

AD-A184 045

FATIGUE '87 VOLUME 1(U) VIRGINIA UNIV CHARLOTTESVILLE

1/7

SCHOOL OF ENGINEERING AND APPLIED SCIENCE

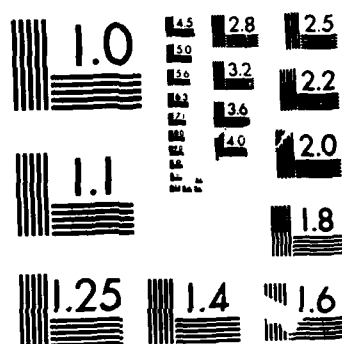
R O RITCHIE ET AL. JUN 87 ARO-24134.1-MS-CF

UNCLASSIFIED

NO0014-87-G-0008

PAG 20/11

NL



MICROCOPY RESOLUTION TEST CHART
NATIONAL BUREAU OF STANDARDS-1963-A

DTIC FILE COPY

①

FATIGUE '87

VOLUME I

AD-A184 045

DTIC
ELECTE
SEP 03 1987
S D

DISTRIBUTION STATEMENT A
Approved for public release
Distribution Unlimited

Papers present at the Third International Conference
on Fatigue and Fatigue Thresholds
held at the University of Virginia, Charlottesville, Virginia
June 28 -- July 3, 1987

87 9 1 203

UNCLASSIFIED
SECURITY CLASSIFICATION OF THIS PAGE

AD-A184045

MASTER COPY

FOR REPRODUCTION PURPOSES

REPORT DOCUMENTATION PAGE

1a. REPORT SECURITY CLASSIFICATION Unclassified		1b. RESTRICTIVE MARKINGS	
2a. SECURITY CLASSIFICATION AUTHORITY		3. DISTRIBUTION/AVAILABILITY OF REPORT Approved for public release; distribution unlimited.	
2b. DECLASSIFICATION/DOWNGRADING SCHEDULE		5. MONITORING ORGANIZATION REPORT NUMBER(S) ARO 24134.1-MS-CF	
4. PERFORMING ORGANIZATION REPORT NUMBER(S)		7a. NAME OF MONITORING ORGANIZATION U. S. Army Research Office	
6a. NAME OF PERFORMING ORGANIZATION Univ. of Virginia	6b. OFFICE SYMBOL (If applicable)	7b. ADDRESS (City, State, and ZIP Code) P. O. Box 12211 Research Triangle Park, NC 27709-2211	
6c. ADDRESS (City, State, and ZIP Code) Charlottesville, VA 22904		9. PROCUREMENT INSTRUMENT IDENTIFICATION NUMBER DAAL03-87-G-0102	
8a. NAME OF FUNDING/SPONSORING ORGANIZATION U. S. Army Research Office	8b. OFFICE SYMBOL (If applicable)	10. SOURCE OF FUNDING NUMBERS	
8c. ADDRESS (City, State, and ZIP Code) P. O. Box 12211 Research Triangle Park, NC 27709-2211		PROGRAM ELEMENT NO.	PROJECT NO.
		TASK NO.	WORK UNIT ACCESSION NO.
11. TITLE (Include Security Classification) Fatigue "87", Volume I			
12. PERSONAL AUTHOR(S) R. O. Ritchie, E. A. Starke, Jr. (Editors)			
13a. TYPE OF REPORT Final	13b. TIME COVERED FROM 6/1/87 TO 5/1/88	14. DATE OF REPORT (Year, Month, Day) August 1987	15. PAGE COUNT
16. SUPPLEMENTARY NOTATION The view, opinions and/or findings contained in this report are those of the author(s) and should not be construed as an official Department of the Army position, policy, or decision, unless so designated by other documentation.			
17. COSATI CODES		18. SUBJECT TERMS (Continue on reverse if necessary and identify by block number)	
FIELD	GROUP	SUB-GROUP	
		Fatigue, Cyclic Deformation, Crack Initiation, Crack Propagation, Crack Closure	
19. ABSTRACT (Continue on reverse if necessary and identify by block number)			
<p>The current proceedings (3 volumes) of the third conference, "Fatigue 87" which was held at the University of Virginia, Charlottesville, covered a wide range of diverse views of the fundamental and applied aspects of fatigue. This includes questions of cyclic deformation, crack initiation and propagation, small cracks, crack closure, variable amplitude effects, and environemntally-influenced behavior. The proceedings should provide a comprehensive state-of-the-art review of the field, suitable for students, researchers and practising engineers alike. (Volume I)</p>			
20. DISTRIBUTION/AVAILABILITY OF ABSTRACT <input type="checkbox"/> UNCLASSIFIED/UNLIMITED <input type="checkbox"/> SAME AS RPT <input type="checkbox"/> DTIC USERS		21. ABSTRACT SECURITY CLASSIFICATION Unclassified	
22a. NAME OF RESPONSIBLE INDIVIDUAL		22b. TELEPHONE (Include Area Code)	22c. OFFICE SYMBOL

DD FORM 1473, 84 MAR

83 APR edition may be used until exhausted.
All other editions are obsolete

SECURITY CLASSIFICATION OF THIS PAGE
UNCLASSIFIED

SCHOOL OF ENGINEERING AND APPLIED SCIENCE
UNIVERSITY OF VIRGINIA

OFFICE OF THE DEAN
THORNTON HALL-

CORRESPONDENT'S PHONE
(804) 924- 3593

August 26, 1987


Dr. Ralph Judy
Scientific Officer
Code 1131M
Office of Naval Research
818 Connecticut Avenue, N.W.
Washington, D.C. 20006

RE: ONR #N00014-87-G-0008
Fatigue '87 - The Third International Conference
on Fatigue and Fatigue Thresholds
June 28-July 3, 1987

Dear Dr. Judy:

As specified in the grant agreement, I am mailing today three sets of the Proceedings of Fatigue '87. One set will be sent to you and the other two sets will be mailed to: ACO, Resident Representative, ONR, and Defense Technical Information Center.

Sincerely,


Edgar A. Starke, Jr.
Earnest Oglesby Professor
and Dean

EASjr/tbh

cc: ACO, Resident Representative
Defense Technical Information Center
R. Nixon

FATIGUE '87

VOLUME I

EDITORS:

R.O. Ritchie and E.A. Starke, Jr.

Papers presented at the
Third International Conference on Fatigue and Fatigue Thresholds
held at the University of Virginia, Charlottesville, Virginia.
June 28 - July 3, 1987

EDITORIAL PANEL

R.P. Gangloff, R.O. Ritchie, E.A. Starke, Jr., and J.A. Wert.

ORGANIZING COMMITTEE

E.A. Starke, Jr., R.O. Ritchie, R.P. Gangloff, J.A. Wert, R.O. Ritchie.

RE: Distribution Statement

Approved for Public Release. Distribution
Unlimited.

Per Dr. Ralph Judy, Office of Naval Research,
Code 1131

For	
&I	<input checked="" type="checkbox"/>
S	<input type="checkbox"/>
ed	<input type="checkbox"/>

per call

Library Codes

Approved/Or
Revised

A-1

EMAS

ENGINEERING MATERIALS
ADVISORY SERVICES LTD.
339, Halesowen Road, Cradley Heath,
Warley, West Midlands, B64 6PH, U.K.



PREFACE

Fracture by the progressive growth of incipient flaws under cyclically varying loads, i.e., by fatigue, must now be considered as the principal cause of in-service failures of engineering structures and components, whether associated with mechanical sliding and friction (fretting fatigue), rolling contact, aggressive environments (corrosion fatigue), or elevated temperatures (creep-fatigue). Of particular importance are the early stages of fatigue damage, involving the initial extension of microcracks and their subsequent growth at very low velocities, as these processes tend to dominate overall lifetime. This has been reflected by trends in fatigue research over the past five years, which have focused largely on so-called "small cracks," of dimensions comparable with the scale of microstructure or local plasticity, and on crack growth in the near-threshold regime, i.e., at stress intensities approaching the fatigue threshold below which cracks are presumed dormant. In addition, associated mechanistic studies have highlighted the critical role of crack tip shielding in fatigue, which arises predominantly from crack closure and deflection, and this has proved to be important in modeling aspects of environmentally-assisted cracking and behavior under variable amplitude loads, and in rationalizing the classical stress-strain-life and defect-tolerant design approaches.

The series of international conferences on Fatigue and Fatigue Thresholds, although devoted to all aspects of fatigue, has emphasized these topics of small cracks and near-threshold behavior, and consequently, has become an international forum for the exchange of information in this field. The series, which has been run under the auspices of a steering and international committee with representatives from Australia, Austria, Canada, China, Czechoslovakia, France, Holland, Japan, Norway, Sweden, U.K., W. Germany and the U.S.A., began in Stockholm, Sweden, in 1981, and continued at the University of Birmingham in England in 1984.

The current proceedings of the third conference, "Fatigue '87," which was held at the University of Virginia, Charlottesville, covered a wide range of diverse views of the fundamental and applied aspects of fatigue. This includes questions of cyclic deformation, crack initiation and propagation, small cracks, crack closure, variable amplitude effects, and environmentally-influenced behavior. The proceedings should provide a comprehensive state-of-the-art review of the field, suitable for students, researchers and practising engineers alike.

The Editors would like to thank the Editorial Committee, particularly Professors R.P. Gangloff and J.A. Wert, the International Committee and the University of Virginia for their help over the past couple of years. We express our sincere thanks to Dr. A.H. Rosenstein of the Air Forces Office of Scientific Research, Dr. G. Mayer of the Army Research Office, Dr. B.A. MacDonald of the Office of Naval Research, and Dr. G. Hartley of the National Science Foundation for their financial support, and to Ms. Tana B. Herndon for her sterling efforts as the conference secretary.

R.O. Ritchie
E.A. Starke, Jr.
June 1987.



FATIGUE 87

RECOMMENDED SYMBOLS

a	Crack-Length - One-Half the Total Length of an Internal Crack or Depth of a Surface Crack
Δa	Crack Growth Increment
a.c.	Alternating Current
B	Test Piece Thickness
C	Compliance
$C_1 - C_5$ & D	Constants
da/dN	Rate of Fatigue Crack Propagation
$\Delta \frac{da}{dN}$	Additional Growth Rate due to Environment
$\left[\frac{da}{dN} \right]_{CTB}$	Growth Rate Retarded by Crack Tip Blunting
$\left[\frac{da}{dN} \right]_{LHE}$	Growth Rate Enhanced by Localised Hydrogen Embrittlement
$\left[\frac{da}{dN} \right]_{TCF}$	Overall Growth Rate for 'True Corrosion Fatigue'
$\left[\frac{da}{dN} \right]_{SCF}$	Stress Corrosion Fatigue Crack Growth Rate
$\left[\frac{da}{dt} \right]_P$	Stress Corrosion Plateau Growth Rate Per Second
da/dt	Crack Extension Rate
d.c.	Direct Current
δ	Value of Crack Opening Displacement (see British Standard BS5762)
δ_c	Critical Crack Opening Displacement, being One of the Following: <ol style="list-style-type: none"> (1) Crack Opening Displacement at Fracture (2) Crack Opening Displacement at First Instability or Discontinuity (3) Crack Opening Displacement at which

FATIGUE 87

an Amount of Crack Growth Commences

δ_m	Crack Opening Displacement at First Attainment of Maximum Force
D_H	Diffusion Coefficient for Hydrogen in Iron
E	Young's Modulus of Elasticity
\exp	Exponential Base of Natural Logarithms
ϵ	Creep Strain
$\dot{\epsilon}_S$	Secondary Creep Rate
ϵ_T	Transient Creep Strain
F	Cyclic Frequency
G	Strain Energy Release Rate
$G_I G_{II} G_{III}$	Crack Extension Forces for Various Modes of Crack Opening
I	Current
i_a	Anodic Current Density
K	Stress Intensity Factor - a Measure of the Stress-Field Intensity Near the Tip of a Perfect Crack in a Linear-Elastic Solid
K_C	Fracture Toughness - The Largest Value of the Stress-Intensity Factor that exists Prior to the Onset of Rapid Fracture
K_{cl}	K in Fatigue Cycle Below which Crack is Closed
K_I	Opening Mode Stress Intensity Factor
K_{IC}	Plane-Strain Fracture Toughness as Defined by ASTM Standard Designation E 399-74 or British Standard BS 5447
K_{Ii}	Elastic Stress-Intensity Factor at the Start of a Sustained-Load Flaw-Growth Test
K_{ISCC}	Plane-Strain K_I Threshold Above which Sustained Load Flaw-Growth Occurs

FATIGUE 87

K_{IH_2S}	Value of K_{ISCC} in Dry H_2S Gas
K_Q	Provisional Fracture Toughness Value Corresponding to a 5% Deviation of the Load/Displacement Relationship from Linearity
K_{max}	Maximum Stress-Intensity Factor
K_{min}	Minimum Stress-Intensity Factor
ΔK	Stress Intensity Range
ΔK_{th}	Threshold Stress Intensity Factor Below which Fatigue Crack Growth will not occur
ΔK_i^O	ΔK_i to just cause Fatigue Initiation
ΔK_n	Next Value of ΔK
ΔK_{th}^O	Value of ΔK_{th} at $R = 0$
ΔK_O	Constant Value of ΔK_{th}
$d\Delta K$	Notional Extra Stress Intensity due to Environment
k_T, k_N	Stress Concentration Factor, Neuber Correction Factor
\ln	Natural Logarithm
\log	Common Logarithm
m	Power Exponent in Paris-Erdogen Expression $\frac{da}{dN} = A \Delta K^m$
N	Cycles
N_i	Cycles to Initiate
N_F	Cycles to Failure
ΔN	Cycles Increment
n	Strain Hardening Exponent
ΔP	Load Range
ν	Poisson's Ratio

FATIGUE 87

Q	Flaw Shape Parameter
σ	Stress
$\Delta\sigma$	Stress Range
σ_{\max}	Maximum Stress
σ_{ps}	Proof Stress
σ_{\min}	Minimum Stress
σ_u	Ultimate Tensile Strength
σ_y	Yield Stress under Uniaxial Tension
$\Delta\sigma_{\text{net}}$	Stress Range on Net Section
R	Minimum Load/Maximum Load
R_{cl}	R below which Crack Closure Occurs
r_p	Plastic Zone Size
ρ	Crack Tip Radius
ρ_o	Notional Minimum Value of ρ
T	Temperature
t	Time
t_h	Hold Time in Load Cycle
t_r	Rise Time in Load Cycle
t_r^o, t_r^{\max}	Values of t_r at Minimum and Maximum Environmental Enhancement
V	Potential Difference
V_o	Reference Potential Difference
$V(a)$	Potential Difference at Crack Length, a
W	Test Piece Width
ϕ	Electric Potential
x, y	Cartesian Co-ordinates

FATIGUE 87

Y Compliance Function

Ω Ohms

RECOMMENDED ABBREVIATIONS

BFS Back Face Strain

BRF Blunting Retardation Factor

CCP Centre Cracked Plate

COD Crack Opening Displacement

CT Compact Tension

CTB Crack Tip Blunting

DCPD Direct Current Potential Drop

EEF Environmental Enhancement Factor

LHE Localised Hydrogen Embrittlement

PD Potential Drop

SENB Single Edge Notched Bend

SENT Single Edge Notched Tension

SCC Stress Corrosion Cracking

SCF Stress Corrosion Fatigue

TCF True Corrosion Fatigue

T-Type WOL T-Type Wedge Open Loading

UTS Ultimate Tensile Strength

FATIGUE 87

CONTENTS

VOLUME I

CYCLIC DEFORMATION AND CRACK INITIATION

Cyclic Deformation and Crack Initiation - P. NEUMANN AND A. TONNESSEN	3
Effect of Grain Orientation on the Origin- ation and the Initial Growth of Fatigue Cracks in Pure Iron - TSUNESHICHI TANAKA	23
The Growth of Persistent Slip Bands - W.J. BAXTER	43
The Mechanics of Fatigue-Crack Nucleation in a Low-Alloy Steel under Fretting Conditions - J. BEARD AND P.F. THOMASON	53
The Effects of Thin Anodic Films on the Cyclic Microstrain/Macrostrain Behavior of Tungsten - KEITH J. BOWMAN AND RONALD GIBALA	63
Surface Deformation and Fatigue Crack Initia- tion of Alpha-Iron Single Crystals - C.S. KIM, Y.W. CHUNG AND M.E. FINE	73
The Effect of Ion Beam Mixed Ni-Al Surface Layers on PSB Extrusion Morphology in Fatigued Nickel - D.S. GRUMMON AND J.W. JONES	83
The Evolution of Local Mechanical Properties of Al 2219-T851 During Fatigue - W.L. MORRIS, M.R. JAMES AND B.N. COX	93
Cyclic Deformation of an Extruded AlMgSi Alloy - KETILL PEDERSEN	103

FATIGUE 87

The Orientations of Dipolar Walls Produced by Cyclic Deformation - J.I. DICKSON, S. TURENNE, L. HANDFIELD AND G. L'ESPERANCE	113
---	-----

CRACK CLOSURE

Closure Behavior Under Constant Effective Stress Intensity Loading Conditions - C.D. CARMAN AND B.M. HILLBERRY	125
The Influence of the Topography of Fracture Surfaces on Crack Closure - K. HAMBERG, J. WASEN AND B. KARLSSON	135
Growth of Short Fatigue Cracks in a Squeeze Formed Aluminum Alloy - B.P.D. O'CONNOR AND A. PLUMTREE	145
Influence of Microstructure and Aging Condition on the Fatigue Crack Propagation in Age Hardened Aluminum Alloys - R. SCHEFFEL, O. IBAS AND K. DETERT	155
Fatigue Crack Growth Behaviour of A356-T6 Cast Aluminum Alloy - C.C. WIGANT AND R.I. STEPHENS	165
Striations and the Fatigue Growth Mechanism in a Micro-Alloyed Steel - H.J. ROVEN, M.A. LANGOY AND E. NES	175
Significance of Fatigue Crack Closure Under Spectrum Loading - R. SUNDER	185
Near-Threshold Short Crack Growth Behaviour in Nimonic 105 - J. BYRNE	195

SMALL CRACKS

Fatigue Crack Propagation of Short and Long Cracks: Physical Basis, Prediction Methods and Engineering Significance - H. NOWACK AND R. MARISSEN	207
--	-----

FATIGUE 87

Low Cycle Fatigue Life Predictions of a 1CrMoV Steel in Terms of a J-Controlled Short Crack Growth Model - V. BICEGO	231
The Statistics of the Shape of Small Fatigue Cracks - B.N. COX AND W.L. MORRIS	241
The Effect of Alpha-Platelet Morphology and Beta-Grain Size on the Initiation and Growth of Short Fatigue Cracks in Ti65S - P.J. HASTINGS, M.A. HICKS AND J.E. KING	251
The Initiation and Growth of Small Fatigue Cracks in Copper at Room and Cryogenic Temperatures - I.B. KWON, J. WEERTMAN AND M.E. FINE	261
Behaviour of Short Cracks in a 2024 Aluminum Alloy Sheet Tested at Several Stress Ratios - A. ANDRADE AND M. FREITAS	271
The Effect of Microstructure on the Surface Crack Length: Crack Depth Relationship for Short Cracks - R.K. BOLINGBROKE AND J.E. KING	281
On the Role of Crack Tip Shielding in Influencing the Behavior of Long and Small Fatigue Cracks in Aluminum-Lithium Alloy 2090 - K.T. VENKATESWARA RAO, W. YU AND R.O. RITCHIE	291
The Influence of Slip Mechanism on Fatigue of Mg and Mg-2.3Li - J.K. GREGORY	303
The Growth Behaviour of Small Fatigue Cracks; The Effect of Microstructure and Crack Closure - K. TOKAJI, T. OGAWA, S. OSAKO AND Y. HARADA	313
The Influence of Microstructure and Residual Stresses on the Initiation and Propagation of Short Surface Cracks on AlMgSi - B. MEIER AND V. GEROLD	323
Threshold Stress for Fatigue Crack Initiation from a Small Crack - Y. MURAKAMI AND K. MATSUDA	333

FATIGUE 87

An Experimental Study of Closure Behavior of Naturally Initiated Small Cracks - X. SU AND W.N. SHARPE, JR.	343
Behaviour of Long and Short Fatigue Cracks in a Powder Metallurgy Superalloy at Room and at High Temperature - F. SONIAK AND L. REMY	351
Propagation of Small Fatigue Cracks in 2024-T3 Aluminum Alloy - K. TANAKA, Y. AKINIWA AND E. MATSUI	361
Closure and Propagation Behavior of Short Fatigue Cracks at Different R-Ratios - Y. VERREMAN, J.-P. BAILLON AND J. MASOUNAVE	371
A Unified Model for Fatigue Crack Initiation, Short Crack Growth, Long Crack Propagation, and Closure Effects - A.O. OBABUEKI, C.H. LEE, T. TANAKA AND A.K. MILLER	381

VARIABLE AMPLITUDE LOADING

Fatigue Crack Retardation in Aluminium Alloys - D.J. ALEXANDER AND J.F. KNOTT	395
Fatigue Crack Growth Under Random Overloads - R. ARONE	407
A Dislocation Model for Fatigue Crack Propag- ation under Variable Amplitude Loading - A. BIA, C. ROBIN AND G. PLUVINAGE	415
Observations on the Effect of Overloads on Fatigue Crack Growth - S.K.P. CHEUNG-MAK AND I. LE MAY	425
A Study of Fatigue Crack Growth Life Under Random Stresses - J.M. HU, W.P. YAO AND K.X. LI	435
Crack Growth in Contrasting Titanium Alloys Under the Conjoint Action of High and Low Cycle Fatigue - B.E. POWELL	443

FATIGUE 87

Variable Amplitude Fatigue Crack Growth in Aluminum Alloys 2090-T8E41 and 7075-T651 - J.S. THOMAS, JR., J.C. VAN SICE AND A.F. GRANDT, JR.	453
Crack Growth Prediction in 3D Structures under Aeronautical-Type Spectrum Loadings - R. LABOURDETTE, G. BAUDIN AND M. ROBERT	461
Fatigue of 30CrMnSiNi2a Notched Specimens Under Spectrum Loading - Y.S. WU, J.H. HUAN AND A.H. ZHOU	471
The How and Why of Variable Amplitude Testing - W. SCHUTZ AND P. HEULER	479

FATIGUE AND MICROSTRUCTURE

Near-Threshold Growth of Defects in Engineer- ing Materials - J.F. KNOTT	497
Effects of Mn Dispersoids on Near Threshold Fatigue Crack Growth in 2134 Type Alloys - K.V. JATA, J.A. WALSH AND E.A. STARKE, JR.	517
Interaction of Microstructure and Fatigue in Tool Steels - H. BERNS	527
Tensile Mean Stress Effects on Uniaxial Fatigue Behavior of 1045 Hr Steel - A. FATEMI AND R.I. STEPHENS	537
Fatigue Strength of Alloy A286 at Cryogenic Temperature - A. INOUE, S. YOSHIOKA, S. TAKAYANAGI, K. HIRAGA, T. OGATA, K. NAGAI, T. YURI AND K. ISHIKAWA	547
The Initiation and Growth of Fatigue Cracks in Carburised 9Cr1Mo Steel - P.J. JEFFCOAT	557
Fretting Wear and Fretting Fatigue Damage - C. COLOMBIE, Y. BERTHIER, L. VINCENT AND M. GODET	567
Crack Propagation Properties of Sintered Steel - I. BERTILSSON AND B. KARLSSON	577
The Role of Inclusions in Corrosion Fatigue Crack Initiation in Q1N - R.A. COTTIS AND A. MARKFIELD	587

FATIGUE 87

**CYCLIC DEFORMATION
AND
CRACK INITIATION**

FATIGUE 87

CYCLIC DEFORMATION AND CRACK INITIATION

P. Neumann and A. Tönnessen*

Fatigue loading hardens most metals in a peculiar way forming metastable dislocation configurations and favouring strain localization. Therefore, fatigue crack nucleation usually occurs at highly localized slip bands. Modern sectioning techniques revealed preferred crack initiation sites within these slip bands which are not yet understood. In common microstructures fatigue crack nucleation can also occur at weak inclusions or special grain boundaries. In spite of their low energy, twin boundaries were found to be a pre dominant crack nucleation site in high cycle fatigue. Usually the environment is found to be very important for the formation of fatigue cracks.

INTRODUCTION

After fatigue crack propagation has been studied extensively in the past, crack initiation remains a phenomenon which is not well understood yet. The issue is darkened to some extent by the ambiguity to separate true crack initiation from the growth of microcracks. It has been proposed by various authors to limit crack initiation to that domain in which stress concentrations at the crack tip are not dominant if compared to the applied stress. In some cases the limit between crack initiation and propagation is suggested by different mechanisms. If, for example, the material contains inclusions of low strength, the first application of any appreciable load will break these inclusions in a brittle manner. This is clearly distinct from the consecutive slow ductile growth of the microcrack. Finally some authors pragmatically define the regime of crack initiation as that within which cracks cannot be detected with some given technique.

In the following various physical processes, which are capable of forming crack nuclei, will be considered in some detail.

* Max Planck Institut für Eisenforschung GmbH,
Postfach 140260, D 4000 Düsseldorf, F R G

FATIGUE 87

without emphasizing such formal borderlines. Although various subjects will be touched upon in a rather brief way this paper is not intended to be review of the current literature at all. The topics are selected in order to reach a certain understanding of the relevant processes and stimulate more research in this difficult area.

CYCLIC DEFORMATION

The dislocation structure after cyclic deformation is well studied and is characterized by veins of high edge dislocation density and channels which have a very low dislocation density and separate the veins. The width of the veins as well as that of the channels is roughly equal to the Orowan distance. This is reasonable since the dislocations must form by multiplication due to bow out.

The plastic strain amplitude which can be carried by such structures is typically of the order of 10^{-4} . Such strains can be accomplished by moving all dislocations over distances of the order of their mutual distances (in the veins as well as in the channels). In contrast to the structures after unidirectional deformation no pile ups are found after cyclic deformation. This is due to the changing direction of the applied stress which effectively mixes dislocations of both signs. As a consequence, the long range stresses which are found after cyclic deformation are much smaller than those after unidirectional deformation.

In pure metals there are no obstacles available and therefore the only interaction which hinders gross dislocation motion and thus determines the flow stress is the mutual interaction between dislocations of opposite sign which have trapped each other. Such a hardening by mutual trapping of dislocations is highly metastable: If the flow stress is exceeded, a significant number of dipoles is destroyed. The freed dislocations pile up against remaining more stable dipoles and help to break them up also. This causes local avalanches of free dislocations and local work softening. As a consequence, very coarse slip lines are observed during tensile deformation after cyclic deformation (1,2). The corresponding stress strain curve shows a small yield drop and a long range of zero work hardening (1,3,4). The most striking evidence of such a metastable behavior are the strain bursts which can be observed when the stress amplitude is slowly increased in a truly stress controlled testing system (4).

During a slow increase of the stress amplitude the same things happen over and over again at an ever decreasing dislocation distance according to Kuhlmann Wilsdorf's principle of similitude. However, at a certain stress level, the saturation stress, something new happens. At this point the dipole width which is necessary for mutual trapping is approaching atomic dimensions. Most likely the most narrow dipoles pop up into rows

of point defects. Because of the different formation energies rows of vacancies are much more easily produced than rows of interstitials. Therefore, although vacancy dipoles and interstitial dipoles are equally abundant below the saturation stress level (because they form by random encounters) at the saturation stress level the number of vacancy dipoles will be decreased by forming the corresponding number of vacancies. This is in good agreement with the high resistivity of fatigued pure metals found by various authors (5,6).

The abundance of interstitial dipoles has an important consequence: If interstitial dipoles and vacancy dipoles are equally abundant in a random shuffling during cyclic deformation no significant slip steps are produced on the surface. If, however, interstitial dipoles are more abundant than vacancy dipoles in some region, then, on the average, more interstitial dipoles will be pushed out of the material than vacancy dipoles. Therefore bumps should develop on the surface where an excess of interstitial dipoles is present underneath. This is a qualitative explanation of the formation of extrusions (7). Quantitatively the situation is quite complex since the excess vacancies inside the material will be either precipitating in the form of dislocation loops or will be swept up by moving dislocations. In the latter case dislocation climb will occur and reduce the unbalance between vacancy and interstitial dipoles. Everything depends in a critical way on the fate of the excess vacancies. In any case the contents of vacancies cannot be increased without limit inside the material. Therefore the growth of extrusions should be fast in the beginning and level off afterwards, as observed experimentally (8,9)

At the saturation stress the dislocation structure underneath the extrusions changes in a very specific way. The vein structure transforms into a very regular ladder structure in which the highly dislocated areas are narrow edge dislocation walls separated by about 10 times wider dislocation free areas (10-13). The tendency to form wall like structures from the veins is understandable from computer simulations (14). If dislocations are packed with a minimum mutual distance, d_{min} , (given by the decomposition of dipoles into vacancy rows) in a vein structure or in a ladder configuration, the former was found to decompose at a lower applied stress level.

PHENOMENOLOGICAL CYCLIC STRESS STRAIN RELATIONS

The plastic strain amplitude is a crucial variable for crack initiation during cyclic deformation. In many applications, however, the stresses can be calculated only from finite element analysis or direct measurements. In this case it is important to be able to calculate from a phenomenological stress strain relationship the plastic strains which develop under these

FATIGUE 87

conditions. Extensive experimental studies showed that cyclic deformation behavior is rather complex in detail but with some reasonable accuracy considerable simplifications can be accomplished. Nowadays the most widely used model for describing the cyclic stress strain response is the Masing model (15) stating that all hysteresis loops which are observed during a random loading of a specimen are composed of pieces of one universal function $\Delta\sigma=f(\Delta\epsilon)$ in the following way:

If $\sigma(\epsilon)$ is the observed stress strain relation and if the last change of the loading direction occurred at (ϵ_0, σ_0) , then we have

$$\sigma(\epsilon-\epsilon_0)-\sigma_0 = f(\epsilon-\epsilon_0) \text{ or } -f(-(\epsilon-\epsilon_0)) \dots\dots\dots[1]$$

for tensile and compressive loading respectively. Obviously, if the mean strain is zero and the strain amplitude is increased continuously, the locus of the upper hysteresis tips is given by

$$\sigma_1(\epsilon_1) = 1/2 f(\epsilon_1/2) \dots\dots\dots[2]$$

This is usually called the cyclic stress strain curve.

The second ingredient which has to be added to the existence of a cyclic stress strain curve is the cyclic memory. It is displayed in fig.1. If the loading path AB is interrupted by a change in the loading direction and if the new loading curve CD is continued beyond the former maximum strain value then the loading curve does not follow the dashed line which is a continuation of CD according to the Masing model. Instead, in most materials loading continues approximately along the old loading curve AB to E. In a sense the material remembers when returning from C to D that it has deformed on the branch AD. It is immediately clear that for the material behavior after D the loop BCD is irrelevant for the plastic deformation. This is the reason why cyclic memory allows to neglect even nested closed loops for prediction of plasticity behavior. This is a considerable simplification and leads immediately to the algorithm of rain flow counting of loops. Combining the cyclic stress strain curve with the cyclic memory thus allows to calculate the plastic strain from a given stress history efficiently and with a reasonable accuracy in most alloys.

The cyclic stress strain curve can usually be described with reasonable accuracy by a power law

$$\Delta\sigma(\Delta\epsilon) = C \cdot \Delta\epsilon^m \dots\dots\dots[3]$$

The value of the parameters C and m do, however, depend considerably on the details of the load history because of cyclic hardening or softening. Such effects can be largely eliminated by only using so-called saturated hysteresis loops for the

FATIGUE 87

determination of the cyclic stress strain curve. I.e. most often the cyclic stress strain curve is determined from an incremental step test. In such a test the strain amplitude is raised stepwise (or continuously) from zero to a maximum value, ϵ_{\max} . Then the strain amplitude is decreased to zero again and the same pattern is repeated several times. After a number of such repetitions the observed locus of the hysteresis loop tips becomes stationary and is used as the cyclic stress strain curve. This procedure is quite useful to predict the plastic stress strain behavior as long as the strain amplitude stays below ϵ_{\max} .

CRACK INITIATION IN SLIP BANDS

For studying crack initiation it is very important to section the specimens perpendicular to the original surface in order to detect crack nuclei reliably (8,16). Figs. 3 shows examples of crack nuclei which are impossible to detect without a sectioning cut. The sectioning technique has been developed to considerable edge resolution. Under optimum circumstances it is of the order of 20 nm.

In materials which are pure enough to avoid major inclusions, crack initiation during cyclic deformation usually occurs in localized slip bands within the single grains. This mechanism works the same way in polycrystals as well as in single crystals. Fig.4 shows an example of a persistent slip band with crack nucleus in a copper polycrystal, which resembles in many details those found in single crystals (fig.13 in (8)). The most striking feature of this localized slip is the fast development of extrusions. The extrusions extend above the original surfaces and in many cases the valleys between the extrusion are the only depressions relative to their surrounding, but they do not extend below the original surface. These valleys, which are usually called intrusions, can be easily identified by their finite vertex angle at the bottom which is typically of the order of 20 to 30°.

After this extrusion-intrusion topography has developed, a completely different process starts out, namely the formation of very narrow crack nuclei at the bottom of the intrusions with their finite vertex angle. These crack nuclei are always closed or, in other words, have a zero crack tip angle, which makes them distinct from the intrusions. Therefore the process of crack formation in fatigue is not a continuous development from a flat surface via an increasing surface roughness towards small cracks.

Surprisingly enough in a single crystal these crack nuclei are very unevenly distributed over a persistent slip band. Early in the life they are found preferentially at one interface between persistent slip band and matrix. Fig.2 shows the number of crack nuclei found in various positions within the persistent slip band. The rightmost position is obviously strongly favoured as long as

the crack nuclei are of the order of 5 to 10 microns deep. At a later stage in life, however, the preferred position for cracking is on the other interface between persistent slip band and matrix. Both sides of the PSB are definitely different physically. E.g. elastic stress concentrations should be smaller at the interface on the right in fig.4 because of the asymmetric surface profile of the PSB. But the reasons for these details of crack nucleation process are not understood yet.

It has been demonstrated several times that the development of the topography of extrusions and intrusions is independent of the environment and that it occurs un-modified even in ultra-high vacuum. But the true crack nucleation at the root of the intrusions is delayed considerably in vacuum. Also the growth of the crack nuclei is reduced, most likely by rewelding of previously formed crack surfaces (17,18). Therefore the most likely model for crack nucleation due to single slip is that of Thompson and Wadsworth (19) which is shown in fig. 5. Single slip alone produces slip steps only. They can be annihilated again by reverse slip and can therefore grow only in a random walk fashion (20). This corresponds to the vacuum situation with its very slow crack growth. Surface reactions with an active environment make the formation of slip steps more irreversible such that crack nuclei can develop parallel to the slip planes of the active slip systems. Again, the details, such as the preferred crack nucleation in persistent slip bands can be understood only in a more detailed theory. Vacancy clustering or annihilation at dislocations is definitely an important process. Also the vacancies may move to the crack tip and thus extend the crack. All these processes were not considered in detail yet. Vacancy transport is of course always a problem at room temperature where diffusion is extremely slow. However, the transport of point defects due to on-going plasticity seems to play a crucial role, but such processes are not well understood either.

CRACK INITIATION AT GRAIN BOUNDARIES

During fatigue the tendency to form cracks in localized slip bands within the grains is rather strong. In polycrystals crack initiation on grain boundaries is a rather uncommon feature. When a strong slip band impinges on a grain boundary, a so-called "L-shaped crack" forms at the intersection of grain boundary and slip band (21,22). Some authors (23) report that the tendency to form crack nuclei may increase if crack nucleation in slip bands is reduced by performing the test in vacuum. In such tests the slip band density increases due to the prolonged life. Still, the number of cracks found in grain boundaries is not very high. In a few papers concerning different fracture modes (LCF, high temperature fatigue, brittle fracture) the correlation between the nature of the grain boundaries and the probability to form intergranular cracks was studied (24-27). In most cases cracks

FATIGUE 87

were found at high angle grain boundaries with no simple correlation with the nature of the boundaries.

In recent studies of fatigue crack initiation in copper polycrystals a large number of persistent slip bands and microcracks was found parallel to and coinciding with twin boundaries (fig.6,7). A sectioning technique was used which unequivocally allowed to detect microcracks. The cracks are not very striking if observed on the surface (see fig.7) and can easily be overlooked. Furthermore, in high cycle fatigue experiments the persistent slip bands coinciding with the twin boundary are often the only slip trace in twin and matrix grain. Then it is impossible to detect the twin boundary from surface observations and the PSB is mistaken as a plain PSB crossing the grain. Only by systematic measurements of the local orientations such ambiguities can be avoided.

In our studies the local orientations of all grains involved were obtained by a modified electron channeling technique in the SEM. A spiral deflection mode was used instead of the usual line scan in order to be able to re-focus the SEM automatically and continuously as a function of the current radius of the spiral. In this way the positional accuracy of the rocking beam on the specimen surface could be kept below $3\text{ }\mu\text{m}$ for a rocking range of 15° . The intensity signal from the SEM was evaluated in an analog circuitry for sudden changes in contrast (channeling lines) and their position was recorded digitally. The resulting digital image of the channeling patterns was evaluated by a computer program to obtain the orientation. The accuracy of this fully automatic method to obtain the relative orientation of grains larger than $3\text{ }\mu\text{m}$ is better than 0.2° and will be described in detail elsewhere (28).

As mentioned above, in low amplitude tests with lifetimes of the order of 10^6 cycles, the cracking at twin boundaries becomes even more pronounced in the sense that cracks do form almost exclusively coincident with twin boundaries. Under such circumstances very few slip bands were introduced in the interior of the grains. Almost all slip bands were parallel to twin boundaries and most of them developed cracks.

Cracking at twin boundaries is to some extent surprising because twin boundaries are known to be the grain boundaries with the lowest possible energy. Even more surprising is the fact that in a stack of lamellar twins there is a strong tendency that slip bands and cracks formed only on every other twin boundary as shown in fig.8. These observations are in agreement with older papers (19,29-31). In these papers no explanation is given, it is only pointed out vaguely that the activation of secondary slip may be of importance (31). Similar observations are not reported in more recent literature.

In order to understand this crack initiation the local stress distribution near grain boundaries must be examined more closely. Obviously in elastically anisotropic materials like copper incompatibilities would develop across grain boundaries if a uniform tensile stress, σ_0 , would be present in all grains. Therefore, if the strains are supposed to be continuous across the grain boundary, stresses must have a discontinuity there. From anisotropic elasticity these additional stresses, which add to σ_0 can be determined from the boundary condition of continuous strains. In some grains these additional stresses enhance the external stresses in others they may reduce them. Thus a systematic variation of local stresses in a twin lamella stack may explain, that only every other twin boundary in such a stack has high local stresses for crack initiation. The variations of the local stresses can be considerable in copper since the anisotropy ratio is 3.2, which means that the value of the shear modulus varies by a factor of 3.2 depending on the direction of the shear elements within the lattice.

The stress concentrations discussed so far do exist at every elastically incompatible grain boundary and are highest at the boundary, which is the source of incompatibility. In fcc metals the twin boundaries are unique among these since they are parallel to the slip planes, so that long PSB simply fit into the region of high local stresses. Thus the exceptional role of twin boundaries may be due to just this geometrical relationship to the slip planes and may not be connected to energy arguments at all.

If local stress concentrations are relevant, twin boundaries can act in two different ways to promote crack initiation: 1) Persistent slip bands form preferentially in the highly stressed region near the twin boundary and trigger crack formation. 2) In the stress concentrations twinning dislocations move along the boundary which results in a motion of the twin boundary. The region over which the boundary moves undergoes an cyclic local strain of 70% (the twinning strain). This high local cyclic strain either promotes crack initiation on its own or again triggers persistent slip bands.

Both hypotheses can be tested experimentally from the data available. From the orientation measurements the local stresses can be calculated and compared with the occurrence of persistent slip bands and cracks. Furthermore the change of the resolved shear stress for the primary dislocations in the grains as well as for the partial dislocations can be calculated from the local stresses. High resolved shear stress on both types of dislocations can then be correlated with the appearance of persistent slip bands and cracks. If one of these explanations is correct, it should be possible to predict which of the two twin boundaries in a stack of twin facets is prone to crack initiation.

To carry out such a program it is crucial to calculate the local stresses at twin boundaries. Wang and Margolin (32) calculated with the help of a finite element program the stress distribution near special twin boundaries. In order to cover all possible twin orientations in a polycrystal we tried the following more simple way:

We consider a stack of twins as shown in fig.9. If the undisturbed uniaxial tensile stress tensor, σ^a , would be present homogeneously in all twins, the two differently oriented groups of twins, 1 and 2, would deform differently due to the elastic anisotropy and therefore would not fit together any more. In equations: Due to elastic anisotropy the compliance tensor, s_{iklm} , has different components, s_{iklm}^1 and s_{iklm}^2 in twins 1 and 2 respectively, if given in the same specimen coordinate system. Thus the misfit strains are

$$\Delta \epsilon_{ik} = \epsilon_{ik}^1 - \epsilon_{ik}^2 = (s_{iklm}^1 - s_{iklm}^2) \sigma_{lm}^a \dots\dots\dots [4]$$

Let α be the volume fraction of twins 1 and consider the situation that

$$\sigma^a + \sigma^b/\alpha \text{ and } \sigma^a - \sigma^b/(1-\alpha) \dots\dots\dots [5]$$

are the two homogeneous stresses acting in twins 1 and 2 respectively, with some arbitrary stress tensor σ^b . Then the stress averaged over both twins is still σ^a . σ^b is uniquely determined by the requirements of compatibility and stress equilibrium at the twinning planes:

Compatibility: The misfit strains have to vanish:

$$(s_{iklm}^1 \sigma_{lm}^b)/\alpha + (s_{iklm}^2 \sigma_{lm}^b)/(1-\alpha) = -\Delta \epsilon_{ik} \dots\dots\dots [6]$$

Equilibrium: The tractions of σ^b on the twinning planes have to vanish, i.e. if n_k are the components of the normal of the twinning planes,

$$\sigma_{ik}^b n_k = 0 \text{ for } i=1,2,3 \dots\dots\dots [7]$$

Because of [7] the contribution of the homogeneous stress σ^b to the shear stress on the planes parallel to the twin interfaces in any direction b_i is zero:

$$\tau^b = b_i \sigma_{ik}^b n_k \dots\dots\dots [8]$$

The determination of σ^b is straightforward since [6] and [7] provide six equations, which are just enough to calculate the six unknown components of the symmetric tensor σ^b . However, due to the anisotropic s_{iklm} it is rather cumbersome to collect the terms for determining the coefficients in these six equations for σ_{ik}^b .

Therefore an iterative scheme was preferred. From the known 3 misfit components in the twinning plane the stress which is required to compensate for this misfit is calculated for the isotropic case as a first approximation to σ^b (using a value for s_{44} , which is adjusted for isotropy). From σ^a and the approximate σ^b the (reduced) boundary misfit is recalculated (using the correct anisotropic $s_{ijk|m}$) and then the procedure is repeated. After about seven iterations the misfits are negligibly small (10^{-6} of their original value) and the iteration is stopped.

The piecewise homogeneous stress state [5] fulfills the compatibility and equilibrium conditions on the twin boundaries and elsewhere. However, σ^b_{ik} produces tractions, $\sigma_0 t^1_i = (\sigma^b_{ik} s_k)/\alpha$, $\sigma_0 t^2_i$, on the surfaces of twins 1 and 2 respectively (s_k is the outer surface normal, σ_0 the skalar value of the applied tensile stress). Because of [5] we have

$$t^2_i = -\alpha/(1-\alpha) t^1_i \dots\dots\dots [9]$$

The solution for a traction-free specimen surface is therefore obtained by adding σ^c to [5], where σ^c is the stress distribution due to the opposite surface tractions. The solution σ^c can be obtained for the isotropic case from Muskhelishvili (33). It is known to have logarithmic singularities where the tractions change sign, i.e. at the twin boundaries. For our purposes we do not require the full solution, but just a few properties of σ^c : Since the average of the σ^b -contributions in [5] is zero, the average of the surface tractions vanishes, too. Thus, due to St. Venant's principle, their effects, i.e. σ^c , reaches only into a depth comparable to the thickness of the twins. Fig.10 illustrates this situation. Because of [7] the direction of the tractions is parallel to the twin boundaries. It is evident from fig.10 that the maximum shear stresses will be produced in the immediate neighbourhood of the twin boundaries. The maximum shear stress will be on planes parallel to the twin interfaces (normal n_i) in a direction which is parallel to the tractions t^1_i . The resolved shear stress in a given direction b_i in these planes will be proportional to the component of the tractions in this direction

$$\tau^c = s \beta \sigma_0 t^1_i b_i \dots\dots\dots [10]$$

with some unknown positive coefficient β and $s=+1, -1$. Since we have to distinguish the two different twin interfaces, it is important to specify the sign of τ^c via s unambiguously: If [10] is used to calculate the resolved shear stress increment on a plane in the vicinity of a twin interface and the normal of that plane is pointing from twin 1 to twin 2, then $s=+1$, otherwise we have $s=-1$. The total resolved shear stress is given by the sum of the regular Schmid factor due to σ^a and [10]:

$$\tau = \sigma_0 (b_i a_i a_k n_k + s \beta t^1_i b_i) \dots\dots\dots [11]$$

FATIGUE 87

where a_j is the tensile direction. Thus the factor β measures the weight with which the logarithmic singularities due to the tractions are used to modify the Schmid factor. Since s changes sign at every other twin interface, the shear stress increments τ^c alternately favour and hinder slip at every other twin interface in agreement with the experimental observations.

With these possibilities to calculate the modification of the applied stress in the vicinity of twin boundaries it is possible to predict for each individual twin interface whether it is prone to crack initiation or not. For this purpose the local resolved shear stress in the most highly stressed slip system was calculated from the measured orientations as discussed above, assuming $\alpha=0.5$. The results are shown in fig.11. Each of the 138 evaluated twin interfaces is represented by a plus sign if there is a persistent slip band - which frequently contains cracks - connected with the boundary and by a square if no slip is visible. The arbitrary numbering of the interfaces is given on the abscissa and the modified Schmid factor, τ/σ_0 according to [11] is given on the ordinate. It is obvious that there is a strong correlation between the value of the modified Schmid factor and the appearance of PSB's and cracks. Above a critical value of $\tau/\sigma_0=0.44$ (the horizontal line in fig.11) almost all twin interfaces show localized slip and below they do not. In this sense only 11% (15 out of the total number of 138 symbols) lie on the wrong side of this line. A value of $\beta=1.5$ was used in fig.11. It was fitted to give the best correlation.

The same evaluation was repeated but now instead of the most highly stressed primary slip system which has a Burgers vector of the type $1/2[110]$, the most highly stressed twinning system which has a Burgers vector of the type $1/6[112]$ was considered. The correlation obtained is as good as with the perfect Burgers vectors. Since there is only an angle of 30° between neighbouring $[110]$ and $[112]$ directions in an (111) plane, the most highly stressed systems of both kinds are so similarly oriented that the corresponding results of the type shown in fig.11 are not significantly different.

The correlation of the occurrence of PSB's with the modified Schmid factor is good in fig.11 but not perfect. This is understandable since in the discussion of the local stresses near the twin boundaries only the effect of the twin boundary itself was taken into account and the effect of all the other nearby grain boundaries were neglected.

The analysis given above seems to be well suited to explain the high crack initiation frequency at twin boundaries and resolves the apparent paradox that the lowest energy boundary is the most frequent crack initiation site. The twin boundaries do not crack in a brittle sense but simply act as stress raisers due

to elastic anisotropy. Other grain boundaries provide also such stress concentrations, however, these become the more effective the larger pieces of slip planes fit into the stressed region near the boundary in order to form a persistent slip band there. In the case of coherent twin boundaries which are parallel to the (111) slip planes in both grains this condition is fulfilled ideally. In the case of other grain boundaries this can be the case only incidentally. In addition the twin boundaries ($\Sigma 3$) are by far the most abundant large angle boundaries in the strain annealed polycrystalline copper which we studied. Fig. 12 shows the relative abundance of the different types of boundaries in our material. Lim and Raj published similar observations on nickel polycrystals (34).

These ideas can of course be applied to other materials and systems. A few experiments were done in pure Ni confirming the above results. Although segregated grain boundaries of considerable brittleness were known to exist in the material (from studies of the stress corrosion cracking and hydrogen embrittlement) in high cycle fatigue the most sensitive crack nucleation sites were annealing twins again.

After knowing about the importance of twin boundaries the crack nucleation sites in stainless steels which have been studied in another program were examined more closely. In many cases crack nucleation was indeed found at twin boundaries.

In bcc crystals the relation between slip planes and twinning planes is different and therefore it would be interesting to study the situation near twin boundaries in bcc metals in similar details. Some results discussed by Tanaka and Kosugi (35) seem to point into the same direction.

CRACK INITIATION AT INCLUSIONS

In commercial materials varying quantities of unwanted inclusions are always present due to the production process. These inclusions are detrimental because they have a low strength themselves or the interface between the inclusions and the matrix is of low strength. Therefore these inclusions are weak spots in the material and when it is loaded, cracks form at a reduced stress there. Fig. 13 gives one example. Depending on the size of the inclusions the crack nuclei size ranges from a few microns to a few 10 microns. In this type of crack initiation there is no question about the mechanism; it is simply the reduced strength of the inclusions.

Crack initiation at inclusions is very important for commercial steels. The growth of short cracks starting from such crack nuclei determines the fatigue lifetime and can be used for rather reliable lifetime predictions for random loading (36).

FATIGUE 87

There is only one way to improve the fatigue properties of such materials: To avoid low strength inclusions, either by increasing their strength or by avoiding them totally. However, the efforts to produce "purer" materials cannot increase the fatigue strength indefinitely. If the inclusions are eliminated, crack initiation in slip bands is still operative. Therefore it must be checked carefully whether the costs to eliminate inclusions are justified by the possible improvements.

A certain limiting case is found in high temperature fatigue. At elevated temperatures the oxidation rates are considerable and oxidation is enhanced due to the deformation induced fracture of the protecting oxide film. Therefore, slip localization causes localization of the oxidation. This leads to the development of extensive oxide clusters. Fig.14 shows a section through the oxidized surface (which on average is vertical in this figure) of a specimen after creep fatigue. A cracked oxide cluster (dark areas) is penetrating into the base material (light areas on the right). These cracked oxide clusters propagate into the interior and trigger new plasticity. The kinetics of these synergic processes and their mutual triggering are not studied in a quantitative way. But these phenomena are essential to an understanding of crack initiation in high temperature fatigue.

In summary it may be said that the most important fatigue crack initiation mechanism seems to be that of strain localization and the synergic effect of large local strains and environmental attack. The kinetics and quantitative description of these phenomena are still not well understood. The effect of grain boundaries seems to be reduced to that of stress raisers for slip crack initiation. Therefore twin boundaries are in fcc polycrystals the most likely crack initiation sites at low amplitudes. In many commercial alloys the crack initiation is still governed by the fracture of low strength inclusions. Certain (limited) improvements are possible in these systems by avoiding these inclusions, however, sooner or later the slip band crack nucleation will limit the fatigue strength. At high temperatures the synergic interdependence of strain localization and localized oxidation governs crack initiation. Unfortunately, quantitative theories which predict the rate of crack nucleation with any acceptable accuracy are still lacking and are left for future research.

Acknowledgement: The authors wish to thank the Deutsche Forschungsgemeinschaft for financial support under contract number 193/12.

FATIGUE 87

SYMBOLS USED

a_j	tensile axis
α	volume fraction of twins
b_i	Burgers vector
C, n	coefficient and exponent of the cyclic stress-strain curve
ϵ_{ik}	strain tensor
n_i	normal of twin interface
s_i	surface normal
s_{iklm}	tensor of elastic compliances
σ_{ik}	stress tensor
σ_0	applied stress
t_i	tractions
τ	resolved shear stress

REFERENCES

- (1) Broom, T. and Ham, R. K., Proc. Roy. Soc., Vol. A251, 1959, pp. 186.
- (2) Neumann, P., Z. Metallk., Vol. 58, 1967, pp. 780.
- (3) Paterson, M. S., Acta Met., Vol. 3, 1955, pp. 491.
- (4) Neumann, P., Z. Metallk., Vol. 59, 1968, pp. 927.
- (5) Polak, J., Scripta Met., Vol. 4, 1970, pp. 761.
- (6) Charsley, P. and Robins, B. A., Mat. Sci. Eng., Vol. 14, 1974, pp. 189.
- (7) Partridge, P. G., Acta Met., Vol. 13, 1965, pp. 517.
- (8) Hunsche, A. and Neumann, P., Acta Met., Vol. 34, 1986, pp. 207.
- (9) Wang, R., Bauer, B. and Mughrabi, H., Z. Metallk., Vol. 73, 1982, pp. 30.
- (10) Laufer, F. E. and Roberts, W. N., Phil. Mag., Vol. 10, 1964, pp. 883.
- (11) Lukas, P., Klesnil, M., Krejci, J. and Rys, P., Phys. Stat. Sol., Vol. 15, 1966, pp. 71.
- (12) Mughrabi, H. and Wang, R., In "Deformation of Polycrystals: Mechanisms and Microstructures", Proc. 2nd Riso Int. Symposium on Metallurgy and Materials Science, eds. N. Hansen, A. Horswell, T. Leffers, and H. Lilholt (Riso National Laboratory, Roskilde, Denmark), 1981, pp. 87.
- (13) Neumann, P., "Fatigue" in "Physical Metallurgy", edited by R. W. Cahn and P. Haasen, Elsevier Science Publ., 1983, pp. 1554.

FATIGUE 87

- (14) Neumann, P., *Mat. Sci. Eng.*, Vol. 81, 1986, pp. 465
- (15) Masing, G., *Z. Tech. Phys.*, Vol. 6, 1925, pp. 569
- (16) Basinski, Z. S. and Basinski, S. J., *Acta Met.*, Vol. 33, 1985, pp. 1319
- (17) Fuhlrott, H. and Neumann, P., *Proc. of "Mechanisms of Environment Sensitive Cracking of Materials"*, Guilford, UK, 1977, pp. 375
- (18) Hunsche, A. and Neumann, P., *Int. ASTM Symp. on Fundamental Questions and Critical Experiments on Fatigue*, Dallas, USA, 1984
- (19) Thompson, N., Wadsworth, N. J. and Louat, N., *Phil. Mag.*, Vol. 1, 1956, pp. 113
- (20) Dillert, K., Easman, U. and Mughrabi, H., *Phil. Mag.*, Vol. A54, 1986, pp. 237
- (21) Porter, J. and Levy, J. C., *J. Inst. Metals*, Vol. 89, 1960-61, pp. 86
- (22) Figueroa, J. C. and Laird, C., *Mat. Sci. Eng.*, Vol. 60, 1983, pp. 45
- (23) Mendez, J. and Violan, P., *Int. ASTM Symp. on Fundamental Questions and Critical Experiments on Fatigue*, Dallas, USA, 1984
- (24) Kim, W. H. and Laird, C., *Acta Met.*, Vol. 26, 1978, pp. 789
- (25) Lim, L. C. and Raj, R., *Acta Met.*, Vol. 32, 1984, pp. 1183(22)
- (26) Watanabe, T., *J. de Phys.*, Colloque C4, 1985, pp. 555
- (27) Hanada, S., Ogura, T., Watanabe, S., Izumi, O. and Masumoto, T., *Acta Met.*, Vol. 34, 1986, pp. 13
- (28) Tonnessen, A. and Neumann, P., to be published
- (29) Kemsley, D. S., *J. Inst. Metals*, Vol. 85, 1956-57, pp. 153 and pp. 420
- (30) Thompson, N., "Fracture", edited by Averbach, B. L., Felbeck, D. K., Hahn, G. T. and Thomas, D. A., John Wiley and Sons, New York, 1959, pp. 354
- (31) Boettner, R. C., McEvily, A. J. and Liu, Y. C., *Phil. Mag.*, Vol. 10, 1964, pp. 95
- (32) Wang, Z. and Margolin, H., *Met. Trans.*, Vol. A16, 1985, pp. 873
- (33) Muskhelishvili, N. I., "Some Basic Problems of the Mathematical Theory of Elasticity", Noordhoff Int. Publ., Leyden, 1977
- (34) Lim, L. C. and Raj, R., *Acta Met.*, Vol. 32, 1984, pp. 1177
- (35) Tanaka, T., Kosugi, M., private communication
- (36) Heitmann, H. H., Vehoff, H. and Neumann, P., *Proc. Sixth Int. Conf. on Fracture*, edited by Valluri, S. R., Knott, J. F., Rama Rao, P. and Tamplin, D. R. M., Pergamon Press, Oxford, 1986, Vol. 5, pp. 3599

FATIGUE 87

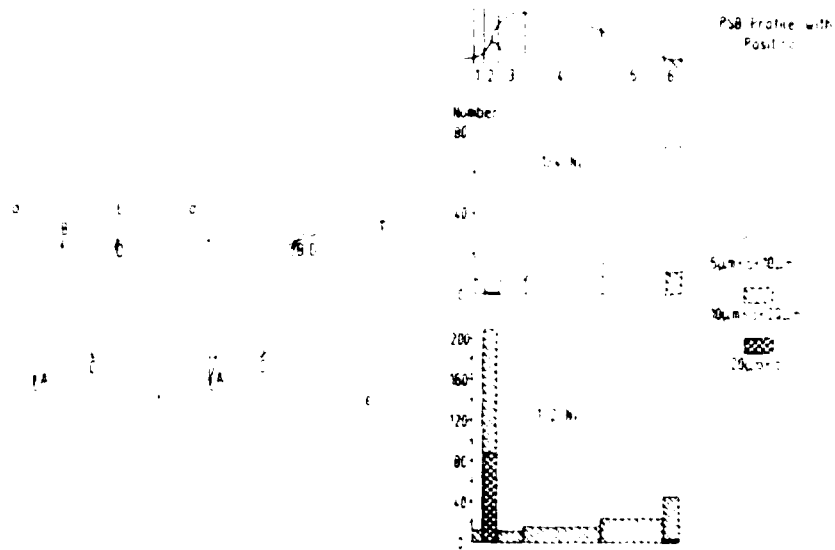


Fig. 1 Cyclic memory behaviour which is found in most metals

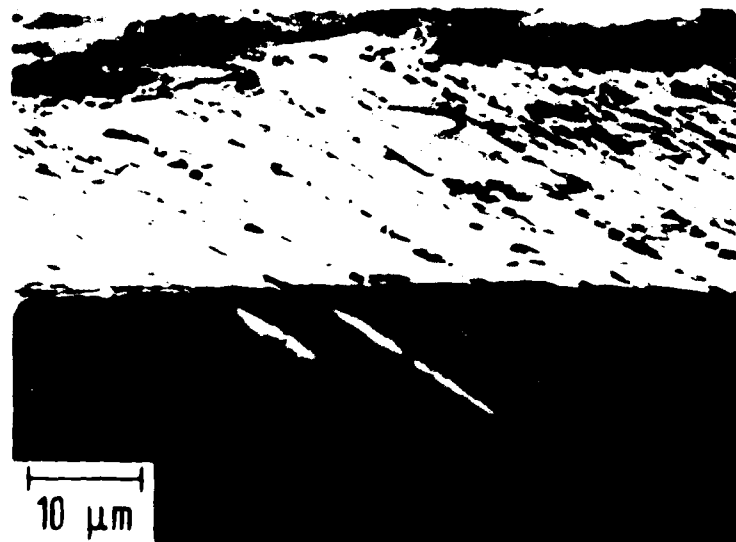


Fig. 3 Slip band crack nuclei which are not detectable from the surface



Fig. 4 Protruding PSB with crack nucleus similar to those found in single crystals (e.g. fig 13 in (8)).

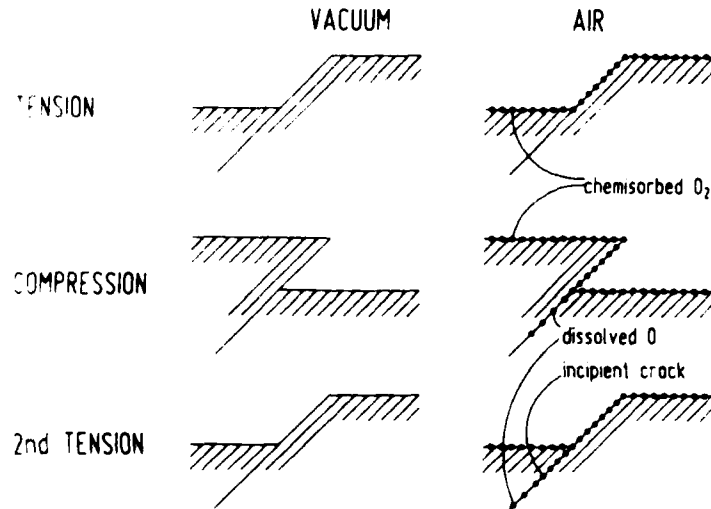


Fig. 5 Model of crack nucleation by the combined effects of single slip and environment reactions (19).

FATIGUE 87



Fig. 6: PSB at twin boundary (at white arrow).

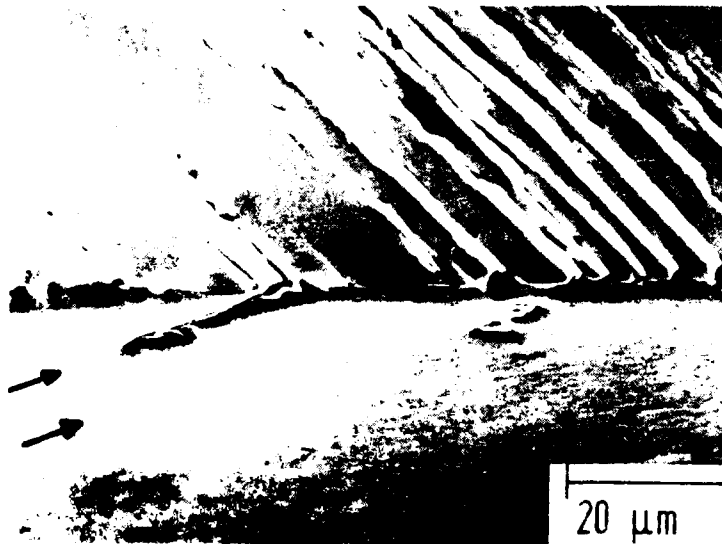


Fig. 7: Crack (not visible on the surface!) at one of the two twin boundaries (at arrows).

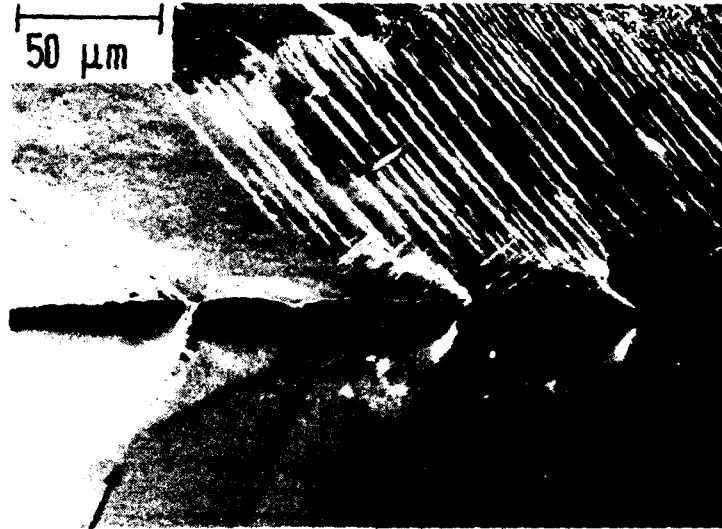


Fig. 8: Crack nucleation at every other twin boundary (at arrows) in a stack of twins.

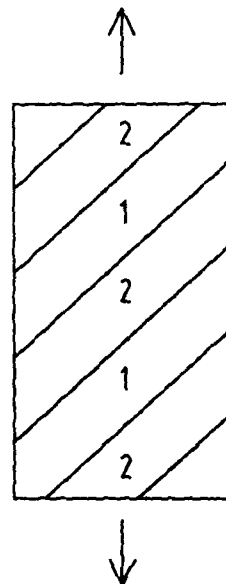


Fig. 9: Stack of twins loaded in tension.

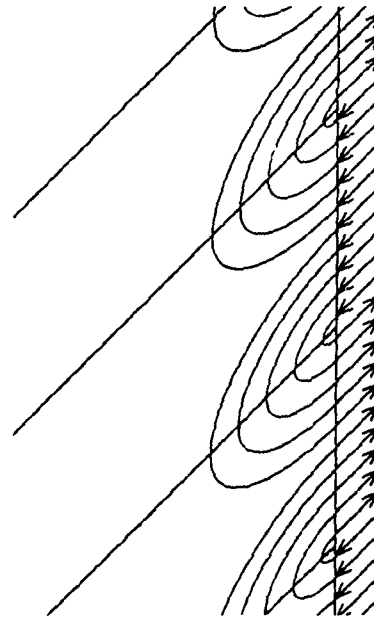


Fig. 10: Tractions on the surface due to σ^c

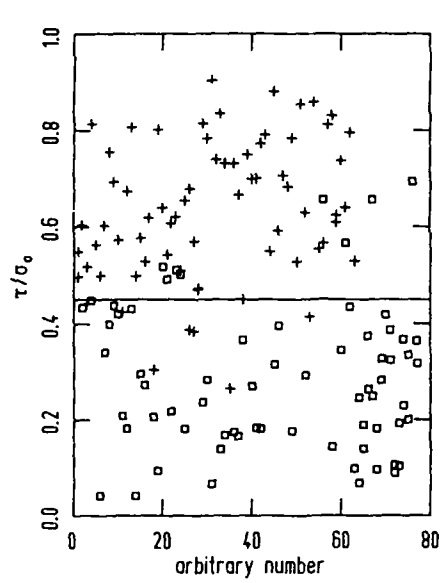


Fig. 11: Correlation between local stress and PSB appearance

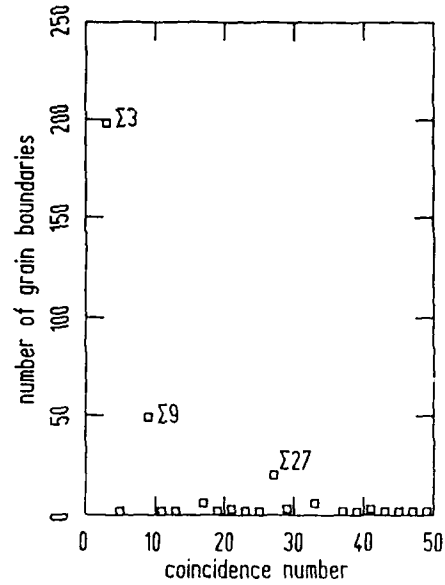


Fig. 12: Frequency of various types of grain boundaries.

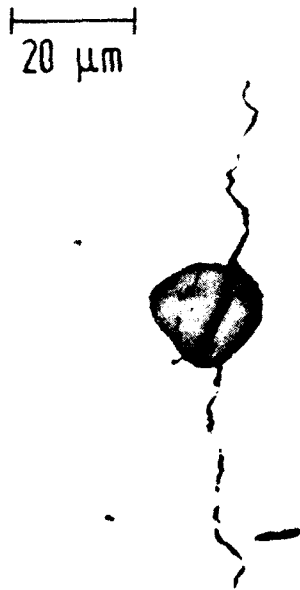


Fig. 13: Crack at an inclusion in a structural steel.



Fig. 14: Localized oxidation after creep fatigue in 316

FATIGUE 87

EFFECT OF GRAIN ORIENTATION ON THE ORIGINATION AND THE INITIAL GROWTH OF FATIGUE CRACKS IN PURE IRON

Tsuneshichi Tanaka*

Nucleation and initial growth of fatigue cracks in pure iron plate specimens were observed under reversed bending and axial stresses and under alternating tension. Grain orientation was determined by the etch pit method developed by the author. It was found that cracks originated at grain boundaries under reversed stress but they nucleated along slip bands under alternating tension. The shift of the crack nucleation sites may be caused by the degree of development of slip bands activated by the maximum applied stress. Another finding was that the morphology of early cracks was the same as that of the pencil glide observed in the slip motion of b.c.c. metals.

INTRODUCTION

Recently, much attention has been paid to the problem of short fatigue cracks, since this problem is closely connected to that of the fatigue threshold. And a number of works have been reported on various aspects of short cracks (1). The behavior of short cracks is, however, strongly affected by the crystallographic structure of materials; namely the grain orientation, Schmid factor, dominating slip system and grain boundaries. Therefore, it is important to have the information of these factors in most of the studies of short cracks.

The author recently developed a technique of grain orientation analysis in the case of commercial base polycrystalline pure iron by etch pit method (2), and have made a series of observations on the origination and initial growth of cracks under bending and axial stresses in high cycle fatigue tests.

The observation results were analyzed in relation to the structural factors of the matrix surrounding cracks to make clear

* Department of Mechanical Engineering, Ritsumeikan University,
Kita-ku, Kyoto 603, Japan

the conditions satisfied at the crack nucleation sites. The analysis was also made on the morphology of crack growth in individual grains and crack penetration into neighboring grains (2)-(5).

This paper is a summary of some of recent works together with a brief explanation of grain orientation analysis by the etch pit method. An emphasis is placed on the discussion of the preferential crack nucleation sites and of the morphology of early cracks subsequent to nucleation.

GRAIN ORIENTATION ANALYSIS BY ETCH PIT METHOD

Crystallographic orientation of surface grains of a commercial base pure iron plate specimen is successfully determined by the etch pit method recently developed by the author (2). The etchants and etching conditions, which were first suggested by Taoka et al. (6), and improved by the author after several trials are listed in Table 1.

By soaking a specimen first in etchant A and then in etchant B under the respective conditions, etch pits of different patterns are developed in grains of different orientations as shown in Figure 1. The normal direction of the specimen is indicated in each photograph by the point in a standard stereographic projection triangle. The ridge lines of an etch pit are clearly observed in a scanning electron microscope owing to its deep focus, and since the matrixes surrounding etch pits have different contrasts depending on individual orientations, the grain boundaries are easily traced.

All the etch pit walls are made of $\{110\}$ planes and all the ridge lines are in $\langle 111 \rangle$ direction. Hence, each etch pit has such a shape that is produced by indenting a rhombic-dodecahedron composed only of the $\{110\}$ planes shown in Figure 2 onto the specimen surface from an arbitrary direction. In Figure 2, a_1, a_2, a_3 are unit vectors of the cubic crystal forming a cartesian coordinate system O-XYZ, and e_1, e_2, e_3 are three ridge line vectors emerging from a vertex denoted by -P. The angle between each pair of ridge lines is $\theta_0 = \cos^{-1}(-1/3) = 109.5^\circ$, and there is a simple relation between e and a vectors:

$$\begin{bmatrix} e_1 \\ e_2 \\ e_3 \end{bmatrix} = L_0 \begin{bmatrix} a_1 \\ a_2 \\ a_3 \end{bmatrix}, \quad L_0 = \begin{bmatrix} -1/\sqrt{3} & 1/\sqrt{3} & 1/\sqrt{3} \\ 1/\sqrt{3} & -1/\sqrt{3} & 1/\sqrt{3} \\ 1/\sqrt{3} & 1/\sqrt{3} & -1/\sqrt{3} \end{bmatrix}. \quad (1)$$

Now, let n be the normal direction of the specimen surface, and l and m be the longitudinal and transverse directions of the specimen, and suppose that the vertex -P is indented onto the specimen surface from an arbitrary direction which is supposed here as $-n$ direction. Then on a photograph of the etch pit thus produced, projections of three e vectors in $-n$ direction are observed as photographs (b), (c) and (d) in Figure 1. This situation is

illustrated in Figure 3 where -P is relabelled by O. Here e_1'', e_2'', e_3'' are the orthogonal projections of e vectors in $-n$ direction on the equatorial plane (projection plane), and e_1', e_2', e_3' are stereographic projections of e vectors on the same plane with respect to the pole O'. It is obvious that mutual angles $\theta_1, \theta_2, \theta_3$ between e_1'', e_2'', e_3'' are equivalent to the angles between e_1', e_2', e_3' . This fact enables us to use the stereographic geometry (7) to find the directions of e vectors with respect to l, m and n directions.

Figure 4 shows the angles to be measured on an etch pit photograph. From angles $\theta_1, \theta_2, \theta_3$, direction cosines n_1, n_2, n_3 of e_1, e_2, e_3 vectors with respect to n direction are found by trial and error method. However, by doing the tedious trial and error calculations by computer, and making the "master table" relating the angles θ_2 and θ_3 to the values of n_1, n_2 and n_3 for a possible range of θ_2 and θ_3 , one can find the direction cosines n_1, n_2 and n_3 immediately from the measured angles. A first few lines of this master table are shown in Table 2.

The direction cosines l_1, l_2, l_3 and m_1, m_2, m_3 of e_1, e_2, e_3 with respect to the directions l and m are calculated by the following formulas:

$$l_i = \sqrt{1 - n_i^2} \cos \alpha_i, \quad m_i = \sqrt{1 - n_i^2} \cos \beta_i, \quad (i = 1, 2, 3) \quad (2)$$

where α_i and β_i are angles shown in Figure 4 and are measured on the etch pit photograph. Thus we obtain the relation:

$$\begin{bmatrix} e_1 \\ e_2 \\ e_3 \end{bmatrix} = L_1 \begin{bmatrix} l \\ m \\ n \end{bmatrix}, \quad L_1 = \begin{bmatrix} l_1 & m_1 & n_1 \\ l_2 & m_2 & n_2 \\ l_3 & m_3 & n_3 \end{bmatrix}. \quad (3)$$

Combining the equations (1) and (3), we obtain:

$$\begin{bmatrix} a_1 \\ a_2 \\ a_3 \end{bmatrix} = L \begin{bmatrix} l \\ m \\ n \end{bmatrix}, \quad L = L_0^{-1} L_1. \quad (4)$$

This is the equation providing the relationship between the base vectors of the cubic crystal and the base directions of the specimen.

Returning to Figure 2, the point -P is a vertex where three ridge lines meet, and an adjacent vertex, say, the point D' has four ridge lines, three of which are parallel to e_1, e_2 and e_3 ; an etch pit pattern corresponding to such a vertex as D' is given in photograph (a) in Figure 1. Therefore, from the etch pit pattern produced by the vertex D' we can build the pattern corresponding to the point -P. Thus the above analysis is applied to all the etch pit patterns.

FATIGUE 87

FATIGUE TEST

Pure iron (99.9%) of commercial base was used in the experiment in the fully annealed state. The heat treatment conditions and mechanical properties are listed in Table 3. The mean grain size was approximately 160 μm . Plate specimens shown in Figure 5 were prepared with a final finish by electrolytic polishing. Plate thickness was $t = 1.0\text{mm}$ for the specimens used in reversed bending tests and $t = 1.5\text{mm}$ for those used in axial loading tests.

Reversed bending tests were carried out by using a magneto-electric type cantilever plane bending machine with zero mean stress at the frequency of 60Hz. Axial loading tests were carried out under two loading conditions of fully reversed tension-compression ($R = -1$) and alternating tension ($R = 0$), by using a hydro-electric servo type axial loading machine at the frequency of 30Hz. The obtained $S-N$ relations are shown in Figures 6 and 7, respectively for reversed and axial loading tests.

The nucleation of cracks and their early growth were observed at stress levels just above the endurance limits under respective loading conditions. In practice, the test was interrupted at every 10^5 cycles and a specimen was removed from the machine for SEM observation. After repetition of such surveys, the test was finally interrupted at above 50-80% of the fracture life and the specimen underwent a series of treatments. In the first place, the specimen surface was treated by the etchants A and B in Table 1 to yield crystallographic etch pits, and the orientation of grains surrounding cracks were determined. Since two slip systems, $\langle 111 \rangle - \{110\}$ and $\langle 111 \rangle - \{112\}$, exist in b.c.c. metals, which are equally operative under repeated stress (8), and each slip system has twelve systems in the combination of slip directions and slip planes, geometrical configuration and Schmid factor of all the systems were determined to make clear their influence on the nucleation and subsequent growth of cracks. After fixing the grain orientation, the surface layer of the specimen was successively removed by electrolytic polishing to find the morphology of cracks and grain boundaries below the surface. Micro-vickers indentation marks were conveniently used as fixed points when thin layers were removed.

OBSERVATION OF CRACKS

Cracks under Reversed Bending Stress

Under reversed bending stress, cracks were observed at the stress $\sigma_a = 140\text{MPa}$. Fine cracks were first observed at about 10^6 cycles, and they grew continuously until the test was interrupted at 2.1×10^6 cycles. Approximate locations of the observed cracks on the specimen surface were indicated at the lower left corner of Figure 8; they are labelled as crack G, K and L. Finer cracks other than these were also observed on the surface, but their

FATIGUE 87

growth was limited and disappeared by the removal of thin surface layer. In the following, the observation results are explained for crack K and G by showing the morphology of these cracks.

Morphology of crack K. The growth of the crack K on the specimen surface is presented in Figure 8 where numbers in each photograph indicate the distinctions of grains. A fine crack was found at 10^6 cycles at the boundary of grains 2 and 9 (boundary 9-2) and grew along the same boundary until 1.4×10^6 cycles. And at 1.8 and 2.1×10^6 cycles, the upper part of the crack entered into grain 2, while its lower part progressed along the boundary 9-12 and reached a triple point of grains 9, 12 and 18, and then entered into grain 18 with a short discontinuity at the triple point. Symbols π_{ij}^{kl} express dominating slip planes in each grain and arrows attached to the symbols indicate the directions of intersections of the slip planes with the surface.

Table 4 shows the Schmid factors of 24 slip systems in grain 2 as an example, where S_i^k and π_{ij}^{kl} mean a slip direction and a slip plane, and K_j^l is Schmid factor. Four suffixes have the following meanings; k indicates grain number, l is 0 for $\langle 111 \rangle$ - $\{110\}$ slip system and 2 for $\langle 111 \rangle$ - $\{112\}$ slip system, i ($=1, 2, 3, 4$) indicate the distinctions of four different slip directions in b.c.c. metal, j indicates three different slip planes belonging to each slip direction and j takes 1, 2 and 3 in the order from the largest to the least Schmid factors. Dominating slip systems were defined as those having the Schmid factors larger than 0.38 which was selected rather arbitrarily as in the author's previous report (3).

In Figure 8, it is found that the directions of the dominating slip planes coincide with slip band directions. Especially, it is noted that the boundary 9-2 where the first crack emerged is parallel to the dominating slip plane π_{22}^{90} and cracks in the grains 2 and 18 are exactly in the directions of π_{31}^{22} and $\pi_{31}^{18,2}$.

Photographs in Figure 9 show the inner surfaces of indicated depths from the outer surface. Photograph (a) is the outer surface after etch pit treatment. These photographs indicate that the grain boundary crack on the outer surface tends to part from the boundary under the surface (photographs (b) and (c)), and the continuous crack on the specimen surface is disjoined inside, and at the depth of about $30\mu\text{m}$ it becomes three separate cracks in the grains 2, 9 and 18 (photograph (c)). In photographs (d) and (e), a crack remains only in grain 2 and cracks in other two grains are only traces and almost disappear. Grain N1 in photograph (e) is a new grain appeared at this depth.

Three illustrations in Figures 10, 11 and 12 show the morphologies of the cracks in respective grains 2, 9 and 18. In each

FATIGUE 87

figure, the frame is in the directions of the specimens base vectors l , m and n . Bold lines (solid and broken) indicate grain boundaries and fine lines indicate dominating slip planes. Coarsely shadowed area is a crack surface resting on dominating slip planes and finely shadowed area is a part of crack not resting on any dominating slip plane or a crack on a grain boundary.

Figure 10 shows the morphology of crack in grain 2 in the inside layer deeper than $30\mu\text{m}$ where the crack is separated from those in the other grains. It is observed that the crack progressed into grain 2 in the direction of S_3^2 along two dominating slip planes Π_{31}^{20} and Π_{31}^{20} . Moreover, comparing to the crack length measured at the upper surface of the given frame in Figure 10 (about $120\mu\text{m}$), its length in the direction of S_3^2 (about $200\mu\text{m}$) is much larger, and therefore it seems that the crack propagated into the grain mainly as a mode II crack.

Figure 11 shows a part of crack from a to b in the photograph (a) in Figure 9. Although this crack lay on the grain boundaries 9-2 and 9-12 on the specimen surface, it penetrated into grain 9 as shown in the photographs in Figure 9. The shadowed area A is a part of crack on the grain boundary to the depth of about $25\mu\text{m}$. The similar area B is partly on the grain boundary but the other part is inside the grain 2 without lying on any dominating slip system. It is again observed that in grain 9 the crack progressed in the direction of S_2^9 along two slip planes Π_{21}^{90} and Π_{22}^{90} .

The illustration in Figure 12 shows a crack in grain 18 in the inside deeper than $12\mu\text{m}$. In this case the crack is lying on three dominating slip planes $\Pi_{11}^{18,2}$, $\Pi_{11}^{18,0}$ and $\Pi_{12}^{18,0}$, which all belong to the same slip direction S_1^{18} .

Morphology of crack G Crack G was observed to originate at grain boundary 8-5 in Figure 13. This grain boundary is parallel to the slip plane Π_{31}^{82} of grain 8. Until 2.1×10^6 cycles, the crack grew along the boundary 8-7 and entered into grain 9 in its lower part, and its upper part entered into grain 5.

Three dimensional morphology of this crack given in Figure 14 shows that the first cracked part along the boundary 8-5 is lying on the same boundary to a certain depth as shown by the fine shadowing, but most part of the crack is in grains 8 and 9. In each grain the crack surface is on the two dominating slip planes and penetrates into the common slip direction; slip planes Π_{31}^{80} and Π_{31}^{82} with the direction S_3^8 in grain 8, and slip planes Π_{31}^{90} and Π_{31}^{92} with the direction S_3^9 in grain 9. Moreover, in this case of crack which extended to two grains, it is found that the adjacent dominating slip planes in two grains intersects with small mismatch and two slip directions S_3^8 and S_3^9 are almost parallel.

FATIGUE 87

Cracks under Reversed Axial Stress

Under completely reversed axial stress ($R = -1$), the observation was made at the stress $\sigma_a (= \sigma_{max}) = 115\text{MPa}$, and cracks were found at 3×10^5 cycles. The test was interrupted at 10^7 cycles.

Figure 15 shows one of such cracks observed on a specimen surface. It was found first at grain boundary 3-4 and until 5×10^5 cycles, its upper part grew along another boundary 1-2, and its lower part entered into grain 5. It is noted that the first crack-
ed boundary 3-4 is parallel to the dominating slip plane Π_{31}^{22} of grain 3, that is in the same mode as in the previous cases observed under reversed bending stress. Patterns of this crack on several inner surfaces are shown in photographs (b), (c) and (d) in Figure 16. Photograph (a) is the outer surface after etch pit treatment. These photographs show that the almost straight crack on the specimen surface is no longer straight inside but it is bent at two points (photographs (b) and (c)), and in the deepest part it becomes straight again (photograph (d)).

The morphology of this crack is shown in Figure 17. The upper surface of the frame corresponds to $38\mu\text{m}$ deep inner surface shown in photograph (b), and at this stage grain 3 disappeared. Although the illustration is rather complicated, by paying attention to the shadowed area presenting the crack surface, it is found that the crack is resting on one or two dominating slip planes having the same slip direction in each grain; the crack is on Π_{41}^{20} and Π_{41}^{22} with S_4^2 in grain 5, and on Π_{21}^{60} and Π_{21}^{62} with S_2^6 in grain 6, and on Π_{31}^{12} with S_3^1 in grain 1. Moreover, the above three slip directions are almost parallel as in the case of Figure 14. It is therefore suggested that the crack propagated in these grains in almost the same direction in the shear mode.

Figure 18 shows another crack observed at the same stress level. This crack was found also at 3×10^5 cycles at grain boundary 1-2, and at 10^6 cycles it entered into grain 3 after passing through the boundary 1-2 (photograph (a)). At the depth of $55\mu\text{m}$ from the surface (photograph (b)), the upper part of the crack has two branches along the boundaries 1-4 and 2-4, and its lower part is bent along the two slip planes Π_{41}^{32} and Π_{41}^{30} .

The morphology of this crack is given in Figure 19, in which grain boundaries inside the frame are not drawn to avoid complication. It is observed that the crack is on the grain boundaries to a certain depth at the first cracked site and at the branched parts, but in grain 3 it penetrated deep into the grain along the slip planes Π_{41}^{32} and Π_{41}^{30} in the direction S_4^3 .

Cracks under Alternating Tensile Stress

Observations of cracks were made at $\sigma_{max} = 190\text{MPa}$ under

FATIGUE 87

alternating tensile stress ($R=0$). Under this stress condition, slip motion was much more active than in the case of reversed stress due to high maximum stress, and most of the surface grains were covered by dense slip bands. Figure 20 shows such surface grains photographed at 5×10^5 and 2.2×10^6 cycles. Cracks are found in the grain 1 along the slip bands whose directions coincide with the direction of slip planes π_{11}^1 and π_{11}^2 belonging to the same slip direction S_1^1 . Since these cracks disappeared after the first removal of $14\mu\text{m}$ thin surface layer, no illustration is given in this case. The important thing is that no cracks were found at grain boundaries under this load condition of $R=0$.

Figure 21 shows another crack observed at the same stress level, and Figure 22 shows the morphology of this crack. The crack nucleated again along slip band inside a grain (grain 1), and it penetrated into the grain along the dominating slip system $S_2^1-\pi_{21}^1$ in the shear mode.

DISCUSSION

As mentioned in the introduction, one of the purposes of this study was to make clear the location of the nucleation of fatigue cracks. So far there have been both assertions; whether fatigue cracks nucleate at grain boundaries or they emerge along slip bands inside grains (9)-(13). The observation in this study clearly shows that the crack nucleation site is not inherent in the structure of material but shifts its location depending on the applied maximum stress which is varied by the stress ratio R . Under the reversed stress of $R=-1$, development of slip bands is suppressed due to low maximum stress and cracks nucleate at grain boundaries without exception, regardless of whether the stress is bending or tension-compression. But under the alternating stress of $R=0$, all cracks nucleate at well developed slip bands inside grains that are activated by high maximum stress.

The second point that was aimed was to make clear the fundamental morphology of early growth of cracks following their nucleation in relation to the crystallographic structure of the materials. It is now clear that an early crack penetrates into grains along one or more dominating slip systems having a common slip direction in respective grains, regardless of whether it nucleated at a grain boundary or along a slip band. This morphology of early cracks is quite the same as that of pencil glide commonly observed in the slip motion in b.c.c. metals, as already suggested by Otsuka et al. (14) and Asami and Terasawa (15). In this sense, the propagation of early cracks occurs in the shear mode.

The observation of the crack K showed that the crack continuous in thin surface layer disjoined in the inside and separate cracks penetrated deep in individual grains. Hence, it seems that they will coalesce again when their growth reaches some threshold

FATIGUE 87

value. However, there is another case as shown in Figures 14 and 17, where cracks extended over two or three grains. In such cases, the crack propagates preferentially to the dominating slip system of an adjacent grain which has a closer orientation to that of the slip system in the first grain on which the crack already exists. The existence of such preferential slip systems in neighboring grains may be a cause of occurrence of the latter case.

In the previous report, the author pointed out that, when cracks nucleated at grain boundaries, high orthogonality conditions were satisfied between two dominating slip systems adjacent to each other at a grain boundary where a preferential crack nucleation occurred, and one of the dominating slip planes was always parallel to the grain boundary (3). The parallelism of a dominating slip plane to the cracked boundary is again confirmed in this study as frequently mentioned in the explanation of observation results. Regarding the orthogonality conditions, the results of analysis for the cracks K, G and I are listed in Table 5. It is found that the angles between two dominating slip plane normals each in adjacent grains are close to a right angle and those between the slip directions are also close to a right angle excepting the case of crack K.

CONCLUSION

The nucleation and early growth of fatigue cracks in pure iron plate specimens were observed under reversed bending and axial stresses and also under alternating tension. The orientation of grains surrounding cracks was determined by the etch pit method, and three dimensional morphology of cracks were drawn based on the observation of cracks on inner surfaces created by removing surface layers. The major results are summarized as follows.

(1) Under reversed bending and axial stresses ($R = -1$), cracks nucleate always at grain boundaries, but under alternating tension ($R = 0$), cracks nucleate along slip bands inside grains. Slip motions activated by a high maximum stress in the latter stress condition give rise to well developed slip bands in surface grains, and thus produced persistent slip bands may be the source of crack nucleation.

(2) Early growth of cracks subsequent to nucleation takes place along one or more dominating slip systems having the same slip direction in individual grains, regardless of the nucleation sites. Its morphology is just like the pencil glide observed in b.c.c. metals and the progress of cracks occurs mostly in the shear mode.

(3) When a crack extended to more than one grain, two cases were observed; one is the case where the crack becomes discontinuous below the surface and separate cracks penetrate deep into individual grains, and the other is the case where the crack

FATIGUE 87

propagates to an adjacent grain having a preferential slip system whose orientation is close to that in the first grain.

(4) In the case when cracks originate at grain boundaries, several crystallographic conditions were found at those boundaries, in the previous study. Some of these conditions were confirmed to hold again in this study.

SYMBOLS USED

\mathbf{a}_i	= base vectors of cubic crystal ($i = 1, 2, 3$)
\mathbf{e}_i	= ridge line vectors of rhombic-dodecahedron emerged from a vertex ($i = 1, 2, 3$)
\mathbf{e}_i'	= orthogonal projection of \mathbf{e}_i
\mathbf{e}_i''	= stereographic projection of \mathbf{e}_i
$\mathbf{l}, \mathbf{m}, \mathbf{n}$	= base vectors of the specimen coordinate system
α_i	= angle between \mathbf{e}_i ($i = 1, 2, 3$)
α_i'	= angles between \mathbf{e}_i' ($i = 1, 2, 3$)
α_i	= angle between \mathbf{e}_i' and \mathbf{l}
β_i	= angle between \mathbf{e}_i' and \mathbf{m}
l_i, m_i, n_i	= direction cosines of \mathbf{e}_i with respect to $\mathbf{l}, \mathbf{m}, \mathbf{n}$
L_1, L_2, L	= transformation matrixes
$S_{ij}^{kl}, -kl$	= slip direction and slip plane
κ_j^l	= Schmid factor
suffix k	= grain number
suffix l	= 0 for $\cdot 111 \cdot \sim \cdot \bar{1}10 \cdot$ slip system and 2 for $\cdot 111 \cdot \sim \cdot 112 \cdot$ slip system
suffix i	= distinctions of four slip directions ($i = 1, 2, 3, 4$)
suffix j	= distinctions of three slip planes belonging to each slip direction in the order of the magnitude of Schmid factor ($j = 1, 2, 3$)

REFERENCES

- (1) For instance, MRS, Vol.1, "Current Research on Fatigue Cracks", edited by T. Tanaka, M. Jono and K. Komai, the Society of Materials Science, Japan, 1985.
- (2) Tanaka, T. and Kosugi, M., Proc. 26th Japan congress on Materials Research, 1983, p.84.
- (3) Tanaka, T. and Kosugi, M., Journal of the Society of Materials Science, Japan, Vol.33, 1984, p.659.

FATIGUE 87

- (4) Tanaka, T. and Murai, Y., Journal of the Society of Materials Science, Japan, Vol.36, 1987 (to be published).
- (5) Tanaka, T. and Murai, Y., Bulletin of the JSME, Vol.53, 1987 (to be published).
- (6) Taoka, K. et al., Journal of the Japan Institute of Metals, Vol.30, 1966, p.820.
- (7) Kovacs, T., "Principles of X-Ray Metallurgy", ILLIFFE Books Ltd., London, 1969.
- (8) Wei, R.P. and Baker, A.J., Philosophical Magazine, Vol.12, 1965, p.1005.
- (9) Sugano, M. and Kojima, K., Journal of the Society of Materials Science, Japan, Vol.19, 1970, p.656.
- (10) Yoshida, A. et al., Journal of the Society of Materials Science, Japan, Vol.19, 1970, p.722.
- (11) Nakazawa, H. et al. Trans. JSME, Vol.40, 1974, p.9.
- (12) Kurobe, T. et al., Journal of the Society of Materials Science, Japan, Vol.26, 1977, p.355.
- (13) Takao, K. and Nisitani, H., Trans. JSME, vol.46, 1980, p.123.
- (14) Otsuka, A. et al., Journal of the Society of Materials Science, Japan, Vol.29, 1980, p.568.
- (15) Asami, K. and Terasawa, M., Journal of the Society of Materials Science, Japan, Vol.30, 1981, p.803.

FATIGUE 87

TABLE 1 - Etchants and etching conditions

Etchant A
Reagent: HCl 0.1cc, H ₂ O ₂ 1cc, H ₂ O 50cc
Soaking time and temperature: 20-30sec at 25°C
Etchant B
Reagent: Saturated aqueous solution of FeCl ₃ ·6H ₂ O 10cc H ₂ O 50cc, HNO ₃ 5cc
Soaking time and temperature: 50sec at 25°C

TABLE 2 - Master table (first few lines)

x2= 90.00	x3= 90.00	n1=-0.5773	n2= 0.5773	n3= 0.5774
x2= 90.25	x3= 90.25	n1=-0.5723	n2= 0.5773	n3= 0.5773
x2= 90.50	x3= 90.50	n1=-0.5672	n2= 0.5773	n3= 0.5773
x2= 90.75	x3= 90.75	n1=-0.5621	n2= 0.5772	n3= 0.5773
x2= 91.00	x3= 91.00	n1=-0.5570	n2= 0.5772	n3= 0.5772
x2= 91.25	x3= 91.25	n1=-0.5519	n2= 0.5771	n3= 0.5771
x2= 91.50	x3= 91.50	n1=-0.5467	n2= 0.5770	n3= 0.5770

X2, X3=θ₂, θ₃; N1, N2, N3=n₁, n₂, n₃

TABLE 3 - Heat treatment and mechanical properties of material

Material	Heat treatment	Yield point	Tensile strength	Elongation
Pure iron	960°C 3hr, F.C.	115 MPa	239 MPa	48 %

TABLE 4 - Slip systems and Schmid factors in grain 2

GNO.	s.d.	<111>-{110} slip system						<111>-{112} slip system					
		s.p.	s.f.	s.p.	s.f.	s.p.	s.f.	s.p.	s.f.	s.p.	s.f.	s.p.	s.f.
		S ₁ ²	-1 ₁ ²	K ₁ ²	-1 ₁ ²	K ₁ ²	-1 ₁ ²	K ₁ ²	-1 ₁ ²	K ₁ ²	-1 ₁ ²	K ₁ ²	-1 ₁ ²
2	i=1	ij=11	0.03	ij=12	0.02	ij=13	0.00	ij=11	0.33	ij=12	0.24	ij=13	0.09
	2	21	0.34	22	0.23	23	0.11	21	0.33	22	0.26	23	0.06
	3	31	0.46	32	0.38	33	0.08	31	0.48	32	0.31	33	0.17
	4	41	0.22	42	0.13	43	0.08	41	0.21	42	0.18	43	0.02

Key: GNO.; grain number, s.d.; slip direction, s.f.; Schmid factor, s.p.; slip plane

TABLE 5 - Angular relationship between two dominating slip systems in the grains adjacent at cracked boundary

Crack	Grain boundary i - j	Schmid factor K _i - K _j	Angle (degree)	
			between the normals of the slip planes	between the slip directions
K	9 - 2	0.40 - 0.48	∠(n ₂₂ ⁹⁰ , n ₃₁ ²²) = 80.5	∠(S ₂ ⁹ , S ₃ ²) = 42.4
G	8 - 5	0.48 - 0.47	∠(n ₃₁ ⁸² , n ₃₁ ⁵⁹) = 82.9	∠(S ₃ ⁸ , S ₃ ⁵) = 80.9
L	10 - 12	0.40 - 0.47	∠(n ₃₁ ¹⁰⁰ , n ₃₁ ¹²⁰) = 80.5	∠(S ₃ ¹⁰ , S ₃ ¹²) = 80.7

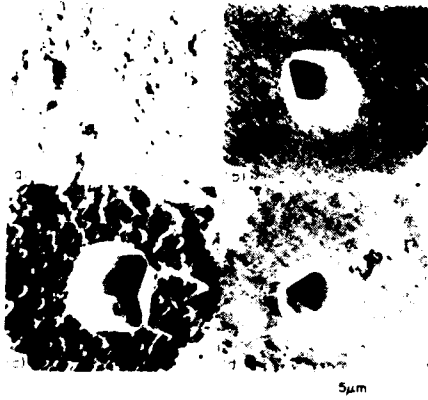


Figure 1 Etch pit patterns

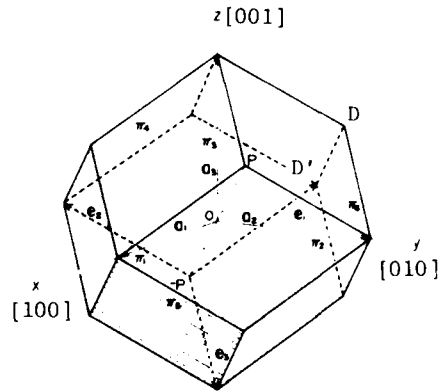


Figure 2 Rhombic-dodecahedron composed of $\{110\}$ planes in the cubic system

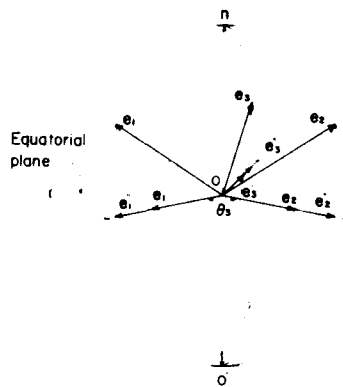


Figure 3 Orthogonal and stereographic projections of e_1 , e_2 and e_3



Figure 4 Angles to be measured on the etch pit photograph

FATIGUE 87

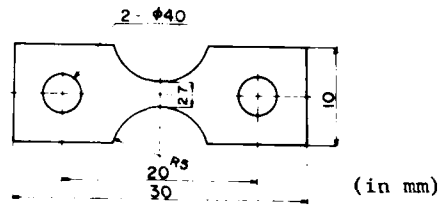


Figure 5 Specimen ($t = 1.0$ and 1.5)

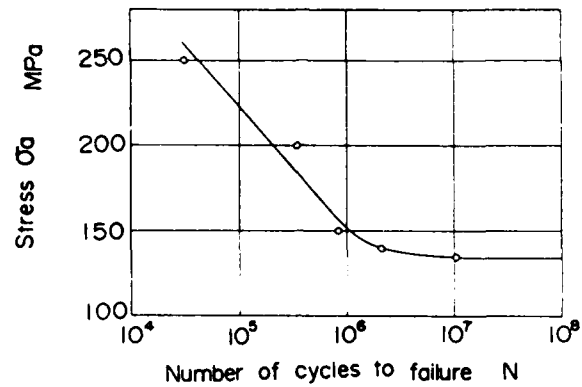


Figure 6 S-N curve under reversed bending stress

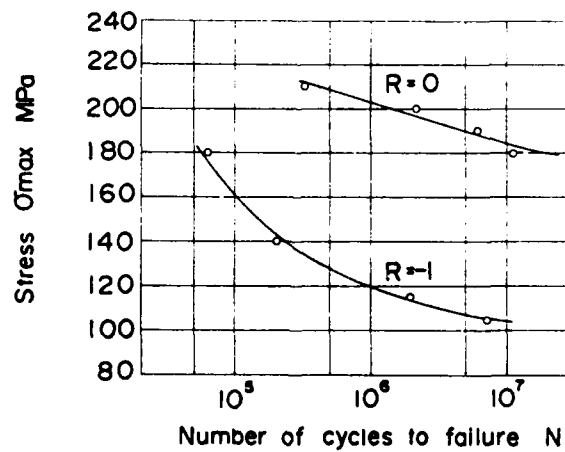


Figure 7 S-N curves under reversed and alternating axial stresses

FATIGUE 87

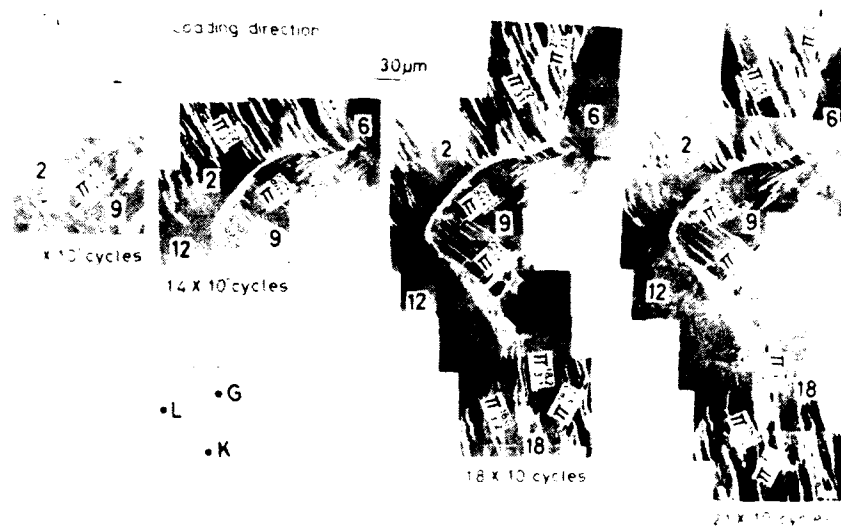


Figure 8 Origination and growth of crack K on the specimen surface

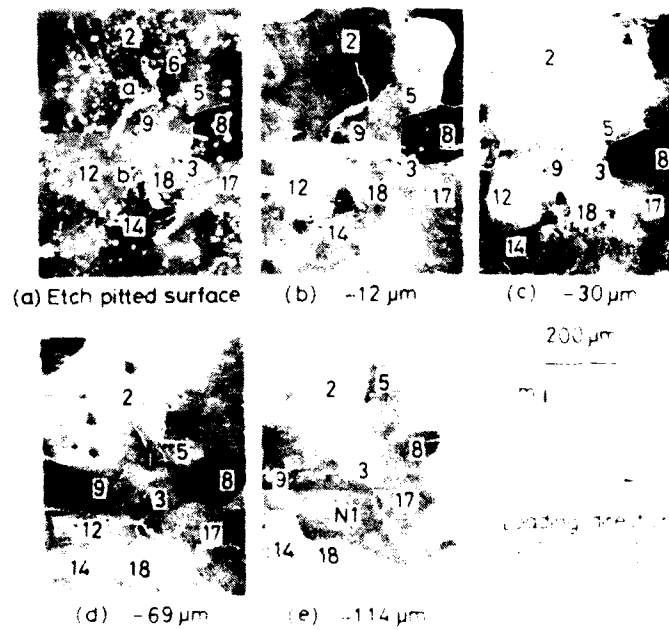


Figure 9 Patterns of crack K on the inner surfaces of given depth

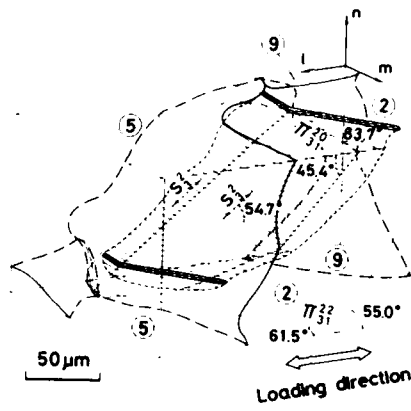


Figure 10 Morphology of a part of crack K in grain 2

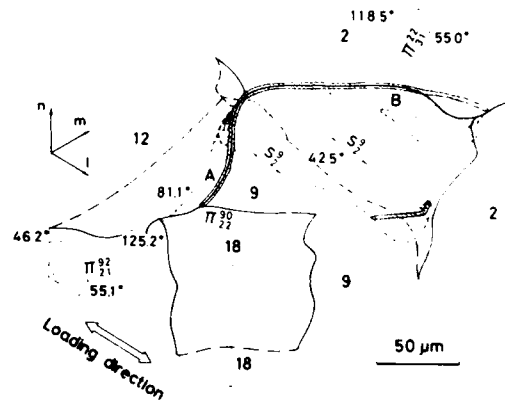


Figure 11 Morphology of a part of crack K in grain 9

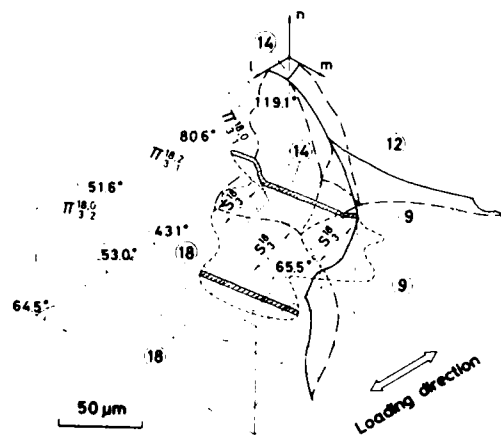


Figure 12 Morphology of a part of crack K in grain 18

FATIGUE 87

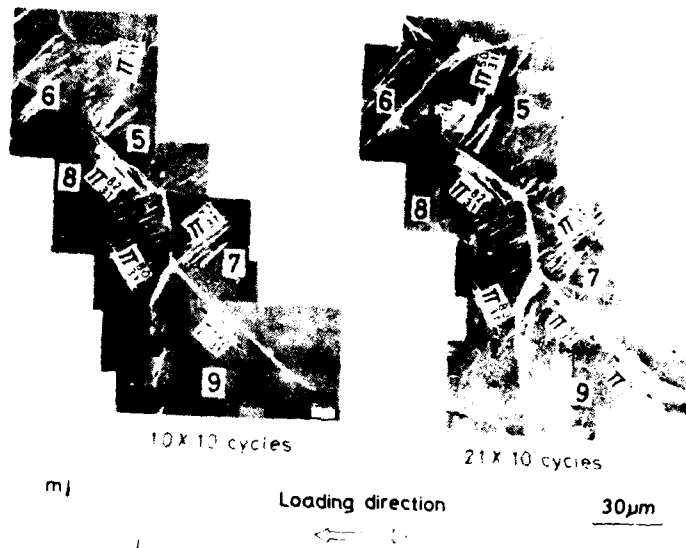


Figure 13 Crack G on the specimen surface

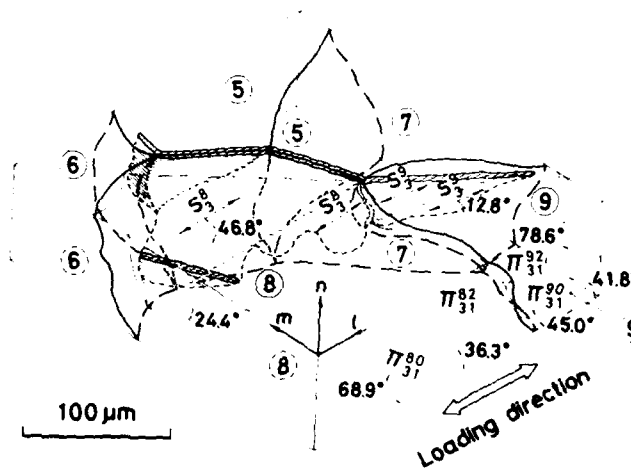


Figure 14 Morphology of crack G

FATIGUE 87

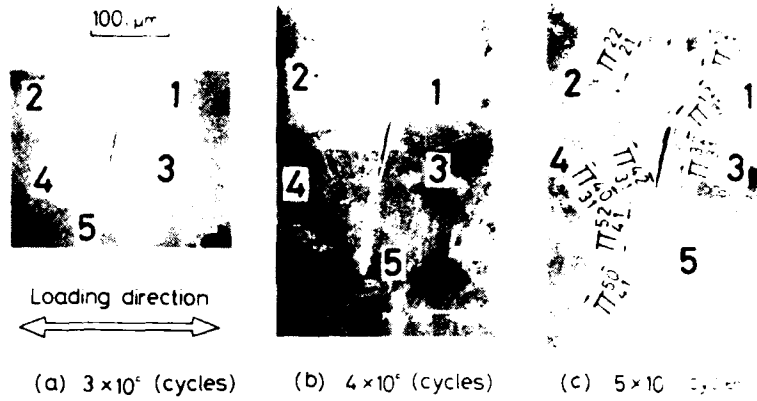


Figure 15 Surface crack under reversed axial stress



Figure 16 Crack patterns on the inner surfaces of given depth

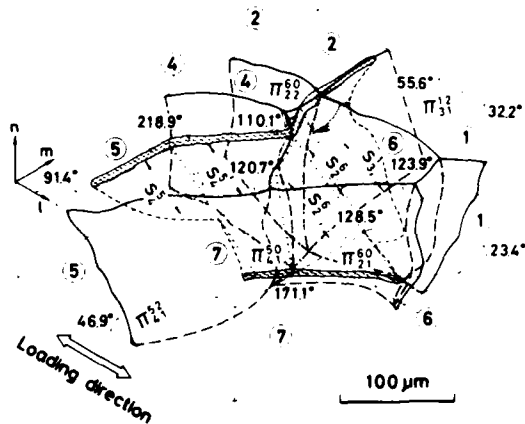


Figure 17 Morphology of the crack

FATIGUE 87

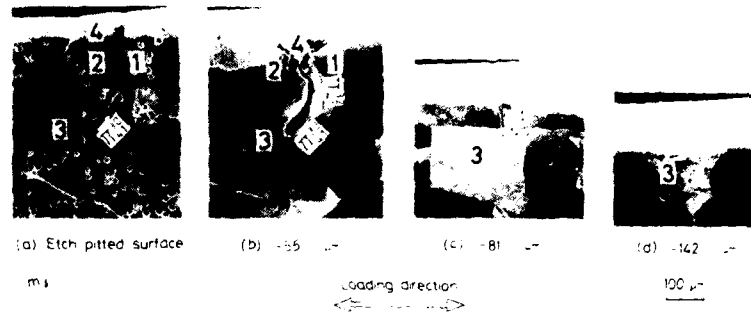


Figure 18 Another crack under reversed axial stress; patterns on the inner surfaces of given depth

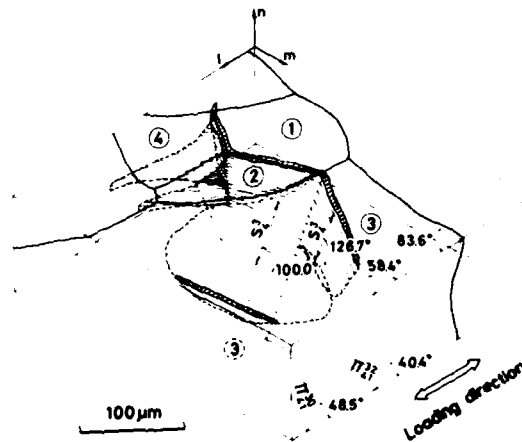


Figure 19 Morphology of the crack

FATIGUE 87

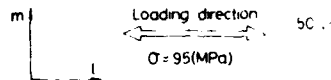
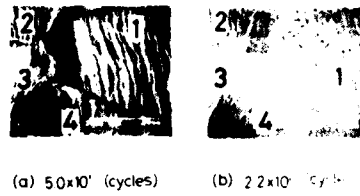


Figure 20 Slip band crack under alternating tension

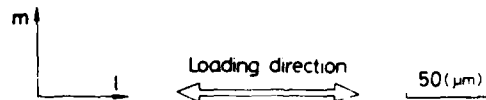


Figure 21 Another slip band crack under alternating tension

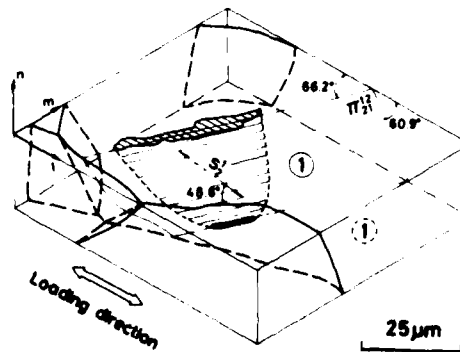


Figure 22 Morphology of the crack

THE GROWTH OF PERSISTENT SLIP BANDS

W. J. Baxter*

The growth of persistent slip bands (psb) in 6061-T6 aluminum was measured with a photoelectron microscope equipped with a fatigue stage. The psb appeared initially as a small extrusion and elongated across the surface by the sequential addition of new extrusions. As the psb elongated, the initial extrusion became more pronounced. The rate of elongation in polycrystalline material varied inversely as the length, whereas in a single crystal the rate remained constant. This difference is attributed to the constraints imposed upon a small grain by the surrounding material. The growth laws are described by a simple model in which the psb is softer than the matrix of the grain.

INTRODUCTION

In many materials the initial surface manifestation of fatigue is the appearance of persistent slip bands (psb), some of which later become sites for fatigue cracks (see, e.g., Forsyth (1), Laird (2) and Mughrabi et al. (3)). This process can occupy a major fraction of the fatigue life particularly at low stress levels. But whereas the growth of fatigue cracks has been studied extensively for many years, there is still little corresponding information on the growth of psb. One reason for this is the difficulty of detecting the early stages of psb formation with conventional techniques of surface examination. In this study a photoelectron microscope (PEM) equipped with a fatigue stage provided sufficient sensitivity to observe the early stages of growth of individual psb in single crystal and polycrystalline 6061-T6 aluminum. The topography of the psb was then examined in more detail by scanning electron microscopy. These experiments have revealed that initially a psb appears in the form of a small extrusion, then elongates across the surface by the sequential addition of new extrusions. Further it is shown that in a single crystal the rate of elongation is constant, but in polycrystalline material the rate of elongation varies inversely as the length of the psb. These growth laws are

* Physics Department, General Motors Research Laboratories, Warren, Michigan 48090-9055

FATIGUE 87

accounted for by a model in which the material of the psb has a lower yield stress than the matrix of the grain. The difference between the single crystal and polycrystalline behavior is attributed to the constraints imposed upon a small plastically deforming grain by the surrounding elastically deforming material.

EXPERIMENTAL

Small cantilever beam specimens, with a tapered gauge section (~2 mm wide x 4 mm long) were fatigued at maximum cyclic surface strains of $\pm 3.0 \times 10^{-3}$ in the vacuum chamber of a photoelectron microscope (Baxter and Rouze (4)). Specimens with small grains (average diameter ~30 μm) were machined from sheet material 1.5 mm thick. A specimen with large grains was machined from a forging such that the gauge section consisted of a single crystal. (The only observable difference in the microstructures was a slightly smaller concentration of $\text{Fe}_3\text{SiAl}_{12}$ and Mg_2Si precipitates in the large grain specimen.) The surface was mechanically polished with 1 μm diamond paste, then etched for four minutes in a solution of 2 mL H_2SO_4 , 1 mL HF and 97 mL H_2O to reveal the grain boundaries. Finally, the specimens were exposed to ambient air for 24 hours to form a thin surface oxide film.

In the PEM, photoelectrons emitted from the specimen pass through a magnetic lens system and form a magnified image of the surface on a fluorescent screen. As the specimen is fatigued, the thin oxide film is ruptured by the emerging psb, exposing fresh metal surfaces. These surfaces emit more photoelectrons (so called exoelectrons (Baxter (5))) than the surrounding oxide-covered metal, and appear as white spots or lines on the micrographs shown in the next section.

RESULTS

Photoelectron Microscopy

A complicating factor in the measurement of psb growth rates is that a large number appear, and grow, simultaneously. In these experiments, the psb were imaged at regular intervals during a fatigue test and the measurements were confined to psb which elongated in a simple manner without the complication of interactions with other psb.

Single Crystal. The early stages of growth of some psb are illustrated by the photoelectron micrographs in Figure 1. This sequence depicts the characteristic behavior of the initial appearance of many small spots of emission and the subsequent elongation of many (but not all) of them, as the psb grow across the surface. The number of cycles required to create an initial spot of emission varies considerably from one psb to another, new spots appearing even after some psb have elongated substantially. The psb A-E in Figure 1 were measured because they were relatively isolated.

Within the range of observation the length of all these psb increased in direct proportion to the number of fatigue cycles (Figure 2). Similar behavior was also observed for other psb at other locations on the specimen; however, the rate of growth differed from one psb to another, as is evident in Figure 2.

Polycrystal. As has been reported previously by this author (Baxter (6) and (7)), in polycrystalline specimens the length of a psb increases as the square root of the number of fatigue cycles. This parabolic growth law differs substantially from that for a single crystal as is illustrated by Figure 3, where the measurements of a psb in a polycrystalline specimen are compared with those of psb A of Figures 1 and 2. (Note that the number of fatigue cycles plotted in Figure 3 is that in excess of those required for the initial onset of exoelectron emission N_0). In this example, the length (ℓ) of the psb is given by

$$\ell = 8 \times 10^{-3} (N - 3.5 \times 10^3) \mu\text{m for the single crystal} \quad (1)$$

and

$$\ell = 0.36 (N - 2.7 \times 10^3)^{1/2} \mu\text{m for the polycrystal} \quad (2)$$

and the respective growth rates are $8 \times 10^{-3} \mu\text{m/cycle}$ and $6.5 \times 10^{-2} \ell^{-1} \mu\text{m/cycle}$.

Scanning Electron Microscopy

Examination of the specimens in a scanning electron microscope did not reveal any obvious differences in terms of the topography of the psb extrusions. Each contained psb with similar structures, ranging from simple to more complex depending upon their maturity. In this regard, comparison with PEM images showed that the initial or mature portions of a psb had more pronounced extrusions than the freshly formed regions near an advancing tip. This tapering of the extent of extrusion is illustrated by the scanning electron micrograph in Figure 4.

DISCUSSION

The important finding of this investigation is that the growth kinetics of persistent slip bands in a single crystal are quite different from those in polycrystalline material. The rate of growth in the single crystal is constant, but in the polycrystal it varies as ℓ^{-1} . Therefore we conclude that in a single crystal a psb can elongate in a relatively unconstrained manner, whereas the growth of a psb in a small grain of a polycrystalline specimen is restrained by the surrounding material.

Model

The physical basis of our model is that i) the material within a psb has a lower yield stress than that of the surrounding matrix,

and ii) the elongation of the slip band involves a systematic conversion of the original matrix microstructure to a different and weaker form. This approach is based upon well documented evidence in the literature. For example, transmission electron microscopy of psb in aluminum alloys (Vogel et al. (8) and Stubbington (9)) has shown that the very small strengthening precipitates are dispersed or dissolved by the repetitive dislocation motion, creating a thin ($\sim 0.1 \mu\text{m}$) planar layer of material relatively free of precipitates. This permits dislocations to move more easily and can even lead to the formation of dislocation cell walls within the slip band ((9) and Lynch (10)). In fact very large cyclic strains (0.3 to 0.6) in psb have been measured directly by interferometry (Lee and Laird (11)). Other evidence for the creation of softer material within a psb has been found in single crystals of copper, nickel, and silver (Mughrabi (12)).

Thus, a grain containing psb can be regarded as a composite material consisting of a strong matrix containing thin planar lamella of softer material. Such a two phase composite model has been proposed previously to describe the cyclic stress strain curve of polycrystalline material (Pedersen et al. (13)). The cyclic stress creates a large predominantly-plastic deformation (ϵ_c) within the psb, but only elastic deformation (ϵ_g) in the matrix. The primary source of fatigue damage is the severe deformation in the psb, consisting of extensive dislocation motion which creates the surface extrusions, and simultaneously emits dislocations from the tip of the psb into the adjacent matrix material. This flux of emitted dislocations changes the microstructure in the adjacent matrix material and thereby elongates the psb. The rate at which this process occurs is assumed to be given by

$$\frac{d\ell}{dN} = \beta \epsilon_c \quad (3)$$

The total macroscopic strain (ϵ_T) contributed by a grain containing a slip band is

$$\epsilon_T = f \epsilon_c + (1 - f) \epsilon_g \quad (4)$$

where f is the fraction of the grain occupied by the slip band. For a slip band of length ℓ and thickness t in a grain of diameter D , $f \approx t\ell/D^2$. Since $t \sim 0.1 \mu\text{m}$ (8), the value of f is always very small ($< 10^{-2}$) even for fine grain material. Thus, to a good approximation

$$\epsilon_T = f \epsilon_c + \epsilon_g \quad (5)$$

Comparison with Experiments

The contribution to the macroscopic strain from the psb ($f \epsilon_c$) depends upon the experimental loading conditions.

FATIGUE 87

Polycrystalline Specimen. Consider a small grain containing a psb, surrounded by grains of different orientation which are only deforming elastically (a common occurrence in the early stages of fatigue). This neighboring material constrains the deformation of the grain under consideration, so that under the condition of constant cyclic amplitude ϵ_T is held constant. This constraint also maintains ϵ_g at a constant level throughout most of the grain. Thus to a first approximation

$$f \epsilon_c = \text{constant} \quad (6)$$

and $dL/dN \sim L^{-1}$, as was observed experimentally.

Single Crystal. In this case psb are initiated with equal probability across the entire width of the specimen so there is no constraint on the value of ϵ_T . As a soft psb develops ϵ_T will increase slightly, the additional contribution to elongation being accommodated elastically in the relatively long ends of the specimen. Thus, to a first approximation the crystal experiences a constant cyclic stress, and ϵ_c is constant. In this case dL/dN is constant, as was observed experimentally.

Single Crystal Under Constant Plastic Strain. An experiment in which a single crystal is fatigued under constant cyclic plastic strain would provide an additional test of our model, since $f \epsilon_c$ would be constant and should result in parabolic growth of the psb. While this experimental condition is not attainable in the PEM, it has often been employed in studies of psb formation in copper crystals. Unique among these is the work of Wang (14) who measured the vertical height of psb extrusions by a profiling technique in a scanning electron microscope. Wang's data is replotted in Figure 5 and clearly demonstrates a parabolic relationship. These results support our model and show that the processes of psb elongation and extrusion growth are controlled by the same driving force (ϵ_c).

SYMBOLS

- β = constant
- D = grain diameter (μm)
- ϵ_c = strain in psb
- ϵ_g = strain in matrix of grain
- ϵ_T = total strain of grain
- f = fraction of grain occupied by psb
- L = length of psb (μm)
- N = number of fatigue cycles

FATIGUE 87

N_0 = number of fatigue cycles to initiate psb

t = thickness of psb (μm)

REFERENCES

- (1) Forsyth, P. J. E., "The Physical Basis of Metal Fatigue", Blackie and Son, Ltd., London, 1969.
- (2) Laird, C., in "Dislocations in Solids", Edited by F. R. N. Nabarro, North Holland, 1983, pp. 54-120.
- (3) Mughrabi, H., Wang, R., Differt, K., and Essmann, U., in "Fatigue Mechanisms: Advances in Quantitative Measurement of Physical Damage", ASTM STP811, 1983, pp. 5-45.
- (4) Baxter, W. J. and Rouze, S. R., Met. Trans., Vol. 7A, 1976, pp. 647-654.
- (5) Baxter, W. J., Treatise on Materials Science and Technology, 19, "Experimental Methods, Part B", Academic Press, New York, 1983, pp. 1-66.
- (6) Baxter, W. J., in "Fundamental Questions and Critical Experiments on Fatigue", ASTM STP, 1985, In Press.
- (7) Baxter, W. J., Proceedings European Group on Fracture, Sheffield, England, 1985, In Press.
- (8) Vogel, W., Wilhelm, M., and Gerold, V., Acta Met., Vol. 30, 1982, pp. 21-30.
- (9) Stubbington, C. A., Acta Met., Vol. 12, 1964, pp. 931-939.
- (10) Lynch, S. P., in "Fatigue Mechanisms", ASTM STP 675, 1979, pp. 174-213.
- (11) Lee, J. and Laird, C., Phil. Mag. A, Vol. 47, 1983, pp. 579-597.
- (12) Mughrabi, H., Scripta Met., Vol. 13, 1979, pp. 479-484.
- (13) Pedersen, O. B., Rasmussen, K. V., and Winter, A. T., Acta Met., Vol. 30, 1982, pp. 57-62.
- (14) Wang, R., Doctorate Thesis, Stuttgart 1982. (Quoted by Mughrabi, H., ICSMA, 7, Montreal, 1985).

FATIGUE 87

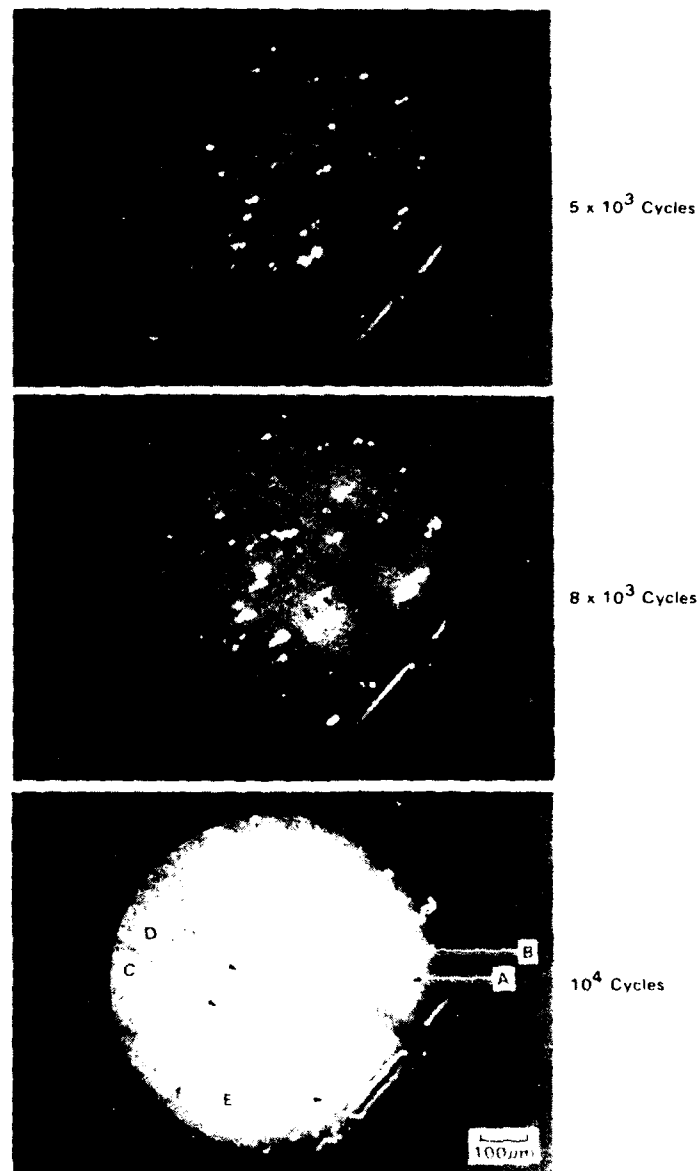


Figure 1. Photoelectron micrographs showing development of exoelectron emission from psb during fatigue of a single crystal of 6061-T6 aluminum.

FATIGUE 87

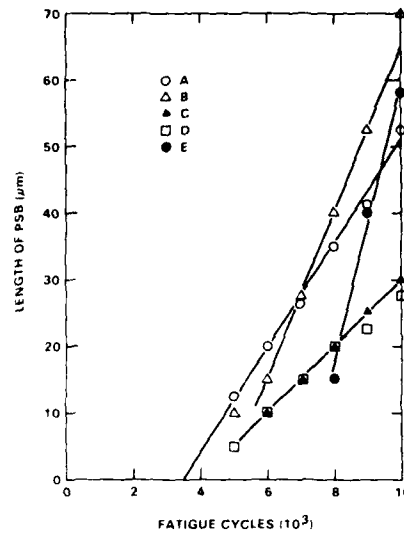


Figure 2. Effect of fatigue cycles on the length of the psb identified in Figure 1.

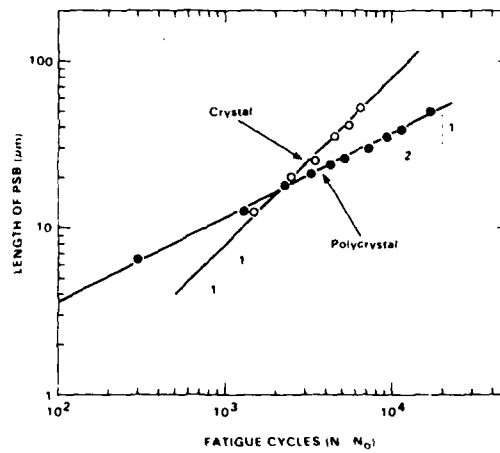


Figure 3. The elongation of a psb in a polycrystal compared to one in a single crystal. Note that the number of fatigue cycles (N) is corrected for the number of cycles (N_0) required to initiate the psb.

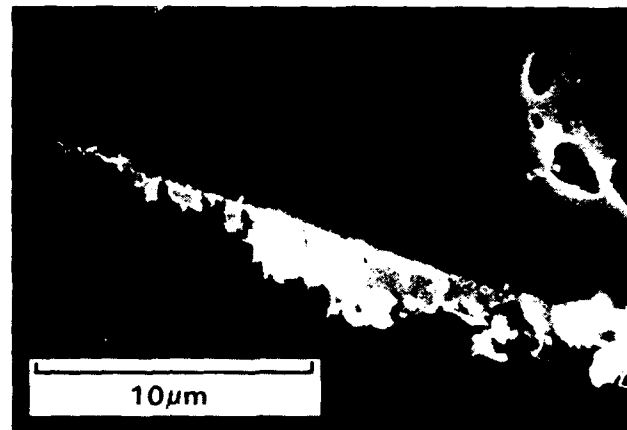


Figure 4. Scanning electron micrograph of a portion of psb C in Figure 1.

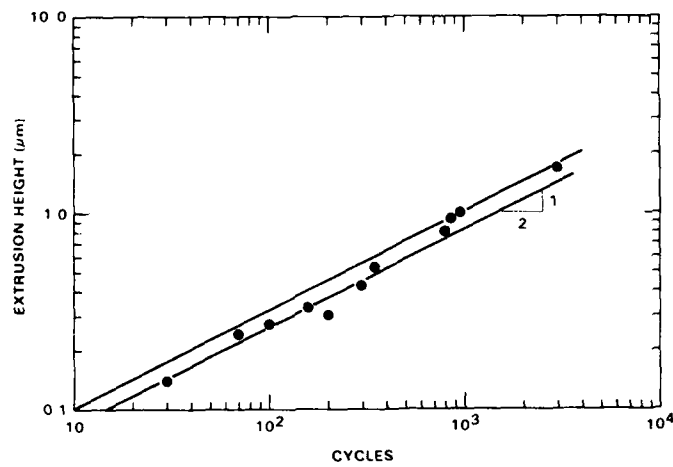


Figure 5. Effect of fatigue cycles on the average height of psb extrusions on a single crystal of copper. From the data of Wang (14).

FATIGUE 87

THE MECHANICS OF FATIGUE-CRACK NUCLEATION IN A LOW-ALLOY STEEL
UNDER FRETTING CONDITIONS

J. Beard* and P.F. Thomason*

A novel fretting-fatigue test rig, giving close control and monitoring of contact stresses and slip-amplitude at a spherical "Hertzian" fretting contact, was used to establish the progressive mechanism of fretting-fatigue. Metallographic analysis by SEM and TEM methods revealed the presence of very hard white-etching layers which were found to fragment and break away from the fretting-contact surface at regular intervals. The paper contains tentative proposals for the mechanism of fatigue-crack nucleation under fretting conditions, in the presence of white-etching layers.

INTRODUCTION

The present work was carried out with the object of establishing the detailed mechanism of fatigue-crack nucleation, in a low-alloy steel, under fretting conditions. The fretting experiments were performed as a series of interrupted tests, to various fractions of the total fretting-fatigue life, to observe the progressive development of fretting-fatigue damage with the aid of SEM and TEM methods.

An important feature of the present experiments was the choice of a spherical 'Hertzian' fretting-contact pad which gave a controlled contact-stress field, without the presence of the large localised stress concentrations and discontinuities which are present at a flat fretting pad. The experiments showed that an unusual metallurgical transformation occurs in the surface layers of material at a fretting contact which results in the formation of an extremely hard and brittle layer. These transformed surface-layers began to develop at isolated points over the

* Department of Aeronautical and Mechanical Engineering,
University of Salford, Salford M5 4WT, UK.
Now at National Centre of Tribology, UKAEA, Warrington, WA3 6AT,
UK.

fretting surface and were found to have a featureless appearance after metallographic etching; they are therefore referred to subsequently as white-etching layers. These hard and brittle layers were found to have an important influence on the mechanisms of both fretting-wear and fatigue-crack nucleation.

THE FRETTING-FATIGUE EQUIPMENT

In most previous experimental work on fretting the low levels of cyclic-slip amplitude at the fretting contact have been obtained by direct utilisation of the cyclic elastic straining of a fatigue specimen. Various flat-faced fretting pad and bridge arrangements (1) (2) (3) have been used to give a relative slip-displacement across the 'feet' of the bridge device, when the specimen is subjected to cyclic fatigue loading. The completely 'floating' bridge device used by Field and Waters (1) has the primary disadvantage that neither end of the bridge is fixed relative to the specimen and hence only the sum of the slip amplitudes at the two fretting pads is known; a disproportionate and varying amount of slip may therefore occur at the two pads over the course of an experiment. Attempts to eliminate this 'floating' effect have been made by Ording and Ivanova (2) and McDowell et al (3) by fixing one end of the 'bridge' relative to a point on the specimen. However, in these experiments no attempts were made to measure directly the magnitude of relative displacements at the pad/specimen interface during testing and since relatively large clamping forces are required with a flat-pad contact, any changes in the mean coefficient of friction at the pad/specimen interface could have produced substantial variations in the estimated levels of slip amplitude.

An additional limitation of the flat-pad type of fretting contact concerns the large stress concentration which develops in the substrate, adjacent to the square corners of the pad, when the fretting interface is subjected to shear loading. The theoretical solution for a band of uniform shear stress on the surface of the half-plane (Muskhelishvili (4)) gives the result in Fig. 1a, which shows the presence of stress singularities at the ends of the loading band. Wright and O'Connor (5) have studied the stress-concentration effect at the corners of a flat pad in contact with the half-plane, using finite-element models, and have confirmed the complexity of the stress and displacement fields at an ostensibly simple contact geometry. It seems reasonable to conclude, therefore, that in order to achieve a clear understanding of the fatigue-crack nucleation process under fretting conditions, it is necessary to utilise a fretting contact geometry which has been analytically modelled, and which is free from singularities and discontinuities in the contact stress field.

Following a wide-ranging review of the surface-contact problem it became clear that only the Hertzian "sphere and plane" geometry

(6)(7) fulfills the above requirements. Hamilton and Goodman's results (7) for the surface stress component σ_x , on the longitudinal axis of symmetry of a sliding Hertzian contact are plotted in Fig. 1(b); this graph shows that the σ_x stress reaches a sharp tensile maximum at the trailing edge of the spherical contact, but unlike the flat-pad type of contact (Fig. 1(a)) there is no stress singularity. A further important feature of the circular Hertzian contact, in the present context, is the low level of micro-slip before the onset of gross sliding and the fact that the extent of micro-slip can be readily determined analytically. It was therefore decided to base the design of the present fretting-fatigue equipment on the 'sphere and plane' fretting-contact geometry. The spherical-contact geometry does not appear to have been used before in fretting-fatigue experiments, even though it has the major advantage of being a self-aligning geometry.

The fretting-test equipment used in the present experiments is shown schematically in Fig.2 and this incorporates a bridge arrangement designed to eliminate the uncertainties in measuring slip amplitude which would have been present with a floating bridge of the type used in previous work (1). The equipment was designed to fit in the standard specimen holders on an Ansler Vibraphore fatigue machine, and the spherical fretting pad is mounted on the end of a lever arm which has a fulcrum positioned at the lower end of the fretting-fatigue specimen. This arrangement restrains the fretting-pad base plate in the direction of sliding, whilst allowing free movement in the direction of normal contact loading. Dead weight loading via a pulley-wheel system is a simple and precise method of applying the relatively small normal contact loads that are needed to give high stresses at a Hertzian contact. This loading arrangement also has the added advantage of being self-compensating for wear of the fretting contact (with a proving-ring loading system, where the compliance is very low, small amounts of wear can cause considerable load variation). A second lever arm is utilised to hold a small rolling element bearing against the opposing flat of the fatigue specimen and by this means a side load, equal and opposite to the normal fretting load is applied to eliminate any bending stress which might otherwise be induced in the specimen. An important feature of the present fretting-test equipment is the incorporation of a pre-loaded bearing at the lever-arm fulcrum. The fulcrum is composed of a needle roller bearing which has had the external surface of the outer race ground back to leave three raised platforms (Fig.2). When fitted in the housing the outer race is located on two of the platforms; a load is then applied, by means of a screw, to the third platform which is just sufficient to distort the race and induce a slight pre-load on the bearing. In this way any free radial play is removed from the bearing, thus eliminating a possible source of inaccuracy when measuring the slip amplitude in the fretting experiments.

The fretting pad is mounted on a fretting-head assembly (Fig.2) which contains a piezo-electric transducer polarised to measure the tangential fretting-contact force. The fretting-head assembly can be positioned and clamped to the lever arm (Fig.2), at any required position over the full gauge length of the fatigue specimen, to give an extensive range of variations in the fretting slip-amplitude. The precise magnitude of the slip-amplitude in a given experiment is monitored by means of a small inductive transducer which measures the relative displacement between the specimen and fretting pad adjacent to the contact surface. The output signals from both the tangential-force and slip-displacement transducers were used to give continuous monitoring of the fretting shear-force and slip-amplitude, respectively, throughout each fretting experiment.

THE FRETTING-FATIGUE EXPERIMENTS

The material used for the manufacture of the fretting fatigue specimens was a low-alloy manganese molybdenum steel supplied to En 16T(BS 970-1955) specification; the cast analysis was 0.34% C, 0.31% Si, 1.49% Mn, 0.23% Mo, 0.031% S, 0.007% P. The steel was in the form of 25.4mm diameter rolled bar hardened by oil quenching at 850°C and tempered at 600°C for two hours. Preliminary experiments established that the specimen material had a 0.2% proof stress of 765 MN/m², and the fatigue limit in the absence of fretting was found to be $\pm 420\text{MN m}^{-2}$. The fretting fatigue specimen was in the form of a standard push-pull type of fatigue specimen with a reduced working section of 4.25mm diameter. Two parallel tangent planes were fine ground over the gauge length of the fatigue specimens; one of the flat surfaces was then chosen as the test surface and polished to a metallographic finish. The spherical fretting pads used throughout the present work were machined by a wire-erosion process from a commercial 50.8mm diameter 1% chrome steel ball bearing of En 31 specification.

The present experiments were designed to investigate the progressive development of fretting damage and not, as in the majority of previous work, rely solely on observations made at the end of a completed fretting test. The procedure consisted of establishing the total fretting-fatigue life under a particular set of loading conditions, and then carrying out experiments on separate specimens under identical test conditions but for varying proportions of the total fretting fatigue life. For the main series of experiments reported in this paper the specimens were subjected to a bulk fatigue stress of $\pm 290\text{MN m}^{-2}$ (69% of the normal fatigue-limit stress) and a normal contact load on the fretting pads of 46N. Tests were carried out with the fretting pads located at either the top or bottom of the specimen gauge length which gave slip amplitudes of either 18 microns or 6 microns, respectively. In the subsequent discussion, the terms high and low slip amplitude will be adopted to indicate that the slip levels are nominally 18μ

FATIGUE 87

and 6 μ respectively. All the tests described in the present paper were carried out in the normal laboratory environment at room temperature; the test frequency used throughout the experiments was 69 Hz.

RESULTS

Although only a limited amount of information was obtained by the direct SEM examination of the fretting scar surface there were nevertheless several interesting features; damage to the fretting contact surface was found to be extremely rapid and a well established wear scar had developed after low-amplitude fretting of 1300 cycles (9). The surface damage continued to increase in severity, with increasing number of fretting cycles, until the deterioration in surface finish appeared to stabilise at about 10,000 cycles, beyond this stage a new feature began to develop in the form of micro-pitting (9). With further increase in fretting to 35,000 cycles and beyond, the fretting scar began to develop an extensive smeared layer of oxide debris which concealed microscopic surface features in direct SEM examinations. All subsequent examinations of fretting damage were therefore made by longitudinal microsectioning of the wear scar.

The micro-sections showed that the fretting scar surfaces invariably developed very hard white etching layers, the magnitude and extent of which was found to increase approximately in proportion to the level of the slip amplitude. Thin-foil TEM analysis revealed that these white etching layers were of b.c.c. ferrite with a cell size of the order of 100 \AA (9). Under low slip amplitude conditions there was evidence as early as 1000 cycles of white etching layer formations covering the central area of the scar. The white etching layers were found to be in the form of lens shaped platelets, the largest of which measured less than 2 μ thick by 8 μ long on the micro section. The initial rapid surface roughening and micro pitting observed in the fretting experiments appeared to be the result of a proportion of these white etching platelets breaking up and becoming detached. Many of the white etching platelets were found to exhibit signs of internal micro cracking and loss of cohesion with the substrate, with the micro-cracks often being oriented at a shallow angle to the surface of the platelets.

With increasing number of cycles the white etching platelets which were still strongly bonded to the substrate showed a tendency to merge together to form an almost continuous layer over the entire central region of the scar. From this point on, which occurred at around 10,000 cycles, the layer increased in size until by 90,000 cycles it had grown to a length of 90 μ and a thickness of 6 μ , Fig.3. For the present set of fretting conditions the white etching layer did not have the opportunity to develop much beyond this size since converging micro-cracks were invariably nucleated

FATIGUE 87

at the boundaries of the layer. These cracks, which were inclined at approximately 20° to the surface, eventually linked up to dislodge the white-etching layer and produce a large pit on the surface of the specimen. Measurements of the average fretting-scar diameter clearly indicated the onset of crack coalescence and pitting by a sudden increase in the fretting scar size (9). Micro-hardness tests on residual pieces of white-etching layer on a specimen which had been subjected to fretting for 100,000 cycles gave hardness values in the range 946Hv to 1312Hv. At the same time micro-hardness readings of the substrate material, immediately adjacent to the white-etching layers, were still equal to that of the bulk material before fatigue testing; i.e. 285Hv.

DISCUSSION

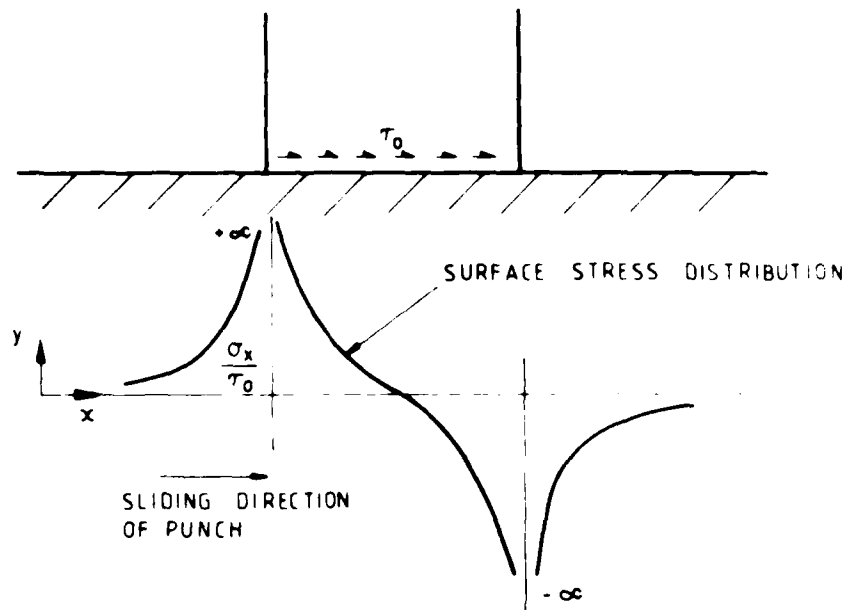
The metallographic observations of the fretting scar indicate that white etching material forms over the centre of the contact area where, according to the Hertz theory, the shear traction and contact pressure are at a maximum. The results also show that increased slip-amplitude levels promote increases in both the rate of formation and the total size of the white etching layer. At the high slip-amplitude level the white etching layers were found to grow to more than 30μ thick before becoming so extensively fatigue cracked (Fig.4) that spalling often occurred resulting in, for a short interval, a rapid increase in the wear rate, (9). In the early stages of fretting (typically up to 10,000 cycles) a deterioration in the surface finish of the contact region appeared to be largely due to the spalling of microscopic platelets of white etching material, which were typically less than 10μ in length by 2μ thick.

It appears from the present experimental results that the mechanism for the nucleation of fretting fatigue cracks in a low-alloy steel is strongly influenced by the formation of hard and brittle white-etching layers on the fretting contact surface. The intermittent formation and spalling of the white-etching layers (Figs. 3 and 4) not only influences the wear rate, but also leads directly to the nucleation of fatigue cracks. This general effect is illustrated by the microsection of a fretting scar in Fig 5 where the fatigue-crack nucleus originates at the apex of an approximately triangular fragment of white etching layer, this white-etching fragment is situated in a region where a large white etching layer has been broken down by the spalling effect (9). The precise mechanism of white etching layer formation and fatigue-crack nucleation, at a fretting contact, will be considered in a later paper when a more detailed SEM and TEM analysis of the results will be presented.

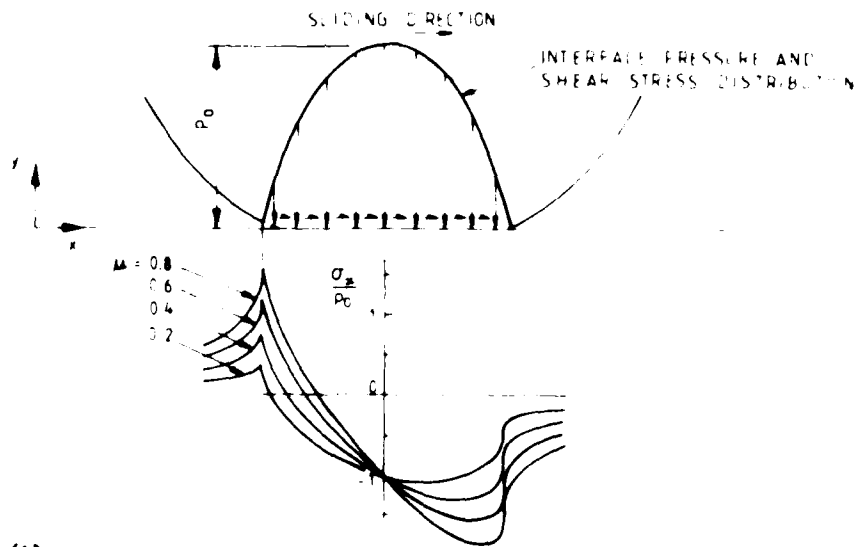
FATIGUE 87

REFERENCES

- (1) Field, J.E. and Waters, D.H., NEL Report No.275, 1967.
- (2) Ording, I.A. and Ivanova, V.S., Proc. Int. Conf. on Fatigue in Metals, Instn. of Mech. Engrs., 1956, p. 408.
- (3) McDowell, J.R., Tierney, W.D. and McClallan, A., ASTM STP No.144, 1952.
- (4) Muskhelishvili, N.I., "Some Basic Problems of the Mathematical Theory of Elasticity", Nordhoff, The Netherlands, 1963.
- (5) Wright, G.P. and O'Connor, J.J., Proc. Instn. of Mech. Engrs., Vol.186, 1972, p.827.
- (6) Hertz, H., "Miscellaneous Papers", (transl. by Jones, D.E. and Schott, G.A.), Macmillan, New York, 1896.
- (7) Hamilton, G.M. and Goodman, I.E., Trans. ASME, J. Appl. Mech., Vol.33, 1966, p.371.
- (8) Feng, I.M. and Rightmore, B.G., Proc. Instn. of Mech. Engrs., Vol.170, 1956, p. 1056.
- (9) Beard, J., PhD Thesis, University of Salford, 1982.



(a)



(b)

Figure 1 The surface stress distribution σ_x when (a) a band of uniform shear stress τ_0 acts on the surface of the half plane. (b) a spherical contact slides on the surface of a semi infinite body

FATIGUE 87

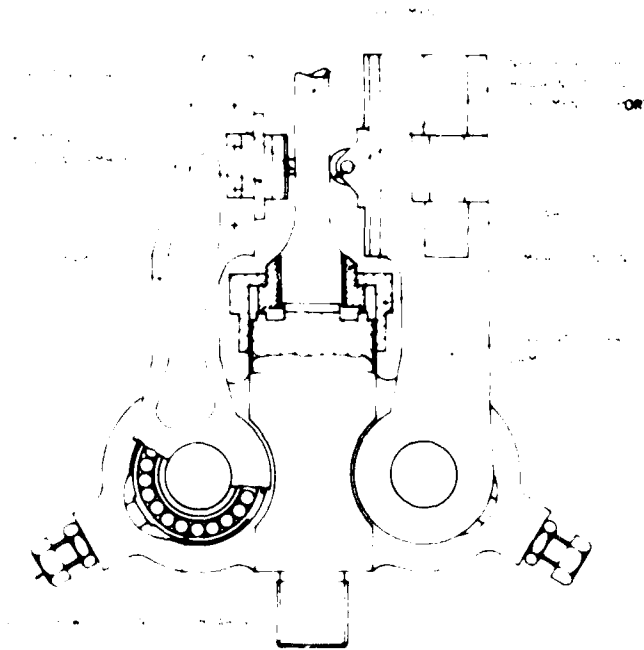


Figure 2 The fretting fatigue equipment



Figure 3 Microsection of white etching layer after 90,000 fretting cycles, low slip amplitude, low bulk-fatigue stress

FATIGUE 87



Figure 4 Optical microsection of white etching layer after 20,000 cycles, high slip amplitude, low bulk fatigue stress



Figure 5 Nucleation of a fretting fatigue crack at site of fragmented white etching layer after 100,000 cycles, high slip amplitude, low bulk fatigue stress

FATIGUE 87

THE EFFECTS OF THIN ANODIC FILMS ON THE CYCLIC MICROSTRAIN / MACROSTRAIN BEHAVIOR OF TUNGSTEN

by Keith J. Bowman* and Ronald Gibala*

The occurrence of film softening or hardening effects in bcc metals is dependent on the relative mobilities of edge and screw dislocations at different homologous temperatures. In this investigation, the difference in the contributions of edge and screw dislocations to plastic flow at different strain levels is used to evaluate the role of thin anodic films in cyclic deformation of W at 298 K. Large reversible hardening effects observed at cyclic microstrains and smaller softening effects which occur at cyclic macrostrains are described in terms of the dominant dislocation species for the two plastic strain regimes.

INTRODUCTION

An understanding of surfaces and the effects of surface modification processes is critical in evaluating mechanical behavior because minute differences in the weight or volume fraction of a material that is directly modified can produce extraordinary changes. The dramatic softening effects of thin oxide films demonstrated by Gibala and co-workers on the monotonic flow behavior of bcc metals (e. g. Figure 1) (1,2) and the B2 intermetallic alloy NiAl (2,3) are examples of large changes in mechanical response from surface modification. At low homologous temperatures ($T \leq 0.10T_m$), these materials have displayed reductions in flow stress greater than 50% and remarkable increases in ductility through the application of thin (50-350nm) thermal or anodic oxide films. It is now recognized that preferential generation of mobile edge dislocations at the film-substrate interface allows plastic flow at stresses much lower than normally required for macroscopic deformation by motion of less mobile screw dislocations at these temperatures. At

*The Department of Materials Science and Engineering
The University of Michigan, Ann Arbor, Michigan 48109

higher temperatures, ($0.10T_m < T < 0.5T_m$), the same anodic films effect an increase in flow stress associated with inhibited egress of dislocations under conditions in which the mobilities of edge and screw dislocations are not greatly different. In the present investigation, the effects of thin anodic films have been explored in two distinct regimes of cyclic stress-strain behavior, viz, cyclic macrostrain and cyclic microstrain. The results illustrate that a small softening effect occurs in high-stress cyclic macrostrain and an enormous, remarkably reversible hardening effect occurs in low-stress cyclic microstrain for W single crystals tested at room temperature. The reversible nature of these effects during film removal/re-application experiments and associated slip behaviors is described in terms of the current understanding of dislocation dynamics for bcc metals.

Both hardening and softening effects have been observed when thin films are applied to pure crystals (4). The change in flow stress, whether an increase or decrease, appropriately illustrates the dislocation dynamics governing mechanical behavior. Most observations of film hardening occur under circumstances in which macroscopic deformation is accomplished by cooperative motion of edge and screw dislocations possessing similar intrinsic mobilities. In bcc metals this corresponds to moderate homologous temperatures, e.g. $T > 0.10T_m$, whereas for fcc metals, flow is dominated by the combined glissile motion of edge and screw dislocations to very low temperatures. Hardening under these circumstances is usually attributed to hindered egress of dislocations by the surface film. An example of film hardening is shown in the lower part of Figure 1 for Nb single crystals deformed at $0.11T_m$ (1). Note the higher flow stress in the surface anodized, i.e. modified (M) vis-a-vis unmodified (U) Nb.

Softening effects are observed for different reasons. For example, an increased mobile dislocation density in an otherwise dislocation-starved material (e.g. whiskers) or an increase in the fraction of specific higher mobility dislocation types can produce a softening effect. As with any mechanical behavior phenomena, softening effects must be analyzed in relative terms. In bcc metals, softening can be observed easily because the flow stress becomes very large at low temperatures. Typical film softening is shown for Nb at $0.03T_m$ and $0.07T_m$ by comparison of the behavior of modified and unmodified single crystals in the upper portion of Figure 1. Since a much greater force is necessary for screw dislocations to

achieve mobile core configurations at low temperatures, screw dislocations are less mobile than edge dislocations (5). Low-stress motion of the available glissile edge dislocations prior to macroscopic flow at much higher stress levels is termed microstrain. Microstrain is very limited in extent in well annealed crystals. Therefore, evaluation of microstrain in monotonic deformation usually requires some prior prestrain (6). Because the surface film softening effect produces an increased supply of edge dislocations, it can be considered to increase the extent of microstrain, or at least to increase the amount of plastic flow at similarly low stress levels. Thus, low-stress monotonic flow behavior of bcc metals is dependent on the amount of plastic strain which can be accommodated by the more mobile dislocation species prior to motion of the less mobile dislocation species at higher stress levels. For moderate temperatures where the cooperative motion of edge and screw dislocations possessing similar mobilities persists to large strains, relatively low work hardening rates are observed. For low temperatures where there is a difference in the mobilities of edge and screw dislocations, the supply of the more mobile dislocation species, in this instance edge dislocations, determines the extent of microstrain-type flow. The range of temperature, applied stress and plastic strain for which this low-stress flow occurs is shown in Figure 1 by the cross-hatched region.

Cyclic deformation provides a unique opportunity to explore film effects under essentially constant dislocation structure in a way not possible in monotonic experiments. In cyclic deformation, the distinct regimes dominated by motion of edge dislocations and screw dislocations, respectively microstrain and macrostrain, can be sustained to large accumulated strains without failure of the specimen as occurs in monotonic deformation to large strains. Thus, film effects can be explored for two very different types of dislocation motion under the near steady-state conditions of cyclic saturation. Such experiments are described in this paper.

EXPERIMENTAL

W single crystals of a $\langle 123 \rangle$ orientation with the same surface modification which produces substantial softening effects in monotonic tensile deformation (7) were used in the present cyclic deformation experiments. For the W data reported here, the unmodified (U) condition corresponds to zone melted and ultra-high vacuum annealed

single crystals. The modified (M) condition corresponds to anodization of the W crystals in 0.01M H_2SO_4 at a potential of 40V which produces an ~80nm anodic film. Film removal was accomplished by dissolution of the anodic film in 0.05M NaOH solution. This solution removes the visible blue interference color film in less than one second. To insure that removing the specimen from the machine did not influence subsequent testing, film removal procedures were repeated *in situ* during a pause at zero strain in the tension half of a cycle by squirting the specimen gage section with the dilute NaOH solution and immediately afterwards with a tap water rinse. Both solutions were at room temperature when applied and caused only small, insignificant zero shifts from changes in specimen temperature. Similar application of tap water to the specimen in the unmodified and modified conditions did not alter the observable film color and produced no hardening or softening effect. The cyclic deformation experiments were performed using a controlled plastic strain amplitude and a fixed total strain rate. Details of the specimen preparation and experimental procedures have been given elsewhere (8).

RESULTS AND DISCUSSION

The relationship between modulus-compensated saturation stress and plastic strain amplitude at various homologous temperatures and strain rates for several different bcc metals is shown in Figure 2. The results for unmodified (U) and modified (M) W are from our current research and those for other bcc metals are from investigations which utilized similar specimen orientations with no surface modification (9-12). For results from investigations on other bcc metals smooth curves were drawn through data, with the thickness of the lines corresponding approximately to errors in extracting data from published figures. Tensile saturation stresses are shown normalized to Young's modulus. Cyclic deformation of unmodified bcc metals at low homologous temperatures produces two distinct regimes of cyclic deformation behavior corresponding to cyclic macrostrain at high stresses and cyclic microstrain at low stresses (8). At higher homologous temperatures the difference between the two regimes becomes small and the cyclic stress-strain behavior of bcc metals begins to resemble the behavior shown for fcc metals. When normalized by elastic modulus, the cyclic stress-strain curves for fcc metals for $T \leq 0.50T_m$ will

generally fall within the thickness of the line so designated, however a relatively small temperature dependence of saturation stresses has been reported for Cu (13, 14). The cyclic stress-strain behavior in Figure 2 and the monotonic deformation behavior shown in Figure 1 are related. Multiplication and difficult motion of both primary and secondary screw dislocations in cyclic macrostrain leads to the formation of a cell-type dislocation structure with large accumulations of dislocation loop debris at large accumulated strains (9). Additionally, the stress level for cyclic macrostrain is a very strong function of temperature and strain rate. Monotonic flow behavior to macrostrains at low homologous temperatures like that shown for Nb in Figure 1 results in the same type of dislocation structures and is also very temperature and strain rate sensitive. Cyclic microstrain is characterized by relatively little dislocation multiplication and easy back and forth glide of edge dislocations. The extent to which cyclic microstrain persists increases with increasing temperature and decreasing strain rate, even though the actual stress level is fairly insensitive to temperature and strain rate. This increased extent of the low-stress microstrain regime with increasing temperature is a result of an increased contribution from thermally-assisted motion of screw dislocations. Microstrain measurements made in monotonic deformation have the same characteristics. Note the similarity between the persistence of low-stress cyclic microstrain behavior to greater strain levels at higher homologous temperatures and the increased extent of low stress flow in monotonic deformation of Nb when the temperature is increased from $0.03T_m$ to $0.11T_m$. For the conditions in which the experiments on W were conducted, the difference between the cyclic macrostrain and cyclic microstrain stress levels is very large, $\sim 600\text{MPa}$. The two primary observations of this investigation are a small film-induced softening effect in cyclic macrostrain and a very large film-induced hardening effect in cyclic microstrain. Because the deformation mechanisms involved are very different, the effects of thin anodic films on cyclic macrostrain and cyclic microstrain will be described separately.

Cyclic Macrostrain

At macroscopic plastic strain amplitudes $\epsilon_p > 1 \times 10^{-3}$,

the interaction of surface film softening effects with cyclic hardening produces a reduction in saturation stresses of 30-50MPa. This cyclic softening effect occurs by an edge dislocation pumping effect as for monotonically film-softened Nb in Figure 1. Although in fractional terms this is a small effect, the absolute size of this effect is very close to the observed macroscopic softening effect in tensile deformation of W on the first quarter cycle of the experiment (15). This effect is easiest to produce in specimens which have been anodized prior to cyclic deformation, but, as shown in Figure 3, it is observed as well by applying the anodic film soon after cyclic saturation is reached. At accumulated strains, ϵ_{acc} , well beyond saturation, anodization produces little or no effect and *in situ* removal of the film does not produce observable hardening or softening effects. Furthermore, from observations on both $\langle 123 \rangle$ and $\langle 110 \rangle$ oriented crystals (15) the softening effect occurs primarily in tension, with little or no effect in compression. Note in Figure 3 that the compression peak stresses are nearly identical in the unmodified and modified conditions. This result corresponds to a greater monotonic softening effect observed in tensile deformation than in compressive deformation of anodized W by Talia (16). It is also consistent with the determination of tensile anodization growth stresses in W thin foils by Bowman (17). In cyclic macrostrain, very different surface slip behavior is observed at the same ϵ_{acc} for the unmodified and modified conditions (15). At $\epsilon_{pl}=0.00375$ surface modification produces coarse, wavy-slip combined with fairly straight slip bands corresponding to anomalous, low Schmid factor $\{110\}$ planes. This is contrary to fairly fine slip observed on $\{112\}$ planes for the unmodified material. This substantial difference in surface slip features in the unmodified and modified conditions suggests that the thin anodic film has a very strong effect on deformation behavior near the surface, even though the change in mechanical response is relatively small in cyclic macrostrain.

Cyclic Microstrain

At microstrain levels, $2.5 \times 10^{-5} < \epsilon_{pl} < 1 \times 10^{-4}$, saturation stresses are very sensitive to the presence of thin anodic films. At $\epsilon_{pl} = 7.5 \times 10^{-5}$ the increase in saturation stress is greater than 400MPa! The clearest demonstration of the film hardening effect in cyclic microstrain is shown in experiments wherein the film is repeatedly ap-

plied to the surface and later removed by *in situ* dissolution, Figure 4. Application of an 80nm anodic film to a soft, cyclically microstrained specimen at $\epsilon_p \approx 7.5 \times 10^{-5}$ resulted in rapid cyclic hardening when cyclic deformation was resumed under the same conditions. The specimen hardened over 300MPa in 125 cycles and had not yet reached saturation. Upon removal of the anodic film in a dilute NaOH solution, cyclic softening was immediate. The rate of softening was nearly equal to the prior hardening rate and the peak stresses quickly approached the original saturation level. Although still substantial, the rate of softening or hardening diminished as further re-application/removal iterations were carried out. Nonetheless, at $\epsilon_{acc} \approx 1$, the peak stress still dropped by over 100MPa upon removal of the film. The difference in visible slip features between unmodified and modified W is dramatic for specimens cycled to $\epsilon_{acc} = 0.05$ at $\epsilon_p = 5 \times 10^{-5}$ (15). For the unmodified material $\langle 111 \rangle$ slip is prevalent on both $\{110\}$ and $\{112\}$ planes, whereas the presence of the anodic film almost totally suppresses the occurrence of visible slip markings. This observation, coupled with rapid cyclic hardening upon re-application of the anodic film, suggests that the hardening effect is associated with difficult egress of dislocations at the surface in the modified condition.

With the exception of the magnitude, the cyclic film hardening effect in microstrain at low homologous temperatures parallels the monotonic film hardening observed in bcc metals at moderate homologous temperatures during macroscopic flow. In both instances, a low stress level is maintained by the fairly easy motion of available mobile dislocations. In cyclic microstrain at low homologous temperatures there is a steady-state supply of high mobility edge dislocations and in monotonic deformation to macrostrain levels at moderate homologous temperatures both edge and screw dislocations are mobile. For both types of deformation an effective reduction in the supply of mobile dislocations produces hardening. An argument complimentary to that expressed earlier for film softening is that film hardening is likely to occur mainly in materials that are intrinsically soft. Any disruption of dislocation motion or dislocation multiplication and exhaustion processes in a material that already has an abundant supply of mobile dislocations will produce a hardening effect as observed at cyclic microstrain at low

temperatures and in monotonic macrostrain at higher temperatures in bcc metals. On the other hand, it is difficult to make a very hard material even harder. Providing an increased supply of more mobile edge dislocations by the presence of anodic films at macrostrains and low homologous temperatures is expected to produce a softening effect.

ACKNOWLEDGEMENTS

This research is supported by the National Science Foundation, Grant No. DMR-850675

REFERENCES

- (1) Sethi, V.K. and Gibala R., Acta Met., Vol. 24, 1977, 321.
- (2) Noebe, R. D. and Gibala R., "Structure and Deformation of Boundaries", Edited by K. N. Subramanian and M. A. Imam, TMS, Warrendale, Pennsylvania, 1986, 89.
- (3) Noebe, R. D. and Gibala R., Scripta Met. Vol. 20, 1986, 1635.
- (4) Latanision, R. P. and Fourie, J. T., Editors, "Surface Effects in Crystal Plasticity", NATO Advanced Study Inst., Noordhoff, Leyden, Netherlands, 1977.
- (5) Christian, J. W., Met. Trans., Vol. 14A, 1983, 1256.
- (6) McMahon, C. J., Editor, "Microplasticity", Wiley Interscience, New York, New York, 1968.
- (7) Talia, J. E., Fernandez, L., and Gibala, R., Scripta Met., Vol. 12, 1978, 737.
- (8) Bowman, K. and Gibala, R., Scrip. Met., Vol. 20, 1986, 1451.
- (9) Mughrabi, H., Herz, K., and Stark, X., Int. J. of Fracture Vol. 17, 1981, 193-203.
- (10) Mughrabi, H., Herz, K., and Stark, X., Acta Met., Vol. 24, 1976, 659.
- (11) Guiu, F., Planell, J. A. and Anglada, M., "Dislocations in Real Materials", Edited by M. H. Loretto, Institute of Metals, London, England, 1985, 263.
- (12) Anglada, M. and Guiu, F. Phil. Mag., Vol. 44, 1981, 499.
- (13) Basinski, Z. S., Korbel, A. S. and Basinski, S. J. Acta Met., Vol. 28, 191.
- (14) Laird, C. and Buchinger, L., Met. Trans., Vol. 16A, 2201.
- (15) Bowman, K. J., Ph.D. Thesis, The University of Michigan, Ann Arbor, Michigan, 1987.
- (16) Talia, J. E., and Gibala, R., unpublished results.
- (17) Bowman, K. J., EMSA Proceedings, 1986, 700.

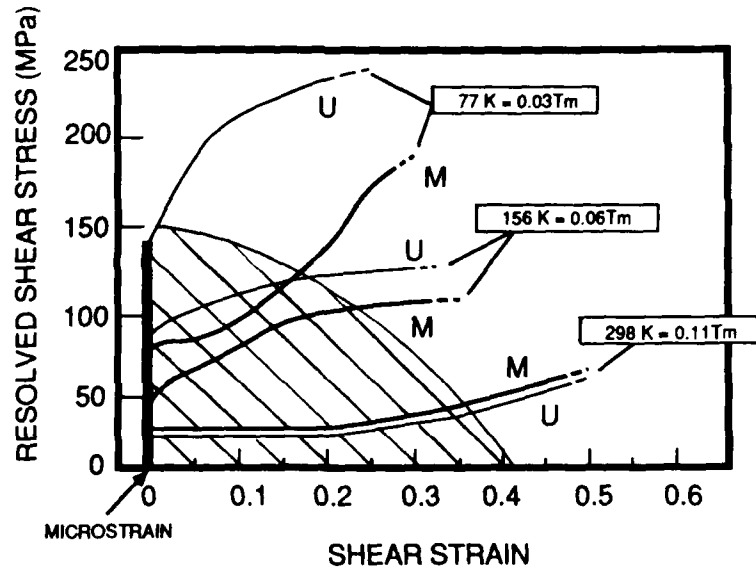


Figure 1: The effects of a thin oxide film on the monotonic flow behavior of Nb single crystals. See reference (1) for details.

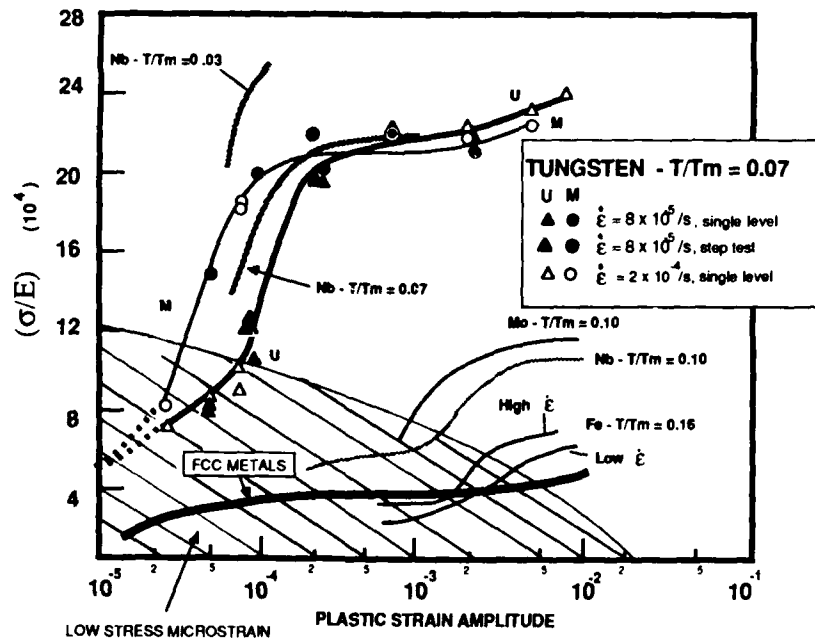


Figure 2: Modulus-compensated saturation stresses for modified and unmodified W as compared to other bcc metals (9-12).

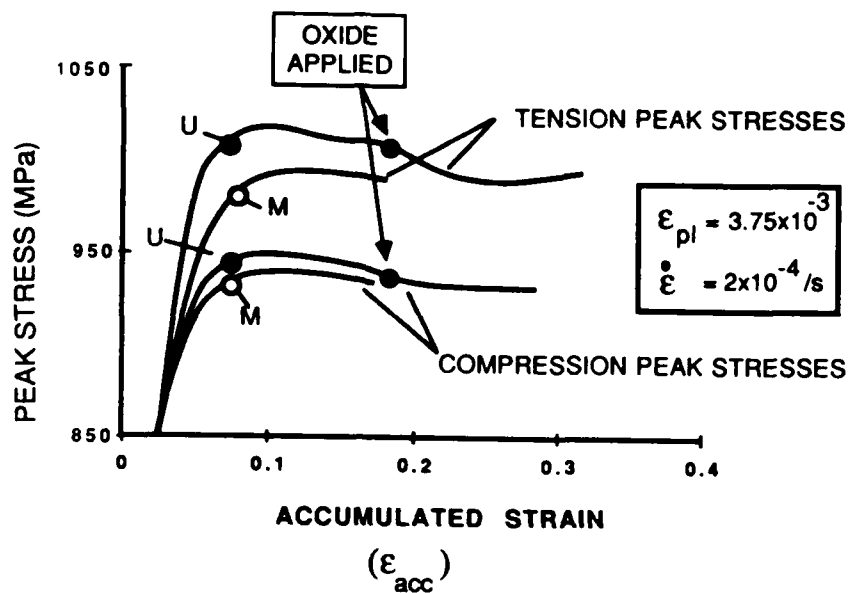


Figure 3: The effect of the thin anodic film on cyclic hardening behavior in cyclic macrostrain of W.

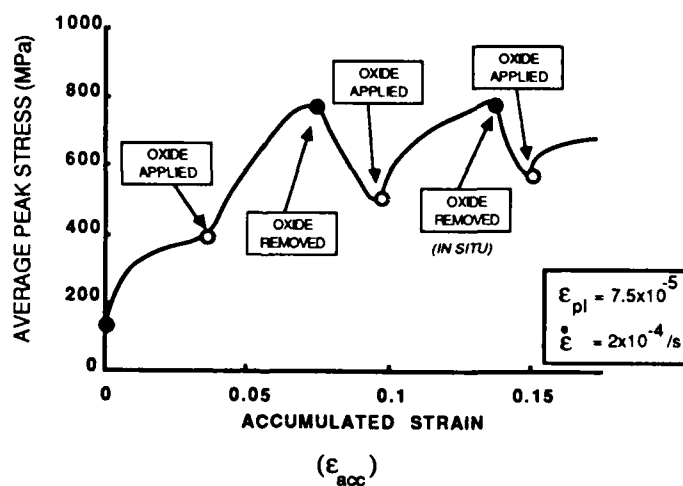


Figure 4: The effects of successive application and removal of the anodic film on cyclic hardening behavior in cyclic microstrain of W.

FATIGUE 87

SURFACE DEFORMATION AND FATIGUE CRACK INITIATION OF α -IRON SINGLE CRYSTALS

C. S. Kim, Y. W. Chung and M. E. Fine*

The cyclic deformation and fatigue crack initiation properties of α -iron fatigued under plastic strain control were investigated as a function of orientation. Single slip, double slip and localized deformation in the form of macroscopic deformation bands brought about by plastic instability were observed. Cracks were found to initiate at slip lines anywhere from 100 to 20,000 cycles depending on crystal orientation at a plastic strain amplitude of 5×10^{-4} .

INTRODUCTION

Much work has been done on the monotonic deformation properties of α -iron (1-7) and of BCC materials in general (8-10). More recently, the cyclic plastic deformation behavior of α -iron has been studied more extensively (11-13). It was not clear from the literature how the cyclic deformation behavior of α -iron varies as the crystal orientation was changed. The point of this research was to fatigue single crystals of various orientations at a constant plastic strain amplitude and at a constant total strain rate and note any significant changes in the crack initiation behavior as well as any significant changes in the surface deformation.

EXPERIMENTAL PROCEDURES

Single crystals of α -iron were grown by the strain anneal technique (14) from vacuum melted iron obtained from the Inland Steel Research Laboratories. Two vacuum melted lots were used, VMI-1 and VMI-2. VMI-1 contained .005 wt.% C, .03 wt.% Mn, .005 wt.% P,

* Department of Materials Science and Engineering and Materials Research Center, Northwestern University, Evanston, IL.

FATIGUE 87

.002 wt.% S, .013 wt.% Si, .002 wt.% N, .008 wt.% Al and 119 ppm of O. VMI-2 contained .003 wt.% C, .01 wt.% Mn, .003 wt.% P, .002 wt.% S, .003 wt.% Si, .002 wt.% N, .008 wt.% Al and ~ 1500 ppm of O. Crystals 1 and 3 were grown from VMI-2 and all the other crystals were grown from VMI-1. The single crystals were grown in an environment of 95% argon and 5% hydrogen, in a furnace with an imposed steep temperature gradient. The iron specimens were slowly moved through the temperature gradient at a rate of 0.25 cm/hr or less. The set-up is described elsewhere (15).

Crystal orientations were determined by the Laue back reflection technique and specimens were rotated to the tensile directions given in Figure 1. The specimens, cut out by electrical discharge machining, were flat and dogbone shaped with gage sections of 7.6 mm x 2.0 mm x 5.1 mm. Each specimen was chemically polished in a solution of 33% hydrogen peroxide and 67% phosphoric acid until approximately 50 μ m from all surfaces and a sharp Laue pattern was obtained. The specimens were then mechanically polished to 0.05 μ m Al_2O_3 . This was done to avoid any pitting caused by chemically polishing.

The specimens were axially loaded and fatigued under plastic strain control using a conventional servohydraulic controlled fatigue set-up. The fatigue wave form used was triangular with R equal to minus one. A constant plastic strain amplitude of 5.0×10^{-4} and a constant plastic strain rate of 5.0×10^{-4} per sec were used throughout these experiments.

Fatigue crack initiation was studied with the replica technique. At specific intervals, plastic replicas were taken of the specimen surface to be observed at a later date. These replicas were shadowed with Au-Pd and subsequently examined in an SEM for deformation markings and crack formation.

SURFACE DEFORMATION

Figure 1 is a standard stereographic triangle containing the tensile directions of all the single crystals investigated. Table 1 summarizes the surface deformation behavior of each of the crystals. In general, deformation occurred in two forms. One being slip band formation, sometimes wavy and sometimes straight, and the other being a macroscopic plastic instability resulting in localized deformation in the form of plastic deformation bands (or surface undulations).

The "harder" the crystal orientation for the plastic strain amplitude investigated, the more likely the crystal formed these macroscopic plastic deformation bands. This can be seen in the last four orientations listed in Table 1. The first entry and

FATIGUE 87

TABLE 1 - Summary Table of the Surface Deformation Behavior and the Number of Cycles to Crack Initiation

Crystal Number	Slip Trace Planes	Macroscopic Deformation Bands	Tensile Yield Stress (MPa)	"Saturation" Stress (MPa)	Number of Cycles to Crack Initiation N_i
1	8° from $\langle \bar{1}10 \rangle \langle 111 \rangle$ a. S b. S	No	37.2	50.0 -50.0	> 20,000
2	$\langle \bar{1}12 \rangle \langle 111 \rangle$ a. PG b. S $\langle 1\bar{1}2 \rangle \langle 111 \rangle$ a. S b. PG	No	56.4	82.5 -87.0	3000
3	$\langle \bar{1}01 \rangle \langle 111 \rangle$ a. PG b. PG $\langle \bar{1}\bar{1}2 \rangle \langle 111 \rangle$ a. S b. S	No	64.55	89.5 -80.0	100
4	$\langle 121 \rangle \langle 1\bar{1}1 \rangle$ a. S b. S $\langle 2\bar{1}3 \rangle \langle \bar{1}11 \rangle$ a. S b. PG	One	73.8	84.0 -84.0	100
5	$\langle 2\bar{1}3 \rangle \langle 111 \rangle$ a. PG b. PG $\langle \bar{1}10 \rangle \langle 111 \rangle$ a. PG b. PG	One	75.1	78.5 -78.0	1500
6	6° from $\langle 231 \rangle \langle 1\bar{1}1 \rangle$ a. S b. PG	Many	77.5	89.5 -85.0	1000
7	5° from $\langle 112 \rangle \langle \bar{1}\bar{1}1 \rangle$ a. S b. PG	Many	89.9	82.0 -80.0	1000

note: a. front face of specimen b. side face of specimen
S- Straight PG- Pencil glide

FATIGUE 87

last two entries exhibited straight single slip traces on the front face of the specimen. For crystal 1, the slip traces on the side surface were also very straight whereas the side faces of crystal 6 and 7 exhibited pencil glide. The macroscopic slip traces may actually be made up of slip occurring on some combination of BCC slip planes ($\{101\}$, $\{112\}$ and $\{123\}$) on a microscopic level with the overall apparent slip "plane" falling on a non-slip plane. The Laue patterns of all the specimens tested were checked at the end of cyclic fatiguing, and only crystals 6 and 7 were too blurred (due to excessive deformation) to check for crystal rotation. All the other crystals had either sharp Laue patterns or Laue patterns with slight asterism where rotation was found to be insignificant. The blurriness of crystals 6 and 7 is further evidence for multiple slip having occurred.

Figure 2 contains 8 photomicrographs illustrating the surface deformation behavior of α -iron single crystals. The stress directions are indicated by arrows. Figure 2a is a photomicrograph of the surface of crystal 1 after 20,000 cycles. It illustrates the parallel slip plane traces formed on this crystal. A replica taken of the surface after 20,000 cycles is illustrated in Figure 2b. Slip lines can be seen, but no cracks could be found anywhere on the replicas taken from the surface of this crystal even after 20,000 cycles. Figure 2c illustrates double slip. This was taken of the surface of crystal 2 after 20,000 cycles of fatiguing. One set of slip traces are seen to be wavy in appearance and the other set appears to be quite straight. Figure 2d is a side surface view of crystal 2. The wavy slip traces from the front face become very straight slip lines on the side face. The single set of slip lines of crystal 7 are illustrated in Figure 2e. The side face of crystal 7 exhibited pencil glide as can be seen in Figure 2f. An example of localized deformation in the form of macroscopic deformation bands is illustrated in Figure 2g. Notice that the macroscopic deformation bands are approximately 1 mm in width and run at an angle of ~ 75 degrees to the slip line traces. An example of fatigue crack initiation detection is illustrated in Figure 2h. Crack initiation was noted to take place at 100 cycles for this crystal (No. 3). Notice the small crack observed to have initiated at the slip line. The cracks are less than 1 μ m in length and a fraction of a micron in depth. Figure 2i is a micrograph illustrating pencil glide on the surface of crystal 3.

FATIGUE CRACK INITIATION

Fatigue cracks for the orientations examined initiated at slip lines only. No cracks were found to initiate in the valleys of the macroscopic deformation bands.

The crystals investigated exhibited crack initiation at anywhere from 100 to greater than 20,000 fatigue cycles. Table 1

FATIGUE 87

summarizes the data on the number of cycles to crack initiation. The "softest" crystal, i.e., the one with the lowest yield stress, smallest saturation stress and the least amount of surface deformation, did not exhibit crack initiation for the total number of cycles investigated, i.e., $N_i > 20,000$ cycles. It should be noted that the slip traces were straight on both faces of this crystal. This was the only crystal that exhibited this type of slip trace. Crystals 3 and 4 were of intermediate yield strength, had more than one slip trace and little or no macroscopic deformation bands. They exhibited crack nucleation at an early number of cycles ($N_i \sim 100$). The last two crystals (6 and 7) with the highest yield strength values, the highest saturation stress, one slip trace (with pencil glide on the edge face) and a large amount of macroscopic surface deformation took a little longer to initiate cracks than the intermediate crystals ($N_i \sim 1000$). Since a large part of the plastic strain was accommodated by plastic instability the crack initiation at the slip lines might be expected to start at a larger number of cycles.

Figure 3 is a plot of the number of cycles to crack initiation, N_i , versus the tensile yield strength. The yield strength was obtained from the first hysteresis loop from the intersection of the tensile elastic line with the plastic deformation curve. The plot can be broken down into two regions, higher and lower stress. At the lower stress level only slip lines were found to occur and as the tensile stress decreased the number of cycles to crack initiation increased, as would be expected. In the higher tensile stress region, surface deformation was found in the form of slip lines and macroscopic deformation bands. As the amount of strain taken up by the large deformation bands increases and less strain is accommodated by the slip lines, the number of cycles to crack initiation at slip lines increases but the effect seems to saturate.

In Figure 4 the tensile yield stress is plotted versus the degrees of the tensile axis away from the $[001]$ pole on the standard stereographic projection towards the $[011]$ pole. The position of the tensile axis was determined by projecting the tensile axis onto the $[001]$ - $[011]$ line through a great circle passing through the slip direction (determined by measuring the slip traces on two surfaces of the crystal and using standard stereographic procedures for determining the slip system). A peak in the tensile yield stress is seen to occur at 25-30 degrees from the $[001]$ pole. This data correlates with the theoretical curves developed by Opinsky and Smoluchowski (16). A peak in the curve, according to Opinsky and Smoluchowski, would correspond to slip occurring mostly on $\{112\}$ and/or $\{123\}$ type planes as was found to occur in the present data.

FATIGUE 87

CONCLUSIONS

1. There was a surprisingly large variation in the number of cycles to fatigue crack initiation depending on orientation. At the constant plastic strain amplitude of 5×10^{-4} , N_f varied from 100 to more than 20,000 cycles. The variation correlated with the plastic deformation markings.
2. The yield stress varied with orientation being maximum when the tensile axis projected on the $[001]-[011]$ side of the stereographic triangle is approximately 30° from $[001]$.

REFERENCES

- (1) Fahrenhorst, W. and Schmid, E., Z. für Physik, Vol. 78, 1932, pp. 383-394.
- (2) Low, J. R., "Iron and Its Dilute Solid Solutions", Interscience, New York, 1963, pp. 217-269.
- (3) Stein, D. F., Low, J. R. and Seybolt, A. U., Acta Metall., Vol. 11, 1963, pp. 1253-1262.
- (4) Stein, D. F. and Low, J. R., Acta Metall., Vol. 14, 1966, pp. 1183-1194.
- (5) Yamashita, T. and Taneda, Y., Trans. Japan Inst. Metals, Vol. 9, 1968, pp. 465-469.
- (6) Keh, A. S. and Nakada, Y., Trans. Japan Inst. Metals, Vol. 9, 1968, pp. 876-884.
- (7) Allen, N. P., Hopkins, B. E. and McLennan, J. E., Proc. Roy. Soc. A, Vol. 234, 1955, pp. 221-246.
- (8) Hirsh, P. B., Trans. Japan Inst. Metals, Vol. 9, 1968, pp. xxx-xxxix.
- (9) Taoka, T., Takeuchi, S. and Furubayashi, E., J. Phys. Soc. Japan, Vol. 19, No. 5, 1964, pp. 701-711.
- (10) Christian, J. W., Proc. SICSMA, 1970, pp. 31-70.
- (11) Nine, H. D., J. Appl. Phys., Vol. 44, 1973, p. 4875.
- (12) Mughrabi, H. and Wüthrich, Ch., Phil. Mag., Vol. 33, No. 6, 1976, pp. 963-984.
- (13) Mughrabi, H., Herz, K. and Stark, X., Int. J. Fract., Vol. 17, No. 2, 1981, pp. 193-220.

FATIGUE 87

- (14) Stein, D. F. and Low, Jr., J. R., Trans. Met. Soc. AIME, Vol. 221, 1961, pp. 744-746.
- (15) Kim, Clarissa, Ph.D. Thesis, Northwestern University, Evanston, Illinois, in progress.

ACKNOWLEDGEMENTS

This research was sponsored by the National Science Foundation, Grant No. DMR83-03904 to Inland Steel Company and Northwestern University under the Industry/University Cooperative program. Use of the Central Facilities of Northwestern University's Materials Research Center, supported under the NSF-MRL program (Grant Nos. DMR82-16972 and DMR85-20280), is gratefully acknowledged.

Figure 1 appears on page 10. Figure 2 appears on pages 8 and 9.

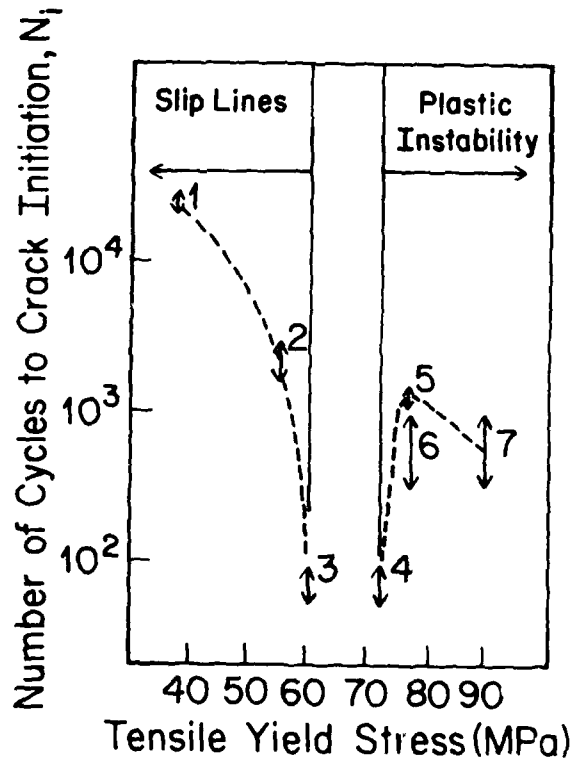


Figure 3 Tensile yield stress versus number of cycles to crack initiation

AD-A184 045

FATIGUE, 87 VOLUME 1(U) VIRGINIA UNIV CHARLOTTESVILLE
SCHOOL OF ENGINEERING AND APPLIED SCIENCE
R O RITCHIE ET AL. JUN 87 ARO-24134.1-MS-CF

27

UNCLASSIFIED

N00014-87-G-0008

F/G 20/11

NL

210
210
120

210
210
210



27

210
210
210

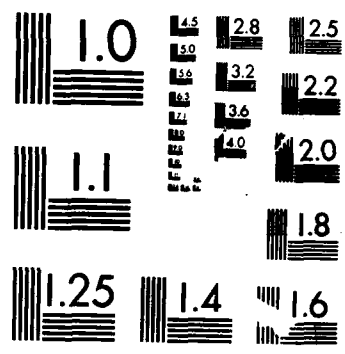
210
210

210
210

210
210

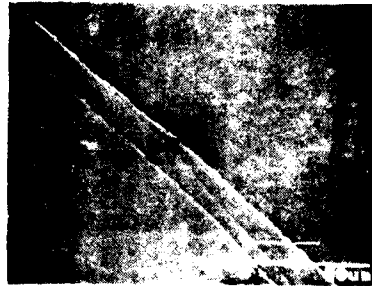
210
210
210

210
210

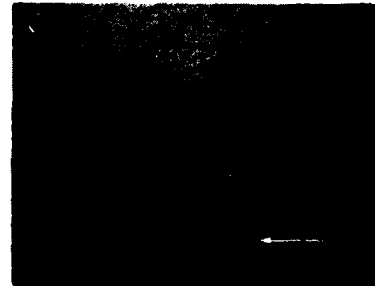


MICROCOPY RESOLUTION TEST CHART
NATIONAL BUREAU OF STANDARDS-1963-A

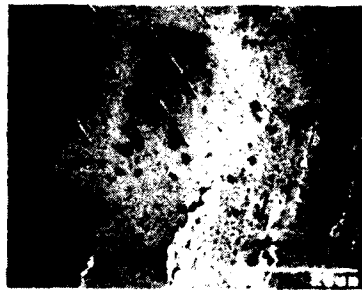
FATIGUE 87



a) Surface of crystal 1 after 20,000 cycles



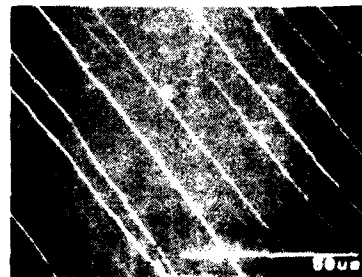
b) Replica of crystal 1 surface after 20,000 cycles. No cracks are noted



c) Surface of crystal 2 after 20,000 cycles



d) Corner view of crystal 2 after 20,000 cycles. Pencil glide slip lines on front face appear straight on edge face



e) Surface of crystal 7 after 10,000 cycles



f) Side face of crystal 7 after 20,000 cycles. Notice the pencil glide

Figure 2 SEM photomicrographs of single crystal surfaces and surface replicas

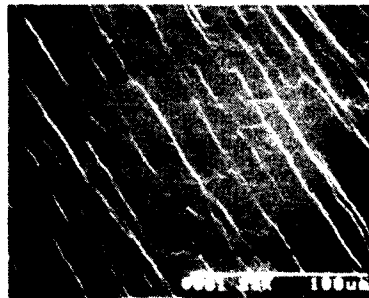
FATIGUE 87



g) Surface of crystal 7 after 10,000 cycles. Note large microscopic deformation bands



h) Replica of crystal 3 after 100 cycles. Slip band cracks are seen



i) Surface of crystal 3. Pencil glide in (101) plane is seen

Figure 2 SEM photomicrographs of single crystal surfaces and surface replicas

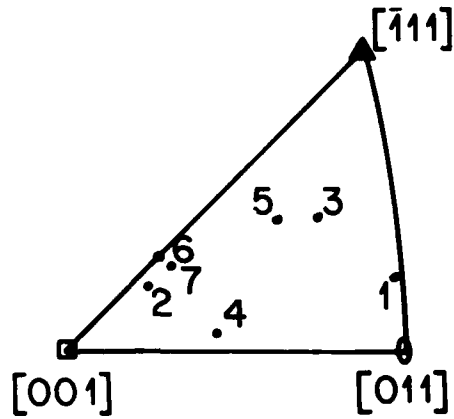


Figure 1 Standard stereographic projection showing the tensile axes directions of the crystals studied

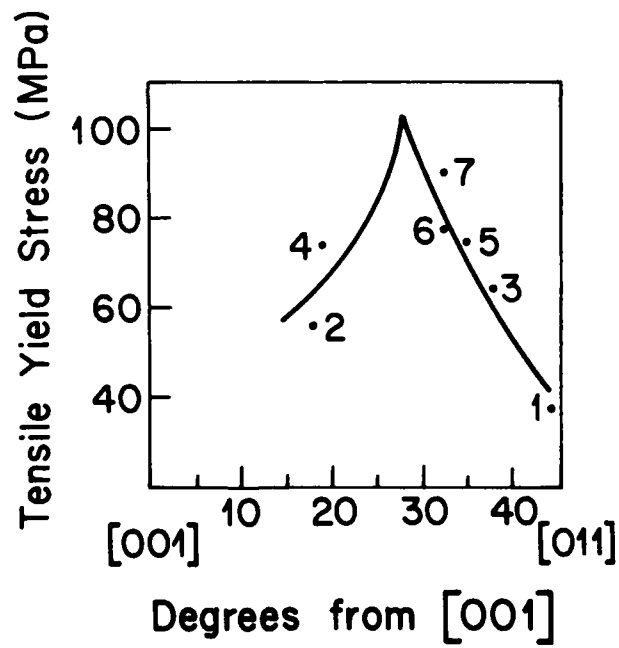


Figure 4 Tensile yield stress versus orientation of the projection of the tensile axis onto the [001]-[011]

THE EFFECT OF ION BEAM MIXED NI-AL SURFACE LAYERS ON
PSB EXTRUSION MORPHOLOGY IN FATIGUED NICKEL

D. S. Grummon* and J. W. Jones**

Experiments have been performed to study the effect of ion beam mixed Ni-Al surface layers on mechanical behavior and surface damage accumulation associated with crack initiation during fatigue of nickel. Supersaturated solid solutions of Al in Ni and Ni₃Al structures were produced, in layers less than 100 nm thick, by ballistic mixing of vacuum-evaporated films. Such surface alloying altered the number, distribution, and morphology of persistent slip band extrusions. The results are discussed in terms of stresses imposed on the surface film in response to plastic strain localization in the bulk.

INTRODUCTION

Several recent studies have reported on the effects of surface modification by ion implantation on metal fatigue (1,2). In many cases, ion implanted specimens have shown increases in fatigue life accompanied by a decrease in the number of slip band features present at the surface. Since surface initiation of fatigue cracks is closely linked to details of the three-dimensional structure of slip band extrusions, it is important to understand the effect of surface modifications on such morphological features. Few reports exist, however, which describe the detailed local structure of surface slip features found on ion beam modified materials. The present work is part of an interdisciplinary effort to study both the kinetics and thermodynamics of ion beam mixing in the Ni-Al system, and the influence of such surface modification on cyclic deformation phenomena associated with

* Department of Metallurgy, Mechanics and Materials Science, Michigan State University.

** Department of Materials Science and Engineering, The University of Michigan.

fatigue crack initiation. In this paper, measurements of changes in mechanical behavior are reported, and a description is presented of the distribution and detailed local morphology of persistent slip band structures observed during fatigue of nickel with ion beam modified surfaces. Additional results, pertaining to process kinetics and the thermodynamics of phase stability during ion beam mixing of Al and Ni, have been published elsewhere (3).

EXPERIMENTAL METHODS

Fatigue specimens were machined from nickel alloy 270 into 4 inch long cylindrical bars. The specimens were mechanically polished and then annealed in dry argon-3% hydrogen for 3 h. at 1073 K. The resultant average grain diameter was approximately 0.4 mm. Annealed specimens were electropolished in a cold solution of perchloric acid and ethanol. (Further details may be found in reference 4.)

Surface modification by ion beam mixing was accomplished in two steps. First, alternate layers of nickel and aluminum were deposited by vacuum evaporation. Two average compositions were obtained by varying the thickness of the layers. In one, an average composition of 16 at.% Al was produced by depositing alternating 15.6 nm Ni layers and 6.7 nm Al layers. A second composition of 23 at.% Al was achieved with 15.6 nm Ni layers and 11.5 nm Al layers. In each case, five layers were deposited, with nickel as the outermost layer, as shown schematically in Fig. 1. After deposition of these films by vacuum evaporation, the specimens were irradiated with 0.5 MeV krypton ions to a dose of 1×10^{16} ions/cm². The 23 at.% composition specimens were subsequently given an annealing treatment for 1 h. at 723 K. to precipitate the gamma-prime (Ni₃Al) phase.

Surface layer characterization was carried out using Rutherford backscattering spectroscopy and electron diffraction analysis. The 16% Al surface modification was confirmed to have produced a supersaturated solution of Al in Ni, and the annealed 23% composition produced gamma-prime precipitates in a dual-phase structure. The depth of the surface modifications was approximately 70 to 100 nm. (Further details are contained in reference 5.)

FATIGUE 87

Specimens were fatigued at constant plastic strain ranges of .0003. Surface observation was carried out periodically throughout the tests using scanning electron microscopy and Nomarski phase contrast optical microscopy.

RESULTS

Mechanical Behavior

Figure 2 shows cyclic hardening curves for .0003 plastic strain range tests of plain and ion beam modified nickel. A slight increase in saturation stress is noted for the surface modified material, but the initial hardening rate is slightly lowered. The hardening curves were generally observed to cross at accumulated strains of approximately 3 to 4. The behavior of supersaturated solid solution specimens and gamma-prime specimens was identical.

Development of Surface Damage Structures

Observation of unmodified specimens fatigued at .0003 plastic strain range revealed the presence of distinct slip band features at accumulated strains as low as 0.6 . At this accumulated strain no evidence of surface slip bands could be detected by phase contrast microscopy in ion beam mixed specimens. Slip band features in ion beam modified nickel were not detected until accumulated strains of 3 to 4 had been reached. At approximately 4.0 accumulated strain, well developed PSB structures were common in unmodified material, whereas only sporadic and much less intense slip band features were found in ion beam modified specimens. Differences in PSB frequency at the surface persisted up to cyclic saturation. It is interesting to note that the first emergence of PSBs at the surface of surface modified nickel corresponds with the point at which the cyclic hardening curves for modified and unmodified material cross.

The effect of the ion beam modified surface layer in suppressing the extrusion of PSBs at the surface is illustrated by observations made at the boundary between modified and unmodified regions in the gage section of an individual specimen. Figure 3 shows such a region on the surface of a 16% Al surface modified specimen saturated at .0003 plastic strain range. The upper half of the scanning electron micrograph has not

been surface modified, and shows widespread and intense surface slip band activity. It is also apparent that a fatigue crack has nucleated in this region. The lower portion, which has been ion beam modified, displays a marked reduction in the number and intensity of slip band features, and shows several grains in which PSBs have not appeared at all. Such behavior was typical of ion beam modified specimens: no crack nuclei were ever observed in the ion beam modified portions of a specimen at saturation. [Additional statistical treatment of this behavior can be found in reference (5).]

PSB Extrusion Morphologies

The scanning electron micrograph in Figure 4 shows a persistent slip band structure which typifies those found at the surface of unmodified nickel fatigued to saturation at .0003 plastic strain range. PSB extrusions such as this one were nearly always found to intersect grain boundaries, and often propagated across them. This morphology is the "classic" PSB structure which has been extensively observed in fatigued copper. It consists of multiple notch-peak features and a net extrusion of material above the surface plane.

In contrast to this morphology, the structure of typical PSB features at the surface of ion beam modified specimens are illustrated in Figures 5 and 6. The most ubiquitous feature on modified specimens was the "microband" feature shown in Fig. 5. The slip band is very narrow, and has apparently extruded material in the form of chips, or filaments, from the bulk. These chip-like extrusions were very fragile, and could be destroyed even by routine cleaning procedures. The slip band in Fig. 6, herein referred to as a PSB "double-microband", was less frequently observed, but still fairly common. This type of feature consisted of two parallel microbands spaced about a micron apart. Generally, the double microband features produced pronounced net extrusions of material above the surface. Neither single microbands nor double microbands were generally observed to intersect grain boundaries.

Extensive observation of surfaces modified with the 16 at.% Al modification (superstaturated solid solution) and the 23% Al modification (heat treated to precipitate the gamma-prime phase) showed little difference in the local morphology of slip band

FATIGUE 87

extrusions at saturation. Occasionally, however, the gamma-prime modified surface layers were found to have delaminated and spalled away from the substrate.

DISCUSSION

Surface alloying pure nickel with aluminum by ion beam mixing radically alters the physical and mechanical metallurgy of the near surface region. Although changes in stacking fault energy, alteration of dislocation image forces, and changes in lattice parameter will occur, these effects are likely to be secondary in relation to two principal consequences of the ion beam mixing of aluminum in nickel. First, the shear modulus will be lowered by approximately 15% in the case of the supersaturated solid solution modification (6). Secondly, and more important, the yield strength of the surface layer is greatly increased over that of the bulk. While there is no precise way to determine the exact yield strength of surface layers as thin as those produced in this study, considering the potency of aluminum as a solid solution strengthener in nickel, the additional hardening produced by ion beam induced lattice defects, and the fine grain size in the surface layer, the yield strength there is likely to be quite high.

Lowering the elastic modulus and increasing the yield strength of the surface layer will lower the stress in the surface layer for a given value of total strain, and increase the total strain needed to plastically deform the surface layer (7). It is therefore likely that, in the present case of an initially soft substrate, plastic deformation in the surface layer is delayed or entirely suppressed, even at the total strains associated with cyclic saturation. This means, that for much of the test, the surface deforms elastically, whereas the bulk undergoes plastic deformation which is resolved onto favored slip planes. The displacement tensors are thus different in the bulk than in the surface layer: surface strain is elastic and thus axial, while bulk strain is plastic and thus consists of a shearing deformation. This situation is shown schematically in Figure 7. For the material to deform compatibly, some accommodation must occur near the interface between surface layer and bulk, requiring the motion of secondary dislocations, and effectively extending the influence of the surface layer to some additional depth.

At accumulated strains near saturation, slip bands eventually penetrate the surface layer in substantial numbers (at least at plastic strain ranges above .0003). This is not surprising if it is assumed that plastic strain inhomogeneities develop in the bulk of surface modified nickel in the same manner as they do in unmodified nickel. Even if the surface layer deforms elastically, once bulk plastic strain becomes localized into persistent slip bands, strain in the surface layer above PSBs is substantially increased over the nominal value associated with the applied strain. Referring to Figure 8, which shows a PSB of width B, intersecting the surface at an angle θ , and undergoing an average localized shear γ , and assuming that the surface undergoes both shear and dilational displacements to maintain compatibility at the interface we have for the displacements w and u in the z-direction and the x-direction respectively:

$$w = \frac{Byx \sin \theta}{B \sin^{-1} \theta + \gamma B \cos \theta} ; \quad u = \frac{Byx \sin \theta}{B \sin^{-1} \theta + \gamma B \sin \theta} \quad (1)$$

But for $\theta = \pi/4$ and for small values of γ , we have :

$$\frac{du}{dx} = \frac{dw}{dx} \approx \gamma; \quad \frac{du}{dy} = \frac{du}{dz} = \frac{dw}{dz} = 0 \quad (2)$$

Since the stress in the z-direction must go to zero at the surface, we have:

$$\frac{E}{(1+\nu)} \epsilon_z = \frac{-\nu E}{(1+\nu)(1-\nu)} (\epsilon_z + \epsilon_x) \quad (3)$$

Therefore, the strain and stress state in the surface layer may be given to a first approximation as: (4)

$$\epsilon_{ij} = \begin{pmatrix} \gamma & 0 & \gamma/2 \\ 0 & 0 & 0 \\ \gamma/2 & 0 & \frac{-\nu\gamma}{1-\nu} \end{pmatrix}; \quad \sigma_{ij} = \begin{pmatrix} \frac{\gamma E}{(1+\nu)(1-\nu)} & 0 & G\gamma/2 \\ 0 & \frac{\gamma E}{(1+\nu)(1-\nu)} & 0 \\ G\gamma/2 & 0 & 0 \end{pmatrix}$$

Since the plastic strain associated with PSBs is on the order of 1% (8), it is clear from the above analysis that, in the absence of plastic deformation in

the surface layer, stresses would quickly reach the order of 2 Gpa. Thus, past the point where plastic strain in the bulk localizes into persistent slip bands, the surface layer is subjected to large strains and, in effect, undergoes strain controlled low cycle fatigue at a strain amplitude on the order of .01. It is therefore not surprising that the surface layer eventually ruptures, producing the "microband" features which are observed at the surface.

The production of "double microband" features is believed to result from the link-up of individually nucleated single microbands which form in different locations of the grain, but are associated with a common underlying persistent slip band. The frequency with which the double microband features (i.e., Fig. 6) are observed, and the fact that their widths match that expected of PSBs (about one micrometer) suggests that rupture of the surface layer is favored at the edges of the underlying PSB.

CONCLUSIONS

It has been found that the presence of an ion beam mixed Ni-Al surface layer increases the saturation stress in plastic strain controlled fatigue at .0003 plastic strain amplitude, and decreases the initial cyclic hardening rate. Surface modification delays the emergence of slip band features from 0.6 accumulated strain (in the case of unmodified material) to accumulated strains of 3.0 to 4.0. The degree of macroscopic damage accumulation is reduced both in terms of frequency and intensity of slip band extrusions present in cyclically saturated specimens. In ion beam modified nickel, the classic PSB surface morphology was replaced by surface slip band features consisting mainly of "microband" features with widths much less than 1 micrometer, or "double microband" features with spacings similar to the width of classic PSBs.

A number of important physical characteristics of the near surface region (such as stacking fault energy, etc.) are altered by ion beam modifications. However, the observed delay in penetration of PSBs at the surface, their decreased numbers at saturation, and the resultant slip band morphologies, can be rationalized by a relatively simple model which considers only the

FATIGUE 87

increased yield strength and lowered elastic modulus of the surface film. Surface film rupture eventually occurs where bulk strain inhomogeneity in the form of PSBs imposes large localized stresses in the surface layer. The frequent occurrence of paired microbands suggests that rupture is favored at the edges of underlying persistent slip bands.

Acknowledgements: This research was supported at University of Michigan through grants NSF-G-DMR8310032 & NSF-G-DMR8603174 from the National Science Foundation.

SYMBOLS USED

- B = Width of persistent slip band.
 θ = angle of incidence of persistent slip band.
 u, v, w = displacements in x, y , and z directions.
 γ = shear strain in persistent slip band
 $\epsilon_{ij}, \sigma_{ij}$ = strain and stress tensors, respectively.

REFERENCES

- (1) A. Kujore, S. B. Chakraborty and E. A. Starke "The Effect of Aluminum Ion Implantation on the Fatigue Crack Initiation of Polycrystalline Copper" in Ion Implantation Metallurgy, Proc. Symp. Mat'l's Res. Soc., Cambridge, Mass. 1979. Preece, Hirvonen, Eds. AIME 1980, pp. 132-141.
- (2) K. Hohmuth, E. Richter and B. Rauschenbach, Mat. Sci. Eng 69, pp. 191-201.
- (3) J. Eridon, PhD. Thesis, The University of Michigan, Department of Nuclear Engineering, 1986.
- (4) D. S. Grummon and J. W. Jones, Scripta Met. 20, 1986. p 311.
- (5) D. Grummon, J Jones, J Eridon, G. Was and L. Rehn, Proc. Conf. IBMM86, Catania, Italy, June, 1986. (Nuc. Inst. Meth. B, April 1987, in press.)
- (6) E. Fisher, Scripta Met. 20, 1986. pp. 279-284.
- (7) I. G. Greenfield and A. Purohit, Mat. Sci. Eng., 46, 1980. p. 89.
- (8) C. Laird, J.M. Finney and D. Kuhlmann-Wilsdorf, Mat. Sci. Eng. 50, 1981. 9pp. 127-136.

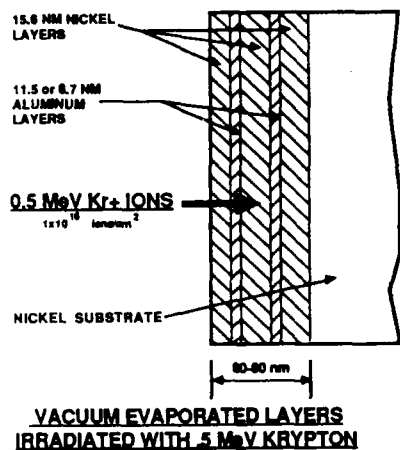


Fig. 1. Schematic of surface films before Kr⁺ irradiation.

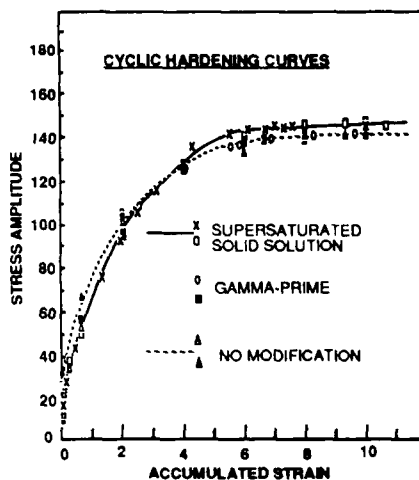


Fig. 2. Cyclic hardening curves.

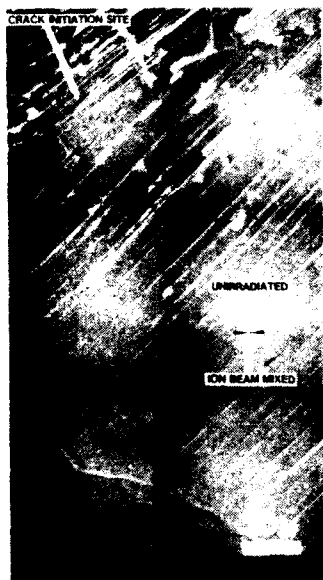


Fig. 3. Transition from unmodified to modified region.



Fig. 4. PSB structure in unmodified specimen



Fig. 5. Microband type PSB, modified specimen.

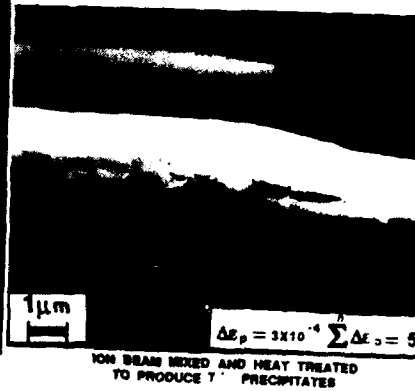


Fig. 6. PSB double microband, modified specimen.

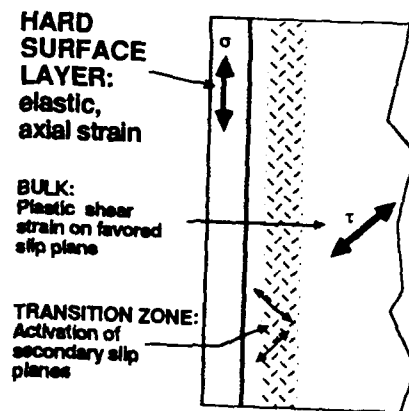


Fig. 7. Modes of strain, surface layer vs. bulk.

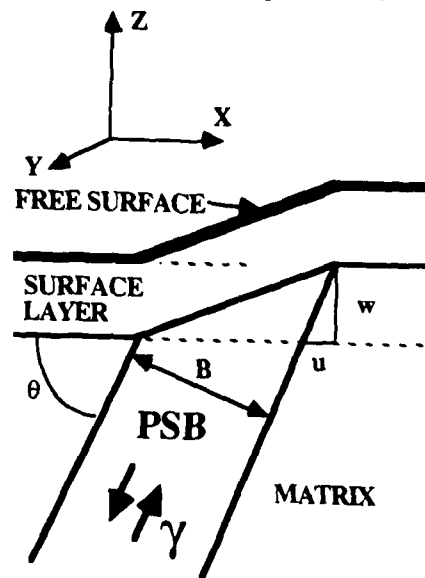


Fig. 8. Geometry of PSB and surface film for eqns. 1-4.

FATIGUE 87

THE EVOLUTION OF LOCAL MECHANICAL PROPERTIES OF Al 2219-T851 DURING FATIGUE

W.L. Morris*, M.R James* and B.N. Cox*

Local strain amplitudes were measured in individual grains of an Al 2219-T851 alloy during fatigue. The alloy has a 360 MPa bulk cyclic yield strength, but its surface is microplastic at cyclic stresses greater than 70 MPa. With fatigue at ± 275 MPa, an upper flow stress of ~ 200 MPa develops in grains much larger than the mean size. Large residual stresses caused by constraint of the localized deformation severely limit the total strain at these softened sites. The use of a load reduction sequence to minimize these residual stresses during strain measurements, so as to obtain more accurate values for the local flow stresses, is discussed.

INTRODUCTION

Large local residual stresses are always present during inhomogeneous deformation (1,2). In fatigue-softened alloys, localized deformation is modified by residual stresses resulting from constraint of flow by the harder surroundings (3,4). Even on a smooth surface, deformation inhomogeneity at the grain level ensures the presence of these residuals, and hence a substantial difference between the local and externally applied stresses. A simple analysis has shown (3) that the residual stress in individual grains can easily be so large that portions of a grain can be in compression while the external stress is tensile. This complicates a simple determination of the local flow stress of individual grains in alloys.

In two recent papers (3,4), we used models of the deformation of a soft ellipsoid in an elastic matrix to calculate the flow stress and strain hardening characteristics of surface grains in Al 2219-T851. The models account for the local residual stress, allowing for the interpretation of strains measured in individual

*Rockwell International Science Center, 1049 Camino Dos Rios,
Thousand Oaks, CA 91360

FATIGUE 87

grains as a function of external stress. We find that fatigue of Al 2219-T851 at stresses below its bulk cyclic yield strength causes a reduction in the local 0.2% offset yield strength of the interiors of the grains, with preference for the largest surface grains. Grains 3-8 times larger than the 60 μm mean are the most affected and are also the eventual sites of crack initiation. Ultimately, the yield strength of these grains falls to half the bulk cyclic value, and well below the applied cyclic stress amplitude. However, the local strain amplitude typically remains less than 10^{-3} in these softened grains because the deformation is constrained by the nearly elastic surface.

These results seem in conflict with ample evidence that many alloys locally harden (5,6). Even in Al 2219-T851, Knoop indentation shows that fatigue hardens the interiors of individual grains, with the change being greatest in the largest grains (Fig. 1). Previous local strain measurements in this alloy have shown that, in large grains, the width of the local strain-external stress hysteresis loop at zero stress reaches a peak with fatigue and then decreases in amplitude, again suggestive of hardening (7).

In this paper, we demonstrate that the small local flow stresses deduced from strains measured within individual grains are not an artifact of our deformation analysis. While strain hardening parameters and deformation depth cannot be accurately obtained without a rigorous theoretical analysis, the local flow behavior can be found directly. A load reduction sequence is used to minimize the local residual stress, causing the external and local stresses to be nearly equal. This technique is used to characterize the evolution with fatigue of flow stresses and strain hardening at low plastic strain amplitudes in a 300 μm grain in Al 2219-T851. The apparent conflict between indentation and local strain measurements is not completely resolved, but the new local stress-strain data provide some clues to possible answers to this problem. We believe that the 10% strains encountered during indentation (8) can make this method a misleading probe of the highly constrained yielding which occurs in isolated softened grains, in which the maximum plastic strains are only 10^{-3} during typical fatigue experiments.

EXPERIMENTAL TECHNIQUES

The 360 MPa yield strength Al 2219-T851 had a 60 μm average grain size in the rolling plane measured at 45° to the rolling direction. The grains were pancake shaped, being nominally 20 μm deep. Tapered flexural specimens (9) of the alloy were carefully machined and polished to minimize initial residual surface stresses and then chemically etched to reveal the grain bound-

FATIGUE 87

daries. Fatigue was in bending at nominally ± 275 MPa in dry nitrogen. The local strains reported were measured using a reference gauge placed within the center of grains and at least $25\text{ }\mu\text{m}$ from the nearest boundary by a micromanipulator, and with the aid of a loading jig in a scanning electron microscope (SEM), as described in Ref. 10. The reference gauge is a thin mica flake used as a convenient ruler and attached to the substrate electrostatically so that the surface can deform freely beneath it. It acts as a stable length, needed to compensate for the $\pm 5 \times 10^{-3}$ magnification instability of our SEM. Distortion and parallax errors from the ruler are smallest at zero load, where we made most of our measurements. For fully reversed loading, the width of the local strain-external stress hysteresis loop at zero load was found by comparing a micrograph taken after completing the compressive cycle to one taken after the next tensile cycle. The information needed to deduce flow stress, strain hardening and constitutive relationships was obtained by changing the loading sequence prior to the loop width measurement (4). We used a stereoscopic analysis of the micrographs to maximize the sensitivity of measurements of the surface displacements relative to the ruler. Since the displacements of nearly identical high contrast objects in each pair of micrographs were found, the accuracy was much better than the point-to-point resolution of the SEM. The displacement of any high contrast profile can easily be determined to a small fraction of the profile width. It is the image reproducibility which actually matters. The quality of our SEM images has been progressively improving over the past few years and we can now achieve about $\pm 15\text{\AA}$ in-plane displacement sensitivity.

RESULTS

To determine how the flow stress of a grain's interior progressively changes during fatigue, we interrupted the constant amplitude cycling at intervals, and determined the local flow stress by measuring strains within the grain for a series of reduced cyclic loads. The local mechanical properties in Al 2219-T851 change slowly, so this measurement activity has no significant effect on the property evolution. The cyclic stress was dropped to a value σ and six cycles were applied to allow the local stress-strain hysteresis to reach equilibrium (4). Then the residual strain at zero external load was measured over a tensile loading cycle. The strain found at each σ is the width, W_0 , of an external stress-local strain hysteresis loop at zero external load. W_0 will always be smaller than the zero load width of a local stress-local strain loop because of local residual stress. As the measurement stress σ is decreased, W_0 at equilibrium becomes progressively smaller. At the same time, the maximum local residual stress within the grain decreases because the maximum local plastic strain amplitude has decreased. For a

sufficiently small plastic strain amplitude, the difference between the external and local stresses at equilibrium will be small, and an accurate determination of the local flow stress can be made from W_0 vs σ . An upper bound on the local residual stress magnitude is given by the product of the local plastic strain and the alloy modulus (3). For aluminum, the modulus is nearly independent of grain orientation, and the maximum plastic strain is rarely 5 times larger than W_0 ; so for W_0 's smaller than 5×10^{-5} , the difference between external and local stress should be less than 20 MPa after equilibrium is reached. Only resolved shear stress variability due to grain orientation should remain.

High sensitivity measurements of W_0 made early in fatigue show the surface is microplastic at stresses greater than 70 MPa (Fig. 2). In fact, the stress dependence of W_0 for a very large (300 μm) and a smaller (120 μm) grain are essentially identical. We would expect to see more scatter in such results from resolved shear stress with more measurements but, clearly, the deformation in the essentially unfatigued alloy is short ranged in that it does not sense the grain boundaries.

With continued fatigue, a dramatic change in loop width occurs in just the largest grains. Figure 3 compares the behavior of a 300 μm grain after 100 and 250 cycles. Within the $\pm 1.5 \times 10^{-5}$ measurement sensitivity, there is little change in the lower flow stress (σ_L , at $W_0 \approx 1 \times 10^{-5}$) with fatigue. But, characteristic of large grains in the alloy is the appearance of an upper flow stress, σ_U , in this case seen clearly after 250 cycles. Below σ_U the grain has apparently strain hardened with fatigue (i.e., $dW_0/d\sigma$ has decreased); above σ_U , the grain has strain softened. We have shown the results in Fig. 3 on a logarithmic scale to clarify the data at small strains. When these and similar data at other fatigue increments are plotted linearly, trends in σ_L and σ_U with fatigue are more accurately defined (Fig. 4a), and indirect information on the strain hardening behavior can also be obtained (Fig. 4b) by treating the strain as linear with σ above and below σ_U . A theoretical analysis of loop widths for such two-stage yielding is presented in Ref. 4.

We see from Fig. 4a that the local flow stresses are nearly constant in a 300 μm grain with perhaps a small fatigue induced decrease in σ_U . The important changes with fatigue are in $dW_0/d\sigma$. The quantity $dW_0/d\sigma$ is shown for the stationary yield surface approximation in Ref. 4 to be equal to $2(1-\alpha)/(2E_p + \alpha E_e)$; where α has a value less than 1 and is a proportionality between the local residual stress and the plastic strain determined by deformation depth, grain shape, and Poisson's ratio. E_p and E_e are plastic and elastic moduli. An increase in $dW_0/d\sigma$ means that either E_p or α has decreased. Typical values for α will be between 1 and 0.6, with very shallow deformation raising α . A full interpretation of the $dW_0/d\sigma$ results in Fig. 4b requires

FATIGUE 87

additional W_0 vs load sequence data so that α and E_p can be independently determined (see Ref. 4). However, if the depth of deformation within the grain is reasonably constant, the results mean that between 100 and 500 cycles E_p has increased below σ_U and has decreased above σ_U , i.e., the grain has strain hardened below σ_U and strain softened above σ_U . A more complete analysis, to be described later, suggests that the fall in $dW_0/d\sigma$ at 800 cycles and above σ_U is a consequence of a reduction in the depth of the deformation within the grain. The results shown at 500 cycles are for a different 300 μm grain, so considerably more data are needed to completely sort out the fatigue-induced evolution of local strain hardening and deformation depth.

DISCUSSION

It is simplistic to think of the fatigue-induced changes in local surface deformation of Al 2219 as reflecting traditional hardening or softening. The changes are complex and partially hidden by the large residual stresses developed by constraint of the local deformation. Analysis in Ref. 4 shows that by 500 cycles σ_U is just below the conventional (0.2% offset strain) yield strength. The loop width measured at maximum cyclic stress is small because the deformation is constrained. Mughrabi's (11) concept of treating the flow of such a material as that of a composite of matrix and penetrating channels or slipbands seems relevant here. But unlike the case of Cu, it appears to us that the upper rather than the lower flow stress more likely corresponds to long-range dislocation motion. The argument for this is indirect. First, σ_U develops after fatigue. While PSB's are not optically visible in Al 2219-T851, banded slip has been found by high resolution strain field analysis in large grains after fatigue (3), suggestive of a connection to σ_U . Second, before there is substantial fatigue damage, the flow above σ_U is independent of grain size and, therefore, probably short range and in the matrix.

No substantial change in the flow characteristics of small grains has been found after 10^4 cycles at ± 275 MPa, while in 300 μm grains changes both above and below σ_U are apparent after a few hundred cycles. So, if there is strain hardening below σ_U in the matrix, it must have accompanied the formation of the long-range dislocation structure which deforms above σ_U , and cannot instead be the cause of the long-range structure. Otherwise, matrix strain hardening would take place over the entire surface early in the lifetime.

How might an indentation test perceive a composite grain in which the matrix had strain hardened, and in which banded slip had developed for which flow above σ_U up to strains of perhaps 10^{-3}

FATIGUE 87

was nearly perfectly plastic? Clearly, on the basis of a lower 0.2% offset yield strength, fatigue has softened the larger grains, but there are several ways that indentation might sense hardening. The strains at the tip of a pyramidal indenter are relatively insensitive to indentation depth and are nearly 10^{-1} (8). Any mechanism which exposes the matrix to indentation and suppresses the contribution of flow from the bands will sense fatigue hardening. Possibilities for this include a saturation of the strain in the bands at the much higher strain of indentation, or the destruction of the long-range slip mode by the indentation. Naturally, we do not believe that softening is being universally misinterpreted as hardening. We have recently found unequivocal local cyclic hardening of an Al-4% Cu alloy with the same local strain measurement techniques. Our results simply call for care in the analysis of local mechanical properties.

We have known since the work reported in Refs. 3 and 4 that deformation in large (300 μm) grains in Al 2219-T851 eventually becomes nearly perfectly plastic during fatigue (i.e., $E_p \approx 0$). While it has been clear that reaching this state involved a dramatic drop in the local yield strength, it was not clear if the evolution of the local mechanical properties entailed a decrease in σ_u , a decrease in E_p , or changes in both these quantities. It now appears likely that, while both may be changing, the most important effect is on E_p .

SUMMARY

Strains measured in individual grains of Al 2219-T851 show a progressive evolution of the local mechanical properties. The entire surface is microplastic at fully reversed stresses greater than ± 70 MPa. Early in fatigue, the deformation strains are independent of grain size, suggesting that the flow resides in a matrix subject to short-range constraints. With continued fatigue, an upper flow stress σ_u becomes visible at ~ 200 MPa in grains substantially larger than the mean size. Below σ_u , the material apparently strain hardens, above σ_u it strain softens. The possibility that the development of σ_u coincides with the penetration of the matrix by slip bands is suggested.

Acknowledgements

This research was supported by NADC under Contract No. N62269-86-C-0261. Our thanks are expressed to R.V. Inman for taking the surface deformation micrographs.

FATIGUE 87

REFERENCES

- (1) Asaro, R.J., Acta Metall. 23, 1975, pp. 1255-1265.
- (2) Margolin, H. Hazaveh, F., and Yaguchi, H., Scripta Met. 12, 1978, pp. 1141-1145.
- (3) Morris, W.L., Cox, B.N., and James, M.R., "Microplastic Surface Deformation of Al 2219-T851," to be published in Acta Metall.
- (4) Cox, B.N., Morris, W.L., and James, M.R., "Two-Stage Microplastic Surface Deformation in Al 2219-T851," to be published in Acta Metall.
- (5) Thompson, A.W., Acta Metall. 23, 1975, pp. 1337-1342.
- (6) Margolin, H., and Stanescu, M.S., Acta Metall. 23, 1975, pp. 1411-1418.
- (7) James, M.R. and Morris, W.L., Mat. Sci. and Engrg. 56, 1982, pp. 63-71.
- (8) Atkins, A.G. and Tabor, D., J. Mech. Phys. Solids 13, 1965, 149-164.
- (9) Zurek, A.K., James, M.R., and Morris, W.L., Met. Trans. 14A, 1983, pp. 1697-1705.
- (10) Morris, W.L., Inman, R.V., and James, M.R., J. Matl. Sci. 17, 1982, pp. 1413-1419.
- (11) Mughrabi, H., Acta Metall. 31, 1983, pp. 1367-1379.

FATIGUE 87

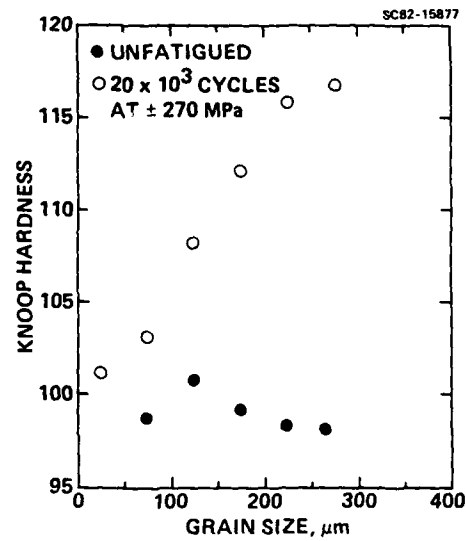


Figure 1 Knoop hardness of Al 2219-T851 vs the individual grain size in a single specimen shows apparent hardening after fatigue. Each datum is an average of approximately ten measurements.

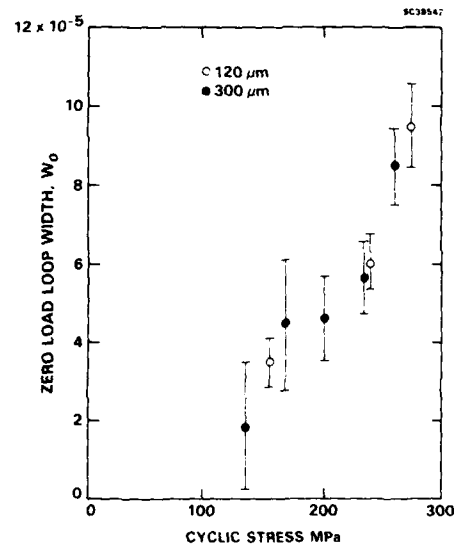


Figure 2 Comparison of loop widths measured at zero load vs cyclic stress amplitude for a 120 and a 300 μm grain. The data were obtained before a substantial fatigue induced change in deformation has occurred.

FATIGUE 87

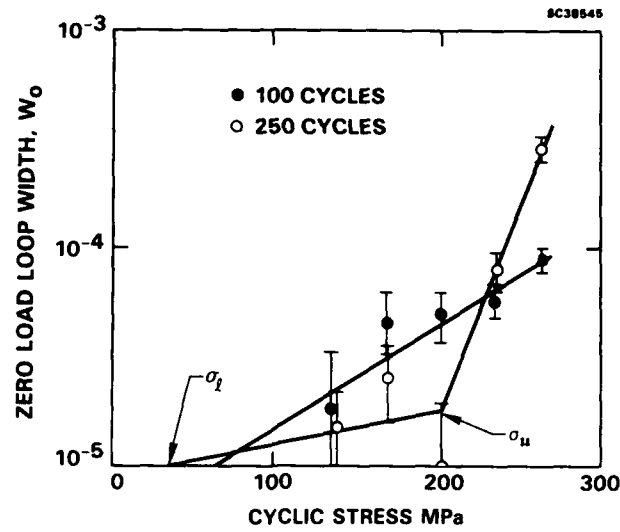


Figure 3 The progressive change in loop width in a 300 μm grain with fatigue.

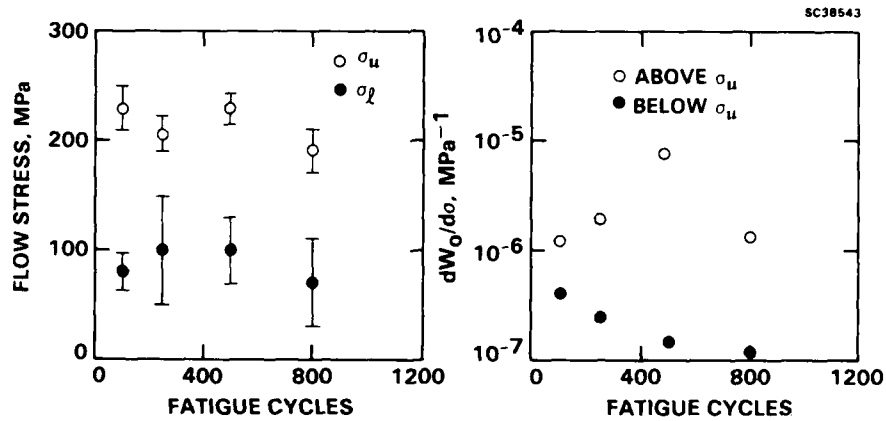


Figure 4 Trends in (a) σ_l and σ_u ; (b) $dW_0/d\sigma$ above and below σ_u for the 300 μm grain.

FATIGUE 87

CYCLIC DEFORMATION OF AN EXTRUDED AlMgSi ALLOY

Ketill Pedersen*

Specimens in under-, peak- and over aged conditions of an extruded commercial AlMgSi alloy have been cycled under constant plastic strain amplitudes. In the under aged condition cyclic hardening to a saturation stress was observed. The cyclic hardening was due to formation of a high density of dislocation loops. In the peak aged condition a saturation stress was obtained after a short period of hardening. Persistent slip bands (PSB) were not observed on the polished specimen surfaces. If the material is recrystallized and aged to peak hardness, cyclic softening occurs and persistent slip bands are formed. A density of $1 \cdot 10^{10}$ dispersoids/mm³ did not prevent formation of persistent slip bands.

INTRODUCTION

Investigations of cyclic stress-strain response and change in microstructure during cyclic deformation are useful for understanding the mechanisms of fatigue failure.

Precipitation hardened aluminium alloys have a cyclic stress strain response that depends on the heat treatment. Alloys in the over aged conditions which contain precipitates impenetrable by dislocations, are cyclically stable. Cyclic saturation is obtained after a short period of hardening (1).

Alloys containing shearable particles, under- to peak aged conditions, show cyclic hardening to a peak stress followed by cyclic softening (2-5). Also in other metals with shearable precipitates, e.g. Cu-2at%Co, a saturation stress is obtained after extensive softening (4). Softening is due to an instability process leading to formation of persistent slip bands, (PSB). Two models for softening have been put forth: 1) The hardening precipitates are repeatedly cut by dislocations, and cause reversion of the precipitates when the size of the precipitates reach a lower

* SINTEF, Division of Metallurgy, N-7034 Trondheim-NTH, Norway.

critical radius. 2) To and fro dislocation motion scrambles the atoms in the precipitates and the ordering component of hardening disappear.

The effect of grain structure on cyclic stress strain response has received less attention (6,7). The aims of this paper is to 1) show the influence of a subgrain structure, obtained by extrusion, on the cyclic stress strain response, 2) compare the cyclic response of this structure with that of a recrystallized structure and 3) show the effect of dispersoids.

EXPERIMENTAL TECHNIQUES

Table 1 shows the chemical composition of the alloy (main alloying elements) in weight %. Other elements are only present as trace elements, except Ti and B which are used for grain refinement.

Table 1 - Alloy composition in Weight %

<u>Mg</u>	<u>Si</u>	<u>Mn</u>	<u>Cr</u>	<u>Fe</u>	<u>Al</u>
0.64	0.72	0.48	0.15	0.29	bal.

The alloy was DC cast, homogenized 2.5 hours at 580°C, and extruded to rods with a diameter of 250 mm. The material was then stored at room temperature for 3 months. An increase in hardness from 50 VHN to 80 VHN was observed during the first week. Further storing made only small increase in hardness. From the extruded rods cylindrical fatigue test specimens were machined with a gauge length of 25 mm and a diameter of 6 mm. For surface observations and thin foil preparation a flat area on the gauge length was ground. The specimens were artificially aged at 175°C in a silicon oil bath for different aging time to produce specimens in peak and different under- and over aged conditions. After the heat treatment the specimens were mechanically polished and finally electro polished in a solution of 5% perchloric acid in methanol at -20°C to produce a scratch free and deformation free surface before fatigue testing.

The fatigue tests were run in laboratory air on a MTS closed loop hydraulic testing machine of 100 KN capacity under total strain control. A MTS elasticity compensator was used for determining and keeping the plastic strain constant during each test. Strain amplitudes were measured using a clip on extensometer with a gauge length of 25 mm.

A JEOL 840 scanning electron microscope equipped with a back scattered electron detector was used for detailed investigations of the specimen surface. The internal microstructures were observed in a JEOL 200KV transmission electron microscope.

RESULTS

Microstructure

The grain structure of the material is fibrous with the longitudinal direction parallel to the load axis. Each grain consists of almost equiaxed subgrains of about 2-5 μm in diameter. The material has a strong $\langle 100 \rangle$ and $\langle 111 \rangle$ -texture.

The presence of Cr and Mn resulted in fine incoherent dispersoids of a size of about 0.1 μm . The density is about $1 \cdot 10^{10}$ dispersoids/ mm^3 . Also coarse, $> 1 \mu\text{m}$, iron rich particles are formed.

Aging at 175⁰C to maximum hardness resulted in a high density of β'' -Mg₂Si precipitates. Near the grain boundaries and the sub-grain boundaries precipitation free zones of about 0.1 μm width are formed. By over aging the precipitates coarsen and lose coherency.

Cyclic stress strain response

The cyclic stress strain responses of the alloy in under-, peak- and over aged conditions when cycled at a plastic strain of $3 \cdot 10^{-4}$ is presented in Fig. 1. The maximum stress is plotted versus the number of cycles to crack initiation. An asymmetrical drop in the tensile and compression peak stresses was used as an indication of crack initiation.

In the under aged condition the cyclic stress strain responses show hardening until a saturation stress of about 290 MPa is reached. This lasts until crack is initiated. By increasing the aging time the initial stress increases and the number of cycles to peak stress is decreased. But the saturation stress seems to be independent of aging time until peak hardness.

In the peak aged condition Fig. 1 initial cyclic hardening during the first 500 cycles is followed by saturation at a level of 295 MPa. No softening or hardening is observed during further cyclic deformation. The increase in stress during the first 500 cycles is not more than 5 MPa.

In the over aged condition initial softening is observed before a saturation stress is obtained. The more the alloy is over aged, the more the saturation stress is reduced.

In Fig. 3 the stress strain responses for under-, peak- and over aged specimens cycled at different plastic strains are presented. Cyclic deformation under constant plastic strain control below $1 \cdot 10^{-4}$ was not possible to obtain with the available equipment. The same behaviour as described above was observed for

all the specimens in the strain range $1 \cdot 10^{-6} < \epsilon < 16 \cdot 10^{-6}$. Varying the strain did not affect the main shape of the cyclic stress strain response. The stress levels are, however, increased by increasing the plastic strain.

Deformation structure

The deformation microstructures after cyclic deforming the specimens at a plastic strain of $3 \cdot 10^{-6}$ to crack initiation, is shown in Fig. 2. In under aged condition a high density of homogeneously distributed dislocation loops are seen in the matrix. Zones which are about $0.1 \mu\text{m}$ wide, and almost free from dislocations, are found near the grain boundaries. Only dislocations normal to the grain boundary are seen in these zones

In the peak aged condition few dislocations were observed in the grain interior. Only in some of the largest subgrains could dislocation loops be seen. Instead the deformation was localized to the precipitation free zones adjacent to the grain boundaries. The grain boundaries in undeformed specimens were straight, with precipitation free zones on both sides. After cyclic deforming the material some of the grain boundaries got a wavy appearance as shown in Fig. 2. Dislocations crossing the PFZ can be seen.

In the overaged condition the dislocations were difficult to observe due to interfering contrast from the precipitates. Single dislocations, however, were observed close to and in the precipitation free zones and dislocations normal to the grain boundaries were also seen in the over aged condition.

After cycling to crack initiation, the specimen surfaces had cracks in the subgrain boundaries for all three aging conditions, as seen in Fig. 4, which is from a specimen in the maximum hardness condition. No PSBs were observed in these specimens either by light or scanning electron microscope investigation of the surfaces, or by transmission electron microscope investigation of the interior of the specimens.

Recrystallized grain structure

The addition of dispersoids to age hardened AlMgSi alloys is reported to improve their low cycle fatigue properties (9). The dispersoids homogenize the slip distribution and thereby reduce the tendency for cyclic softening. Another beneficial effect of dispersoids is preventing grain growth. Reduced grain size is reported to increase the number of cycles to crack initiation (5,6).

To determine whether the high density of dispersoids was the reason for cyclic hardening to saturation in peak aged condition, the material was deformed 5% by cold rolling and recrystallized at 550°C . The grain size obtained was $50 \mu\text{m}$ in the transverse

direction and 100 μm in the longitudinal direction. Apart from the change of the grain structure the density of dispersoids and the density of precipitates were the same as in the fibrous material.

The cyclic stress strain responses of recrystallized and fibrous grain structures may be compared in Fig. 4. In the under aged conditions specimens with recrystallized grain structure show hardening which may be followed by softening. In peak aged conditions a short hardening period is followed by extensive softening. In over aged conditions only softening is observed. The amount of softening is reduced by further over aging. By investigating the surfaces of the fatigued specimens under and peak aged specimens show persistent slip bands.

DISCUSSION

Usually the cyclic stress strain response of age hardened alloys is initial hardening followed by softening and saturation. This kind of cyclic stress strain response has been observed in single crystals and polycrystalline material with recrystallized grain structures. The softening is due to formation of coarse slip bands. In these bands the hardening effect due to precipitates is destroyed.

In the extruded alloy where small subgrains of about 2 - 5 μm in diameter are present, no softening was observed. Light, SEM and TEM investigations of the under-, peak- and over aged conditions did not reveal any PSBs after cycling which could result in softening.

In the under aged condition there is a small difference in hardness between areas near the subgrain boundaries and the grain interior. Cyclic deformation of this structure results in formation of dislocation loops and an increase in strength is observed during cycling. Near the grain boundaries, almost dislocation free zones are found, possibly due to vacancy diffusion to the grain boundaries causing the dislocation loops to shrink and disappear. Since the grain interior is hardened during cyclic deformation, an increase in strength will be created between the dislocation free zone and the grain interior. The strain will then be localized to the weaker zone near the grain boundaries (10) and cracks will be initiated in the grain boundaries as is also observed.

In maximum hardness condition, a large difference in strength between the grain interior and the PFZ already exist. Localization of strain to the PFZ will therefore occur almost immediately and a constant cyclic stress strain response is obtained. Localization of strain into PSB in the matrix is prevented by the existence of small subgrains, see Fig. 4.

In the over aged condition the high density of semicoherent or incoherent needle-like Mg_2Si precipitates makes it difficult to observe the dislocation contrast. Dislocations are only observed in the PFZ and our assumption is that deformation is still concentrated to the PFZ.

It may be argued that the high density of Mn and Cr dispersoids is the reason for homogeneous slip distribution in matrix and a stable cyclic stress strain response. This investigation, where the cyclic stress strain responses are compared for specimens which apart from the grain structure are identical, show that this is not the case. In recrystallized material cyclic softening occurs in under- and peak aged condition and SEM micrograph Fig. 4 shows that persistent slip bands have been formed on the surface at these stress levels.

Since in peak aged condition, cyclic softening occurs and persistent slip bands are formed in the recrystallized material containing shearable precipitates dispersoids did not prevent formation of PSB. Even though dispersoids may homogenize slip to some extent as reported (9), their main effect is to prevent grain growth and thereby improve the fatigue initiation properties. A small grain size has been reported earlier (5,6) to increase the resistance against crack initiation.

CONCLUSION

A commercially extruded AlMgSi alloy containing subgrains of about 2 - 5 μm in diameter did not show cyclic softening in under and peak aged conditions. A cyclic saturation stage was reached after a period of hardening.

Cracks were initiated in or near the grain boundaries due to localization of plastic strain in weak zones adjacent to the grain boundaries.

The reason why peak and over aged material showed a constant cyclic stress-strain response, is the existence of small subgrains which prevent the formation of persistent slip bands before fracture starts in PFZ.

In recrystallized material of the same alloy, extensive cyclic softening was observed after a short period of hardening in peak conditions. Persistent slip bands were formed. A density of Mn and Cr dispersoids of $1 \cdot 10^{10}$ dispersoids/mm³ did not prevent the formation of persistent slip bands.

REFERENCES

- (1) Calabrese, C. and Laird, C., *Matr. Sci. Eng.*, 13 (1974), 159-174.
- (2) Calabrese, C. and Laird, C., *Matr. Sci. Eng.*, 13 (1974), 141-157.
- (3) Wilhelm, M., *Matr. Sci. Eng.*, 48 (1981) 91-106.
- (4) Gerold, V. and Steiner, D., *Scripta Met.* 16 (1982) 405-408.
- (5) Pedersen, K. (1986) *proc. Aluminium alloys their physical and mechanical properties*. vol. 2 Virginia Edit A.E. Starke Jr and T.H. Sanders, Jr.
- (6) Lutjering, G. et al. *Proc of third int. conf. on fracture* (1977) Waterloo, Canada, Edit. D.M.R. Taplin.
- (7) Sanders, R.E. and Starke, A.E. (1977) *Matr. Sci. Eng* 28, 53-69.
- (8) Renaird, A. et al. *Matr. Sci. Eng*, 60 (1983) 113-120.
- (9) Edwards, L. and Martin, J.W. (1982) *proc. 6th Int. Conf. on Strength of Metals and Alloys*. ed: R.C. Gifkings, Melbourne, Australia.
- (10) Graf, M. and Hornbogen, E. (1976) *Acta Met.*, Vol 25.

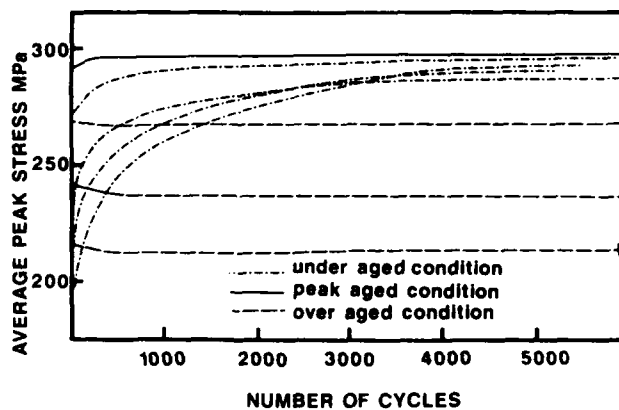


Fig. 1. The cyclic stress strain response as a function of aging conditions.

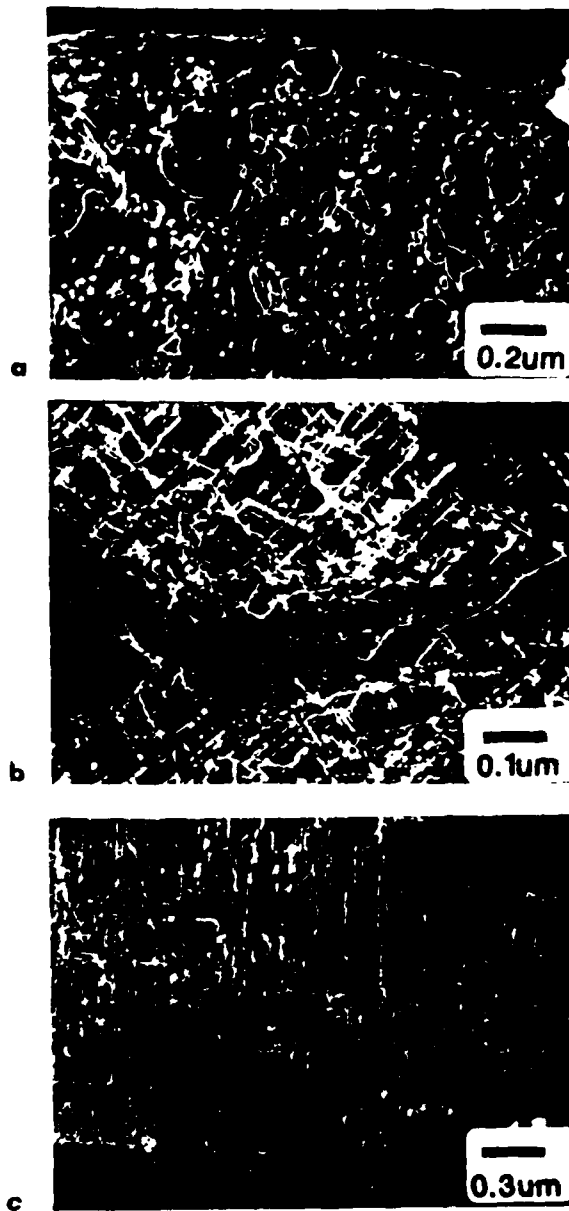


Fig. 2. TEM micrograph of cyclic deformed specimens to crack initiation $\epsilon_p = 3 \cdot 10^{-3}$ a) under aged-, b) peak aged- and c) over aged condition.

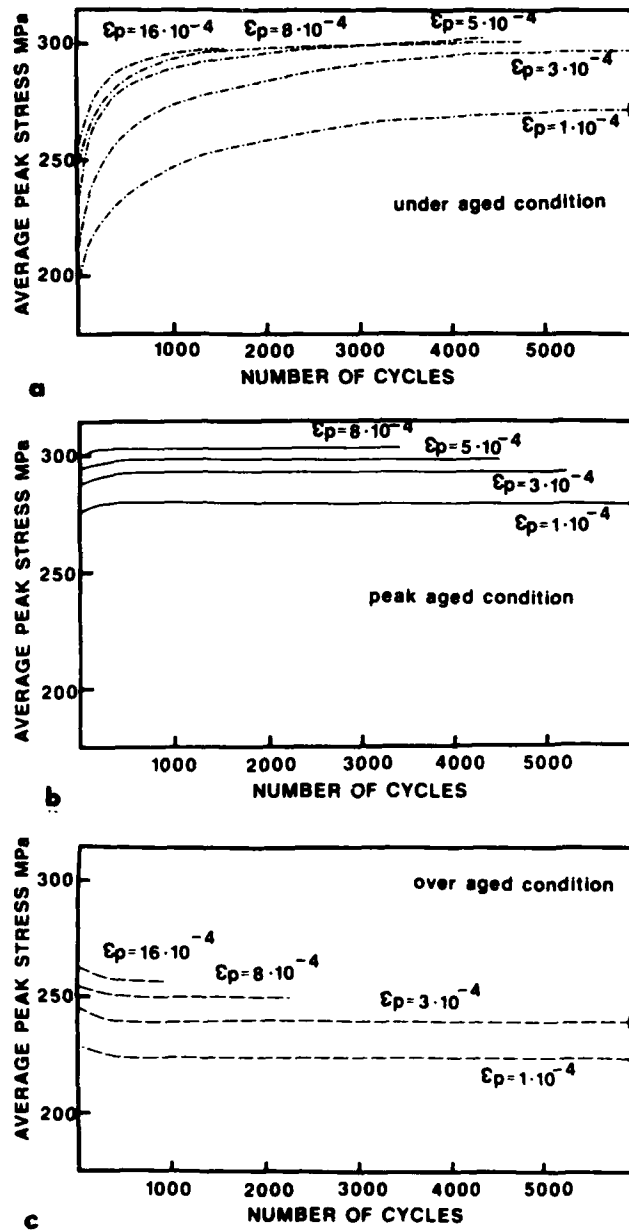


Fig. 3. The stress strain response for a) under-, b) peak- and c) over aged condition cycled at different plastic strains.

FATIGUE 87

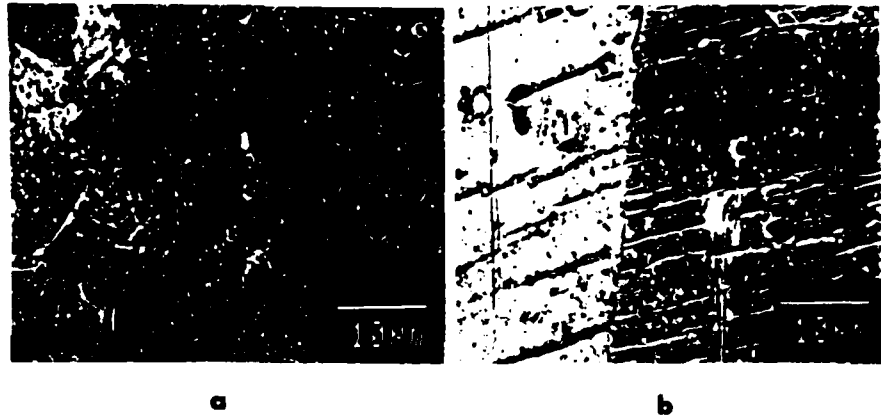
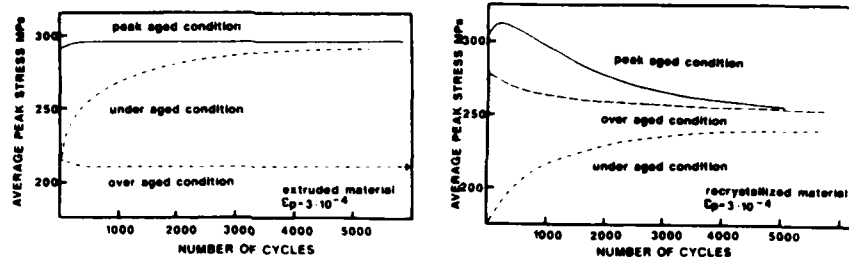


Fig. 4. The cyclic stress strain response for a) subgrain structure and b) recrystallized grain structure. The micrograph show the surface structures when the stress-strain response show that crack has been initiated. The specimens with subgrain structures shows the formation of cracks along the subgrain boundaries. In recrystallized material PSB are formed.

THE ORIENTATIONS OF DIPOLAR WALLS PRODUCED BY CYCLIC DEFORMATION

J.I. Dickson*, S.Turenne**, L. Handfield* and G. L'Esperance*

Dipolar walls produced by cyclic deformation consist largely of dipole loops and can be modelled as a geometrical network of stacked loops, formed by edge-trapping and/or jog-dragging mechanisms and swept together by edge dislocations. Such a model helps to understand the orientations and certain other aspects of dipolar walls in f.c.c., b.c.c. and h.c.p. metals.

INTRODUCTION

The dislocation structures which form during cyclic deformation are known to influence the cyclic stress (e.g., Mughrabi (1)) and, for the initiation of microcracks within persistent slip bands, also to influence the crack initiation behaviour on polished specimens of single-phase metals (e.g., Polak et al (2)). For wavy slip metals cycled at low strain amplitudes, the dislocation structures produced are largely dipolar and contain large numbers of dipole loops. A recent geometrical and mechanistic model (Dickson et al (3,4)) for the formation of dipolar walls consisting of dipole loops has been shown to explain well the available experimental evidence concerning the orientations and certain other aspects of dislocation structures produced by the cyclic deformation of f.c.c. metals. The objectives of the present paper are, firstly, to review this model and the aspects of dislocation structure which it allows to explain in f.c.c. metals and, secondly, to show that this model also helps to explain similar dipolar dislocation structures produced in b.c.c. and h.c.p. metals.

* Departement de genie metallurgique, Ecole Polytechnique, P.O. 6079, Sta. "A", Montreal, Québec, Canada, H3C 3A7.

** Present address: IGM-CNRC, Boucherville, Que., Canada, J4B 6Y4.

FATIGUE 87

In this model, edge-type dipole loops which form from edge-trapping and jog-dragging mechanisms are assumed to be swept to sites where they become stacked in regular arrays. This sweeping is performed by edge dislocations parallel to the long loop segments and of the same Burgers vector as the loops. Only the slip plane of the long segments is considered and, for simplicity, will be referred to as the slip plane of the loops. The idealized three-dimensional stacking network considered as representing the loop stacking aspects of the dipolar wall is schematized in Figure 1, for dipole loops of two orientations, i.e., of either one or two Burgers vectors and of two slip planes for long loop segments. Wall orientations are predicted from the stacking directions of the idealized network. One of these directions is normal to the plane containing both edge dislocation orientations of long loop segments. The other two effective stacking directions, indicated a and b in Figure 1, bisect the acute and obtuse angles between long loop segments. Restricted stacking in one direction results in a wall containing the other two directions; limited stacking in two directions results in a loop patch extended parallel to the third direction. Since the loops are swept into the walls by edge dislocations on the same slip system as the long loop segments, this mechanism always tends to extend the network in the a-direction. The probability of formation of a given wall is also influenced by the angle(s) at which the loops are swept into the walls, as measured by the complement of the angle between the Burgers vector of a loop and the normal to the wall. High dislocation sweeping angles favour tight loop stacking and limited stacking in that direction; low dislocation sweeping angles disfavour the formation of that wall orientation.

OBSERVATIONS AND DISCUSSION

F.c.c. Metals. This model of walls consisting of dipole loops of two Burgers vectors has been shown to explain well the orientations of labyrinth walls in f.c.c. metals ((3,4), L'Esperance et al (5)). Such labyrinth walls have been found to occur in the case of a pair of mutually perpendicular Burgers vectors, with the exact wall orientations obtained depending on the relative number of dipole loops of each Burgers vector. A dominant slip system favours the occurrence of the wall containing both orientations of long loop segments, which wall can better accommodate excess loops of the dominant system as well as individual edge dislocations of both systems. This model of walls involving two Burgers vectors also permits to explain (3,4) the available experimental evidence in f.c.c. metals for the wall orientations which form at the intersection sites of persistent slip bands (PSB's) as well as that for rotations in wall orientations away from perpendicular to the primary Burgers vector which occur as a secondary slip system becomes activated. The orientations of the veins in the matrix structure of single crystals oriented for duplex slip have also

been shown to be well explained (4) by this model.

For single crystals oriented for single slip, the orientations of the veins appear consistent (4), from single trace analysis, with those of walls consisting of dipole loops of the primary Burgers vector and of one of the more probable secondary Burgers vectors. This has now been more convincingly demonstrated (Hong and Bandrup (6)) in polycrystalline copper containing a mixture of matrix structure and of PSB's (Figure 2). The presence of the latter permitted identifying the primary slip system. Dislocations of two secondary Burgers vectors were identified in the matrix structure, and four vein orientations were identified from detailed observations employing four different beam directions. All four vein orientations identified corresponded to walls predicted for the primary slip system combined with a secondary slip system involving one of the other Burgers vectors identified. With this explanation of the vein structure in regions in which one slip system dominates, the elongated aspect (Basinski et al (7)) of such veins approximately parallel to the primary edge dislocations can be explained (Dickson et al (8)) by extended stacking of loops occurring preferentially in the mechanistically favoured a -direction of Figure 1, with the wall shape developing as extended stacking in a second direction occurs with increased cycling.

In the case of dislocation activity of only one Burgers vector, either on a single slip system or combined with cross slip, the consideration of the relevant dipole loop stacking network and of the dislocation sweeping angles results in the only wall orientation expected being that perpendicular to the Burgers vector (4). Thus the transition from veins to ladder-like persistent slip bands (PSB's) is associated with a decrease in the amount of secondary slip activity and with a disappearance within the PSB's of dipole loops of the secondary Burgers vector. As the strain amplitude or the number of cycles is then further increased, a secondary slip system can become reactivated resulting in walls rotating away from the orientation perpendicular to the primary Burgers vector.

In the case of $\langle 100 \rangle$ or $\langle 111 \rangle$ multislip axis single crystals, a dominant wall has been observed (Jin and Winter (9); Lepisto et al (10)) to form normal or roughly normal to the stress axis. In each case, this wall orientation can be explained (3,4) as a composite wall made up of segments whose orientations are predicted by considering the expected slip systems taken in the appropriate pair combinations.

Assuming that a constant dislocation sweeping distance d_s , equal to the width of the channels between $\{110\}$ walls within PSB's, can be applied to the other dipolar wall orientations identified for f.c.c. metals, the widths of the channels between these

FATIGUE 87

other walls should depend on the dislocation sweeping angle ϕ (Dickson et al (11)). according to

$$W_s = d_s \sin \phi \quad (1)$$

The presently available experimental evidence indicates that the values of W_s actually observed (Figure 3) are equal or lower than those predicted by equation 1. This can be explained firstly, since all these other wall orientations are associated with some degree of duplex or multiple slip, which effect can be expected to decrease d_s on any particular slip plane. As well, in the uncondensed walls, the loose stacking of the dipole loops in the walls can be expected to decrease d_s as the wall thickness increases.

B.c.c. metals. The orientation of walls which can be predicted from the consideration of a network of dipole loops of the type schematized in Figure 1 will depend on the individual slip systems considered. For $\{110\} \langle 111 \rangle$ slip, the types of wall orientations, which can be geometrically predicted, are summarized in Table 1. Since the $\langle 121 \rangle$ edge dislocation orientations, perpendicular to both the slip plane normal and the Burgers vector, determine these wall orientations, the walls predicted for $\{110\} \langle 111 \rangle$ slip in b.c.c. metals have exactly the same indices as those predicted for $\{111\} \langle 110 \rangle$ slip in f.c.c. metals, if the slip planes indices in each crystalline structure correspond to the slip direction indices for the other.

In a study carried out on a renitrogenized mild steel, some dipolar dislocation structures similar to these described for f.c.c. metals were studied. These included ladder-like walls having $\{111\}$ orientations within $\{110\}$ PSB's, with the walls perpendicular to the dominant Burgers vectors (Figure 4) and, in regions closer to grain boundaries, misoriented cells forming within such PSB's. Two regions of labyrinth-like walls were also studied in detail, one of which is shown in Figure 5. In both cases, these walls formed in a region in which dislocations of two Burgers vectors were identified. For the region shown in Figure 5, the Burgers vectors identified were $a/2 [\bar{1}11]$ and $a/2 [11\bar{1}]$ and the walls for the different beam directions employed agreed well with $(1\bar{3}1)$ and $(\bar{1}01)$ orientations, which are the two wall orientations expected for $(0\bar{1}1) [\bar{1}11]$ and $(1\bar{1}0) [11\bar{1}]$ duplex slip.

The second region of labyrinth walls studied showed similar good agreement with predicted wall orientations for the identified pair of Burgers vectors, with the best agreement being again for a $\{\bar{3}11\} - \{0\bar{1}1\}$ combination of walls but with reasonable agreement also found for a $\{100\} - \{0\bar{1}2\}$ combination, predicted for the same Burgers vectors but for two different $\{110\}$ slip planes. As will be shown elsewhere (Turenne et al (12)), the dipole loop stacking model of dislocation walls also allows to explain a num-

TABLE 1 - Summary of Geometrically Predicted Wall Orientations for B.C.C. and H.C.P. Metals

First Slip System	Second Slip System	Wall Orientations		
		A	B	C
B.C.C. Metals; {110}<111> Slip				
<u>Perpendicular Slip Planes</u>				
$(\bar{1}01)[111]$	$(101)[\bar{1}\bar{1}1]$	$(02\bar{1})$	(100)	(012)
<u>Common Slip Plane</u>				
$(0\bar{1}1)[111]$	$(0\bar{1}1)[\bar{1}\bar{1}1]$	(100)	(011)	$(0\bar{1}1)$
<u>60° Between Slip Planes</u>				
$(\bar{1}01)[111]$	$(0\bar{1}1)[\bar{1}\bar{1}1]$	$(3\bar{1}2)$	(130)	$(\bar{3}15)$
$(1\bar{1}0)[111]$	$(101)[\bar{1}\bar{1}1]$	$(23\bar{3})$	(011)	$(3\bar{1}1)$
<u>Cross Slip</u>				
$(\bar{1}01)[111]$	$(0\bar{1}1)[111]$	$(\bar{1}10)$	$(\bar{1}\bar{1}2)$	(111)
<u>Single Slip</u>				
$(\bar{1}01)[111]$	-----	$(1\bar{2}1)$	$(\bar{1}01)$	(111)
H.C.P. Metals				
<u>Duplex Basal Slip</u>				
$(0002)[11\bar{2}0]$	$(0002)[1\bar{2}10]$	$(\bar{2}110)$	$(01\bar{1}0)$	(0002)
<u>Single Basal Slip</u>				
$(0002)[11\bar{2}0]$	-----	$(1\bar{1}00)$	$(11\bar{2}0)$	(0002)
<u>Duplex Prismatic Slip</u>				
$(1\bar{1}00)[11\bar{2}0]$	$(10\bar{1}0)[1\bar{2}10]$	(0002)	$(\bar{2}110)$	$(01\bar{1}0)$
<u>Single Prismatic Slip</u>				
$(1\bar{1}00)[11\bar{2}0]$	-----	(0002)	$(11\bar{2}0)$	$(1\bar{1}00)$

FATIGUE 87

ber of literature observations on b.c.c. metals.

H.c.p. metals. Table 1 also lists wall orientations predicted for duplex and single slip on basal or $\{10\bar{1}0\}$ prismatic planes in h.c.p. metals. For duplex basal slip, the $\{10\bar{1}0\}$ type wall predicted should be favoured because of its higher dislocation sweeping angles (60°) than those for the other wall orientations (30° for the $\{2\bar{1}\bar{1}0\}$ wall and 0° for the $\{0002\}$ wall). For duplex prismatic slip, both orientations of long loop segments are parallel to the c-axis, which is then the mechanistically preferred stacking direction. The other two probable stacking directions in the network of dipole loops can be considered to be those which result in symmetrical dislocation sweeping angles for both types of dipole loops. The $\{10\bar{1}0\}$ type wall thus predicted is expected to be the most favoured orientation since it involves the highest dislocation sweeping angles (60°), while the angle associated with the other two geometrically possible wall orientations are 30° and 0° . In the case of single slip, again only walls perpendicular to the active Burgers vector are expected.

Observations were carried out on cyclically deformed commercial-purity (CP) titanium (1200 ppm (wt) oxygen) and zirconium (900 ppm O) and on high-purity (HP) zirconium (100 ppm O). In the CP metals, it was shown (8) that, for low strain amplitudes, the dipole loop patches were strongly elongated parallel to the c-direction. This corresponds to the mechanistically favoured stacking direction in the case of duplex $\{10\bar{1}0\}$ slip. Since extended stacking in this direction is favoured by parallel dislocations on the same or neighbouring slip planes sweeping dipole loops into the walls, stacking in this direction could also be more favoured than that normal to the slip plane in the case of single prismatic slip, even though loop stacking in both directions is associated with the same 0° dislocation sweeping angle. In observations carried out in the basal plane, the loop patches observed in CP Ti and Zr tend to be parallel to the traces of the $\{10\bar{1}0\}$ and $\{1\bar{2}10\}$ (Figure 6). The former orientation is that expected to be favoured for loop patches consisting of dipole loops of two Burgers vectors and the latter that expected to be favoured for patches of loops of a single Burgers vector.

In HP Zr cycled at low amplitudes, the dipolar walls viewed perpendicularly to the c-axis can be seen to consist of lines of loosely stacked dipole loops, elongated perpendicularly to the c-axis, with these lines then loosely stacked in the c-direction (Figure 7). Evidence for similar but less conspicuous gaps in the stacking in the c-direction can also be found in CP Ti (Figure 8) and Zr, both of which also tend to present a few lines of stacked dipole loops, normal to the c-axis. Such observations can be interpreted as showing the sequence in which the loop patches form. The first step in loop patch formation consists of the dipole loops being swept together by edge dislocations gliding on

individual slip planes. This sweeping occurs in the direction parallel to the Burgers vectors. In Zr and Ti, the edge dislocations are relatively short because of the limited mobility of the screw dislocations (Dickson et al (13,14)) and thus the dipole loops swept together by edge dislocations activated from the same sources can be seen as stacked lines of dipole loops normal to the c-axis. The lines produced by edge-dislocations doing the sweeping on the same and neighbouring slip planes then tend to line up above each other to extend the wall in the mechanistically favoured c-direction. Quite similar dipolar walls presenting evident gaps have been observed for magnesium deformed by basal slip (Kwadio and Brown (15)). Such observations can be considered as strongly indicating that the dipolar walls form as a result of a dipole loop sweeping mechanism and that the first stage in wall formation is the sweeping together of dipole loops on individual slip planes.

CONCLUSIONS

From the present study, it can be concluded that modelling dipolar walls produced by cyclic deformation, as regular stacking arrangements of dipole loops, helps to understand the orientations and certain other aspects of the dipolar walls observed in f.c.c., b.c.c. and h.c.p. metals.

ACKNOWLEDGMENTS

Financial support from the NSERC (Canada) and FCAR (Québec) research-support programs is gratefully acknowledged. The authors are grateful to Nicole Roy for typing the manuscript.

REFERENCES

1. Mughrabi, H., Mater. Sci. Eng., Vol. 33, 1978, pp. 207-223.
2. Polak, J., Lepisto, T.K. and Kettunen, P., Mater. Sci. Eng., Vol. 74, 1985, pp. 85-91.
3. Dickson, J.I., Boutin, J. and L'Espérance, G., Acta Metall., Vol. 34, 1986, pp. 1505-1514.
4. Dickson, J.I., Handfield, L. and L'Espérance, G., Mater. Sci. Eng., Vol. 81, 1986, pp. 477-492.
5. L'Espérance, G., Vogt, J.B. and Dickson, J.I., Mater. Sci. Eng., Vol. 79, 1986, pp. 141-147.
6. Hong Bande, L'Espérance, G. and Dickson, J.I., to be published.

FATIGUE 87

7. Basinski, S.J., Basinski, Z.S. and Howie, A., *Phil. Mag.*, Vol. 19, 1969, pp. 899-924.
8. Dickson, J.I., Handfield, L., Turenne, S. et L'Espérance, G., "The Three-Dimensional Shape of Loop Patches Produced by Cyclic Deformation", *Mater. Sci. Eng.*, 1987, in the press.
9. Jin, N.Y. and Winter, A.T., *Acta Metall.*, Vol. 32, 1984, pp. 1173-1176.
10. Lepisto, T.K., Kuokkala, V.T. and Kettunen, P.O., *Mater. Sci. Eng.*, Vol. 81, 1986, pp. 457-463.
11. Dickson, J.I., L'Espérance, G. and Turenne, S., "Factors Influencing the Spacings Between Dipolar Walls in Cyclic Deformation", *Scripta Metall.*, 1986, in the press.
12. Turenne, S., L'Espérance, G. and Dickson, J.I., "The Orientations of Dipolar Dislocation Structures Produced by the Cyclic Deformation of B.C.C. Metals", submitted to *Acta Met.*
13. Dickson, J.I., Handfield, L. and L'Espérance, G., *Mater. Sci. Eng.*, Vol. 60, 1983, pp. L3-L7.
14. Dickson, J.I., Handfield, L. and L'Espérance, G., "A Comparison of the Cyclic Deformation Behaviour of Two Purities of Zirconium", in "Strength of Metals and Alloys (ISMA7)", edited by H.J. McQueen, J.P. Bailon, J.I. Dickson, J.J. Jonas and M.G. Akben, Pergamon Press, 1985, Vol. 1, pp. 355-360.
15. Kwadjo, R. and Brown, L.M., *Acta Metall.*, Vol. 26, 1978, pp. 1117-1132.

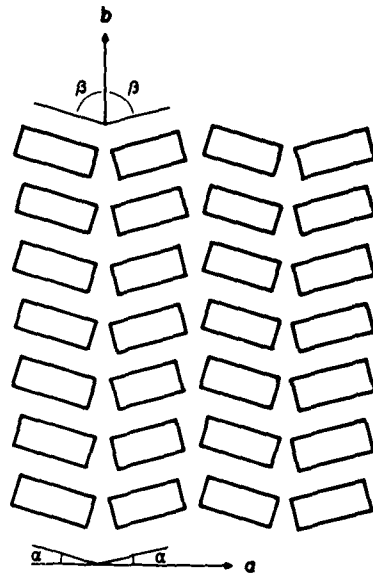


Figure 1 Dipole loop stacking arrangement assumed [3]



Figure 2 Region of PSB's and veins [6], Cu, $\Delta\epsilon/2=0.15\%$

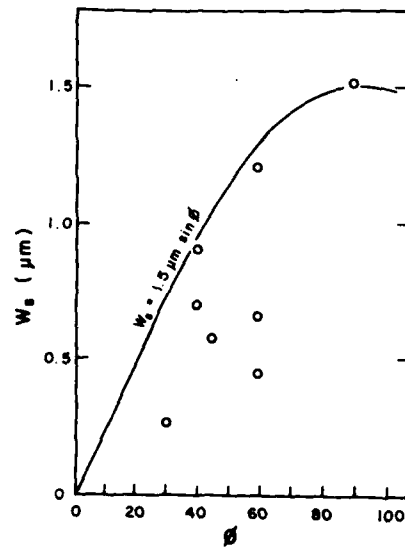


Figure 3 Variation wall spacing with sweeping angle, Cu [11]



Figure 4 Region of PSB's in mild steel, $\Delta\epsilon/2=0.33\%$



Figure 5 Labyrinth walls in mild steel, $\Delta\epsilon/2=0.40\%$



Figure 6 Dipolar walls observed in CP Ti, $\Delta\epsilon/2=0.25\%$, $B=[0001]$



Figure 7 Loose dipolar walls in HP Zr, $\Delta\epsilon/2=0.25\%$, $B=\langle 1210 \rangle$

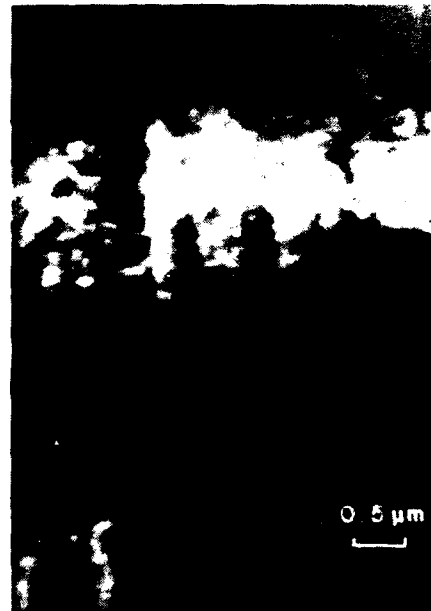


Figure 8 Details of dipolar wall in CP Ti, $\Delta\epsilon/2=0.25\%$, $B=\langle 1210 \rangle$

FATIGUE 87

CRACK CLOSURE

FATIGUE 87

CLOSURE BEHAVIOR UNDER CONSTANT EFFECTIVE STRESS INTENSITY LOADING CONDITIONS

C.D. Carman¹, and B.M. Hillberry²

Crack closure was measured over a wide range of stress intensity levels and stress ratios for 7475-T6 aluminum alloy. These results were used to generate a block loading program that would produce a constant ΔK_{eff} which was then shown experimentally to produce a constant fatigue crack growth rate.

INTRODUCTION

Fatigue crack closure is an important concept in understanding fatigue crack growth behavior. It has been used to correlate such effects as stress ratio, delay due to variable amplitude loading and threshold behavior. Elber(1) first observed that a fatigue crack remained closed over the initial part of the loading cycle and postulated that crack growth only occurs during the portion of the load cycle when the crack is open. In terms of stress intensities, the driving force to propagate the crack is the effective stress intensity, ΔK_{eff} , which is the range from the crack opening load to the maximum load. Although there has been considerable research on crack closure, it is still difficult to measure (eg. Ref. 2).

1 Engineer, General Dynamics Corporation, Ft. Worth Division, Ft. Worth, TX.

2 Professor, School of Mechanical Engineering, Purdue University, W. Lafayette, IN.

Stress Ratio Effects

Crack closure has been used effectively to correlate fatigue crack growth rate at different stress ratios [1, 3-6]. These investigations are generally accomplished by running tests under constant loading conditions while closure is measured at specified intervals during the test. The effective stress intensity range is then fit to a linear function of the stress ratio, R:

$$\frac{\Delta K_{\text{eff}}}{\Delta K} = f(R)$$

where $f(R)$ is linear. Several specimens are tested in order to have da/dN versus ΔK data for different R ratios. The da/dN data are usually found to correlate very well when plotted versus ΔK_{eff} .

Thickness Effects

It has been observed that the crack growth rate is lower in specimens under plane strain conditions (7). However, Daiuto and Hillberry (8) and others (9-10) have concluded that plane strain conditions in thicker specimens result in faster FCG rates than plane stress conditions in thinner specimens. Assuming that if cracks do grow faster under plane strain conditions, then it is expected that a thick specimen would show less closure than a thin specimen because of different degrees of plasticity.

Objective

The objective of this study was to measure fatigue crack closure for a wide range of stress intensities and stress ratios, determine the R dependency, $f(R)$, and then using this $f(R)$, define a new loading pattern with a wide range of R and ΔK that would predict constant growth rate. Finally, this new loading pattern would be verified experimentally to produce constant growth rate.

MATERIALS AND METHODS

The material tested was from a single heat of 7475-T731 aluminum alloy. The mechanical properties of the material are listed in Table 1. The specimens were 158 x 558 mm center cracked tension panels (MT specimen). Two different thicknesses, 2.03 mm and 6.30 mm, were tested. The crack was initiated from a 0.25 x 5 mm electrical discharge machined slot which was centered, perpendicular to the applied load.

The tests were conducted using an 89 KN (20 KIP) electrohydraulic fatigue machine operating in load control. A microcomputer was used for function generation, data acquisition, and control. Crack length was measured with a traversing 100X stereo microscope. The cycle count was normally recorded at 0.2 mm intervals. Specimens were precracked 7.6 mm in accordance with ASTM E647 test method. Tests were performed in room air conditions at 20-22°C. Humidity measurements from wet and dry bulb temperatures indicated that the relative humidity in the laboratory ranged 38-42 percent during the testing period. The fatigue crack was grown at the rate of 12 to 18 Hz (depending on the expected FCG rate) and the load-displacement closure data were recorded at 0.5 Hz. A seven point floating polynomial method was used to differentiate the a vs. N data.

phase one of the test program was designed to determine the closure behavior for various R ratios and load levels. Initially, the specimen was loaded in constant K_{max} conditions and the R ratio was incremented in discrete steps of 0.05 by reducing K_{min} . The phase one loading conditions for the two different thicknesses are shown in Figures 1 and 2. Load-displacement closure data were recorded for each R ratio. After the crack length of 22.86 mm, constant ΔK conditions were applied with the R ratio incremented in discrete steps of 0.05. Again, load-displacement closure data were recorded at each R ratio.

The load profile for phase two of the program was generated to give constant ΔK_{eff} conditions with different stress

ratios, K_{\max} , and K_{\min} , which were determined from

$$K_{\max} = \frac{\Delta K_{\text{eff}}}{(1-R)f(R)} \quad (2)$$

$$K_{\min} = RK_{\max} \quad (3)$$

where $f(R)$ was determined from the closure measurements of the phase one test program. The R ratio was also incremented in steps of 0.05 with increasing K_{\max} and K_{\min} to avoid the influence of delay behavior.

Crack Closure Measurement

Crack closure was measured using an Elber type crack tip opening displacement gage (CTOD). The gage was positioned one-half of the specimen thickness behind the crack tip. The load-CTOD data were digitally recorded. The opening load, P_{op} , was determined as the tangent point between the curved portion and the linear portion of the data using a computer routine to fit the data to a model. This method provided an automated procedure for determining P_{op} and is described in detail by Carman, et al [11].

RESULTS

The material closure response was determined by plotting the ratio of $\Delta K_{\text{eff}}/\Delta K = f(R)$ versus the stress ratio, R . Figures 3 and 4 show the resulting data from the phase one tests for both the thin and thick specimens respectively. The numbers in these plots are the data points corresponding to the loading condition as labeled in Figures 1 and 2. The dashed line represents the least squares fit to the numbered data points. For the 2.03 mm specimens,

$$f(R) = 0.55 + 0.59 \cdot R.$$

For the 6.30 mm specimens,

$$f(R) = 0.70 + 0.42 \cdot R.$$

The thin specimens started in mixed mode and quickly went into the plane stress condition. The thick specimens started in plane strain and eventually moved into mixed mode conditions.

Figures 5 and 6 shows the resulting FCGR from the phase two loading conditions which were predicted to approximate constant ΔK_{eff} conditions and, therefore, constant da/dN . Each of these plots is nearly a horizontal line indicating approximately constant growth rate.

The variation in crack closure results shown in Figures 3 and 4 is considered to be due to the fact that each of the applied load steps as shown in Figures 1 and 2 were only approximately one plastic zone in length. Even with the variation in the crack closure results, nearly constant growth rate as predicted was observed. This suggests that the R dependency might be a secondary effect or that the growth rate is not highly sensitive to crack closure levels.

CONCLUSIONS

Experimentally determined crack closure as a function of stress ratio accurately predicted constant growth rate for a wide range of stress ratio and loading conditions. This was verified for two different thicknesses, however, the R dependency was different for the two thicknesses.

REFERENCES

1. Elber, W., "The Significance of Fatigue Crack Closure," *Damage Tolerance in Aircraft Structures*, ASTM STP 486, American Society for Testing and Materials, 1970.
2. Elber W. and Newman, J.C., Eds., *International Symposium on Crack Closure*, ASTM, 1986.
3. Schijve, J., "Four Lectures on Fatigue Crack Growth," *Engineering Fracture Mechanics*, 11, 1979, pp. 167-221.

4. Ohji, K., Ogura, K. and Ohkubo, Y., "On the Closure of Fatigue Cracks Under Cyclic Tensile Loading," Department of Mechanical Engineering, Osaka University, Suita, Osaka 565, Japan, pp. 1233-124.
5. Shaw, W.J.D. and LeMay, I., "Crack Closure During Fatigue Crack Propagation," ASTM STP 677, American Society for Testing and Materials, 1979.
6. Staal, H.U. and Elan, J.O., "Crack Closure and Influence of Cycle Ratio R on Fatigue Crack Growth in Type 304 Stainless Steel at Room Temperature," Engineering Fracture Mechanics, 11, 1979, pp. 275-283.
7. Wilhem, D.P., "Investigation of Cyclic Crack Growth Transitional Behavior," ASTM 415, American Society for Testing and Materials, 1967.
8. Daiuto, R. and Hillberry, B.M., "Effect of Thickness on Fatigue Crack Propagation in 7475-T731 Aluminum Alloy Sheet," M.S. Thesis, Purdue University, 1984.
9. Heiser, F.A., Mortimer, W., "Effect of Thickness and Orientation on Fatigue Crack Growth Rate in 4340 Steel," Metallurgical Transaction, 3, 1972.
10. McGowan, J.J. and Liu, H.W., "The Role of Three Dimensional Effects in Constant Amplitude Fatigue Crack Growth Testing," Journal of Engineering Materials and Technology, 102, October 1980.
11. Carman, C.D., Turner, C.C., and Hillberry, B.M., "A Method for Determining Crack Opening Load from Load-Displacement Data," International Symposium on Fatigue Crack Closure, ASTM, 1986.

FATIGUE 87

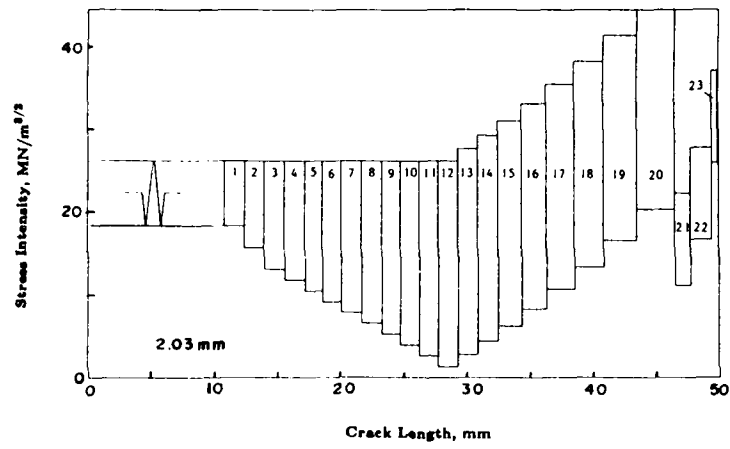


Figure 1. Phase one test program for 2.03mm specimens.

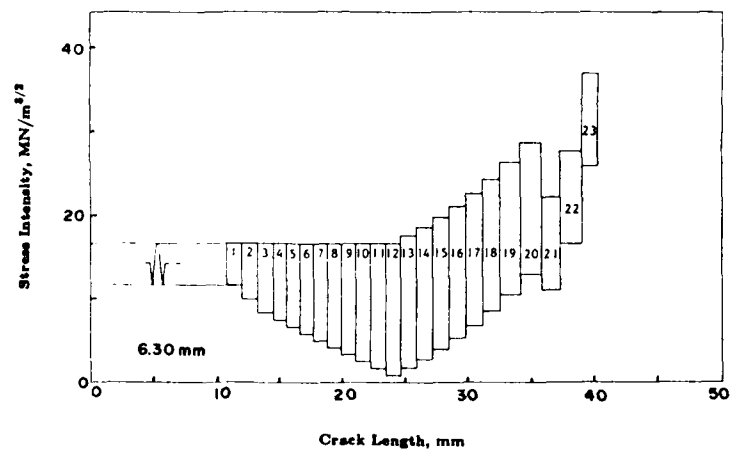


Figure 2. Phase one test program for 6.30 mm specimen.

FATIGUE 87

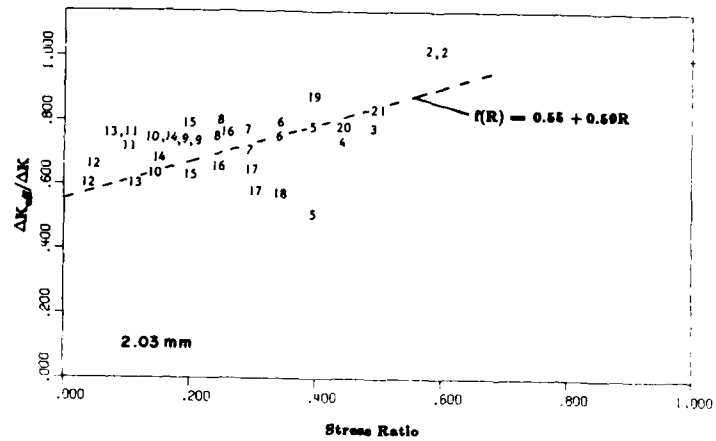


Figure 3. Crack opening as a function of stress ratio for 2.03 mm specimens.

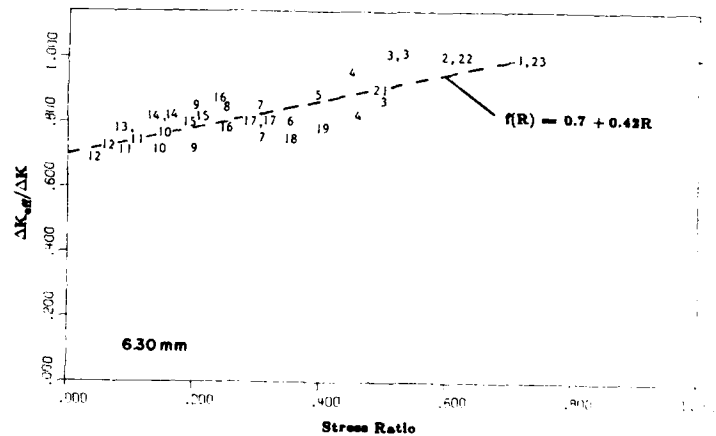


Figure 4. Crack opening as a function of stress ratio for 6.30 mm specimens.

FATIGUE 87

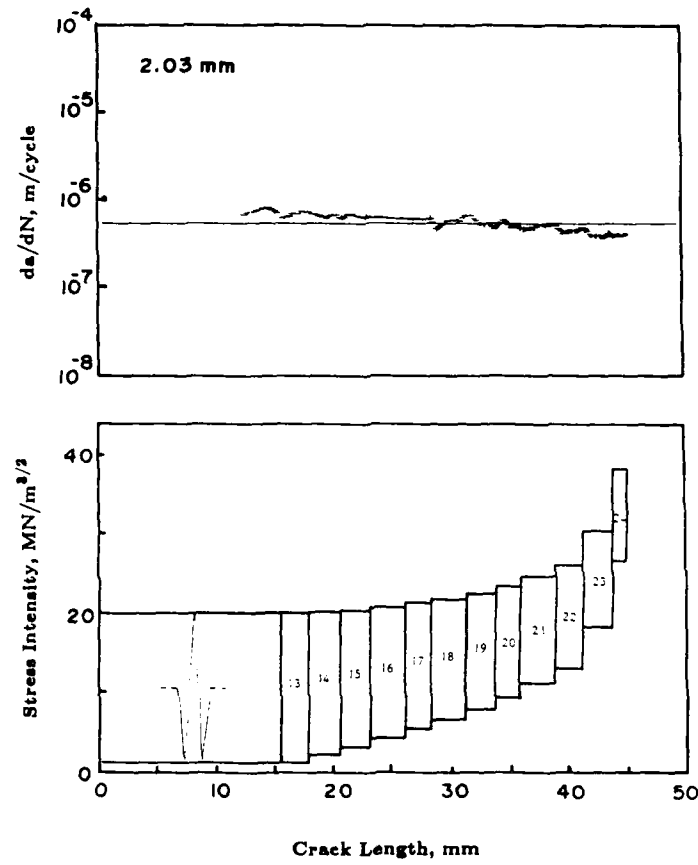


Figure 5. Phase two growth rate and test program for 2.03 mm specimen.

FATIGUE 87

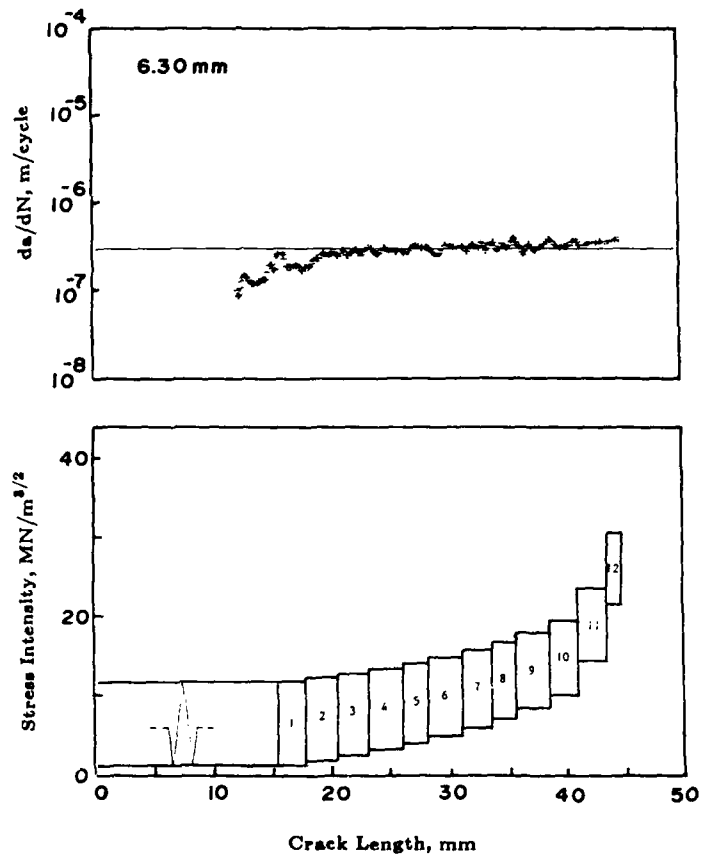


Figure 6. Phase two growth rate and test program for 6.30 mm specimen.

THE INFLUENCE OF THE TOPOGRAPHY OF FRACTURE SURFACES ON CRACK CLOSURE

K. Hamberg*, J. Wasén[†], and B. Karlsson[†]

Roughness induced crack closure of propagating fatigue cracks originates from a complicated interaction between the geometry of the fracture surface at the crack tip and the local microstructure. The fracture surface roughness increases approximately linearly with the size of the microstructural unit for ferritic and pearlitic steels. Mixed structures of ferrite/pearlite or ferrite/martensite in coarse grained steels generally have a larger surface roughness than the individual constituents. Such an effect is not found in fine grained steels. Generally, the crack closure (K_{cl}) increases with the fracture surface roughness (\bar{H}) proportionally to $\bar{H}^{1/3}$.

INTRODUCTION

Since Elber's discovery of the crack closure phenomenon (Elber (1)), evidence has been found for a number of closure mechanisms (Suresh and Ritchie (2)). These mechanisms have been used to rationalize the influence of the microstructure on the near threshold fatigue crack growth rate. Mainly two of these mechanisms, oxide induced closure and surface roughness induced closure, have been discussed in some detail. The roughness induced closure seems to be most relevant since it is related to the fracture surface topography which in turn depends on the underlying microstructure (Hamberg and Karlsson (3), Wasén et al. (4)). The basis of this mechanism is found in the way the crack tip interacts with the local microstructure. Deviations from mode I frequently occur due to the local microstructure (3,4). Consequently local shear displacements take place at the crack tip and cause crack closure (2).

* AB Volvo, Technological Development, Laboratory for Metallic Materials, S-405 08 Göteborg, Sweden.

[†] Department of Engineering Metals, Chalmers University of Technology, S-412 96 Göteborg, Sweden.

FATIGUE 87

The roughness of the serrated fracture surface can be measured in various ways (3,4, Wasén et al. (5), Gray et al. (6), Karlsson et al. (7)). Basically the geometry of the surface can be determined by stereometry or through analysis of profiles from vertical sections perpendicular to the fracture surface (7). The latter technique is used here and is often advantageous as it allows simultaneous analysis of the underlying microstructure. A problem with quantitative fractographic measurements is that no generally accepted definition of the fracture surface roughness exists. This makes a direct comparison between different published results difficult. Huge differences in the absolute values of the surface roughness have been reported for alloys with virtually identical microstructures (3,6).

The aim of the present work is to make a systematic study of the relation between the microstructure, the fracture surface roughness, and the crack closure level.

EXPERIMENTAL PROCEDURE

Plain binary Fe-C alloys with various carbon contents and some commercial, unalloyed steels were used in the present investigation (see table 1). The commercial alloys (from Svenskt Stål AB, Sweden) were tested in the as-received conditions. The pure Fe-C alloys were austenitized at various temperatures (760-1200 °C) in order to develop different grain sizes. All austenitized alloys were furnace cooled (7 °C/min) down to the A_1 -temperature and then either continuously air cooled (15 °C/min) or isothermally transformed in a lead bath at 575 °C for 10 s followed by air cooling. The air cooled materials are denoted soft (S) and the isothermally transformed alloys hard (H). In the case of ferrite/martensite microstructures the specimens were quenched from 788 °C in the ($\alpha+\gamma$) phase region, resulting in a carbon content of 0.40 % in the martensite. Later annealing gave a microhardness of HV 400 in the martensite.

The microstructural variables thus controlled by these heat treatments are the grain size, the volume fraction and the hardness of the second phase and in the case of pearlitic steels the size of the pearlite colonies and nodules as well as the inter-lamellar spacing. These variables were measured with linear intercept methods (3). The values in table 1 are mean values, each one corresponding to a standard deviation of less than 5 %.

For the pearlitic alloys the colony size has been considered as the most relevant microstructural feature in the present context, because the stress field at the crack tip is sensible to the cementite lamellae orientation (3). For the two-phase structures the grain size is defined as the average linear intercepts of the two constituents ferrite/pearlite nodules and ferrite/martensite respectively.

FATIGUE 87

Fatigue crack growth experiments were carried out with single edge notched specimens (thickness 2 mm, width 15 mm). All tests were performed in plain strain condition with $R = 0.05$, using an Instron universal testing machine at constant load amplitude (frequency 55 Hz and laboratory air with 45-55 % relative humidity).

During the propagation, crack opening displacement curves were recorded at different crack lengths. The crack closure load was defined as the intersection point of the two branches of the recorded compliance curve. It is obvious that this point lies between the conventionally defined P_{op} and P_{cl} loads. The advantage of this procedure is that the uncertainties due to evaluation problems are minimised.

The fracture surfaces of the fatigued specimens were geometrically quantified by the aid of profile analysis. The profiles were taken from vertical sections through the interior of the specimens parallel to the main crack propagation direction. High resolution optical micrographs were used for computer aided digitizing of the profile. In the measurements the "real" profile is replaced by a chain of chords with an individual length given by the resolution of the digitalization, in this case 0.5 μm .

The parameters used to characterize the profile should describe the direction and the location of the chords related to some suitable reference line. Parameters that are preferably used in order to quantify the fracture surface are for example the height distribution (4,5,7), the angular distribution (4,5,7), the length weighted angular distribution (7, Wasén and Karlsson (8)), the linear roughness parameter (5,7, Wright and Karlsson (9)), and the wavelength spectrum (7).

A problem in profile analysis (and also in direct surface studies) is that a long-waved irregularity sometimes appears in the profile (3-5,7,8, Park and Fine (10)) and overlays the local fracture geometry. This waviness results in a non-averaged height distribution when the total length of measure is finite. A method to suppress the waviness in order to average the characteristics of the fracture surface over a limited interval is to use a high pass filter technique (5,7). This method creates a mathematically well-defined dividing line formed by the low frequencies of the frequency spectrum of the profile. With this dividing line (that satisfies the geometrically necessary requirement that the height distribution should be symmetric around it) as a reference it is easy to determine the height distribution (5,7). In this context the height distribution of a fracture surface is of special significance. Although the measurements were performed along the profile the results arrived at are truly representative also for the curved area elements on the real fracture surface. The height distributions turned out to be symmetrical around the dividing

line with virtually Gaussian shapes. For this reason the distributions can effectively be described by the standard mean height deviation (\bar{H}). The geometrical meaning of this is that the advancing crack is meandering around the dividing line at a distance essentially within $\pm \bar{H}$. Further experimental details are published elsewhere (5,7).

RESULTS AND DISCUSSION

Surface roughness

The topography of the fracture surface was studied by the quantitative profile analysis technique described above. The number of grains transversed along the crack profile was more than 400 in each case and thus sufficient for good average values to be obtained after filtering. For all microstructures tested the standard mean height deviation (\bar{H}) represents a mean value over the whole crack length, but no significant influence of the ΔK -level was found.

For ferrite there is a linear relationship between the standard mean height deviation (\bar{H}) and the mean intercept grain size (λ), fig 1. By including corresponding data from pearlitic structures and using the mean intercept of the pearlitic colonies as the microstructural unit, a good fit between the data from the two microstructures is found. Fig 1 indicates that the meandering of the crack tip around the dividing line is in general confined to the width of one ferritic grain or one pearlitic colony respectively. However, the sideways movement of the crack tip in relation to the grain size is smaller in the coarser structures as the ratio \bar{H}/λ decreases with increasing λ (fig. 1).

Which of the microstructural features that controls the surface roughness is a matter of controversy. The size of the microstructural unit has been suggested as the prime factor (2-6) and this view is convincingly supported for the "single" phases ferrite and pearlite in this study (fig. 1). In cases of more than one microstructural constituent, the stress field at the crack tip interacts with a phase mixture which is plastically heterogeneous. This makes it more difficult to define a relevant microstructural unit, especially when both constituents have similar volume fractions. When introducing pearlite as the second constituent in a ferritic matrix, \bar{H} may be expected to depend on the crack retarding capacity and the volume fraction of pearlite relative to that of ferrite. In addition the grain size itself might influence. As \bar{H}/λ in ferrite and pearlite respectively depends on λ (fig. 1), one series of coarse and one series of finer phase mixtures were selected for further investigation (figs. 2a and 2b; table 1). In the phase mixtures the mean intercept grain sizes were taken as 45 and 20 μm approximately (slight deviations from λ -values given in table 1).

In coarse microstructures the height deviation \bar{H} increases at increasing volume fractions of pearlite (fig. 2a). The reason for this behaviour is that the advancing crack partly circumvents the pearlitic constituent. As \bar{H}/λ is relatively small in the pure ferrite at such large grain sizes, this circumventing of the inclusions causes large deviations of the propagating crack. Passing the level of shift in the phase continuity then gradually causes \bar{H} to approach the level found in pure pearlite (cf. fig. 1 and table 1). As the inherent retarding effect on a propagating crack increases at decreasing interlamellar spacings (3), harder pearlite inclusions would result in more pronounced crack deviations in the mixed structures. This was indeed found (figs. 2a and 3) and the effect is strongest at equal volume fractions of the constituents. In fully pearlitic specimens, on the other hand, the comparatively low \bar{H} -values are determined by the size of the pearlite colonies created in the heat treatment cycle (ref. (3), fig. 2a and table 1). By introducing martensite instead with still higher hardness a more or less complete circumventing of the inclusions could be created causing a very wide height distribution (figs. 2a and 3). Increasing the hardness of the martensite further results in brittle cracking of the martensitic inclusions with a lower \bar{H} -value as a consequence.

At smaller grain sizes the relative crack deflection (\bar{H}/λ) in ferritic samples is larger. Introduction of inclusions will then cause less change of the crack topography. In fact, at $\lambda \approx 20 \mu\text{m}$ virtually no effect of the pearlitic inclusions is seen, fig. 2b. At very fine grained ferritic structures ($\lambda < 5 \mu\text{m}$) \bar{H} approximately equals the grain size (i.e. $\bar{H}/\lambda \approx 1$), fig. 1, and additions of pearlite or even martensite inclusions will not cause any further increase of the fracture surface roughness (c.f. DOCOL 800 in table 1).

The preference for cracking in the softer ferrite phase leads to a gradual change of \bar{H} at the continuity shift between ferrite and pearlite (fig. 2a). Microhardness measurements indicate noticeable plastic deformation of the pearlite only when this constituent is intersected by the propagating crack; otherwise the plastic zone extends in the softer ferrite leaving the pearlite inclusions elastically strained in the process zone ahead of the crack tip.

Crack closure

The crack closure level increases with increasing roughness of the fracture surface. In fig. 4, K_{C1} and \bar{H} of all the microstructures in table 1 are collected. With a reasonably small scatter

FATIGUE 87

the data fit a relation earlier developed for single phase ferrite (4):

$$K_{Cl} = 1.20 \cdot \bar{H}^{1/3} \quad (K_{Cl} \text{ in } \text{MNm}^{-3/2} \text{ and } \bar{H} \text{ in } \mu\text{m}) \quad (1)$$

This equation predicts that the crack closure level (K_{Cl}) is wholly determined by the roughness as defined by the well-defined standard height deviation \bar{H} . Relation (1) is statistically very secured with a span of the \bar{H} -values of approximately a factor 30 (table 1).

The highest closure values are found in coarse microstructures with second phase inclusions close to being continuous and hard enough to cause a crack tip deflection. To high a hardness might cause transcrystalline cleavage fracture of the inclusions leading to an overall decrease of the roughness and thus of K_{Cl} . This study also shows that for instance fine-grained duplex microstructures (DOCOL grades in table 1) do not result in higher crack closure than do single phase ferritic materials of corresponding grain sizes.

CONCLUSIONS

This investigation on steels with microstructures of ferrite, ferrite/pearlite, ferrite/martensite and pearlite leads to the following conclusions:

1. In the case of single phase materials the fracture surface roughness (\bar{H}) increases linearly with the size of the microstructural unit.
2. Both the volume fraction and the hardness of second phase inclusions are determining factors for the fracture surface roughness in coarse-grained steels. Such a dependence is not seen in fine-grained materials.
3. The crack closure level is closely related to the fracture surface roughness (\bar{H}) and increases proportionally to $\bar{H}^{1/3}$.

ACKNOWLEDGEMENT

The Swedish Board for Technical Development has financially supported this project.

FATIGUE 87

REFERENCES

- (1) Elber, W., ASTM STP 486, Amer. Soc. Test. Mater., Philadelphia, 1971, pp. 230-242.
- (2) Suresh, S. and Ritchie, R.O., Conference Proceedings: "Fatigue Crack Growth Concepts". Edited by D. Davidsson et al., AIME, Philadelphia, USA, 1984, pp. 227-261.
- (3) Hamberg, K. and Karlsson, B., Chalmers Univ. Tech., Göteborg, Sweden. To be published 1987.
- (4) Wasén, J., Hamberg, K., and Karlsson, B., Chalmers Univ. Tech., Göteborg, Sweden. To be published 1987.
- (5) Wasén, J., Karlsson, B., and Hamberg, K., Proceedings of the IV European Symposium for Stereology, Göteborg, 1985. Acta Stereologica, Vol. 6, No. 1, 1987. In print.
- (6) Gray, G.T., Williams, J.C., and Thompson, A.W., Metall. Trans. A, Vol. 14A, pp. 421-433.
- (7) Karlsson, B., Wasén, J., and Hamberg, K., To be presented at Fatigue '87, 1987.
- (8) Wasén, J. and Karlsson, B., Chalmers Univ. Tech., Göteborg, Sweden. To be published 1987.
- (9) Wright, K. and Karlsson, B., J. Microscopy, Vol. 130, pt. 1, 1983, pp. 37-51.
- (10) Park, D.H. and Fine, M.E., In "Fatigue Crack Growth Threshold Concepts". Edited by D. Davidson and S. Suresh, AIME, New York, 1984, pp. 145-161.

TABLE 1 - Microstructures investigated

Material	Micro-structure	v/o of second phase	Microstruct. size λ (μm)	Surface roughness H (μm)	K_{cl} ($\text{MNm}^{-3/2}$)
DOCOL 350	Ferrite	<3	8	5.2	2.0
SS 141147	Ferrite	<3	15	6.9	2.3
Fe-0.02C	Ferrite	-	29	9.9	2.5
Fe-0.02C	Ferrite	-	45	15.0	2.9
Fe-0.02C	Ferrite	-	80	22.0	3.3
Fe-0.8C	Pearlite (S)	-	26	9.2	2.8
Fe-0.8C	Pearlite (S)	-	15	5.6	2.3
Fe-0.8C	Pearlite (S)	-	10	4.3	2.1
Fe-0.8C	Pearlite (H)	-	5	3.9	1.8
Fe-0.8C	Pearlite (H)	-	4.5	2.9	1.9
Fe-0.8C	Pearlite (H)	-	3	2.7	1.5
Fe-0.8C	Pearlite (H)	-	2	1.6	1.2
DOCOL 800	Ferrite/Martensite	42	3.3	3.0	2.2
DOCOL 500BH	Ferrite/Martensite	7	6.1	4.0	2.2
Fe-0.20C	Ferrite/Martensite	45	42	42.9	4.1
Fe-0.20C	Ferrite/Pearlite (H)	22	46	23.0	-
Fe-0.20C	Ferrite/Pearlite (H)	22	19	7.8	-
Fe-0.20C	Ferrite/Pearlite (S)	22	19	7.2	-
Fe-0.38C	Ferrite/Pearlite (H)	42	45	28.0	3.8
Fe-0.38C	Ferrite/pearlite (H)	42	27	6.9	-
Fe-0.38C	Ferrite/Pearlite (H)	42	17	6.0	-
Fe-0.38C	Ferrite/Pearlite (S)	42	45	17.0	3.2
Fe-0.53C	Ferrite/Pearlite (H)	65	75	23.0	3.5
Fe-0.53C	Ferrite/Pearlite (H)	65	23	5.9	2.8

FATIGUE 87

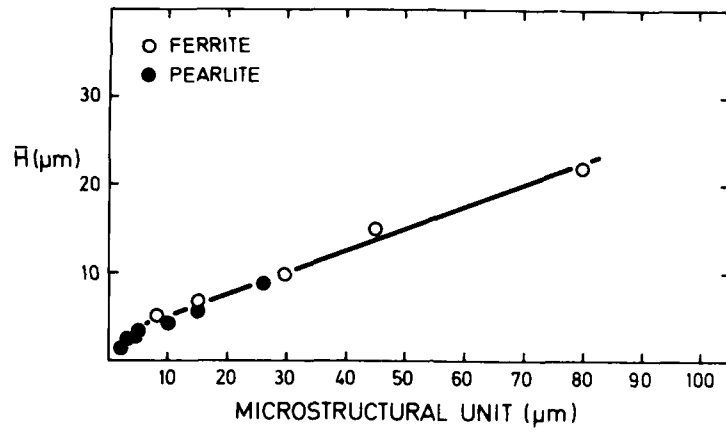


Fig. 1. The fracture surface roughness (\bar{R}) vs. the microstructural unit size for the single phase ferritic and pearlitic steels.

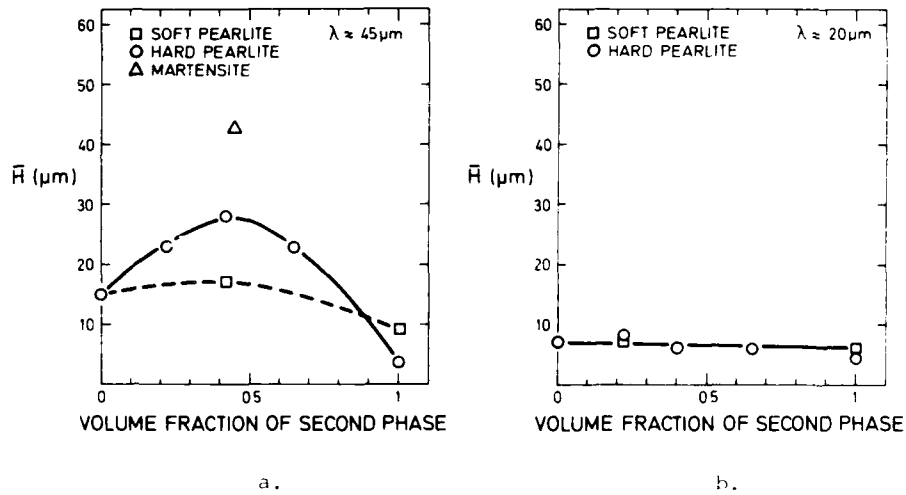


Fig. 2. The fracture surface roughness (\bar{R}) vs. the volume fraction of second phase.
a. Coarse grain structure, $\lambda = 45 \mu\text{m}$.
b. Fine grain structure, $\lambda = 20 \mu\text{m}$.

FATIGUE 87

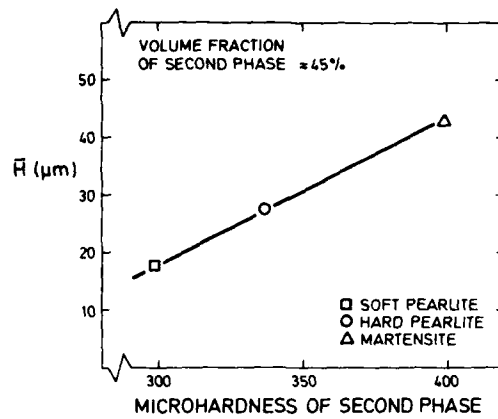


Fig. 3. The fracture surface roughness (\bar{R}) vs. the microhardness of the second phase ($\lambda = 45 \mu\text{m}$).

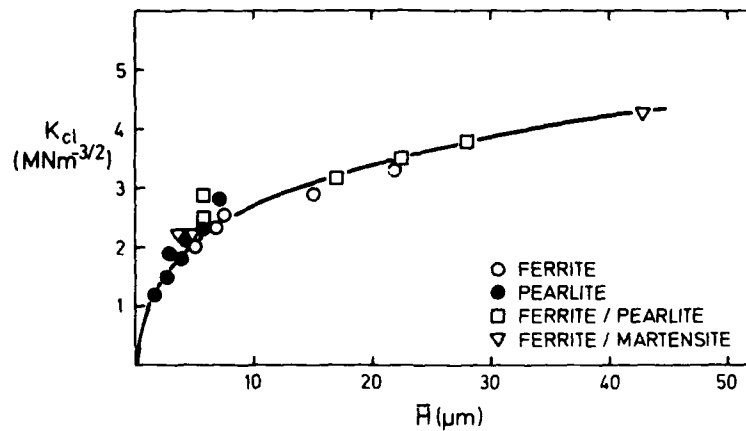


Fig. 4. The crack closure stress intensity (K_{cl}) vs. the fracture surface roughness (\bar{R}). Drawn line indicates K_{cl} predicted from equ. 1.

GROWTH OF SHORT FATIGUE CRACKS IN A SQUEEZE
FORMED ALUMINUM ALLOY¹

B.P.D. O'Connor and A. Plumtree¹

The initiation and early growth of fatigue cracks in strain cycled squeeze-formed 6066-T6 aluminium alloy have been investigated using single-stage replication techniques. Cracks initiated at the second phase particles in the interdendritic region. Fatigue cracks propagated through these regions.

Short crack growth behaviour may be expressed using a model based on crack tip plasticity where the barriers are second phase particles at triple junctions. These barriers influenced the growth at low strain amplitudes more than at higher amplitudes.

INTRODUCTION

The anomalous growth behaviour of short cracks has been shown by many investigators to be associated with such microstructural features as grain boundaries [1], eutectic colony boundaries [2] and second phase particles [3]. In all cases, short cracks were observed to grow at rates faster than those predicted by linear elastic fracture mechanics (LEFM). One possible explanation is that the size of the plastic zone associated with short cracks is several times greater than that of a large crack with a similar driving force [4]. The tip of a short crack does not witness the material as a continuum. In this respect, impediments presented by grain boundaries have little effect until the crack is in their immediate neighbourhood.

An attractive model for the prediction of short crack propagation rates is that proposed by Chan and Lankford [5], in which the growth rate of a short crack is dependent upon the proximity of the

¹Department of Mechanical Engineering, University of Waterloo, Waterloo, Ontario, Canada N2L 3G1

FATIGUE 87

crack tip to a grain boundary and the orientation of the neighbouring grain. The observed phenomena of crack arrest, crack retardation followed by crack acceleration and continuing crack acceleration is incorporated in this model by a parameter, $k(\theta)$, representing the misorientation between neighbouring grains. Growth of this type is assumed to continue until the plastic zone size is of the order of a grain, at which stage long crack behaviour is assumed [6].

The object of this work was to examine the microstructural features which initiate short cracks together with those which impaired crack growth at various applied stress/strain levels. It also provides the opportunity to examine the applicability of the crack growth model based on crack tip plasticity [5].

EXPERIMENTAL PROCEDURE

Completely reversed strain controlled fatigue tests were performed at room temperature on smooth cylindrical specimens of 5mm diameter with a gage length of 10 mm. The material examined was AA6066-T6 in a squeeze-formed condition having a 0.2% offset stress of 345 MPa, an ultimate tensile strength of 365 MPa and a strain to failure of 1.4%. All tests were performed on an MTS servocontrolled closed-loop electrohydraulic testing machine. Single stage replication was used to determine crack growth at various intervals of the fatigue life.

MICROSTRUCTURE

Squeeze-forming AA6066 resulted in a refined microstructure, consisting of cast primary aluminum rich dendrites and a second phase of $\alpha\text{FeAlMnSi}$ in the interdendritic regions, as shown in Fig. 1. Grain boundaries surrounded many dendrite arms indicating that the pressures involved in the squeeze-forming process were sufficient to break them from the primary cores. This resulted in a fine-grained structure with an average dendrite spacing of 84 μm . Dendrite size distribution ranged from 25 μm to 300 μm . The average width of the precipitate free interdendritic region was 15 μm . Second phase particles ranged from 3-30 μm in length. Coring in primary dendrites produced during squeeze-forming persisted after the T6 heat treatment. The strengthening precipitates in this system are Mg_2Si .

RESULTS

Metallurgical Examination

Low Cyclic Strain Amplitudes. $0 \leq \Delta\epsilon_t/2 \leq 0.3$ [maximum stress < 60% σ_y] Upon cycling, short cracks initiated in the soft (115 HV) precipitate-free interdendritic regions. In the majority of cases, initiation occurred by debonding of second phase particles orien-

tated normally to the applied stress. Initially, crack growth was from particle to particle. Indeed, propagation over the first 1.5 mm in the depth direction at $\Delta\epsilon_t/2 = 0.15\%$ was along the interdendritic region, shown in Fig. 2, as opposed to propagation through the harder aluminum dendrite matrix (140 HV). Figure 3 shows the evolution of a short crack which caused failure at $\Delta\epsilon_t/2 = 0.15\%$. It may be seen that growth to the right is blocked (position 1) whilst the crack grows to the left at an angle of 45° to the applied stress. Changes in crack growth direction occurred at second phase particles labelled 2-6 until a crack length of 350 μm was attained. At this stage the barrier to the right was overcome and growth continued as shown. The fracture surface associated with this crack was examined using back scattered electrons (BSE), Fig. 4, where higher atomic number elements in the intermetallic second phase particles appear brighter than the lower atomic number aluminum. The region marked by the arrow corresponds to the initiation site whilst the fretted (black) region in the centre represents the inclined region of Fig. 3. Lighter second phase particles can be seen to outline dendrites and faceting is apparent throughout. A secondary crack, labelled 1, associated with a second phase particle at a depth of 30 μm behind the initiation site indicates that the crack was blocked at this location. Other secondary cracks can be seen at depths of 100, 150 and 290 μm , labelled 2-4. In general secondary cracks followed the light second phase particles in the interdendritic regions at grain boundaries and triple junctions suggesting these represented the strongest barriers to growth at this strain amplitude. Knowing, however, that growth was taking place along the interdendritic regions, parallel to grain boundaries, secondary cracking is due to the crack interacting with triple junctions. This is confirmed by examining Figure 2 which shows the greatest 'confusion' in crack growth occurring at the triple junctions, represented by 'A'.

High Strain Amplitudes. $0.30 \leq (\Delta\epsilon_t/2) \leq 0.5$ [maximum stress $< 70\% \sigma_y$]. At strain amplitudes exceeding 0.35% initiation occurred both by second phase particle debonding and fracture, which took place at many locations. As a result, early crack growth was by crack coalescence. Once again the easiest path for growth was along the interdendritic region but in this case the driving force was sufficient to break second phase particles at triple junctions leading to a combination of inter and transdendritic growth. The fracture surface in Fig. 5 shows a small faceted region (to a depth of 550 μm). When compared to that at lower strain amplitudes, slow crack growth occurred to a smaller depth. The initiation site shown by an asterisk has a faceted thumbnail appearance in the depth direction representing growth to the first triple point. Early growth appears to be at approximately 45° to the stress axis in the depth direction and is halted approximately 70 μm from the surface. The depth of the crack was 70 μm whilst the surface length was approximately 200 μm . Only one secondary crack was located on the fracture surface, implying that triple junctions no

longer represented major impediments to crack growth.

Crack Growth Studies

Surface crack lengths at various intervals of the fatigue life were measured for the strain amplitudes examined. The retardations in crack advancement occurred at distances up to 900 μm on the crack surface, which far exceeded the dendrite size. However, knowing that in plane strain, growth along the surface is easier than that in the radial direction, a series of tests were performed to determine the depth associated with surface cracks up to 10 mm. Corresponding depths were determined by the penetration of a dye applied prior to breaking the specimen on an impact machine. The resulting data showed that the crack depth, a , could be approximated from the surface crack length, ℓ , by the relation

$$a \approx 0.365 \ell \quad (1)$$

This relationship was used to determine the crack depth shown in Figure 6 for various intervals of the fatigue life. Retardations occurred over the depth range of 20-300 μm corresponding to the range of dendrite sizes. Crack propagation rates were determined by the secant method. These were plotted against crack depth in Fig. 7. At low strain amplitudes, retardations in growth occurred at average crack depths of 40, 90, 120 and 250 μm corresponding approximately to the depths at which secondary cracks at triple junctions 1-4 in Fig. 4 were observed. At $\Delta\epsilon_t/2 = 0.5\%$ retardations were smaller in magnitude and this is consistent with the larger crack driving force and hence reduced resistance of triple junctions.

DISCUSSION

The micromechanism of crack retardation observed in this work is similar to that modelled by Lankford et al [4] using the equation

$$da/dN = C \Delta K^n [1 - k(\phi)((D-2x)/D)^m] \quad (2)$$

where da/dN = crack growth rate
 C = constant obtained at $\Delta K = 1 \text{ MPa}\sqrt{\text{m}}$ and $k(\phi) = 0$
 ΔK = stress intensity factor
 $k(\phi)$ = measure of the misorientation between grains
 x = distance of crack tip from a dendrite boundary
 D = dendrite size
 n and m = constants

To apply this model the values of C , n , $k(\phi)$ and m must be known. The term $k(\phi)$ is significant since it determines the degree of retardation imposed by dendrites of different orientation. The value of ΔK at which this occurs is independent of the actual value of $k(\phi)$ and for this reason, together with the experimental difficulty associated with its determination, a value of 0.8 was assumed throughout. The slope, n , can be approximated by the growth of short cracks when they are distant from a neighbouring grain bound-

ary. In this case, $n=0.49$ indicating that short cracks grow with a different ΔK dependency than long cracks ($n \approx 2.5$). The value of C from Fig. 7 is clearly dependent upon strain amplitude and was determined to be 4.0×10^{-10} , 2.0×10^{-8} and 2.0×10^{-6} for the strain amplitudes of 0.15, 0.20 and 0.50% respectively. The relationship between C and strain amplitude has been determined and values from a similar strength squeeze-formed material [7] have also been included for greater accuracy. In all cases the average dendrite size of $84 \mu\text{m}$ was assumed, together with a value of $m=2$ determined by Chan and Lankford [5] on 7075-T651. Plotting Equation (2) with these values produced the plots of da/dN against crack depth for the strain amplitudes of 0.15, 0.2 and 0.5% and these are included in Fig. 7. The predicted retardations in growth occur at crack depths corresponding to multiples of the average dendrite size. The predicted growth with $k(\phi)=0$ is shown for comparison. This value is appropriate for the higher strain amplitudes. The rationale will be discussed later. For the lowest strain amplitude, $\Delta\epsilon/2=0.15\%$, the retardation at $40 \mu\text{m}$ corresponds to microstructural features less than the average dendrite size. Again this may be due to the distribution of dendrite spacings but the predominately interdendritic mode of crack advancement suggests that the observed behaviour is associated with second phase particles at dendrite boundaries and triple junctions. The greater number of retardations observed at this strain amplitude in comparison to the higher levels further suggests that these microstructural features have a mitigated effect at higher amplitudes due to the greater stresses which can cut through second phase particles, even those at triple points, leading to a combination of trans and interdendritic growth.

Since short cracks grow with a different ΔK dependency than long cracks, it is important to know at what stage the short cracks become "large". Lankford observed that short crack data merges into long crack data when the plastic zone is of the order of a grain size and suggested that his model should be applied to that point. Assuming the plastic zone size, r_p , to be given by an equation of the form [8]

$$r_p = 0.196 (K_{\max}/\sigma_y)^2 \quad (3)$$

where K_{\max} = maximum applied stress intensity
 σ_y = yield stress

then short and long cracks should merge at depths of 1500, 700 and $175 \mu\text{m}$ at strain amplitudes of 0.15, 0.20 and 0.50% respectively. This phenomenon was not observed where the short crack data merged with long crack data at depths of 40-300 μm over the range of strain amplitudes examined. For crack depths of 300 μm the size of the plastic zone was 20, 38 and $150 \mu\text{m}$ at strain amplitudes of 0.15, 0.20 and 0.50 % respectively, implying that the crack depth at which short and long cracks merge is independent of the plastic zone size. It thus appears that short crack growth in this case is due to the lack of constraint of the surface grains. El Haddad et

al [9] proposed that short crack data may produce long crack curves provided the stress intensity equation is modified according to

$$\Delta K_{\text{eff}} = A \Delta \sigma \sqrt{\pi(a+a_0)} \quad (4)$$

$$\text{where } a_0 = (1/\pi)(\Delta K_{\text{th}}/\Delta \sigma_e)^2 \quad (5)$$

ΔK_{th} = threshold stress intensity value
 $\Delta \sigma_e$ = fatigue or endurance limit

Using a threshold value of 7 MPa $\sqrt{\text{m}}$ and an endurance limit of 220 MPa at 10^6 cycles a value of $a=330 \mu\text{m}$ is obtained. This represents four grain sizes and corresponds quite well to the crack depth at which short crack behaviour is no longer observed.

Practical Application of Short Crack Data

Having found that Lankford's model can predict decelerations in crack propagation rate at triple junctions it is interesting to speculate how this model may be used to estimate the number of cycles spent in the short crack regime. The risk one takes in applying the model is that it assumes a very regularly distributed microstructure with each grain separated by the average grain size. Thus any decelerations caused by features above or below this dimension cannot be predicted. Furthermore, the misorientation between grains is the major factor which determines whether or not a short crack arrest or deceleration will occur. One cannot predict apriori that any crack arrest or acceleration will occur. The conservative approach therefore is to assume the worst possible case of continuous crack growth with no decelerations whatsoever. This can be incorporated into the model by assuming the value of $k(\phi)$ to be zero. In this case

$$da/dn = C \Delta K^n \quad (6)$$

Knowing $n=0.49$ and C , it is possible to integrate this equation in order to estimate the number of cycles spent in the short crack regime. The limits of integration vary from the size of the initiation site to the upperbound ($=a_0$) for short crack growth. The former may be taken as the average second phase particle size of $15 \mu\text{m}$ whilst the latter is $330 \mu\text{m}$ as determined from equation (5). Integration of equation (6) yields the values given in Table 1 for the short crack regime. The actual number of cycles are given for comparison. Integration of the Paris equation from a crack depth of $330 \mu\text{m}$ gives the number of cycles to failure in the long crack growth region. Combining the results of this integration with that for short cracks results in an estimated fatigue life (C), Table 1. The life predictions at the two lower strain amplitudes are conservative whilst that at 0.5% is less so, indicative of the absence of severe crack arrests in this case. The outcome of incorporating the number of cycles in short crack regime into the lifetime prediction has been to reduce the grossly over-conservative estimate produced by assuming only the Paris regime to apply.

FATIGUE 87

TABLE 1 - Comparison of Predicted and Actual Fatigue Lives

	STRAIN AMPLITUDE %		
	0.15	0.20	0.50
A. Predicted short crack growth (cycles) from integration of eqn. 6. (15 μm - 330 μm)	404,000	7,000	47
B. Predicted Long Crack Growth (330 μm - 5000 μm)	246,100	50,790	593
C. Estimated Life (A+B)	650,100	57,790	640
D. Actual short crack growth	1,225,000	55,000	420
E. Actual long crack growth	144,900	78,500	508
F. Actual life (D+E)	1,369,900	133,500	928

CONCLUSIONS

1. Short fatigue cracks in a squeeze-formed aluminum-6066 alloy initiate at second phase particles in the precipitate free interdendritic zone. The process of initiation is by decohesion at the particle/matrix interface for strain amplitudes less than 0.3% and a combination of decohesion and particle cracking at higher strain amplitudes.
2. The early growth rate of short cracks is dependent upon the applied stress/strain level. Short cracks of a given length grow faster at higher strain amplitudes.
3. Short crack growth behaviour may be expressed using a model based on crack tip plasticity where the barriers are second phase particles at triple junctions. These barriers influence growth at low strain amplitudes more so than at higher amplitudes. The tendency for particle fracture at high strain amplitudes appears to result in less drastic growth deceleration before long crack behaviour develops.

REFERENCES

- (1) Lankford, J., Fracture Engng. Struct., Vol. 8, 1985, pp.161-175.

FATIGUE 87

- [2] Taylor, D., and Knott, J.F., *Fatigue of Eng. Materials and Structures*, Vol. 4, 1979, pp.147-155.
- [3] Pearson, S., *Engineering Fracture Mechanics*, Vol.7, 1975, pp.235-247.
- [4] Lankford, J., Davidson, D.L. and Chan, K.S., *Met. Trans. A.*, Vol.15A, 1984, pp.1579-1588.
- [5] Chan, K.S., and Lankford, J.A., *Scripta Met.*, Vol.17, 1983, pp.529-532.
- [6] Lankford, J., *Fatigue of Eng. Materials and Structures*, Vol.5, 1982, pp.233-248.
- [7] Schafer, S., and Plumtree, A., "Initiation and Short Crack Behaviour in Aluminum Castings" in *The Behaviour of Short Fatigue Cracks*, Ed. by K.J.Miller, Mechanical Eng. Publ., London 1986, pp.169-181.
- [8] Rice, J.R., *Fatigue Crack Growth*, ASTM STP415, Philadelphia, 1967, pp. 247-309.
- [9] El Haddad, M.H., Smith, K.H. and Topper, T.H., *Trans. ASME*, Vol. 101H, 1979, p.42.

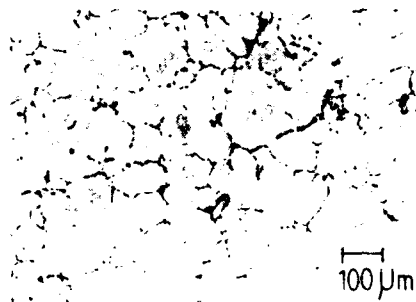


Fig. 1 General microstructure



Fig. 2 Interdendritic fracture path

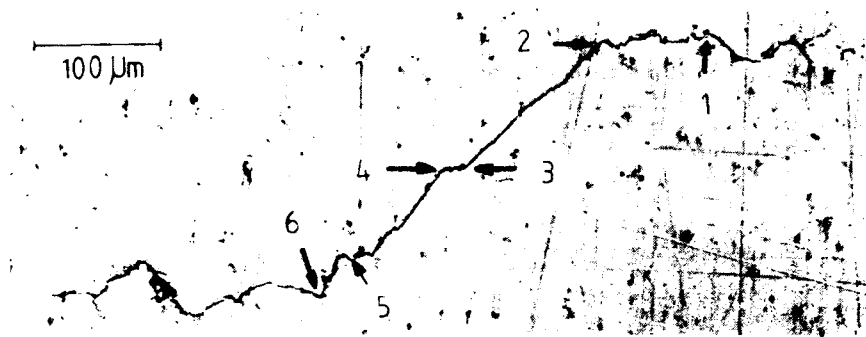


Fig. 3 Short crack evolution: 1-2 (136,000 cycles), 1-4 561,000 cycles; 1-5 (850,000 cycles), 1-6 (946,000 cycles)

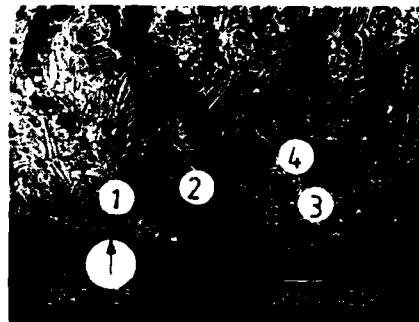


Fig. 4 Fracture surface
 $\Delta\epsilon_t/2=0.15\%$

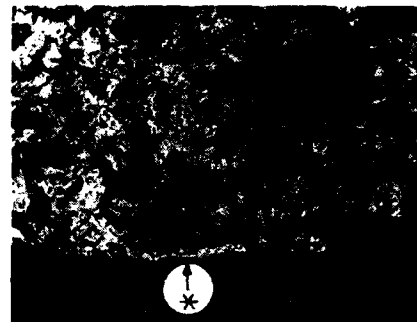


Fig. 5 Fracture surface
 $\Delta\epsilon_t/2=0.50\%$

FATIGUE 87

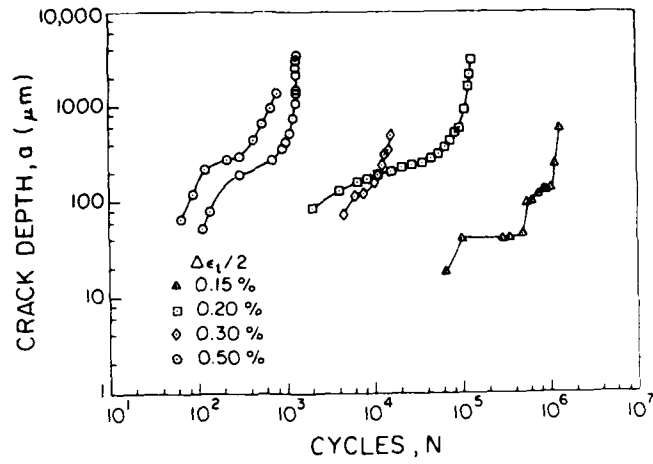


Fig.6 Crack depth versus cycles

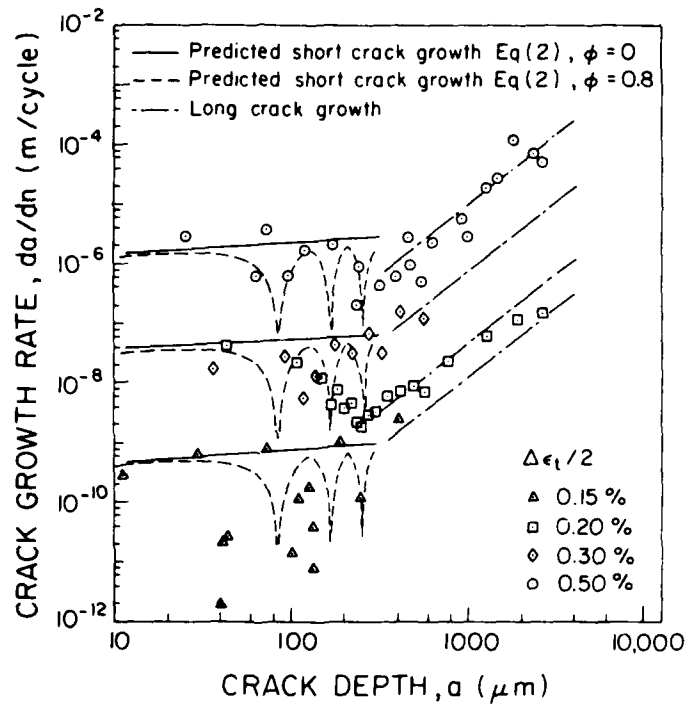


Fig. 7 Actual and predicted crack growth rates

FATIGUE 87

INFLUENCE OF MICROSTRUCTURE AND AGING CONDITION ON THE FATIGUE CRACK PROPAGATION IN AGE HARDENED ALUMINIUM ALLOYS

R. Scheffel, O. Ibas and K. Detert*

Fatigue crack growth rates of age hardened aluminium alloys with different grain sizes were studied. The tests were conducted on CT specimens at increasing ΔK values and on bend specimens at increasing as well as at decreasing ΔK . The stress ratio varied between 0.1 and 0.8. An influence of stress ratio below 0.6 was found with increasing grain size. This could be explained by roughness induced closure, which occurs in coarse grained materials. By taking closure into account good agreement of the data at all stress ratios and for the different aluminium alloys could be obtained. An absolute threshold value is found to be below $1.5 \text{ MPa}\sqrt{\text{m}}$.

INTRODUCTION

Age hardened aluminium alloys such as Al-Mg-Si and Al-Zn-Mg-Cu are commercially used for light weight applications in particular for ground transportation, structures and aeronautical purposes. Since all constructions are usually subjected to alternating stresses during service, the fatigue properties of the above alloys are very important.

It was found for Al-Mg-Si alloys that grain size (Ruch and Gerold (1)), dispersoid content due to Mn or Cr being present (Edwards and Martin (2)) and also the stress ratio R (Scheffel and Detert (3)) are important parameters which control the fatigue crack growth rate (FCGR) at a given level of the applied cyclic stress intensity factor ΔK . The R-ratio effect was shown to occur due to roughness induced closure (Scheffel and Detert (3), (4)).

*Institut für Werkstofftechnik, Universität GH Siegen
D-5900 Siegen, FRG

FATIGUE 87

The present study was undertaken in order to evaluate the influence of grain size, grain shape and aging treatment on crack closure and the FCG behaviour, and to derive simple rules for the use of fatigue data in damage tolerance design concepts.

MATERIAL DETAILS

The Al-Mg-Si alloys were DC cast, extruded to bars, homogenized and hot rolled. They were solution treated at 540° C and aged to a hardness of 95-100 HB at 160° C. The aging time was 3h for the underaged and 2h for the overaged condition. The alloys termed T and T' were commercially manufactured and had nearly the same composition. T was an alloy with coarse and T' an alloy with fine grains (Fig. 1). The other two coarse grained Al-Mg-Si alloys were produced from one melt to contain different Mn additions: Alloy MF is manganese free, whereas MH contains more Mn than T and T'.

The Al-Zn-Mg-Cu1,5 alloy was extruded to rectangular bars of 50.5mmx25mm cross section. It was solution treated at 470°C/30min in a saltbath, plastically strained (1.5%) and then aged in two steps (120°C/12h, 170°C/5.5h) to obtain a hardness of 164 HB. The grain shape was fibrous with an average diameter of 20µm across the thickness. For comparison tests a coarse grained modification with roughly equiaxed grains of approximately 110µm diameter was produced by a special heat treatment (470°C/14h, 540° C/24h) prior to aging (Fig. 1). Some properties of the investigated alloys are compiled in Tab. 1 and Fig. 1.

TABLE 1 - Composition, Grain Dimensions in L, T, S - Directions and Mechanical Properties of the Investigated Alloys (Underaged Condition).

Alloy	Al-Mg-Si				Al-Zn-Mg-Cu1,5	
	MFu	Tu	Tu'	MHu		
Cast No.	41	43	A	45		
Mg (w%)	0.91	1.02	1.00	0.89	2.50	
Si (w%)	0.92	1.05	1.04	0.88	0.14	
Mn (w%)		0.70	0.76	0.97	0.10	
Fe (w%)	0.25	0.21	0.20	0.30	0.26	
Cu (w%)					1.42	
Zn (w%)					5.30	
Cr (w%)					0.20	
Grain L	365	521	46	498	1000	73
diam. T	367	256	55	283	100	113
D (µm) S	196	92	46	134	20	116
Sp (MPa)	219	252	210	202	526	
UTS (MPa)	312	361	322	299	576	

EXPERIMENTAL PROCEDURE

CT-specimens (Al-Mg-Si: W = 100 mm; B = 15 mm, Al-Zn-Mg-Cu_{1,5}: W = 40 mm; B = 15 mm) in LT orientation were machined according to the ASTM specification E647-78T for tests at FCG rates above 10^{-8} m/cycle. The tests were conducted in laboratory air at constant stress ratios up to 0.8 and at a testing frequency of 20 Hz using a servohydraulic testing machine. During each test the maximum and minimum loads were kept constant, which means that ΔK increased with the crack length. At every optically measured crack length a load vs. crack opening displacement (COD) record was taken to check the linearity and to correct ΔK for crack closure (3).

Charpy specimens with a modified cross section (15 mm high, 10 or 5 mm thick) and a 2 mm notch were used in an automatic resonant fatigue testing system under pure bending at approximately 200 Hz to measure the FCGR below 10^{-8} m/cycle at low values of ΔK as well as to determine the threshold. The crack lengths were measured with the indirect potential drop method. During the test the cyclic stress intensity was exponentially decreased with increasing crack-length according to Saxena et al (5). This procedure occurred continuously under microcomputer control. Either the stress ratio R or K_{\max} in each cycle was kept constant throughout the test. A strain gauge was fixed to the specimen to measure the back face strain (BFS). More details about the testing equipment were reported by Scheffel and Detert (4) and Phoplonker et al (6). It could be shown that keeping K_{\max} constant avoids crack closure near the threshold.

RESULTS

Influence of grain size (and shape). The results obtained from tests with CT-specimens at increasing K and $R=0.1$ in Figs. 2a, b show a strong grain size influence on FCG: The FCGR at a given ΔK increases with decreasing grain size in both alloy systems. This is in accordance with the findings of Albrecht et al (7, 8) for Al-Zn-Mg-Cu alloys and those of Ruch and Gerold (1, 9) for Al-Mg-Si. The scatterbands of these literature data are also included in Figs. 2a, b for comparison. For our alloys an influence of crack closure on FCG was taken into account: The crack opening stress intensity, K_{op} , was determined from the load at the intersection of the linear parts of each load-COD curve and the corresponding crack length. When the FCG data are replotted versus the effective stress intensity range $\Delta K_{eff} = K_{\max} - K_{op}$ in Fig. 2c no influence of grain size or shape remains.

Crack closure was detected for all investigated Al-Mg-Si alloys (for coarse grained materials up to $R=0.6$) and also for coarse grained Al-Zn-Mg-Cu_{1,5} below $R=0.6$. No indication of closure was found for the fibrous grained Al-Zn-Mg-Cu_{1,5} alloy.

FATIGUE 87

Some FCG data in the near threshold region (at $da/dN \cdot 10^{-8} \text{ m/cycle}$) obtained from bending specimens tested at decreasing ΔK are given in Figs. 3a, b for those alloys with minimum and maximum crack closure: The fibrous (fine) grained Al-Zn-Mg-Cu1.5 alloy in Fig. 3a did not show any crack closure. It is therefore not surprising that a R-influence was not detectable. The threshold lies around $1.0 \text{ MPa}\sqrt{\text{m}}$. A different result in the low ΔK range is found for the underaged alloy T in Fig. 3b: At constant R tests decreasing thresholds are found as R increases. This behaviour is typical for a strong crack closure influence, which is also indicated by non-linear moment-BFS records (K_{op} was $3 \text{ MPa}\sqrt{\text{m}}$). Comparison of the measured threshold values (open symbols Fig. 3c) and the closure corrected ones (full symbols) with those obtained at $K_{\text{max}} = \text{const}$, from the other Al-Mg-Si alloys MF, MH in Fig. 4 (shaded area) supports an absolute fatigue threshold less than $1.5 \text{ MPa}\sqrt{\text{m}}$ for the present alloys.

Influence of the aging treatment. Fig. 4 summarizes similar results obtained from under- and overaged specimens of the Al-Mg-Si alloys MF and MH. The FCG curves are nearly identical with those in Figs. 3a, b and also consist of two common scatterbands each with a slope $m=2$ but with individual transition ranges between them: Overaging shifts the transition ranges of both alloys to larger ΔK_{eff} but the transition sequence is the same for both aging conditions. The threshold values $\Delta K_{\text{eff,th}}$ are indicated as the shaded area in Fig. 3c.

DISCUSSION

This contribution confirmed for two different aluminium alloy systems that the influence of grain size is mainly to determine the extent of closure which was found to increase with grain size, especially at low R. Ruch and Gerold (9) as well have reported indications for closure in their coarse grained Al-Mg-Si such as oxide particles due to fretting corrosion at touching sections of the crack surfaces. Kim and Griffith (10) published results from a very fine grained ($2.4\mu\text{m}$) P/M 7091 alloy tested at $R=0.3$ which agree very well with our Al-Zn-Mg-Cu1.5 data in Figs. 2, 3a indicating that both alloys, which did not show any closure, have the same resistance to FCG despite different grain sizes (and shapes).

However the amount of closure does not seem to be a material constant controlled by the grain size alone. This must be concluded from the results of alloy Tu where the crack opening stress intensity K_{op} is found to be $7.5 \text{ MPa}\sqrt{\text{m}}$ for CT and only $3 \text{ MPa}\sqrt{\text{m}}$ for the less compliant small clamped specimens under pure bending. McEvily concluded in his survey (11) that (roughness induced) closure caused by contributions of non-mode I deformations might be more pronounced in compliant (eg CT-specimens) than in stiffer (eg SENT or CCP) specimens. From this point of view it is less surprising that Paauw and Bardal's (12) FCG data obtained from SENT

specimens of extruded Al-Mg-Si tested at $R=0.1$ coincide with our data in Fig. 4 including the transition range though they did not correct for closure.

Moderately overaged Al-Mg-Si alloys (72 h/180 °C) still contain shearable precipitates of needle to rodlike shape. This was confirmed by electron diffraction methods (Westengen (13)). The primary effect of overaging is therefore to increase the mean distance between these particles which could give the explanation for the fact that the overaged alloys in Fig. 4 show their transition between the lower and upper scatterband at higher values of ΔK_{eff} . The same result for aluminium alloy 7475 was reported by Carter et al (14). They too did not find a distinct influence of grain size. In both states of aging our manganese containing alloy MH had a lower transition than MF probably due to dispersoids, which tend to homogenize the slip distribution and thus should reduce slip band cracking.

The coincidence of the FCG curves in Figs. 3a, b and 4 and the agreement with the literature discussed above emphasizes, that only ΔK_{eff} should be used for the presentation of FCG data and that the influence of microstructure in this description is limited to the individual positions of the transition ranges if FCG along grainboundaries is not a dominant mechanism (4). The upper scatterband in these figures correspond to the striation mechanism of FCG, whereas the lower band is associated with a crystallographic (faceted) mode. Only in the transition range of alloy MF a certain contribution of intergranular FCG was observed. A similar fracture morphology is reported by Jono and Song (15) for an A5083-0 aluminium alloy and by Stofanek et al (16) for an Al-Mg-Si alloy. Such a transition due to a change of the FCG mechanisms has been reported also for other alloys (eg titanium alloys (15), (16), (17) and nickel base alloys (18)). The FCG behaviour of the present alloys can be described by a modified Paris expression

$$da/dN = A' (\Delta K_{eff}/E)^m \dots\dots\dots(1)$$

with $m=2$, the dimensionless constant $A'=8$ for striated and $A'=0.8$ for faceted growth. Eq 1 and $A'=8$ was reported to describe the macroscopic crack advance (19) as well as the striation spacing (20), (21) of a variety of different metals. No such expression for faceted growth with $m=2$ $A'=0.8$ is reported but also the aforementioned results for titanium- and nickelbase alloys agree with it.

Assuming that the lowest physically meaningful FCGR in the threshold condition occurs in the faceted mode ($A'=0.8$) and is given by the interatomic spacing (eg 0.28 nm for Al). Eq 3 can be rearranged to

$$\Delta K_{th,eff}/E = 1.9 \cdot 10^{-5} \sqrt{m} \dots\dots\dots(2)$$

FATIGUE 87

Eq 2 is in agreement with the result ($1.6 \cdot 10^{-5} \sqrt{m}$) derived by Liaw et al (22), who compiled threshold values of different materials from literature.

All FCG expressions similar to Eq (1) which are applicable over a wider range of ΔK_{eff} , when the mechanisms of FCG change, must therefore have an exponent $m > 2$ as shown convincingly by Speidel (23). He investigated the FCG of the widest variety of materials known to the present authors and suggests to use Eq (1) with $m=3.5$ and $A'=5.1 \cdot 10^{-6}$ (the FCGR da/dN is obtained in m/cycle when K is inserted in $MPa\sqrt{m}$ and E in MPa). This relationship also describes our data in Figs. 3a, b and 4 very well.

This discussion shows clearly that the normalisation of ΔK with the modulus of elasticity used in the empirical Eq (3) is very useful as the FCG and threshold data of different alloys in air are rationalized. $\Delta K/E$ has the physical meaning of a strain-intensity factor (Donahue (24)) and a few theoretical models just predict a simple dependency of the FCGR from the square of the elastic strain intensity factor in a limited range of da/dN (25), (26), (27).

CONCLUSION

The presented results from commercial aluminium alloys show that in the closure corrected da/dN vs ΔK_{eff} presentation of FCG data no grain size/shape influence and only a minor influence of dispersoid content and state of aging could be observed. For damage tolerance design concepts always threshold values and FCG data either measured at high R (eg for the condition $K_{min} \geq K_{th}$) or those corrected for closure should be taken. For a first estimate of the threshold Eq (2) can be used. To be on the safe side Eq (1) with $C=8$ or perhaps Speidel's expression and assumption $\Delta K_{eff} = \Delta K$ should be adopted to calculate the FCGR at low and medium values of ΔK . This concept can also help to estimate the growth of small cracks (a 10 μm) as shown by Detert and Scheffel (28).

REFERENCES

- (1) Ruch, W.; Gerold, V.; ECF 4, Leoben, Austria, 1982, pp 383-390
- (2) Edwards, L.; Martin, J.W.; ICF 5, Cannes, France, 1983, pp 323-328
- (3) Scheffel, R.; Detert, K.; ECF 5, Lisbon, Port., Vol. 3, 1984, pp 805-814
- (4) Scheffel, R.; Detert, K.; ECF 6, Amsterdam, Netherlands, Vol. 3, 1986, pp 1851-1860
- (5) Saxena, A.; Hudak, S.J.; Donald, J.K.; Schmidt, J.W.; J. Test. Eval., Vol. 6, 1978, pp 167-174

- (6) Phoplonker, M.A.; Scheffel, R.D.; Byrne, J.; Duggan, T.V.; Barnes, P.; FEMS, Sheffield, UK, 1986, pp 137-144
- (7) Albrecht, J.; Lütjering, G.; DFVLR Forschungsbericht, DLR-FB 77-07, 1977
- (8) Albrecht, J.; Martin, J.W.R.; Lütjering, G.; Martin, J.W.; ICSMA 4, Nancy, France, 1976, pp 463-467
- (9) Ruch, W.; Gerold, V.; Z. Metallkunde 76, 1985, pp 338-347
- (10) Kim, T.W.; Griffith, W.M.; PM Aerospace Materials, Vol. I, Berne, Switzerland, 1984, paper 33, pp 1-16
- (11) McEvily, A.J.; Metal Science, Vol. 11, 1977, pp 274-284
- (12) Paauw, A.J.; Bardal, E.; Aluminium Weldments III, Munich, W-Germany, paper V.9, 1985, pp 1-6
- (13) Westengen, H.; Ryum, N.; Z. Metallkunde 70, 1979, pp 528-535
- (14) Carter, R.D.; Lee, E.W.; Starke Jr., E.E.; Beevers, C.J.; Metall. Trans. A., 15A, 1984, pp 555-563
- (15) Jono, M.; Song, J.; Fatigue 84, "Proc. 2nd Int. Conference on Fatigue and Fatigue Thresholds" ed. C.J. Beevers, Birmingham, UK, 1984, pp 717-726
- (16) Stofanak, R.J.; Hertzberg, R.W.; Miller, G.; Jaccard, R.; Donald, K.; Eng. Fract. Mechanics 17, 1983, pp 527-539
- (17) Chesnutt, J.C.; Wert, J.A.; "Fatigue Crack Growth Threshold Concepts" ed. D. Davidson, S. Suresh, Fall Meeting of the Metall. Soc., Philadelphia PA, USA, 1983, pp 83-97
- (18) Yuen, J.L.; Roy, P.; (same as Ref. 17), pp 185-203
- (19) Hahn, G.T.; Serrate, M.; Rosenfield, A.R.; Air Force Conf. on Fatigue of Aircraft Structures and Materials, Miami Beach, USA, AFFDLTR 70-144, 1969, pp 425-499
- (20) Bates, R.C.; Clark Jr., W.G.; Trans. of the ASM 62, 1969, pp 380-389
- (21) Rhodes, D.; Nix, K.H.; Radon, J.C.; ECF 4, 1982, pp 443-448
- (22) Liaw, P.K.; Leax, T.R.; Logsdon, W.A.; Acta Metall, 31, 1983, pp 1581-1587
- (23) Speidel, M.O.; Platinum Metals Review, 1981, pp 24-31

- (24) Donahue, R.J.; Clark, H.McI.; Atanomo, P.; Kumble, R.;
McEvily, A.J.; Int. J. Fracture Mechanics 8, 1972, pp 209-219
- (25) Pook, L.P.; Frost, N.E.; Int. Journal of Fracture 9, 1973,
pp 53-61
- (26) Sadamanda, K.; Shahinian, P.; Int. Journal of Fracture 13,
1977, pp 585-594
- (27) Wertmann, J.; "Three-dimensional constitutive relations and
ductile fracture", ed. Nemat-Nasser, North-Holland, Leyden,
Netherlands 1981, pp 111-122
- (28) Detert, K.; Scheffel, R.; Proc. Fall Meeting of the E-MRS,
Advanced Materials Research and Development for Transport,
Strasbourg, France, 1985, Light Metals Vol. 7, pp 265-272

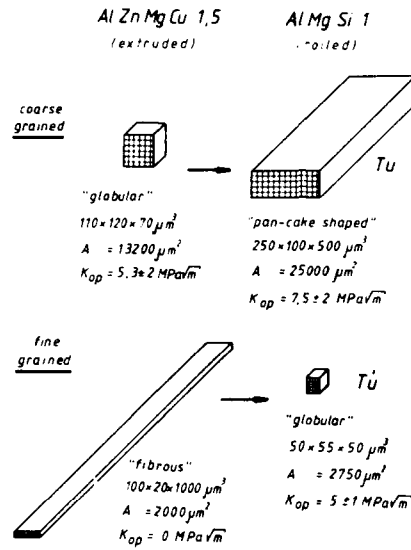


Figure 1 Grain size/shapes. Arrows indicate directions, shaded areas A plains of FCG.

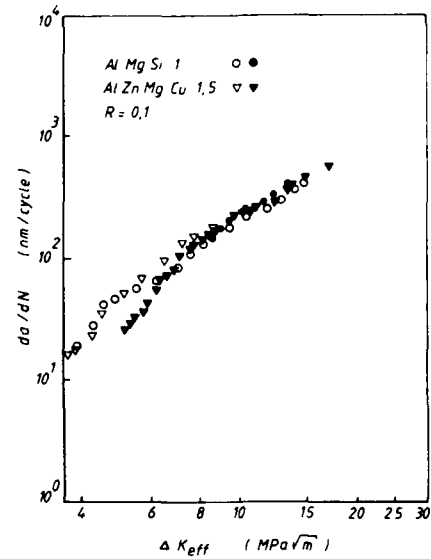


Figure 2c Crack closure corrected data from Figs. 2a, b.

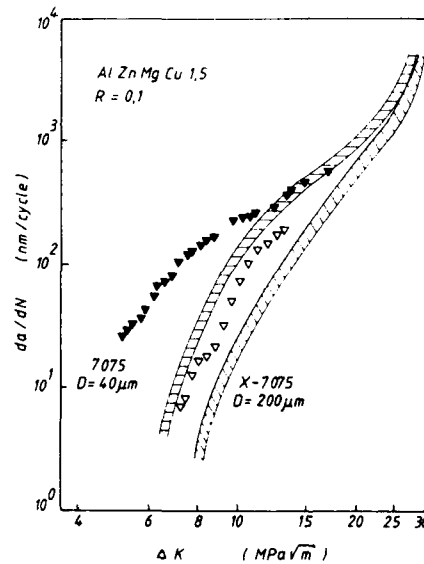
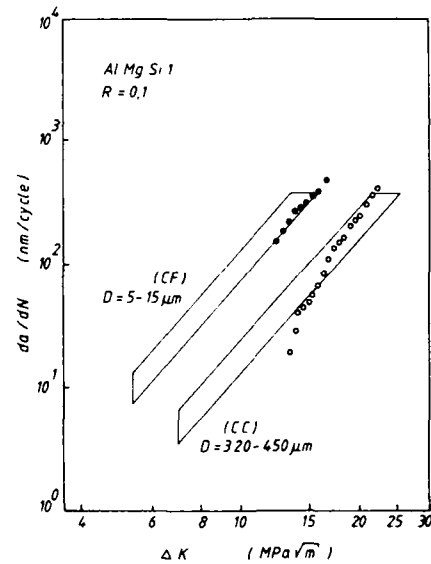


Figure 2a, b FCGR vs ΔK for fine grained (full) and coarse grained (open symbols). Scatterbands indicate literature data. a) (7), (8) b) (1)



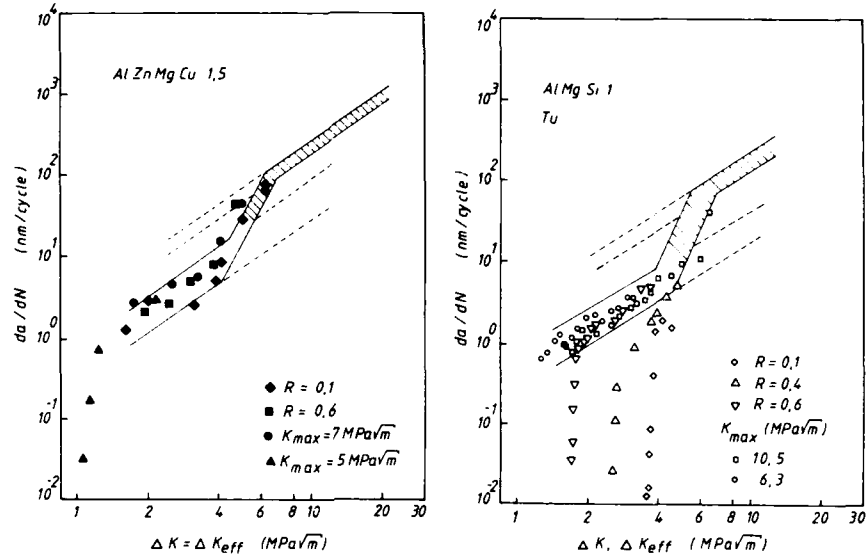


Figure 3a, b FCGR vs ΔK near the threshold (bend spec.). Shaded areas indicate FCG data vs ΔK_{eff} from CT spec. (0.1 R 0.8).

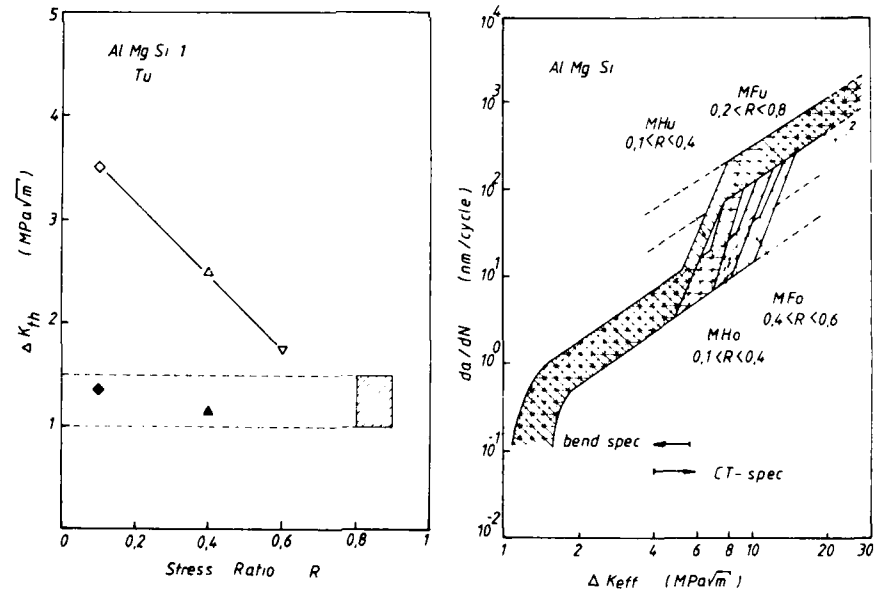


Figure 3c ΔK_{th} vs R from Fig. 3b. Figure 4 FCGR vs ΔK_{eff} . Influence of aging. u=underaged o=overaged

FATIGUE CRACK GROWTH BEHAVIOUR OF A356-T6 CAST ALUMINUM ALLOY

C.C. Wigant* and R.I. Stephens*

Constant amplitude fatigue crack growth behavior was obtained for A356-T6 (Al7SiMg) cast aluminum alloy for crack growth rates between 10^{-11} and 10^{-6} m/cycle with R ratios of 0.1 and 0.5. Three different mold temperatures resulted in secondary dendritic arm spacings (DAS) to vary from about 80 to 90 μm , resulting in only coarse microstructure. Threshold levels, ΔK_{th} , and the Paris exponent, m, were approximately twice the values usually found for wrought aluminum alloys. The influence of R ratio was quite pronounced and crack closure, as measured with a crack mouth COD gage, did not eliminate threshold and near-threshold R ratio differences. Roughness-induced crack closure was no doubt more important than plasticity-induced closure.

INTRODUCTION

Fatigue crack growth behavior of cast aluminum alloys has been investigated recently by only a few researchers (1-5). This paper involves the fatigue crack growth behavior from 10^{-11} to 10^{-6} m/cycle for A356-T6 (Al7SiMg) cast aluminum alloy. The material was part of the recent SAE Fatigue Design and Evaluation committee's round robin low cycle fatigue program. The material was chosen because of its use in the ground vehicle industry.

TEST MATERIALS AND PROCEDURES

The chemistry of the A356-T6 cast aluminum alloy is given in Table 1. Castings were formed as 25 mm thick near net shape compact type, CT, blocks that were formed by pouring the molten aluminum alloy, at 704°C, into permanent molds. The permanent molds were at room temperature, 538°C or 982°C in order to hopefully obtain three different cooling rates and hence three different microstructures or secondary dendritic arm spacing (DAS). The three

* Research Assistant and Professor, respectively, Mechanical Engineering Department, The University of Iowa, Iowa City, Iowa 52242, USA.

174

FATIGUE 87

materials are designated X, Y and Z, respectively. After solidification, all castings were heat treated to the T6 condition. The microstructures resulting from the three mold temperatures and heat treatment however were all very similar with respect to eutectic structure and DAS. The DAS was about 80 μm for X and about 90 μm for Y and Z materials. Thus, even though three different permanent mold temperatures were used, essentially only one cooling rate or microstructure was obtained in these CT castings. The microstructure was classified as coarse. Porosity was less than one percent in all three materials.

Monotonic tensile properties were obtained from axial cylindrical specimens poured under the same conditions as the CT specimens. However the as-cast cylindrical test diameters were about 11 mm which were then ground to 9.5 mm. These smaller size castings had smaller DAS values and hence slightly different properties than the CT castings. The monotonic properties are listed in Table 2 as reasonable values for the CT specimens. Values of hardness and Young's modulus were essentially the same for all three materials, while the ultimate strength, S_u , and the .2% yield strength, S_y , varied by less than 10 percent. The low percent elongation ($\leq 3\%$) and low percent reduction in area ($\leq 3\%$) indicated brittle tensile behavior for all three materials. Under low cycle strain-controlled fatigue conditions, all three materials had similar cyclic strain hardening behavior (6).

Compact type, CT, specimens were used for all fatigue crack growth tests. Two 9.1 mm thick specimens with $H/w = 0.49$ and $w = 71$ mm were machined from each cast block. Both sides of the specimen were polished in the crack growth region in order to

TABLE 1 - Chemistry A356-T6 Cast Aluminum Alloy (% Weight)

Cu	Fe	Mn	Si	Mg	Zn	Ti	Al
0.01	0.01	0.01	7.25	0.36	0.01	0.02	BASE

TABLE 2 - Average Tensile Properties and Hardness of A356-T6

	X	Y	Z
S_y - MPa	231	224	218
S_u - MPa	276	267	255
E - GPa	71	70	71
% RA	3.3	2.5	3.2
HB (10/500/15)	93	93	93

FATIGUE 87

better monitor crack growth using a 32X travelling telescope. Tests were run at room temperature with a frequency between 30 and 40 Hz using an 89 kN closed-loop electrohydraulic test system. Crack closure was monitored using a crack mouth opening displacement (COD) clip gage. Load versus COD data were obtained periodically during the testing at which time the frequency was dropped to 1 Hz. Precracking was done following ASTM standard E647 using a manual load shedding procedure. Crack extension during each preloading step was usually less than the E647 recommendation, but greater than the plane stress plastic zone size. Fatigue crack growth data were obtained for all three materials with R ratios (P_{min}/P_{max}) equal to 0.1 and 0.5. Region I data (threshold and near threshold) were obtained using a manual decreasing and increasing load step procedure suggested by Bucci (7). Load steps were from 2 - 8% and crack extensions at a given load were between 0.2 and 1.6 mm. The absolute value of the K-gradient C given by

$$C = \left| (1/K)(dK/da) \right| \quad (1)$$

was always less than 0.08 mm^{-1} as recommended by Bucci (7). The secant method was used to reduce the step test data to da/dN versus ΔK . Region II data (10^{-8} - 10^{-6} m/cycle) were obtained principally under constant load amplitude as recommended in ASTM Standard E647. However, some of the increasing load step tests reached 10^{-8} m/cycle and after that rate, these specimens were run at constant load amplitude. Some decreasing load step tests also had da/dN values greater than 10^{-8} m/cycle.

The nominal crack growth surface path was essentially perpendicular to the applied load, however the local surface crack paths were very erratic. This caused less continuity in the a vs. N data than usually found with wrought aluminum alloys. All crack growth data were reduced to da/dN vs. ΔK using either a secant method or a seven point second order incremental polynomial.

TEST RESULTS AND DISCUSSION

da/dN versus applied ΔK are shown in Fig. 1 for each of the three A356-T6 cast materials. Solid data points are for $R = 0.5$ and open data points are for $R = 0.1$. Substantial scatter is evident along with the effect of R ratio. The greatest scatter occurred with $R = 0.1$ principally in Region II. Here, higher da/dN values resulted with the increasing or decreasing load step tests than with the constant load amplitude tests. This unusual scatter is attributed to differences in crack closure and experimental procedures. All the da/dN vs. applied ΔK data have been superimposed in Fig. 2 for better comparison. The solid inclined line separates the two R ratios. The greater $R = 0.1$ scatter is

FATIGUE 87

evident, along with the definite shift in R ratio results. For a given R ratio, the three cast materials have very nearly the same fatigue crack growth behavior. Threshold values, ΔK_{th} , at 10^{-10} m/cycle and the Paris equation coefficients and exponents are given in Table 3, where

$$\frac{da}{dN} = A(\Delta K)^m \quad (2)$$

Only constant load amplitude data were used in determining the values of A and m.

From Figs. 1 and 2 and Table 3, it is seen that the Region II exponent m is very high with values for R = 0.1 ranging from 7.9 to 11.2 and values for R = 0.5 ranging from 5 to 8.4. ΔK_{th} values are also very high with values for R = 0.1 ranging from 6.0 to 6.9 MPa \sqrt{m} and values for R = 0.5 ranging from 3.6 to 4.0 MPa \sqrt{m} . The highest values of ΔK for stable fatigue crack growth were approximately 20 and 10 MPa \sqrt{m} , respectively, for R = 0.1 and 0.5. Thus, fatigue crack growth has a very narrow band of ΔK for these similar A356-T6 castings. Wrought aluminum alloys usually have a wider range of applicable ΔK values.

Crack opening loads were determined from load vs. COD curves obtained in both Regions I and II. P_{op} was determined by extending the two linear portions of the curves. The intersections were defined as P_{op} . No deviation from linearity occurred for R = 0.5 tests which indicated no crack closure was involved with R = 0.5 tests, based upon COD measurements. A plot of P_{op}/P_{max} vs. applied ΔK for R = 0.1 is given in Fig. 3 for the three materials. The open data points represent Region I while the closed data points represent Region II. In Region I, the P_{op}

TABLE 3 - Threshold Values and Paris Equation Parameters of A356-T6 (units: MPa \sqrt{m} and m/cycle)

Material Designation	Loading Condition	ΔK_{th} MPa \sqrt{m}	$(\Delta K_{th})_{eff}$ MPa \sqrt{m}	A	m
X	R = 0.1	6.0	3.7	1.5×10^{-20}	11.2
	= 0.5	4.2	4.2	2.2×10^{-15}	8.4
Y	R = 0.1	6.2	3.0	5.4×10^{-17}	8.0
	= 0.5	3.6	3.6	7.0×10^{-15}	7.9
Z	R = 0.1	6.9	1.3	8.6×10^{-17}	7.9
	= 0.5	4.0	4.0	1.2×10^{-12}	5.0

FATIGUE 87

values ranged from about 50 to 75 percent of P_{max} while in Region II this percentage was about 20 to 80 percent. Thus, crack closure is of greater importance in Region I compared to Region II for these cast aluminum materials.

P_{op} was used to determine the crack opening stress intensity factor K_{op} . An effective stress intensity factor ΔK_{eff} was then defined as

$$\Delta K_{eff} = K_{max} - K_{op} \quad (3)$$

da/dN vs. ΔK_{eff} data are given in Fig. 4 for each of the three materials. The solid data points are for $R = 0.1$ and the open data points are for $R = 0.5$. Since no closure occurred for $R = 0.5$, ΔK_{eff} and applied ΔK are the same for this R ratio. For each material, it appears that crack closure can account for the R ratio effect in Region II, while for Region I, the $R = 0.1$ effective data "overshoot" the $R = 0.5$ data. This may be due to insufficient COD gage sensitivity. Superposition of all the data from Fig. 4 is given in Fig. 5 where again, solid data points are for $R = 0.1$ and open data points are for $R = 0.5$. Effective values of ΔK_{th} were obtained using a linear regression and extrapolation to 10^{-10} m/cycle. These values, $(\Delta K_{th})_{eff}$, are given in Table 3. All values are quite similar except for material Z with $R = 0.1$ which had extremely high crack opening loads and could be suspect.

Figure 6 shows the macro fatigue crack growth surfaces of material X at near threshold regions for R ratios of 0.1 and 0.5. It is seen that higher growth rates produced rougher textured areas, with the near threshold growth rates producing a smooth texture. This was seen for all three materials and was due to greater crack closure and fretting at low ΔK values. The $R = 0.5$ surfaces also exhibited this smoothness, indicating crack closure was present during $R = 0.5$ near threshold testing. This is contrary to the load vs. COD results.

Figure 7 shows the macro fatigue crack growth surfaces of material Y for Region II constant load amplitude testing. These surfaces are similar to that for the other two materials in Region II. Both $R = 0.1$ and 0.5 fatigue surfaces have the same rough texture.

Figure 8a and 8b show typical low magnification SEM fractographic features. The crack growth direction is from bottom to top. Figure 8a shows narrow ridges that formed as the crack advanced. This feather-like feature was common for the lower crack growth rates. Figure 8b shows β -platelets and porosity which were common for all crack growth rates.

FATIGUE 87

Figure 9a and 9b show typical higher magnification SEM fractographic features. In Fig. 9a it appears that rubbing of the near threshold crack surfaces due to crack closure occurred. This was often found in the $R = 0.1$ tests, but was also found for the $R = 0.5$ tests providing more evidence that crack closure was present, at times, during $R = 0.5$ tests. The secondary cracking and elongated cellular structure seen in Fig. 9b were very common for $da/dN > 10^{-6}$ m/cycle. Localized poorly defined striations were occasionally found.

SUMMARY AND CONCLUSIONS

1. The microstructure, fatigue crack growth behavior and fracture surface morphology were very similar for all three A356-T6 cast materials.
2. ΔK_{th} and the Paris exponent m were much higher (about a factor of 2^{th}) than for most wrought aluminum alloys.
3. Crack growth rates were increased and ΔK_{th} was decreased by increasing the R ratio from 0.1 to 0.5.
4. Crack closure was no doubt roughness-induced rather than plasticity-induced.
5. Crack closure as measured with a crack mouth COD gage did not eliminate R ratio effects in the near threshold and threshold regions and even over-corrected some data.

REFERENCES

- (1) Hertzberg, R.W. et al., in Advances in Fracture Research, ICF-5 Proceedings, Vol. 2, pp. 907-914.
- (2) Saxena, A., Hudak, S.J., Donald, J.K., and Schmidt, D.W., Journal of Testing and Evaluation, Vol. 6, 1978, pp. 167-174.
- (3) Gunther, C.K., Technical Report AFWAL-TR-80-3021, Part II, The Boeing Co., 1980.
- (4) Doyle, C.E., Jr., Technical Report AFWAL-TR-84-4070, Vol. I and II, General Dynamics, Fort Worth Division, 1984.
- (5) Oswalt, K.J., and Lii, Y., Technical Report AFWAL-TR-4117, Northrop Corp., 1985.
- (6) Wigant, C.C. and Stephens, R.I., "Low Cycle Fatigue of A356-T6 Cast Aluminum Alloy," SAE International Congress and Exposition, Detroit, 1987, paper No. 8700096.
- (7) Bucci, R.J., in Fatigue Crack Growth Measurement and Data Analysis, ASTM STP 738, 1981, pp. 1-33.

FATIGUE 87

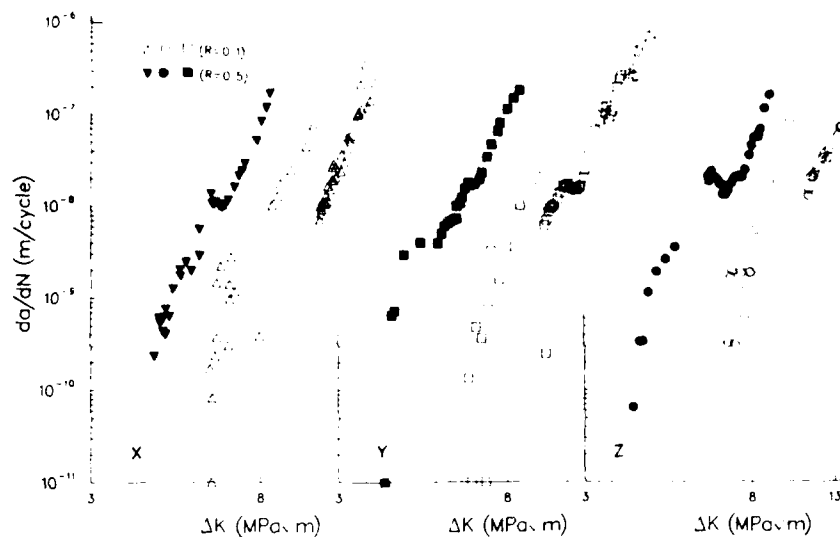


Figure 1. da/dN versus applied ΔK , material X, Y and Z

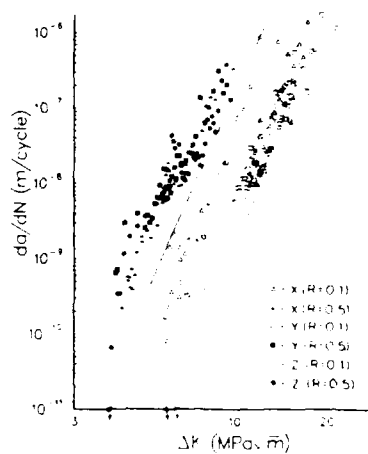


Figure 2. Composite da/dN versus applied ΔK

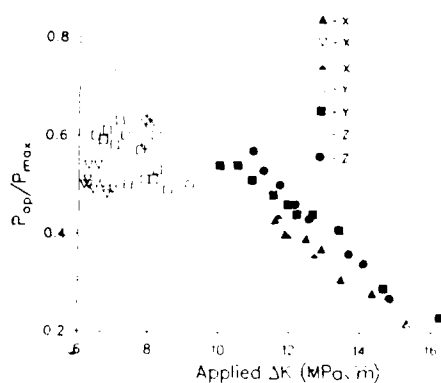


Figure 3. P_{op}/P_{max} versus applied ΔK

FATIGUE 87

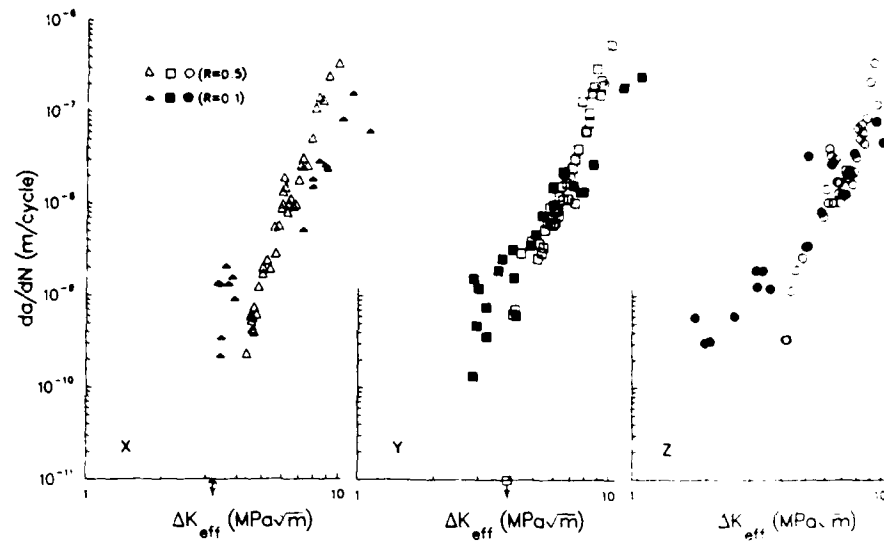


Figure 4. da/dN versus effective ΔK , material X, Y and Z

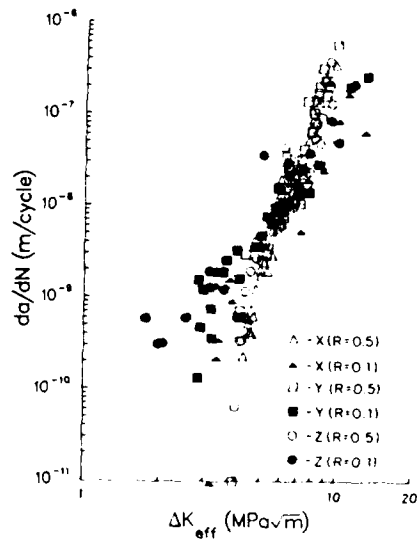


Figure 5. Composite da/dN versus effective ΔK

FATIGUE 87

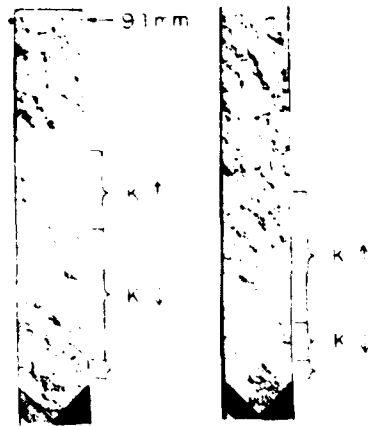


Figure 6. Typical macro fatigue surfaces, Region I

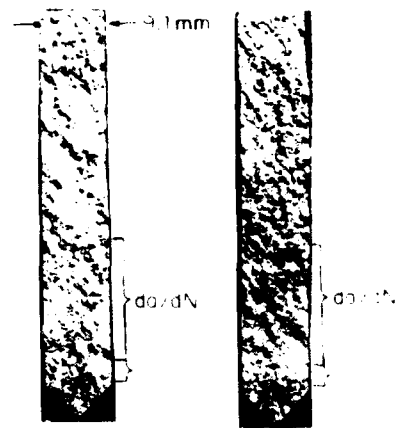
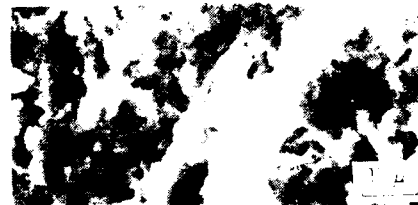


Figure 7. Typical macro fatigue surfaces, Region II



(a) Feather-like Feature



(a) Region I Ruttling



(b) β -platelets and Porosity



(b) Region II

Figure 8. Low magnification SEM features $da/dN \approx 10^{-9}$ m/cycle

Figure 9. Higher magnification SEM features

FATIGUE 87

STRIATIONS AND THE FATIGUE GROWTH MECHANISM IN A MICRO-ALLOYED STEEL

H.J. Roven¹, M.A. Langøy² and E. Nes²

The fatigue crack growth mechanism has been studied in a microalloyed steel in laboratory air at constant load ratio. A striation mechanism was found to dominate both the ΔK_{th} - and Paris law region. The striation spacing was constant over four orders of magnitude of crack growth rates whereas the classical "one cycle per striation" spacings only occurred in a small fraction of the Paris law regime. The crack deformation zone contained subgrains with a decreasing size as the fracture plane was approached. A model is developed to describe the observed empirical connection between ΔK and N_s (number of cycles per striation). The crack growth equation in this model is in accordance with the "accumulated damage" philosophy.

INTRODUCTION

During the last 20 years a series of models for the fatigue crack propagation process (FCP) have been suggested. The models can be divided into three groups, as suggested by Bailon and Antolovich (1): (I) Empirical models (2-8), (II) dislocation based models (9,10), and (III) micro low-cycle fatigue models (11-14). Among the empirical models, the Paris equation developed from the concepts of linear elastic fracture mechanics, seems to fit well to experimental data in general:

$$da/dN = C_1 (\Delta K)^m$$

Where C_1 and m are experimental constants and ΔK is the stress intensity factor lying between two asymptotic values: the threshold stress intensity (ΔK_{th}) and the critical stress intensity ($K_{max,c}$), the specimen toughness ($K_{max,c}$).

¹ SINTEF, Div. of Metallurgy, N-2034 Trondheim
² The Norwegian Institute of Technology, Div. of Metallurgy, N-2034 Trondheim NTH

AD-A184 045

FATIGUE '87 VOLUME 1 (U) VIRGINIA UNIV CHARLOTTESVILLE
SCHOOL OF ENGINEERING AND APPLIED SCIENCE
R O RITCHIE ET AL. JUN 87 ARO-24134.1-MS-CF

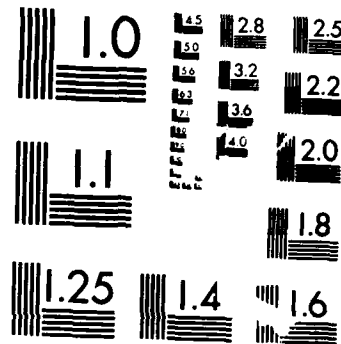
3/7

UNCLASSIFIED

N00014-87-G-0008

F01 20/11

NL



MICROCOPY RESOLUTION TEST CHART
NATIONAL BUREAU OF STANDARDS-1963-A

Laird and Smith (16) maintained that there is one general mechanism of fatigue crack growth in ductile materials which is formation of ductile striations by the crack tip "plastic blunting process". Based upon the experiments from Forsyth and Ryder (17) it was generally agreed that one striation is formed during each load cycle. Extensive fractographic research over the last 30 years, however, have shown that this basic idea is not always fulfilled and alternative mechanisms have been suggested (9-15). Fractographic examinations of Al, Cu, γ -Fe and Ti-alloys have shown that striation formation is limited to crack growth rates approximately between 10^{-8} to 10^{-6} m/cycle (18). At crack growth rates below a certain value, the striation spacing, s , has been reported to exceed the corresponding macroscopic growth increment per cycle in ferritic steels (19), maraging steels (20), austenitic steels (21-22), QT-steels (23) and two Al-alloys (24). A one cycle per striation mechanism is normally observed at crack growth rates above 10^{-6} - 10^{-7} m/cycle (19-24). However, ultralow macroscopic growth rates much lower than a Burgers-vector advance per cycle have been observed in conventional metallic alloys (18). This may indicate that the crack advances in a discontinuous fashion, extending by some multiple of the Burgers-vector and then arresting for some cycles. The objective of the present work was to follow in detail the striation formation over a wide range of crack growth rates in a microalloyed steel. Emphasis was directed towards an establishment of a detailed quantitative picture of the striation formation and the deformation zone substructure. A micro-mechanism model for fatigue crack growth in the low and intermediate ΔK -region is developed and discussed in terms of the experimental data.

MATERIAL AND EXPERIMENTAL INVESTIGATION

A normalized microalloyed steel (0.09 C, 0.38 Si, 1.46 Mn, 0.25 Ni, 0.025 Nb, 0.02 Cr, 0.003 V, 0.011 Ti, 0.029 Al) with yield strength 373 MPa and UTS 494 MPa was used in this investigation. The pearlite content was 10%, ferrite grain size $10\ \mu\text{m}$ and pearlite grain size was $6\ \mu\text{m}$. Standardized compact tension specimens (25) with dimensions $W=60\ \text{mm}$ and $B=10\ \text{mm}$ was used in the crack growth experiments. The crack growth data were obtained in laboratory air (25 - 55 % relative humidity) by using a servo-hydraulic 100 kN MTS machine, $R=0.5$, $F=50\ \text{Hz}$ sine ($\Delta K < 20\ \text{MPam}^{1/2}$) and $F=10\ \text{Hz}$ ($\Delta K > 20\ \text{MPam}^{1/2}$). Crack advance was measured from both sides on electropolished surfaces with optical microscopes (63x) and a stepped load shedding technique (26) was used to obtain the ΔK versus da/dN data for $\Delta K < 20\ \text{MPam}^{1/2}$. For $\Delta K > 20\ \text{MPam}^{1/2}$ the tests were conducted at constant load amplitude.

Crack closure measurements were carried out by using both a back face strain gage and a clip on gage at $F=0.1\ \text{Hz}$. Fracture surfaces of fatigued specimens were examined in a JEOL JSM 840

scanning electron microscope. The primary goal was to establish a detailed quantitative picture of the fracture surface morphology. Fractographs at 10.000x magnification were used and striations spacings, s -values, were measured from, in average, 50 striations at each ΔK -level. In this work the quantity "striation spacing" means the distance between "tops" of two neighbouring striations in the direction parallel to the microgrowth direction. From the measured macroscopic crack growth rate and the striation spacing the quantity N_s (=number of cycles per striation) was calculated. To study the deformation substructure close to the fatigue fracture plane, the fracture surfaces were Fe-plated, sectioned and electropolished before SEM investigation in the channeling contrast mode. Thin foil sections were also studied in a 200 kV TEM. The surface plated specimens used were taken normal to the crack plane and contained the crack growth direction. The investigated specimens corresponded to the upper part of the linear Paris region.

RESULTS AND DISCUSSION

Fatigue crack growth

The fatigue crack growth rate versus effective stress-intensity data for the investigated material are shown in Figure 1. Crack closure was detected for the given experimental conditions for $\Delta K < 11 \text{ MPam}^{1/2}$. The closure stress intensity, K_{cl} , seemed to be influenced by the previous load block and hence a plasticity induced closure (6) may be operating. The Paris law relation was assumed to apply in the crack growth rate range 1×10^{-9} to $6 \times 10^{-7} \text{ m/cycle}$. In the statistical calculations a logarithmic normal distribution of crack growth data was assumed (27).

Fractography - striation formation

Fractographic studies in SEM showed that formation of transgranular ductile striations is the most dominating feature in the ΔK_{th} -region (Figure 2), in the linear Paris region and still occurs to a large extent as the crack propagation rate approaches the unstable fracture mode. The frequent observations of striations in the ΔK_{th} -region, where the macroscopic crack growth rate per cycle is only a fraction of the Burgers-vector, are not in accordance with the faceted growth reported in this regime in carbon and QT-steels (30), Al-, Cu-, Ti- and Ni-alloys (31). The present work showed the presence of striations in addition to such intergranular facets as the ΔK_{eff} approached values corresponding to a reversible plastic zone diameter equal to the ferrite grain size. Above and below this narrow ΔK -regime where some faceted growth was observed, striation formation was the dominating feature. According to (18) striations are not detected below

2×10^{-8} m/cycle since their spacings are reduced below the resolution limit of the electron microscope. This is true only if the striation spacings correspond to the incremental advance of the crack after each cycle. A constant striation spacing, $s = 0.23 \pm 0.05 \mu\text{m}$, is observed over almost four orders of magnitude of crack propagation rates from $da/dN = 3 \times 10^{-11}$ m/cycle ($\Delta K_{\text{eff}, \text{th}} = 2.3 \text{ MPam}^{1/2}$) to $da/dN = 2.3 \times 10^{-7}$ m/cycle ($\Delta K = 34 \text{ MPam}^{1/2}$). It follows from these results that as long as $da/dN < 2.3 \times 10^{-7}$ m/cycle the striation spacing is greater than the crack advance increment per cycle indicated by the measured macroscopic growth rate. The same tendency has been reported by other investigators on different steels and Al-alloys (19-24). In Ref. (23) they suggest that a greater striation spacing is caused by a decreasing area fraction of striations at low stress intensities. This is not in accordance with our observation. Close to the threshold stress intensity, the area fraction of striations is still close to a 100%. In addition, the presence or absence of intergranular facets do not appear to have much direct affect on near threshold crack rates (31). Experiments carried out on an Al-Cu alloy (29), showed that a constant striation spacing was left behind the advancing crack when $K_{\text{min}} < K_{\text{cl}}$, while at $K_{\text{min}} > K_{\text{cl}}$, varying spacing was observed. Our results are not in accordance with these observations since a constant striation spacing is observed at ΔK -levels where there are no measured crack closure.

ΔK versus N_s relationship

In quantitative terms the number of cycles per striation, N_s , versus the effective stress intensity range, ΔK_{eff} , (Figure 3) fit well to an empirical relationship of the form:

$$\Delta K_{\text{eff}} = C_2 \cdot N_s^{-q} \quad (2)$$

where C_2 and q are constants. In the present work $C_2 = 33.1 \text{ (MPam}^{1/2})$ and $q = 0.34$. The validity of this relation over three orders of magnitude in N_s is demonstrated in Figure 3. The spacing seems to increase towards a value which fits the classical "one cycle per striation" (16,17) for $\Delta K > 34 \text{ MPam}^{1/2}$. It is worth emphasizing that this latter correspondence between striation spacing and macroscopic crack growth rate only operates in approximately one third order of magnitude of growth rate in the upper ΔK -range from $34 \text{ MPam}^{1/2}$ ($da/dN = 2.3 \times 10^{-7}$ m/cycle) to $\Delta K = 45 \text{ MPam}^{1/2}$ ($da/dN = 5.2 \times 10^{-7}$ m/cycle). In this regime we have the following relationship between the spacing s and ΔK :

$$s = C_3 \cdot (\Delta K)^{m_s} \quad (3)$$

where C_3 and m_s are constants. Our data give $m_s = 2.69$.

Such relationships have been reported by other authors (20, 32). The exponent m_s should in this case approach the exponent m (Eq. 1) in accordance with the present observations.

Deformation structure

The sectioned plated specimens used for deformation structure studies close to the fracture plane revealed the formation of an almost equiaxed subgrain structure. Both micrographs in SEM (Figure 4) and TEM showed subgrain formation. The subgrain size seemed to decrease rapidly as the fracture plane was approached. An interesting observation was that the subgrain size very close to the crack plane was in the same range as the constant striation spacing, i.e. approximately 0.2 - 0.3 μm . A strain gradient reflected by a decreasing subgrain size has also been observed in a low carbon steel (33), but the minimum size was considerably larger (1 - 2 μm). On the other hand, in Cu and Al the minimum subgrain size have been reported down to 0.1 - 0.2 μm (34,35). From this we suggest that there is a close connection between the striation growth mechanism and the plastic zone deformation substructure and further work should be carried out along these lines.

A model for striated growth

From the above results on striation formation and striation spacings, it is reasonable to believe that below $da/dN = 2.3 \times 10^{-7}$ mm/cycle the crack front advances in a discontinuous way. A fraction X of the crack front extends by an increment equal to the striation spacing during one cycle. In the same cycle the remaining fraction of the crack front (1-X) is resting. This process is continued until the entire crack front have advanced the striation spacing distance s . In other words, each striation with a width corresponding to the fraction X of the specimen

thickness, rests for N_s cycles. Then it suddenly, during one cycle, advances the distance s again. In our model it is assumed that the number of cycles required to generate a local incremental jump of the crack front is related to the plastic zone strain, $\Delta\epsilon_p$, through a Coffin-Manson relation $\Delta\epsilon_p = C_o (N)^{-b}$. Further, by assuming that the plastic strain range at the crack tip is $\Delta\epsilon_p = \text{CTOD}/d$ (where d is a parameter of dimension length and a characteristic of the material) and that cyclic CTOD $= \Delta K_{\text{eff}}^2 / E \cdot \sigma_{yc}$, the following relationship is derived:

$$\Delta K_{\text{eff}} = (C_o \cdot E \cdot \sigma_{yc} \cdot d)^{1/2} \cdot N_s^{-b/2} \quad (4)$$

When using low cycle fatigue (LCF) data from the same material ($C_o = 1.19$, $b = 0.62$, $E = 206 \text{ GPa}$ and $\sigma_{yc} = 373 \text{ MPa}$) and assuming Eq. 2 identical to Eq. 4 the parameter d becomes $d = 12 \mu\text{m}$. It is interesting to note that this value of d is almost identical to the ferrite grain size ($10 \mu\text{m}$). Further, LCF data have confirmed that the exponent in Eq. 2, $q (=0.34)$, is very close to $b/2 (=0.31)$. Eq. 4 is in convincingly good agreement to experimental data under the given experimental conditions. This model shows an interesting connection between the LCF and the FCP-process on both a micro- and macroscopic level. By assuming $N_s > 1$ the following equation for the FCP-process is derived:

$$da/dN = s \cdot \frac{(\Delta K_{\text{eff}})^{2/b}}{(E \cdot \sigma_{yc} \cdot C_o \cdot d)^{1/b}} \quad (5)$$

This equation is only valid when the striation spacing is independent of ΔK and $N_s > 1$. Eq. 5 is very similar to the "accumulated damage" philosophy models suggested by other authors (11,12). At higher stress intensity levels where $N_s = 1$, the mechanisms taken care of by the above model are considered to have neglectable influence to the fatigue crack growth rate. Other models based upon a crack advance per cycle proportional to the CTOD (36) may be of importance in the upper part of the Paris region (37).

CONCLUSIONS

From the present work on fatigue crack growth in a microalloyed steel, we conclude (constant load ratio, laboratory air):

- the fatigue striation mechanism is dominating the FCP-process in the crack growth range 3×10^{-11} to $6 \times 10^{-7} \text{ m/cycle}$.
- a constant striation spacing is operating over almost four decades of crack propagation rates and the classical "one cycle per striation" appears only in a narrow regime of one third decade of propagation rates.

FATIGUE 87

an "accumulated damage" model for the FCP-process where the number of cycles per striation is greater than one, is developed. The model shows convincingly good agreement between LCF-data, crack growth rate data and the measured constant striation spacing.

ACKNOWLEDGEMENTS

The authors want to thank NTNF (the Royal Norwegian Council for Natural Science and Industrial Research) and STATOIL (The Norwegian State Oil Company) for their financial support of this work.

SYMBOLS USED

b	= power exponent in the Coffin-Manson expression
C_o	= constant in the Coffin-Manson expression
d	= material constant of dimension length
m_s	= power exponent in s versus N_s expression
N_s	= number of cycles per striation
q	= power exponent in ΔK_{eff} versus N_s expression
s	= striation spacing
$\Delta K_{eff} = K_{max} - K_{cl}$	
σ_{yc}	= cyclic yield strength
$\Delta \epsilon_p$	= plastic strain range
X	= fraction of crack front

REFERENCES

- (1) Bailon, J.P., Antolovich, S.D., "Fatigue Mechanisms: Advances in Quantitative Measurements of Physical Damage", ASTM STP 811, 1983, pp. 313-349.
- (2) Paris, P., Erdogan, F., Journal of Basic Engineering, Trans. of ASME, D, 85, 1963, pp. 528-539.
- (3) Forman, A.G., Journal of Basic Engineering, Vol. 89, 1967, pp. 459-469.
- (4) Nicholson, C.E., in Proc., Conference of Mechanics and Mechanisms of Crack Growth, Churchill College, Cambridge, England, 1973.
- (5) Frost, N.E., Dixon, J.R., Int. Journal of Fracture, Vol. 9, 1967, pp. 301-316.
- (6) Elber, W., in "Damage Tolerance in Aircraft Structures", ASTM STP 486, ASTM, 1971, pp. 230-242.
- (7) Fitzgerald, J.M., Journal of Testing and Evaluation, Vol. 5, 1977, pp. 343-353.
- (8) Sullivan, A.M., Crooker, T.W., Trans. ASME, Vol. 98, 1976, pp. 179-184.
- (9) Weertman, J., in "Fatigue and Microstructure", ASM, Metals Park, Ohio, 1979, pp. 279-306.

FATIGUE 87

- (10) Yokobori, T., Konosu, S., Yokobori, A.T.Jr., in "Fracture", ICF4, Waterloo, Canada, Vol. 1, 1977, pp. 665-681.
- (11) McClintock, F.A., Fracture of Solids, Wiley, New York, 1963, pp. 65-102.
- (12) Antolovich, S.D., Saxena, A., Chanani, G.R., Eng. Fract. Mech., Vol. 7, 1975, pp. 649-652.
- (13) Chanani, G.R., Antolovich, S.D., Gerberich, W.W., Met. Trans., Vol. 3, pp. 2661-2672.
- (14) Lantaigne, J., Bailon, J.P., Met. Trans., Vol. 12A, 1981, pp. 459-466.
- (15) Chakraborty, S.B., Fat. of Eng. Mat. and Struct., Vol. 2, 1979, pp. 331-344.
- (16) Laird, C., Smith, G.C., Phil. Mag., 8, 1963, p. 1945.
- (17) Forsyth, P.J.E., Ryder, D.A., Aircraft Engineering, Vol. 32, No. 374, 1960, p. 96.
- (18) Hertzberg, R.W., Mills, W.J., ASTM-STP 600, 1976, pp. 220-224.
- (19) Bates, R.C., Clark, W.G., 68-1D7-RPAFC-P1, Westinghouse Research Laboratories, Pittsburg, Penns., 1968.
- (20) Miller, G.A., Trans. ASM, Vol. 62, 1969, pp. 651-658.
- (21) Bathias, C., Pelloux, R.M.N., Met. Trans., 1973, 4, pp. 1265-1273.
- (22) Wareing, J., Vaughan, H.G., Met. Sci., Oct, 1977, pp. 439-446.
- (23) Masuda, C., et al., Journ. of Met. Sci., 15, 1980, 1663-1670.
- (24) Broek, D., Proc. 2nd Int. Conf. on Fract., Chapman and Hall, London, 1969, p. 754.
- (25) ASTM standard E 647-78T.
- (26) Bucci, R.J., ASTM STP 738, 1981, pp. 5-28.
- (27) Rausand, M., "Statistical analyses of Fatigue Test Data", SINTEF report STF18-A81047, 1981.
- (28) Suresh, S., Parks, D.M., Ritchie, R.D., Proc. Fat. Thresholds, Stockholm, Sweden, June, 1981, pp. 391-408.
- (29) Sunder, R., Dash, P.K., Int. J. Fatigue, April, 1982, pp. 97-105.
- (30) Beevers, C.J., Met. Sci., 11, 1977, pp. 362-367.
- (31) Ritchie, R.D., Int. Met. Rev., Nos. 5 and 6, 1979, pp. 205-230.
- (32) Rhodes, D., Nix, K.J., Radon, J.C., Int. J. Fract., Vol. 6, 1984, pp. 3-7.
- (33) Davidson, D.L., Lankford, J., Int. J. Fract., 12, 1976, pp. 579-585.
- (34) Saxena, A., Antolovich, S.D., Met. Trans. 6A, 1975, p. 1809.
- (35) Grosskreutz, C., Phys. Stat. Sol. (b), 1971, p. 359.
- (36) McClintock, F.A., in Fat. Crack Prop., ASTM STP 415, 1967, p. 170.
- (37) McEvily, A.J., "Fatigue Mechanisms: Advances in Quantitative Measurements of Phys. Dam.", ASTM STP 811, 1983, pp. 283-312.

FATIGUE 87

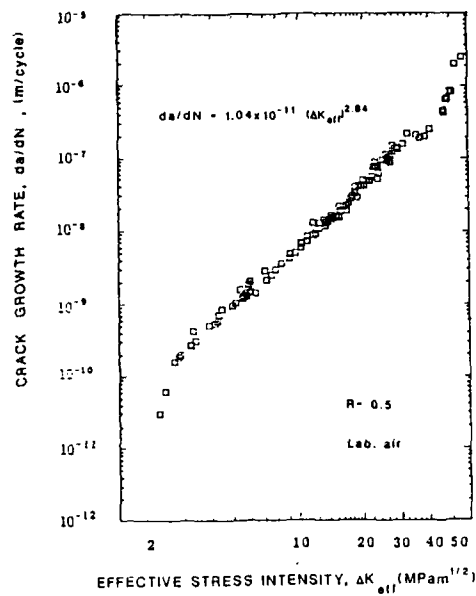


Figure 1. Fatigue crack propagation, da/dN , versus ΔK_{eff} data obtained in laboratory air, $R=0.5$.

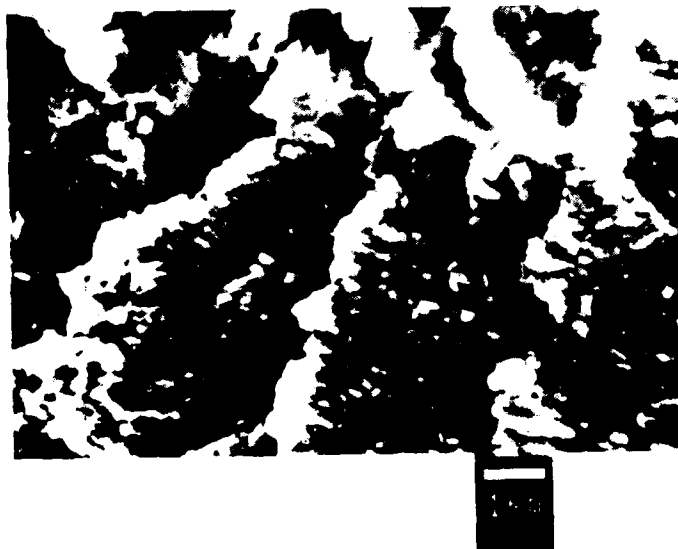


Figure 2. Striations in the threshold region, $\Delta K_{eff,th} = 2.3$ $MPam^{1/2}$, $da/dN = 3 \times 10^{-11}$ m/cycle. Striation spacing $s = 1.6 \times 10^{-7}$ m (10.000X; SEM).

FATIGUE 87

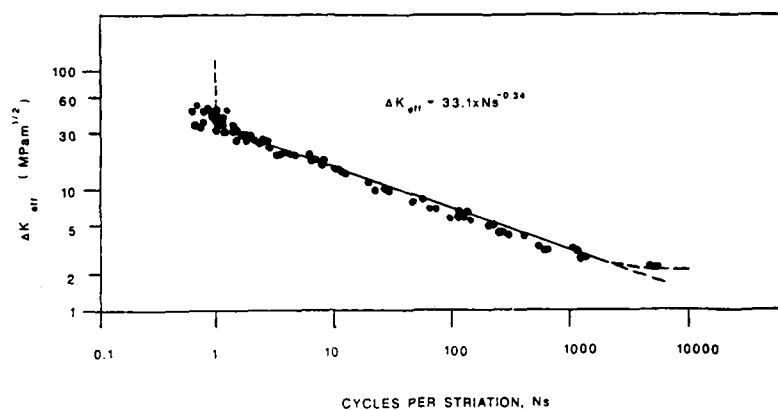


Figure 3. Experimental data: ΔK_{eff} versus the number of cycles per striation, N_s .



Figure 4. Deformation substructure (right) in the plane normal to the crack plane. Crack growth direction from bottom to top. $\Delta K = 32 \text{ MPa}\sqrt{\text{m}}$.

**SIGNIFICANCE OF FATIGUE CRACK CLOSURE
UNDER SPECTRUM LOADING**

R. Sunder*

A numerical study was made to evaluate the significance of fatigue crack closure under spectrum loading. It uses a reasonably accurate crack growth prediction model to assess the effect of variation in crack closure stress on predicted life. It is shown that precise knowledge of crack closure stress can be crucial to life estimates. The degree to which this precision will affect accuracy of life estimates depends on crack growth properties of the material as well as the nature of the load spectrum. dK/da and net stress effects on crack growth are also considered.

INTRODUCTION

The fatigue crack closure phenomenon (Elber (1)) explains fatigue crack propagation (FCP) behaviour under complex load sequences. A number of closure-based methods are now available to predict the FCP process under spectrum loading (Newman (2), de Koning and Linden (3), Sunder (4)). The ones proposed by Newman (2) and de Koning (3) actually permit a cycle-by-cycle estimate of crack closure stress and related crack extension under any given load sequence. The method proposed by Sunder (4) is an 'engineering' one which essentially permits extrapolation of constant amplitude FCP and closure data to spectrum loading without resorting to a protracted cycle-by-cycle analysis.

Crack growth rate is a power function of effective stress intensity range, K_{eff} . Obviously, errors in estimates of the crack opening stress intensity, K_{op} will be magnified through this power relationship. This raises a number of questions: How will inaccuracies in closure estimates affect predictions for the case of spectrum loading? Will the influence vary from material to material and spectrum to spectrum? Experimental studies of FCP under spectrum loading point to sizeable dK/da and net stress effects (Schijve et al (5), Sunder (6)). Such effects appear to go unnoticed under constant amplitude loading. Are they related to closure?

*NRC Research Associate, Air Force Materials Laboratory
AFWAL/MLLN, Wright-Patterson AFB, Oh. 45433

FATIGUE 87

This study addresses the above questions. A numerical analysis of FCP under various aircraft spectra was made with a simulation of minor variations in crack closure stress, S_{op} . The next section describes the load spectra and life prediction technique used. This is followed by an analysis of the spectra and evaluation of variation in predicted FCP life with change in S_{op} .

ANALYTICAL PROCEDURES

This section describes the analytical procedures used in the study. These include the material and load spectra considered and the FCP life prediction technique.

Material and Load Spectra were the same as those used in an elaborate round robin study carried out in the United States to evaluate the FCP life prediction capability of five different techniques under random loading. Ref. 2 contains a detailed description of this study. Its salient features are listed below.

The study was on 6.35 mm thick, 150 mm wide center cracked specimens of 2219-T851 aluminium alloy sheet material. Baseline crack growth rate (da/dN) data for the material at different stress ratios were provided for use in the predictions. The five load spectra were provided as tables of load sequences (peak/trough excursions). These are graphically shown in Fig.1. Repetitive blocks of these loads were applied in the tests. Typically we see characteristic manoeuvre loads in the fighter spectra and gust loads in the transport spectrum. In some of the sequences one can clearly see the periodic downward load excursions associated with the Ground-Air-Ground (GAG) cycle.

The experimental programme in (2) included tests under each of the spectra at two or three stress levels. Thus a total of 13 tests were conducted, 11 for the fighter spectra and two under the transport spectrum. The FCP lives were compared to predictions from individual methods. Interestingly, almost all predictions were within a factor of two.

Life Prediction Method. For this study, we chose the method proposed by Sunder (4) in view of its simplicity, minimal computational overhead and good prediction accuracy. The technique assumes that crack closure accounts for all of the retardation and acceleration one may observe under spectrum loading FCP. Further, it is assumed that crack closure under repetitive blocks of random loading is stable and controlled by the extreme loads in the block (provided of course such blocks repeat before the crack grows out of the plastic zone created by a previous block). Observations by Elber (7), Newman (2) and Schijve (8) strongly support this assumption.

The load sequences in Fig.1 show excursions - not complete (fatigue) load cycles. To enable FCP analysis, these sequences have first to be 'reduced' to closed fatigue cycles. This is done using the Rainflow cycle counting technique (Matsuishi and Endo (9)) whose validity for FCP analysis

under random loading was experimentally validated by Sunder et al (10). Assuming $S_{op} = \text{Const.}$ and K to change insignificantly over a block of loading, average growth rate $(da/dN)_{av}$ over a block of n cycles can be considered load sequence insensitive and described by the following relationship representing linear damage accumulation in FCP:

$$\left(\frac{da}{dN}\right)_{av} = \frac{1}{n} \sum_{i=1}^n f(K_{eff,i}) = \frac{1}{n} \sum_{i=1}^n f\left\{\bar{K} [S_{max,i} - \max(S_{op}, S_{min,i})]\right\}$$

where, \bar{K} - is stress intensity due to unit stress and $S_{max,i}$ and $S_{min,i}$ are the maximum and minimum stress respectively in cycle i . The max function accounts for the possibility that S_{min} can exceed S_{op} . S_{op} is determined from constant amplitude closure data corresponding to the highest S_{max} and lowest S_{min} in the block. The da/dN equation as a function of K_{eff} can be any suitable one. In this study, we used the modified Elber equation proposed by Newman (2).

In view of the sequence independence of the above equation, FCP life can be determined by numerical integration of its inverse from initial crack length to failure. This procedure requires negligible computation time when compared to cycle-by-cycle analysis.

RESULTS AND DISCUSSION

Fig.2 summarises the analysis of the five spectra in Fig.1. Results for the Air-to-Ground case were similar to Air-to-Air and excluded from the figure. Three curves are shown for each spectrum. All three are plotted as percentage versus exceedance.

The first curve is exceedance of applied ranges. This curve shows the results of Rainflow analysis which counted closed cycles, each with a range and mean. Ignoring the mean, ranges were plotted as percentage of maximum counted range (highest load minus lowest load) versus exceedance. This curve describes spectrum severity.

The second curve provides the crack closure viewpoint on the spectrum. It shows the exceedance of effective ranges (percentage of maximum applied range) - Rainflow counted after accounting for crack closure. In the first curve, we lost all information on stress ratio. The second curve overcomes this loss by considering closure - and through it, accounting for stress ratio and history effects.

The third curve represents relative damage contribution from the different effective ranges. In computing this curve, it was assumed that growth rate is proportional to effective range raised to the power 3 (the exponent in da/dN equation for 2219-T851 was 3.18 (2)). This damage curve is valid for the intermediate range of growth rates. At very low and very high stress intensity, the exponent would be higher.

The format representing the three curves in Fig.2 permits a qualitative assessment of the significance of crack closure. We find that in all the fighter spectra, closure accounts for some reduction in

effective range. In the case of the transport spectrum, the applied and effective range curves coincide for almost 99% of the load cycles - indicating a fully open crack. A glance at Fig.1 explains why this is so - the bulk of load cycles in the transport spectrum were at high stress ratio. The damage curve provides the weightage to draw meaningful conclusions. We find for example that in case of the fighter spectra, 10% of the severest load cycles contribute to 50% of damage (crack growth). In the transport spectrum, 60% of the damage is caused by just 1% of the cycles (the GAG cycle).

The applied ranges curve essentially represents the spectrum itself. The effective ranges curve and consequently the damage curve also reflect crack closure and growth rate behaviour of a specific material under the spectrum. If there was no crack closure, the effective and applied ranges would coincide (provided no negative loads were involved). Any change in closure stress will correspondingly shift the effective range curve downwards. The effect of that shift will not be uniform from the damage viewpoint. For example, the small ranges will react differently depending on the load spectrum. Consider the Air-to-Air and transport spectra. In the Air-to-Air case, some 90% of the cycles (towards the lower ranges) have an effective range about 70% of the applied range. A variation in S_{op} causing a small (10%) variation in effective range for the larger cycles would cause a much greater change (20 to 50%) in the effective range of smaller cycles, leading to an appropriate effect on FCP life. This will not happen in the case of the transport spectrum. Here we have 99% of the cycles seeing no closure - if S_{op} varies only slightly, these cycles may not see the difference (being always open).

The effect of small variations in S_{op} presents a question of practical relevance. Crack closure - based predictions of FCP life rely heavily on the precision of S_{op} estimates. It was shown in (6) that dK/da and net stress can strongly influence FCP under spectrum loading, supposedly through closure.

The effect of small variations in S_{op} was simulated in the present study. The validity of the life prediction technique used hinges on the assumption that a block of loading will repeat at least once within the monotonic plastic zone created by the last occurrence of the highest load. To verify this assumption for all the cases studied, crack extension per block was represented as a fraction of the current plastic zone size and plotted versus crack length (see Fig.3). The bulk of FCP life is exhausted in the first few mm of crack growth. From Fig.3 we find that in this interval of crack length, the crack grew less than 20% of the plastic zone per block (a block repeats at least five times within a plastic zone). Even in extreme situations (high stress levels, longer crack) a block occurs at least once within a plastic zone. These data validate the assumption that crack closure is fairly stable and controlled by the extreme loads.

The FCP life prediction method assumes that the current crack opening stress intensity, K_{op} is controlled by a previous K_{max} and K_{min} , specifically, their values when the crack was shorter by 25% of the current

plastic zone (Sunder (4)). This is based on the nature of closure being a consequence of the crack wake. It makes crack closure sensitive to dK/da . Calculations were made of S_{op} variation due to K_{max} (affects plastic zone size) and dK_{max}/da . The results appear in Fig.4 for a practical range of these values. We find that the dK/da effect can cause upto 10% variation in S_{op} .

Newman (2) observed that the ratio of S_{max} to yield stress, S_y can also affect closure. His data show a greater sensitivity to this ratio under plane stress conditions and at low stress ratios. From his results, one may conclude that a 20% variation in S_{op} related exclusively to S_{max}/S_y may not be unusual, particularly with reference to spectrum loading where the fairly high infrequent load excursions have a low stress ratio and cause near yield conditions.

To estimate the extent to which FCP life predictions can be affected by variations in S_{op} , FCP life was computed for the five different spectra and (for comparison) under constant amplitude loading. These results are summarised in Figs.5,6. Fig.5 shows data for the 2219-T851. Fig.6 covers the hypothetical case of a much higher baseline S_{op} ($S_{op}/S_{max}=0.5$). Calculations were made for all 13 test conditions reported in (2) but only two are shown in the figures.

From Fig.5, we see that for constant amplitude loading, a 20% change in S_{op} causes a 30% change in growth rate (life). Under the fighter spectrum however, the same change in S_{op} induces almost a factor of two variation in FCP life. Similar variations were observed for the other fighter spectra. Interestingly, FCP life under transport spectrum loading remained relatively insensitive to the S_{op} change, even when compared to constant amplitude loading. For the hypothetical baseline $S_{op}/S_{max}=0.5$ the changes in FCP life are more dramatic but still less so for the transport spectrum. The discussion earlier on the relationship between applied and effective ranges for the different spectra as influenced by closure provides a qualitative explanation for these observations.

CONCLUDING REMARKS

The study showed that depending on the load spectrum (fighter/transport) and the material (high/low closure, growth rate exponent), the effect of change in crack closure stress on FCP life can be varied. Specifically, one may conclude that fighter spectrum FCP life prediction will be more sensitive to the precision of crack closure estimates than constant amplitude FCP life. This sensitivity will be greater for materials exhibiting higher closure stress. Transport spectrum life predictions will be less sensitive to errors in S_{op} estimates (while closure occurs below the bulk of load cycles). Variations in S_{op} caused by such 'secondary' effects as dK/da and net stress can noticeably affect FCP life. It is hoped that this study can assist more confident FCP life estimates under spectrum loading. The format of exceedance curves showing effective range and damage exceedance can provide the basis for spectrum editing for testing purposes.

REFERENCES

- (1) Elber, W., ASTM STP 486, 1971, p.230.
- (2) Many authors, ASTM STP 748, 1981.
- (3) de Koning, A.U., and van der Linden, H.H., Proc. 11th ICAF Symposium, NLR, 1981, The Netherlands.
- (4) Sunder, R., "Measurement and Fatigue - EIS'86", EMAS, 1986, pp. 227-240.
- (5) Schijve, J., Jacobs, F.A., and Tromp, P.J., NLR TR 72018, Amsterdam, 1972.
- (6) Sunder, R., Fatigue '84, vol. II, EMAS, 1984, pp. 881-892.
- (7) Elber, W., ASTM STP 595, 1976, pp.236-247.
- (8) Schijve, J., Report LR-485, Delft University, 1986.
- (9) Matsuishi, M., and Endo, T., Fatigue of Metals Subjected to Varying Stresses, JSME, 1968.
- (10) Sunder, R., Seetharam, S.A., and Bhaskaran, T.A., Int. J. Fatigue, v.6, 1984, p.147.

FATIGUE 87

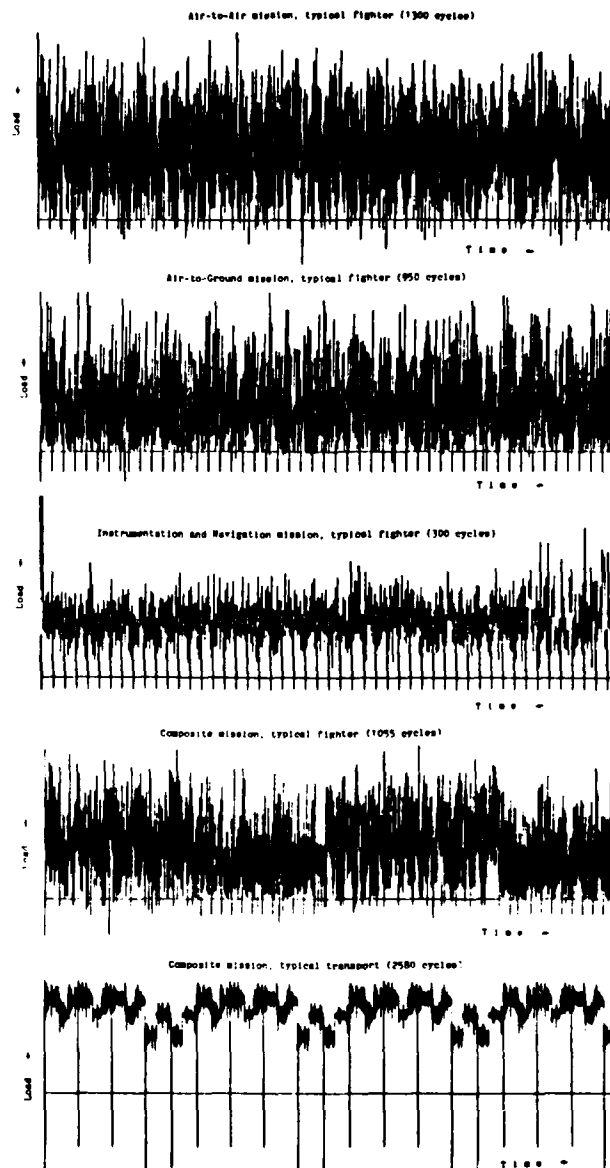


Fig.1. The five load spectra considered in the study. Data from (2).

FATIGUE 87

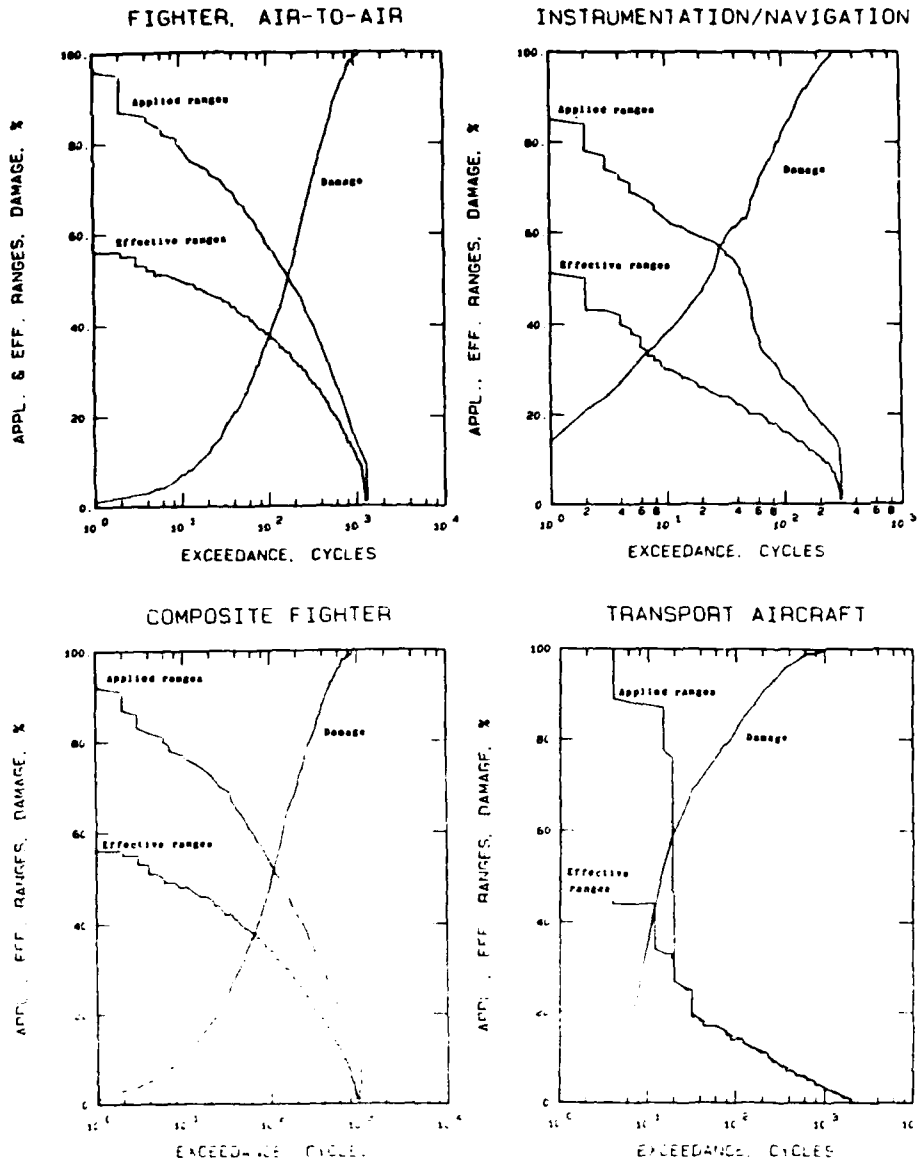


Fig.2. Exceedance and damage curves. Applied ranges refer to Rainflow counted cycles in one block. Effective ranges account for crack closure. Damage curve reflects relative contribution to crack extension. Ranges are percent of maximum counted range. Air-to-Ground mission excluded from figure - results similar to Air-to-Air case.

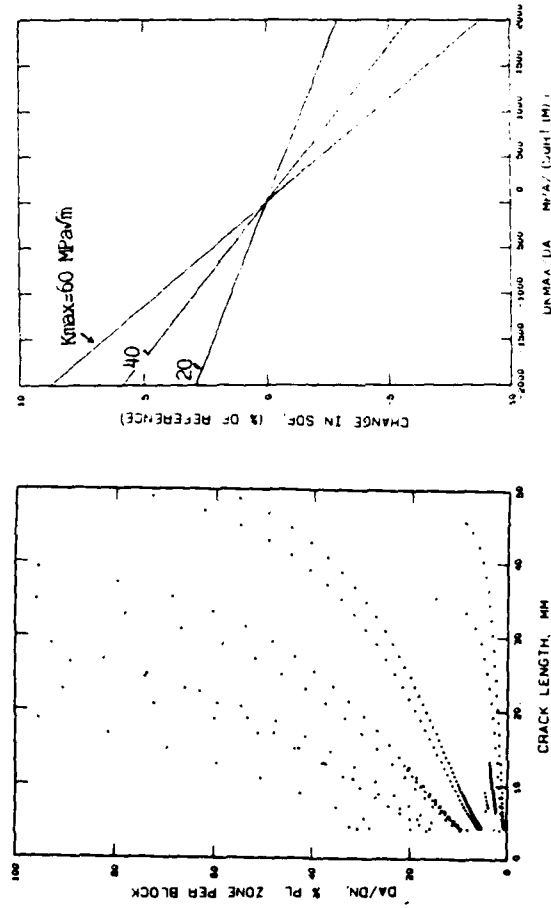


Fig. 3. Growth rate versus crack length - summarised for all 13 specimens and shown relative to plastic zone size.

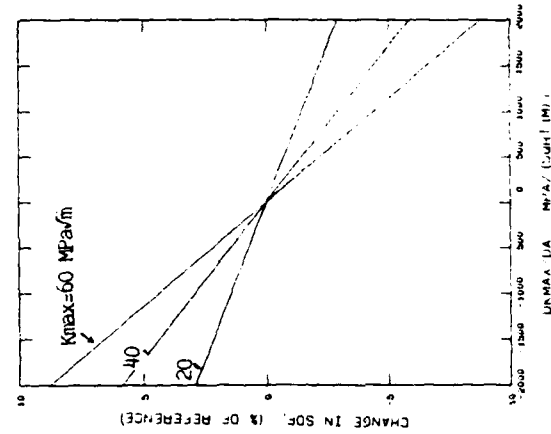


Fig. 4. Effect of dK_{max}/da on S_{np} . Results computed for K_{max} values representative of test conditions studied.

FATIGUE 87

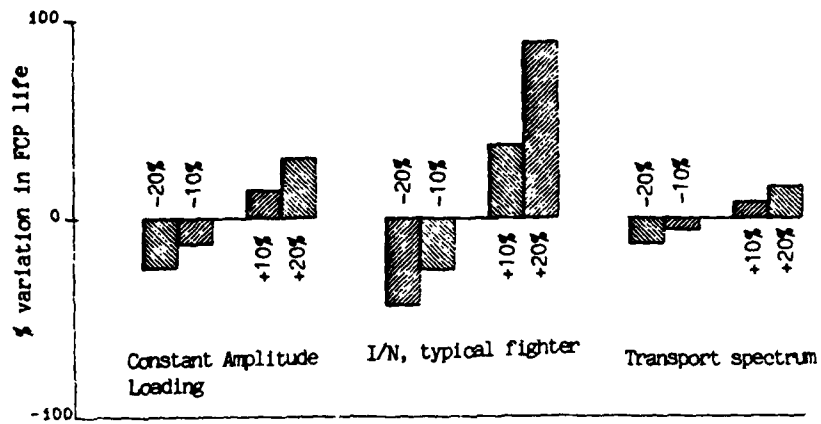


Fig.5. Percentage variation in predicted FCP life due to percentage change in Sop (indicated on bars). Results for 2219-T851 (Sop/Smax = 0.25).

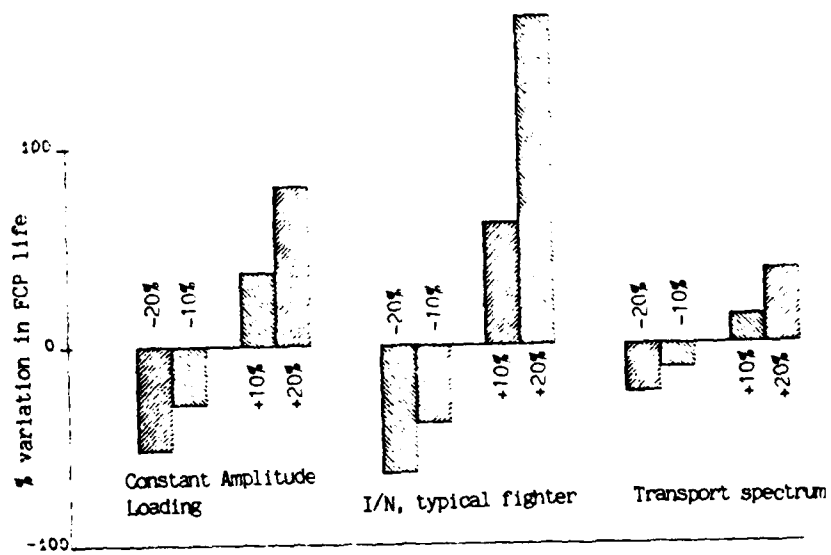


Fig.6. Percentage variation in predicted FCP life due to percentage change in Sop (indicated on bars). Results for hypothetical case of Sop/Smax = 0.5)

NEAR-THRESHOLD SHORT CRACK GROWTH BEHAVIOUR IN
NIMONIC 105

J. Byrne*

Physically short semi-elliptic and through-cracks, 0.1 to 0.4 mm in depth, were generated in Nimonic 105. These short cracks propagated at less than the nominal ΔK_{th} for long cracks at $R = 0.1$ and crack growth rates blended with the long crack results at between 0.5 to 0.65 mm crack depth. A similar crystallographic FCG mechanism was observed for both the short and long cracks. It is proposed that this physically short crack growth behaviour is due to a reduced effect of crack closure on the short crack results.

INTRODUCTION

There continues to be a major interest in the fatigue crack growth (FCG) behaviour of short cracks. This stems from the observation for short cracks of faster FCG rates and lower threshold stress intensity ranges (ΔK_{th}) than found for long cracks in conventional fracture mechanics specimens(1,2). The practical relevance of these studies lies in the fact that defects of small size may be significant in highly stressed critical components(3) and short crack FCG may constitute a high proportion of cyclic life(4). Thus it is important to establish the lower limits of crack length for which linear elastic fracture mechanics (LEFM) may satisfactorily be applied in assessing defect tolerance and fatigue life integrity of components and structures.

There is no unique definition of a "short" crack, though in general short crack effects have only been observed for cracks less than about 0.5 mm in depth (or 1 mm surface length). Three main categories have been proposed by Suresh and Ritchie(2):

*Department of Mechanical Engineering, Portsmouth Polytechnic, Portsmouth, U.K.

FATIGUE 87

- (i) the crack length is less than that of some microstructural parameter e.g. grain size;
- (ii) the crack size may exceed that of the microstructure, but characterisation of the crack tip stress field breaks down e.g. under excessively high bulk stress or local stress due to notches;
- (iii) the crack is "physically small" such that crack closure and possibly environmental effects differ from those found for long cracks.

In engineering components and structures, short (and indeed many long) cracks will tend to have semi-elliptical and corner geometries rather than be through-cracks. The behaviour of such defect types has received considerable attention in recent years (e.g. 5-12) and is of particular importance for gas turbine components(13). In an earlier paper(6) on Nimonic 105, it was found that effective fatigue thresholds ($\Delta K_{eff,th}$) for corner and semi-elliptic cracks were consistent with those for through-thickness cracks. However, the depths studied for the corner and semi-elliptic cracks were in the range 0.33 to 2.42 mm which may not be considered to be truly "short". The present paper describes further FCG studies on Nimonic 105 which have been carried out with initial crack/defect sizes between 0.11 and 0.37 mm depth.

EXPERIMENTAL DETAILS

The material studied is a nickel base alloy, Nimonic 105, in the age-hardened condition, with a 0.2% Proof Stress (S_p) of 888 MPa and grain size of 52 μm . Full details of the material have been published earlier(6).

Long Crack FCG Data

Specimens were machined longitudinally from bar to produce 6 mm thick single edge notched (SEN) bend specimens (Fig. 1). Fatigue testing was performed in room temperature air using an Amsler Vibrophore in four-point bending, giving a test frequency in the region of 80 to 100 Hz. A load shedding procedure was carried out to obtain ΔK_{th} followed by grow-out to obtain FCG data at $R = 0.1$ and 0.5 . Threshold was defined as the condition where no further crack growth could be detected by the direct current potential drop (DCPD) technique after at least 10^7 cycles. This corresponds to an FCG rate of less than 5×10^{-9} mm/cycle for a crack length increase detection sensitivity of 0.05 mm.

Crack closure was measured using DCPD, crack mouth opening displacement (CMOD) measured by a conventional clip gauge and back face strain (BFS) gauges. The procedures are described in more detail in (6) and (8).

FATIGUE 87

Short Crack Development and FCG Data

Short cracks were developed by two different methods:-

(i) Spark Erosion Damage (semi-elliptic crack). A small crater was developed on the tension surface of plain specimens by striking an arc from a 0.5 mm diameter nichrome wire. The cratered surface was then polished to achieve a smooth flat surface with a central defect with a diameter of between 0.20 to 0.40 mm. The resulting defect was, as a first approximation, initially assumed to have an aspect ratio (c/a) of 1.

Testing was carried out in cantilever bending at 16.7 Hz on a machine developed from the design of Pearson(10). Single stage plastic film replication was used to monitor surface crack length change to a sensitivity of 1 μm . Heat tinting was carried out (a) at 300 °C for 2 hours when the crack had grown to about twice the original surface length and (b) at 500 °C for 4 hours when the crack was near to breaking through the edges of the specimen. This procedure together with scanning electron microscope (SEM) fractographic measurement of the original crater dimensions enabled an assessment of the actual crack aspect ratio to be made.

(ii) Far-Field Cyclic Compression (through crack development). Here SEN specimens were loaded in the cantilever bend rig with the notched face in compression, as previously carried out by Christman and Suresh(14). This generates a very local decaying tensile stress field at the notch root and the development of a short through-crack with decelerating FCG rate and a small crack tip plastic zone size. The notch containing material was then machined off leaving a remnant short through-thickness crack with an average depth of about 0.2 mm. This was followed by a stress relief heat treatment at 600 °C for 1 hour under a vacuum of $< 5 \times 10^{-6}$ torr.

FCG was then monitored for these short cracks under tension in the same cantilever bend rig at 16.7 Hz again using single stage plastic replication (on both faces of the specimen) to monitor crack depth increase.

For both short crack cases testing was carried out in room temperature air at $R = 0.1$.

Analysis of Crack Growth Data

FCG rates were calculated in all cases from crack depth (a) versus cycles (N) data using a simple 3-point secant finite difference method(15).

For the long crack data the stress intensity factor for pure

FATIGUE 87

bending(16) was used.

For the short through-crack results in cantilever bending a finite element based solution(17) was used where:

$$K_I = \frac{6M}{BW^2} (\pi a)^{\frac{1}{2}} \cdot Y \quad \dots (1)$$

and,

$$Y = 1.1332 - 1.2748\left(\frac{a}{W}\right) + 4.9936\left(\frac{a}{W}\right)^2 - 3.2515\left(\frac{a}{W}\right)^3 + 2.9572\left(\frac{a}{W}\right)^4 \quad \dots (2)$$

For the semi-elliptic short cracks, which developed from the spark erosion craters, the stress intensity factor was calculated for the deepest point on the crack front using the calibration of Shah and Kobayashi(18), where K_I is given by equation (1), a is the maximum depth of the crack, $2c$ the surface length and Y is a function of both a/c and a/W . For the a/c and a/W values of this study, the review by Scott and Thorpe(19) indicates little variation between the different stress intensity solutions proposed for semi-elliptic cracks in bending.

RESULTS AND DISCUSSION

The FCG data and ΔK_{th} values for both $R = 0.1$ and 0.5 are shown in Fig. 2. Crack growth rates down to 0.1 nm/cycle were monitored and average ΔK_{th} values of 8.8 , 6.1 and 4.3 MPa/m were found for $R = 0.1$, 0.5 and 0.7 respectively. A typically strong R dependence of near-threshold crack growth is evident with reduced sensitivity for the mid-range ("Paris" law) regime.

Values of effective threshold stress intensity range ($\Delta K_{eff,th}$), allowing for closure, were found to be 5.1 and 4.9 MPa/m for $R = 0.1$ and 0.5 ; closure was not detected at $R = 0.7$. Here $\Delta K_{eff} = K_{max} - K_{cl}$ where K_{cl} defines the stress intensity value at which the crack is indicated to stop closing by compliance change using a clip gauge. An approximate ΔK_{eff} versus da/dN plot for the $R = 0.1$ long crack data, based on DCPD estimates, is also shown in Fig. 2.

Crack growth from the spark damage craters started at less than the nominal ΔK_{th} value for $R = 0.1$ (Fig. 3). FCG rates were monitored from surface crack lengths but are presented as crack depth rates based on initially assuming the crack aspect ratio $c/a = 1$, and subsequently correcting for aspect ratio when the specimens were broken open. Figure 3 shows the results from

FATIGUE 87

four different specimens with initial defect depths estimated to be between 0.110 and 0.178 mm (Table I). FCG data was only analysed where fatigue cracking was detectable at both edges of the original defect. Thus FCG rates were established for greater than 0.1 nm/cycle. Whilst there is scatter between the sets of data there is a similar trend evident in every case, i.e. to grow initially at a ΔK value consistent with the $\Delta K_{eff,th}$ value and for the FCG plots eventually to blend with the $R = 0.1$ long crack data.

Values of crack depth at which the short crack FCG data blended with the long crack data were estimated to be 0.48, 0.64, 0.48 and 0.40 mm. This is considered to be consistent with defects experiencing initially little or no closure but increasingly developing closure with increasing crack length. Closure would be developed by increasing asperity contact because of the faceted crystallographic FCG mode occurring in this alloy near the threshold.

TABLE I - Details of Initial Short Cracks

c/a	a_i (mm)	ΔK (MPa \sqrt{m})	σ_{max} (MPa)	$\frac{\sigma_{max}}{S_p}$	r_{pr} , plane strain (μm)	"Blend" crack depth (mm)
1.0	0.150	6.0	469	0.53	0.65	0.48
0.74	0.157	5.2	354	0.40	0.49	0.64
0.85	0.110	5.3	428	0.48	0.51	0.48
0.85	0.178	7.5	475	0.53	1.01	0.40
through crack	0.369	7.6	220	0.25	1.04	0.65
" "	0.243	6.0	215	0.24	0.64	0.63

Criticisms of this spark damage defect approach are first that the original defect cannot be controlled to be a true semi-ellipse (although the resulting fatigue cracks did develop in this way) and second that some local metallurgical damage must be caused. On the latter count it should be noted that no FCG data was taken until at least a further 0.05 mm crack growth had occurred. To counter these criticisms short through-crack results were generated using the far-field cyclic compression method.

FATIGUE 87

A comparison between the short through crack and long crack results is made in Fig. 4. The initial short crack lengths developed were 0.243 and 0.369 mm (Table I) and the trend is observed to be very similar to that for the spark damage generated cracks. The crack lengths at which this short crack data blended with that for long cracks at $R = 0.1$ were about 0.65 and 0.63 mm. This behaviour again is consistent with the development of increasing crack closure with increasing crack length.

It is considered that the cracks studied in this paper are physically short cracks according to Suresh and Ritchie's categorisation(2), with reduced crack closure primarily explaining the short crack behaviour. The initial crack/ defect sizes developed were between two and seven times the average grain diameter (52 μm) in depth. Also even the shorter crack fronts for the semi-elliptic cracks would have sampled at least 7 grains whilst the short through-cracks would sample over 100 grains over the full 6 mm width of the specimen. Thus it would appear unlikely that a significant microstructural short crack effect is being observed. This proposal is further reinforced by examining the relationship between the plain specimen fatigue limit (established in (8)) and both ΔK_{th} and $\Delta K_{eff,th}$ for $R = 0.1$.

The values of crack length, a_0 , below which short crack behaviour would be expected are indicated in the Kitagawa-Takahashi (5) plot for semi-elliptic cracks, Fig. 5. It is considered that the most realistic case is the semi-elliptic crack since this is how cracks were mainly observed to initiate in plain specimen fatigue limit testing(8). Fig. 5 indicates that physically short (closure controlled) crack growth behaviour would be expected between 77 μm and 230 μm crack depth. Making use of $\Delta K_{eff,th}$ a value of $a_0 = 77 \mu\text{m}$ is obtained which approaches the average grain diameter. It is therefore indicated that a crack depth of the order of the grain size would be needed before microstructurally short crack behaviour would be expected.

The FCG results are presented in the well established form of $\log \Delta K$ versus $\log da/dN$ plots for comparison of short and long FCG rates. Such comparison if it is to be valid requires that small-scale crack tip yielding is satisfied and that a similar FCG mechanism occurs for both the short and long cracks. As shown in Table I, in the worst case the maximum bending stress reached was 53% of the 0.2% proof stress for the semi-elliptic cracks and the through-cracked specimens were only subjected to a 25% level. The value of reversed plastic zone size (plane strain) for the smallest crack size is less than 1/200 of crack length (or 1/77 for the plane stress plastic zone size). It is considered that both the nominal stress levels and plastic zone sizes indicate that LEFM is being reasonably satisfied.

Fractographic examination on the SEM of samples from repre-

FATIGUE 87

sentative short and long crack specimens showed similar FCG mechanisms. Thus in the near-threshold regime a predominantly transgranular, faceted FCG mechanism was observed (Fig. 6) for both short and long cracks. For both cases a transition in fracture mode occurred at greater than a ΔK of about 15 MPa \sqrt{m} from the crystallographic faceted mode to a predominantly striated mode, typical of mid-range FCG in a ductile alloy. This transition from crystallographic to striated FCG mode always occurred for the short cracks after the data had blended with the long crack data.

CONCLUSIONS

1. The physically short cracks studied of between 0.1 to 0.4 mm depth propagated at stress intensity range values less than the nominal ΔK threshold value determined for long cracks at the same stress ratio, $R = 0.1$.
2. This physically short crack growth behaviour is considered to be due to a reduced effect of crack closure on the short crack results and a blend with the long crack results occurred at between 0.5 and 0.65 mm depth.
3. A similar crystallographic "faceted" FCG mechanism was found for both the long and short cracks studied and use of the stress intensity factor K for these cracks appears reasonable.
4. The relationship between the fatigue limit and effective ΔK_{th} indicates that a microstructurally short crack effect on FCG rate and threshold would not be expected down to crack lengths of the order of the grain size.

ACKNOWLEDGEMENTS

The provision of material by Rolls-Royce, Derby Aeroengine Division and assistance in testing by G.L. Wakeford, K.M. Blakemore and P.J. Wolstencroft are gratefully acknowledged.

REFERENCES

- (1) K.J. Miller, Fat. Eng. Mat. Struct., 5, (1982), p. 223.
- (2) S. Suresh & R.O. Ritchie, Int. Met. Rev., 25, (1984), p.445.
- (3) R.H. Jeal, Metals and Materials, 1, (1985), p. 528.
- (4) J. Schijve, in Proc. "Fatigue '84", (1984), p. 751.
- (5) H. Kitagawa & S. Takahashi, Proc. Second Int. Conf. on Mechanical Behaviour of Materials, Boston, ASM, (1976), p.627.

FATIGUE 87

- (6) J. Byrne & T.V. Duggan, in "Fatigue Thresholds - Fundamentals and Engineering Applications", ed. C.J. Beevers et al, EMAS, (1982), p. 759.
- (7) J. Byrne, T.V. Duggan & C.J. Beevers, Proc. 7th Int. Conf. on Strength of Metals and Alloys, Montreal, Vol. II, (1985), p. 1393.
- (8) J. Byrne, "Fatigue Resistance in Alloys - Influence of Crack Geometry and Closure", PhD Thesis, CNAA, Portsmouth Polytechnic, (1981).
- (9) A.F. Blom, A. Hedlund, W. Zhao, A. Fathula, B. Weiss and R. Stickler, Proc. Symp. on Behaviour of Short Fatigue Cracks, Sheffield, EGF Publication No. 1, (1986), p.37.
- (10) S. Pearson, Engng. Fracture Mechanics, 7, (1975), p.235.
- (11) M.N. James & G.C. Smith, Int. J. Fatigue, 5, (1983), p.75.
- (12) C.W. Brown & M.A. Hicks, Int. J. Fatigue, 4, (1982), p.73.
- (13) A.C. Pickard, C.W. Brown & M.A. Hicks, in "Advances in Life Prediction Methods", A.S.M.E, 1983, p.173.
- (14) T. Christman & S. Suresh, Engng. Fract. Mech., 23, (1986), p. 935.
- (15) I.M. Austen, in "Measurement of Crack Length and Shape During Fracture and Fatigue", ed. C.J. Beevers, EMAS, (1980), p. 164.
- (16) W.F. Brown & J.E. Srawley, STP 410, ASTM, (1966).
- (17) A.P. Smith, Welding Institute Report 3826/1/84, August 1984.
- (18) D.P. Rooke & D.J. Cartwright, "Compendium of Stress Intensity Factors", HMSO, (1976).
- (19) P.M. Scott & T.W. Thorpe, Fat. Eng. Mat. Struct., 4, (1981), p. 291.

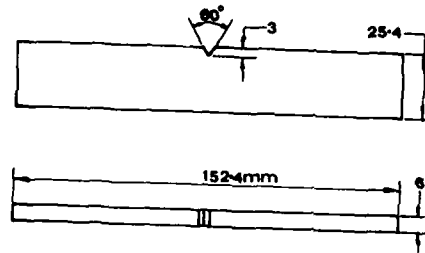


Fig. 1. Specimens: notched for long and short through cracks; plain for semi-elliptic cracks.

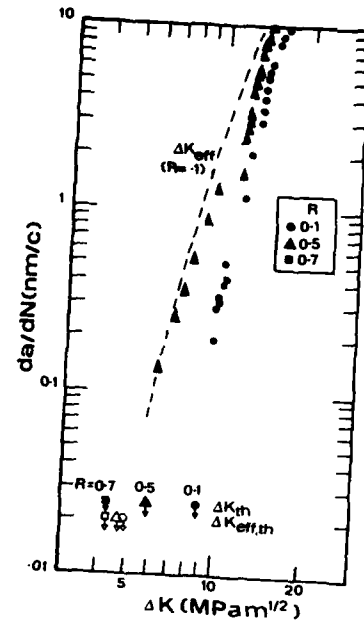


Fig. 2. Long crack FCG data.

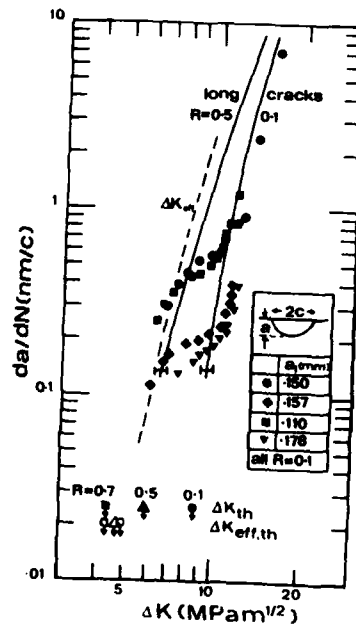


Fig. 3. Short semi-elliptic crack FCG data.

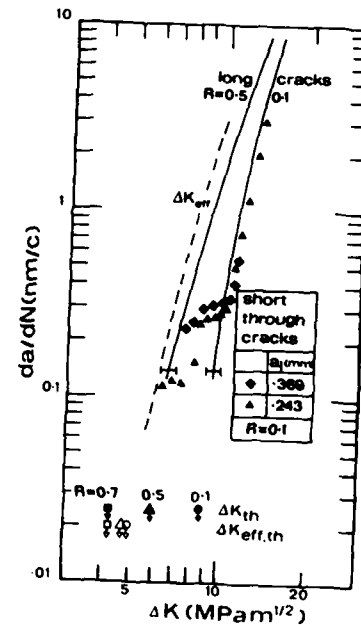


Fig. 4. Short through-crack FCG data.

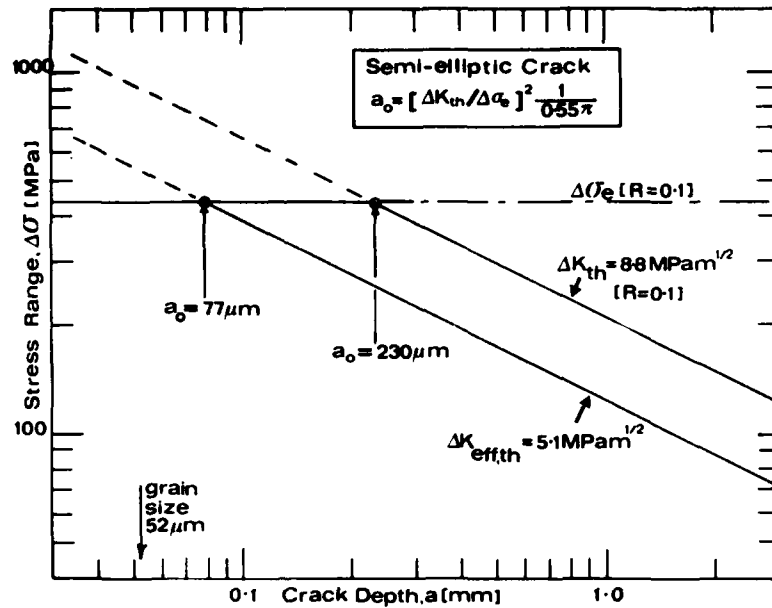


Fig. 5. Relationship between endurance limit stress range ($\Delta \sigma_e$) and threshold stress intensity ranges (ΔK_{th} and $\Delta K_{eff,th}$).

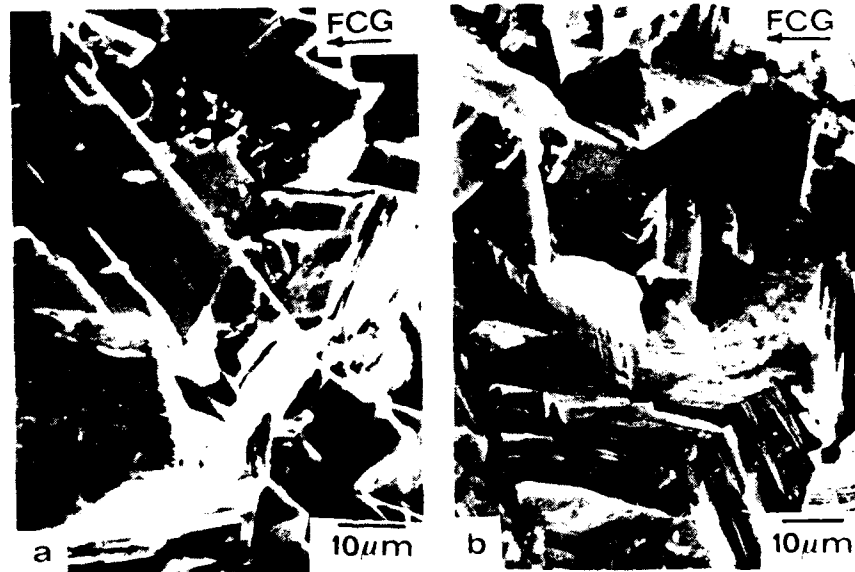


Fig. 6. SEM fractographs for between 0.1 and 1.0 nm/c FCG rate; (a) typical long crack, (b) typical short crack.

FATIGUE 87

SMALL CRACKS

FATIGUE 87

FATIGUE CRACK PROPAGATION OF SHORT AND LONG CRACKS: PHYS.
BASIS, PREDICTION METHODS AND ENGINEERING SIGNIFICANCE

H. Nowack, R. Marissen*

In the present paper recent developments regarding the macrocrack stage and the short crack stage are described. It is shown that the advanced macrocrack propagation analysis schemes are based upon the effective stress intensity factor, but it is also shown that the mere consideration of ΔK_{eff} was not always sufficient.

Both from engineering and from physical viewpoints concepts for the evaluation of fatigue threshold values are of importance. Three different concepts are compared. It is shown that the "precracking in compression" concept offers advantages from an engineering viewpoint.

Regarding the short crack stage a low ΔK -regime and a high ΔK -regime have to be distinguished. In the low ΔK -regime the threshold value of short cracks and the microstructure are of special importance, whereas in the high ΔK -regime the mechanical environment of the cracks plays the predominant part. Further aspects which are important from an engineering viewpoint as the scatter of the short crack data and cumulative damage analyses are also discussed.

INTRODUCTION

Mainly economical viewpoints, but also the growing competition of new high strength materials as ARALL (1) and carbon fibre reinforced plastics are main reasons, why the design levels for metallic structures are steadily increased. That means that further improved fatigue life prediction methods are required, which account for the physical causes of the (nonlinear) damage accumulation in metallic materials and which include improved

* Deutsche Forschungs- und Versuchsanstalt für Luft- und Raumfahrt (DFVLR), Institute for Materials Research, Fatigue Branch, D-5000 Köln 90, F.R.G.

mechanics tools. The consequences of the fact that the physical basis of the cumulative damage hypotheses has to be improved are:

- that in the field of fatigue crack propagation numerous projects have been initiated, which deal with details of the crack propagation process on a macroscopic, as well as on a microscopic and submicroscopic level, and
- that that part of fatigue life where short cracks are present is carefully investigated, whether there exists a potential to further increase the span in life which can be activated together with the design of engineering components.

The present paper deals with both areas. Regarding the macrocrack propagation stage those fields and aspects, which have been thoroughly investigated in the past and which are published in the open literature (comp., for example, (2, 3)) will not be repeated here. The present paper concentrates on special topics as the crack closure mechanism, the threshold for fatigue crack propagation, and the influences of dK/da and of compression loads.

Since threshold tests can become extremely time consuming if an ASTM proposal (4) is applied, two alternative methods are considered in more detail in the present study.

For predictions of the crack propagation especially also under variable amplitude loading conditions ΔK_{eff} -concepts are commonly used. A brief overview of these concepts will be given. However, there exists also some experimental evidence, that the consideration of ΔK_{eff} -values only may not be sufficient. These investigation results will be given.

Regarding short cracks the question frequently arises, in how far extrapolations of the macrocrack behavior can be performed to predict the behavior of short cracks. Short cracks exhibit various essential anomalies, which will be outlined. This will be done once for the range of low ΔK -values and once for the range of high ΔK -values. At low ΔK -values the threshold problem is important because the threshold values of short cracks are commonly (significantly) lower than those as derived from long crack studies. At high ΔK -values the adequate mechanics representation of the short cracks becomes the predominant problem.

Predictions of the crack growth behavior under vari-

able amplitude loading conditions at low ΔK -values turn out to become difficult because of microstructural incompatibilities. This will be shown on the basis of new results, which stem from a cooperative work together with the University of Essen, Germany.

The last part of the present paper deals with engineering aspects as the consideration of notches, the problem of the large variation ("scatter") of short crack data (especially at low ΔK -values), the demand for the formulation of a prediction concept for which combines the short crack and the macrocrack stage.

CRACK PROPAGATION IN THE MACROCRACK AND IN THE SHORT CRACK STAGE, CONSTANT AMPLITUDE AND VARIABLE AMPLITUDE BEHAVIOR

Macrocrack Stage

Because macrocracks can easily be observed during fatigue tests and because post-failure analyses of the fracture surfaces reveal numerous details of the crack propagation processes - on the one side - and because the mechanics tools to represent the macrocrack behavior have reached a high standard in their development - on the other side - the phenomenological macrocrack propagation behavior is fairly well known.

Crack closure, ΔK_{eff} . Since the crack closure behavior has a predominant influence on the cycle by cycle crack propagation the instantaneous effective stress intensity factor, ΔK_{eff} (which is the range in the stress intensity factor between that instant where a fatigue crack fully opens in a cycle and the maximum stress intensity in the cycle), is most often used as a parameter to describe the crack advance, not only under constant amplitude loading but also under variable amplitude loading conditions. The instantaneous crack opening level in a cycle is the result of the simultaneous action of several individual contributions, which are commonly denoted as plasticity induced crack closure, roughness induced crack closure (5), etc.. There exist already numerous investigations where these individual contributions and related aspects have been worked out in detail.

If the outer loading conditions of a specimen/component are considered the crack opening/closure level is predominantly influenced by the stress ratio and by compression loads, which may be present.

In order to briefly show the potential of the (crack closure based) effective stress intensity factor to

correlate fatigue data, the results of test series with constant amplitude loading at different R-ratios on a high strength aluminum alloy (Al 7475-T7351) are plotted once vs. $(\log)\Delta K$ and once vs. $(\log)\Delta K_{eff}$ in Figure 1 (7). (The procedure for the determination of the ΔK_{eff} values is described in the paper by Zhang et al. (7).)

Under compression loads fatigue cracks are usually closed. If cracks are closed the stress intensity factor has no longer a physical meaning (although it is quite often (formally) calculated). As it has been shown in (8) the actual magnitude of the compression stress as applied at a specimen/component relative to the compression yield stress of the material being used becomes important. In (8) an estimation formula for the crack opening stress intensity factor, K_{op} , relative to the maximum stress intensity in a cycle, K_{max} , for negative R-ratios has been proposed. This formula, which holds predominantly for plane stress conditions, is given in Figure 2, where also other concepts for the determination of K_{op} -values from the literature are included.

The effective stress intensity variation is also influenced by dK/da (8, 9). dK/da is responsible for the size of the plastic wake zone at the crack tip. It turned out that the dK/da influence is less important under constant amplitude conditions than under variable amplitude loading conditions. (Especially in connection with the evaluation of the effect of small load cycles in a variable amplitude loading history dK/da is of importance.)

If a more general statement regarding the present state of the art to describe the macrocrack propagation for constant amplitude loading conditions is tried, it can be said that the crack closure concept represents a generally complete analysis scheme.

Threshold value in the macrocrack stage. The visible manifestation of the threshold behavior of macrocracks is the lower end of the constant amplitude $(\log)da/dN$ - $(\log)\Delta K$ -curve, which usually tends to approach some certain $\Delta K_{(th)}$ -value below which crack propagation does no longer occur. The threshold behavior is important from an engineering viewpoint, as for example in those cases where some certain (crack like) defects can be present in a structural part just from the beginning and where predictions have to be made if cracks will grow from the defects. Threshold considerations are also important for crack propagation analyses under variable amplitude loading conditions, because the question

frequently arises if smaller load variations will contribute to the macrocrack growth or not.

From numerous investigations in the literature it is known that the threshold stress intensity factor, ΔK_{th} , is not always a constant but that it may depend strongly on the testing conditions, especially on the stress ratio. (There exist also other important influences as, for example, the testing environment, which will not be considered here.)

For the determination of threshold values different procedures can be applied. Three of them will be considered in the following:

- (A) the ASTM proposal after Bucci (4)
- (B) a procedure after Döker et al. (10) and after Castro et al. (11)
- (C) a new procedure which is denoted as "precracking under compression" method.

The general procedure after the ASTM proposal (A) is schematically indicated in Figure 3a. The threshold tests start with a running fatigue crack. Then the K-values are reduced as the crack length (a) increases. This has to be done in a way that a certain prescribed K-value is always reached as a function of a (dK/da-requirement). The stress ratio remains always constant. In practice the load shedding technique is commonly applied. If the load shedding cannot be performed continuously the stress is stepwise reduced, whereby each reduction in the stress is limited at 10 % of the previous stress value. The ASTM proposal represents a quite restrictive procedure. That is the reason why the tests usually last extremely long, and that there is a strong demand for other less expensive methods. The two other concepts as they were mentioned above fulfill this requirement.

In Figure 3b the general procedure after the concept after Döker et al. (10) and Castro et al. (11) is shown. The threshold tests again start with a running fatigue crack. In contrast to the ASTM proposal for the determination of threshold values the maximum stress in tests is kept constant and the minimum stress is increased until no further crack propagation occurs. From that stress range the threshold value is calculated. It turned out, that above a certain level of K_{max} -values always about the same threshold values were found. From that the conclusion is drawn that the threshold value is independent of the R-ratio, if the R-ratio is high

FATIGUE 87

enough to prevent crack closure. This value is seen as a "physical" threshold in terms of a material constant. The described procedure can be preformed within a very short time. Unfortunately, the threshold values after this procedure are immediately applicable to high R-ratios only. For a general application of the threshold values further informations about the instantaneous crack opening level have to be available.

Method (C) is a new procedure which includes several individual steps. First a precracking procedure under compression is applied as indicated in Figure 3c. A specimen where a saw cut (for example of a size of 7 mm) is applied is subjected to pure compression fatigue loading. A crack starts immediately to grow but its propagation rate decreases as it become longer and, finally, crack arrest occurs. This situation represents an optimum condition for the start of a threshold test since there exists no (positive) plastic wake zone at the crack tip and because the crack opening level is extremely low. The threshold test itself is then started with the R-ratio of interest. The loading level in the test is chosen a little below that amount where the threshold value is expected to occur. If the crack does not start running or if it stops running after it has started to grow, the actual threshold value has not yet been reached. The loading level is then increased by some amount and the test is continued. The procedure is repeated until the crack continuously grows. Although this method seems to be time consuming, this is in reality not the case, because the transition in the stress below which a crack will stop to grow and above which it continuously grows is quickly found. In Figure 4 the fatigue crack growth rates which were observed during the compression precracking part along with the application of this method in case of the high strength aluminum alloy Al 7475-T7351 are shown.

In Figure 5 the results of the application of the threshold evaluation procedures after the "precracking in compression" concept (C) and after the ASTM proposal (A) are shown. From the figure it can be seen that the threshold stress intensity after method (C) was smaller than after the ASTM proposal (A). However, the scatter of the crack propagation data was also somewhat larger, when the "precracking in compression" method was applied. The time which was needed for the application of method (C) turned out to be less than 20 % of that time which was needed for the application of the ASTM proposal (A).

From these investigation results and from the gener-

al features of the methods (A) - (C) the following conclusions may be drawn:

- The ASTM proposal required by far the largest expenses in time because of the very restrictive dK/da requirement. Independently of that the threshold value turned out to be not conservative. The introduction of more severe conditions into the general procedure cannot be recommended because the testing time is already extremely large.
- The concept (B) after Döker et al. (10) and Castro et al. (11) appears to be attractive from a physical viewpoint, however, the "physical" threshold value after this method cannot directly be applied to situations, where crack closure plays some part. In a recent publication Döker et al. suggested a rational method for the determination of the crack opening level. This procedure (which itself stands in a very close correlation to the basic principles of the "physical" threshold concept) in connection with the "physical" threshold value after method (B) may develop to an attractive concept.
- At present method (C) represents a most promising tool for the solution of threshold problems in practice. This is why it can be applied to arbitrary R-ratios, and because the threshold values themselves tend to be conservative, and because the expenses in time for its application are relatively low.

Variable amplitude loading conditions. Under variable amplitude loading conditions significant load sequence effects on the macrocrack propagation behavior are observed. As already mentioned earlier the crack closure mechanism is assumed to be the most essential cause for the load sequence effects. That is the reason why most of the advanced crack propagation prediction concepts are built up upon the effective stress intensity factor, ΔK_{eff} . In Figure 6 a brief survey of the present crack propagation prediction models is given (also comp. (2,3,12)). The highest level models which explicitly account for the crack closure behavior is represented by those models which include a complete or a Dugdale-Barenblatt type analysis of the stresses and displacements around the crack. The high numerical expenses which are required for the application of these models were the reason why the simulation models (where the main contributions to crack closure and to the crack propagation behavior are simulated by analytical expressions) were developed and also the models as mentioned on the third level in Figure 6, where empirical trends (as, for example, the observation that under various types of

service loading conditions the crack opening level does no longer vary much after it has reached some equilibrium condition (12)) are further included. At the lowest level in Figure 6 those models are summarized, which are simply adjustment models or which use only one "characteristic" K-value, or which are linear analyses which ignore the presence of sequence effects at all.

For engineers quite often difficulties arise if they have to select one crack propagation prediction method for the solution of a certain practical problem. Although the prediction capability of the models as mentioned on the higher levels in Figure 6 is commonly better, the authors should like to emphasize that it may be in most cases more efficient - from a practical viewpoint - to select a model where the user is able to overlook all basic assumptions and analytical procedures rather than to choose a more complicated model, which needs the special insider knowledge of the author of the model for its general application.

Since ΔK_{eff} is used as a basis of nearly all models for the prediction of the macrocrack propagation behavior it is an essential question, if ΔK_{eff} is in fact the only important parameter. In this context the results of a recent investigation by Zhang et al., where simple but systematically varied periodic loading patterns were applied, give some important informations. They showed, that there are commonly no contradictions between the ΔK_{eff} -concept and the actual crack propagation behavior in most cases. However, under one loading condition, which is shown in Figure 7, the crack opening stresses which were derived from the striation measurements and using the $(\log) da/dN$ vs. $(\log) \Delta K_{eff}$ correlation in Figure 1b, turned out to be not compatible with the actual physical behavior of the crack opening stresses. For a further evaluation of this result where microstructural causes may play a significant part further systematic investigations are required.

Short Crack Stage

As already outlined in the beginning the basic question in how far predictions of the short crack properties become possible on the basis of the long crack behavior (which itself is fairly well known) is of interest. Short cracks exhibit various anomalies (as compared to long cracks) which are schematically indicated in Figure 8. Two general ranges can be distinguished, a range where the stress intensity variations, ΔK , and the crack propagation rates, da/dN , are low and another range, where

both become high.

Low ΔK -regime. If the range with low ΔK -values is considered significant deviations from the long crack behavior are observed. This refers to the threshold value and to the crack propagation rates, and to the microstructural influences.

The threshold values of short cracks are probably significantly lower than the threshold values for long cracks and the crack propagation rates are higher. In (13) several possible reasons for the differences in this material behavior were given. One "physical" key for the differences is seen in different slip mechanisms at the crack tip. As indicated in Figure 9 the steep stress gradient which is present at the tip of long cracks and the strong elastic-plastic interface favor the slip reversibility at the tip of long cracks. In case of short cracks the net section stresses are commonly significantly higher than for long cracks leading to a flat stress distribution (except very close to the crack tip). This is also indicated in Figure 9. The dislocations emanating from the tip of short cracks can freely move. This may be the predominant cause for the lower threshold value and for the high propagation rates of short cracks.

Microstructural features which have also a significant influence are mainly the inhomogeneity of the crystallographic microstructure as such and the presence of obstacles in form of grain boundaries, phase boundaries, textures, etc. Most of the variations of the da/dN vs. ΔK -curves which are also (schematically) indicated in Figure 8 are due to these special microstructural features. If grains are favorably orientated the short cracks in these grains propagate faster. If the short cracks approach obstacles their growth rate drops down. For the quantitative prediction of the short crack behavior under these circumstances several models/approaches have been suggested (14). Miller et al. proposed a model, which is based on the shear deformations at the specimen surface where the short cracks start to grow (15). If the shear deformations are really taken at those local areas where the short cracks actually initiate and start to grow this model is a most interesting one from a physical viewpoint. Another advantage is that the effect of microstructural obstacles is also explicitly accounted for.

Another approach has been proposed by Topper et al. (16). In this approach a fictitious crack length, l_0 , is used, which is based on the threshold value of

the material and on its endurance limit. The principle of the model is schematically shown in Figure 10. The relevant ΔK -vs. a -curve is shifted such far (by l_0) to the left that ΔK -values which fall below the selected ΔK_{th} -value of the material cannot occur.

Another (rough) estimate of the $(\log) da/dN$ vs. $(\log) \Delta K$ -behavior of short cracks in the low ΔK -regime can often be performed if the straight part of the long crack $(\log) da/dN - (\log) \Delta K$ -curve is elongated into the range of low ΔK -values by a straight line. In Figure 11 results which fit into this approach are shown, as an example. (The elongated straight line has to be seen as an average line.)

High ΔK -regime. The transition from the low ΔK -regime to the high ΔK -regime (in the short crack stage) usually leads to the following consequences:

- the fatigue threshold problem becomes less significant,
- the influence of the microstructure is also less important,
- the principles of linear elastic fracture mechanics are commonly no longer applicable.

The fact that the parameters of linear elastic fracture mechanics are usually no longer applicable for the representation of short crack data, and that elastic-plastic fracture mechanics parameters have to be applied is a most essential problem, and most of the deviations from the long crack behavior which are reported in the literature may be due to the utilization of uncorrect parameters.

Several methods have been proposed for the representation of short crack data. Among these are:

- the cyclic J -integral concept after Dowling, where the range of the original J -integral (which is limited to a monotonic nonlinear material behavior) is left for the consideration of cyclic loading. This concept does not account for crack closure.
- the ΔZ -integral after Neumann (17) where the overall σ - ϵ hysteresis loops at a test piece is determined, and where the area under the instantaneous loop and the instantaneous length of the short crack are combined to estimate the cyclic J -integral. (Crack closure is accounted for by taking one of the empirical long crack relationships (comp. Figure 2).) The life which is spent in the short crack stage is

derived from an integration of the short crack behavior.

- the equivalent $K^{(*)}$ -concept by Foth et al. (18), where the cyclic J-integral is determined at the end of each half cycle in a loading history and where corresponding $K^{(*)}$ -values are calculated using the elastic K-J-relationship. These $K^{(*)}$ -values are then introduced into an Elber type equation to account also for crack closure.

The concepts (especially the two last mentioned concepts) still need further systematic investigations for their general verification. An essential problem is, that suitable J-integral approaches are presently available for a very small number of cases only.

Variable amplitude loading conditions. In (19) it has been shown that sequence effects occur not only in the macrocrack stage but also in the short crack regime. That means that simple linear calculation methods (if they are applied to predict the short crack behavior under variable amplitude loading conditions) cannot lead to realistic results. Recently an investigation program has been performed in cooperation with the University of Essen, Germany (20), where the crack initiation process at the surface of Ck15 specimens were studied. In the program the influence of positive and negative mean stresses under constant amplitude loading was investigated. Furtheron, tests with simple program loading patterns were performed, where blocks of small cycles were introduced once into the tension and once into the compression direction. From the SEM-observation of the specimen surfaces it came out, that the microscopical processes differed depending on the direction, where the mean stresses or the blocks of small cycles were applied. If they occurred into the tension direction fatigue bands with a high density were formed at the ferritic grains. Cracks initiated at these grains and at the transitions to the phase and grain boundaries. However, if the mean stresses or the blocks of small cycles occurred into the compression direction, much less fatigue bands were observed which appeared as sharp lines. Due to the lower number of fatigue bands the number of nuclei for the initiation of cracks was lower, as well (comp. Figure 12). From the existence of these basic differences it can be concluded that if under variable amplitude loading a mixture of cycles with different mean stresses and amplitudes occurs incompatibilities in the microstructural mechanisms can quite often occur. That means, that realistic crack propagation prediction methods can become even more complicated.

FATIGUE 87

From a mechanics viewpoint it would be quite worthwhile if an effective stress intensity factor concept could also be formulated for the short crack stage. Under such circumstances the development of a unique crack propagation prediction concept where a homogeneous transition from the short crack stage to the long crack stage is included would become more easily possible.

Engineering aspects. From an engineering point of view (among others) the following questions are of special importance:

- Under which special circumstances the short crack behavior has explicitly to be considered?
- In which way the variation ("scatter") of the short crack data can be accounted for?
- What is the effect of stress concentrations?

Regarding the first point Figure 13 gives an informative overview. It can be seen, that the short crack stage turns out to become important if the applied stress/strain levels are low. The available life time depends strongly on the crack size which can be permitted. On the other hand it is not convenient to perform special inspections in this life regime.

The variation ("scatter") of short crack data is as it has been shown previously extremely large. So it is highly advisable to evaluate the upper band of the da/dN vs. ΔK -variations carefully and to take this as the basis for fatigue life predictions in the short crack stage.

The consideration of notches is predominantly a problem of mechanics and in the literature some approaches have already been developed.

SUMMARY AND CONCLUSIONS

In the present paper the long crack stage and the short crack stage were considered. Regarding the macrocrack stage the present investigations concentrate on refinements of the crack propagation analyses in order to improve their prediction capability. In the short crack stage various anomalies occur which hinder simple extrapolations from the long crack behavior. The present short crack investigations concentrate on the development of basic analysis schemes and on the evaluation of the microscopical and mechanics details.

In the macrocrack stage ΔK_{eff} -concepts are commonly

used to predict the crack propagation under constant amplitude as well as under variable amplitude loading conditions. Recent investigation results show, however, that ΔK_{eff} may not be the only parameter but that other, especially microstructural contributions, may be important, as well.

For the determination of threshold values of long cracks various methods can be applied. In the present paper three different methods were considered, an ASTM-proposal, the "physical" threshold concept after Döker et al. and after Castro et al., and a new "precracking in compression" method. From a special experimental program on the high strength aluminum alloy Al 7475-T7351 and based on practical considerations it came out that the "precracking in compression" method may be preferred for engineering purposes. From a physical viewpoint the method after Döker et al. and after Castro et al. includes various interesting aspects.

Regarding the short crack stage the low ΔK -regime and the high ΔK -regime have to be distinguished. In the low ΔK -regime the threshold value (which is lower than the long crack threshold), the higher crack propagation rates, and the microstructural influences have to be considered, whereas in the high ΔK -regime the adequate mechanics representation of the short crack behavior stands in the foreground. A recent concept by Miller et al. opens up new possibilities to explicitly consider the microstructural processes from a physical viewpoint. From an engineering viewpoint the large scatter of the short crack data and the fact that cumulative damage analyses based on constant amplitude data may lead to significant microstructural incompatibilities are of special importance.

ACKNOWLEDGEMENT

The authors should like to thank Mrs. Schmitz, Mr. Trautmann, Mr. Strunck, Mr. Nurtjahjo and Mr. Hermanns for their help in preparing the present manuscript. Parts of the present investigations were financially supported by Deutsche Forschungsgemeinschaft (DFG).

REFERENCES

- (1) Marissen, R., "Fatigue Mechanisms in ARALL, a Fatigue Resistant Hybrid Aluminum-Aramid Composite Material", Proceedings of the present Conference. Editors R.O. Ritchie, E.A. Starke.

FATIGUE 87

- (2) Nowack, H., "Macro- and Micromechanisms of Fatigue Crack Initiation and Propagation under Constant and Variable Amplitude Loading", Proceedings of the Int. Conf. on "Application of Fracture Mechanics to Materials and Structures (AFMMS)", Martinus Nijhoff Publ., The Hague, Netherlands, 1984, pp. 57-102.
- (3) Nowack, H., "Fatigue Behaviour of Metallic Components under Variable Amplitude Loading: Influencing Factors and Prediction Methods", Proceedings "Fatigue 84". Edited by C.J. Beevers, EMAS Ltd., Warley, U.K., 1984, pp. 961-986.
- (4) Bucci, R.J., "Development of a Proposed ASTM Standard Test Method for Near-Threshold Fatigue Crack Growth Rate Measurement", ASTM STP 738. Edited by S.J. Hudak, Jr., and R.J. Bucci, American Society for Testing and Materials, 1981, pp. 5-28.
- (5) Nowack, H., Trautmann, K.H., Schulte, K. and Lütjering, G., "Sequence Effects on Fatigue Crack Propagation; Mechanical and Microstructural Contribution", ASTM STP 677. Edited by C.W. Smith, American Society for Testing and Materials, 1979, pp. 36-53.
- (6) Suresh, S., Eng. Fract. Mech., Vol. 21, No. 3, 1985, pp. 453-463.
- (7) Zhang, S., Marissen, R., Schulte, K., Trautmann, K.H., Nowack, H. and Schijve, J., "Crack Propagation Studies on Al 7475 on the Basis of Constant Amplitude and Selective Variable Amplitude Loading Histories", to be publ. in: Fatigue Fract. Engng. Mater. Struct.
- (8) Marissen, R., Trautmann, K.H. and Nowack, H., Eng. Fract. Mech., Vol. 19, No.5, 1984, pp.863-879.
- (9) Schijve, J., Jacobs, F.A. and Tromp, P.J., "Fatigue Crack Growth in Aluminum Alloy Sheet Material under Flight Simulation Loading. Effects of Design Stress Level and Loading Frequency", NLR-Amsterdam, The Netherlands, Report No. NLR-TR 72018U, 1972.
- (10) Döker, H. and Bachmann, V., "Determination of Crack Opening Load by Use of Threshold Behaviour", Proceedings of the Int. Symp. on "Fatigue Crack Closure". Symp. Chairman J.C. Newman, W. Elber, American Society for Testing and Materials, to be publ.

FATIGUE 87

- (11) Castro, D.E., Marci, G. and Munz, D., "A Generalized Concept of a Threshold", to be publ. in: Fatigue Fract. Engng. Mater. Struct.
- (12) Nowack, H. and Marissen, R., "Recent Aspects of Crack Propagation Analyses under Variable Amplitude Loading Conditions and Prediction Methods", Proceedings on Second Int. Conf. on "Structural Failure, Product Liability and Technical Insurance". Technical University Vienna, Austria, to be publ.
- (13) Schijve, J., "Prediction of Fatigue Crack Growth in 2024-T3 Alclad Sheet Specimens under Flight-Simulation Loading", Delft University of Technology, Dept. of Aerospace Engineering, Delft, The Netherlands, Memorandum M-415, 1981.
- (14) Nowack, H., Marissen, R. and Trautmann, K.H. and Foth, J., "Significance of the Short Crack Problem as a Function of Fatigue Life Range", Proceedings of the Int. Conf. on "Fatigue of Engineering Materials and Structures". The Institution of Mechanical Engineers, London, U.K., 1986, pp. 511-524.
- (15) Miller, K.J. "Retrospective and Prospective Views of Fatigue Research", Proceedings of the Int. Conf. on "Fatigue of Engineering Materials and Structures". The Institution of Mechanical Engineers London, U.K., 1986, pp. 5-12.
- (16) Topper, T.H. and El Haddad, M.H., "Fatigue Strength Prediction of Notches Based on Fracture Mechanics", Proceedings of the Int. Conf. on "Fatigue Thresholds". EMAS, Warley, U.K., 1982, pp. 777-797.
- (17) Neumann, P., Vehoff, H. and Heitmann, H.H., "Untersuchungen zur Betriebsfestigkeit von Stahl: Reihenfolgeeffekte während der Rissinitiationsphase", Bundesministerium für Forschung und Technologie, Bonn, Germany, Report No. BMFT-FB-T 84-040, 1984.
- (18) Foth, J., Marissen, R., Trautmann, K.H. and Nowack, H., "Short Crack Phenomena in a High Strength Aluminium Alloy and Some Analytical Tools for Their Prediction", EGF Pub.1 "The Behaviour of Short Fatigue Cracks". Edited by K.J. Miller and E.R. de los Rios, Mechanical Engineering Publications, London, U.K., 1986, pp. 353-368.

FATIGUE 87

- (19) Foth, J., Marissen, R., Nowack, H. and Lütjering, G., "Fatigue Crack Initiation and Microcrack Propagation in Notched and Unnotched Aluminium 2024-T3 Specimens", Proceedings of the ICAS Symposium, Toulouse, France, 1984, pp. 791-801.
- (20) Middeldorf, K., Nowack, H., Fischer, A. and Harig, H., "Cumulative Damage under Constant Amplitude and Variable Amplitude Loading: Some New Physical Aspects", Proceedings on the 2nd Int. Conf. on "LCF and Elasto-Plastic Behavior of Materials", Munich, Germany, 1987. Elsevier, Amsterdam, The Netherlands, to be publ.

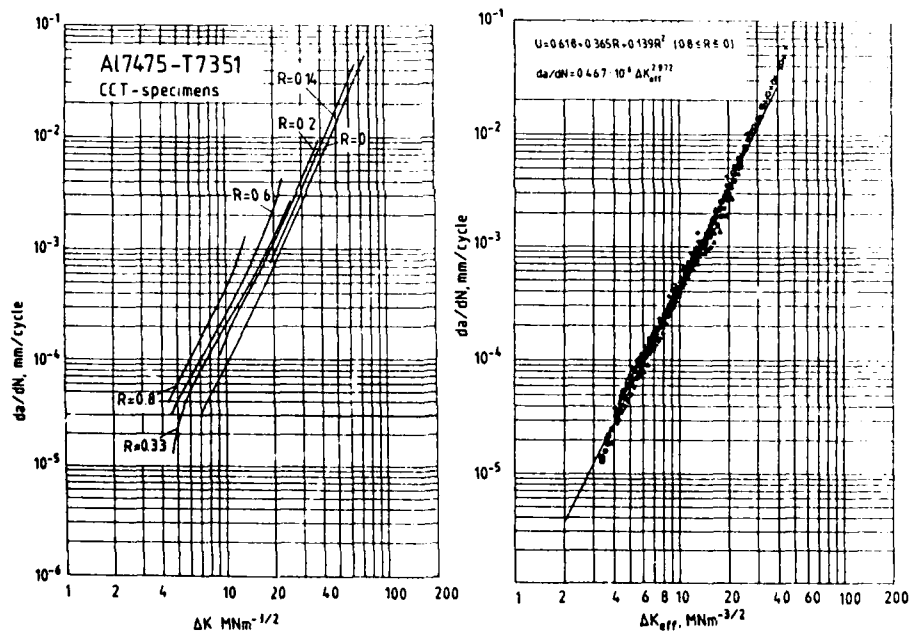


Figure 1 Crack propagation behavior of Al 7475-T7351, once plotted vs. ΔK and once plotted vs. ΔK_{eff}

FATIGUE 87

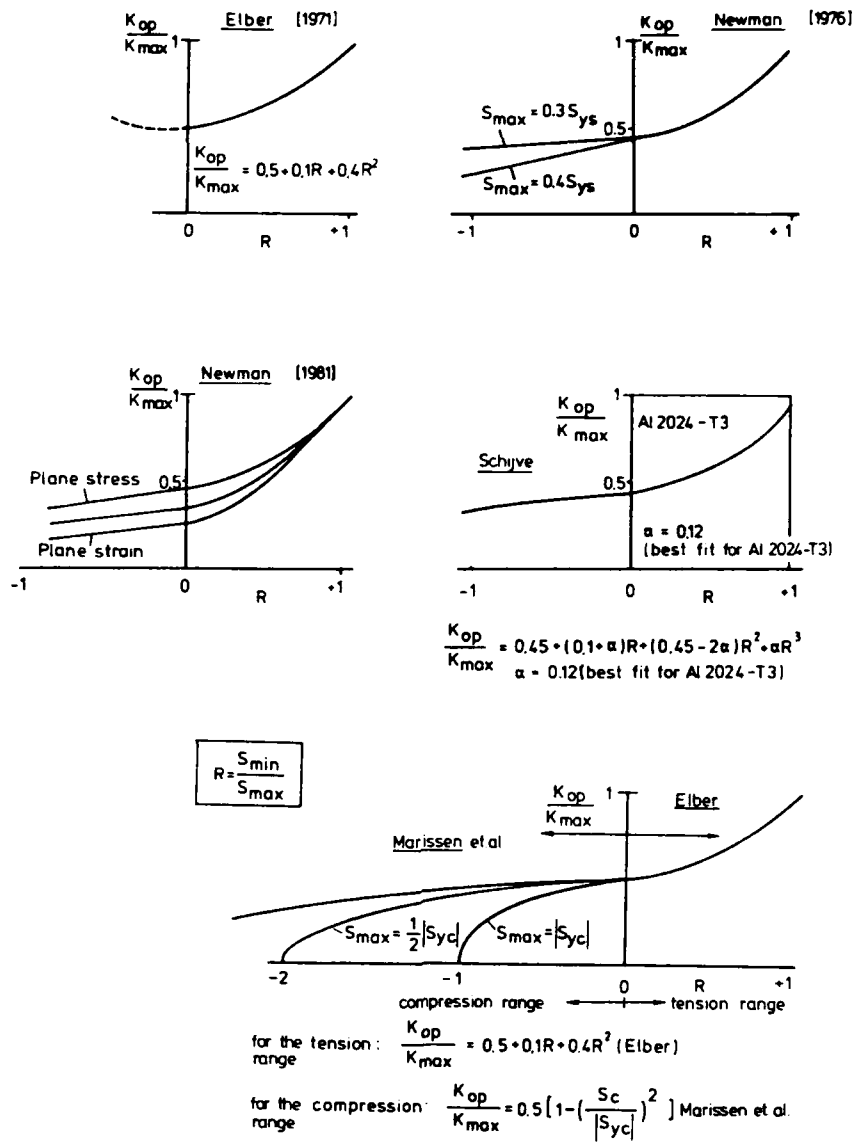


Figure 2 Approaches for the consideration of the crack opening behavior under positive and negative R-ratios

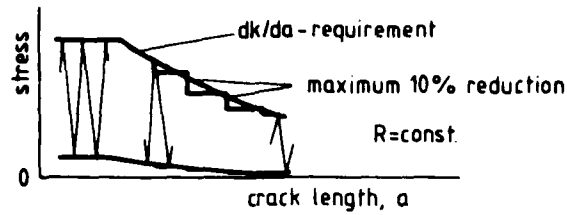
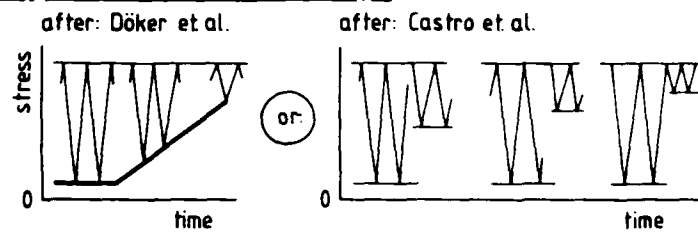
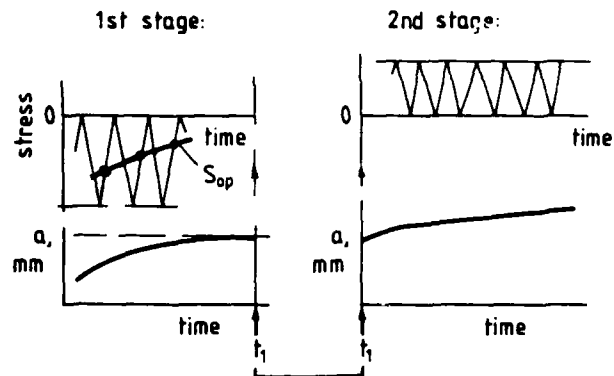
(a) ASTM-proposal (after Bucci)(b) 'Physical' threshold concept(c) 'Precracking in compression' -method

Figure 3 Different concepts for the determination of (long crack) threshold values: (a) ASTM proposal (4), (b) "physical" threshold concept after Döker et al. (10) and after Castro et al. (11), (c) "precracking in compression" method

FATIGUE 87

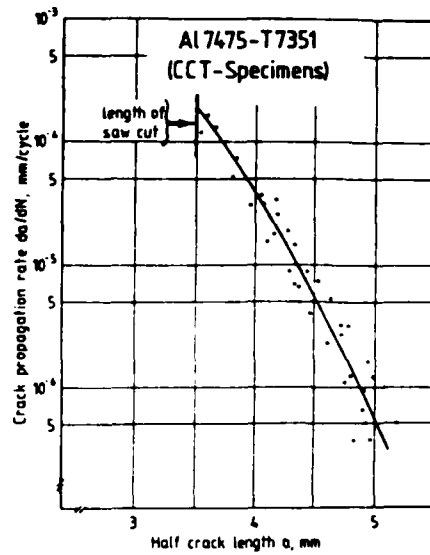


Figure 4 Fatigue crack behavior under compression precracking

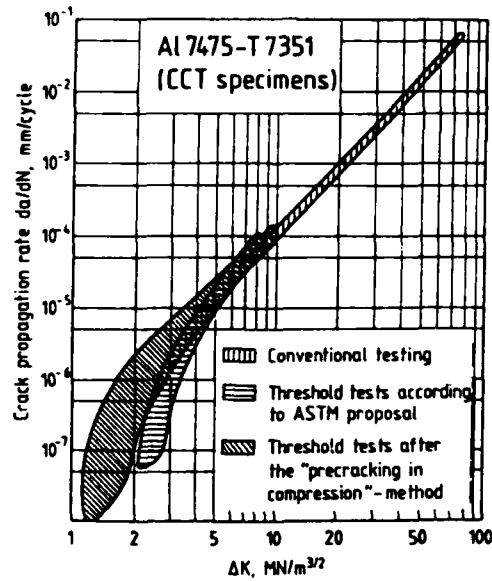


Figure 5 Comparison of the threshold behavior for the Al 7475-T7351 alloy after the ASTM proposal and after the "precracking in compression" method

FATIGUE 87

I	Analyses of the stresses/displacements at the cracks	Explicit calculation of the el.-plast. stresses/displacements around a crack	Analyses of stresses/displacements based on Dugdale-Barenblatt Model
II	Simulation models	The most important influences are <u>simulated</u> by simple analytical routines	
III	Simplified simulation models	Procedure as before, empirical trends further included	
	Adjustment models	Crack closure and its causes are <u>not explicitly</u> considered	
	Characteristic K-value concept, $K_{R.M.S.}$ -concept		
	Linear prediction models based on constant amplitude equations		

Figure 6 Survey of crack propagation prediction concepts which account for crack closure

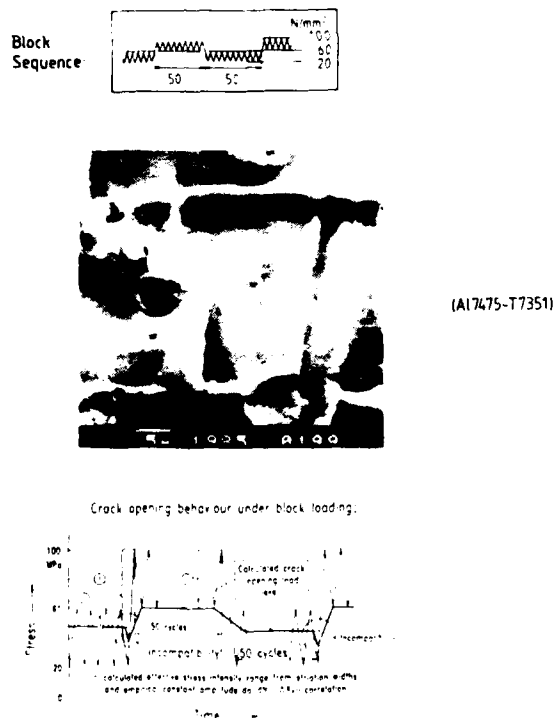


Figure 7 Prediction of the crack opening behavior under block loading

FATIGUE 87

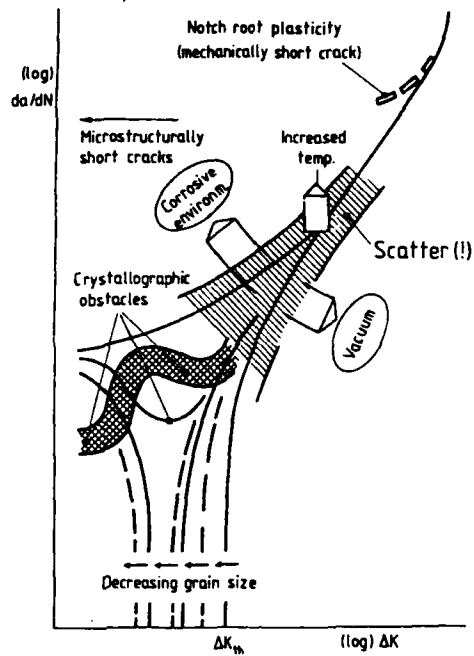


Figure 8 Typical anomalies of short cracks as compared to the long crack behavior

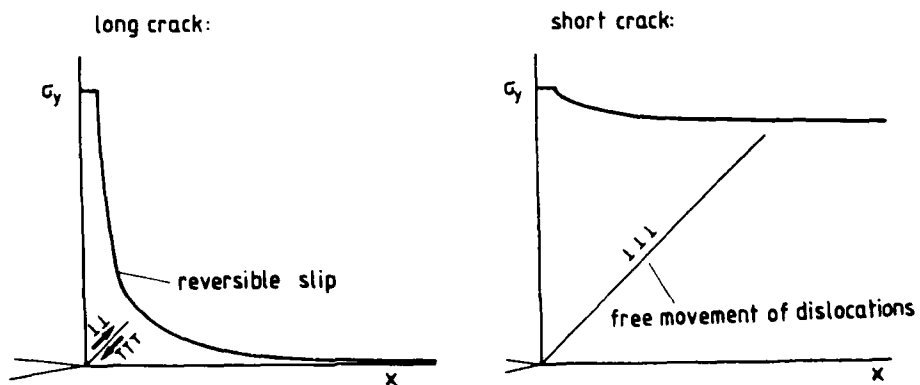
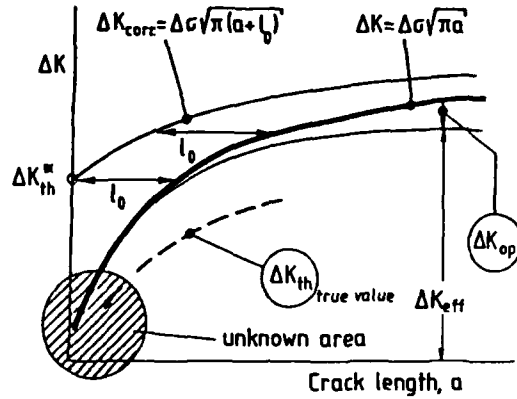


Figure 9 Interaction between the stress fields and the dislocation processes at the tip of long and short cracks

FATIGUE 87



ΔK_{th}^{∞} = (long crack-) threshold

l_0 = size of an "intrinsic damage"

Figure 10 l_0 -concept after Topper et al. for short cracks (16)

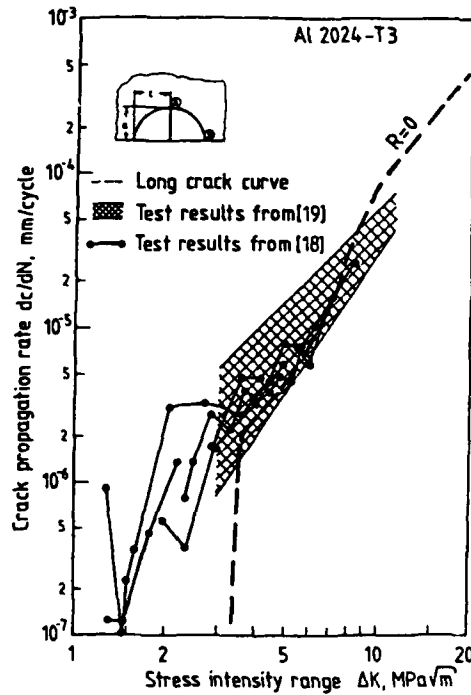


Figure 11 Short crack behavior of the high strength aluminum alloy Al 2024-T3

FATIGUE 87

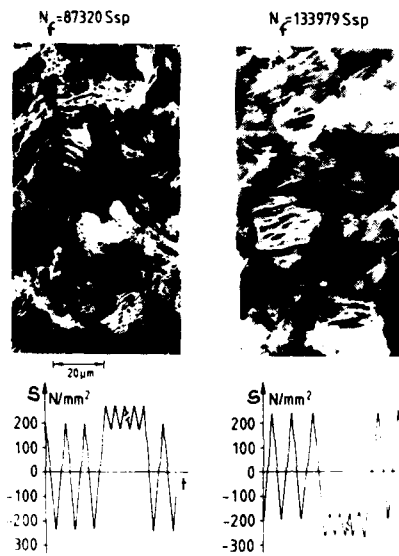


Figure 12 Microstructural processes at the surface of Ck15 specimens under two different types of load sequences

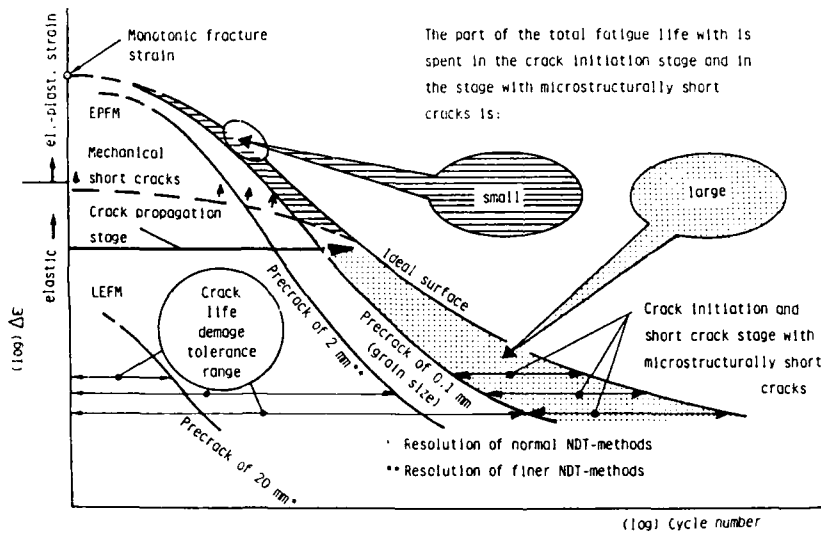


Figure 13 Engineering significance of the short crack stage

FATIGUE 87

FATIGUE 87

LOW CYCLE FATIGUE LIFE PREDICTIONS OF A 1CrMoV STEEL IN TERMS OF A J-CONTROLLED SHORT CRACK GROWTH MODEL

V. Bicego*

The propagation of cracks under Low Cycle Fatigue (LCF) conditions is modelled in terms of Rice's cyclic parameter ΔJ , specifically formulated for short cracks. Simply relying on the values of Paris coefficients from conventional Fatigue Crack Growth tests under elastic conditions, it is shown that life predictions obtained by integrating the crack growth expressions for the LCF cracks comply quite favourably with actual lives found in tests at 480 and 540°C on a 1CrMoV steel.

INTRODUCTION

It is generally accepted (Coffin (1), Grosskreutz (2), Tompkins (3)) that the period of the slow stable growth of short cracks occupies the major portion of what is usually meant as Low Cycle Fatigue (LCF) life, whereas only small life fractions are spent in the crack initiation phase (multiple cracks formation and coalescence into single dominating small cracks) and in the period of accelerated growth of large cracks leading to the final failure. A marked distinction has become popular (Novack et al. (4)) between two different definitions of short cracks, i.e. microstructurally short cracks and physically short cracks. In the former case models must take into account physical parameters of the microstructure, responsible for crack accelerations (favourably oriented slip systems, etc.) or retardation (at grain boundaries, hard particles etc.). In the latter case continuum mechanics crack models apply, mostly related to Elastic-Plastic (EP) representations of stress-strain fields at crack tip. It has been pointed out (Miller (5)) that in fatigue at low load amplitudes on an initially uncracked specimen the growth of microstructurally short cracks governs the majority of the life, whereas physically small cracks become in-

* CISE - Tecnologie Innovative SpA, Segrate (Milano)-I.

FATIGUE 87

creasingly important at high loads. Modelling small crack behavior under EP conditions should therefore provide a valuable tool for predicting lives of test specimens and of plant components subjected to LCF damage.

Following Dowling and Begley's original work (6), the following law has become extensively used for correlating da/dN data under EP conditions:

$$\frac{da}{dN} = A \Delta J^m \quad (1)$$

where A and m are material constants, and ΔJ is the applied range of Rice's J integral. This equation was applied by Mowbray (7), Dowling (8), Starkey and Irvin (9) and Ebi et al. (10) to small cracks on smooth bar specimens; life predictions have also been derived (9), (10), mostly in the limited domain of small cyclic plasticity. In these studies no particular attention was put to the peculiar characteristics of the kinetics of short cracks, as formulas directly derived for large cracks were thought to be adequate for small cracks too. On the other hand it was reported by El Haddad et al. (11) and in ref. (8) that expressions of Fracture Mechanics parameters for large cracks do not provide good correlations of da/dN data down to crack lengths smaller than some tenths of a mm. In addition, as observed by Minzong and Liu (12), no attempt was ever made to correlate da/dN data with ΔJ calculated by finite element methods for the specific test specimen configurations.

In the present work ΔJ expressions used previously have been refined and applied to cracks growing at the surface of smooth specimens. The derivation is accomplished in two steps: expressions of ΔJ for a typical configuration of a Fracture Mechanics test specimen are firstly considered, and the solution obtained is then modified according to a short crack model due to El Haddad et al. (13). The crack growth expressions in eq. 1 have then been integrated, providing LCF life predictions which have been checked against actual data on a 1CrMoV steel.

THE MODEL

EPFM: J estimation schemes. In order to derive expressions of J applicable to edge cracks on smooth LCF specimens it is convenient to rely on a suitable Fracture Mechanics test specimen idealization, for which formulas are readily available from handbooks. Reference is here made to the case of a Single Edge Notched (SEN) specimen loaded in uniform tension under plane stress conditions. For this specimen configuration ΔJ can be determined according to EPRI Engineering Approach (Kumar et al. (14)) from a summation of elastic and plastic components of ΔJ , determined as:

FATIGUE 87

$$\Delta J_e = F_{SEN}^2(a/b) \frac{\pi a \Delta P^2}{b^2 E} \quad (2)$$

$$\Delta J_p = \alpha \Delta \epsilon_o \Delta \sigma_o \frac{c a}{b} \left(\frac{\Delta P}{\Delta P_o} \right)^2 h_{SEN}(a/b, n) \quad (3)$$

where b is the specimen width, c is the ligament ($b-a$), α , $\Delta \epsilon_o$, $\Delta \sigma_o$, and n are constants in the cyclic Ramberg Osgood representation of material stress-strain curve as in (14), P_o is the reference load of EPRI limit load analysis, $F_{SEN}(a/b)$ is the elastic geometry factor given by Tada et al. (15), and $h_{SEN}(a/b, n)$ is a plastic coefficient for SEN geometry which has been evaluated (by f.e. analysis) and reported in tabular form in EPRI handbook (14). By rewriting eqs. 2 and 3 in terms of the elastic and plastic strain energy densities far from the crack tip,

$$w_e = \frac{\Delta \sigma^2}{2 E} \quad (4)$$

$$w_p = \frac{\Delta \sigma \Delta \epsilon_p}{1 + 1/n} \quad (5)$$

and in the limit $a \ll b, c$, the following relationship is obtained:

$$\Delta J = 2 \pi a F_{SEN}^2 (w_e + f_{EPRI}(n) w_p) \quad (6)$$

with F_{SEN}^2 (for $a=0$) being 1.122, and

$$f_{EPRI}(n) = (1+1/n) \frac{1}{2 \pi F_{SEN}^2} h_{SEN}(0, n) \left(\frac{1}{1.072} \right)^{n+1} \quad (7)$$

(with the coefficient 1.072 taken from the expression of P_o in EPRI limit load analysis). Unfortunately for the various specimen configurations considered in EPRI handbook no f.e. solutions are given for the plastic factors $h(a/b, n)$ in the limit $a/b \rightarrow 0$, the shortest crack length analyzed being $a/b = 1/8$. Therefore alternative estimates have to be considered. Simply relying upon the fact that for a Center Cracked Tension (CCT) panel a simple analytical expression was made available by Shih and Hutchinson (16) for the case $a/b=0$, the following J estimation scheme has become widely in use (8-10):

$$\Delta J = 2 \pi a F_{SEN}^2 (w_e + f_{CCT}(n) w_p) \quad (8)$$

with:

FATIGUE 87

$$f_{CCT}(n) = (1+1/n) \frac{1}{2\pi} \left[3.85 \sqrt{n} \left(1 - \frac{1}{n} \right) + \frac{\pi}{n} \right] \quad (9)$$

Values of $f_{EPRI}(n)$ and of $f_{CCT}(n)$ are reported in Table 1. Though it is recognized that use of a CCT expression has no theoretical justification, to the author's knowledge numerical checks of ΔJ estimates from eqs. 8-9 against f.e. solutions have never been reported.

TABLE 1 - Values of factor $f(n)$ in eq.: $\Delta J = 2\pi a F^2 (W_e + f(n) W_p)$, according to 5 estimation schemes.

n	1	2	3	5	7	10	13	16	20	
f_{CCT}	1.00	1.02	1.17	1.44	1.67	1.97	2.24	2.47	2.76	
f_1	1.00	0.95	1.07	1.54	2.35	4.60	9.13	18.3	46.4	for
f_2	1.00	0.84	0.84	0.95	1.14	1.55	2.14	2.99	4.68	$\frac{a}{b} = 0$
f_{EPRI}	1.00	- - -	- - -	NOT EXISTING	- - -	- - -	- - -	- - -	- - -	
f_{SEN}	1.00	1.07	1.18	1.40	1.57	1.80	1.97	2.18	2.52	
f_{CCT}	1.06	- - -	- - -	NOT EXISTING	- - -	- - -	- - -	- - -	- - -	
f_1	1.00	1.63	3.16	13.5	61.0	$6.1 \cdot 10^2$	$6.1 \cdot 10^3$	$6.3 \cdot 10^4$	$1.3 \cdot 10^6$	for
f_2	1.00	0.92	1.01	1.37	1.97	3.51	6.38	11.7	26.3	$\frac{a}{b} = \frac{1}{8}$
f_{EPRI}	1.00	1.17	1.42	2.02	2.72	4.07	5.88	8.51	14.2	
f_{SEN}	1.00	1.17	1.42	2.02	2.72	4.07	5.88	8.51	14.2	

(f_{CCT} from (13) and (16), f_1 and f_2 from (17), f_{EPRI} from (14) and f_{SEN} from present scheme)

A different J estimation scheme was recently proposed by Broek (17), with the aim of providing a simple method for the prediction of loads in tearing instability analyses. Based on suitable (but theoretically unjustified) extrapolations to the plastic case of J expressions valid in the elastic regime, two possible expressions of the plastic geometry coefficient in eq. 6 result from this method:

$$f_1 = (1+1/n) \frac{1}{2\pi F_{SEN}^2} \left(\pi F_{SEN}^2 \right)^{(n+1)/2} \quad (10)$$

$$f_2 = (1+1/n) \frac{1}{2\pi F_{SEN}^2} F_{SEN}^{n+1} \quad (11)$$

It is seen in Tab. 1 that abnormally high estimates are obtained with eq. 10 at large n values, whereas more reasonable results are found with eq. 11 with respect to existing EPRI data at $a/b = 1/8$.

FATIGUE 87

Based on this finding, it may be expected that reliable results are to be found by eq. 11 even for $a=0$. In addition, taking advantage of the discrepancies with respect to EPRI data at $a/b=1/8$, a further refinement of the estimate can be accomplished as follows:

$$\left[f_{\text{SEN}}(n) \right]_{a/b=0} = \left[f_2(n) \right]_{a/b=0} \cdot \left[\frac{f_{\text{EPRI}}}{f_2} \right]_{a/b=1/8} \quad (12)$$

$$\left[f_{\text{SEN}}(n) \right]_{a/b=1/8} = \left[f_{\text{EPRI}}(n) \right]_{a/b=1/8} \quad (13)$$

It is seen from Tab. 1 that these estimates do not differ much from the CCT solutions for $a=0$ usually assumed (present analysis therefore is also an indirect validation of the possible use of f_{CCT} coefficients even for a SEN geometry). In lack of more definite f.e. results, in the following the simple estimation scheme of eq. 12 will be used, which was specifically derived for a SEN geometry, and for which a reliable check against EPRI data has been possible, at least for $a/b=1/8$.

Short crack considerations. By extending to EP situations the empirical concept of an intrinsic crack length a_0 , originally developed (ref. (11)) for correlating da/dN data and threshold values of ΔK in conventional Kitagawa-Tagahashi (18) plots, El Haddad et al. (13) proposed the following short crack redefinition of ΔJ :

$$\Delta J = 2 \pi F^2 (W_e + f(n) W_p) (a + a_0) \quad (14)$$

with:

$$a_0 = \frac{1}{\pi} \left(\frac{\Delta K_{\text{th}}}{\sigma_{\text{end}}} \right)^2 \quad (15)$$

being F the geometry factor, ΔK_{th} the fatigue threshold stress intensity factor for large cracks under elastic conditions, and σ_{end} the endurance limit. According to this model, the expression of ΔJ for an edge crack in a smooth LCF specimen is:

$$\Delta J = 2 \pi \left(\frac{2}{\pi} F_{\text{SEN}} \right)^2 (W_e + f_{\text{SEN}}(n) W_p) (a + a_0) \quad (16)$$

where the usual coefficient of $2/\pi$ has been introduced to account for the semicircular shape of conventional LCF cracks.

LCF predictions. It is assumed that a unique relationship, eq. 1, is adequate in modelling conventional LEFM cracks as well as short LCF cracks. In addition, for an easy check of this method effects of a negative R ratio on da/dN curves determined in Fatigue Crack Growth (FCG) tests under elastic conditions are assumed to be negligible, only affecting threshold values in the definition of a_0 (eq. 15). Therefore from the values of Paris coefficients from FCG

FATIGUE 87

tests with $R=0$ the constants A and m (eq. 1) for LCF cracks with $R=-1$ can be simply determined using the elastic equivalence $J=K/E'^2$. A life prediction for a smooth LCF test specimen with diameter D is derived by integrating eq. 1 (with ΔJ from eq. 16) between appropriate values of initial (a_i) and final (a_f) crack lengths (the particular choice of a_f is not of great importance, as the final stage of crack growth is normally rapid). In the following it will be assumed $a_i=0$ and $a_f=D/3$, this latter being the length of cracks typically found at the instant chosen to define failure in LCF tests.

EXPERIMENTAL VERIFICATION

Life prediction capability of present model has been verified on a number of LCF test results carried out at CISE's laboratories on a 1CrMoV forging rotor steel, of an ASTM type A470 Cl. 8. Chemical composition, mechanical properties, test procedures and an extensive overview of LCF results have been reported in previous papers by Bicego et al. (19,20). Test data on specimens from the Rim region of the High Pressure rotor stage are here considered, with stress axis parallelly oriented with respect to the rotor axis, for which cracks develop in radial-tangential planes. For this same rotor region and identical crack orientation the values of Paris coefficients were available (21) from Fatigue Crack Growth (FCG) tests on CT specimens, carried out at 450°C with triangular waveforms at frequencies of 0.1 and 1 Hz. No time dependent effects were found, and a unique Paris curve was given as:

$$\frac{da}{dN} = 7.7 \cdot 10^{-12} \Delta K^{3.0} \quad (17)$$

This equation has been used to derive life predictions applicable to LCF tests at 480°C, with applied strain ranges in the interval 0.5 - 4% and a constant strain rate $\dot{\epsilon} = 3 \cdot 10^{-3} \text{ s}^{-1}$ (resulting in frequencies in the same interval as the FCG data; the difference in temperature with respect to FCG tests is not thought to be of importance, as LCF results were found to be relatively temperature independent for these test conditions). Values of energies W_e and W_p in eq. 16 were derived from mid-life stress-strain hysteresis loops. In lack of high temperature data with $R=-1$, a_0 was estimated from room temperature parameters in eq. 15. A threshold value of $7.7 \text{ MPa}\sqrt{\text{m}}$ was assumed at $R=0$, on the basis of an extensive collection of thresholds data reported by Taylor (22) for perlitic and bainitic steels. For the case $R=-1$ a reduction factor of 2/3 was introduced, again on the basis of literature findings (Morgan (23), Lee and Stephens (24), Yu et al. (25), Greenfield and Suhr (26)), resulting in $\Delta K_{th}(R=-1) = 5.0 \text{ MPa}\sqrt{\text{m}}$. Being $\sigma_{end} = 403 \text{ MPa}$, the estimated value of a_0 is then $49 \cdot 10^{-6} \text{ m}$. Finally, being $n=11.8$, the value of the coefficient $f_{SEN}(n)$ is 1.71. In fig. 1 the life predictions calculated in this way are compared with actual LCF test results: notwithstanding the uncertainties in some

FATIGUE 87

numerical coefficients of the model, it is seen that the agreement is excellent.

Fig. 2 reports further results of a similar analysis for LCF tests at 540°C (with $n = 12.7$ and $f_{SEN}(n) = 1.95$). Predictions were obtained from Westinghouse data determined by Swaminathan et al. (27) from tests at 538°C on CT specimens of a nominally identical rotor steel, with ramp times (t_r) and hold times (HT) in the ranges 5-30 s and 0-1680 s respectively. The time-dependent crack growth curve is in this case:

$$\begin{aligned} \frac{da}{dN} = & 6.8 \cdot 10^{-11} \Delta K^{2.5} + 2.2 \cdot 10^{-9} ((2t_r)^{0.24} - 0.64) \Delta K^{1.5} \\ & + 1.2 \cdot 10^{-9} (HT)^{0.36} \Delta K^{1.3} \end{aligned} \quad (18)$$

As hold periods in FCG tests were applied at constant maximum loads, a strong conservatism is expected when using eq. 18 to predict LCF lives under constant strain hold conditions. This is clearly confirmed in fig. 3. Strain rate dependence is analyzed in fig. 4 (here the data with $\dot{\epsilon} = 3 \cdot 10^{-6} \text{ s}^{-1}$ represent far extrapolations beyond the limits of experimental validity of eq. 18). A constant factor of conservatism is seen in figs. 2 and 4. This might be attributed to the intrinsic conservatism of Westinghouse crack growth equation in test with no hold, as recognized in the original paper (27), or to the different heats used in CISE (LCF) and Westinghouse (FCG) tests. On the other hand the fixed amount of conservatism found in tests with different $\dot{\epsilon}$ is an indication that present approach can adequately represent time-dependent damage: see fig. 5.

CONCLUSIONS

The analysis here carried out on a low alloy steel supports the use of an EPFM description of short cracks for LCF life prediction purposes. The importance of this approach is not merely a speculative one, i.e. supporting a crack growth interpretation of LCF: the method provides life predictions on the basis of a limited amount of material data, and is therefore a natural candidate for engineering applications.

Acknowledgements

The author wish to express his gratitude to A. Barbieri for cooperation in running the LCF tests, and to ENEL (Italian Electricity Board) for having supported this activity.

SIMBOLS USED

a, a_0 = Crack length and intrinsic crack length (m)
 b, c_0 = Specimen width and ligament (m)

FATIGUE 87

t_r	=	Rise time of a triangular waveform (s)
A, m	=	Constants of the crack growth eq. 1
D	=	Diameter of a smooth LCF specimen (m)
E, E'	=	Plane stress and plain strain Young's moduli (MPa)
HT	=	Hold time (s)
N	=	Cycle number
N_f	=	Actual LCF life to failure
N_p	=	Predicted LCF life to failure
P, P_0	=	Applied load and reference load (N)
W	=	Strain energy density (MPa)
W_e, W_p	=	Elastic and plastic parts of W (MPa)
α, n	=	Ramberg-Osgood's coefficient and strain exponent
$\dot{\epsilon}$	=	Strain rate (s^{-1})
σ_{end}	=	Fatigue endurance limit (MPa)
$\Delta\epsilon_t, \Delta\epsilon_p$	=	Total and plastic strain ranges (m/m)
$\Delta\epsilon_0, \Delta\sigma_0$	=	Reference strain (m/m) and reference stress (MPa)
$\Delta\sigma$	=	Stress range (MPa)
ΔJ	=	Applied range of Rice's J integral (MPa \cdot m)
$\Delta J_e, \Delta J_p$	=	Elastic and plastic parts of ΔJ (MPa \cdot m)
ΔK	=	Range of stress intensity factor (MPa \sqrt{m})
ΔK_{th}	=	Threshold value of ΔK (MPa \sqrt{m})

REFERENCES

- (1) Coffin, L.F. Jr., Proc. IMechE, Vol. 188, 1974, pp. 109-127.
- (2) Grosskreutz, J.C., ASTM STP 495, 1971, p. 60.
- (3) Tompkins, B., Phi. Mag., Vol. 18, 1968, pp. 1041-1066.
- (4) Nowack, H., Marissen, R., Trautmann, K.H. and Foth, J., Proc. IMechE, 1986-9, pp. 511-519.
- (5) Miller, K.J., Proc. ECF6, 1986, ed. Van Elst Bakker, pp.2149-67.
- (6) Dowling, N.E. and Begley, J.A., ASTM STP 590, 1976, pp. 83-104.
- (7) Mowbray, D.F., ASTM STP 601, 1976, pp. 33-46.
- (8) Dowling, N.E., ASTM STP 637, 1977, pp. 97-121.
- (9) Starkey, M.S. and Irvin, P.E., ASTM STP 770, 1982, pp. 382-398.
- (10) Ebi, G., Riedel, H. and Neumann, P., in ref. (5), pp.1587-1598.
- (11) El Haddad, M.H., Smith, K.N. and Topper, T.H., Proc. ASME-CSME Conf. PVP Nucl. En. Mat., 1978, Paper 78-Mat-7.
- (12) Minzhong, Z. and Liu, H.W., J. Eng. Mat.T., Vol. 108, 1986, pp. 201-205.
- (13) El Haddad, M.H., Dowling, N.E., Topper, T.H. and Smith, K.N., Int. J. of Fr., Vol. 16, 1980, pp. 15-30.
- (14) Kumar, V., German, M.D. and Shih, C.F., GE, EPRI NP-1931, 1981.
- (15) Tada, H., Paris, P.C. and Irwin, G.R., The Stress An. of Cr. Handbook, Del R.C., Hellertown Penn., 1973.

FATIGUE 87

- (16) Shih, C.F. and Hutchinson, J.W., J.E.Mat.Tech., Oct. 1976, pp. 289-295.
- (17) Broek, D., in ref. (5), pp. 745-759.
- (18) Kitagawa, H. and Takahashi, S., Proc. 2nd I. Conf. Mech. B. Mat., Met. Park, 1976, ASM.
- (19) Bicego, V., Fossati, C. and Ragazzoni, S., ASTM Sym. LCF, N.Y., 1985 (to be published in ASTM STP, 1987).
- (20) Bicego, V., Borghi, L. and Ricci, N., Proc. Liege Conf. 1986, ed. Betz et al., pp. 1537-1546.
- (21) Private comm., courtesy of ENEL-DSR (Italian Electr.B.-R&D Div.) Jan. 1986.
- (22) Taylor, D., Proc. Conf. FATIGUE 84, ed. Beevers, 1984, pp. 327-337.
- (23) Morgan, H.G., UKAEA ND-R-985(S), UK, 1985.
- (24) Lee, H.W. and Stephens, R.I., in ref. (22), pp. 255-264.
- (25) Yu, M.T., Topper, T.H. and Au, P., in ref. (22), pp. 179-190.
- (26) Greenfield, P. and Suhr, R.W., Proc. IMechE 1986-9, pp. 165-186.
- (27) Swaminathan, V.P., Shih, T.T. and Saxena, A., Eng. Fr. Mech. Vol. 16, No. 6, 1982, pp. 827-836.

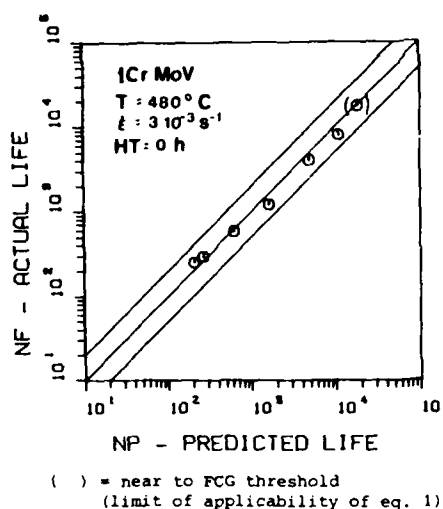


Figure 1 Correlation of actual and predicted lives at 480°C

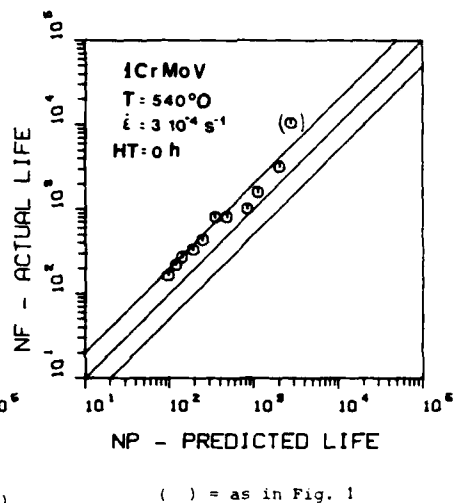
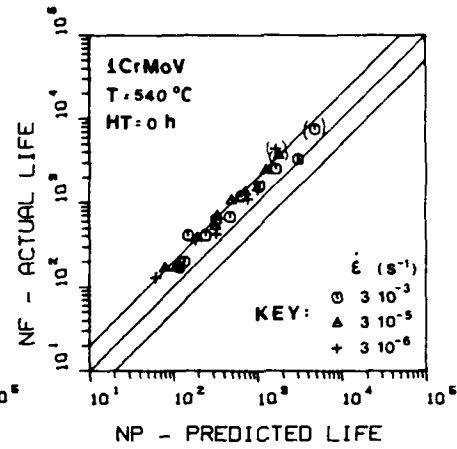
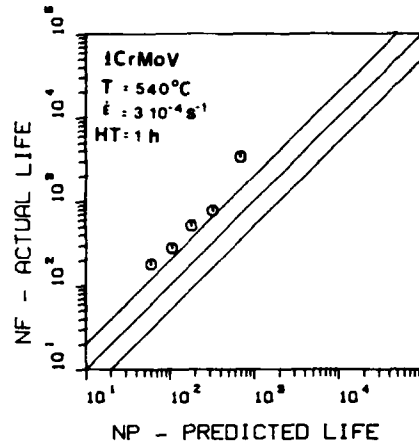


Figure 2 Correlation of actual and predicted lives at 540°C

FATIGUE 87



() = as in Fig. 1

Figure 3 Analysis of tests with a hold time (HT)

Figure 4 Analysis of tests with different strain rates ($\dot{\epsilon}$)

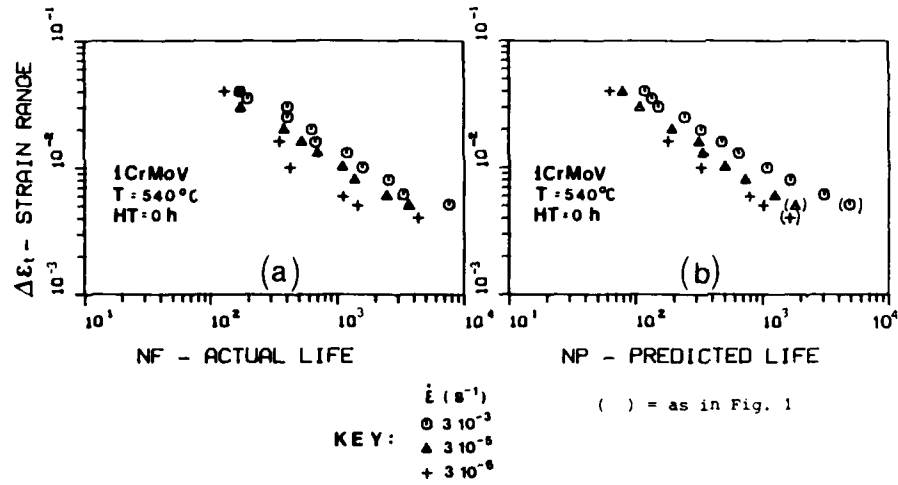


Figure 5 Strain life diagrams showing strain rate effects for actual (a) and predicted (b) fatigue lives

FATIGUE 87

THE STATISTICS OF THE SHAPE OF SMALL FATIGUE CRACKS

B.N. Cox* and W.L. Morris*

This paper presents Monte Carlo simulations of the growth of small fatigue cracks through stochastic microstructures. The simulations are based on canonical formulae for the stress intensity factor around an irregular crack front, and laws of crack growth extracted from prior experiments or theories to describe the influence of the microstructural environment. The simulations allow the convenient examination of the statistics of crack shape, which may be compared with easily obtained experimental data. The magnitude and persistence of fluctuations in crack shape may be used to test postulated laws of growth. The physical insight available from the Monte Carlo simulations will ultimately permit more accurate predictions of fatigue lifetime.

INTRODUCTION

Small fatigue cracks having no dimension greater than a few grain diameters are subject to large stochastic variations in the driving force acting at different points along the crack front. Therefore, the crack front does not remain smooth, but shows irregularities which may be large or small depending on the strength of the stochastic factors generating them. In this paper, Monte Carlo simulations of the growth of such irregular cracks are presented. The Monte Carlo simulations can be used to validate postulated laws of crack growth by comparison with observations of crack shape; and to illuminate the sources of various statistical properties of small cracks, which may allow more accurate predictions of fatigue lifetime.

For small cracks, the stochastic variations in the driving force originate in the stochastic nature of the microstructure encountered by the advancing crack front. The rate of advance of a segment of the crack front can be influenced by several mechan-

*Rockwell International Science Center, 1049 Camino Dos Rios,
Thousand Oaks, CA 91360

isms whose impact depends on the size, orientation, and mechanical properties of the grains in the immediate vicinity. The mechanisms include temporary arrest at grain boundaries, deceleration caused by back stress or by fracture surface roughness, acceleration caused by enhanced local plasticity, and fluctuations in the local stress field caused by elastic inhomogeneity and anisotropy. The Monte Carlo simulations allow the consideration of one or all of these mechanisms, as long as a corresponding law is available to express their influence on the growth rate of each segment of the crack front.

The tendency of the stochastic microstructure to make the crack front irregular is balanced by the dependence of the stress intensity factor on crack shape. For example, for an embedded irregular plane crack, the mode I stress intensity factor, K_I , is generally reduced on protrusions and enhanced on retarded segments, so that, in the absence of microstructural fluctuations, the crack always tends to be circular. For a surface breaking crack under mode I loading, the equilibrium shape is approximately a smooth semi-ellipse of aspect ratio 0.4. For the Monte Carlo simulations, a simple algorithm has been derived to estimate K_I for either an embedded or surface breaking plane crack of any shape.

STOCHASTIC MICROSTRUCTURES

A single instance of a stochastic microstructure is generated as follows. Nucleation sites of a prescribed average density are placed on the plane of the crack in a Poisson process (i.e., with no correlation in their locations) by invoking a pseudo-random number generator. The grain boundaries are then determined by the Wigner-Seitz construction, which defines each grain as the area bounded by the perpendicular bisectors of the lines joining that grain's nucleation site to the nucleation sites of all its contiguous neighbors. Nonequiaxed grain structures are generated by rescaling one of the axes. The locations of the vertices and the total area of each grain are stored until the next microstructure is generated.

To enable convenient reference to the information contained in a given microstructure, a discrete square grid is defined on the plane of the crack. Each point on this grid is then associated with the number of the grain containing it and with other measures of the local microstructure. For example, for modeling crack growth in Al alloys, an appropriate measure upon which plasticity-induced closure depends is the distance from the grid point to the next grain boundary measured along the line emanating from the center of the crack. Other characteristics, such as grain orientation, might be preferred for other materials.

APPROXIMATE, FAST ALGORITHM FOR K_I

The feasibility of the Monte Carlo simulations depends critically on being able to estimate K_I very quickly for plane cracks of arbitrary shape. Exact calculation of K_I would be prohibitively slow and, therefore, simple approximations to K_I have been derived. The approximations are based on estimates, $K_I(P)$, of K_I at the zenith, P, of a protrusion and $K_I(Q)$ at the nadir, Q, of a retarded segment. Both the protrusion and the retarded segment considered have the square-shouldered geometry shown in Figure 1. A combination of analytical and numerical work has led to the following expressions for $K_I(P)$ and $K_I(Q)$:

$$K_I(P) = 2\sigma_\infty \sqrt{t/\pi} \cdot \frac{2}{\pi} \tan^{-1} \left[\frac{3 + s/t}{1 - s/t} \tan \frac{\alpha}{2} \right], \quad (1)$$

and

$$K_I(Q) = 2\sigma_\infty \sqrt{s/\pi} / \frac{2}{\pi} \tan^{-1} \left[\frac{3 + s/t}{1 - s/t} \tan \frac{\alpha}{2} \right], \quad (2)$$

where s , t and α are defined in Figure 1. The identification of α for a smooth rather than square-shouldered protrusion or retarded region is subjective and, therefore, the term $\alpha/2$ in Equations (1) and (2) was replaced by $\pi/2 \cdot \alpha/\alpha_0$, with the parameter α_0 evaluated by calibration against K_I for elliptical cracks.

For crack fronts of arbitrary profile, the half-width α of a protrusion or retarded segment was defined as half the angle between the points on either side of the extrema at which the radius of the crack was equal to its average radius (Figure 2a). The value of K_I between the zenith of a protrusion and the nadir of a retarded segment is then written simply as

$$K_I(\theta) = [(r(\theta) - s)K_I(P) + (t - r(\theta))K_I(Q)]/(t - s), \quad (3)$$

where $r(\theta)$ is the radius of any point and s and t are defined in Figure 2a. The exact results for an elliptical crack with $s = t$ can be fitted perfectly by Equation (3) by adjusting α_0 . With this value of α_0 (viz., $\alpha_0 \approx 0.201$) retained for all cases, the agreement with other known solutions is as illustrated in Figure 3. Even for protrusions and retarded segments of significant magnitude ($s/t \sim 0.5$), the approximation is always accurate to within a few percent. Most importantly for the present application, it gives fair estimates of the dependence of K_I on α and of the relative magnitudes at extrema on the same crack. These are

the properties essential to balancing the tendency of $K_I(\theta)$ to make a crack regular against the disrupting effects of the microstructure. Note that $K_I(Q)$ is correctly predicted to diverge and $K_I(P)$ to vanish as $\alpha \rightarrow 0$. This implies that very sharp irregularities of the crack front are unlikely to be found.

K_I on Surface Breaking Cracks

Convenient algorithms for estimating K_I around semi-elliptical surface cracks have been given by Newman and Raju (2,3). If $2c$ is the crack's length on the surface, and a its depth, then for $2c \geq a$,

$$K_I(\phi) = \sigma \frac{\sqrt{\pi a}}{E(k)} F\left(\frac{a}{c}, \phi\right) \quad , \quad (4)$$

where E is the elliptic integral of the second kind, $k^2 = 1 - a^2/c^2$, and F is a polynomial in a/c and c/a and a simple trigonometric function of ϕ , the parametric angle of the ellipse.

To account for departures of the crack front from the semi-elliptical shape, Equation (4) was combined with Equation (3) by the following ansatz. The center of mass and the moments of inertia I_x and I_y of an irregular crack were found, and taken to define the center and semi-axes ($c = 2\sqrt{I_y}$ and $a = 2\sqrt{I_x}$) of a smoothed semi-elliptical crack. The x axis was rescaled by the factor a/c , so that the fitted semi-elliptical crack would become a semi-circular crack, and the mirror image was added (Figure 2(b)) to generate an entire irregular, approximately circular crack. Equation (3) was then used to generate values of $K_I(\theta)$ around this scaled crack, normalized to $K_I(a) = 2\sigma_\infty\sqrt{a/\pi}$. These normalized values of $K_I(\theta)$ represent the relative acceleration and retardation of local protrusions and retarded segments. These values were then multiplied by the results of Equation (4) for the semi-elliptical crack of semi-axes c and a , to account for gross shape and size effects.

MONTE CARLO SIMULATIONS

A Monte Carlo simulation begins by generating a random, two-dimensional pattern of grains lying in the plane of growth. A small crack is introduced, spanning a few grains or perhaps just one. The crack front is divided into discrete segments, which increase in number as the crack grows, so that they remain small relative to the microstructure. The position of the crack front is updated at regular intervals according to the laws governing

the growth of each segment, which embody the dependence of the growth rate on the details of the surrounding microstructure. The advance of the crack front is always assumed to be in the direction of the normal to it at any point. If a newly calculated crack front possesses unphysical loops or overlapping spurs, these are eliminated by deleting the offending segments.

CLOSURE-INDUCED SHAPE EFFECTS IN AL 7075-T6

A typical simulation of a surface crack is shown in Figure 4. The grain structure there corresponds to that exposed on a plane cut normal to the rolling direction and normal to the surface of a rolled sheet of Al 7075-T6. The average grain length normal to the rolling direction is $\sim 120 \mu\text{m}$, and the average depth normal to the surface is $\sim 20 \mu\text{m}$. After a brief crystallographic phase immediately following initiation, small fatigue cracks in such specimens grow in a transgranular noncrystallographic mode. Plasticity-induced closure causes them to slow down upon reaching each grain boundary and accelerate as each grain is being traversed (Zurek et al (4)). Observations on just the visible surface outlines of individual cracks have led to laws relating the rate of advance of each surface tip to its distance, z , from the next grain boundary. In the simulations shown here, the same law has been assumed to prevail all around the crack front, with z always measured along a line radiating from the original center of the crack. The law has the form

$$\frac{dw}{dN} = A\Delta K^2 (1-\beta z/2\bar{r})^2 H(1-\beta z/2\bar{r}) \quad (5)$$

where w refers to displacement of the crack front along the normal direction, \bar{r} is the average radius of the crack, and β is a parameter whose value for visible surface crack tips in Al 7075-T6 is ~ 0.5 . H is the Heaviside step function, and its presence signifies the possibility of part or all of the crack front being arrested by closure. Small cracks in Al alloys are also arrested temporarily by grain boundaries, but this effect is relatively weak in large-grained specimens and it has been ignored here. (Note, however, that grain boundary arrest is readily treated in the simulations, and it will be a principal subject of future studies.)

The simulation shown in Figure 4 exhibits some important general characteristics of small crack growth. When the crack is small relative to the microstructure (less than or equal to a few grains), the crack front can be highly irregular. Parts of it may be arrested by closure (or grain boundary blockage), and the aspect ratio, i.e., the ratio of the average depth to the surface

length, fluctuates widely from crack to crack and as the crack grows.

Some statistics of the aspect ratio, defined to be $a/2c$, where $a = 2\sqrt{I_x}$ and $c = 2\sqrt{I_y}$, are shown in Figure 5 as functions of the average crack radius, defined as $\bar{r} = \sqrt{ac}$. Both experimental and theoretical data in Figure 5 were calculated from observations or simulations of many cracks: 16 experimental cracks and 100 simulations. The experimental data were obtained by splitting open specimens after various fatigue exposures and measuring the outline of the fatigue crack front. One striking feature of the experimental data is that many cracks show $a/2c > 0.5$ at $50 \mu\text{m} \leq \bar{r} \leq 100 \mu\text{m}$. This characteristic is reproduced in the simulation (continuous curves of Figure 5), and can be traced to the fact that the grains are highly nonequiaxed. Values of z tend to be much smaller for those segments of the crack front propagating down into the specimen, and Equation (5) then implies that $a/2c$ will be augmented. The agreement between the experimental data and the simulations, both in average and deviation, supports the hypothesis that the law of growth obtained from surface observations is also valid for segments of the crack growing down into the bulk.

When the crack spans more than a few grains, the relative strength of microstructural factors decreases, and in the simulations the crack front is restored to its smooth equilibrium configuration, with aspect ratio ~ 0.4 , by the variation of $K_I(\theta)$ according to Equations (1)-(4). For very small cracks, $a/2c$ is found experimentally to be ~ 0.2 . This was mimicked in the simulations by assuming that initiation (e.g., by fracture of stringers of particles or by persistent slip bands forming microcracks) generates relatively long, shallow cracks, about $90 \mu\text{m} \times 4 \mu\text{m}$. Such an assumption is, of course, testable by appropriate experiments. For the largest cracks, the experimental values of $a/2c$ in Figure 5 fall below 0.4 because the cracks were grown in bending.

OTHER STATISTICS OF THE SHAPE OF SMALL CRACKS

There are many other statistical properties of small cracks that can be conveniently studied by Monte Carlo simulations. These include: (1) the degree of irregularity of the crack front; (2) the covariance between the rates of advance of different segments of the crack front; (3) the persistence of fluctuations in the degree of irregularity or the aspect ratio; (4) the relationships between either the aspect ratio or the degree of irregularity and the rate of growth averaged around the crack front; and (5) the correlation between the visible surface crack velocity and the velocity of the invisible subsurface crack.

CONCLUSIONS

Statistical data for small cracks can be directly related to the stochastic nature of the microstructure by appropriate laws of growth. Monte Carlo simulations present a powerful and flexible method of exploring this relationship.

Comparison of the simulations with experimental data allows existing laws of growth to be tested and optimized. This process both illuminates the physical mechanisms controlling growth, and forms the basis for accurate, calibrated models for predicting fatigue lifetime. The utility of the experimental data available for comparison with the simulations does not depend on being able to measure the actual pattern of grains through which each individual crack grows.

The simulations offer a powerful and convenient way of investigating whether the laws of growth for subsurface portions of a crack are the same as those deduced for growth of the visible surface crack tips. They give immediate insight into the question of whether fluctuations seen in the velocity of surface crack tips are generated by local surface phenomena or can be attributed to stochastic variations in the subsurface crack shape and growth rate.

Acknowledgements

The authors are grateful to D.C. Lim for her assistance with the computer programming. The research was sponsored by the Air Force Office of Scientific Research (AFSC) under Contract No. F49620-85-C-0034. The United States Government is authorized to reproduce or distribute reprints for governmental purposes notwithstanding any copyright notation hereon.

REFERENCES

1. Mastrojannis, E.N., Keer, L.M. and Mura, T., Int. J. Fract., 15, 1979, pp. 247-58.
2. Newman, J.C., Jr and Raju, I.S., Eng. Fract. Mech. 15, 1981, pp. 185-92.
3. Newman, J.C., Jr. and Raju, I.S., NASA Technical Memorandum 85793, April 1984.
4. Zurek, A.K., James, M.R., and Morris, W.L., "Met. Trans. A 14, 1983, pp. 1697-1705.

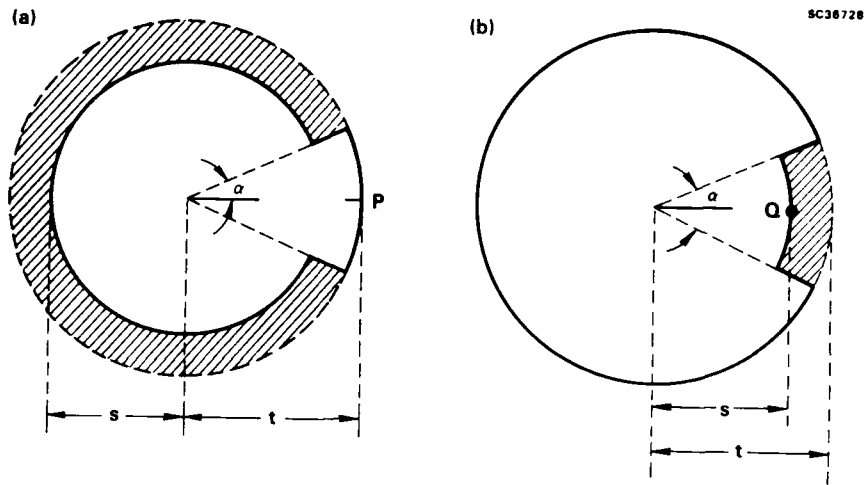


Figure 1. The geometries of (a) the protrusion and (b) the retarded segment used to estimate K_I at the extrema of an irregular plane embedded crack.

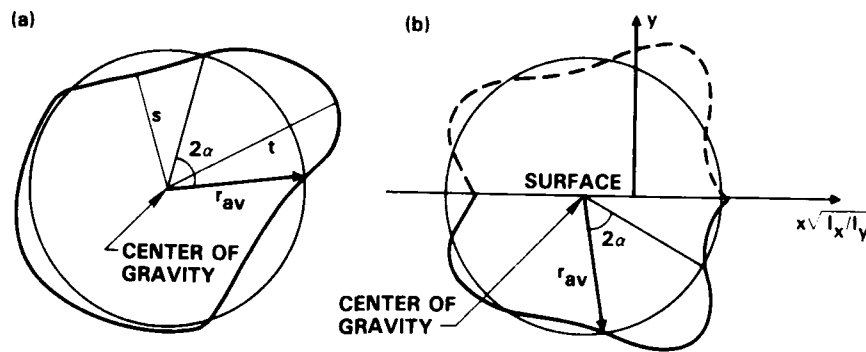


Figure 2. Illustrating the procedures used to define protrusions and retarded segments on an irregular crack for the purpose of invoking Equations (1)-(3).

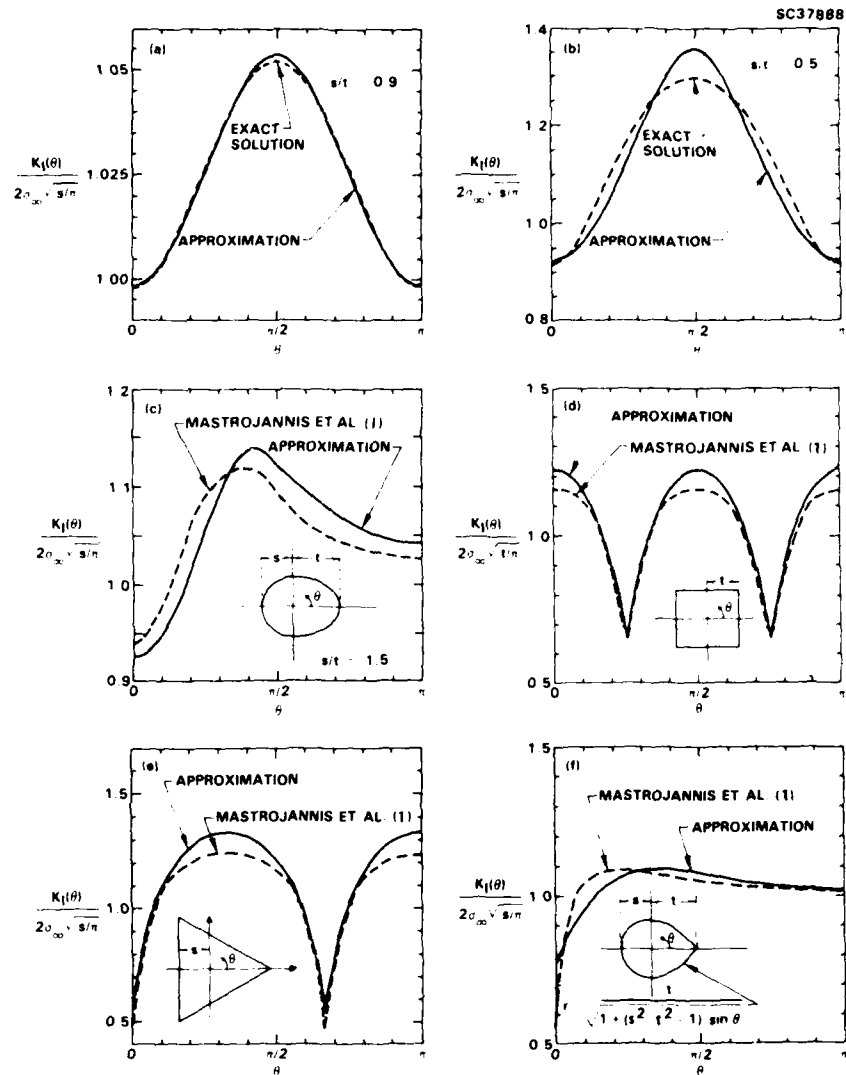


Figure 3. Testing the algorithm Equations (1)-(3) against known solutions for embedded irregular cracks. (a) and (b) are for ellipses with semi-axes as marked. The shapes of the cracks in (c)-(f) are shown in insets.

FATIGUE 87

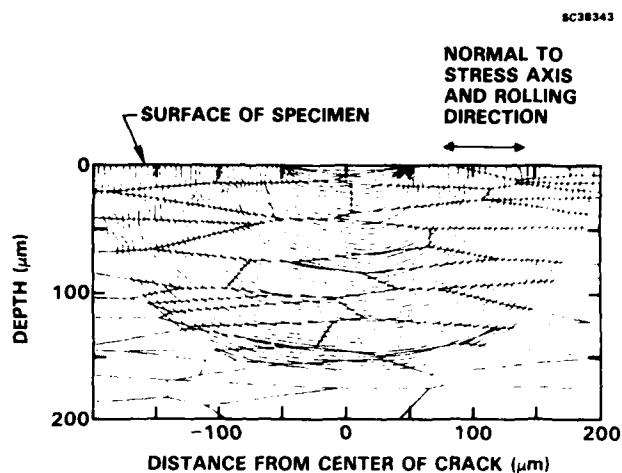


Figure 4. A simulation of the growth of a surface crack in AL 7075-T6. The position of the crack front is recorded at approximately equal intervals in crack size \sqrt{ac} , rather than in cycles.

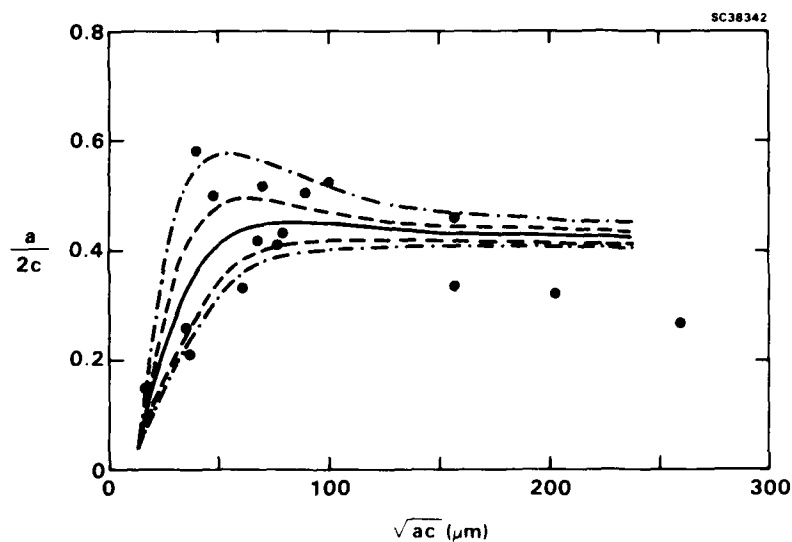


Figure 5. Aspect ratios of small cracks in AL 7075-T6 as a function of the crack size \sqrt{ac} . The data (circles) were taken at a stress amplitude of 408 MPa. The curves show the distribution of $a/2c$ found in simulations of 100 cracks. The solid curve shows the average of $a/2c$ in the simulations. The dashed curves should contain 70%, and the chain-dot curves 95%, of the data.

THE EFFECT OF α -PLATELET MORPHOLOGY AND β -GRAIN SIZE ON THE INITIATION AND GROWTH OF SHORT FATIGUE CRACKS IN Ti65S

P.J. Hastings*, M.A. Hicks[†] and J.E. King*

The effects of α -platelet alignment and prior β grain size on short fatigue crack growth in a β -heat treated titanium alloy Ti65S have been investigated. At crack depths of the order of the α colony size faster crack growth was seen in aligned than in basketweave structures, although the shortest cracks grew at similar rates in both. Large increases in prior β grain size appear to increase crack growth rates.

INTRODUCTION

Ti65S is a near- α titanium alloy widely used as a compressor disc and blade material in aeroengines. A typical heat-treatment would involve β -heat treatment followed by conventional ageing to give a microstructure consisting of colonies of α -platelets within equiaxed prior β grains with average grain diameter around 1.5mm.

The degree of alignment of the α -platelets is dependent on the cooling rate from above the β -transus temperature. Fast cooling produces a 'basketweave' Widmanstätten morphology, whereas a slow cooling rate results in an aligned structure. Within a compressor disc forging there will be variations in prior β grain size and α platelet alignment and colony size due to both the level of work and the local cooling rate.

With relatively large grain sizes such as that used in Ti65S cracks can be physically quite large, i.e. several hundred microns, but still "microstructurally short". Thus cracks which may well be detectable by conventional NDI methods can still show the features of "short" crack growth, and thus the study of this regime of crack

*Dept. of Metallurgy & Materials Science, University of Nottingham.

[†]Rolls-Royce plc, Derby.

FATIGUE 87

propagation in Ti65S is important in understanding component behaviour.

A number of investigations on β -processed titanium alloys have shown that microstructurally short cracks can propagate at much higher rates than long cracks at the same nominal ΔK values (14). The object of the current work has been to determine the effects of microstructural variations, i.e. α -platelet morphology and prior β -grain size, in this short crack regime, in the β processed alloy Ti65S.

EXPERIMENTAL

Material

The material was taken from a forged compressor disc, supplied by Rolls-Royce plc, which had undergone the following heat-treatment: solution treat at 1050°C (in the β phase field), forced air cool, age at 550°C for 24 hrs., air cool.

This produces a basketweave Widmanstätten distribution of α -platelets within the prior β grains, which will be referred to as the as-received microstructure. A second microstructure was studied, developed by furnace cooling from the β phase field to give a structure of coarser more aligned α platelets, but with the same prior β grain size. This will be called the aligned structure. Figure 1(a) shows a well developed basketweave microstructure formed on rapid cooling from the β phase field and 1(b) shows an aligned structure characteristic of the slower cooling rate. Due to the large size and variation in thickness across a typical disc forging there are occasional aligned regions in the as-received structure because of the difficulty of maintaining a sufficiently fast cooling rate throughout the disc. The nominal composition of the alloy, Ti65S, (in wt.%) is 6Al-5Zr-0.5Mo-0.25Si-0.2Fe-100 ppm Hf, balance Ti.

Testing Procedures

Fatigue testing was carried out in 1 point bend on a Mayes servohydraulic testing machine at 20°C in laboratory air. The specimens used were smooth 10mm square bars with top surfaces electropolished to eliminate any residual stresses from specimen machining and grinding operations. Tests were run at a frequency of 10 Hz with a maximum top surface stress σ_{\max} of 850 MPa, at a stress ratio ($\sigma_{\min}/\sigma_{\max}$) R = 0.1. Tests were stopped at varying intervals, depending on whether or not a crack was present and acetate replicas of the surface region experiencing the maximum bending moment were taken at mean load.

After gold sputter coating the replicas to increase their reflectivity, surface crack length was measured using an optical microscope. Where possible, the two crack ends were treated

FATIGUE 87

separately, as this method showed more clearly any interaction of either of the crack tips with microstructural features.

Crack growth rates were calculated by dividing the increment of crack length by the number of cycles over which this increment occurred. The alternating stress intensity range was calculated using the Shah and Kobayashi (5) solution for a semi-elliptical crack in pure bending.

Measurements of crack shape were carried out using previously tested specimens, containing fatigue cracks. The specimens were loaded up in 3 point bend to the test mean load, to open the crack. The specimen was then heated, under load, to 500°C for 1 hour, to oxidise the specimen surface and the crack faces. The colour of the oxide formed was light brown. After cooling down, the specimen was broken open, leaving the fatigued region of the fracture surface clearly distinguishable from the rest. The 'top surface' length and depth at the mid point of the fatigue region were then measured using a travelling microscope and the a/c ratio calculated.

RESULTS

Figure 2 shows crack growth rate (da/dN) vs. nominal stress intensity range (ΔK) and crack depth (a) for the as-received (2(a)) and aligned (2(b)) microstructures. The data are presented as scatter bands of points for a number of tests on each microstructure. The as-received data were taken from eight individual cracks and the aligned data from five cracks.

Initiation was usually found to occur late on in the life of the specimen from slip bands in small α platelet bundles (≈ 5 -10 platelets) although deep, long slip bands formed within the α colonies within the first 10% of the test life. Crack arrest was seen to occur at the first α -platelet bundle boundary. By the time cracks had reached lengths of the order of the prior β grain size, microstructural features such as grain and colony boundaries produced no obvious retardation of crack growth as can be seen in figures 3(a) and 4(a). Crack paths were tortuous with occasional crack branching, propagating across α platelets and occasionally along α -platelet boundaries.

Figures 3 and 4 show typical plots of da/dN vs. ΔK and a for cracks in the as-received and aligned microstructures respectively, and micrographs showing early stages of growth. The first growth rate minimum in each case corresponds to crack retardation at the boundary of the α platelet bundle in which the crack has initiated (3(b), (c) and 4(b), (c)). The plots show considerable fluctuation in growth rate in the early stages, as the cracks experience microstructural variations. These two figures show clearly the similar initiation behaviour in both microstructures.

Initial crack shape measurement at lengths of the order of 1 mm

FATIGUE 87

showed a generally semi-elliptical form, with an a/c ratio of about 0.85.

DISCUSSION

Initiation Behaviour

Occurrence of initiation late in the specimen life agrees with the findings of Bolingbroke and King (2) working on β heat treated IMI318. Deep, long slip bands were also found to appear within the first 10% of life in the IMI318, but initiation finally occurred in grain boundary α -platelets. Such platelets were not present in the as-received Ti65S examined here, and although some grain boundary α -platelets were present in the aligned Ti65S microstructure, initiation was not observed in these particular features, but in α -platelet bundles within α colonies.

Effect of α -platelet alignment

The effect of α -platelet alignment can most readily be seen by comparing the upper bound lines of the scatter bands for the two sets of data, i.e. the maximum growth rates seen for a particular ΔK or a . These lines are shown in figure 5 with an additional scale of approximate microstructural dimensions.

When the crack depth is of the order of α platelet bundle size there is a lot of scatter in the data due to retardation taking place at platelet boundaries but essentially there is no difference between the aligned and as-received structures. This is to be expected, as at this crack depth microstructural features encountered are similar in both structures. A clear difference can be seen, however, when the crack is moving through α colonies, i.e. at crack depths between platelet bundle size and prior β grain size. The growth rates in the as-received structure are lower than growth rates in the aligned structure because the crack has to take a more tortuous path in the basketweave microstructure, crossing α -platelets in different orientations. In the aligned structure cracks have a relatively easy path right across a colony of α platelets in similar orientations. By the time crack depth reaches the prior β -grain size the crack no longer behaves like a short crack and microstructure (especially α platelet alignment) ceases to have a strong effect. Thus the lines for the two microstructures merge.

Effect of Prior β Grain Size

Figure 6 shows the data of Brown and Hicks (1) for a coarse grained highly aligned structure in IMI685. Prior β grain size in this material was approximately 5mm compared to an average grain size of approximately 1.5mm in the Ti65S. The growth rates are considerably higher than those measured in this work. This suggests that prior β grain size is also important although it

FATIGUE 87

should be noted that the coarser grained material was also more aligned than the material in the current study. Further work is continuing on this aspect of behaviour.

CONCLUSIONS

1. The first microstructural barrier experienced by short cracks is the first 'platelet bundle' boundary. This is the same for aligned and basketweave microstructures, and similar growth rates are seen in the two structures at crack depths of the order of the α -platelet bundle size.
2. The degree of alignment of the α platelets is important, especially when crack depth is of the order of the colony size (i.e. travelling through the first colony). The aligned microstructure shows higher growth rates than the as-received microstructure, because the crack is not deflected by meeting platelets in widely differing orientations as in the basketweave (as-received) structure.
3. It appears that prior β -grain size is important; a larger grain size increases the crack growth rate for a given ΔK (and crack depth), but there is also a colony size and alignment effect.

ACKNOWLEDGEMENTS

The authors are grateful to Professor J.S.L. Leach for providing laboratory facilities and to Dr. M. Cope of Rolls Royce plc for helpful discussions. Financial support from Rolls Royce plc and the SERC for one of the authors (PJH) is gratefully acknowledged. Material and specimens for the work were provided by Rolls Royce plc.

REFERENCES

- (1) Brown, C.W. and Hicks, M.A., *Fat. Eng. Mat. Struct.*, Vol. 6, No. 1, 1983, pp. 67-76.
- (2) Bolingbroke, R.K. and King, J.E., "The Growth of Short Fatigue Cracks in Titanium Alloys IMI550 and IMI318", Proceedings of the Second Engineering Foundation Conference on "Small Fatigue Cracks", Edited by R.O. Ritchie and J. Lankford, the Metallurgical Society AIME, Pennsylvania, 1986.
- (3) Gerdes, C., Gysler, A. and Lütjering, G., "Propagation of Small Surface Cracks in Ti-Alloys", Proceedings of the AIME Conference on "Fatigue Crack Growth Threshold Concepts", Edited by D.L. Davidson and S. Suresh, AIME, New York, 1984.
- (4) Hicks, M.A., Howland, C. and Brown, C.W., "The Metallurgy of Light Alloys", No. 20, pp. 252-259, Institution of Metallurgists, 1983.
- (5) Rooke, D.P. and Cartwright, D.J., "A Compendium of Stress Intensity Factors", pp. 297-299, HMSO, London, 1976.

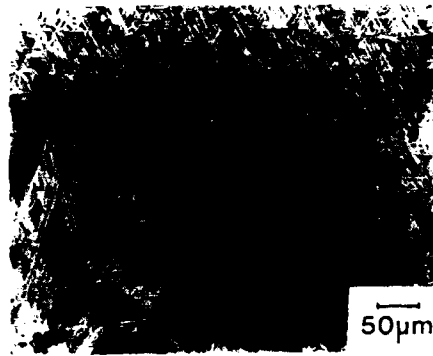


Figure 1(a) As-received (basketweave) microstructure.

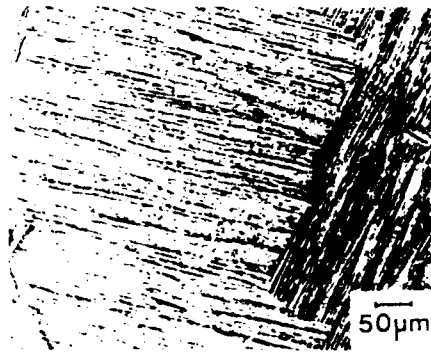


Figure 1(b) Aligned microstructure.

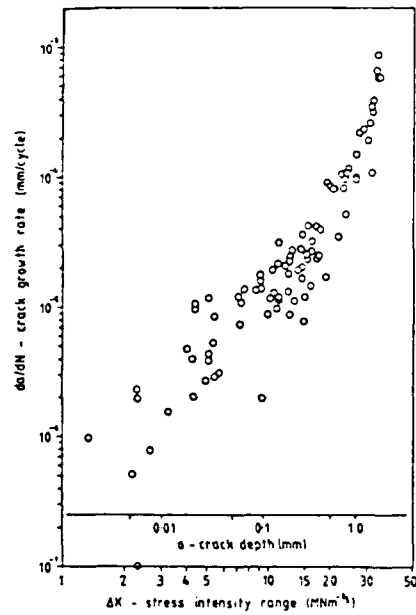


Figure 2(a) Crack growth data for as-received material.

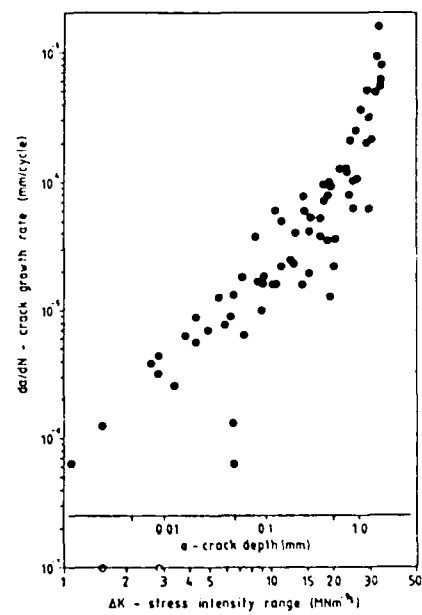


Figure 2(b) Crack growth data for aligned material.

FATIGUE 87

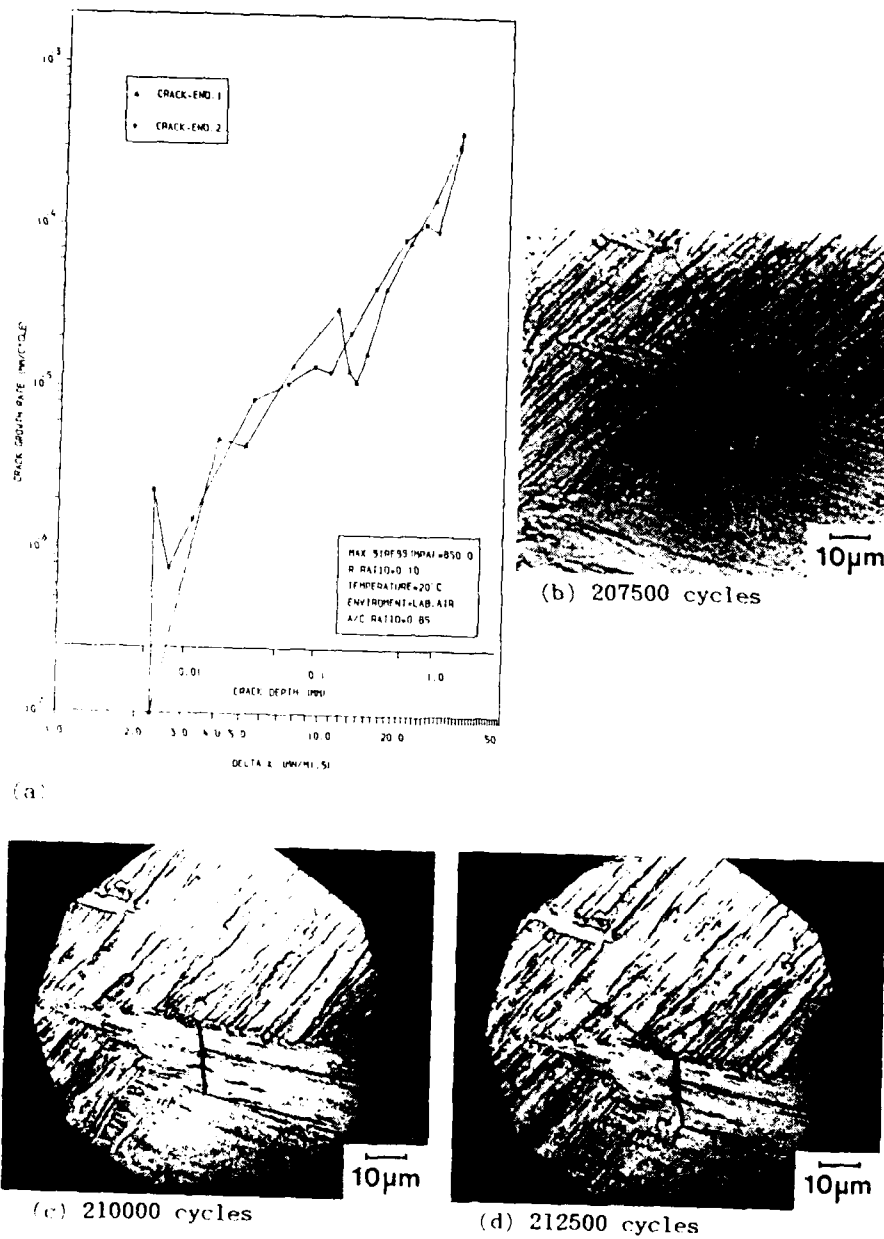


Figure 3 (a) - Typical da/dN vs. ΔK plot for as-received material; (b), (c), (d) - replicas of early stages of crack growth.

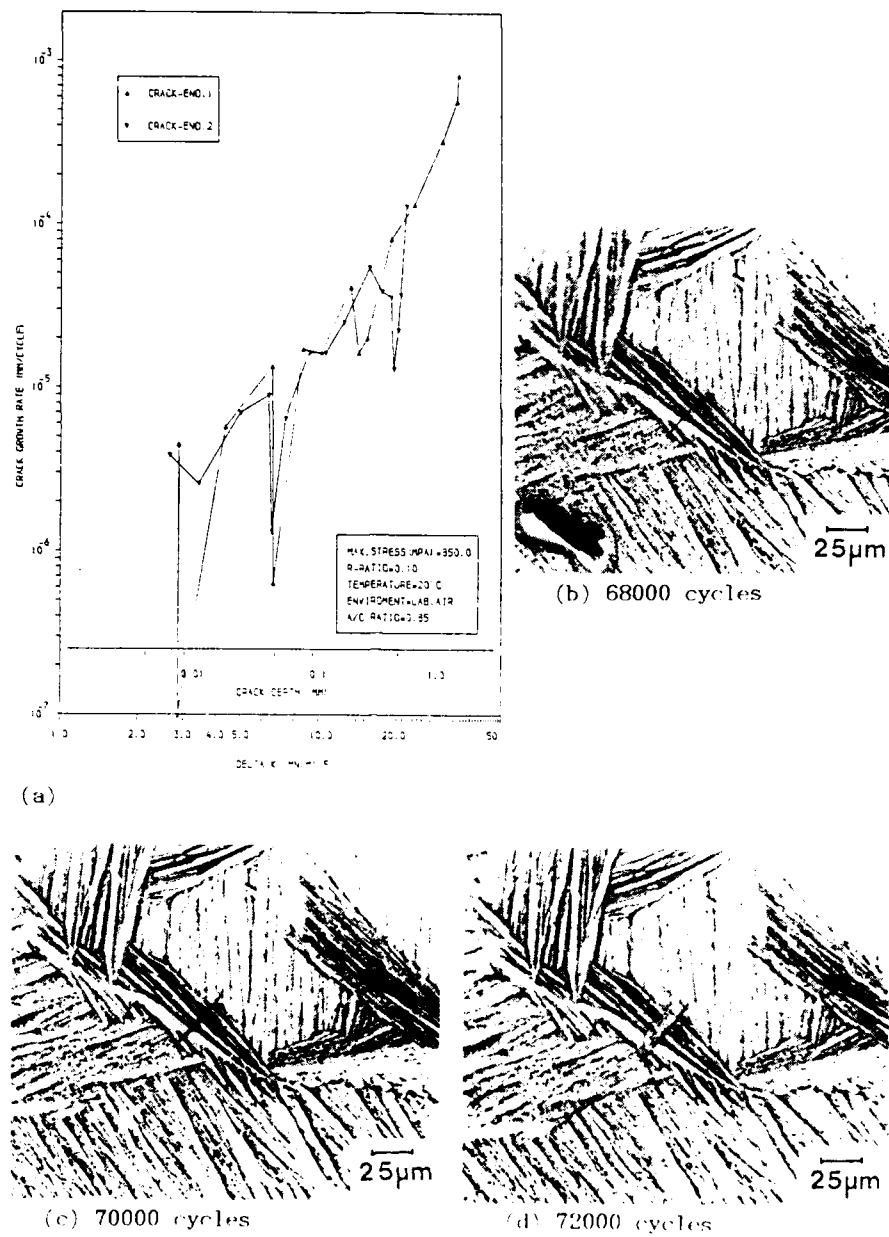


Figure 4 (a) Typical da/dN vs. ΔK plot for aligned material; (b), (c), (d) - replicas of early stages of crack growth.

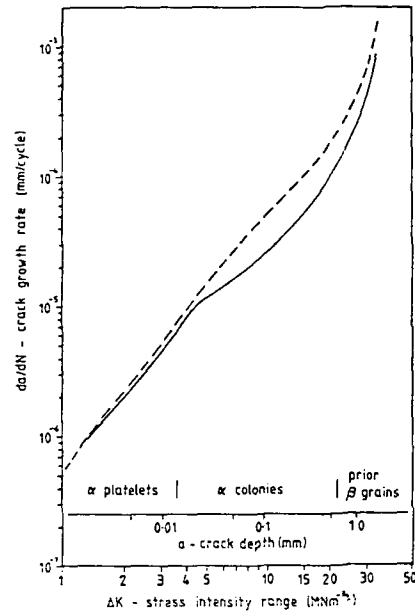


Figure 5 Comparison between growth rate data in as-received and aligned microstructures (approximate microstructural dimensions shown).

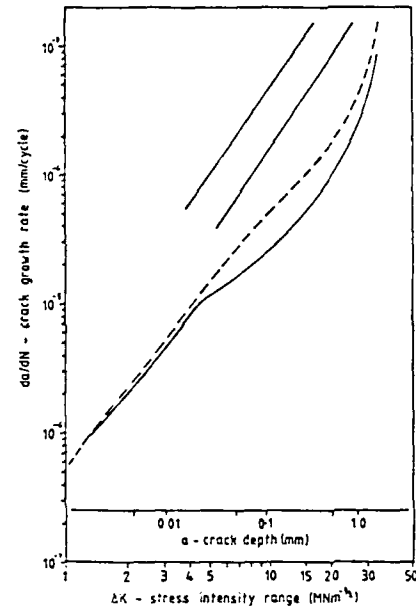


Figure 6 Comparison of growth rate data (Figure 5) with data band of Brown and Hicks.

FATIGUE 87

FATIGUE 87

THE INITIATION AND GROWTH OF SMALL FATIGUE CRACKS IN COPPER AT ROOM AND CRYOGENIC TEMPERATURES

I. B. Kwon, J. Weertman and M. E. Fine *

The microstructural evolution of small fatigue cracks in copper, both polycrystals and single crystals, has been investigated by OM, SEM and TEM using surface replicas at 298°K, 77°K and 4.2°K. The basic initiation processes of small fatigue cracks are unchanged at different test temperatures and in different environments even though the lower temperatures and inert environments retard the fatigue crack initiation. The temperature and environmental dependences of fatigue damage during the early stages of fatigue are discussed based on the microscopic observations.

INTRODUCTION

Just initiated small fatigue cracks often with pit shapes have been observed along slip bands emerging on the surface by the optical microscope (OM) or electron microscopes (SEM and TEM) beginning about 85 years ago as reviewed in reference (1). Often these cracks are periodically spaced. Although the characteristics of persistent slip bands (PSB's) including the corresponding dislocation structures in fatigue have been extensively studied in the recent decade (for example, see reference (2)), the detailed microscopic mechanism for the development of small fatigue cracks during the very early stages of fatigue is still incompletely known. It is generally accepted that fatigue cracks are initiated along slip bands or grain boundaries in notch-free pure metals. Since the free surfaces of materials are more energetically unstable than the bulk, cracks are thought to originate at the surface. Strong evidence for this is that repeated removal of surface layers during fatigue testing of copper extends the fatigue life enormously (3).

* Department of Materials Science and Engineering and Materials Research Center, Northwestern University.

FATIGUE 87

It is well known that the fatigue life in FCC metals is longer at low temperature than at room temperature (4), implying that the test temperature influences the initiation and/or propagation processes of fatigue cracks. However, relatively little attention has been given to the operating microstructural processes at cryogenic temperature during the early stages of fatigue. Since the fatigue tests at low temperatures are generally performed in cryogenic liquids or inert atmospheres, the environmental effect must be taken into consideration for the correct analyses of experimental results obtained at low temperatures. Definitive and critical experiments are needed to elucidate the temperature and environmental dependences of fatigue crack initiation.

In the present research, the microstructural processes leading to the initiation and growth of fatigue cracks as small as $0.1\text{ }\mu\text{m}$ in depth were investigated by OM, SEM and TEM at different test temperatures (298°K , 77°K and 4.2°K) with different environmental conditions. High purity copper was chosen for study, single as well as polycrystalline specimens, because more is known about fatigue of copper than any other metal. Qualitative and quantitative analyses were made based on the microstructural observations to develop a comprehensive theoretical model of fatigue crack initiation.

EXPERIMENTAL PROCEDURES

Polycrystalline Copper

Dog-bone-shaped specimens were machined from 99.98 % OFHC copper plate, annealed and then polished. Fatigue tests at 298°K and 77°K were made at low strain amplitude of about 10^{-3} to 10^{-4} under fully reversed total strain control. Cyclic responses such as cyclic hardening curves and cyclic stress-strain curves were monitored during the fatigue tests. At 4.2°K , fatigue tests were performed under load control due to experimental limitations. Corresponding strain amplitudes were determined using foil strain gages at this temperature. The cycling at 298°K was done in laboratory air (40 % relative humidity) and in paraffin oil which has a very low dissolved oxygen and water vapor content whereas the specimens fatigued at 77°K and 4.2°K were immersed directly in cryogenic liquids.

Copper Single crystals

Copper single crystals were grown by the Bridgman technique from high purity copper shot (99.999 %). Fatigue specimens oriented for single slip (Schmid factor = 0.47) were prepared by EDM and chemically polished. The primary slip system is $(11\bar{1})$ $[101]$. Fatigue tests were carried out under load control in the push-pull mode at the different temperature and environmental

FATIGUE 87

conditions, laboratory air and He gas at 298°K, He gas and liquid N₂ at 77°K and liquid He at 4.2°K. The stress amplitude was built up gradually to the final stress amplitude during the first 500 cycles in order to avoid severe specimen deformation during the initial stages of the test. The hysteresis loops were recorded using foil strain gages during the fatigue tests.

The primary observation methods were to examine surface replicas taken periodically from the fatigued specimens using OM, SEM and TEM. Particularly, the replication technique with SEM has several advantages. The whole gage section can be examined easily and the biggest crack after a certain amount of cycling can be located. The length and depth of small fatigue cracks can be measured by means of the shadowing geometry. Furthermore, the microstructural evolution of fatigue cracks can be investigated at the same site on the specimen as a function of number of fatigue cycles.

RESULTS AND DISCUSSION

Polycrystalline Copper

Microscopic observations of the fatigued specimen surfaces reveal that slip bands formed at the lower temperature are relatively thin and closely spaced when compared to those at the higher temperature. This result is in good agreement with Hull (5). On the other hand, the features of slip bands observed after fatiguing at 298°K in paraffin oil is rather similar to that at 77°K in liquid N₂. Thus the uniform slip process observed at the lower temperature seems to result at least in part from the inert environment.

A periodical array of pit shaped small fatigue cracks forms along slip bands during the very early stages of fatigue at less than 1 % of the fatigue life. This phenomenon is observed at 298°K in air and in paraffin oil, at 77°K and even at 4.2°K. These pits grow and coalesce into continuous microcracks. Figure 1 shows a typical SEM micrograph of a replica taken from a specimen cycled for 500 cycles at 4.2°K. The plastic strain amplitude corresponding to the applied stress amplitude of 200 MPa was determined to be approximately 3×10^{-3} . Two possible mechanisms may be considered for the formation of such small fatigue cracks; primarily localized accumulation of fatigue damage due to irreversible slip and secondly fatigue damage due to accumulation of lattice defects such as vacancies perhaps assisted by thermally activated processes. In view of the pit shape of small fatigue cracks, it was suggested that the first factor is not solely responsible for the formation of cracks (6). While thermal activation may accelerate fatigue crack initiation by cross slip and/or vacancy diffusion under an appropriate

FATIGUE 87

circumstance, the basic mechanism for fatigue crack initiation must operate in the absence of thermal activation since pit shaped cracks have been observed down to 4.2°K.

In order to explain the formation of such small fatigue cracks, two dislocation glide mechanisms have been suggested (1, 6). In both dislocation glide mechanisms, vacancies are suggested to be swept by dislocations from the bulk to the surface, a process originally imagined by Wilkov and Shield (7). One process is the dislocation spiral mechanism coupled with an inverse whisker growth process and the second is the glide of dislocation dipoles in the slip bands to form a short depression on the surface of specimen. In addition, the periodical configuration of small fatigue cracks seems to be related to the ladder-like dislocation structure of slip bands since the spacing between the small fatigue cracks observed on the surface is almost the same as the ladder rung spacing reported by Basinski et al. (8).

Observations of the same site on the specimen versus number of fatigue cycles by SEM using the replication technique have facilitated the quantitative analysis of the fatigue crack initiation processes. Cracks as shallow as 0.1 μm in depth were identified with reasonable certainty and thus the number of cycles to initiate such cracks, N_i , was bracketed. Figure 2 shows the fatigue crack initiation data at 298°K and 77°K under different strain amplitudes. The cumulative plastic strains, $4N(\Delta\epsilon_p/2)$, for various numbers of cycles were obtained by summing up the measured plastic strain amplitudes. It was found that the cumulative plastic strain required to initiate fatigue cracks greater than a 0.1 μm in depth along slip bands at 77°K in liquid nitrogen is over ten times higher than that required at 298°K in laboratory air. This change between tests run in liquid nitrogen and in air arises from the combined temperature and environmental effects. As shown in Figure 2, the cumulative plastic strain required to initiate small fatigue cracks at 298°K in paraffin oil is considerably greater than that at 298°K in air.

It is of interest to compare specimens B, F and G which have been fatigued near the same plastic strain amplitude at cyclic saturation under different temperature and environmental conditions. Designating the cumulative plastic strain required to initiate small fatigue cracks in various test conditions by F_{RA} (at 298°K in air), F_{RP} (at 298°K in paraffin oil) and F_N (at 77°K in liquid nitrogen), the ratios are obtained as follows;

$$F_N / F_{RA} = 30 \quad (\text{due to combined temperature and environmental effects})$$

$$F_{RP} / F_{RA} = 10 \quad (\text{due to the environmental effect alone})$$

$$F_N / F_{RP} = 3 \quad (\text{due to the temperature effect alone})$$

Therefore, it is concluded that the initiation processes of small fatigue cracks is more sensitive to the change of environment than to the change of temperature. A similar analysis of the separate effects of temperature and environment on the fatigue life in copper, published by Holt and Backofen (9), shows the same trend.

The growth behavior of individual fatigue crack can be investigated by means of a series of SEM micrographs taken from the same site on the specimen. It is observed during the early stages of fatigue that small fatigue cracks are initiated in almost all slip bands in a grain and grow continuously at 298°K whereas at 77°K these are limited to form and grow along certain slip bands. After the small fatigue cracks initiate along slip bands, the cracks grow as stage I cracks having a semi-elliptical form. Through these observations, the growth rate of small fatigue cracks in stage I is measured to be on the order of 0.1 nm/cycle at 298°K and 77°K. This value is comparable with those of Basinski et al. (one Burgers vector/cycle, 10) and Laird et al. (1 angstrom/cycle, 11). On the other hand, the growth rate is higher at 77°K than at 298°K in the case of near the same plastic strain amplitude. For example, the growth rates in specimen A and D are 0.5 nm/cycle and 0.8 nm/cycle respectively (refer to Figure 2 for fatigue conditions). This result may indicate that fatigue damage at 77°K is focused on the initiated cracks, which are fewer and sharper at 77°K than at 298°K, rather than towards the initiation of new cracks.

In the present research, it is found that the formation of extrusions is considerably reduced but still occurs at low temperatures. In addition, slip bands consist of extrusions and cracks (or intrusions), however sometimes only cracks (or intrusions) were observed along slip bands on the surface of specimen when fatigued particularly at low strain amplitudes. It thus appears that the formation of extrusions may not be a requirement for fatigue crack initiation.

Copper Single Crystals

The microstructural evolution of small fatigue cracks in copper single crystals has been examined with surface replicas taken periodically during fatigue testings. Figure 3 shows typical SEM micrographs of replicas taken from the (321) plane of copper single crystals fatigued under various test conditions. Since the stress axis is $[\bar{1}4\bar{5}]$, the most severe fatigue damage is produced on the (321). Figure 3a shows the fatigue damage in a specimen fatigued at 298°K in purified helium gas for 1000 cycles with τ of 30 MPa. Several cracks not greater than 0.4 μm in depth form along slip bands. The features of fatigue cracks developed in a specimen fatigued for 5000 cycles at 77°K in He gas with τ of 50 MPa and at 4.2°K in liquid helium with τ of 70

FATIGUE 87

MPa are shown in Figure 3b and 3c. The depth of biggest crack along slip bands is 0.1 μm and 0.06 μm , respectively. Fatigue conditions and experimental results on copper single crystals are summarized in Table 1. When the crack depths measured after the numbers of fatigue cycles given in Table 1 are compared, it is concluded that the initiation of small fatigue cracks is retarded at lower temperatures and in inert environments in a manner similar to that observed in polycrystalline copper.

Table 1 - Experimental Data on Copper Single Crystals

Temperature- Environment	τ * (MPa)	$\Delta\gamma_p/2$ * ($\times 10^{-4}$)	Spacing of slip bands	Thickness of a slip band	Deepest crack; cycles
298°K-Air	30	2	4.8 μm	1 - 1.8 μm	0.5 μm ; 500
298°K-He gas	30	2	3.1 μm		0.4 μm ; 1000
77°K-Liq. N ₂	50	4.2	1.9 μm	0.8 - 1 μm	0.2 μm ; 5000
77°K-He gas ²	50	4.2	1.8 μm		0.1 μm ; 5000
4.2°K-Liq. He	70	9	1.5 μm	< 0.5 μm	0.06 μm ; 5000
4.2°K-Liq. He	60	4	1.5 μm		0.04 μm ; 5000

* τ and $\Delta\gamma_p/2$ are resolved shear stress and resolved plastic shear strain after 5000 cycles estimated using foil strain gages respectively.

According to the microstructural observations with OM and SEM, the configuration of the slip bands on fatigued copper single crystals depends on the test temperature and environment. Table 1 also lists the details of the slip bands such as the spacing of slip bands and the thickness of a slip band under different temperatures and environments. The spacings of slip bands were measured by optical microscopy and the thicknesses of a slip band were measured from the SEM micrographs. The spacing of slip bands becomes smaller at lower temperatures and in inert environments while the thickness of each slip band decreases with the temperature but seems to be independent of environment. In addition, the whole surface is covered with fine slip lines at 77°K and 4.2°K as shown in Figure 3b and 3c.

The thickness of a PSB is reported to be almost the same as the ladder rung spacing of about 1.3 μm at room temperature (12). This optimum ladder rung spacing seems to lower the elastic strain energy of a system. Basinski et al. (8) investigated the dislocation structures of copper single crystals at 295°K, 77.4°K and 4.2°K. PSB's were observed at all temperatures but the ladder rung spacing in the PSB's decreased from 1.3 μm to 0.45 μm as the

FATIGUE 87

temperature was lowered. It is of interest to consider that the thickness of a slip band obtained in this experiment (refer to Table 1) approximately corresponds to the ladder rung spacing observed by Basinski et al. (8). Since PSB's are thought to be produced throughout the whole bulk copper single crystals, the temperature effect is thought to govern mainly the bulk properties of fatigued specimens such as the dislocation structure. The narrowing of the slip bands as the temperature is lower is probably due to the role of thermally activated cross slip in the formation of slip bands.

As shown in Table 1, the spacing of slip bands at 298°K decreases in an inert environment. The effect of environment on fatigue has been investigated in copper single crystals oriented for single slip by Mughrabi and his coworkers (13). At a plastic shear strain amplitude of 2×10^{-3} , the fatigue life to final failure in vacuum of 10^{-4} to 10^{-5} torr is increased by a factor of 15 or more although the cyclic hardening curves in vacuum and air are almost identical with the exception that the data for vacuum extend to much larger values of accumulated plastic strain. This means that the effect of environment is mainly a surface or near surface effect. How the environmental effect plays a role in the development of slip bands is still not understood. Therefore, in order to explain these results on copper single crystals in terms of near-surface dislocation structures, the near surface region where the fatigue cracks have just-initiated is being examined by TEM.

SYMBOLS USED

- F_{RA} = cumulative plastic strain required to initiate small fatigue cracks at 298°K in laboratory air
- F_{RP} = cumulative plastic strain required to initiate small fatigue cracks at 298°K in paraffin oil
- F_N = cumulative plastic strain required to initiate small fatigue cracks at 77°K in liquid nitrogen

REFERENCES

- (1) Fine, M. E. and Kwon, I. B., "Fatigue Crack Initiation along Slip Bands", Proceedings of the Second Engineering Foundation International Conference/Workshop, Santa Barbara, CA, "Small Fatigue Cracks", Edited by P. O. Ritchie and J. Lankford, The Metallurgical Society of AIME, Warrendale, PA, 1986, pp. 29-40.

FATIGUE 87

- (2) Laird, C., Charsley, P. and Mughrabi, H., *Mat. Sci. Eng.*, Vol. 81, 1986, pp. 433-450.
- (3) Thompson, N., Wadsworth, N. and Louat, N., *Phil. Mag.*, Vol. 1, 1956, pp. 113-126.
- (4) McCammon, R. D. and Rosenberg, H. M., *Proc. Roy. Soc.*, Vol. A 242, 1957, pp. 203-211.
- (5) Hull, D., *J. of Inst. Met.*, Vol. 86, 1957-58, pp. 425-430.
- (6) Fine, M. E., "Fatigue Crack Initiation on Slip Bands", *ICSMA 6*, Edited by R. C. Gifkins, Pergamon Press, 1982, pp. 833-838.
- (7) Wilkov, M. A. and Shield, R., "Crack Initiation in Fatigue of Metals", U. S. Department Comm., AD 640419, 1966.
- (8) Basinski, Z. S., Korbil, A. S. and Basinski, S. J., *Acta Metall.*, Vol. 28, 1980, pp. 191-207.
- (9) Holt, D. L. and Backofen, W. A., *Trans. Metall. Soc. AIME*, Vol. 239, 1967, pp. 264-269.
- (10) Basinski, Z. S. and Basinski, S. J., "Surface Geometry in Fatigued Copper Crystals", *Eshelby Memorial Symposium, "Fundamentals of Deformation and Fracture"*, Edited by B. A. Bilby et al., Cambridge Univ. Press, 1985, pp. 583-594.
- (11) Ma, B.-T. and Laird, C., "Distributions of Small Crack Sizes in Fatigued Copper Single Crystals - Statistical Aspects of Competitive Growth", "Small Fatigue Cracks", Edited by R. O. Ritchie and J. Lankford, *The Metall. Soc. AIME*, Warrendale, PA, 1986, pp. 9-28.
- (12) Mughrabi, H., "Cyclic Plasticity of Matrix and Persistent Slip Bands in Fatigued Metals", "Continuum Models of Discrete System 4", Edited by O. Brulin and R. K. T. Hsieh, North-Holland Pub. Comp., 1981, pp. 241-257.
- (13) Wang, R., Mughrabi, H., McGovern, S. and Rapp, M., *Mat. Sci. Eng.*, Vol. 65, 1984, pp. 219-233.

ACKNOWLEDGEMENT

This research was supported under the NSF-MRL program through the Materials Research Center of Northwestern University (Grant No. DMR82-16972).

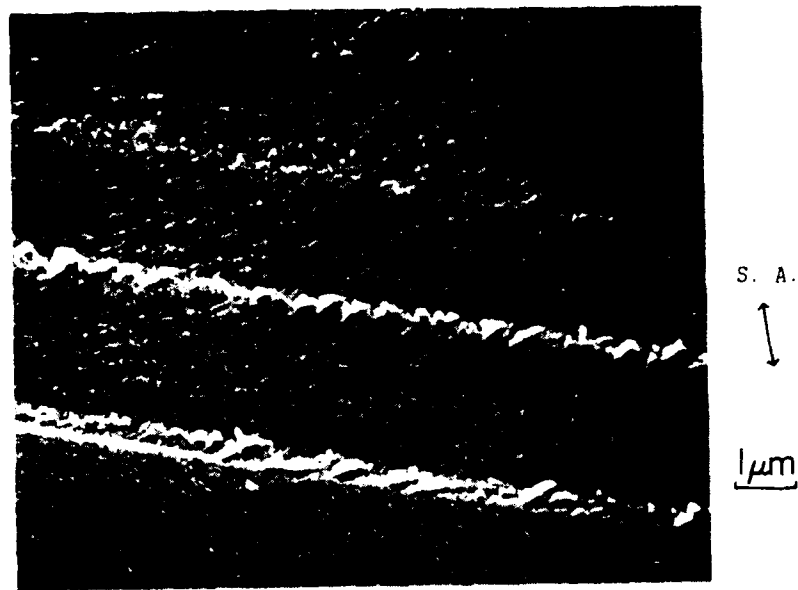


Figure 1 SEM micrograph of a replica₃ of a polycrystalline Cu specimen fatigued with $\Delta\epsilon_p/2$ of 3×10^{-3} at 4.2°K for 500 cycles

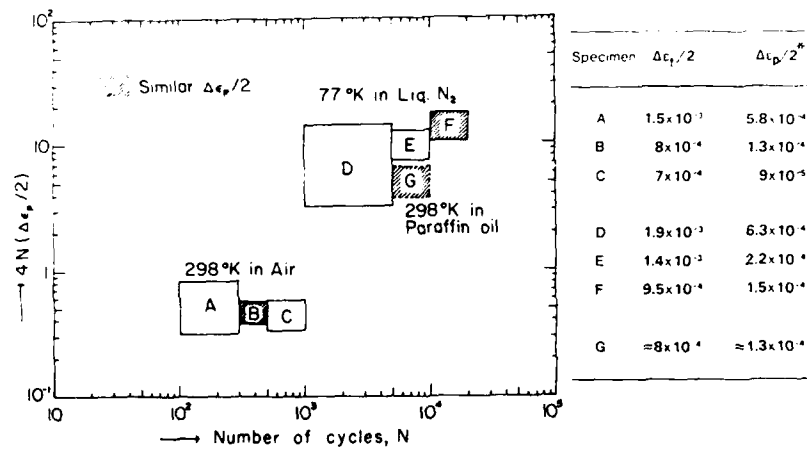


Figure 2 Fatigue crack initiation data at 298°K and 77°K (* after cyclic saturation)

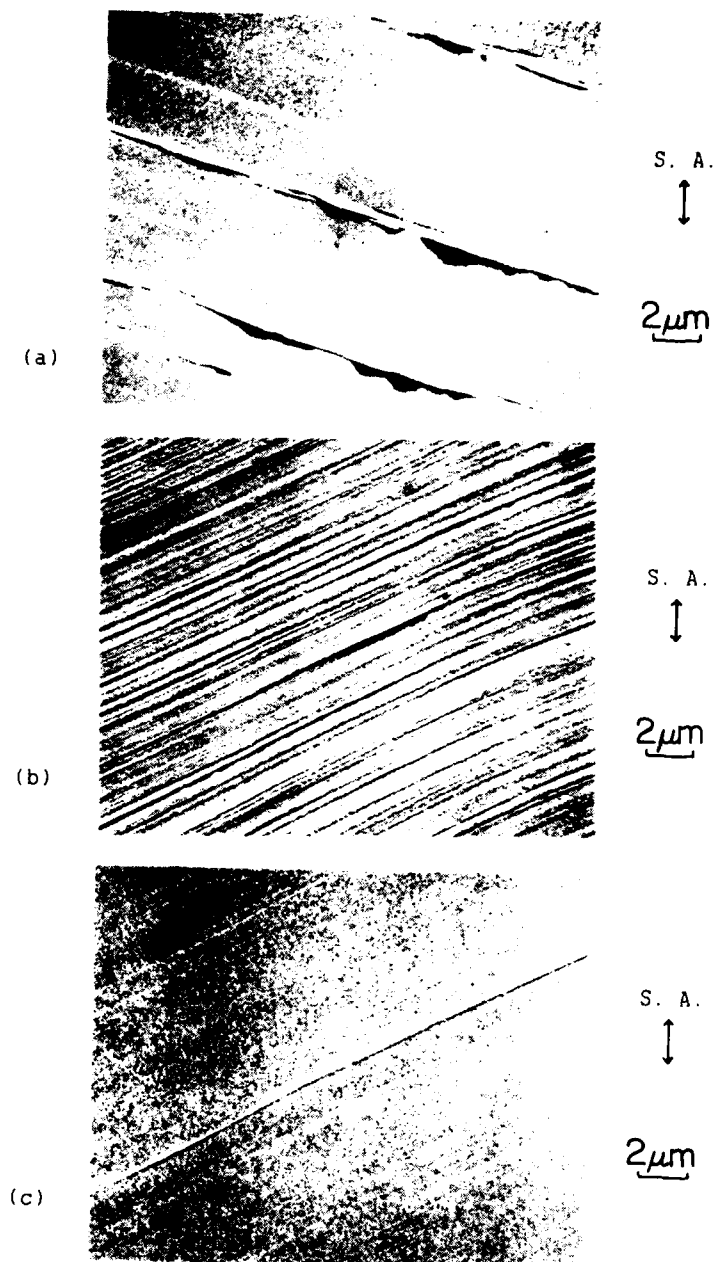


Figure 3 SEM micrographs of replicas of Cu single crystals specimens fatigued (a) at 298°K in He gas (b) at 77°K in He gas (c) at 4.2°K in liquid He (refer to text for fatigue conditions)

FATIGUE 87

BEHAVIOUR OF SHORT CRACKS IN A 2024 ALUMINIUM ALLOY SHEET TESTED AT SEVERAL STRESS RATIOS

A. Andrade * and M. Freitas *

The initiation and growth of small cracks ($>3 \mu\text{m}$) from edge notches in 2024 T3 aluminium alloy sheets were studied under constant amplitude loading for a wide range of stress ratio. The surface crack length was monitored by taking surface replicas at regular intervals. Crack initiation were mainly voids associated with inclusions due to decohesion or at cracked inclusions. Crack growth rates were plotted against the stress intensity factor ranges. Results showed that small cracks grow faster than large cracks at the same stress-intensity factor range. An effect of the stress range on the number of initiated cracks was detected, as being there a more significant factor than either R or S_{max} by themselves.

INTRODUCTION

A short crack effect whereby small cracks growth rate differs from that of long cracks has been frequently reported in literature for several steels (1) and different aluminium alloys (2,3). On the basis of linear-elastic fracture mechanics, the small cracks were found to grow much faster than would be predicted from long crack data and grow at stress-intensity factor range levels well below the threshold (ΔK_{th}) obtained for large cracks.

It has been related that the differences in the behaviour of short and long cracks can arise from a number of distinct phenomena (4) such as the interaction of short cracks with microstructural features (grain boundaries, inclusions) or differences in the local cracks tip environments or the effect of crack closure varying with crack length (5).

In order to study the behaviour of short crack and his effect, a collaborative effort programme on short cracks was implemented by AGARD under the coordination of Dr. P. R. Edwards (RNL-UK) and Dr. J. C. Newmann (NASA-USA) (6). It was within this programme that the

* CEMUL/IST, Av. Rovisco Pais, 1096, Lisboa Codex, Portugal

AD-A184 045

FATIGUE '87 VOLUME 1(U) VIRGINIA UNIV CHARLOTTESVILLE

47

SCHOOL OF ENGINEERING AND APPLIED SCIENCE

R O RITCHIE ET AL JUN 87 ARO-24134.1-MS-CF

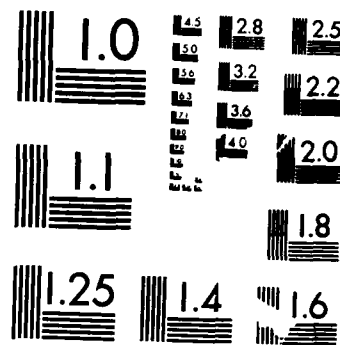
UNCLASSIFIED

N00014-87-G-0008

F/G 20/11

NL

12
13
14
15
16
17
18
19
20
21
22
23
24
25
26
27
28
29
30
31
32
33
34
35
36
37
38
39
40
41
42
43
44
45
46
47
48
49
50
51
52
53
54
55
56
57
58
59
60
61
62
63
64
65
66
67
68
69
70
71
72
73
74
75
76
77
78
79
80
81
82
83
84
85
86
87
88
89
90
91
92
93
94
95
96
97
98
99
100



MICROCOPY RESOLUTION TEST CHART
NATIONAL BUREAU OF STANDARDS-1963-A

FATIGUE 87

initiation and growth of small fatigue crack in 2024-T3 aluminium alloy sheet specimens were studied under constant amplitude loading for a wide range of stress ratio.

It has been reported in the literature a number of different techniques to measure the growth of small cracks under fatigue loading, notably optical microscopy, scanning electron microscopy of replicas, cyclic-load changes to mark the fatigue surface (7).

The present paper describes measurements of crack growth rates of small cracks initiated at semi-circular edge notch in 2024-T3 aluminium alloy sheet specimens. The scanning electron microscopy of replicas was used; this technique provided accurate information not only on crack length but also on crack initiation sites.

Experimentally determined crack growth rates for small cracks are compared with data obtained for long cracks on this alloy obtained in literature.

MATERIAL, SPECIMEN AND EXPERIMENTAL PROCEDURE

Material

Tests have been conducted on specimens made of 2024-T3 aluminium alloy sheet material, which has typically a yield strength (σ_{ys}) of 346 MPa and a ultimate strength (σ_u) of 496 MPa. For this material it was found that the monotonic and cyclic stress strain data (6) could be well approximated by

$$\sigma = E\epsilon \text{ for } \epsilon < \epsilon_1; \sigma = k_1\epsilon^{n_1} \text{ for } \epsilon_1 < \epsilon < \epsilon_2 \text{ and } \sigma = k_2\epsilon^{n_2} \text{ for } \epsilon > \epsilon_2$$

where

TABLE 1

	E	K ₁	K ₂	ϵ_1	ϵ_2	n ₁	n ₂
Monotonic	73.100	1013	431	0.0047	0.006	0.2	0.032
Cyclic	73.100	5135	917	0.0049	0.0071	0.499	0.15

Specimens

Chemically polished single edge notched tensile specimens (2,3 mm thick) were used; the notches were semi-circular with 3,18 mm radius with a stress concentration factor $K_t = 2,3$ based on gross-section stress.

A wide interval of stress ranges was covered by using four stress ratios and three different maximum stress for each one, as shown in Table 2.

FATIGUE 87

TABLE 2

Stress Ratio R	-2			-1			0			0.5		
Max gross Stress S_{max}	75	60	50	105	80	70	145	120	110	225	205	170

Experimental Procedure

Guide plates lined with teflon sheets were loosely bolted on both sides of the specimen to prevent buckling under compressive loads.

A careful alignment of the testing rig was carried out; bending strains from lateral and rotational misalignment were kept below 20 and 10 microstrain ($\mu\epsilon$) respectively; longitudinal misalignment was kept less than 0.05.

The surface crack length was monitored by interrupting the fatigue tests and taking replicas of the notch surface at regular intervals until one continuous crack went all the way across the notch root. While taking replicas, a specimen was loaded to about 0.8 S_{max} so that any crack present would be opened. Replicas were spretter-coated with a thin layer of Au and examined then in the scanning electron microscope.

The replicas taken at the highest number of cycles were observed first, as the cracks were large and easy to locate. By following in sequence from the last replica to the earlier ones, the inclusion pattern and faintly visible grain boundaries were used to locate the initiation of the small cracks; replicas were then observed again from the first to the last one and their crack length measured.

When many cracks were present, only the 5 more important cracks that contributed to the final crack were monitored.

For each test condition, one specimen was tested until the total crack length was about 50% of the specimen thickness and then broken statically; this procedure allowed to obtain information about the shape and dimensions of the crack (crack length versus maximum depth).

RESULTS AND DISCUSSION

Experimental Results

The scanning electron microscopy examination of replicas

FATIGUE 87

provided accurate information since the thinness of the replica material (about 0.04 mm thick) and the observation method (SEM) allowed the detection of cracks as small as 3 μm long.

Data generated in fatigue crack growth studies are characterized by two variables: crack length and cycles. Crack growth data were obtained on length versus cycles coordinates, and were analysed on crack growth rate - ΔK coordinates. Growth rate is calculated as the slope between two points and reported as a function of the stress-intensity factor range, ΔK , corresponding to the average crack length for a given growth rate. The stress-intensity factor range, ΔK , is defined in the usual fashion, for a semi-elliptical surface crack located at the center of a semi-circular edge notch subjected to remote uniform stress (7,8,9)

$$\Delta K = \Delta S \sqrt{\pi a/Q} F_{sn} \quad (2)$$

Where Q is the shape factor and F_{sn} is changed by F_{cn} for corner cracks (7,8,9); ΔS is the full stress range ($S_{\text{max}} - S_{\text{min}}$) in all types of loading.

The number of cracks initiated and monitored strongly depended on stress range. Table 3 represents the number of cracks observed and monitored

TABLE 3

R	0.5			0			-1.0			-2.0		
ΔS (MPa)	97.5	102.5	122.5	110	120	145	140	160	210	150	180	225
S_{max} (MPa)	195	205	225	110	120	145	70	80	105	50	60	75
N° cracks	1	1	1	1	5	>5	2	5	>5	4	5	>5

Crack Initiation

Crack initiation sites were easy to locate with the technique of replicas SEM examination. They were mainly voids associated with inclusions and due to the polishing procedure or to decohesion from the matrix during processing; cracks were also observed to initiated at cracked inclusions; in a very few cases a crack was initiated in a grain (10). No relation was obtained between crack initiation site and stress ratio or maximum stress.

Only one crack was initiated in the corner (corner crack) while

FATIGUE 87

all the others were initiated in single or multiple midthickness sites (central cracks).

When multiple crack initiation is present the first crack initiated is not always the dominant. Sometimes one crack initiates and goes dormant, while another one initiates and becomes pre-dominant.

Typical multiple initiation is observed at high stress ranges; for these load conditions and specimen, the stress range $\Delta S = 120$ MPa is the transition value for multiple crack initiation. For $R = 0.5$, single crack initiation was obtained (Table 3) but the maximum stress at the notch root is greater than yield strength and approaches the ultimate tensile for the three test conditions. So this fact does not lead to multiple crack initiation since ΔS remains in the value mentioned above.

Crack Growth Behaviour

Figures 1, 2, 3 and 4 present crack growth rate as a function of the stress-intensity factor range for $R = 0.5$, $R = 0$, $R = -1$ and $R = -2$ respectively, for data obtained on short crack tests, long crack data is shown in order to be compared to short crack data.

It should be noted that in this analysis we are using an approach; the method of calculating stress-intensity factor used (7,8,9) does not take into account for multiple crack iteration, which is important for stress ratio greater than 0 (zero) (see Table 3); for example when two cracks joint, the ratio a/c (crack length versus crack depth) is different for the final crack in relation with the previous ones, so, care must be taken in interpreting these data.

There is a large evidence of growth of crack for stress intensity factors well below the long crack threshold ΔK_{Th} ; this behaviour is observed for all stress ratios tested in the program.

When a single crack is present ($R = 0.5$) fig. 1, there is a minimum crack growth for the three stress conditions tested, which correspond to crack size of $a = 21 \mu\text{m}$ for $S_{max} = 195$ MPa, $a = 53 \mu\text{m}$ for $S_{max} = 205$ MPa and $a = 95 \mu\text{m}$ for $S_{max} = 225$ MPa. Typical grain dimensions in the crack growth directions, $2a$ and c , were $25 \mu\text{m}$ and $55 \mu\text{m}$ respectively. In this case notch plasticity is present and so the crack growth rate depends on the geometry of the notch and on the extent of the notch plastic zone which is proportional to S_{max} .

CONCLUSIONS

The following conclusions are considered to hold for 2024-T351 aluminium alloy tested at several stress ratio:

1. The growth of short cracks is faster than predicted on the basis

FATIGUE 87

of long crack data and at stress-intensity factor ranges well below the threshold K_{th} for long cracks.

2. Crack initiation sites were mainly voids associated with inclusions or grain boundaries.

3. The number of cracks initiated strongly depends of the stress range even when maximum stress is higher than yield strength.

4. Work must be done in order to take into account interaction between multiple crack because LEFM has significant limitations in this case.

ACKNOWLEDGEMENTS

The authors are grateful to Mrs. M. Helena Carvalho, LNETI, for permission to include the metallographic results presented in this paper. Financial support by AGARD and LNETI are also acknowledged.

SYMBOLS USED

ΔK	= stress intensity factor range (MPa \sqrt{m})
K_t	= stress concentration factor
σ	= stress (MPa)
E	= Young's modulus (MPa)
n_i	= strain-hardening exponent
K_i	= strain-hardening coefficient
R	= stress ratio
S	= gross section stress (MPa)
Q	= shape factor
a	= crack length (m)
c	= crack depth (m)
F_{sn}	= boundary correction factor for central crack
F_{cn}	= boundary correction factor for corner crack
ϵ	= strain

REFERENCES

- (1) Leis, B.N., Ahmad, J., Kanninen, M.F., Multiaxial Fatigue, ASTM STP 853, pp. 314-339

FATIGUE 87

- (2) Taylor, D. and Knott, J.F., Fatigue of Engineering Materials and Structures, Vol. 4, n° 2, pp. 147-155, 1981
- (3) Lankford, J., Fatigue of Engineering Materials and Structures, Vol. 5, n° 3, pp. 233-248, 1982.
- (4) Lankford, J., Fatigue Fracture Engineering Materials and Structures, Vol. 8, n° 2, pp. 161-175.
- (5) Suresh, S. and Ritchie, O., International Metals Reviews, Vol. 29, n° 6, pp. 445-475, 1984.
- (6) Edwards, P. and Newmann, J., AGARD Collaborative Effort on Short Cracks, 1984.
- (7) Swain, M. and Newmann, J., presented at AGARD Specialists Meeting on Fatigue Crack Topography, 1984.
- (8) Bowie, O.L., Journal of Mathematics and Physics, Vol. XXXV, n° 1, pp. 60-71, 1956.
- (9) Newmann, J., ASTM STP 791, pp. I 238-I 265
- (10) Carvalho, M.H., LNETI, Internal Report SIM/DTM, n° 1/86.
- (11) Leis, B. and Galliher, R., ASTM STP 7701, pp. 399-421, 1982.

FATIGUE 87

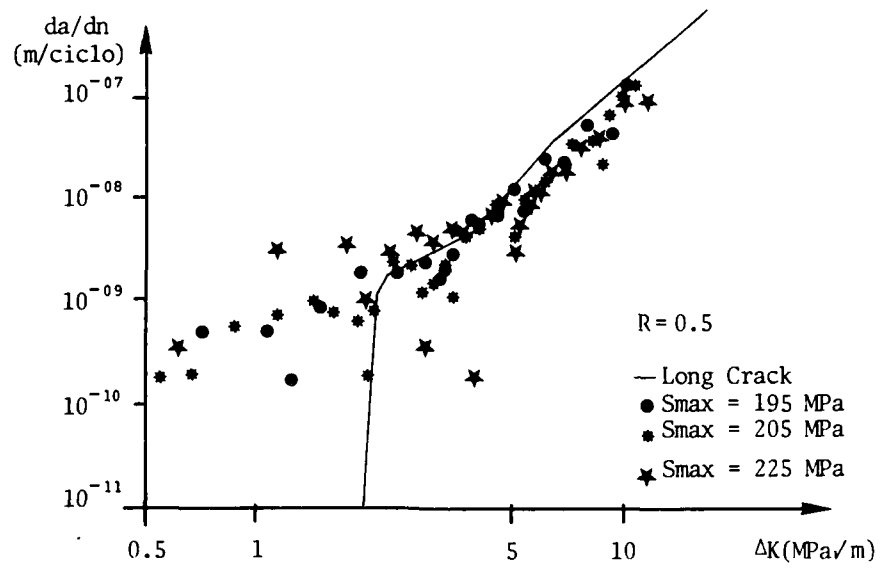


Figure 1 Crack growth rate vs stress intensity factor range

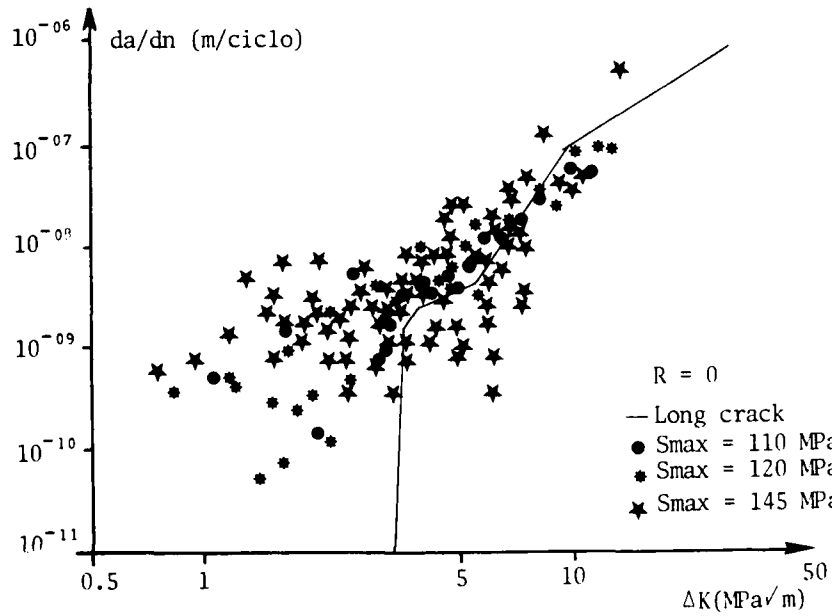


Figure 2 Crack growth rate vs stress intensity factor range

FATIGUE 87

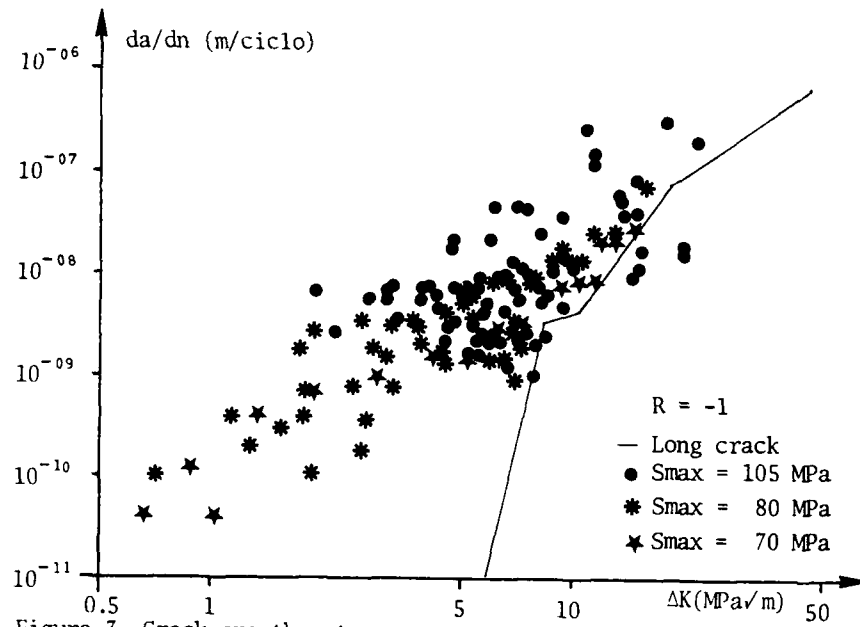


Figure 3 Crack growth rate vs stress intensity factor range

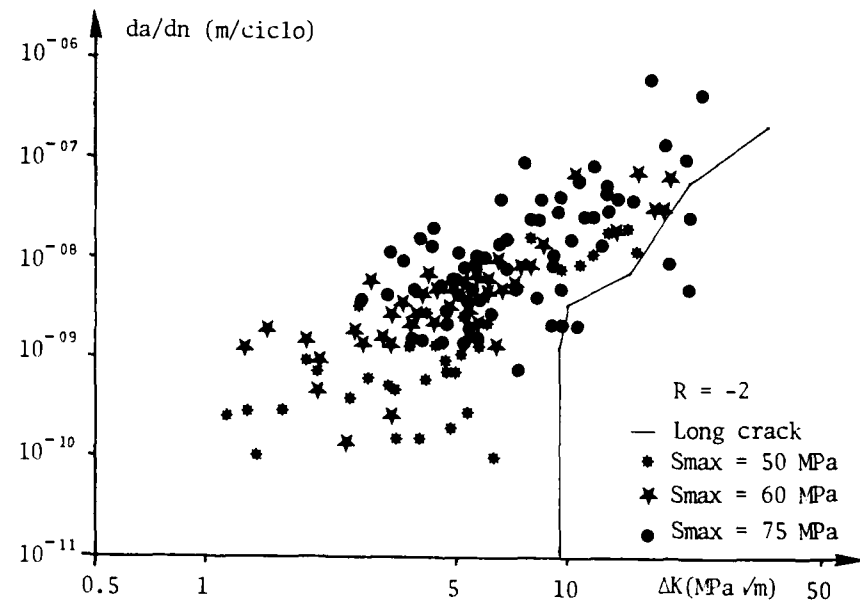


Figure 4 Crack growth rate vs stress intensity factor range

FATIGUE 87

THE EFFECT OF MICROSTRUCTURE ON THE SURFACE CRACK LENGTH: CRACK DEPTH RELATIONSHIP FOR SHORT CRACKS

R.K. Bolingbroke* and J.E. King*

Observations of crack shape development have been made for surface cracks varying in length between 40 μ m and several mm, in aluminium and titanium alloys.

In the aluminium alloy aspect ratio was found to vary with specimen orientation for short cracks, however when the change in aspect ratio was taken into account the da/dN vs. a (or ΔK) curves were not shifted very significantly. Similar behaviour was seen in α /transformed β microstructures in Ti alloys, however in coarse grained β -annealed microstructures very high a/c ratios can be obtained, indicating that growth rate comparisons based on surface crack length could be very misleading in some cases.

INTRODUCTION

To apply any kind of fracture mechanics to microstructurally short cracks, measured using a surface monitoring technique, the relationship between the surface crack length ($2c$) and crack depth (a) must be established.

Many investigations (1-10) have shown that the local microstructure close to the crack tip can influence short crack growth behaviour. For example, Lankford (1,2) observed crack tip arrest at or near grain boundaries in a high strength aluminium alloy. Others (3-5) have demonstrated that propagation can cease in dual phase microstructures when the crack tip reaches the second phase. Such observations suggest that an irregularly shaped crack front will develop when the crack depth is small and will be maintained until the microstructure no longer influences crack propagation.

Evidence for such behaviour, obtained by Hoshide et al (6) and by Tokaji et al (7) for a range of materials, shows changing aspect ratio with crack length. Similarly, observations by Wagner et al

*Department of Metallurgy & Materials Science,
University of Nottingham, UK.

(8) have highlighted the effect of microstructure on crack shape for a Ti-8.6Al alloy. Cracks initially took semi-circular or semi-elliptical shapes, however after crossing the first grain boundary, faster propagation was observed in the region close to the specimen surface, rather than into the specimen interior, resulting in a crack with a shallow profile. The same behaviour was observed at each grain boundary until the surface crack length was approximately 5x the grain size, after which cracks were essentially semi-circular.

Smith et al (11) have shown for an aluminium alloy that aspect ratio can change with crack depth for longer cracks. The upper bound of their experimental data indicates that an initially semi-circular crack will become more semi-elliptical ($a/c < 1.0$) as the crack depth (a) tends to the specimen thickness (b). However, this is an effect of specimen boundaries and not microstructure.

As part of an ongoing research programme concerning the effect of microstructure on short crack growth in Al and Ti alloys, the data presented here show how the relationship between aspect ratio and crack depth can vary for these materials. The effect of altering crack propagation orientation with respect to the pancake grain structure of a high strength aluminium alloy, 7010, has been studied and the resulting influences on propagation rates considered. In addition changes in the effective grain size of two $\alpha + \beta$ titanium alloys (IMI318 and IMI550) have been examined.

EXPERIMENTAL

For all three materials under study a variety of different microstructures were obtained by heat treatment. All material was supplied in 25mm plate form and prior to any heat treatment square section bar specimens 12.5mm x 12.5mm x 70.0mm were cut from the plate with their largest dimension parallel to the rolling direction (RD).

For the 7010 aluminium alloy an overaged microstructure was produced with a 0.2% proof stress of 495 MPa. [Published data for a commercial temper (DT05120) (12) shows similar tensile properties in the L and LT directions ($\sigma_{0.2\%} = 486$ and 478 MPa respectively), though a reduced $\sigma_{0.2\%}$ of 439 MPa in the S direction]. The pancake grain structure had typical grain sizes in the three directions of L, 100 μm -1mm; LT, 60 μm -200 μm ; ST, 10 μm -40 μm . Figure 1, the grain structure in the plane parallel to the ST direction, shows grains are approximately twice as long as they are high.

Table 1 shows the heat treatments and resulting grain sizes for the two titanium alloys (IMI318 and IMI550). The microstructures can be broadly divided into two groups. Those heat treated at temperatures below the β -transus, consisting of $\alpha +$ transformed β phases (318A, 318B, 318C, 550A) and those treated within the β -phase region composed totally of Widmanstätten α (318D, 318E,

FATIGUE 87

TABLE 1 - Titanium Alloy Heat Treatments and Grain Sizes

Material	Heat Treatment (1 hour at)	α grain size (μm)	trans β g.s. (μm)	prior β g.s. (μm)	packet size (μm)
318A	A.R.	8.6	4.2	-	-
318B	950°C F.C.	8.6	1.8	-	-
318C	950°C A.C.	8.5	13.0	-	-
550A	A.R.	6.8	5.5	-	-
318D	1100°C A.C.	-	-	350.0	-
318E	1100°C F.C.	-	-	360.0	65.0
550B	1100°C F.C.	-	-	337.0	161.0

550B). Optical micrographs of examples of each group are shown in figure 2. Figure 2(a) is the as-received IMI318 (recrystallisation anneal, 318A) and figure 2(b) a Widmanstätten type (318E). Heat treatments were performed with specimens encapsulated in silica tubes, back filled with argon, to prevent oxygen contamination.

Specimens were ground, polished, electropolished and etched prior to any fatigue testing. Testing was carried out in 4-point bend, with crack initiation and subsequent growth monitored by a replication technique, in an area of approximately 10mm^2 on the top surface which experienced a constant maximum value of bending moment. Specimens were fatigued at $R = 0.1$ and at a maximum tensile stress on the top surface (σ_{max}) equal to $\approx 0.9 \times$ yield stress (σ_y). (7010, $\sigma_y = 495\text{ MPa}$, $\sigma_{\text{max}} = 440\text{ MPa}$; IMI318, $\sigma_y = 890\text{ MPa}$, $\sigma_{\text{max}} = 750\text{ MPa}$; IMI550, $\sigma_y = 990\text{ MPa}$, $\sigma_{\text{max}} = 850\text{ MPa}$). Cracks were grown to various surface crack lengths between $40\mu\text{m}$ and 10mm before cycling was stopped and specimens broken open to reveal crack shape. In some cases an overload technique was used to produce 'beach marks' on fracture surfaces of the 7010 alloy. In addition, crack front markings for the Ti alloys were obtained by oxidising specimens at 600°C to colour the extent of fracture.

The effect of changing the specimen orientation of the 7010 alloy and therefore the direction of crack growth was examined. Specimens were fatigued with their top surfaces parallel to either the rolling direction or to the plane normal to the rolling direction, resulting in propagation either in the LS or LT directions respectively.

RESULTS

Figure 3 represents data for testing performed on specimens orientated with the rolling direction perpendicular to the stress axis (LS direction cracks). Changes in a/c ratio with crack depth

(a) are highlighted for the overaged microstructure. It is clear from both individual cracks and overload tests that there is a trend for decreasing a/c ratio with increasing crack depth, although there is a wide scatter band. Aspect ratio values fall from between 1.25 and 1.0 to between 1.1 and 0.85 as crack depth increases from $\approx 25\mu\text{m}$ to 2.5mm. The insert in figure 3 indicates that values continue to fall slowly as crack depth increases further.

Overload testing produced direct evidence of this behaviour. Figure 4, the fracture surface of such a test showing two 'beach marks', indicates a drop in a/c ratio from 1.28 to 1.05 with an increase in crack depth from $25\mu\text{m}$ to $327\mu\text{m}$. The larger 'beach mark' also highlights the irregularities of the crack front. Microstructural interactions with the crack tip produce local misorientations at the periphery of the crack.

When the specimen orientation is rotated through 90° so that cracks now grow in the LT direction, a change in the crack shape is also noted. In figure 5 data for LT direction cracks are presented in terms of a/c vs. a . In comparison with figure 3, little difference can be seen between a/c values for cracks in both directions greater than approximately $500\mu\text{m}$ in depth. However, a significant difference is noted for some shorter cracks, with a/c ratios up to 1.6 being observed. Figure 6 shows the fracture surface of such a crack, with a depth of $263\mu\text{m}$, and should be compared with figure 4.

Figures 7 and 8 show, for LS and LT direction cracks respectively, the effect of the changing aspect ratio on crack propagation rates. Data, previously obtained measuring the increase in surface crack length during the fatigue life, were analysed assuming a constant semi-circular crack shape, $a/c = 1.0$ (full line). In addition, a changing a/c ratio was also considered (broken line) according to the mean relationship between a/c and a in figures 3 and 5. For both LS and LT direction cracks, the effect of the changing aspect ratio is to shift the curves to the right.

Fig. 9 shows the a/c vs. a relationship for both titanium alloys over a range of crack depths from $\approx 100\mu\text{m}$ to $\approx 3.2\text{mm}$. Values of a/c for the dual phase α /transformed β microstructures (318A, 318B, 318C, 550A) generally fall into a band between 0.8 and 1.0, independent of crack depth. The same can be seen for the Widmanstätten microstructures for crack depths $> 1\text{mm}$. Below this depth aspect ratios were seen to vary dramatically. Values are scattered between 0.75 and 2.50. Fig. 10 shows the fracture surface of a crack $570\mu\text{m}$ deep that has an aspect ratio = 2.50. From the initiation site marked at the top of the figure, growth can be seen to have occurred on a single slip plane almost through an entire grain.

DISCUSSION

The general trend of falling aspect ratio with increasing crack depth shown in figures 3 and 5, indicates that when cracks are no longer considered to be microstructurally short, a/c ratios fall to approximately 1.0 (semi-circular). At shorter crack depths, <400 μm for example, microstructural influences on the crack tip are more apparent and a wider scatter of a/c ratios is observed. The impedance of the crack tip at grain boundaries in aluminium alloys, as reported by Lankford (1,2), has been explained in terms of crack tip deflection (13) reducing the local crack tip driving forces, and to the containment of slip within the grain (9). Such a mechanism delays further growth until slip can reorientate and reinitiate in an adjoining grain. The relative misorientation of neighbouring grains determines the degree of arrest.

For a material with a non-equiaxed grain structure like 7010, the crack shape is therefore expected to depend on the relative number of grain boundaries in the direction of propagation. The higher aspect ratios of the LT direction cracks can be explained in terms of the number of grain boundaries encountered by the crack tip. Figure 11 schematically shows that there is less resistance to propagation into the interior of the specimen due to the smaller number of grain boundaries encountered for the LT direction crack compared to the LS direction crack. For growth along the specimen surface the reverse is true, with the greater number of crack tip grain boundary interactions occurring in LT direction cracks.

Differences in yield strength between the LS and LT direction could be an influencing factor on crack shape. However, as both specimens are loaded in the same direction, parallel to the rolling direction, the effects are thought to be minimal.

The effects of texture on short crack propagation behaviour as shown by Gregory et al (10) for a textured, extruded 7475 alloy may also affect crack shape. The texture of the present material is currently under investigation in order to assess any influence it may have on crack shape.

The continued gradual reduction in a/c shown in figure 3, as the crack depth (a) approaches the specimen thickness (b) may be because of a mechanical effect of the finite specimen size rather than any microstructural effect. Similar behaviour has been reported by Smith (11) for a 2219-T87 alloy.

The effect of the changing a/c ratio on crack propagation rates, figures 7 and 8, is to displace the curves further to the right. The amount by which they curve is shifted is strongly dependent on the direction of propagation. The fairly constant crack shape of the LS direction crack produces only a small shift in the da/dN vs. a curve. However, for the LT direction crack, the shortest crack length (2c) measurements correspond to a change in

FATIGUE 87

a/c ratio from 1.0 to 1.8, producing a significant shift in the curves. In engineering terms, the consequences of considering crack shape for the 7010 alloy are not particularly damaging, especially when the large amount of scatter of short crack data is taken into account. Indeed, if the da/dN vs. a or ΔK curves are pushed further to the right, slightly better fatigue resistance may be expected.

The effect of grain size, rather than grain shape, was considered from testing the titanium alloys. Both groups of microstructures, $\alpha +$ transformed β and β -annealed, had an equiaxed grain structure, though with widely different grain sizes (table 1). The $\alpha +$ transformed β microstructures (318A, 318B, 318C, 550A) all exhibited similar short crack behaviour (3), with initiation along slip bands in α grains or at α/α boundaries. Discontinuous growth occurred when crack tips interacted with transformed β grains and at changes in lath orientation within these grains. The fairly constant crack shape associated with these microstructures over the range of crack depths studied may be a consequence of the small grain size. Even for the shortest crack, the depth was an order of magnitude larger than the grain size and the microstructure may no longer significantly influence the crack shape.

However, cracks in the considerably coarser grained β -annealed microstructures (318D, 318E, 550B) showed wide variations in aspect ratio up to $500\mu\text{m}$ in depth. This corresponds to only approximately $2\times$ grain size or $5\times$ packet size and the microstructure still strongly influences crack shape. Growth characteristics are also different to the α /transformed β structures (3). Propagation along slip bands within Widmanstätten grains is rapid, but grain or packet boundaries produce very effective barriers to crack tip advance.

The faceted nature of the fracture surfaces generated (figure 10) coupled with the large effective grain size leads to erratic crack shapes even at crack depths in excess of $500\mu\text{m}$. Propagation rates in the crack depth direction would be substantially altered with respect to surface growth rates by such varied aspect ratios.

CONCLUSIONS

1. Aspect ratios for microstructurally short cracks in 7010, IMI318 and IMI550 are affected by the local microstructure.
2. For the 7010 alloy, a change in the crack propagation direction from the LS to LT direction is accompanied by a significant increase in a/c ratio at short crack depths. Aspect ratios of cracks with depths $>330\mu\text{m}$ for both orientations are similar and close to 1.0.
3. Little effect on overall crack propagation behaviour of 7010 is observed when changes in aspect ratio are taken into account.

FATIGUE 87

4. Over the range of crack depths studied (100 μ m-3mm) little change in a/c ratio has been observed for fine grained α + transformed β titanium microstructures. However, for β -annealed microstructures in the same alloy widely varying ratios between 0.75 and 2.50 are reported up to crack depths \approx 500 μ m.
5. In coarse grained microstructures such as β -annealed Ti alloys it is important to take crack shape into account when considering short crack growth behaviour.

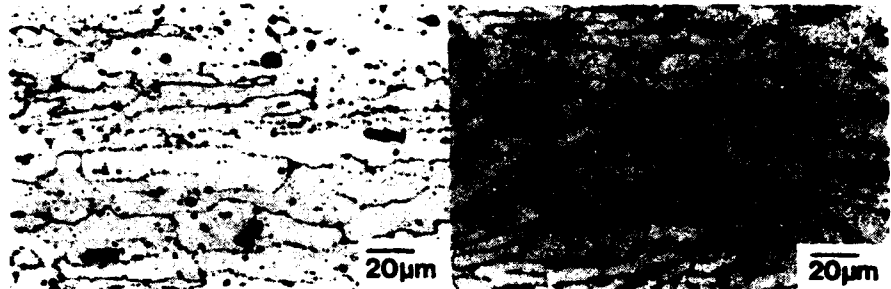
ACKNOWLEDGEMENTS

The MOD are thanked for financial support for one of the authors (RKB) and provision of materials. The authors are grateful to Professor J.S.L. Leach for making available laboratory facilities, and to Dr. R.N. Wilson of the Royal Aircraft Establishment, Farnborough, for helpful discussions.

REFERENCES

- (1) Lankford, J., Fat. Eng. Mat. Struc., Vol. 5, 1982, pp. 233-248.
- (2) Lankford, J., Fat. Eng. Mat. Struc., Vol. 6, 1983, pp. 15-31.
- (3) Bolingbroke, R.K. and King, J.E., "Small Fat. Cracks", Eds. Ritchie, R.O. and Lankford, J., ASTM, 1986, pp. 129-144.
- (4) De Los Rios, E.R., Mohamed, H.J. and Miller, K.J., Fat. Fract. Eng. Mat. Struc., Vol. 8, 1985, pp. 49-63.
- (5) De Los Rios, E.R., Tang, Z. and Miller, K.J., Fat. Fract. Eng. Mat. Struc., Vol. 7, 1984, pp. 97-108.
- (6) Hoshide, T., Yamada, T., Fujimura, S. and Hayashi, T., Eng. Frac. Mech., Vol. 21, 1985, pp. 85-101.
- (7) Tokaji, K., Ogana, T., Harada, Y. and Ando, Z., Fat. Frac. Eng. Mat. Struc., Vol. 9, 1986, pp. 1-14.
- (8) Wagner, L., Gregory, J.K., Gysler, A. and Lütjering, G., "Small Fat. Cracks", Eds. Ritchie, R.O. and Lankford, J., ASTM, 1986, pp. 117-128.
- (9) Morris, W.L., Met. Trans. A., Vol. 11A, 1980, pp. 1117-1123.
- (10) Gregory, J.K., Gysler, A. and Lütjering, G., "Fatigue '84", Ed. Beevers, C.J., EMAS, Warley, UK, 1984, pp. 847-856.
- (11) Smith, C.W., Peters, W.H. and Kirby, G.C., "Analytical and Experimental Fracture Mechanics", Eds. Sih, G.C. and Mirabile, M., Sijthoff and Noordhoff, 1981, pp. 699-710.
- (12) Reynolds, M.A., Fitzsimmons, P.E. and Harris, J.G., "Aluminium Alloys in the Aircraft Industry - Sym.", Tech. Ltd., Glos., UK, 1978, pp. 115-124.
- (13) Suresh, S., Met. Trans. A., Vol. 14A, 1983, pp. 2375-2385.

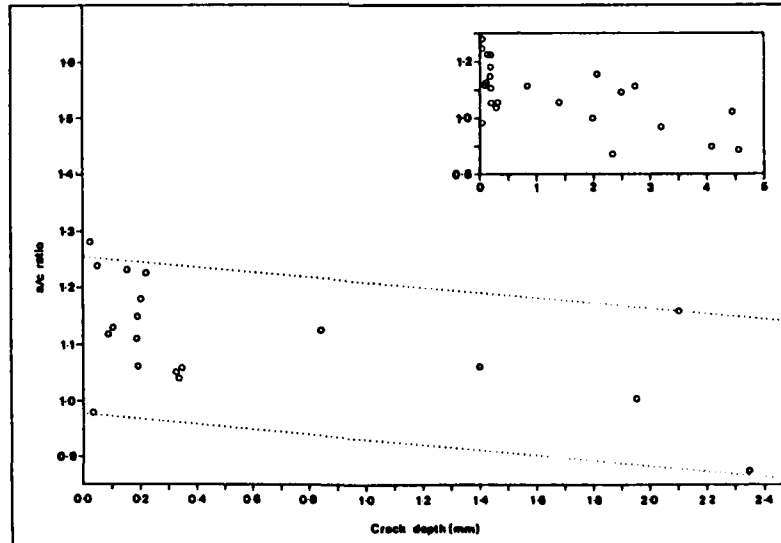
FATIGUE 87



(1) Optical micrograph 7010 plane parallel to ST direction. (2) (a) Optical micrograph IMI318 as-received (318A).

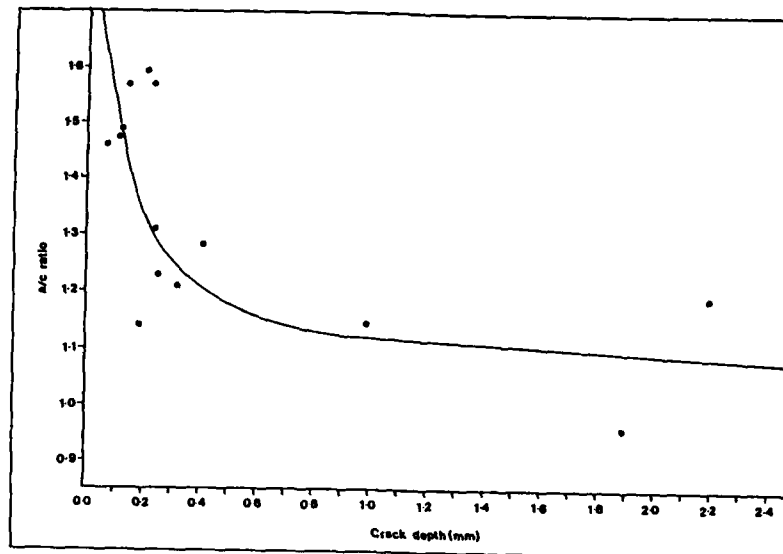


(2) (b) Optical micrograph IMI318(4) Widmanstatten microstructure (318E). (4) Fracture surface 7010 LS direction crack showing 'beach marks'.

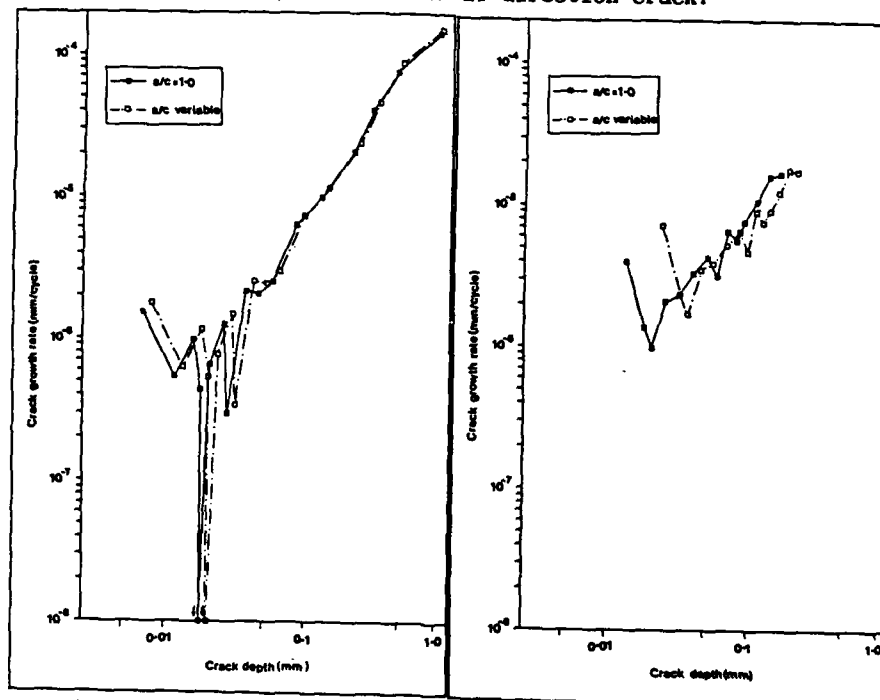


(3) a/c vs. a, 7010 LS direction crack.

FATIGUE 87

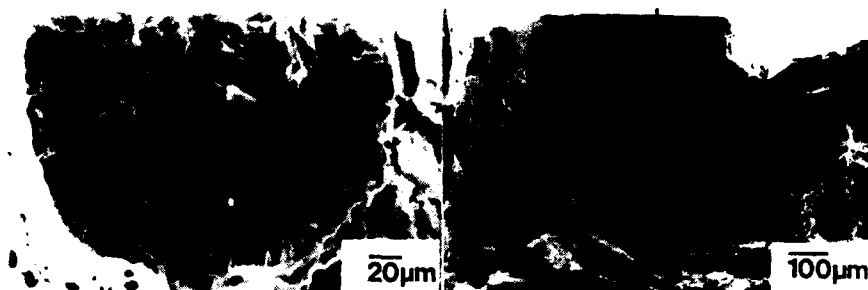


(5) a/c vs. a 7010 LT direction crack.

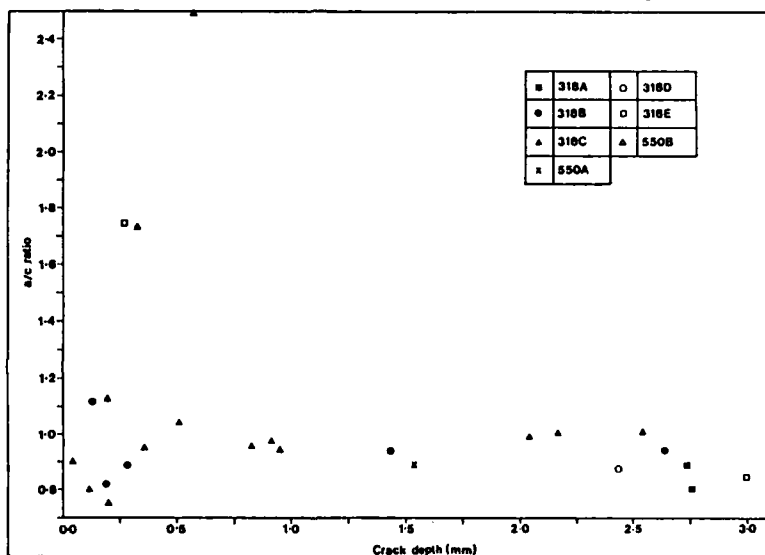


(7) & (8) da/dN vs. a, 7010 LS direction crack (7) and LT direction crack (8) with a/c ratio = 1.0 and variable (>1.0).

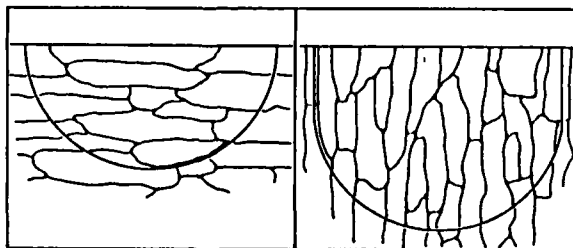
FATIGUE 87



- (6) Fracture surface 7010 LT direction crack.
 (10) Fracture surface β annealed titanium alloy.



- (9) a/c vs. a for titanium alloys, black points are for $\alpha +$ transformed β microstructure, white points are for β annealed microstructures.



- (11) Schematic diagram showing number of grain boundary: crack tip interactions in (a) LS direction cracks and (b) LT direction cracks.

ON THE ROLE OF CRACK TIP SHIELDING IN INFLUENCING THE BEHAVIOR OF LONG AND SMALL FATIGUE CRACKS IN ALUMINUM-LITHIUM ALLOY 2090**K. T. Venkateswara Rao, W. Yu, and R. O. Ritchie***

The fatigue crack growth behavior of long (≥ 5 mm) through-thickness cracks is compared with that of microstructurally small (2 to 1000 μ m) surface cracks in aluminum-lithium alloy 2090-T8E41. Although long crack growth rates are in general significantly slower than in traditional high strength aluminum alloys and show marked anisotropy, corresponding growth rates of small cracks are up to 3 orders of magnitude faster, and propagate at stress intensities far below the long crack threshold ΔK_{TH} . Such behavior is attributed to the role of crack tip shielding, primarily from crack deflection and asperity-induced crack closure.

INTRODUCTION

The demand for high strength, high stiffness materials with lower density for advanced aerospace applications has led to increasing interest in the development of ultra-light weight aluminum-lithium alloys, specifically for airframe and cryogenic applications (1-4). In general, these alloys show 7-10% lower density, 7-12% higher stiffness and improved toughness at cryogenic temperatures (4), yet often suffer from poor short-transverse properties. Moreover, although their fatigue crack growth properties appear to be superior to most traditional high strength aluminum alloys (5-10), there is some question over the origin of these properties, and over the fatigue resistance in the presence of microstructurally small cracks (11).

As described in refs. 7-11, the excellent fatigue crack growth resistance of aluminum-lithium alloys has been attributed primarily to a marked tendency for planar slip and to the anisotropic nature of the unrecrystallized microstructure, both

* Center for Advanced Materials, Lawrence Berkeley Laboratory, and Department of Materials Science and Mineral Engineering, University of California, Berkeley, CA 94720, U.S.A.

of which promote tortuous crack paths. This induces lower growth rates through crack deflection and subsequent crack closure, primarily from enhanced fracture surface asperity contact (Fig. 1). Such mechanisms constitute forms of crack tip shielding, which act locally to reduce the "crack driving force" actually experienced at the crack tip (12,13). Although the use of shielding mechanisms represents a potent means of impeding crack growth, as shown for example by transformation toughening in ceramics (14) and crack bridging in composites (15), the result is often crack-size dependent behavior, in the form of resistance curve toughness behavior and "anomalous" small crack effects (13).

Such considerations are particularly significant to aluminum-lithium alloys, as they appear to derive their excellent fatigue crack growth properties principally from crack tip shielding (7-11). Accordingly, it might be anticipated that under conditions where shielding is restricted, such as with small cracks of limited wake, their fatigue resistance may be compromised. It is thus the objective of this paper to examine the fatigue behavior of long and microstructurally small cracks in an aluminum-lithium alloy, and specifically to study the role of shielding mechanisms.

EXPERIMENTAL PROCEDURES

The material studied was a 12.7 mm thick plate of Al-Li-Cu alloy 2090, received from ALCOA in the peak aged T8E41 condition. The alloy had a composition in wt% of 2.86 Cu, 2.05 Li, and 0.12 Zr, with 0.02 Fe, 0.01 Si, 0.01 Mg, 0.005 Mn and 0.02 Ti. The microstructure, which was unrecrystallized and highly anisotropic with large pancake shaped grains, roughly 20 μm thick, 500 μm wide and elongated several mm along the rolling direction (Fig. 2), was hardened by spherical δ' (Al_3Li), plate-like T_1 (Al_2CuLi) and T_2 (Al_5CuLi_3) precipitates, and β' (Al_3Zr) dispersoids (16). Room temperature mechanical properties were strongly sensitive to plate orientation; yield strength and elongation varied between 460 MPa and 10.9%, respectively, in the L+45 orientation to 550 MPa and 5.4% in the L-T orientation. Fracture toughness values similarly varied markedly, from 16 $\text{MPa}\sqrt{\text{m}}$ (S-L) to 35 $\text{MPa}\sqrt{\text{m}}$ (L-T).

Crack growth tests were conducted in controlled room air using automated servo-hydraulic testing machines operating at a frequency of 50 Hz (sinusoidal) with a load ratio ($R = K_{\min}/K_{\max}$) of 0.1. Tests on long (≥ 5 mm) through-thickness cracks were performed with 6-7 mm thick compact, double-cantilever beam, and 4-point single-edge-notched bend specimens, in the L-T, T-L, T-S, S-L, S-T and L+45 orientations. Continuous, in situ monitoring of crack length and crack closure was achieved using d.c. electrical potential and back-face strain methods, respectively. The latter measurements involved determining the closure stress intensity K_{cl} , defined at first contact of the fracture surfaces during unloading (13). Growth rate data are presented in terms

of the nominal stress intensity range ($\Delta K = K_{\max} - K_{\min}$), and the effective stress intensity range ($\Delta K_{\text{eff}} = K_{\max} - K_{\text{cl}}$).

Tests on naturally-occurring, microstructurally small (2 to 1000 μm) surface cracks were performed by replicating the electropolished top surface of 7.6 mm thick, unnotched, rectangular 4-point bend specimens (maximum tensile surface stress less than 0.9 times the yield stress). Surface crack lengths were taken as the projected length normal to the direction of the tensile stresses; a half surface-crack-length-to-depth ratio of 0.8 was assumed, based on serial sectioning studies. Stress intensities K_I were computed from Newman and Raju's solution for semi-elliptical surface flaws (17). Use of K_I to characterize small crack growth was deemed appropriate, as computed maximum and cyclic plastic zone sizes remained small (0.4 to 150 μm and 0.1 to 30 μm , respectively) compared to specimen dimensions.

RESULTS AND DISCUSSION

Long Cracks

Growth rate behavior. The fatigue behavior of long cracks in 2090-T8E41, as a function of the nominal stress intensity range ΔK , is compared to that of traditional high strength aluminum alloys 2124 and 7150 (13,18) in Fig. 3 for the T-L orientation. Despite having 30% higher strength, growth rates in the aluminum-lithium alloy are consistently slower over the entire range of growth rates (except close to ΔK_{TH} in 2124-T351), consistent with higher measured levels of crack closure (10). Behavior in 2090, however, is strongly anisotropic. This is shown by the 4 orders of magnitude difference in growth rates (at fixed ΔK), and associated variation in crack closure, between the various orientations (Figs. 4 & 5). The T-L, L-T and T-S orientations, which develop the highest closure levels (e.g., K_{cl} in the L-T orientation approaches 0.9 K_{\max}), show the slowest growth rates, with threshold ΔK_{TH} values between 3 and 4 $\text{MPa}\sqrt{\text{m}}$. Conversely, the S-L and S-T orientations, which develop the least closure, show the fastest growth rates. The lowest threshold ($\Delta K_{\text{TH}} = 2.4 \text{ MPa}\sqrt{\text{m}}$) is found in the L+45 orientation, which has 16 pct lower strength.

Crack path morphology. The high levels of closure in 2090 were associated with highly deflected and meandering crack paths. As shown in Fig. 6, the marked planar slip characteristics of the alloy can induce crystallographic crack growth, with cracking along slip bands. This may be manifest as macroscopic crack branching, where the entire crack extends at some angle ($\sim 45^\circ$) to the plane of maximum stress, as shown by the L-T orientation in Fig. 6a, or more commonly as faceted crack growth, where the crack undergoes periodic "zig-zags" (on the scale of the grain size) but still grows primarily along the plane of maximum tensile stress, as shown by the L+45 orientation in Fig. 6b. A third type of

(milder) crack deflection occurs in the S-L and S-T orientations (Fig. 6c), where linkage occurs between intergranular delamination cracks in the rolling plane, as discussed in ref. 19.

Such tortuous crack paths lead to much slower growth rates i) by increasing the path length of the crack, ii) by promoting crack tip shielding by deviating the crack from the plane of maximum tensile stress (20), and iii) by developing shielding from closure via wedging of asperities within the crack (21). Thus, the fastest growth rates are expected in the short-transverse S-L and S-T orientations, where the unrecrystallized, elongated grain structure provides a weak path along the grain boundaries, with little consequent crack path deviation. Conversely, the slowest growth rates are expected in the L-T, T-L, T-S orientations where crack advance is normal to the weaker rolling plane and where the cracks undergo crystallographic deflection and delamination perpendicular to the crack plane.

Such crystallographic crack path morphologies are not uncommon in precipitation-hardened alloys, particularly close to ΔK_{TH} in planar slip microstructures (17,22,23). Behavior in 2090, however, is striking in that this fracture mode, and associated high closure levels, persist to much higher growth rates, accounting for the improved crack growth properties above $\sim 10^{-9}$ m/cycle (Fig. 3). For most aluminum alloys, the crystallographic fracture mode occurs only at low ΔK , typically where the cyclic plastic zone size is less than the order of the grain size (21).

Extrinsic toughening. The reliance on crack tip shielding to achieve superior crack growth properties in Al-Li alloys is an example of "extrinsic toughening", where crack extension is impeded, not by increasing the microstructural crack growth resistance, but rather by microstructural, mechanical or environmental mechanisms which reduce the local "crack driving force" (13). Although commonly employed to toughen brittle materials (14,15), this approach is generally less applicable to metallic materials due to their high intrinsic toughness, except where cracking proceeds at low K_I levels, such as in fatigue. The drawback of this approach, however, is that shielding acts primarily in the crack wake, such that propagation behavior becomes crack-size dependent. As the magnitude of shielding grows with increase in size of the crack wake, this results in resistance-curve toughness behavior and in accelerated growth rates for small cracks (13), as discussed below.

Small Cracks

Growth rate behavior. A comparison of the growth rate data for microstructurally small surface cracks with that measured for long cracks (for T-L orientation) is shown as a function of the nominal ΔK in Fig. 7. The scatter in small crack results is inherent as

they initiate naturally within a few favorably oriented grains and suffer local impedance during early growth on encountering grain boundaries. It is clear that whereas long and small crack behavior is comparable at higher ΔK levels, typically above $\sim 8 \text{ MPa}\sqrt{\text{m}}$, the near-threshold propagation rates of small flaws are between 1 to 3 orders of magnitude faster than those for long flaws (at the same ΔK). Moreover, small crack growth is apparent at ΔK levels as low as $0.7 \text{ MPa}\sqrt{\text{m}}$, far below the long crack threshold ΔK_{TH} .

Crack closure. The primary reason for such differences in long and small crack behavior can be readily appreciated by replotting the long crack data in terms of ΔK_{eff} , after allowing for closure. As shown in Fig. 7, the scatter bands for small crack growth rates now come into close correspondence with long crack data, indicating that accelerated small crack behavior results primarily from reduced shielding. This implies a critical role of shielding in the fatigue of Al-Li alloys, both in promoting superior long crack resistance and, when restricted with cracks of limited wake, in causing enhanced small crack growth rates. With increasing crack size, however, closure gradually approaches a saturation long crack level, such that small crack growth rates merge with long crack results (Fig. 7). Moreover, at the higher ΔK levels, the role of wedge shielding mechanisms, such as roughness-induced closure, become diminished even for long cracks, due to the larger crack tip opening displacements (12).

Although a reduced role of crack closure at small crack sizes appears to be the major reason for their accelerated growth rates, it is apparent from Fig. 7 that the smallest cracks, typically below $\sim 5 \mu\text{m}$, show no indications of an intrinsic threshold. Moreover, they continue to grow at ΔK levels as low as $0.7 \text{ MPa}\sqrt{\text{m}}$, well below the long crack ΔK_{eff} threshold, implying that factors other than closure may be pertinent. One such difference may be related to evidence that suggests that small flaws may experience higher cyclic plastic strains at their tips (24). Another factor may be associated with differences in the statistical sampling of microstructural features encountered by large and small cracks (25). For example, naturally-occurring small cracks will tend to initiate at preferred "soft spots" in the microstructure and, unlike large pre-existing cracks, will not have their growth averaged over many disadvantageously oriented grains. Furthermore, microstructurally small cracks, corresponding to three-dimensional flaws with plastic zones typically smaller than key microstructural dimensions, will advance as if in a single crystal, preferentially oriented for operation of the relevant crack extension mechanism. Clearly, in such cases, where crack sizes are below any continuum approximation, it is inappropriate to talk of an intrinsic threshold for crack propagation (25).

Aluminum-Lithium Alloys

In summarizing the fatigue resistance of aluminum-lithium alloy 2090-T8E41, it is clear that the superior long crack growth properties and anomalously high small crack growth rates paradoxically are a consequence of the same phenomenon, namely significant crack tip shielding from crack deflection and particularly roughness-induced crack closure, resulting from highly deflected and meandering crack paths. Characteristic of "extrinsic toughening" (13), such mechanisms are extremely potent in impeding crack advance at low applied K_I levels, yet are less relevant to crack initiation or the growth of cracks with limited wake. However, where shielding remains effective, such as with long crack growth under constant amplitude or tension-dominated variable amplitude loading, 2090 shows a remarkable combination of high strength and fatigue crack growth resistance. Conversely, for the early growth of small fatigue cracks, which may provide a major contribution to fatigue life, 2090 is less attractive (19).

Behavior in 2090 is thus analogous to an aligned composite, as planes of weakness perpendicular to the short-transverse direction actually promote beneficial crack growth properties perpendicular to these planes. Accordingly, attempts at improving the short-transverse properties, through refinements in processing and thermomechanical treatments, may actually compromise the superior fatigue and fracture properties in the other directions.

CONCLUSIONS

Based on a study of the fatigue behavior (at $R = 0.1$) of long (≥ 5 mm) through-thickness cracks and naturally-occurring small (2 to 1000 μm) surface cracks in 12.7 mm thick plate of Al-Li-Cu-Zr alloy 2090-T8E41, the following conclusions can be made:

1. Rates of fatigue crack propagation in 2090 were found to be generally slower than in 2124 and 7150 aluminum alloys, despite having 30% higher strength. Such superior crack growth properties were associated with highly deflected crack paths, which promote significant crack tip shielding from crack deflection and crack closure from the wedging of fracture surface asperities.

2. Crack growth and closure behavior in 2090 was highly anisotropic, with growth rates varying by up to 4 orders of magnitude. The fastest growth rates occurred in the rolling plane, (S-L & S-T), where a delamination-type fracture path induced little crack deflection and resulting crack closure. Conversely, the slowest growth rates occurred perpendicular to the rolling plane (L-T, T-L & T-S), where a heavily deviated crack path induced significant shielding from crack deflection and closure.

3. Small surface cracks were observed to propagate at rates up to 1 to 3 orders of magnitude in excess of long cracks at the same ΔK , and were found to grow at ΔK levels well below the fatigue threshold, ΔK_{TH} . The close correspondence of small crack data with long crack results expressed in terms of ΔK_{eff} , suggests that the restriction in shielding for cracks of limited wake is a primary reason for their "anomalously" high growth rates.

ACKNOWLEDGEMENTS

This work was supported by the Director, Office of Energy Research, Office of Basic Energy Sciences, Materials Sciences Division of the U.S. Department of Energy under Contract No. DE-AC03-76SF00098. Thanks are due to the Aluminum Company of America for supplying the alloy and to H. Hayashigatani for experimental assistance.

REFERENCES

- (1) Sanders, T.H. and Starke, E.A. eds., "Aluminum-Lithium Alloys", Proc. First Intl. Conf., Stone Mountain, GA, TMS-AIME, Warrendale, PA, U.S.A., 1981.
- (2) Sanders, T.H. and Starke, E.A. eds., "Aluminum-Lithium Alloys II", Proc. Second Intl. Conf., Monterey, CA, TMS-AIME, Warrendale, PA, U.S.A., 1983.
- (3) Baker, C., Gregson, P.J., Harris, S.J. and Peel, C.J. eds., "Aluminium-Lithium Alloys III", Proc. Third Intl. Conf., Oxford, U.K., Institute of Metals, London, U.K., 1986.
- (4) Glazer, J., Verzasconi, S.L., Dalder, E.N.C., Yu, W., Emigh, R.A., Ritchie, R.O. and Morris J.W., Advances in Cryogenic Engineering, Vol. 32, 1986, pp. 397-404.
- (5) Coyne, E.J., Sanders, T.H. and Starke, E.A., in ref. 1, pp. 293-305.
- (6) Harris, S.J., Noble, B. and Dinsdale, K., in ref. 2, pp. 219-33.
- (7) Vasudévan, A.K., Bretz, P.E., Miller, A.C. and Suresh, S., Mater. Sci. Eng., Vol. 64, 1984, pp. 113-22.
- (8) Jata, K.V. and Starke, E.A., Metall. Trans. A, Vol. 17A, 1986, pp. 1011-26.
- (9) Petit, J., Suresh, S., Vasudévan, A.K. and Malcolm, R.C., in ref. 3, pp. 257-62.

- (10) Yu, W. and Ritchie, R.O., J. Eng. Matls. Tech., Trans. ASME, Series H, Vol. 109, 1987.
- (11) Venkateswara Rao, K.T., Yu, W. and Ritchie, R.O., Scripta Met., Vol. 20, 1986, pp. 1459-64.
- (12) Suresh, S. and Ritchie, R.O., in "Fatigue Crack Growth Threshold Concepts", Edited by D. L. Davidson and S. Suresh, TMS-AIME, Warrendale, PA, U.S.A., 1984, pp. 227-61.
- (13) Ritchie, R.O. and Yu, W., in "Small Fatigue Cracks", Edited by R. O. Ritchie and J. Lankford, TMS-AIME, Warrendale, PA, U.S.A., 1986, pp. 167-89.
- (14) Evans, A.G. and McMeeking, R.M., J. Amer. Cer. Soc., Vol. 65, 1982, pp. 242-246.
- (15) Marshall, D.B., Cox, B.N. and Evans, A.G., Acta Metall., Vol. 33, 1985, pp. 2013-2021.
- (16) Rioja, R.J. and Ludwiczak, E.A., in ref. 3, pp. 471-482.
- (17) Newman, J.C. and Raju, I.S., Eng. Fract. Mech., Vol. 15, 1981, pp. 185-192.
- (18) Zaiken, E. and Ritchie, R.O., Mater. Sci. Eng., Vol. 70, 1985, pp. 151-60.
- (19) Venkateswara Rao, K.T., Yu, W. and Ritchie, R.O., Metall. Trans. A, Vol. 18A, 1987, in press.
- (20) Suresh, S., Metall. Trans. A, Vol. 14A, 1983, pp. 2375-2343.
- (21) Ritchie, R.O. and Suresh, S., Metall. Trans. A, Vol. 13A, 1982, pp. 937-40.
- (22) Suresh, S., Vasudévan, A.K. and Bretz, P.E., Metall. Trans. A, Vol. 15A, 1984, pp. 369-379.
- (23) Carter, R.D., Lee, E.W., Starke, E.A. and Beevers, C.J., Metall. Trans. A, Vol. 15A, 1984, pp. 555-563.
- (24) Lankford, J. and Davidson, D.L., in "Small Fatigue Cracks", Edited by R. O. Ritchie and J. Lankford, TMS-AIME, Warrendale, PA, U.S.A., pp. 51-71.
- (25) Ritchie, R.O. and Lankford, J., Mater. Sci. Eng., Vol. 84, 1986, pp. 11-16.

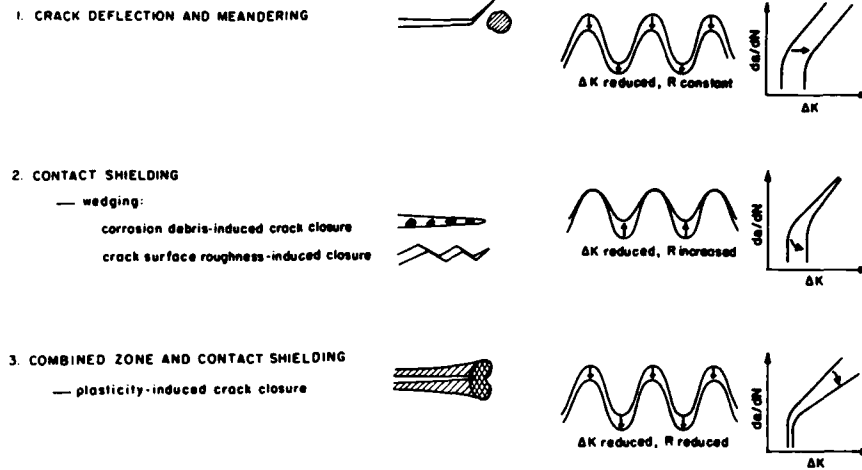


Figure 1 Primary mechanisms of crack tip shielding in aluminum-lithium alloys, and their consequences to crack growth behavior.

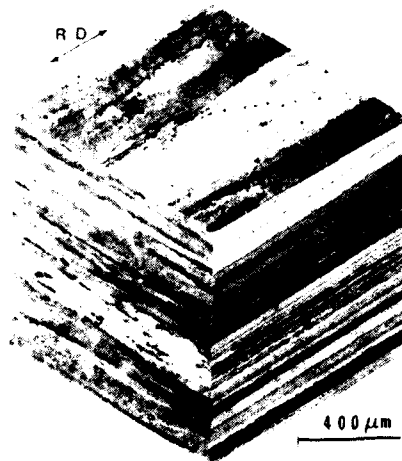


Figure 2 Optical micrograph of the grain structure in 12.7 mm plate of aluminum-lithium alloy 2090-T8E41 (Keller's reagent etch).

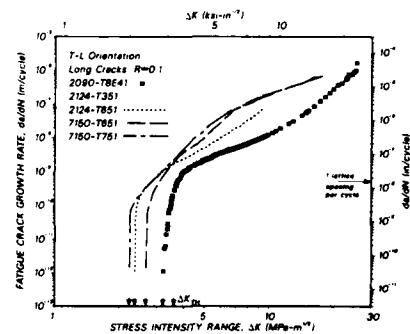


Figure 3 Comparison of fatigue crack growth behavior (long cracks) in 2090-T8E41 with 2124-T351 and 7150-T651 alloys.

FATIGUE 87

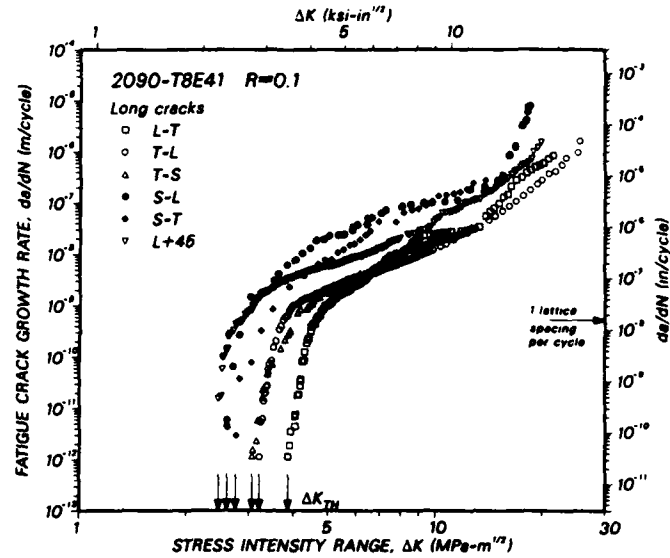


Figure 4 Variation in fatigue crack growth rates (long cracks) with ΔK in 2090-T8E41 at $R = 0.1$ as a function of plate orientation.

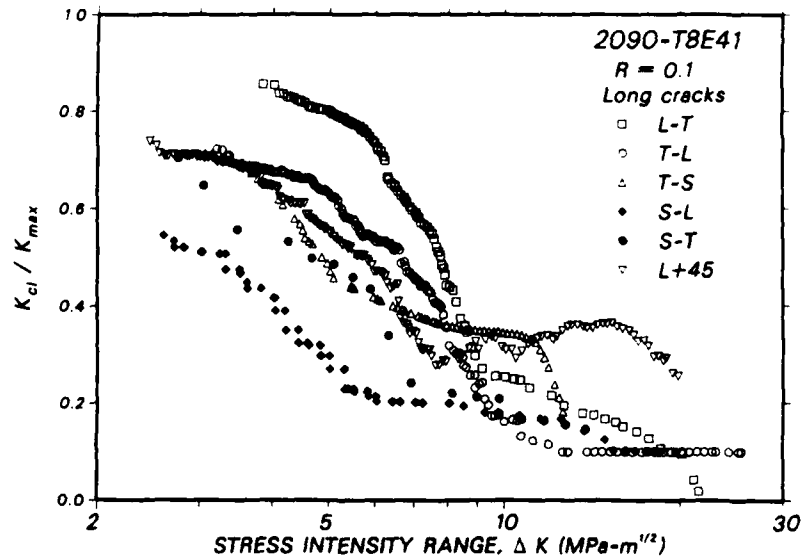


Figure 5 Variation in normalized closure stress intensity, K_{cl}/K_{max} , with ΔK (long cracks) in 2090-T8E41 at $R = 0.1$ as a function of orientation.

FATIGUE 87

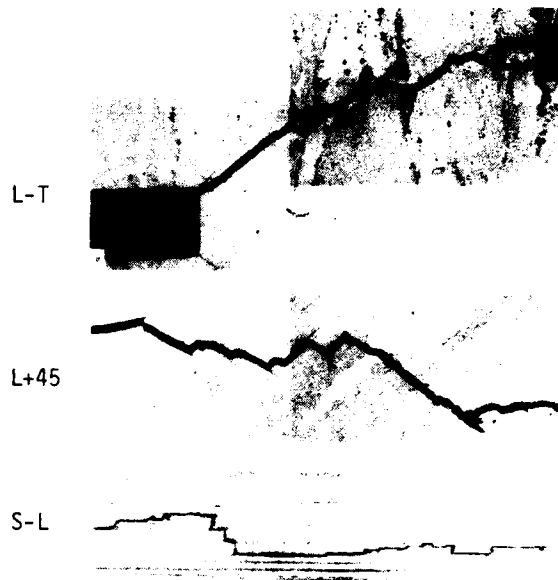


Figure 6 Crack path meandering during fatigue of 2090-T8E41, showing a) macroscopic crack branching, b) crystallographic slip-band cracking, and c) intergranular delamination.

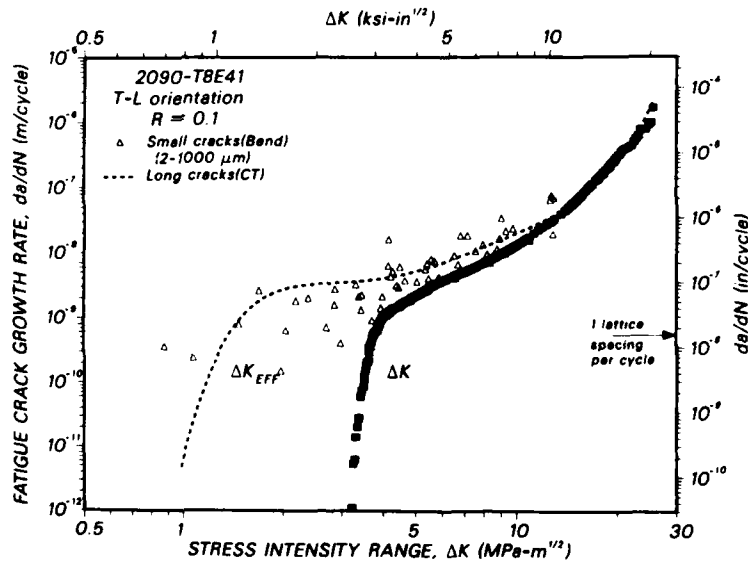


Figure 7 Comparison of fatigue growth rates of long (≥ 5 mm) and microstructurally-small (2 to 1000 μm) cracks in 2090-T8E41.

FATIGUE 87

FATIGUE 87

THE INFLUENCE OF SLIP MECHANISM ON FATIGUE OF Mg AND Mg-2.3Li

J.K. Gregory*

The fatigue behavior of pure magnesium is compared with that of Mg-2.3Li on smooth S-N specimens. To obtain a lifetime of 10^5 cycles at $R=0.1$, σ_{max} is 80 MPa for Mg, and 125 MPa for Mg-2.3Li. Surface cracks nucleate at roughly the same fraction of the total life, and grow at the same rates. This similarity in behavior, despite the difference in stress levels, is explained by two effects: 1) The proportional limit is increased from 4 MPa to 32 MPa by the addition of lithium, reducing the effective stress range driving crack growth; 2) Crack orientations in Mg-2.3Li are more strongly influenced by slip, resulting in deflection to unfavorable growth directions.

INTRODUCTION

Work by Hauser, Landon, and Dorn [1] showed that the tensile ductility of magnesium is substantially increased when lithium is added. Pure magnesium deforms by basal slip and twinning only, while solid solutions of magnesium containing a sufficient amount of lithium deform by prismatic slip as well. This effect is attributed to a reduction in the c/a ratio as lithium is added. The fatigue behavior of the Mg-Li system was investigated later by Lee and Jones [2], who found that adding lithium shifts the S-N curve upward in stress as much as 50 MPa. They assumed that only a small fraction of the fatigue life involved crack propagation, and thus they did not examine surface cracks. Their explanation for the improved fatigue resistance was based on an increase in the cyclic microyield stress. The present work focuses on the fatigue behavior of Mg and Mg-2.3Li. It is expected that a change in the crystallography of slip will correspond to a change in the orientations of cracks. In particular, it is anticipated that cracks will have greater difficulty crossing grain boundaries in pure Mg, since fewer slip systems are available.

*McDonnell Douglas Research Laboratories, P.O. Box 516, St. Louis, MO 63166

FATIGUE 87

EXPERIMENTAL PROCEDURE

Materials

Rods of pure magnesium and magnesium containing nominally 3 wt% Li were received as extrusions from the Dow Chemical Company. Chemical analysis gave values for the actual lithium content between 2.1 wt% and 2.6 wt%. The grain sizes of the as-received Mg and Mg-2.3Li were approximately 80 μm and 50 μm , respectively, and were not affected by annealing at 300°C. Neutron-diffraction pole figures (Figs. 1 and 2) indicate a strong fiber texture in both materials. In the pure magnesium, the fiber axis is close to $[11\bar{2}1]$, and in the magnesium with lithium the fiber axis is $[11\bar{2}0]$.

Mechanical Testing

Threaded-end specimens were used for both tensile and fatigue tests. After machining, specimens were annealed to reduce surface damage. Tensile properties were measured on cylindrical specimens, where strain gages were used to obtain Young's moduli. With one exception, hour-glass specimens were used to determine the S-N curves and measure surface crack growth rates. A cylindrical specimen was used to measure the growth rates in pure Mg to increase the number of cracks available for observation. Fatigue specimens were chemically polished in a 20% nitric acid solution to render a finish suitable for studying cracks, and to remove residual surface damage. Virtually no deformation twins were present after chemical polishing. Fatigue tests were done at $R=0.1$ at 30 Hz in air. Crack growth rates were measured by interrupting the fatigue tests and photographing the cracks in a light microscope. The surface crack length, $2l$, was taken to be the total length projected onto the plane perpendicular to the stress axis.

RESULTS

Tensile Properties

Tensile data are given in Table 1. As expected, the Mg-2.3Li is more ductile than the pure Mg. The Mg-2.3Li work hardens more slowly, resulting in similar values of σ_u . Figure 3 shows the initial portion of the stress-strain curve obtained with strain gages, along with extrapolations of the elastic regimes. The proportional limit for the Mg-2.3Li is significantly higher than for the Mg--about 32 MPa as opposed to 4 MPa. A chemically

FATIGUE 87

Table 1. Tensile data for Mg and Mg-2.3Li.

	Material			
	E (GPa)	$\sigma_{0.2}$ (MPa)	σ_u (MPa)	Elongation (%)
Mg	40	95	172	8
Mg-2.3Li	45	93	161	13

GP61 1420 1 R

polished tensile sample loaded to 10 MPa contained deformation twins, giving additional evidence for early yielding in Mg.

Fatigue Behavior

As Fig. 4 shows, the addition of 2.3 wt% lithium improves the S-N behavior significantly. The curve for Mg-2.3Li lies approximately 60 MPa higher than the curve for Mg. To achieve a lifetime of 10^5 cycles, maximum stresses of 80 MPa and 125 MPa for the Mg and Mg-2.3Li, respectively, were chosen for the crack growth studies.

Cracks appeared after roughly 10% of the total life in Mg, and after 20-30% of total life in Mg-2.3Li. Plots of the surface crack growth rate as a function of crack length are shown in Figs. 5 and 6. Growth rates for the two materials are almost identical, ranging from 10^{-9} to 10^{-3} m/cycle up to 1000 μ m. Arrest was observed more often in Mg, although it is remarkable that a crack as long as 550 μ m was arrested in Mg-2.3Li.

Crack initiation occurred at grain boundaries in both systems. However, mechanisms of propagation and arrest were different. Fig. 7 shows an arrested crack in pure Mg. This crack had been propagating near the grain boundaries. However, it branched and, while it stopped at A, grew transgranularly at B. Another arrested crack is shown in Fig. 8. The initiation site is indicated by the arrow. Although slip bands can be seen on the left side, the crack tends to propagate in the direction determined at initiation. Evidently, this direction is unfavorable, and the crack eventually propagates along a slip band. Figure 9 illustrates the propagation mechanism that is characteristic of cracks in Mg-2.3Li. Transgranular propagation is tortuous, containing segments which are parallel to the stress axis. Figure 10 shows the crack in Mg-2.3Li that apparently arrested. Although there is a change between 8 and 3.5×10^4 cycles, the direction of propagation is parallel to the stress axis and thus does not contribute to an increase in Δl . Examples of 1000 μ m-long cracks in Mg and Mg-2.3Li are given in Figs. 11 and 12. The crack in pure Mg (Fig. 11) is relatively smooth and does

FATIGUE 87

not necessarily propagate along slip bands. In Mg-2.3Li (Fig. 12), crack propagation often occurs parallel to the stress axis, making the crack trace much rougher.

DISCUSSION

The addition of 2.3 wt% lithium to magnesium has two separate effects: 1) the proportional limit is raised significantly, and 2) crack orientations become more consistent with expected prismatic and basal slip orientations. The first effect was discussed extensively by Lee and Jones, who performed detailed analyses of the tensile [3] and fatigue [2] behavior. They assumed that the majority of fatigue life is spent in nucleating cracks, which then propagate rapidly to failure. Hence, their explanation was based on an accumulated plastic work model and relied on the dependence of the cyclic plastic strain amplitude on the difference between σ_{\max} and σ_{py} . The present work shows that cracks initiate at a relatively short fraction of the lifetime. Therefore, failure is determined by the length and growth rate of the longest crack, which presumably would also depend on $\sigma_{\max} - \sigma_{\text{py}}$, or, more exactly, on the difference between the maximum stress and the proportional limit. For Mg, this study found a proportional limit of 4 MPa, as compared with a σ_{py} of 3.5 MPa [3] and a $\sigma_{0.01}$ of 14 MPa [1]. For Mg-2.3Li, the proportional limit is 32 MPa, compared with a value of 34.5 MPa for $\sigma_{0.01}$ [3]. (Mg-2.3Li was not examined in [2].) In this study, the stress range driving crack growth in Mg is actually 80 MPa - 8 MPa (since $R=0.1$), or 72 MPa, and for Mg-2.3Li, it is 125 MPa - 32 MPa, or 93 MPa.

The reduction in effective stress range caused by the increase in the proportional limit still leaves a 20 MPa difference in stress range to produce equivalent crack growth rates and lifetimes in Mg and Mg-2.3Li. This difference may be explained by a change in propagation mechanism, as indicated by crack trace orientations. The texture in pure magnesium is characterized by basal plane normals approximately 73° from the stress axis and the prism plane normals 33° and 90° from the stress axis. Crack traces do not reflect this texture. Instead, crack nucleation and propagation appear to be dominated by slip near grain boundaries. This is probably caused by incompatible slip in neighboring grains. Transgranular slip bands are observed, but cracks tend not to propagate along them. These observations agree with those of Hauser et al. [4] for tensile cracks. They proposed that alternate shear and cleavage might be responsible for the noncrystallographic transgranular cracks. For the preferred orientation in Mg-2.3Li, the basal plane normals should be 90° from the stress axis and the prism normals 30° and 90° from the stress axis. These orientations are found in some of the crack traces in Mg-2.3Li; in particular, segments parallel to the stress axis are often observed. Deflection of growth in this unfavorable direction undoubtedly plays a role in slowing the effective growth rates in Mg-2.3Li.

FATIGUE 87

CONCLUSIONS

1. The addition of 2.3 wt% lithium to pure magnesium increases the proportional limit from 4 MPa to 32 MPa and thus reduces the effective stress range driving crack growth.
2. Crack orientations in Mg are more strongly influenced by grain boundaries than by slip, while in Mg-2.3Li crack orientations can be correlated with slip. This correlation with slip in Mg-2.3Li results in unfavorable growth directions, further slowing crack growth rates.

SYMBOLS USED

- l = one half the crack length projected onto the plane perpendicular to the stress axis (μm)
- $\sigma_{10^{-6}}$ = tensile stress at 10^{-6} plastic strain (MPa)
- $\sigma_{0.01}$ = tensile stress at 0.01% plastic strain (Mpa)
- $\sigma_{0.2}$ = tensile stress at 0.2% plastic strain (MPa)

ACKNOWLEDGMENTS

The author would like to thank Dr. P.J. Meschter for drawing attention to the alloy system used in this study, Prof. W.J.D. Jones for providing information regarding extruding conditions for these materials, Prof. A.D. Krawitz for providing the neutron pole figures, and Dr. B. London for helpful discussions. This research was conducted under the McDonnell Douglas Corporation Independent Research and Development program.

REFERENCES

- (1) F.E. Hauser, P.R. Landon, and J.E. Dorn, Trans. A.S.M., Vol. 50, 1958, pp. 856-883.
- (2) R.E. Lee and W.J.D. Jones, J. Mater. Sci., Vol. 9, 1974, pp. 476-481.
- (3) R.E. Lee and W.J.D. Jones, J. Mater. Sci. Vol. 9, 1974, pp. 469-475.
- (4) F.E. Hauser, C.D. Starn, L. Tietz, and J.E. Dorn, Trans. A.S.M., Vol. 47, 1955, pp. 102-134.

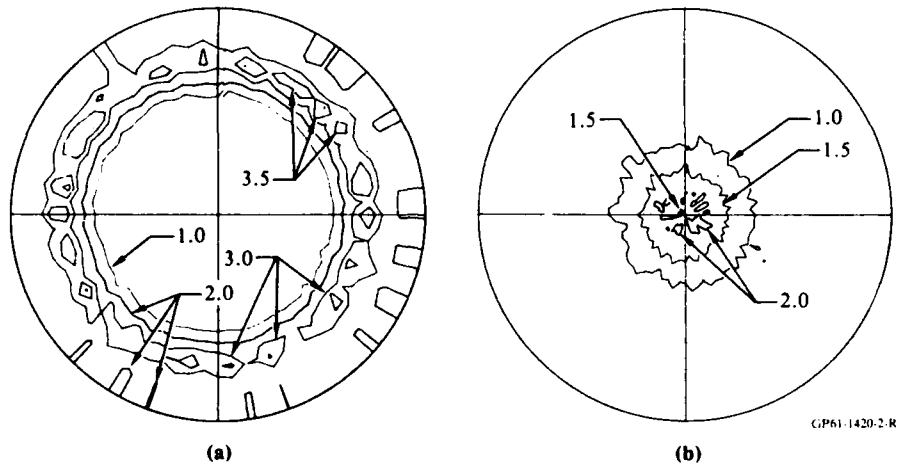


Fig. 1. a) (0002) and b) (11 $\bar{2}$ 0) pole figures for pure Mg.

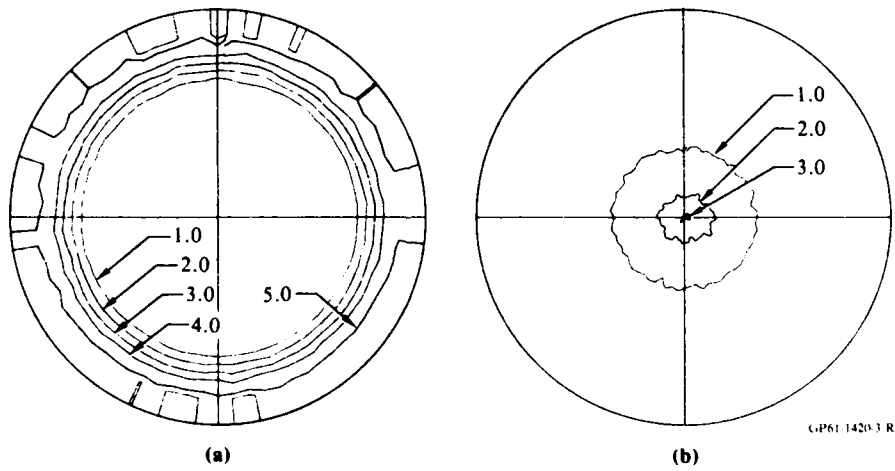


Fig. 2. a) (0002) and b) (11 $\bar{2}$ 0) pole figures for Mg-2.3Li.

FATIGUE 87

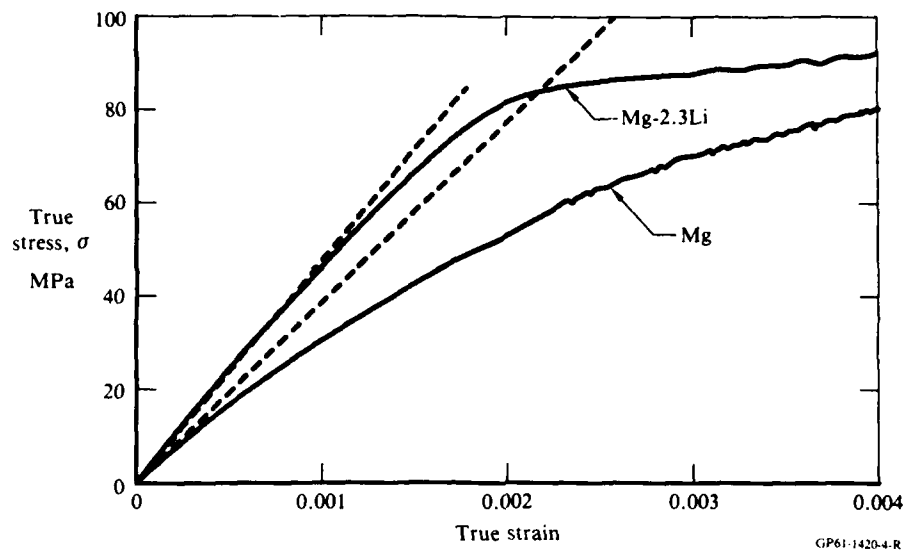


Fig. 3. Initial portions of stress strain curves with elastic regimes extrapolated.

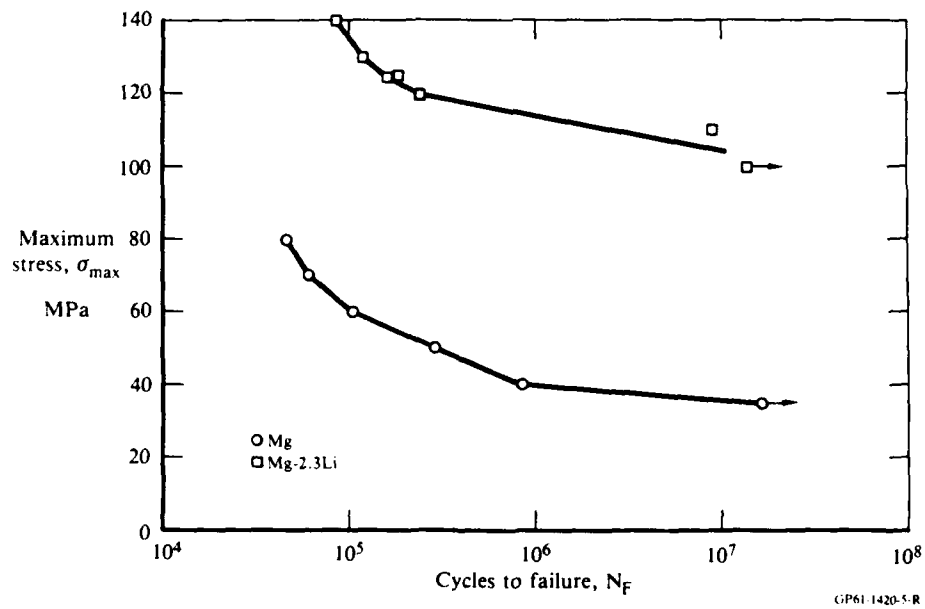


Fig. 4. S-N curves for Mg and Mg-2.3Li. Arrows indicate run-out.

FATIGUE 87

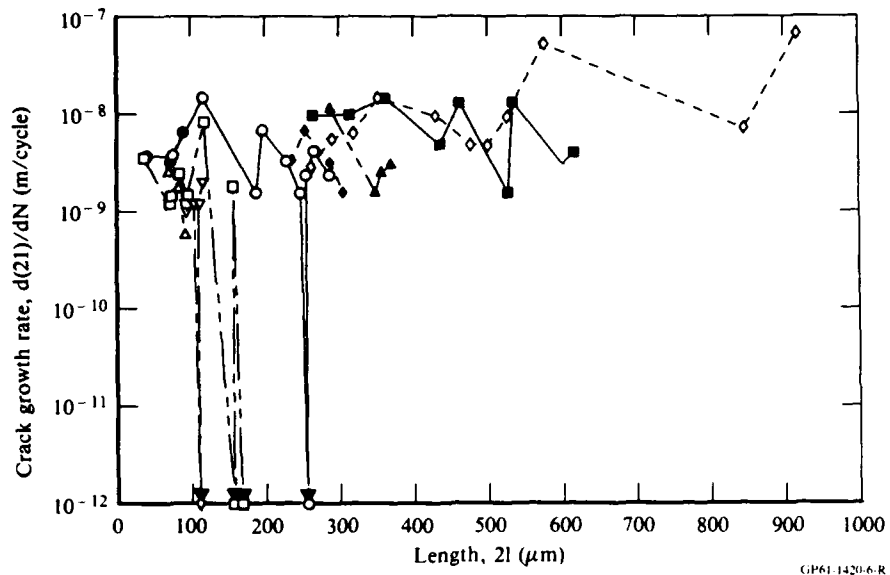


Fig. 5. Crack growth rates for pure Mg. Arrows indicate arrest.

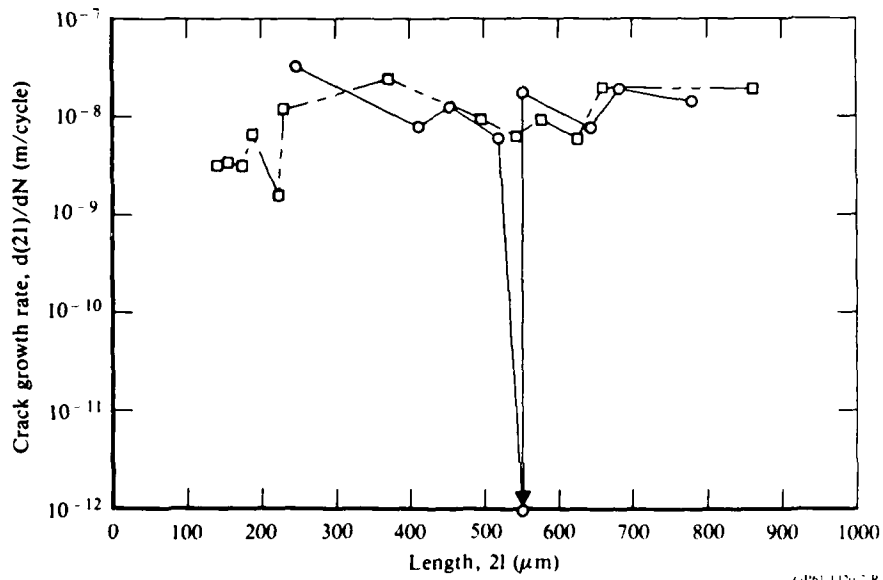


Fig. 6. Crack growth rates for Mg-2.3-Li. Arrow indicates arrest.



Fig. 7. Crack in pure Mg at a) 3×10^4 cycles and b) 3.5×10^4 cycles. Arrest has occurred at A, but growth continues at B.

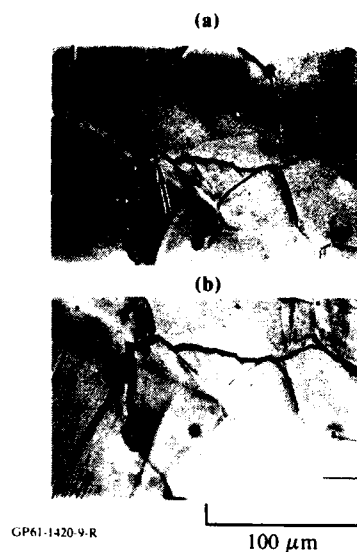


Fig. 8. Crack in pure Mg at a) 6.5×10^4 cycles and b) 8×10^4 cycles. Arrow indicates initiation site.

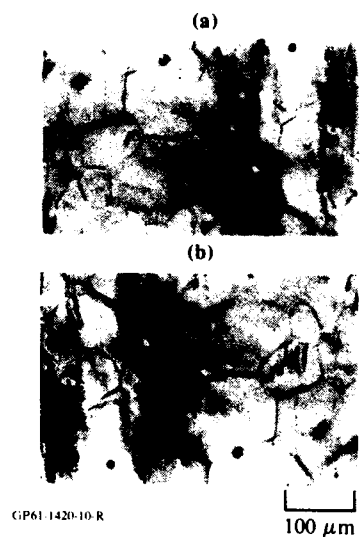


Fig. 9. Crack in Mg-2.3Li at a) 3×10^4 cycles and b) 6×10^4 cycles.

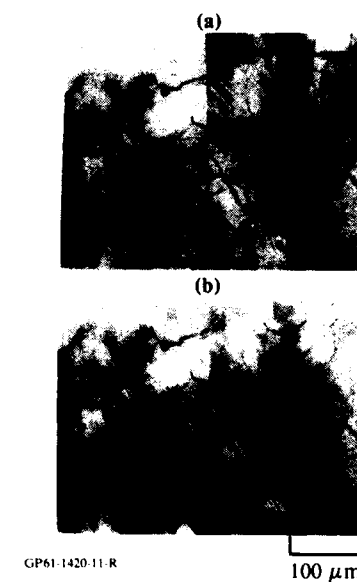


Fig. 10. Apparently arrested crack in Mg-2.3Li at a) 8×10^4 cycles and b) 8.5×10^4 cycles.

FATIGUE 87



Fig. 11. 1000 μm-long crack in Mg.



Fig. 12. 1000 μm-long crack in Mg-2.3Li.

FATIGUE 87

THE GROWTH BEHAVIOUR OF SMALL FATIGUE CRACKS; THE EFFECT OF MICROSTRUCTURE AND CRACK CLOSURE

K.Tokaji*, T.Ogawa*, S.Osako* and Y.Harada**

The small fatigue crack growth behaviour was studied under rotary bending in a low carbon steel prepared with two ferrite grain sizes, and was compared with the growth behaviour of large through cracks. The critical crack length above which linear elastic fracture mechanics (LEFM) is applicable was evaluated for small crack growth, and the effect of microstructure on crack growth rates and crack closure were examined experimentally. It was found that small cracks grew much faster than large cracks and also showed growth rate perturbations due to grain boundaries. Crack opening stress increased with increasing crack length and tended to be constant near the critical crack length. The anomalous or rapid growth behaviour of small cracks is discussed in terms of growth mechanisms and crack closure.

INTRODUCTION

It has been recognized that cracks shorter than a critical length tend to grow more rapidly than corresponding large fatigue cracks subjected to the same nominal driving force and also show growth rate perturbations(1-8).

The authors have indicated that the growth rate perturbations were attributed to grain boundaries, and that both the length below which cracks showed growth rate perturbations and the critical crack length above which LEFM was applicable were closely related to the microstructural unit size(9). Thus, microstructure is considered to be one of the most important parameters controlling the growth of small cracks. On the other hand, crack closure has been considered as a major cause for rapid crack growth rates of small cracks. However, crack closure data are limited because of considerable difficulty in the measurement(10-12).

In the present paper, the small fatigue crack growth behaviour is investigated under rotary bending in a low carbon steel prepared with two ferrite grain sizes. The critical crack length is

*Department of Mechanical Engineering, Gifu University, Gifu, Japan

**Nippon Sharyo, Ltd., Nagoya, Japan

FATIGUE 87

evaluated for small crack growth, and the effect of microstructure on crack growth rates and crack closure are examined experimentally. The anomalous or rapid growth behaviour of small cracks is discussed in terms of growth mechanisms and crack closure.

EXPERIMENTAL PROCEDURES

The material used in this study is a low carbon steel (S10C) which was supplied as 25mm thick plate. The chemical composition is listed in Table 1. Heat treatment was used to prepare materials in two average ferrite grain sizes \bar{d} , 24 μ m for fine grained material and 84 μ m for coarse grained material; the former was normalized for 1h at 900°C and the latter was annealed for 4h at 1100°C. The mechanical properties for both materials are given in Table 2.

Rotary bending fatigue plain specimens were machined to a diameter of 8mm and a gauge length of 10mm with the stress axis in the rolling direction; subsequently they were polished mechanically using emery-papers and finished by electropolishing to facilitate the observation of fatigue crack growth.

Tests were conducted on a 98Nm Ono-type rotary bending fatigue testing machine operating at 33Hz. All tests were performed at room temperature in laboratory air. Crack extension was measured by periodically replicating the surface of the specimen section. Crack closure data were obtained by measuring displacement between two microvickers indentations which were impressed at the positions straddling the center of the crack.

TABLE 1-Chemical Composition
of Material(wt%).

C	Si	Mn	P	S
0.11	0.20	0.38	0.013	0.019

TABLE 2-Mechanical Properties of Materials.

Upper yield point	Lower yield point	Tensile strength	Breaking strength on final area	Elongation	Reduction of area	Average ferrite grain size
σ_{su} MPa	σ_{sl} MPa	σ_B MPa	σ_T MPa	ϕ %	ψ %	\bar{d} μ m
298	286	432	977	33	70	24
233		402	789	32	63	84

EXPERIMENTAL RESULTS

Growth Characteristics of Small Cracks

The relationships between da/dN and ΔK for main cracks are

illustrated in Fig.1 with individual data points omitted in the interest of clarity. Since no exact solution of ΔK exists for a round bar specimen subjected to rotary bending, $\sigma\sqrt{\pi c}$ was used as a measure of ΔK . In the long crack regime, except for the data at $\sigma=310\text{MPa}$ which is higher than yield stress σ_{ys} ($1.08\sigma_{ys}$ for fine grained material and $1.33\sigma_{ys}$ for coarse grained material), there is no stress level-dependence of dc/dN , and the dc/dN vs ΔK curves for small cracks are coincident with the da/dN vs ΔK curves for large cracks represented by solid curve. A similar trend has been obtained in a high strength low alloy steel(9). Therefore, the crack growth under rotary bending could be characterized uniquely by $\sigma\sqrt{\pi c}$ when the stress level is small relative to the yield stress. In the small crack regime, dc/dN is sensitive to stress level, being higher with increasing stress level, and small cracks grow much faster than large cracks and below the threshold values for large cracks. Moreover, the growth behaviour in this regime is very complex and significant retardations in dc/dN are observed, particularly in coarse grained material.

The dc/dN vs ΔK curves for rapidly growing small cracks gradually approach the da/dN vs ΔK curves for large cracks as the ΔK value increases, i.e. crack length increases; both curves converge at a certain ΔK value which depends on stress level. The ΔK values and resulting values of $2c$ at the points of convergence are represented in the figures. These $2c$ values mean the critical crack length $2c_c$ above which LEFM can be used. The $2c_c$ values for growing small cracks range from 1.81mm to 1.96mm for fine grained material and 2.32mm to 2.82mm for coarse grained material. Since the relationship between σ and $2c_c$ is not always clear in this study, the $2c_c$ value would be established as the maximum length of $2c_c$ in different stress levels.

Effect of Grain Boundaries

The effect of grain boundaries are shown in Fig.2. Crack growth rates dc/dN are presented as a function of c . Traces of the cracks including grain boundaries are also given in order to appreciate the crack growth path and the position of grain boundaries. Characters labelled on these figures show the position of grain boundaries crossed by cracks. In both materials, small cracks grow in an irregular manner with dc/dN decreasing when crack tips cross grain boundaries or reach triple points of grain boundary. However, the decrease in dc/dN also takes place at positions other than grain boundaries. This appears to be due to grain boundaries within the bulk(9). Similar effects of grain boundaries could also be recognized at $\sigma=310\text{MPa}$, but the stress level dependence was unclear. However, the effect of a grain boundary depends strongly on crack length and becomes obscure with increasing crack length. The crack lengths $2c_m$ below which the effect of a grain boundary was observed are approximately 200 and 250 μm for fine and coarse grained materials, respectively. In this sense, small cracks shorter than $2c_m$ are termed microstructurally

FATIGUE 87

small crack. In the region longer than $2c_m$, the effect of grain boundaries disappears completely and da/dN increases monotonously with increasing crack length.

Fractography

As a typical example, fractographs associated with small crack growth in coarse grained material are shown in Fig.3. Fracture surface appearance over a certain distance from the initiation point, region A, clearly differs from that of the other regions B and C. The surface length of region A, $313\mu\text{m}$, is represented on the micrograph. For fine grained material, this length was $133\mu\text{m}$. It should be noted that these lengths approximately correspond to the length below which the effect of grain boundaries was observed, i.e. $2c_m$. As can be clearly seen at high magnification, the fracture surface in region A is relatively flat and consists of many straight lines parallel to the direction of crack growth. This fracture surface morphology has a crystallographic feature which was formed by a pencil-glide mechanism of slip(13,14). Apart from the question of the terminology, Stage I crack or shear type crack, it is not doubted that in region A the crack grew along a slip plane. It should be emphasized that the region is not confined within one grain size and extends over several grain sizes. Fracture surfaces B and C correspond, respectively, to the region in which there was no effect of a grain boundary but da/dN was faster than large cracks ($2c_m < 2c < 2c_0$), and to the region in which da/dN was coincident with that of large cracks ($2c > 2c_0$). There is no significant difference in fracture surface morphology between both; the fracture surfaces are almost totally covered with striation-like markings.

Crack Closure Measurements

Crack opening stress is presented in Fig.4 as a function of $2c$. Measurements were made in the region of crack length $2c_m$ to $2c_0$ at $\sigma = 240\text{MPa}$. In both materials, crack opening stresses increase with increasing crack length(10-12), and cracks are open under compressive load in $2c < 1.3\text{mm}$ for fine grained material and whole crack length for coarse grained material. Moreover, crack opening stresses for coarse grained material are lower than those for fine grained material. In the region $2c \geq 1.3\text{mm}$ for fine grained material and $2c \geq 2\text{mm}$ for coarse grained material, crack opening stresses tend to be constant independent of crack length. That is, at these crack lengths, crack opening stress is considered to attain the same level as large cracks. It should be noted that these crack lengths are approximately equal to $2c_0$ ($2c_0$ values at this stress level are represented in the figure). Therefore, it was confirmed that small cracks in the region of crack length $2c_m$ to $2c_0$ are in the process of increasing crack closure.

Figure 5 shows the observations of plastic deformation surrounding the crack. Ferrite grains in which slip lines were observed are regarded as plastic deformed grain and hatched lines

FATIGUE 87

are drawn in the illustrations. As can be seen from the figure, extensive plasticity is observed at the circumference of the crack rather than the crack tip, and is more remarkable for coarse grained material than fine grained material.

DISCUSSION

Growth rate perturbations of small fatigue cracks in the low ΔK regime are attributed to a blockage effect of ferrite grain boundaries as shown in Fig.2. The regions in which the effect of grain boundaries was observed are $2a < 200 \mu m$ ($\sim 8d$) for fine grained material and $2a < 250 \mu m$ ($\sim 3d$) for coarse grained material. It was confirmed by the fractographic analysis of the fracture surface (Fig.3) that cracks in this region grew along slip planes, i.e. in Mode II. Therefore, the effect of a grain boundary appears to be due to the orientation of ferrite grains (15). For example, when the orientation between the grain containing the crack and the neighbouring grain are similar, there would be little decrease in growth rates at the boundary. In fact, there were some cases in which cracks were not impeded by boundaries in their paths (see Fig.2). In general, it has been recognized (15) that when cracks are of a length comparable to the scale of the microstructure, the growth is affected by the microstructure and hence the relevance of continuum mechanics is limited. It is interesting that the results in this study indicate such regions extending over the length of several grain sizes. Therefore, the anomalous crack growth behaviour in this region may be related to different growth mechanisms from large cracks.

In the region $2a_m < 2a < 2a_c$, there was no effect of a grain boundary and the fracture surface morphology was the same as that in the region $2a > 2a_c$. However, da/dN was still faster than large cracks. This is due to less crack closure of small cracks as shown in Fig.4. It is considered that the less crack closure of small cracks may be attributed to elastic-plastic effect surrounding the crack. When cracks are extremely small ($\sim 2a_m$), plastic deformation occurs extensively at the circumference of the crack rather than the crack tip and thus the constraint of elastic material surrounding plastic region is decreased, leading to the small amount of plasticity-induced crack closure; then crack opening stress of small cracks would decrease. With increasing crack length, cyclic plastic deformation progressively concentrates at the crack tip and crack closure results from a consequence growing through the crack tip plastic zone generated by the crack itself, that is, the crack closure behaviour of small cracks approaches that of large cracks. Thus, less crack closure is responsible for rapid growth of small cracks in the region $2a_m < 2a < 2a_c$, and cracks in this region can be termed mechanically small crack.

Based on the above results and discussions, small fatigue cracks can be classified to three regimes corresponding to mechanisms and characteristics as shown in Fig.6. Cracks which are

FATIGUE 87

simply physically small are defined as physically small crack and are below several millimeters in length. The physically small cracks can be classified to microstructurally small crack, mechanically small crack, and crack regarded as large cracks, corresponding to their lengths. The microstructurally small cracks are Stage I crack or shear type crack; their growths are strongly affected by microstructure. The mechanically small cracks, i.e. from $2c_m$ to $2c_c$, are the process of increasing crack closure and the crack closure level is lower than large cracks. Cracks regarded as large cracks should be called small crack when only their lengths are considered, but the mechanical behaviour is similar to large cracks.

CONCLUSIONS

The conclusions obtained are summarized as follows:

(1) Small cracks grew much faster than large cracks and below fatigue crack thresholds for large cracks.

(2) The critical crack lengths above which LEFM is applicable were approximately 1.96mm for fine grained material and 2.82mm for coarse grained material.

(3) The crack growth rates of small cracks decreased at ferrite grain boundaries or at triple points of grain boundary.

(4) In the region where the effect of grain boundaries on crack growth rates was observed, cracks grew along slip planes, i.e. in Mode II, and extended over several grain sizes.

(5) Crack opening stress increased with increasing crack length and tended to be constant at a certain crack length. This length was approximately equal to the critical crack length.

Acknowledgments—The authors wish to thank Mr M.Niinomi for experimental assistance.

SYMBOLS USED

c	=surface half crack length
c_m	=surface half crack length below which the effect of a grain boundary is observed
c_c	=critical surface half crack length above which LEFM is applicable
d	=average ferrite grain size
da/dN	=crack growth rate per cycle for a large fatigue crack
dc/dN	=surface crack growth rate per cycle for a small fatigue crack
ΔK	=stress intensity factor range
N	=number of cycles

FATIGUE 87

- 1 stress amplitude
- 2 crack opening stress
- 3 yield stress of the material

REFERENCES

- (1) Pearson, S., Engng Fract. Mech., Vol.7, 1975, pp.235-247.
- (2) Taylor, D. and Knott, J.F., Fatigue Engng Mater. Struct., Vol.4, No.2, 1981, pp.147-155.
- (3) Lankford, J., Fatigue Engng Mater. Struct., Vol.5, No.3, 1982, pp.233-248.
- (4) Lankford, J., Fatigue Engng Mater. Struct., Vol.6, No.1, 1983, pp.15-31.
- (5) Tanaka, K., Hojo, M. and Nakai, Y., ASTM STP811, 1983, pp.207-232.
- (6) Brown, C.W. and Hicks, M.A., Fatigue Engng Mater. Struct., Vol.6, No.1, 1983, pp.67-76.
- (7) Brown, C.W. and Taylor, D., TMS AIME, 1984, pp.433-446.
- (8) Gerdes, C., Gysler, A. and Lutjering, G., *ibid.*, 1984, pp.465-478.
- (9) Tokaji, K., Ogawa, T., Harada, Y. and Ando, Z., Fatigue Fract. Engng Mater. Struct., Vol.9, No.1, 1986, pp.1-14.
- (10) James, M.R. and Morris, W.L., Metall. Trans. A, Vol.14A, 1983, pp.153-155.
- (11) Breat, J.L., Mudry, F. and Pineau, A., Fatigue Engng Mater. Struct., Vol.6, No.4, 1983, pp.349-358.
- (12) Jono, M., Song, J., Okabe, M., Uesugi, N., Ohgaki, M. and Eguchi, N., J. Soc. Mater. Sci. Japan, Vol.33, No.368, 1984, pp.560-565(in Japanese).
- (13) Otsuka, A., Mori, K., Miyata, T. and Yamamoto, S., Trans. JSME, Vol.42, No.357, 1976, pp.1313-1323(in Japanese).
- (14) Asami, K. and Terasawa, M., J. Soc. Mater. Sci. Japan., Vol.30, No.335, 1981, pp.803-808(in Japanese).
- (15) Suresh, S. and Ritchie, R.O., Int. Metal Reviews, Vol.29, No.6, 1984, pp.445-476.

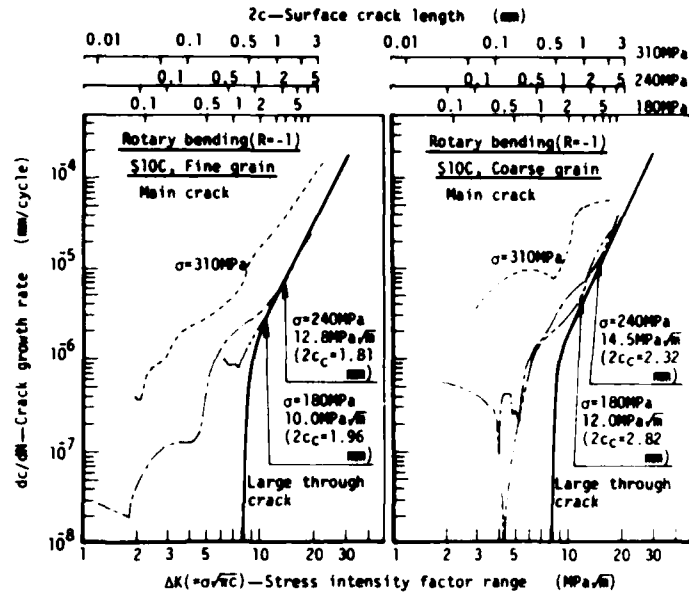


Figure 1 Growth characteristics of small fatigue cracks (main crack); individual data points are omitted in the interest of clarity.

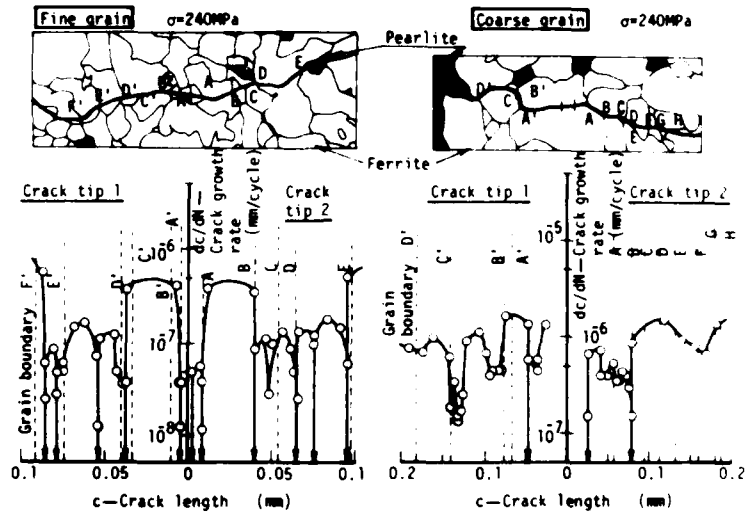


Figure 2 Effect of grain boundaries on crack growth rates.

FATIGUE 87

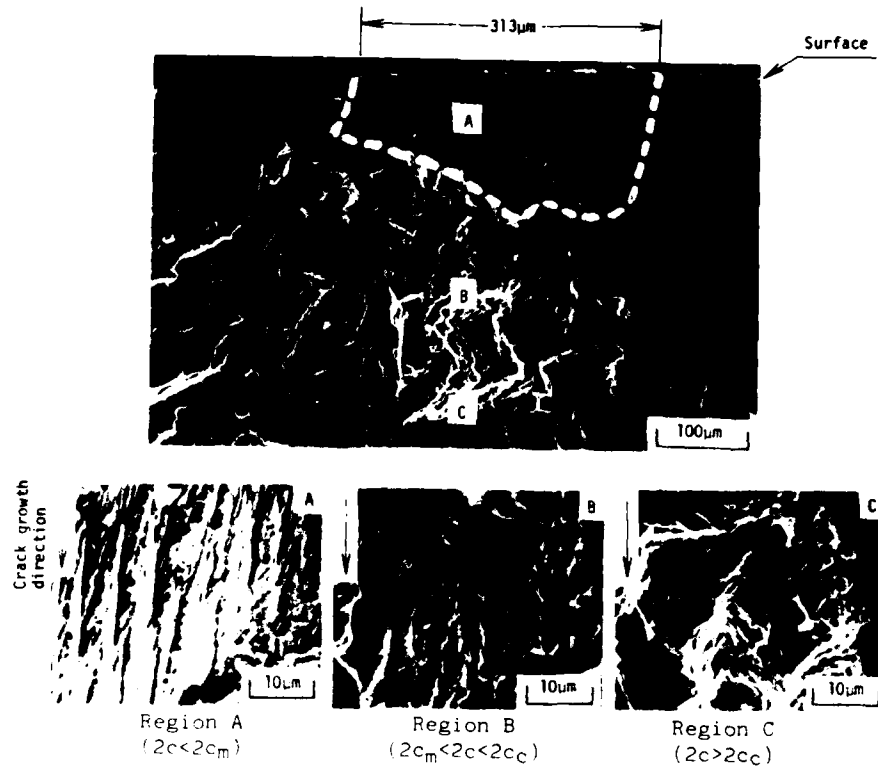


Figure 3 Fractographs of a small fatigue crack in coarse grained material.

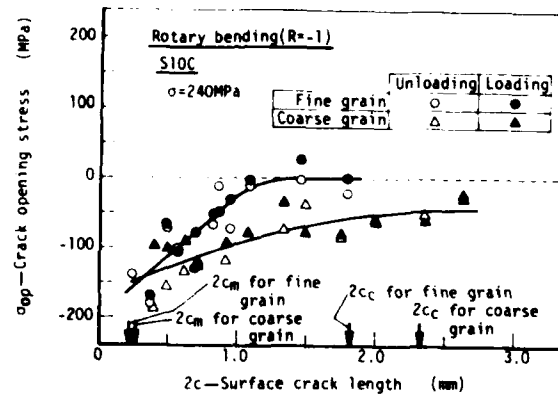
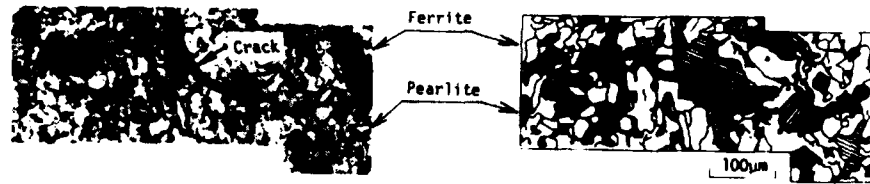
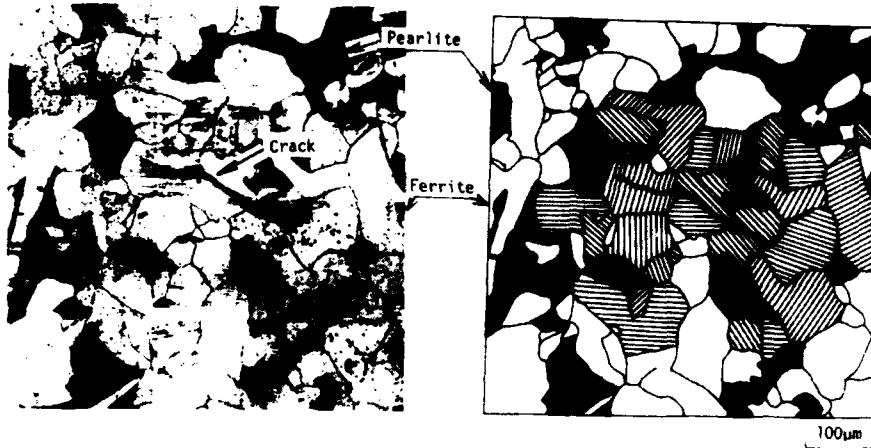


Figure 4 Variation of crack opening stress with surface crack length.



(a) Fine grained material ($2c=327\mu\text{m}$)



(b) Coarse grained material ($2c=294\mu\text{m}$)

Figure 5 Observations of plastic deformation surrounding the crack.

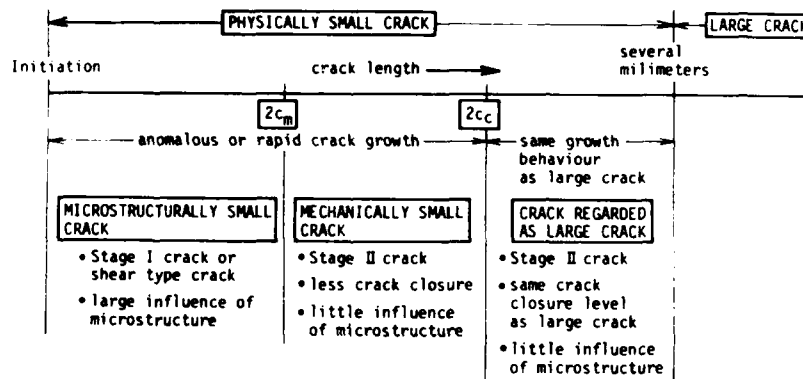


Figure 6 Three regimes of small fatigue cracks and their corresponding mechanisms and characteristics.

THE INFLUENCE OF MICROSTRUCTURE AND RESIDUAL STRESSES ON THE
INITIATION AND PROPAGATION OF SHORT SURFACE CRACKS ON AlMgSi1

B. Meier and V. Gerold*

The effect of microstructural features and residual compression stresses on crack initiation and growth of short surface cracks in Al-1 wt.% Mg-1 wt.% Si alloys in the peak-aged condition has been investigated. A clear influence of slip distribution on crack initiation mechanisms has been found. In the high cycle regime the interface inclusion-matrix transverse to the loading direction plays a dominant role in crack initiation. In the growth behaviour of surface cracks exists a regime with a slope $m = 2$ (Paris). In that regime nearly no influence of microstructural features and residual compression on the growth rate in contrast to that found by through-thickness cracks could be observed.

INTRODUCTION

The total lifetime N_f during fatigue can be divided into three regimes:

$$N_f = N_i + N_{SC} + N_{MC} \quad (1)$$

where N_i is the number of cycles necessary to initiate the first crack of a predetermined length, N_{SC} that for the growth of short surface cracks and N_{MC} that for the growth of through-thickness cracks. In this study we are interested in the influence of dispersoid distribution, grain size and near surface residual stresses on the first two regimes. Aluminium-based alloys are widely used for aircraft and ground transport systems. Typical components of these alloys are the shearable coherent or semicoherent precipitates promoting a localization of slip, small incoherent particles (0.1 - 1 μm) often called dispersoids, which act against this localization, and large intermetallic inclusions (5 - 20 μm) which can act as preferred crack initiation sites (1-6).

* Max-Planck-Institut für Metallforschung, Institut für
Werkstoffwissenschaften and Institut für Metallkunde der
Universität Stuttgart, D-7000 Stuttgart, F.R.Germany

FATIGUE 87

Two commercial AlMgSi1 alloys comparable to Al 6170 with the same chemical composition in the peak-aged condition but with a coarse and a fine dispersoid distribution (1) and therefore different grain sizes were selected for surface modification by thermomechanical treatment (TMT). The coarse dispersoid distribution (P-type alloys) results in a inhomogeneous slip distribution with a localization of plastic deformation in slip bands, whereas the fine distribution (S-type alloy) hinders dislocation movement and leads to a more homogeneous slip distribution. Through TMT the surface grain size and near surface residual stress was modified without altering the distribution and size of the hardening precipitates. Dispersoids and inclusions and therefore the slip distribution of the respective alloy also remained the same. The surface microcrack growth rates are compared to the growth rates of through-thickness cracks. The latter show a strong influence of dispersoid content (4) and distribution and of grain size (1) in the usual ΔK description.

MATERIAL PREPARATION AND EXPERIMENTAL PROCEDURE

The two basic structures are

Alloy P: coarse distribution of coarse dispersoids (0.5 μm in extruding direction), large pancake shaped grains

Alloy S: very fine distribution of fine dispersoids (0.1 μm), fine subgrain structure.

Both alloys showed large inclusions of Mg_2Si and another phase enriched by Fe, Si and Mn (5 -20 μm). The net cross section of the mildly notched specimens ($\alpha_K = 1.5$) was 2.5 x 4 mm^2 . They had been prepared out of extruded bars with a cross section of 3 x 20 mm^2 .

Treatment D: The specimens were solution treated in a salt bath (10 min at 808 K), water quenched and aged for 16 h at 433 K to the peak aged condition. After heat treatment the notch surface was deformed by machining the notch. This leads to residual compression stresses in the strain-hardened surface.

Treatment R: The notch was machined before heat treatment, which results in a recrystallized layer at the notch surface (Fig.1).

The received microstructures are described in Table 1. The fatigue experiments were carried out in laboratory air at a constant stress amplitude using 27 Hz with a stress ratio of 0.1. At the notch surface the crack initiation and propagation was observed in-situ by light microscopy in the range from 10 to 500 μm for the crack length. Propagation rates were taken only for such cracks which had a minimum distance larger than 500 μm from the edge of the notch.

FATIGUE 87

TABLE 1 - Microstructures obtained by thermomechanical treatment

Alloy	SD	SR	PD	PR	P
dispersoid distribution	fine		coarse		
grain size (μm) bulk material	5 - 15 subgrains		450 x 320 x 100		
thickness of recryst. surf. layer (μm) grain size (μm)	- -	100-300 20-60	- -	50 10-30	only local regions with fine grains
near surface residual compr. stresses	yes	no	yes	no	no
σ_y (MPa)	350		310		

RESULTS AND DISCUSSION

Fatigue Life and Crack Initiation

Figure 2 shows the ratio of the number of cycles necessary to build up the first crack with a surface length of 100 μm , $N_{i,100}$, to N_f . This quantity enables us to demonstrate the "efficiency" of the surface layer which has a thickness of only 50 μm in alloy PR. One can see that in all cases the contribution of crack initiation to N_f increases with total lifetime. In the low cycle regime ($N_f = 10^4$ - 10^5) 30 to 60% of the total lifetime is necessary for building up a 100 μm crack. This fraction ultimately increases to 95% in the high cycle regime ($N_f = 10^6$ - 10^7), pointing out the great importance of crack initiation and short crack propagation in service of technical components. Since in the high cycle regime the crack formation governs the lifetime, the crack formation and therewith N_f is strongly influenced by grain size and residual stresses (Fig.3):

- $N_{i,100}$ increases under the influence of near surface compression stresses (σ_y) for both dispersoid distributions in the high cycle regime (Fig.3a,b).
- A marked influence of the surface grain size on $N_{i,100}$ was found only for the P-type alloys which contained the coarse dispersoid distribution (Fig.3a). The recrystallized fine grains (PR) showed a larger $N_{i,100}$ than the other (P).

These results on crack initiation can be attributed to the correlation between the mean free path length for dislocation motion and crack formation mechanisms. In the case of coarse dispersoid distributions (P-type), the long free path length produces pronounced localized slip caused by the shearing of

strengthening precipitates. This leads to crack initiation in slip bands. Likewise crack initiation at grain boundaries could be detected, too. However, in the case of a fine dispersoid distribution (S-type) a very homogeneous slip distribution is produced so that in most cases neither grain boundary nor slip band crack initiation could be observed. Thus, a distinct influence of grain size on the crack formation period is only possible in structures with an inhomogeneous slip distribution. Also a marked retardation in crack initiation is only efficient for the inhomogeneous slip distribution in the low cycle regime. Such pronounced retardation is also reported by Gräf and Verpoort (7) for a planar slip alloy in the underaged condition, while in the overaged condition with a homogeneous slip distribution nearly no retardation is observed.

At low stress amplitudes cracks always initiated near the inclusion-matrix interface in both slip distributions. Figure 4 shows two crack initiation sites in P-type alloys. For better contrast conditions Fig.4b is drawn from a SEM-photograph. Fig.4a shows a cluster of inclusions fractured during the hot forming process. The fracture of the inclusions seems to have no marked influence on the crack initiation possibility as can be seen in Figs.4a and b, which are both showing pre-cracked inclusions. In Fig.4a one can see extrusions created during fatigue near the part of the interface which is oriented normal to the vertical loading direction. From that region with strong and irreversible slip activity a slip band starts to grow into the matrix. Fig.4b shows a crack initiation site after specimen failure. A persistent slip band which has been formed at the transverse interface of an inclusion has grown through the whole grain with subsequent transgranular crack growth.

Figure 4 demonstrates the dominant role of the transverse interface for crack initiation. This should be due to an easier onset and higher mobility of dislocation motion near the surface of the specimen and near the interface between inclusion and matrix. The reasons for this are:

- The stress concentrating effect of the hard inclusions at the transverse interfaces undergoing tension deformation (stress concentration factor $\alpha_k \approx 2-5$).
- Weaker bonding forces between the matrix atoms close to the interface compared to those far away from it.

Additionally, there may be a high degree of slip irreversibility near the inclusions caused by the more complex stress field in that region. Due to the easy onset of dislocation motion this crack initiation mechanism is of great importance for technical components in service. The cracking of inclusions as reported by James and Morris (3) could be observed only at high stress amplitudes. Since James and Morris used flexural fatigue specimens it is possible

that there is an influence of flexural strain, which may support a cracking mechanism of the inclusions.

Short Crack Growth

For the sake of comparison with through-thickness crack growth the growth rates for surface cracks are related to ΔK given by

$$\Delta K = 1.18 \cdot \Delta \sigma_{\text{net}} \cdot \sqrt{a} \quad (2)$$

under the assumption of semicircular (radius a) growth (9). The growth rates in this investigation show the typical short crack behaviour:

- crack growth below the macrocrack threshold ΔK_{th} ,
- high growth rates compared to macrocracks,
- pronounced scattering of the data.

In this kind of experiments with constant stress amplitude one or more cracks initiate which could be detected at a minimum length of about 10 μm . So we obtain a very low surface crack threshold of 0.3 MPa $\sqrt{\text{m}}$. With better optical resolution a somewhat smaller threshold should be expected. In comparison to this surface crack threshold for through-thickness cracks a threshold of $\Delta K = 3$ MPa $\sqrt{\text{m}}$ is found (Fig.5). However, quite recent research on bending specimens showed a threshold of $\Delta K_{\text{eff}} \approx 1$ MPa $\sqrt{\text{m}}$ (10).

For the investigated AlMgSi1 alloys three regimes of crack growth behaviour could be distinguished (Fig.5):

Regime I. $0.3 < \Delta K \leq 1.0$ MPa $\sqrt{\text{m}}$: This regime corresponds to crack lengths $2a < 140$ μm . The mean free path length for dislocation motion influences the crack initiation and growth mechanisms. In this regime we find a pronounced influence of slip distribution on the growth mechanisms. In the S-type alloys with a very fine slip distribution cracks grow in a Stage II mechanism. Whereas in the P-type alloys we find slip band crack growth in the initial stage. In the latter case we observe a marked influence of microstructure on the growth rate. For example, in a PD-specimen fatigued near the endurance limit seven slip bands initiated at inclusions in a large surface grain. Before reaching the grain boundary their growth rates decreased practically to zero. Finally, after an incubation time, slip band cracks were initiated in adjacent grains in front of the PSB's with a clear orientation difference. In other cases crack growth retardation was accompanied by a change from slip band cracking to Stage II cracking in the adjacent grain. The growth behaviour in this regime is controlled by microplasticity and in doing so, not only the crack growth mechanism but also the initiation mechanism and for that the volume necessary for crack initiation have to be taken into account for a detailed description. No doubt that ΔK is not sufficient in that regime to describe crack propagation.

Regime II. $1.0 \leq \Delta K \leq 3 \text{ MPa}\sqrt{\text{m}}$: The corresponding crack length ranges from about $2a = 80$ to $500 \mu\text{m}$. The growth rate increases more uniformly with crack length at constant stress amplitude. In our measurements no marked influence of the stress amplitude on the mean value of da/dN for a fixed crack length increment was found. Within the scatterband ($m = 2$) there is no distinct influence of the different microstructures on the growth rates compared to the macrocrack data of S- and P-type alloys measured by Ruch (1) or by Edwards and Martin (8).

Regime III. $\Delta K > 3 \text{ MPa}\sqrt{\text{m}}$: The macrocrack data show a clear influence of microstructure, i.e. slip distribution and grain size on threshold and growth behaviour. Edwards and Martin fatigued AlMgSi alloys with different Mn-content but comparable grain size. With higher Mn content the threshold increases. At $\Delta K > 10 \text{ MPa}\sqrt{\text{m}}$ the alloy with the higher dispersoid volume fraction shows higher growth rates. Also the measurements of Ruch (1) show a 5 times higher growth rate for the S-type alloy. Therefore it can be concluded that a main rate controlling parameter in this regime is the slip distribution.

Detert et al (2) demonstrated that the growth rates of different AlMgSi1 alloys fit into one scatterband using a ΔK value which has been corrected for crack closure effects, ΔK_{eff} . Thus the differences in macrocrack behaviour should be caused by closure effects due to different fracture surfaces. Influenced by grain size and slip distribution the P-type alloys show a distinct three-dimensional macroscopic topography, whereas the S-type topography is more two-dimensional in a macroscopic view. So roughness-induced closure (10) causes the slower growth rates in the P-structures. The scatterband in Regime II has a slope $m = 2$ (Paris law) and its elongation includes the macrocrack data of Detert et al (2) described by ΔK_{eff} . This points to an absence of crack closure effects in the regime II under the assumption that the ΔK description is valid. It has been reported that crack closure effects become significant for longer crack lengths (12,13). But there is still the question if ΔK really describes the driving force for crack growth in regime II because the increase in growth rate is strongly related to the increasing crack length and effectively independent from the stress amplitude. In addition, Morris et al (14) stated the influence of the grain size on the deformation process at the crack tip.

The authors are obliged to Dr. G. Scharf, Vereinigte Aluminiumwerke AG, Bonn, for providing the extruded material.

REFERENCES

- (1) Ruch, W., and Gerold, V. Proc. 4th Europ. Conf. Fracture, Leoben/Austria. Vol.II, 1982, pp. 383-390.
- (2) Detert, K., Scheffel, R., and Stünkel, R., Proc. 7th VIC SMA 7, Montreal/Canada, 1985, pp. 1219-1224.
- (3) James, M.R., and Morris, W.L., in Fatigue Mechanisms: Advances in Qualitative Measurement of Physical Damage, ASTM STP 811, 1983, pp. 46-70.
- (4) Kung, C.V., and Fine, M.E., Met. Trans. 10A, 1979, pp. 603-616.
- (5) Pearson, S., Eng. Frac. Mech. 7, 1975, pp. 235-247.
- (6) Grosskreutz, J.C., and Shaw, G.G., Proc. 2nd Int. Conf. Fracture, Birghton, 1969.
- (7) Gräf, M., and Verpoort, C., ICSMA 5, Aachen, 1979, pp. 1207-1212.
- (8) Edwards, L., and Martin J.W., Proc. 5th Int. Conf. Fracture, Cannes/France. 1981, pp. 323-328.
- (9) Sommer, F., in: "Bruchmechanische Bewertung von Oberflächenrissen", Springer Verlag Berlin, New York, 1984.
- (10) Scheffel, R., Ibas, O., Detert, K., Proc. of this conf.
- (11) Suresh, S., and Ritchie, R.O., Met. Trans. 13A, 1982, pp. 1627-1631.
- (12) Clement, P., Angelis, J.P., and Pineau, A., Fat. Engng. Mat. Struct. 7, 1984, pp. 251-265.
- (13) Fathulla, A., Weiss., B., and Stickler, R., 2nd Int. Conf. on Fatigue and Fatigue Thresholds, Birmingham/UK, 1984, pp. 1913-1928.
- (14) Morris, W.L., James, M.R., and Zurek, A.K., Scripta Met. 19, 1985, pp. 149-153.

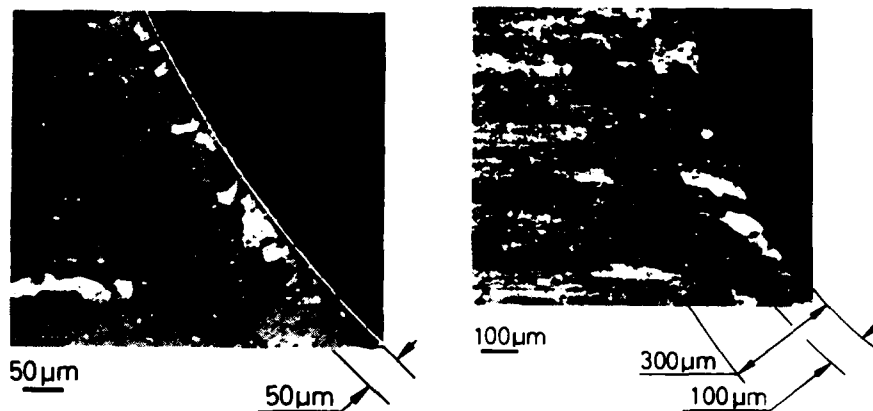


Figure 1a Alloy PR; fine grained recrystallized surface layer and pancake-shaped grains of the bulk material; coarse dispersoid distribution

Figure 1b Alloy SR; recrystallized surface layer and subgrain structure of the bulk material; fine dispersoid distribution

Figure 1 Recrystallized layer in the alloys PR (1a) and SR (1b)

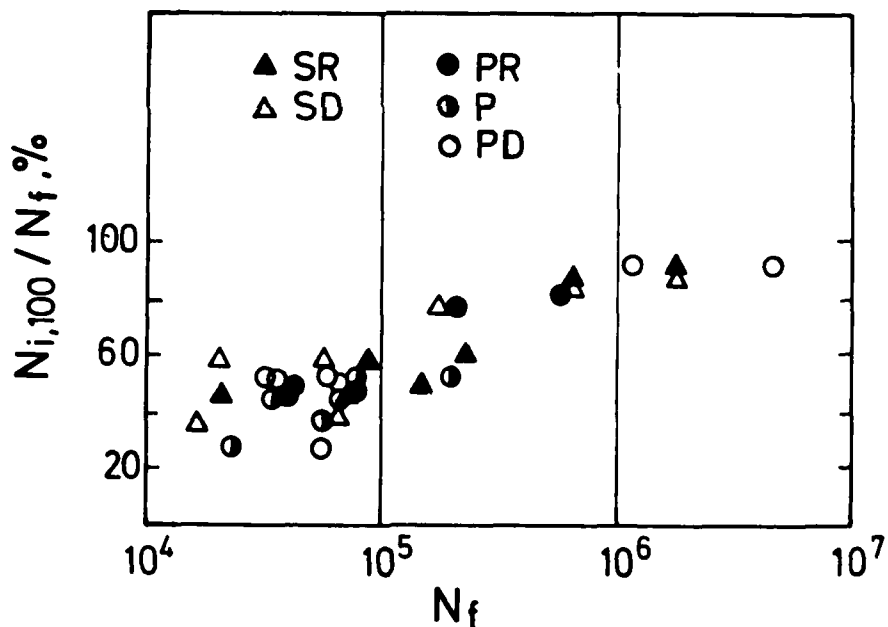


Figure 2 Fraction of total lifetime necessary to build the first 100 μm surface crack versus total lifetime

FATIGUE 87

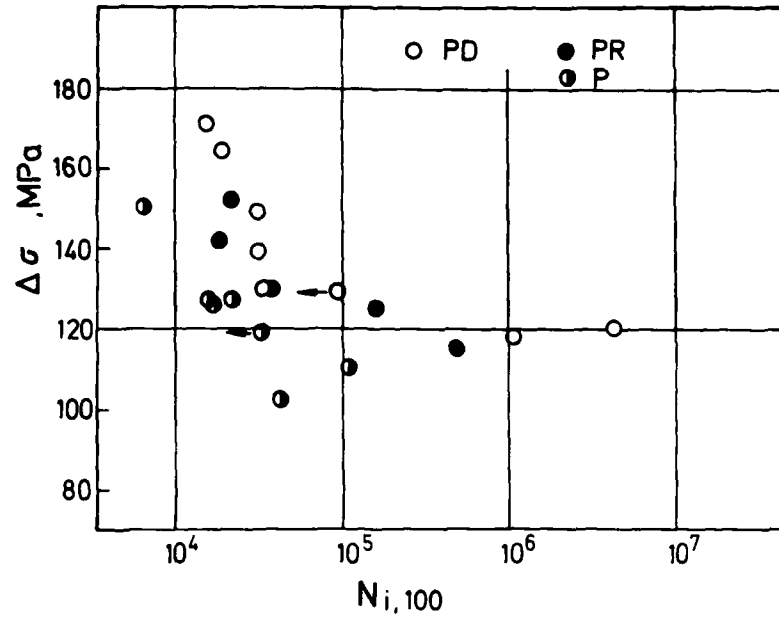


Figure 3a Number of cycles necessary to build the first 100 μm surface crack, coarse dispersoid distribution

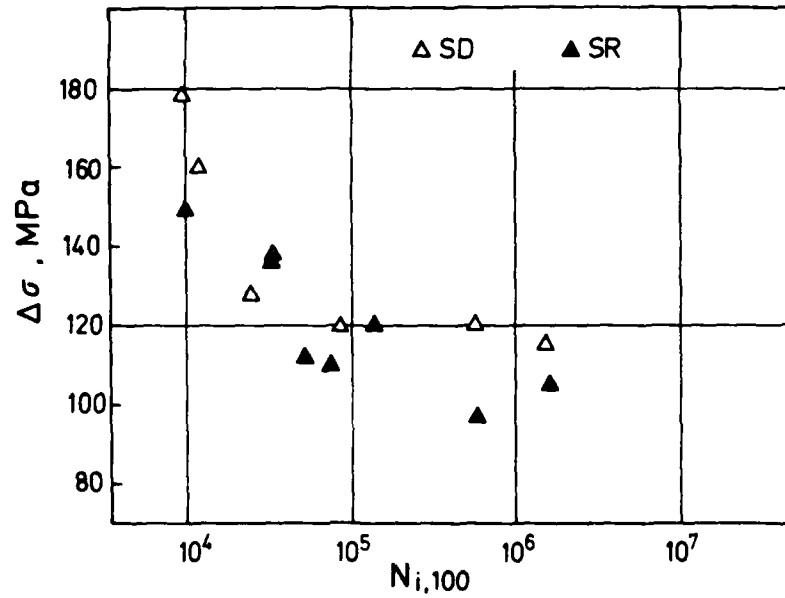


Figure 3b Number of cycles necessary to build the first 100 μm surface crack, fine dispersoid distribution



Figure 4a Extrusion and PSB at the interface inclusion-matrix as crack initiation site; P-type alloy; SEM micrograph

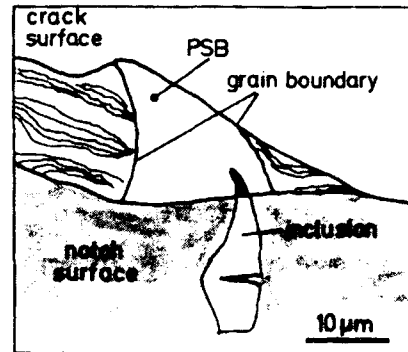


Figure 4b Sketch of a SEM micrograph showing a PSB-crack initiated at the interface inclusion-matrix (black area); P-type alloy

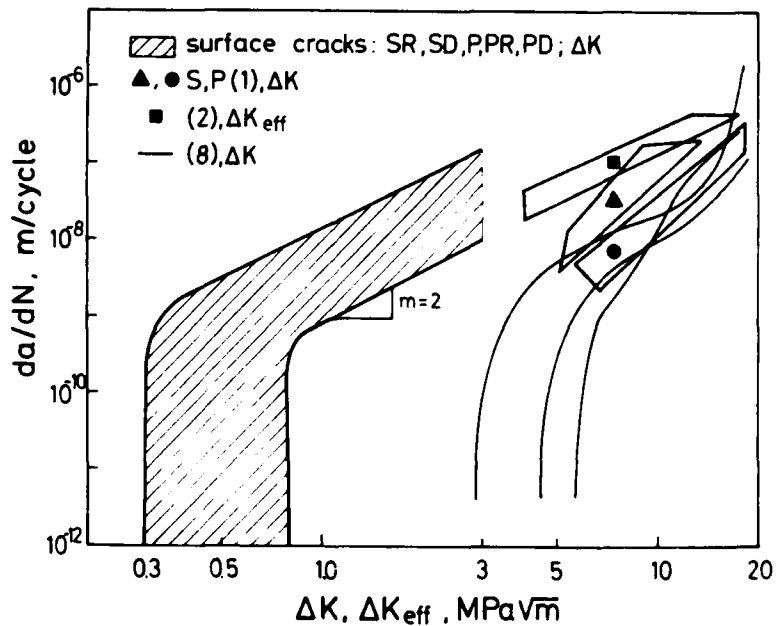


Figure 5 Comparison of fatigue crack growth of surface and through-thickness cracks in AlMgSi1 with $R = 0.1$

THRESHOLD STRESS FOR FATIGUE CRACK INITIATION FROM A SMALL CRACK

Y. Murakami* and K. Matsuda**

The critical stress σ_{wi} for crack initiation from a small crack and effective threshold stress intensity factor range $\Delta K_{eff,th}$ of 0.46% C steel were determined by the annealing method. The specimens containing small cracks were annealed in order to relieve residual stress and were undergone the subsequent fatigue test again at different stress level. The length of nonpropagation crack Δa from the initial crack was measured, and by the extrapolation to $\Delta a = 0$, the critical stress σ_{wi} for fatigue crack initiation from an ideal crack and $\Delta K_{eff,th}$ were determined. The values of $\Delta K_{eff,th}$ for the surface crack length $2a \approx 100, 200, 500$ and $1100 \mu\text{m}$ were independent of crack length; $\Delta K_{eff,th} \approx 3.4\text{--}3.6 \text{ MPa}\cdot\text{m}^{1/2}$.

INTRODUCTION

Recently Murakami et al (1-3) showed that the threshold stress intensity factor range ΔK_{th} and the fatigue limit σ_w for small defects or cracks can be predicted in terms of the Vickers hardness H_v and a geometrical parameter \sqrt{area} which is the square root of the area occupied by projecting defects or cracks onto the plane normal to the maximum tensile stress:

$$\Delta K_{th} = 3.3 \times 10^{-3} (H_v + 120) (\sqrt{area})^{1/3} \dots\dots\dots (1)$$

$$\sigma_w = 1.43 (H_v + 120) / (\sqrt{area})^{1/6} \dots\dots\dots (2)$$

where the units of the quantities in these equations are $\Delta K_{th} : \text{MPa}\cdot\text{m}^{1/2}$, $\sqrt{area} : \mu\text{m}$ and $\sigma_w : \text{MPa}$.

The value of σ_w obtained by Eq.(2) is not the critical stress for fatigue crack initiation from small cracks or defects but the threshold stress under which cracks emanating from the initial original cracks stop propagation. In addition to this value (σ_w), we can define another critical stress σ_{wi} under which no crack

* Department of Mechanics and Strength of Solids,
Faculty of Engineering, Kyushu University.

** Graduate School of Kyushu University.

initiate from the original cracks. These two critical stress play an important role in life prediction of fatigue under variable amplitude loading, because these two quantities give the measure to evaluate the contribution of the variable amplitude stress to fatigue damage; the stress lower than σ_w contributes to fatigue damage, if it is higher than σ_{wi} . It should also be noted that both σ_w and σ_{wi} are the function of crack length, and accordingly these two critical values vary as the progress of the loading process (crack propagation). This means that the interference effect arises between the stress higher and that lower than fatigue limit. The objective of this study is to determine the critical stress σ_{wi} of an annealed medium carbon steel and make clear its dependence on crack size and geometry.

In order to study the threshold condition of crack propagation, we usually use threshold stress intensity factor range ΔK_{th} and effective stress intensity factor range ΔK_{eff} in stead of σ_w and σ_{wi} . Recent studies have shown that ΔK_{eff} characterizes very well the growth behavior of crack almost independently of crack size, specimen shape and loading condition (4,5). However, concerning the existence of the finite threshold value of ΔK_{eff} , which is denoted by $\Delta K_{eff,th}$, the complete agreement has not been arrived at yet. Kikukawa et al (6) pointed out the existence of threshold value of ΔK_{eff} . On the other hand, Nisitani et al (7) concluded from their experiments and analyses that $\Delta K_{eff,th} \approx 0$. Kobayashi et al (8) also suggested that the threshold value of ΔK_{eff} might not exist, because $\Delta K_{eff,th}$ measured in their experiments was very small.

So far, the unloading-elastic-compliance method (6) or the ultrasonic-method (9) has been commonly used for the measurement of $\Delta K_{eff,th}$. New method different from these two method will be useful to obtain more reliable and comprehensive informations. In the present study, a new method (the annealing method) was used for the determination of $\Delta K_{eff,th}$.

MATERIAL, SPECIMEN AND EXPERIMENTAL PROCEDURE

The annealing method adopted in the present study for the measurement of $\Delta K_{eff,th}$ is as follows.

Specimens containing very small artificial holes (diameter: 40 μm , depth: 40 μm) were prepared, the fatigue cracks having the definite length, say 100 μm , 200 μm , 500 μm and 1100 μm , were introduced in these specimens, these specimens were annealed in a vacuum and then, they were undergone again the fatigue test at different stress levels. By annealing, the prior fatigue history at the initial fatigue crack is expected to be relieved and the initial crack can approximately be regarded as an ideal crack.

Figure 1 illustrates the procedure to determine σ_{wi} . If an annealed crack does not propagate under the subsequent fatigue test,

FATIGUE 87

it can be expected that none of the plastically-induced-(10), surface-roughness-(11-13) and oxide-induced-(11,14-16) crack closure will occur. Therefore, if we can estimate the crack opening stress at steady state of loading, the value of $\Delta K_{eff,th}$ will be easily determined. The crack opening stress of a stationary crack, i.e. the stress intensity factor at crack tip opening (K_{op}) was evaluated based on the Dugdale model (see Appendix).

Figure 2 shows the experimental procedure. The material used is a rolled 0.46% carbon steel. Table 1 gives the chemical composition. Table 2 shows mechanical properties after annealing at 844°C. Figure 3 shows the shape and dimension of the specimens. The surface layer removed by the electropolishing was about 40 μm per diameter of the specimen. Four holes with 40 μm diameter were drilled on specimen surface after electropolishing. After drilling, the specimens were annealed in a vacuum at 600°C for 1 hr to relieve residual stress. These specimens were undergone rotary bending fatigue test under the stress of 284.2 MPa in order to introduce initial fatigue cracks and then, they were annealed again at 600°C in a vacuum to relieve fatigue history. All specimens were annealed after every fatigue test and then, the crack length was measured by replica method or by optical microscope. Testing machines used were rotary bending fatigue testing machines with the capacity of 98 Nm and the test speed of 2300 rpm. Fatigue tests were conducted in air at room temperature.

EXPERIMENTAL RESULTS AND DISCUSSION

The dependence of $\Delta K_{eff,th}$ on crack size was investigated using specimens containing cracks with different length, say 100 μm , 200 μm , 500 μm and 1100 μm . The amount of crack propagation Δa from the initial crack is defined by Fig.4.

Figure 5 shows the initial crack and the behavior of cracks after fatigue test, in which the same specimen was repeatedly used for one series of fatigue test in order to save the preparation of many specimens. It should be noted that the specimen was always annealed after every fatigue test of 10^7 cycles and then was undergone the subsequent tests.

Figure 6 shows the relationship among the initial crack length $2a$, the stress amplitude σ and the amount of crack propagation Δa . Nevertheless the scatter of the data, it is evident that the values of Δa approximately linearly increase with increasing stress. The

TABLE 1-Chemical Composition (%). TABLE 2-Mechanical Properties.

C	Si	Mn	P	S	Cu	Ni	Cr	σ_y (MPa)	UTS	Hv (kgf/mm ²)	ψ (%)
0.46	0.22	0.74	0.024	0.026	0.01	0.02	0.15	356	663	170	43.9

ψ : reduction of area (%)

intersection of this linear line and the abscissa, which means $\Delta a = 0$, indicates the critical stress σ_{wi} under which no crack initiates from the initial ideal crack. The values of σ_{wi} estimated from Fig.6 are shown in Table 3. The vertical dotted lines in Fig.6 indicate the critical stress σ_w predicted by Eq.(2), beyond which the crack no longer stops.

Figure 7, which was obtained by the same data as Fig.6, shows the relationship between K_{max} and the length Δa of nonpropagating crack from the initial crack. K_{max} was calculated by the following equation (17):

$$K_{I_{max}} \approx 0.650 \sigma \sqrt{\pi \sqrt{area}} \dots\dots\dots (3)$$

where $K_{I_{max}}$ denotes the maximum stress intensity factor along crack front, σ is the stress amplitude ($R = -1$) and \sqrt{area} is the square root of the area of the surface crack which was assumed to be semi-circular shape. According to the previous report (3), the aspect ratios of surface cracks range from 0.64 to 0.93 and accordingly $K_{I_{max}}$ based on the assumed values of \sqrt{area} may be 2-10% larger than the exact values. Following the same procedure of determination of σ_{wi} , we can determine the critical value $K_{max,th}$ under which no crack initiates from the initial crack and consequently we have $K_{max,th} \approx 1.7-1.8 \text{ MPa} \cdot \text{m}^{1/2}$ independently of crack size (see Table 3).

If the initial crack shows no propagation, it can be regarded as an ideal crack and the value of K_{op} can be estimated by the Dugdale model. By the numerical calculation based on the Dugdale model, we evaluated ΔK_{eff} as $\Delta K_{eff} = 2.0 K_{max}$ under the condition of the present study ($R = -1$) (see Appendix); this means that the crack is open during the complete cycle. Therefore, we have $\Delta K_{eff,th} = 2.0 K_{max,th} \approx 3.4-3.6 \text{ MPa} \cdot \text{m}^{1/2}$.

Table 4 shows the values of $\Delta K_{eff,th}$ obtained by previous works. Although the value of $\Delta K_{eff,th}$ in the present study (0.46% C steel) is close to that of Kikukawa et al (0.38% C steel), the values obtained by other researchers are completely different. At present, it remains unsolved which factor the difference is caused by, the difference of materials, loading condition or method of measurement.

The conventional method of determination of $\Delta K_{eff,th}$ in the previous works picked up the process from propagation to

TABLE 3-Critical Values σ_{wi} and $K_{max,th}$ estimated from Fig.6 and 7.

Initial Crack Length $2a$ (μm)	Critical Stress σ_{wi} (MPa)	$K_{max,th}$ $\approx 0.650 \sigma_{wi} \sqrt{\pi \sqrt{area}}$ ($\text{MPa} \cdot \text{m}^{1/2}$)
100	180	1.7
200	130	1.7
500	90	1.8
1100	60	1.8

FATIGUE 87

nonpropagation and the determination of crack tip opening was dependent on the judgment of each researcher. The present method (annealing method) is substantially different from previous methods. The values σ_{wi} and $\Delta K_{eff,th}$ determined by the annealing method are really important, because they give a reliable value of the lower limit condition of crack initiation from cracks having various prior fatigue history. The disadvantage of this method is that it may not be applied to the materials whose mechanical properties may change by annealing. Any way, these two critical values (σ_{wi} and $\Delta K_{eff,th}$) must be considered in fatigue damage counting under variable amplitude loading; the stress amplitude lower than σ_{wi} never contributes to fatigue damage.

CONCLUSIONS

The critical stress σ_{wi} for crack initiation from a small crack and effective threshold stress intensity factor range $\Delta K_{eff,th}$ of 0.46% C steel were determined by using the specimens which contain ideal cracks. The ideal cracks were prepared by annealing (the annealing method) the fatigued specimens which contain small fatigue cracks emanating from a small drilled hole with 40 μm diameter.

The values of $\Delta K_{eff,th}$ for the surface crack length $2a \approx 100, 200, 500$ and $1100 \mu\text{m}$ were independent of crack length; $\Delta K_{eff,th} \approx 3.4\text{--}3.6 \text{ MPa}\cdot\text{m}^{1/2}$. The critical values σ_{wi} and $\Delta K_{eff,th}$ determined

TABLE 4—The Values $\Delta K_{eff,th}$ obtained by the Unloading-Elastic-Compliance Method or by the Ultrasonic Method.

(a) Unloading-Elastic-Compliance Method

Materials	Hv	Stress Ratio R	$\Delta K_{eff,th}$ $\text{MPa}\cdot\text{m}^{1/2}$	References
0.38% C Steel	182	-1.1, 0, 0.18 0.30, 0.70	3.3	Kikukawa et al. (18)(19)
0.20% C Steel	158 129	-1 -1	0.61 1.30	Nakai et al.(20)
0.17% C Steel	126	-1, 0, 0.4	3.06	Nakai et al.(21)
304 Stainless Steel	183	-1, -3	1.7	Ogura et al.(22)
0.45% C Steel	187	-1	≈ 0	Nisitani et al.(7)

(b) Ultrasonic Method

Materials	Hv	Stress Ratio R	$\Delta K_{eff,th}$ $\text{MPa}\cdot\text{m}^{1/2}$	References
0.36% C, 1.1% Cr, 0.16% Mo, High-strength Steel	506	0.05	0.27	Hirano et al.(8)
	405	0.05	0.50	
	405	0.4	0.58	
	405	0.6	0.52	
	405	0.8	2.48	

FATIGUE 87

by the annealing method have practical importance in fatigue damage counting, because they gives the lower limit condition of crack propagation from cracks having various prior fatigue history.

REFERENCES

- (1) Murakami, Y. and Endo, M., J. Soc. Mater. Sci. Japan, Vol.35, No.395, 1986, pp.991-917.
- (2) Murakami, Y. and Endo, M., The Behaviour of Short Fatigue Cracks, (Edited by K.J. Miller), Mechanical Engineering Publications, London, 1986.
- (3) Murakami, Y. and Matsuda, K., Trans. Japan Soc. Mech. Engrs., Vol.52, No.478, 1986, pp.1492-1499.
- (4) Jono, M. and Song, J., Proc. Fatigue 84, Vol. II, (Edited by C.J. Beevers), 2nd Int. Conf. on Fatigue and Fatigue Threshold, 1984, pp.717-726.
- (5) Jono, M. and Song, J., Current Research on Fatigue Cracks, Materials Research Series 1, Soc. Mater. Sci. Japan, 1985, pp.35-55.
- (6) Kikukawa, M., Jono, M., and Tanaka, K., Proc. of 2nd Int. Conf. on Mechanical Behavior of Materials, special volume, 1976, pp.254-277.
- (7) Nisitani, H. and Chen, D., Trans. Japan Soc. Mech. Engrs., Vol.51, No.465, 1985, pp.1436-1441.
- (8) Hirano, K., Ishii, A., Kobayashi, H., and Nakazawa, H., J. Soc. Mater. Sci. Japan, Vol.32, No.356, 1983, pp.542-548.
- (9) Buch, O., Ho, C.L., and Marcus, H.L., Eng. Fract. Mech., Vol.5, No.1-C, 1973, pp.23-34.
- (10) Elber, W., ASTM Spec. Tech. Publ., Vol.486, 1971, pp.230-242.
- (11) Suresh, S., Zamiski, G.F., and Ritchie, R.O., Met. Trans. A, Vol.12-II, 1981, pp.1435-1443.
- (12) Walker, N. and Beevers, C.J., Fat. Eng. Mat. Struct., Vol.1, 1979, pp.135-148.
- (13) Minakawa, K. and McEvily, A.J., Scripta met., Vol.15, 1981, pp.633-636.
- (14) Endo, K., Komai, K., and Ohnishi, K., J. Soc. Mater. Sci. Japan, Vol.17, No.173, 1968, pp.160-168.
- (15) Ritchie, R.O., Suresh, S., and Moss, C.M., J. Eng. Mater. Technol. (Trans. ASTM, H), Vol.102, 1980, pp.293-299.
- (16) Stewart, A.T., Eng. Fract. Mech., Vol.13, 1980, pp.463-478.
- (17) Murakami, Y., Eng. Fract. Mech., Vol.22, No.1, 1985, pp.101-114.
- (18) Kikukawa, M., Jono, M., Kondo, Y., and Mikami, S., Trans. Japan Soc. Mech. Engrs., Vol.48, No.436, 1982, pp.1496-1504.
- (19) Kikukawa, M., Jono, M., Kondo, Y., Kanetani, T., and Mikami, S., Proc. 20th Symposium, JSME, No.810-7, 1981, pp.291-296.
- (20) Nakai, Y. and Tanaka, K., Proc. 23rd Japan Congress on Materials Research-Metalic Materials, 1980, pp.106-112.
- (21) Nakai, Y., Tanaka, K., and Kawashima, R., J. Soc. Mater. Sci. Japan, Vol.32, No.356, 1983, pp.535-541.
- (22) Ogura, K., Miyoshi, Y., and Nishikawa, I., Trans. Japan Soc. Mech. Engrs., Vol.52, No.474, 1986, pp.275-283.

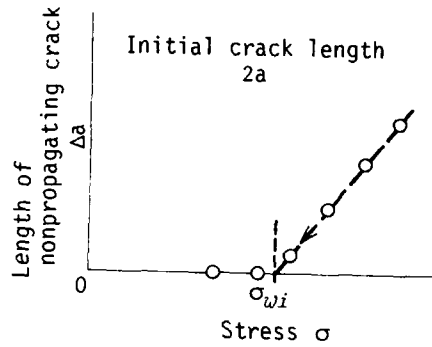


Figure 1 Test procedure for the determination of critical stress σ_{wi}

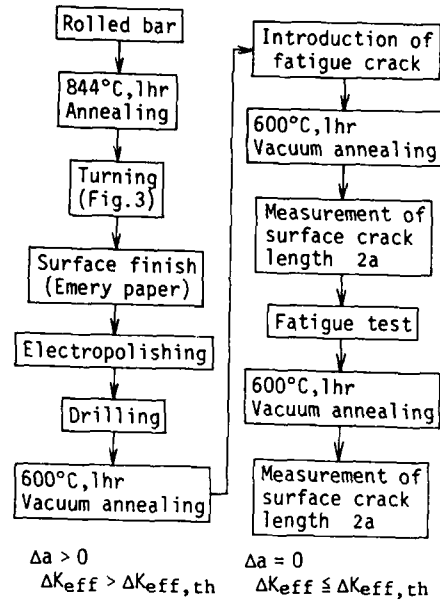
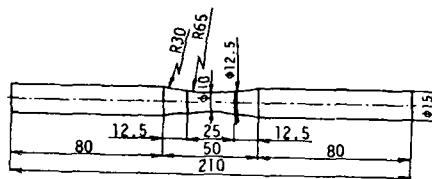
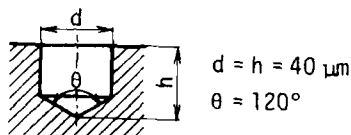


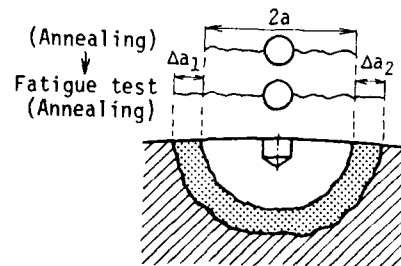
Figure 2 Experimental procedure



(a) Specimen



(b) Shape and dimension of drilled hole



2a :Initial crack length

$(2a + \Delta a_1 + \Delta a_2)$:Total length of nonpropagating crack

$$\Delta a = \Delta a_1 + \Delta a_2$$

Figure 3 Specimen containing artificial small holes

Figure 4 Method to determine the crack growth length Δa

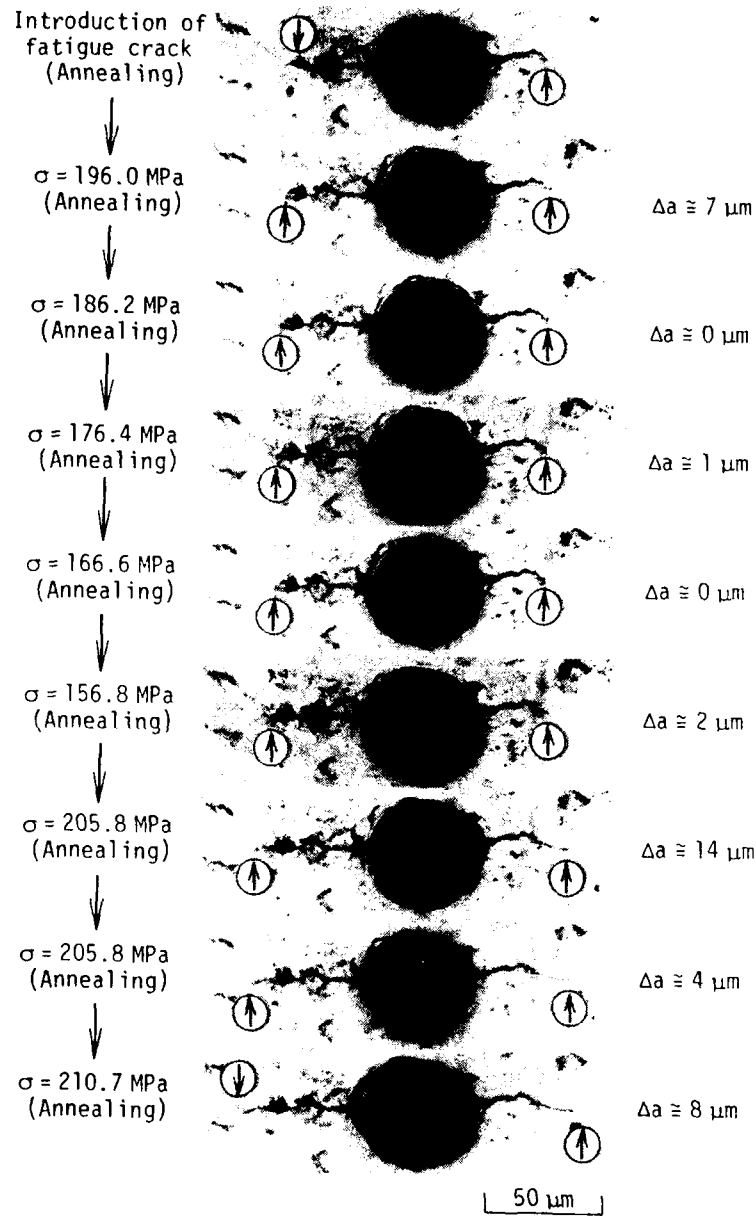


Figure 5 Nonpropagating crack emanating from an initial crack $2a \approx 100 \mu m$

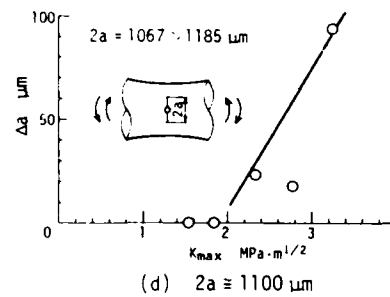
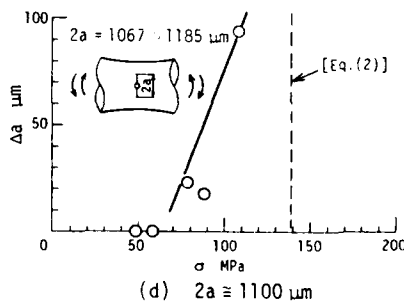
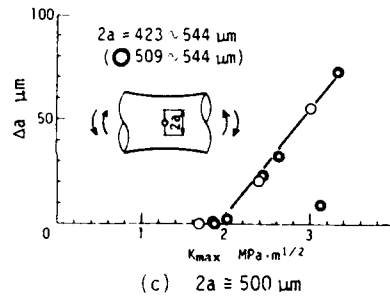
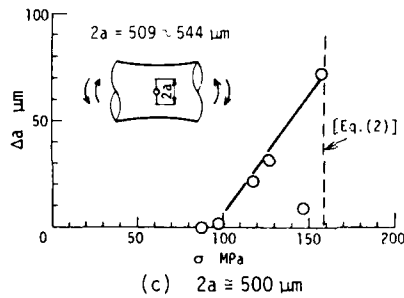
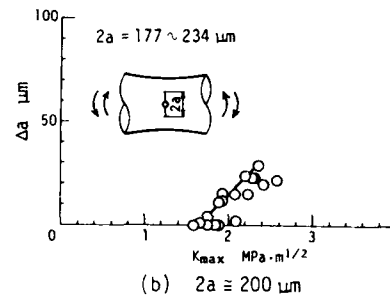
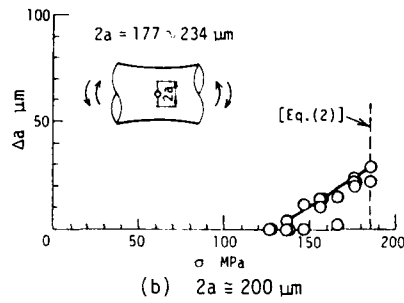
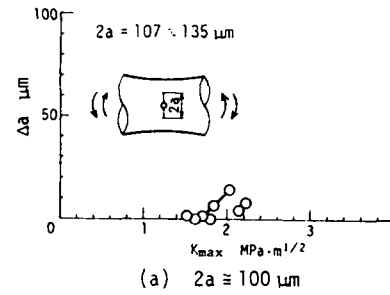
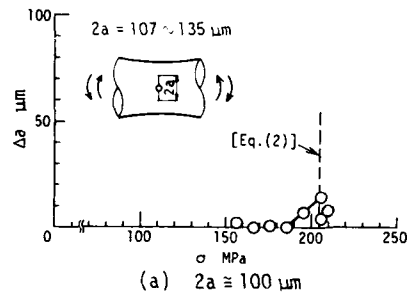


Figure 6 Relationship between stress amplitude and Δa

Figure 7 Relationship between K_{max} and Δa

APPENDIX

Crack Opening and Closure during One Cycle

Figure A1 schematically shows the crack opening and closure behavior based on the Dugdale model during one cycle. When the load is unloaded from $\sigma = \sigma_{max}$ to $\sigma = 0$, the crack is still open along whole surface. If we superpose the loading $\sigma = \sigma^*$ by which the crack tip opening displacement δ_A is cancelled, the displacements at other positions become negative (the upper and lower surface of the crack intersect each other). The value of σ^* can be estimated as $\sigma^* = -(0.4-0.5)\sigma_{max}$. However, this result never happens, because the upper and lower surface of the crack contact each other under the stress higher than σ^* and, therefore, we have the crack closure stress $\sigma_{cl} < \sigma^*$. Considering $V_C = -0.4 V_A$ (see Fig. A1 (A) and (C)) and assuming $\sigma_{cl} = \sigma_{op}$, we can estimate the value of ΔK_{eff} as $\Delta K_{eff} = (1.8-2.0)K_{max}$.

In order to find more exact value of ΔK_{eff} , the numerical analysis based on the Dugdale model was performed. As shown in Fig. A1 (E), a distributed load $p(x)$ which keeps the crack surfaces just in contact under the given loading, was determined and the closure level was calculated from the positive or negative sign of $p(x)$. From the results of the numerical analysis, we concluded that for broad range of σ_{max}/σ_y (0.1-0.75), the crack tips were still open even under the maximum compressive stress $\sigma = -\sigma_{max}$ and accordingly the opening ratio may be regarded as $U = 1$ in case of a stationary ideal crack.

From this conclusion, we used in the present study the estimation, $\Delta K_{eff} = 2.0 K_{max}$, for the critical condition of crack initiation from an annealed ideal crack.

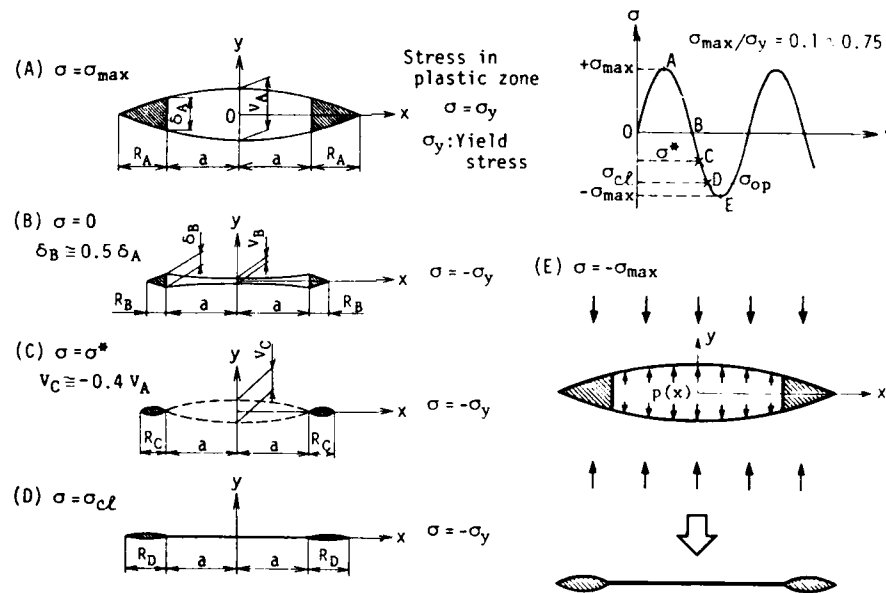


Figure A1

AN EXPERIMENTAL STUDY OF CLOSURE BEHAVIOR OF
NATURALLY INITIATED SMALL CRACKS

X. Su* and W. N. Sharpe, Jr.**

Small cracks were initiated on the edges of 2024-T3 aluminum specimens by fatigue loading with various R-ratios. The crack opening displacement was then measured with a laser-based interferometric technique and used to determine the opening load ratio. This ratio decreased with increasing distance from the tip; however, it remained essentially constant as the crack grew if one used a consistent measurement position.

INTRODUCTION

In many cases the growth rate of small fatigue cracks is different from that of long cracks when both are presented in terms of the stress intensity factor range - ΔK . It has been proposed that a major cause is the difference in closure behavior between small and large fatigue cracks, Suresh (1). An extensive study by Lee and Sharpe (2) of the growth rates and closure behavior of very small cracks initiating at the roots of notches in 2024-T3 aluminum showed that closure effects were somewhat successful in explaining the difference in growth rates. In that work, acetate replicas of the notch root were taken periodically to find surface cracks while they were still very

* Institute of Aeronautical Materials, Beijing, China ** Department of Mechanical Engineering, The Johns Hopkins University, Baltimore, Maryland

small (less than 50 μm). Two indentations were then placed across the crack with a microhardness tester, illuminated with a laser, and the resulting interference fringe motion was monitored to give a displacement resolution on the order of 0.01 μm . Closure was determined from this load-displacement curve.

The scope of this work is similar, but the flat specimens do not have a notch - rather a very gentle curvature to cause the cracks to initiate on the edge in the vicinity of the center of the specimen gage length. The cyclic loading was conducted with R-ratios = 0.5, 0.0, and -1.0 and load-displacement records were taken for various crack lengths (up to 2 mm) and at various positions along the cracks. A very brief description of the measurement technique is given since it is adequately presented by Lee and Sharpe (2); however, the testing procedure is described. The results are presented here in the form of opening load ratio, P_{op}/P_{max} , versus either distance behind the crack tip or crack length.

EXPERIMENTAL PROCEDURES

The specimens were machined from 2024-T3 aluminum sheet 2.23 mm thick with the tensile axis in the rolling direction. The sides were cut to a radius of 37.2 cm to produce a stress concentration at the center of the gage length which was 1.09. The specimens were 19 mm wide at their narrowest portion. This material had $\sigma_y = 380$ MPa and $\sigma_u = 470$ MPa as determined from other tests conducted in the same test machine. The grain size of the material was approximately 70 μm in the direction of rolling and 30 μm in the transverse direction.

All tests were conducted in a carefully aligned electrohydraulic test machine which had been used earlier for a NASA-sponsored round-robin series of tests on notched specimens by Lee and Sharpe (2). Buckling guides were used for negative R-ratios, and tests were run for $R = 0.5$, 0.0, and -1.0. The peak loadings, σ_{max} , were 290 MPa, 290 MPa, and 190 MPa respectively.

It was originally hoped that the naturally initiating cracks could be found on the edges of the specimen near the center without any special treatment to that local region. However, that proved impossible (or at least impractical), and a small area about 3 mm long on one edge of the specimen was etched lightly

with Keller's etch. The grain boundaries were barely visible with a microscope, but this surface treatment localized the initiation of the cracks. Acetate replicas were taken at intervals to find natural cracks that were 35 to 100 μm long. The cracks tended to initiate in the center of the edge of the specimen and grow fairly symmetrically across the thickness. Once the cracks reached the flat side of the specimen, they started growing down the sides, but only grew a short distance before the specimen fractured. The small cracks were therefore surface cracks that initiated on the edge of the specimen.

After the initial crack was found, the specimen was removed from the test machine and one indentation applied above and one below the center of the crack. Figure 1 is a photomicrograph of a pair of indentations across a natural crack that is 70 μm long (it turns up at the right) with indentations that are 50 μm apart. These two indents enable measurement of the crack opening displacement at the center of the surface crack with the laser-based Interferometric Strain/Displacement Gage (ISDG). The ISDG is described adequately elsewhere by Sharpe (3), but its principle is very simple. An incident laser beam is reflected from the sides of the pyramidal indentations, and these reflections overlap to generate interference fringes in space. As the indentations move relative to each other, the fringes move, and one records this motion to determine the relative displacement. One complete fringe motion corresponds to approximately 1 μm displacement, so it is necessary to use a computer-controlled scanning system to measure fractional fringe motion. The measurement system in use has a resolution of 0.01 μm which is quite adequate since the total crack opening displacement of the small crack is on the order of a few μm .

Figure 2 is a typical plot showing load versus crack opening displacement for a surface crack on the edge of a specimen. The first plot was taken when the crack was 0.59 mm long, and the second when it had grown to 0.84 mm long on the surface. Note that the second curve is shifted to the right for clarity and that the R-ratio is -1.0. In each case, the loading curve is higher than the unloading one; there is some hysteresis. This hysteresis decreases as the crack grows, and one usually observes a single curve once the crack is longer than 1 mm. In most cases, additional sets of indentations were applied along the crack after it had grown so that more data could be accumulated on the same specimen.

The opening load was determined manually from the loading curve by the method of tangents which involves fitting a straight line to the initial portion and one to the upper portion of the load-displacement curve. The intersection of these two straight lines defines P_{op} . There is uncertainty in choosing which portions of the curve are to be used, but it is estimated that the relative uncertainty in identifying P_{op} is ± 7 percent for the shortest cracks and ± 3 percent for the longer ones.

RESULTS AND DISCUSSION

The results are presented in terms of the opening load ratio, P_{op}/P_{max} , as a function of either the measurement location behind the crack tip or the length of the crack..

It is well-known that P_{op}/P_{max} depends on the measurement location when one measures near the fatigue crack tip. Macha et al (4) have demonstrated this for longer cracks using the ISDG. As the cracks grew, new sets of indentations were applied to enable recording load-displacement at various positions along the crack length.

The accumulated results for 12 different specimens are presented in Figure 3. These are accumulated into one figure for ease of comparison even though the data is somewhat crowded. Note that there is a mixture of surface, corner, and through-thickness cracks on the plot - the kind of crack is not identified because they all behaved in a similar fashion.

Figure 3 shows that there is a definite decrease in P_{op}/P_{max} as one moves back from the tip, but that P_{op}/P_{max} tends toward a stable value further from the tip. This is consistent with Macha's work on longer cracks which shows that this stable value is the same as would be measured at the crack mouth.

To examine the effect of crack length on P_{op}/P_{max} , measurements were taken near the crack tip. A new set of indentations was placed near the fatigue crack tip after it had grown enough so that the laser beam would not overlap with the previous set. This increment of growth was on the order of 200-400 μm . For surface cracks on the edge of the specimen, the indents were placed 50 μm behind the tip - usually at only one end of the crack. If the crack was a corner crack or it had grown into

a through-thickness crack, the indents were placed on the side of the specimen and always within 90 μm of the tip. These attempts at consistency of location were necessary to eliminate the variability associated with measurement location.

Figure 4 is a plot of the results at various R-ratios on the same 12 specimens. The first observation from Figure 4 is that there is little change in P_{op}/P_{max} as measured at the tip for cracks of various lengths. The very smallest cracks (100 - 200 μm long) showed a P_{op}/P_{max} lower (near zero) for $R = -1$ than for longer cracks at that same R value or for any cracks at other R-ratios. The load-displacement records for these very short cracks had a less clearly defined transition from nonlinear opening to the fully open crack. However, once the crack was longer than ≈ 0.5 mm, the P_{op}/P_{max} was essentially constant at 0.35.

CONCLUDING REMARKS

The partial results from an extensive series of experiments - 127 different load-displacement records on 12 different specimens - are reported here. Measurements of this nature produce a lot of scatter; that is why the raw data is presented here. Most of the data was taken on naturally initiating cracks that were less than 1 mm long. The ISDG is a very effective measurement technique for recording displacements with high resolution on such a small scale.

In general, the results on measurement location are similar to those for long through-thickness cracks. The decrease in P_{op}/P_{max} as one moves the measurement location back from the crack tip is well-established by Macha et al (4). It is not entirely clear which measurement location should be used, but obviously one must be consistent.

P_{op}/P_{max} (as measured close to the tip) is essentially independent of the crack length for each of the R-ratios (within the scatter of the data) for cracks longer than about 0.2 mm. However, it tends to decrease somewhat with decreasing R-ratio. This is consistent with the observations of Schijve (5) and Newman (6) who both predict that P_{op}/P_{max} decreases as R decreases - from a value on the order of 0.6 for $R = 0.5$ to approximately 0.35 at $R = -1.0$. The closure data of Lee and Sharpe (2) for small cracks in notches also shows an even more dramatic decrease in P_{op}/P_{max} with decreasing R.

One of the ideas behind rapid growth of very small cracks is that the closure effect is less pronounced so that the ΔK_{eff} (effective ΔK) is equal to the nominal ΔK ; i.e., there is no reduction in loading due to closure. The data for $R = -1.0$ show an increase in P_{op}/P_{max} until the crack becomes longer than ≈ 0.2 mm which is consistent with this hypothesis. However, data for other R -ratios does not support it.

ACKNOWLEDGEMENTS

This work was supported by NASA-Langley under Grant NAG-1526. The technical encouragement of Dr. J. C. Newman, Jr. is appreciated.

REFERENCES

- (1) Suresh, S. and Ritchie, R. O., Int. Material Rev., Vol.29, No.6, 1984, pp.445-476.
- (2) Lee, J.J. and Sharpe, W. N., Jr., "Small Fatigue Cracks", TMS-AIME, 1986.
- (3) Sharpe, W. N. Jr., Optical Engr., Vol.21, 1982, pp.483-488.
- (4) Macha, D. E., Corbly, D. M. and Jones, J. W., Exptl. Mech., Vol.19, 1979, pp.207-213.
- (5) Schijve, J., Engr. Fracture Mech., Vol.14, 1981, pp.461-465.
- (6) Newman, J. C., Jr., Int'l J. Fracture, Vol.24, 1984, pp.R131-R135.



Figure 1 A naturally initiated crack $70\text{ }\mu\text{m}$ long with two indentations $50\text{ }\mu\text{m}$ apart.

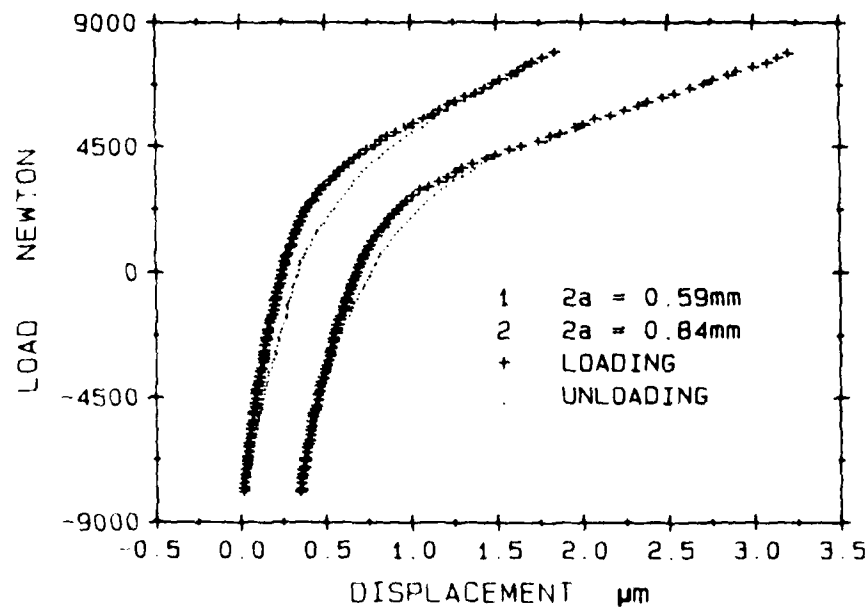


Figure 2 Load-displacement records from a crack at various lengths. Note that the curve for the longer crack has been shifted for clarity.

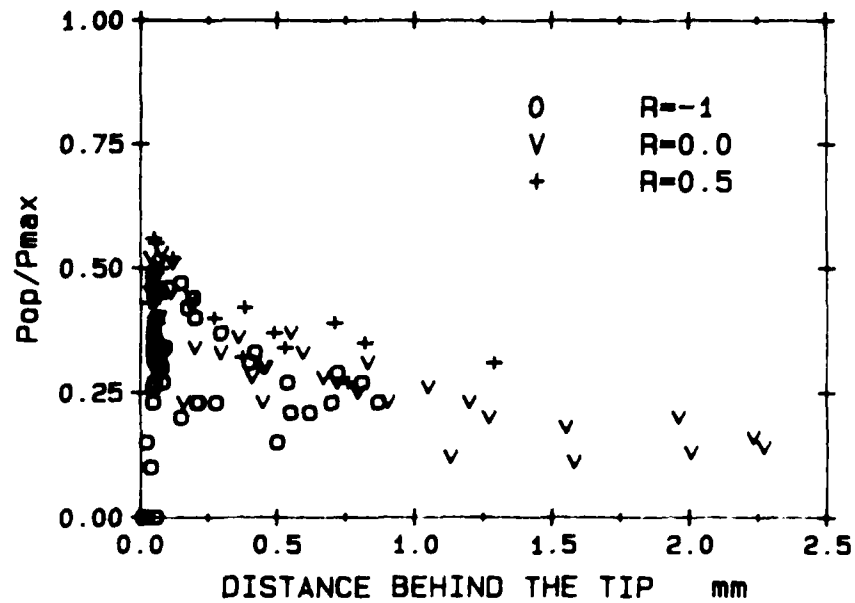


Figure 3 P_{op}/P_{max} versus measurement location behind the crack tip.

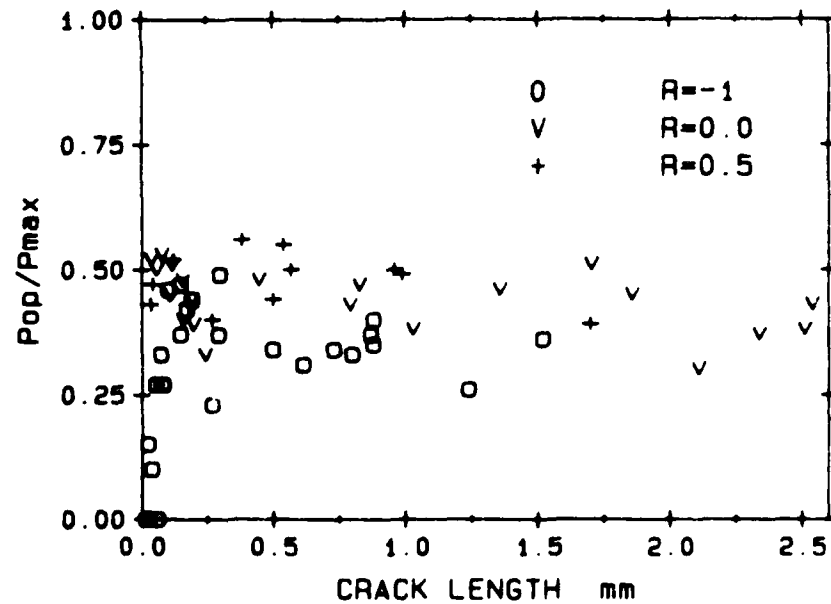


Figure 4 P_{op}/P_{max} measured very close to the tip versus crack length.

BEHAVIOUR OF LONG AND SHORT FATIGUE CRACKS IN A POWDER METALLURGY SUPERALLOY AT ROOM AND AT HIGH TEMPERATURE

F. SONIAK and L. REMY*

ABSTRACT. Fatigue crack growth behaviour of long and short cracks are discussed in this paper, at room and at 650°C for different stress ratios. Tests were carried out on a HIP + forged Astroloy, which has a necklace structure. At room temperature for long cracks, closure was found to depend upon the stress ratio. Short cracks were found to grow faster than long cracks and no intrinsic threshold has been observed at room temperature. At 650°C closure was found to depend upon the maximum stress intensity factor. Unstable crack propagation have been observed on short cracks. Fatigue crack growth rates could be rationalized by crack closure analysis and the intrinsic crack growth law da/dN versus ΔK_{eff} should lead to conservative predictions of fatigue crack growth life at room and high temperature.

INTRODUCTION

Powder metallurgy superalloys are currently being developed for turbine disc applications in advanced jet engines. However, defects are inherent to this manufacturing process and they can initiate short cracks under fatigue cycling. An accurate prediction of fatigue life is needed for aeroengine components. Generally, life calculations are made by the integration of the PARIS law (PARIS [1]) : $da/dN = C(\Delta K)^m$, from the largest size of initial defect to the crack length at final fracture. But the growth rate of short cracks (PEARSON [2], LANKFORD [3]), is faster than that of long cracks, say about 5mm, at low stress ratios (KLESNII and LUKAS [4], USAMI [5]), which are generally used in laboratories, to characterize fatigue crack growth behaviour. It follows that the use of the damage tolerance approach with such laws leads to non-conservative prediction of the fatigue lives of the component. Different mechanisms has been proposed such as fracture roughness, plasticity, environment effects, etc..., which could explain the higher rate of growth of the short cracks. These mechanisms are discussed in this work which reports the results obtained for long and short crack growth rate at room temperature and at 650°C in powder metallurgy superalloy for different stress ratios.

* Centre des Matériaux de l'école des Mines de Paris
 158 CHENES 924 64 40, 92015 EVRY CEDEX, FRANCE

MATERIAL AND EXPERIMENTAL PROCEDURE

The HIP + forged Astroloy studied here has a necklace structure, composed of coarse grains about 50 μm , and fine grains about 2 μm in diameter. The nominal wt composition is 0.022C, 0.003S, 14.6Cr, 5.04Mo, <0.01Cu, 16.9Co, 3.52Ti, 0.044Zr, 3.98Al, 0.02B, bal.Ni. The 0.2 per cent yield strength and ultimate tensile strength at room temperature are 1110 and 1510 MN.m^{-2} respectively. The 0.2 per cent yield strength and ultimate tensile strength at 650°C are 1060 and 1400 MN.m^{-2} respectively.

Long and short fatigue crack propagation studies were carried out at room temperature and at 650°C in laboratory air. The fatigue tests were conducted on a servo hydraulic fatigue testing machine using sine wave loading in the range 30 to 60 Hz at room temperature, and 50 Hz or 2 Hz at 650°C. The growth rates of long fatigue cracks were measured on compact tension specimen 40 mm in width and 8 mm in thickness. A load shedding procedure was adopted for the threshold measurement on the specimens using, a 1 to 2 per cent decrease in load after a growth of about 0.1 mm at 650°C, and a 5 to 10 per cent decrease in load after a growth of about 0.5 mm at room temperature. The growth rates measured under the ΔK decreasing procedure were found to be in agreement with those measured under constant load at increasing fatigue crack growth rates. The short crack behaviour has been studied for different stress ratios in the same growth rate range than that of long cracks and for crack length ranging from 0.1 to 3.5 mm. This study has been restricted to artificial two dimension short cracks. Single edge notched specimens were fatigue precracked at growth rates down to 10^{-10} m/cycle at room temperature and down to about 10^{-9} m/cycle at 650°C. Those SEN specimens were 18 mm in width and 4 mm in thickness. Precracks were grown about 1 mm ahead of the notch using the same load shedding procedure as in CT specimens. The precracked SEN specimens were then machined down to about 11 mm in width and 2 mm in thickness. These machined SEN specimens contain a straight front through-crack of 1 mm in width and about 0.1 to 0.4 mm in depth. No heat treatment was given in order to prevent any modification of the crack surface. The plasticity left after all previous operations was kept to a minimum due to the threshold procedure adopted and the very cautious handling of specimens. The tests on these machined specimens were conducted at constant load when the crack propagate, or using an increasing load procedure with steps of about 5 per cent if crack growth did not occur. Crack growth was monitored using optical measurements on both sides of the specimen, also by a potential drop technique and finally by a clip gauge extensometer located in the front part of the specimen. Load displacement P- δ curves were recorded periodically at low frequency (1 Hz). The load shedding method was determined by the upper break of the loading P- δ curve which indicated that the crack was fully open. Effects of the plasticity

load was more accurately measured using a corrected displacement $\delta' = \alpha P - \delta$ where α is an adjustable constant which was given by an electronic processor. The value of P_{op} was quite difficult to assess but the evolution of the load displacement curve was so regular that the accuracy level was estimated to be about 10 per cent. The stress intensity factor at crack opening K_{op} was deduced from the opening load using the calibration formula for the relevant specimen geometry.

EXPERIMENTAL RESULTS

Fatigue crack growth rates at room temperature of short cracks are reported as a function of the stress intensity range ΔK in figure 1 for a stress ratio of 0.1. It can be seen that short cracks are able to propagate below the long cracks threshold stress intensity range and at a crack growth rate more than thirty times that of long cracks. The results are plotted versus the effective stress intensity range ΔK_{eff} defined as $K_{max} - K_{op}$ in figure 1. All the results fit a single straight line which correspond to the intrinsic law observed on long cracks whatever the stress ratio ranging from 0.1 to 0.9. In figure 2 fatigue crack growth rates of short cracks are reported as a function of the stress intensity range ΔK for a stress ratio R of 0.7. No closure phenomenon has been observed and one can see that results fit the intrinsic law of long cracks data. In figure 3 the value of the opening stress intensity factor K_{op} has been plotted as a function of the maximum stress intensity factor K_{max} for long and short cracks. By increasing the stress ratio from 0.1 to 0.7 the K_{op} value of long cracks increases from 8.3 to 14.9 $\text{MPa.m}^{1/2}$. For short cracks K_{op} increases with K_{max} and merges with long cracks data for a K_{max} value of about 20 $\text{MPa.m}^{1/2}$. The figure 4 reports the variation of the opening stress intensity factor K_{op} as a function of the crack size. It can be seen that K_{op} increases with crack size and merges with the long crack data at crack sizes ranging from 1 to 2 mm.

The FCGR at 450°C of long cracks data at 50 Hz for two stress ratios 0.1 and 0.7 are reported in figure 5 as a function of the stress intensity range ΔK . When the stress ratio increases from 0.1 to 0.7 the nominal threshold decreases from about 9 $\text{MPa.m}^{1/2}$ to about 4.5 $\text{MPa.m}^{1/2}$. For a stress ratio of 0.1 many times cracks have been seen to slow down then stop if the load was not increased. In figure 6 FCGR of long cracks are plotted versus the effective stress intensity range ΔK_{eff} . All the results fit together within a small scatter but an intrinsic threshold of about 4.5 $\text{MPa.m}^{1/2}$ can be observed. For a stress ratio of 0.7 no closure phenomenon has been seen. FCGR of a short crack for a stress ratio 0.1 is reported as a function of ΔK in figure 7. We have observed two distinct stages in this experiment. A few points which

are under the effective stress range, are related with brutal transient crack growth of about 20 μm . It is not very easy to represent on a da/dN - ΔK diagram such a behaviour. These phenomenon occur after a minimum of about 100 000 cycles during which, no crack propagation has been observed. When the load was increased the crack grows in a very few cycles have been seen before it stopped, if the associated ΔK was under the nominal stress intensity range ΔK . Crack growth rates which have been indicated, correspond to the number of cycles at constant load which precede the increasing of the load. The second stage begins when the value of ΔK reaches the nominal threshold of long cracks for the same R ratio. A monotonic increasing fatigue crack growth has been seen for a stress never exceeding half of the 0.2% yield strength. In figure 8 FCGR of short crack for a stress ratio of 0.5 is reported as a function of ΔK . As for a stress ratio of 0.1 two distinct stages are noticeable but the first one looks somewhat different. The load shedding procedure was about an order of magnitude quicker than in the experiment presented before. No crack growth has been observed till ΔK reached the nominal threshold. Then crack growth occurred, but was seen to slow down during a few millions of cycles, then stopped till the load was increased. As the same in figure 7 when the value of ΔK reaches $10 \text{ MPa.m}^{1/2}$ a monotonic increasing fatigue crack growth occurs. For a stress ratio of 0.5 no closure phenomenon has been seen. In figure 10 the opening stress intensity factor K_{op} is plotted versus the maximum stress intensity factor K_{max} for long and short cracks. When K_{max} increases, the values of K_{op} has been seen to increase also up to about $15 \text{ MPa.m}^{1/2}$ when K_{max} reaches $65 \text{ MPa.m}^{1/2}$. Long and short cracks are in good agreement in this figure in a scatter-band of about $3 \text{ MPa.m}^{1/2}$.

DISCUSSION

From the present results it is clear that the range of the stress intensity factor alone cannot account for stress ratio and crack size effects on fatigue crack growth rate, as seen by previous authors KITAGAWA [7], TANAKA et al. [8], HICKS et al. [9], SCHIJVE [10], MINAKAWA et al. [11], PINEAU et al. [12]. Many authors since PEARSON [2] have studied the growth of natural cracks in smooth specimens. Assumptions must be made to calculate the fatigue crack growth rate and also the stress intensity range ΔK as seen by BROWN et al. [13]. For example many studies use observations of cracks on the specimen surface and the assessment of crack shape and depth relies upon a calibration curve which is established from broken specimens. Such data are not easily generated for the smaller crack sizes, and the accuracy of the calibration curve becomes questionable. Natural cracks initiate generally at material inhomogeneities, SCHIJVE [10], RITCHIE and LANKFORD [14], such as inclusions, pores, and second phase particles. When the crack is much larger than the size of the initiation defect it has an equilibrium shape and the calibration curve should apply. However

this becomes questionable at short crack lengths for defects at or near the outer surface where cracks may not be of equilibrium shape LUTJERING et al. [15]. The artificial short cracks as described here, may be accurately described as two dimension through-cracks. The assumptions made, concerning bidimensionality and a uniform stress intensity factor along the crack front are realistic in this case. The artificial short cracks, as used in the present work, are a convenient way to study the crack length dependency of fatigue crack growth behaviour, even though natural cracks are more representative of situations occurring in real components.

A single intrinsic law at room temperature for this HIP + forged Astroloy is observed whatever the crack length ranging from 0.1 to a few tens of mm or the stress ratio ranging from 0.1 to 0.9. For the CT specimens the closure in the wake, as studied by JAMES and KNOTT [16], SONIAK and REMY [17] was observed to be identical to the real crack length ahead of the notch, this behaviour was observed for specimens tested at decreasing ΔK as well as for specimens tested at increasing ΔK . On the other hand the closure in the wake on SEN specimens was always smaller than the crack length. But as seen in figure 4 when the cracks becomes longer than 2 mm, a constant K_{op} value was observed for both CT and SEN specimens. However, this constant K_{op} behaviour corresponds to very different closure behaviours in the wake and so the opening stress intensity factor K_{op} is not simply connected to the closure in the wake for this material. The figure 3 indicates that K_{op} is not so dependent upon K_{max} . That means that at room temperature plasticity should not be simply take into account. Crack closure should be dependent upon surface roughness in the present alloy but other mechanisms could also be operative ignoring any environmental influence at room temperature.

It can be seen in figure 9, which reports at 650°C the value of the opening stress intensity factor K_{op} as a function of the maximum stress intensity factor K_{max} , that the K_{op} value increases with K_{max} and takes the same value for long and short cracks. Those K_{max} values are associate to very different crack lengths on long and on short cracks. Consequently crack closure should be principally dependent upon plasticity phenomenon in the present alloy at 650°C in air. Two different behaviours have been seen on short cracks at 650°C in air. The first one has been related for low ΔK levels on figure 7. It is associated with a great number of cycles at a very low ΔK level ranging from 1 to 5 MPa.m^{1/2} and followed by a brutal crack advance occurring during a few cycles when the load is increased. It means that crack advance could occur under the effective threshold and that during a great number of cycles a damage accumulates ahead of the crack tip when the short crack does not propagate. The second behaviour has been observed on figure 8. The load shedding procedure was quick enough to reach the effective stress intensity range before the crack had propagate.

FATIGUE 87

Then the crack was seen to grow very fast then to slow down during a few millions of cycles, and then to stop. The FCGR decreases continuously at constant load. The decreasing of the rate should be caused in that case by the increasing of the closure phenomenon. No macroscopic closure have been seen on load displacement curves far away from the crack tip. But one may assume the existence of a microscopic closure, probably caused by a thin film of oxide, close to the crack tip, as reported by RITCHIE and SURESH [18]. Crack closure should be responsible at 650°C in air in this alloy of the behaviour of the short cracks, when ΔK ranges from the effective to the nominal stress intensity range. Experiments are actually under way to assess the importance of environmental effects, which should be taken in to account in any realistic prediction of fatigue crack growth at high temperature.

CONCLUSIONS

The present investigation into the influence of stress ratio on long crack behaviour in HIP + forged Astroloy has shown that consideration of crack closure can rationalize fatigue crack growth rate curves. This consideration leads to an intrinsic crack growth law of da/dN versus ΔK_{eff} for long and short cracks at room and at high temperature.

At 650°C in air unstable crack growth events have been observed below the effective threshold. Stable crack growth occurs above the effective threshold.

ACKNOWLEDGEMENTS

The authors are indebted to Turboméca for provision of research facilities and the DRET for financial support.

REFERENCES

- 1 - PARIS, P.C., BURKE, J.J., REED, N.L., and WEIS, V., 1964, Proceed of the 10th Sagamore Army Materials Research Conf., Syracuse University Press, pp.107-127.
- 2 - PEARSON, S., 1975, Eng. Fract. Mech., 7, pp.235-247.
- 3 - LANKFORD, J., 1977, Eng. Fract. Mech., 9, pp.617-624.
- 4 - KLESNIL, M. and LUKAS, P., 1972, Mat. Sci. Eng., 9, pp.231-240.
- 5 - USAMI, S., 1982, "Fatigue Thresholds", J., Backlund, A.F. Blom and C.J. beevers (Eds), E.M.A.S., 1, pp.205-238.

FATIGUE 87

- 6 - ELBER, W., 1971, "Damage Tolerance in Aircraft Structures", ASTM STP 486, Am.Soc. for Test. Mat., pp.230-242.
- 7 - KITAGAWA, H., 1982, "Fatigue Thresholds", J. Backlund, A.F. Blom and C.J. Beevers (Ed.), E.M.A.S., 2, pp.1051-1068.
- 8 - NAKAI, Y., TANAKA, K. and T. NAKANISHI, 1981, Eng. Fract. Mech., 15, pp.291-302.
- 9 - VENABLES, R.A., HICKS, M.A. and KING, J.E., 1984, "Fatigue Crack Growth Threshold Concepts", D. Davidson and S. Suresh (Ed.), T.M.S. AIME, Warrendale, Pennsylvania, pp.341-357.
- 10 - SCHIJVE, J., 1982, "Fatigue Thresholds", J. Backlund, A.F. Blom and C.J. Beevers (Ed.), E.M.A.S., 2, pp.881-908.
- 11 - MINAKAWA, K., NEWMAN, Jr. J.C., and McEVILY, A.J., 1983, Fatigue of Eng. Mat. and Struct., 6, pp.359-365.
- 12 - BREAT, J.L., MUDRY, F., and PINEAU, A., 1983, Fatigue of Eng. Mat. and Struct., 6, pp.349-358.
- 13 - BROWN, C.W., KING, J.E., and HICKS, M.A., 1984, Metal Science, 18, pp.374-380.
- 14 - RITCHIE, R.O. and LANKFORD, J., 1986, Mat. Science and Eng., pp.11-16.
- 15 - FOTH, J., MARISSEN, R., NOWACK, M., and LUTJERING, G., 1984, Proceed of the 5th E.C.F., L. Faria (Ed.), pp.135-144.
- 16 - JAMES, M.N., and KNOTT, J.F., 1985, Fatigue Fract. Eng. Mat. Struct., 8, pp.177-191.
- 17 - SONIAK, F., and REMY, L., 1986, "the Behaviour of Short Fatigue Cracks", EGF Pub.1, K.J. Miller and E.R. de los Rios (Ed), Mechanical Engineering Publications, London, pp.133-142.
- 18 - RITCHIE R.O., and SURESH, S., 1982, Met. trans, 13.A., pp.937-940.

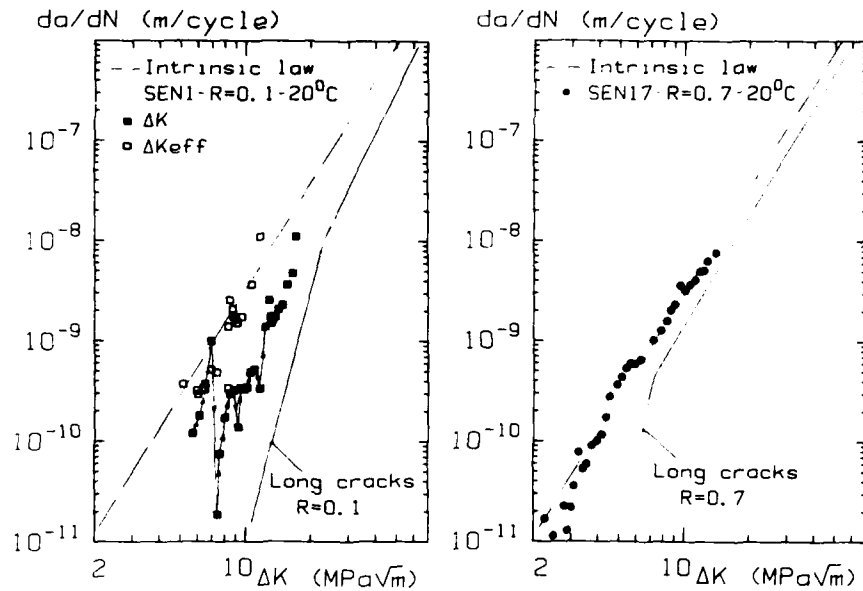


Fig.1 FCGR (da/dN) versus ΔK for **Fig.2** FCGR (da/dN) versus ΔK for $R=0.1, 20^\circ\text{C}$, on short cracks. $R=0.7, 20^\circ\text{C}$, on short cracks.

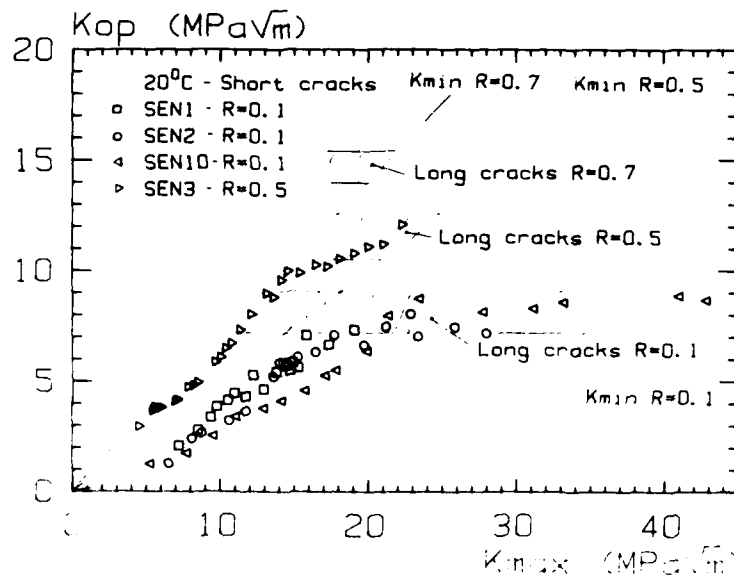


Fig.3 Crack opening stress intensity factor K_{op} versus K_{max} at 20°C on long and short cracks for different stress ratios.

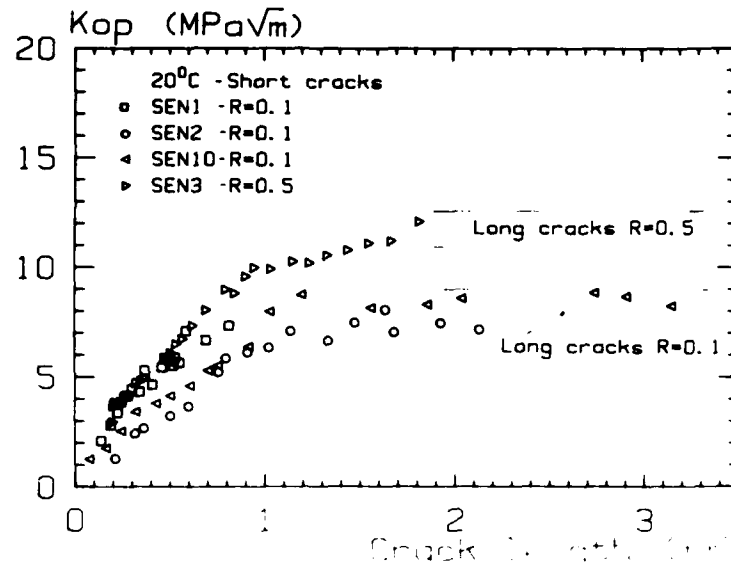


Fig.4 Crack opening stress intensity factor K_{op} versus crack length on short cracks at 20°C for different stress ratios.

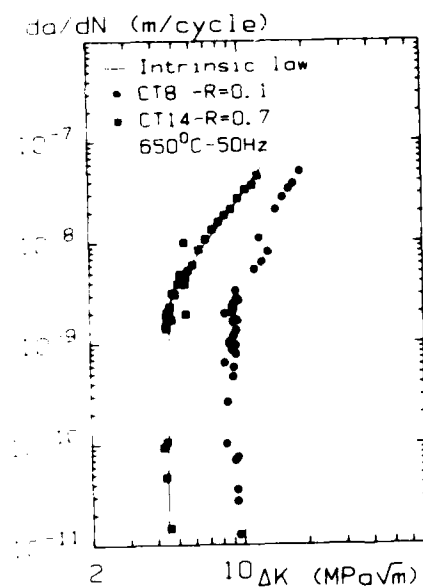


Fig.5 FCGR (da/dN) versus ΔK at 650°C on long cracks.

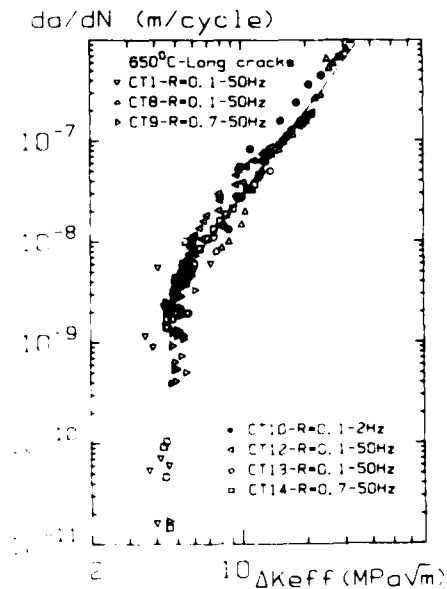


FIG.6 FCGR (da/dN) versus ΔK_{eff} at 650°C on long cracks

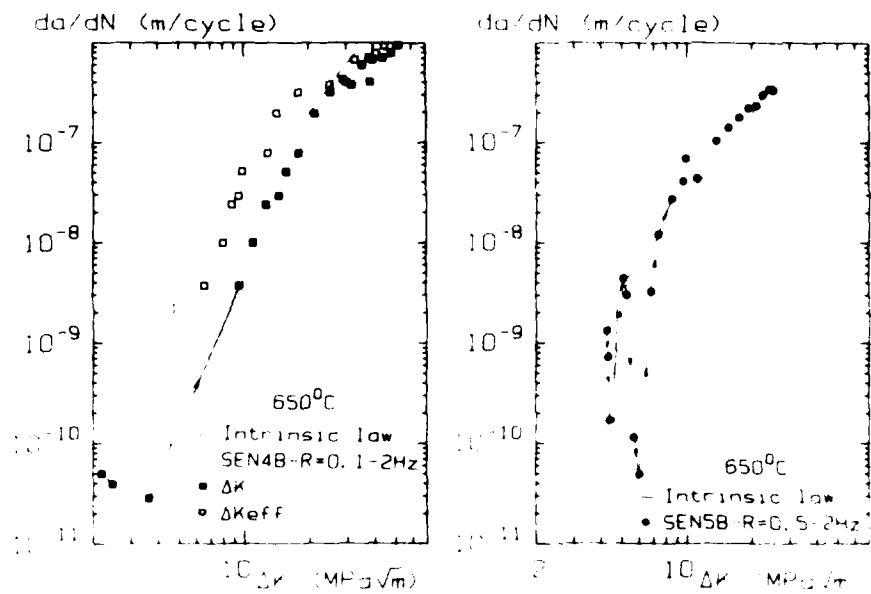


Fig.7 FCGR (da/dN) versus ΔK for **Fig.8** FCGR (da/dN) versus ΔK for $R=0.1, 650^\circ C$ on short cracks. $R=0.5, 650^\circ C$ on short cracks.

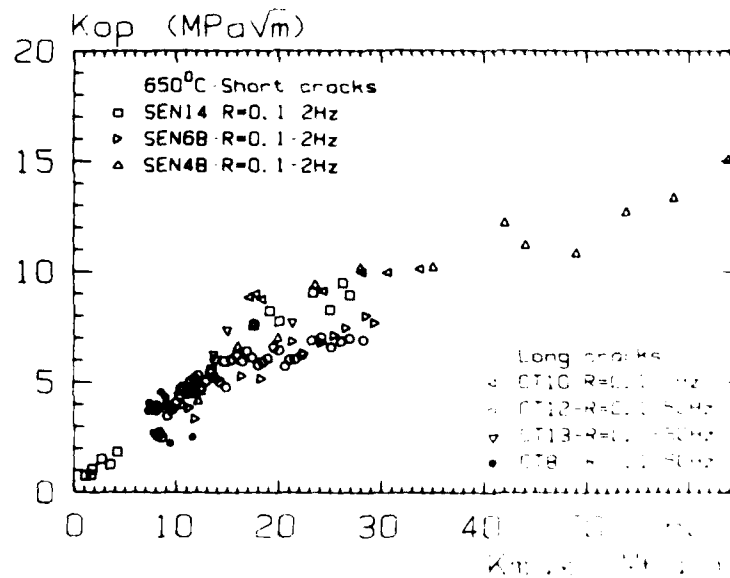


Fig.9 Crack opening stress intensity factor K_{op} versus K_{max} at $650^\circ C$ for different stress ratios.

PROPAGATION OF SMALL FATIGUE CRACKS IN 2024-T3 ALUMINUM ALLOY

K. Tanaka*, Y. Akiyama*, and E. Matsui*

Smooth specimens of 2024-T3 aluminum alloy were fatigued under nominally elastic conditions with several mean stresses. The propagation behavior of many small cracks was analysed statistically. The relation between the crack growth rate and the crack length was divided into three regions: A, B, and C. In region C, where the crack growth rate was higher than 10^{-8} m/cycle, the crack growth data followed the $da/dN-\Delta K$ relation for large cracks. In region A, where the crack length was less than 0.1 mm, the crack grew along slip planes and the scatter of the crack growth rate was large. In region B, the crack growth path was perpendicular to the stress axis; the crack growth rate was higher than that predicted from the $da/dN-\Delta K$ relation. The characteristics of the crack growth behavior in each region were examined, and the growth behavior of a main crack was discussed in relation to life prediction.

INTRODUCTION

Small cracks with dimensions on the order of the material microstructure, e.g., the grain size, are called microstructurally small cracks. They show anomalously high, irregular growth rates when compared with large cracks at the same range of the stress intensity factor (SIF) ΔK (Lankford (1,2), Tanaka (3), Tokaji (4)). This irregular growth behavior is caused by the microstructural inhomogeneity and has a probabilistic nature. To derive a predictive method for small crack growth, the statistical nature of small cracks must be characterized and the limitation of the ΔK -based fracture mechanics needs to be defined.

In the present paper, smooth specimens of 2024-T3 aluminum alloy were fatigued under nominally elastic conditions. The propagation behavior of small cracks was discussed on the basis of microscopic observation. The statistical analysis of the growth rates of many small cracks was used to derive the average growth behavior and to define the limitation of the large crack growth law in predicting small crack growth.

* Department of Engineering Science, Kyoto University,
Kyoto 606, Japan

EXPERIMENTAL PROCEDURE

Material and Specimen

The material is 2024 T3 aluminum alloy with the following chemical compositions in weight %: 0.12Si, 0.20Fe, 0.20Cu, 0.02Mn, 1.48Mg, 0.016Cr, 0.029Zn, 0.032Ti, balance Al. The material was provided in a sheet with a thickness of 5 mm. The grain size measured with the linear intercept method was 32 μm in the rolling direction, 27 μm in the transverse direction, and 19 μm in the thickness direction. The 0.2% off set strength in the rolling direction was 322 MPa and the tensile strength was 485 MPa.

Figure 1 shows the test specimen which is thinned at the center. The rolling direction is longitudinally. The part of the longitudinal axis. The elastic stress concentration factor is 1.9 (Number 100). All the specimens were polished to mirror finish and finished with electropolishing.

Fatigue Test and Microscopic Observations

Fatigue tests were conducted in a servohydraulic test machine under normally sinusoidal stress with a constant frequency of 20 to 30 Hz at laboratory temperature. The mean stress σ_m and the stress ratio R adopted for the test were $\sigma_m = 150$ MPa and $R = 0.1$, respectively. At a given number of cycles, the test was terminated and the cracks were taken from the central part of the specimen. The number of cycles N_f and the crack length a were recorded and given in Table I. The region of microscopic observation of the longitudinal direction and transverse direction at the central part of the specimen. The test was stopped when the longest crack was about 1 mm. The grain boundaries were revealed through optical microscopic observation. A series of typical

EXPERIMENTAL RESULTS AND DISCUSSION

Characteristics of Small Crack Propagation

Fatigue cracks nucleated in smooth specimens tend to grow in an irregular manner because of microstructural inhomogeneities. Figure 2 shows the propagation of a fatigue crack nucleated at an inclusion in the specimen subjected to $\sigma_a = 150$ MPa with $R = 0.1$, where (a) is a micrograph (the stress axis is vertical), (b) is its sketch, and (c) is the crack propagation rate plotted against the crack length. The crack length is the length of the projection of a crack on the plane perpendicular to the applied stress axis measured from the inclusion center. The crack growing along slip planes in the early stage is frequently decelerated when it hits the grain boundary or when it makes a sharp bend, as indicated with letters A, B, C, D in the figure. The peak growth rate is nearly independent of the crack

length, when the crack becomes long, the crack growth path is nearly perpendicular to the stress axis and the crack does not show large irregularity in the crack growth curve.

The statistics of the microstructural state, relative to the grain boundaries, at temporary crack stoppage, and those of the crack growth direction, just after crack stoppage, were obtained for the cases of $\dot{\epsilon}_0 = 1.00$ and $2.30 \text{ MPa}/\text{mm}^2/\text{sec}$ under $\dot{\epsilon}_0 = 1.00$. Table 1 summarizes the results. About sixty percent of the crack terminated at the grain boundaries, 44 percent at eight percent of the cases, where crack stoppage was observed, the crack growth direction was changed when the crack started to propagate.

The relationship between the two variables is supported by the significant positive correlation of the regression between the two variables, $r = 0.61$, $p < 0.001$. The correlation of the regression is not statistically significant when the sample is small ($n = 47$), $r = 0.28$, $p > 0.05$. The regression of the variable "number of visits to the doctor for a chronic condition" was not significant ($p > 0.05$). The regression of the variable "number of visits to the doctor for an acute condition" was not significant ($p > 0.05$). The regression of the variable "number of visits to the doctor for a chronic condition" was not significant ($p > 0.05$). The regression of the variable "number of visits to the doctor for an acute condition" was not significant ($p > 0.05$).

It is evident that the difference between the peak at $\lambda = 2100$ and the peak at $\lambda = 2200$ is due to the difference in the absorption of the two types of radiation. The peak at $\lambda = 2100$ is due to the absorption of the γ rays, and the peak at $\lambda = 2200$ is due to the absorption of the β rays. The difference in the absorption of the two types of radiation is due to the difference in the penetration of the two types of radiation into the material. The γ rays penetrate deeper into the material than the β rays, and therefore the peak at $\lambda = 2100$ is higher than the peak at $\lambda = 2200$.

The scatter of the data in the small α regime is dominated by the data converge to the large α track growth law at a track density of 10.6 μm^{-1} and a growth rate of 10 $\mu\text{m}/\text{cycle}$.

Statistical Distribution of Crack Propagation Rate

The distribution of the crack growth rate at a given crack length was obtained from Fig. 3(b). Figure 4 is the weibull plot of the cumulative probability function, of the crack growth rate for cracks whose lengths are within each interval as indicated. The abscissa is the crack growth rate. The variation of distribution

FATIGUE 5

For marks shorter than 120 points, space for the student's answer is provided, indicated at growth rates as marked by the corresponding number of points on the student's answer. The answers are marked by the number of points on the student's answer, indicated by the number of points on the student's answer.

the 1990s, the number of people in the United States who are 65 years of age or older has increased by 50% (U.S. Census Bureau, 2000). The number of people aged 65 and older is projected to increase to 20% of the total population by the year 2020 (U.S. Census Bureau, 2000). The increase in the number of people aged 65 and older is expected to be even more dramatic in other countries. For example, the number of people aged 65 and older in Japan is projected to increase from 15% of the total population in 1990 to 25% of the total population by the year 2020 (U.S. Census Bureau, 2000). The increase in the number of people aged 65 and older is expected to be even more dramatic in other countries. For example, the number of people aged 65 and older in Japan is projected to increase from 15% of the total population in 1990 to 25% of the total population by the year 2020 (U.S. Census Bureau, 2000).

1. *Journal of the American Medical Association*, 1997; 277: 1033-1036.

1 • 2 3 4

[illegible]

... ..

[illegible]

The transition from crystallographic growth (stage I) to non-crystallographic growth (stage II) takes place at a crack length of about 0.1 mm. The total crack length on the specimen surface was about seven grain sizes. As the crack becomes longer than this crack length, the scatter in the crack growth rate was sharply reduced, and the scatter in the crack aspect ratio was also decreased, approaching to about one (Tanaka *et al.*).

On the basis of above discussion, the \dot{a}/N relation for small cracks can be divided into three regions: A, B, and C. In region C, where the crack growth rate is higher than 10^{-10} m/cycle, the data points follow the \dot{a}/N - ΔK relation for large cracks and the scatter of the crack growth rate is small. In region A, where the crack length is less than about 0.1 mm, the crack grows along the slip plane, and the scatter of the crack growth rate is large.

FATIGUE 53

[illegible]

• • • • •

•

As the crack length increased, the average crack growth rate decreased with increasing crack length. The crack growth rate was the least sensitive to the grain orientation and the stress level. The average crack growth rate was approximately the same for all the crack lengths. The average crack growth rate was fairly insensitive to the crack length, while sensitive to both the stress amplitude and crack length.

the growth rate of the main crack was generally higher than the average crack growth rate. The life prediction based on the average growth behavior of small cracks gives a dangerous estimate, while

Table 1

Table 1. Applied stress conditions.

Table 1. Applied stress conditions.

Table 1. Applied stress conditions.

Table 1. Applied stress conditions.

Table 1. Applied stress conditions.

Table 1. Applied stress conditions.

Table 1. Applied stress conditions.

Table 1. Applied stress conditions.

Table 1. Applied stress conditions.

Table 1. Applied stress conditions.

Table 1. Applied stress conditions.

Table 1. Applied stress conditions.

Table 1. Applied stress conditions.

Test No.	Stress amplitude σ_a (MPa)	Mean stress σ_m (MPa)	Maximum stress σ_{max} (MPa)	Stress ratio $R = \frac{\sigma_{min}}{\sigma_{max}}$	Life N_f	Observation interval Δt
1	150	0	150	-1	7.5×10^5	2.0×10^4
2	230	0	230	-1	1.0×10^5	5.0×10^3
3	150	80	230	-0.3	2.5×10^5	5.0×10^3
4	230	-80	150	-2.07	1.9×10^5	5.0×10^3

TABLE 2 - Statistics of Microstructural Site and Growth Direction at Crack Stoppage.

Stress amplitude	Microstructural site	At grain boundary			Within grain			Within grain, less than 5 μ m from the grain boundary	Branched
$\sigma_a = 150 \text{ MPa}$	Number of cracks	33			22			3	2
	Crack direction after deceleration or stoppage	Bent	Straight	Unknown	Bent	Straight	Unknown	Bent	Straight
	Number of cracks	19	5	9	12	3	7	1	2
	Number of cracks	18			12			1	0
$\sigma_a = 60 \text{ MPa}$	Number of cracks	18			12			1	0
	Crack direction after deceleration or stoppage	Bent	Straight	Unknown	Bent	Straight	Unknown	Bent	Straight
	Number of cracks	14	4	0	9	2	1	0	1
	Number of cracks	18			12			1	0

AD-A184 045

FATIGUE '87 VOLUME 100 VIRGINIA UNIV CHARLOTTESVILLE
SCHOOL OF ENGINEERING AND APPLIED SCIENCE
R O RITCHIE ET AL JUN 87 ARO-24134.1-MS-CF

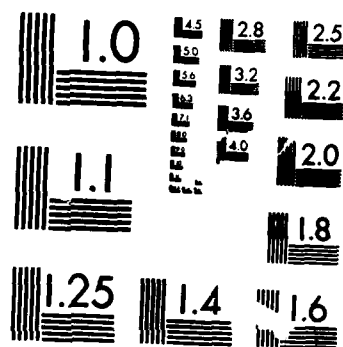
5/7

UNCLASSIFIED

N00014-87-G-0008

F/G 20/11

NL



MICROCOPY RESOLUTION TEST CHART
NATIONAL BUREAU OF STANDARDS-1963-A

FATIGUE 87

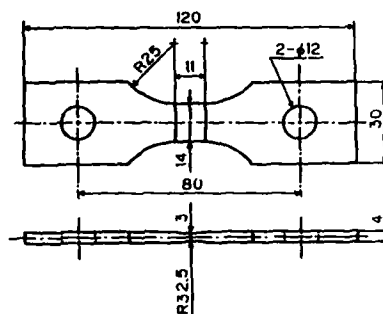


Figure 1. Test specimen. (Dimensions are in mm)

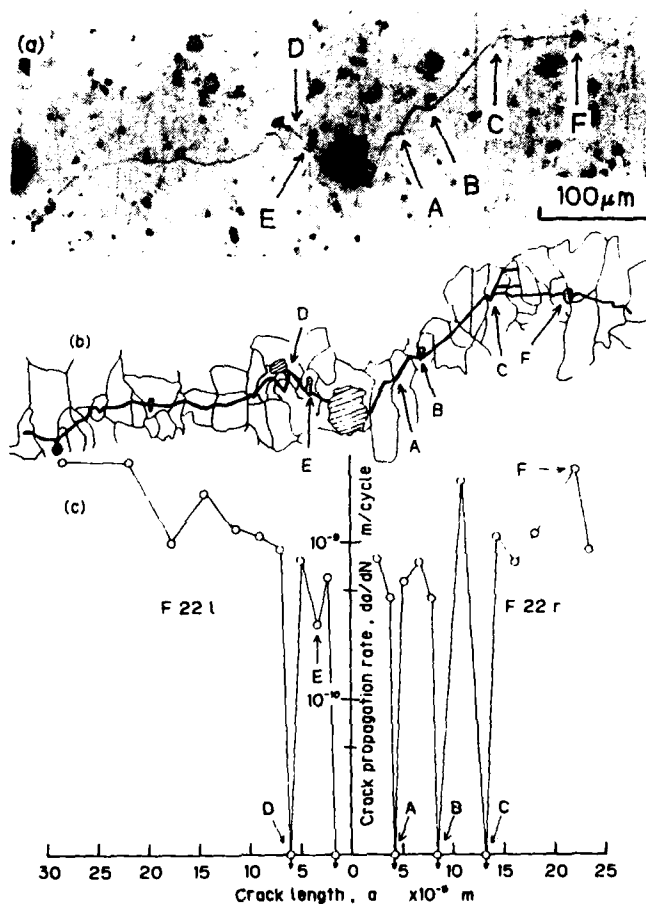


Figure 2. Propagation of a small surface crack. (a) Micrograph. (b) Sketch of crack and microstructure. (c) Crack growth rate.

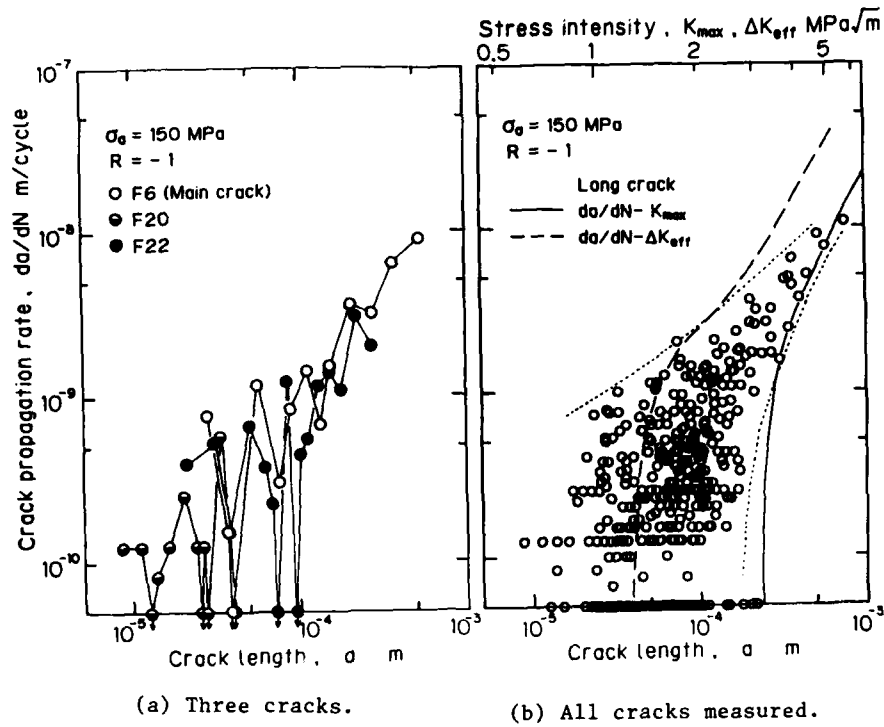


Figure 3. Relation between crack growth rate and crack length.

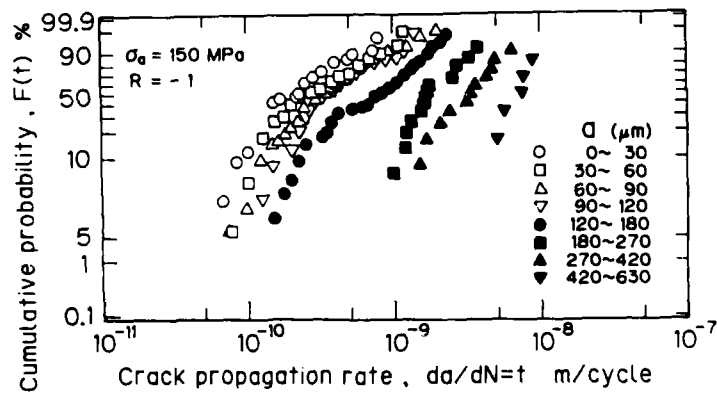


Figure 4. Distribution of crack propagation rate.

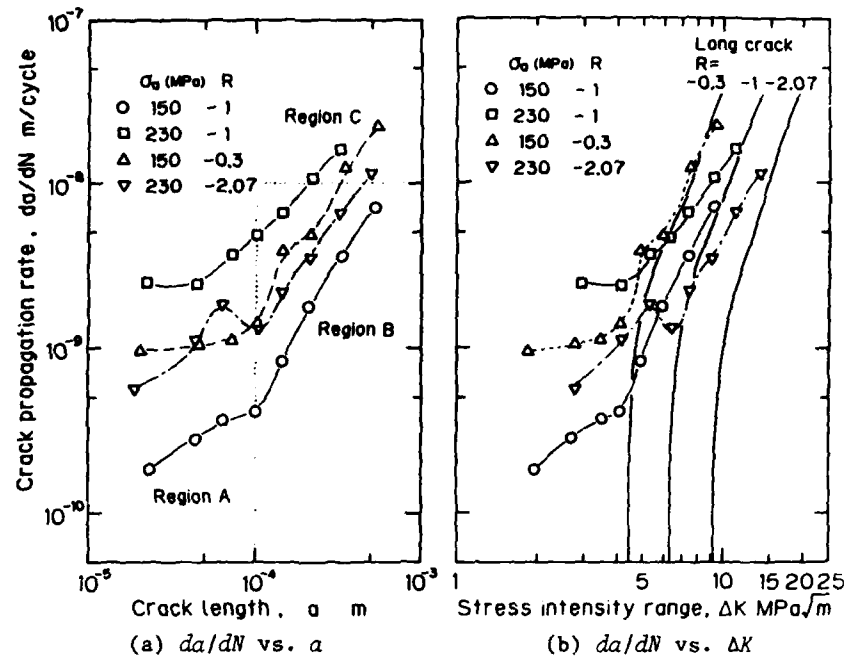


Figure 5. Average growth behavior of small cracks.

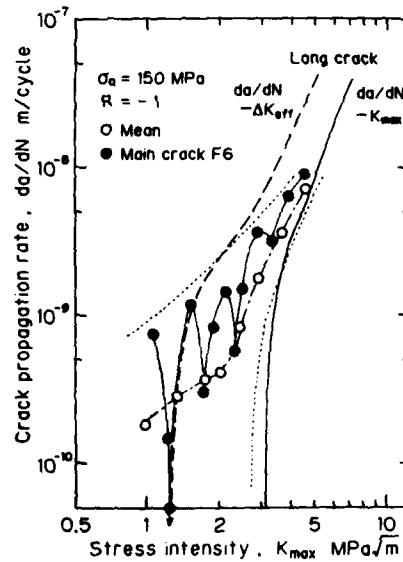


Figure 6. Relation between crack growth rate and stress intensity factor for main crack.

CLOSURE AND PROPAGATION BEHAVIOR OF SHORT FATIGUE CRACKS
AT DIFFERENT R-RATIOS

Y. Verreman*, J.-P. Bailon*, J. Masounave**

A previous investigation on V-notched specimens in plane strain showed that the short crack behavior at $R = -1$ is essentially due to an initial transient variation of the crack opening level within the notch plastic zone. This paper includes new results at $R = 0$ and -2 . Similar closure and propagation behaviors are observed, and the effective SIF range still correlates both short and long crack growth rates. However, the lower the R-ratio, the more pronounced the short crack effect; this results from important differences between the amplitudes of the opening level variation. Micro-strain gages installed close to the crack plane were used to monitor the length and the opening level of short cracks. The notch monotonic and cyclic plastic zone extents were computed from finite element analysis.

INTRODUCTION

The behavior of short fatigue cracks growing at notches is known to differ significantly from the LEFM behavior of long cracks. Higher growth rates at the same ΔK and growth below the conventional long crack threshold have been often reported. A more fundamental disagreement is that short cracks can grow at a decreasing rate and become non-propagating near the endurance limit level, as shown for example by El Haddad et al (1) and Tanaka and Nakai (2). Such a non-LEFM behavior, which was predicted by an earlier theoretical study from Smith and Miller (3), can be attributed to the notch plasticity since the small scale yielding condition is violated as long as the crack is within the notch plastic zone. The notch plasticity influence was well substantiated by Leis (4) who found, for a variety of notches, materials and nominal stress levels, a good correspondence between the plastic zone extent and the crack length at transition to LEFM behavior. However, the data were for only $R = -1$ and the comparison, which covered the range $50 \mu\text{m} - 10 \text{ mm}$,

* Dept of Metallurgy Engng, Ecole Polytechnique, University of Montreal, C.P. 6079, Succ. A, Montreal, Qc, Canada, H3C 3A7.

** Industrial Materials Research Institute (National Research Council), 75 de Mortagne, Boucherville, Qc, Canada, J4B 6Y4.

FATIGUE 87

revealed about half a decade of scatter. Moreover, a number of recent studies, like those compiled by Lankford (5), show that short cracks growing at smooth surfaces also present a non-LEFM behavior even beyond the crystallographic propagation stage.

Numerical analyses were performed by Ohji et al (6) and Newman (7) to simulate the plasticity-induced closure of cracks growing at notches under $R = -1$ loading. The results indicate that the crack opening level S_{op} starts from $S_{min} = -S_{max}$ at zero crack length (the crack is fully open), rapidly increases as the crack grows and finally tends to a stabilized slightly positive value. This initial transient variation explains qualitatively the short crack propagation behavior (6,8). However, nothing indicates that the opening level variation is induced by notch plasticity, and very few experimental data have been generated to verify these simulations and to ascertain that the effective SIF range ΔK_{eff} correlates both short and long crack growth rates.

It is difficult to know the influence of the R-ratio on short crack behavior from the available literature. Most experimental and theoretical results have been obtained under $R = -1$ loading. An experimental study performed under $R = 0$ loading (2) shows an initial transient variation of the opening level similar to those computed in (6,7). However, its amplitude is lower than under $R = -1$ loading because the minimum possible value of S_{op} is obviously 0, which suggests that one can expect less discrepancy between short and long crack growth rates. The opposite would occur under $R = -2$ loading if S_{op} starts from $S_{min} = -2S_{max}$. Therefore, it seems that the lower the value of R, the more pronounced the non-LEFM behavior of short cracks. The extreme case would occur under zero-to-compression loading ($R = -\infty$) for which it has been often reported (e.g. Usami et al (9) and Holm et al (10)) that cracks can initiate but become non-propagating after a certain length even when the stress range is increased.

This paper presents experimental results on the short crack closure and propagation behavior in a V-notched specimen. It includes results obtained at $R = -1$ in a previous investigation (11) and further results obtained at $R = 0$ and -2 . The crack lengths at transition to LEFM behavior are compared with the notch plastic zone extents computed from the elasto-plastic finite element analysis presented in Ref. (8).

EXPERIMENTAL CONDITIONS

The experimental conditions are briefly described. Further details are given in Ref. (11). The specimen investigated was the cruciform fillet welded joint shown in Figure 1. The large width in the Z-direction imposed a plane strain state. A cyclic nominal stress S was applied in the X-direction and the crack propagated from the toe of a fillet weld in the Y-Z plane. The base metal was

ASTM A36 steel and the weld metal was AWS-CSA E70S-7 steel. The MIG automatic process was used with the gravity in the Y-direction, which made the weld toe a severe V-shaped stress concentrator: the curvature radius at the toe apex was less than 50 μm . Welding also introduces a residual stress field and a microstructural heterogeneity (Figure 1). The residual stress influence is not concerned in this paper which presents results in a stress-relieved state. The microstructure of the heat affected zone, which extended to about 1.5 mm below the toe apex, was generally fine ($\sim 5 \mu\text{m}$) and no discernible effect of heterogeneities was found on crack propagation.

An efficient crack monitoring system was developed. It allows to make a continuous monitoring of crack length from 10-20 μm with an accuracy of 5%. The principle consists to measure the response of micro-strain gages installed close to the crack plane and to calibrate this response against crack length by finite element computation. The system also allows to monitor the crack opening level from 10-20 μm with an absolute accuracy of $\pm 6 \text{ MPa}$.

Although very few initial defects were observed, crack initiation life was short as compared to total life whatever the nominal stress range. This is due to the V-notch severity. The elasto-plastic finite element analysis shows that there is a quasi-similitude between the stress-strain field ahead of a V-notch and the one ahead of a crack tip, and that the notch plasticity is still at a macroscopic scale at the endurance limit level (8,11). Uniform through-cracks were systematically observed, even at very small crack lengths and low nominal stress ranges. The main reason is that the welding process gives a straight weld bead and very few defects, but the notch macro-plasticity is also a contributing factor (11). As a consequence, the stress intensity factor increases much more rapidly with crack length than for semi-elliptical cracks, so that nearly 90% of life is consumed within the first millimeter of crack growth.

BEHAVIOR UNDER FULLY REVERSED LOADING ($R = -1$)

The short crack propagation behavior was similar to that already reported for severe notches (1). As soon as the crack initiates, a rapid crack growth is recorded, then the crack growth rate significantly decreases. After a certain crack length increasing with S_{max} , the crack growth re-accelerates until final fracture, which is now in agreement with LEFM. Crack growth data are presented in Figure 2 on a conventional da/dN versus K_{max} plot for different nominal stresses ranging from endurance limit level to general plasticity (the cyclic yield stress is estimated at 167 MPa). Long crack growth rates represented by open symbols are well correlated with K_{max} along the dashed curve, while short crack growth rates represented by solid symbols exhibit important discrepancies with respect to this curve. At low nominal

FATIGUE 87

stresses, short cracks grow below the long crack threshold and can become non-propagating (11). Under general plasticity ($S_{max} = 177$ MPa), short crack growth rate does not decrease and long crack one also deviates with respect to the dashed curve.

The measured variations of the opening level with crack length (Figure 3) are in good agreement with the numerical analyses quoted previously (6,7). Moreover, they show that the crack lengths at transition to the quasi-LEFM behavior, where S_{op} becomes stabilized to a slightly positive value, are approximately equal to the notch plastic zone extents indicated by arrows. In spite of further scatter introduced by the measurement of S_{op} , short and long crack growth rates are well correlated with the effective SIF range, ΔK_{eff} (Figure 4). As a consequence, the short crack behavior in the geometry investigated is essentially due to an initial transient variation of the crack opening level within the notch plastic zone. The absence of closure ($S_{op} < 0$) induced by the notch plasticity surrounding the short crack is responsible for the high growth rates. Moreover, the decrease of the effective fraction U of the nominal stress range (Figure 3) is sufficiently rapid for ΔK_{eff} and thus the short crack growth rate to decrease. The slight amount of closure in the long crack regime is induced by the Elber's mechanism, i.e. by residual plasticity behind the crack tip. It is maximum at low nominal stresses and small crack lengths, which explains the knee at low crack growth rates on the da/dN versus K_{max} plot (Figure 2). Inversely, general plasticity ahead of the crack tip makes negative S_{op} -values re-appear at large crack lengths. Its effect is already marked in the short crack regime at $S_{max} = 177$ MPa where the crack opening level never becomes positive (Figure 3). Although the validity of ΔK_{eff} is somewhat doubtful in this case, the slower decrease of U explains why the short crack growth rate does not decrease.

BEHAVIOR UNDER NON-SYMMETRIC LOADING ($R = 0$ AND -2)

The notch monotonic and cyclic plastic zones have not the same extent when $R = -1$. It is logical to assume that only the notch cyclic plasticity can play a role in the crack driving force. However, the notch monotonic plasticity can induce variations of the crack opening level in the same manner as an overload, i.e. by introducing a residual stress field. Under $R = 0$ loading, the discrepancy between short and long crack growth rates was barely pronounced as compared to $R = -1$ loading. A similar initial increase of the opening level was observed (Figure 5). However, although the maximum value of S_{op} ($\sim 0.35 S_{max}$) is somewhat greater than the corresponding one at $R = -1$, the amplitude of the opening level variation is lower because S_{op} starts from 0 instead of $-S_{max}$: the effective fraction U only decreases by a ratio of $1/0.65 \sim 1.5$ instead of $1/0.40 \sim 2.5$ at $R = -1$. This explains why the short crack effect is barely pronounced. Moreover, for the

FATIGUE 87

same S_{max} , the crack lengths at which S_{op} becomes maximum are smaller than at $R = -1$. They nearly correspond to the extents of the notch cyclic plastic zone (Figure 5): these are theoretically eight times smaller than at $R = -1$, but the finite element computation, which uses a bi-linear stress-strain curve (8), leads to some underestimation of plastic yielding when it is small. Another difference is noticeable. Once the maximum is reached, there is a sensible decrease of the opening level before it becomes stabilized. This second variation suggests a possible role of notch monotonic plasticity, the extent of which (Figure 5) is equal to the plastic zone extent at $R = -1$ for the same S_{max} . The whole variation of the opening level, from zero crack length to stabilization, is quite similar to the one induced by an overload on a long crack. It is also worth noting that the crack becomes again fully open when approaching general plasticity (Figure 5; $S_{max} = 206$ MPa).

The opposite occurs under $R = -2$ loading. The short crack effect is more pronounced than at $R = -1$, with in particular a strong decrease of the short crack propagation rate (Figure 6). The reason is the same as that advanced in the introduction section. The opening level starts effectively from $-2S_{max}$ (Figure 7), which results in a higher amplitude of the opening level variation: for $S_{max} = 88$ MPa, the effective fraction U decreases by a ratio of $1.0.28 \sim 3.6$. The comparison with finite element computations shows that the crack length at which S_{op} becomes maximum corresponds to the extent of the cyclic plastic zone (Figure 7). No subsequent variation is observed here, i.e. the opening level remains stabilized when the maximum is reached, as under $R = -1$ loading. However, the absence of closure induced by general plasticity in the long crack regime is observed for relatively low S_{max} -values. This rapid transition from endurance limit level to general plasticity results from the fact that, at $R = -2$, the total nominal stress range, ΔS is equal to $3S_{max}$. For $S_{max} = 108$ MPa, $\Delta S = 324$ MPa which is nearly twice the cyclic yield stress estimated at 167 MPa. Finally, it is worth noting that short and long crack growth rates are still well correlated on a da/dN versus ΔK_{eff} plot (Figure 8) together with those obtained at $R = -1$ (compare with Figure 6).

CONCLUSIONS

Fatigue tests were performed at different R-ratios on V-notched specimens in plane strain while monitoring the length and the opening level of cracks as small as $10\text{-}20\ \mu\text{m}$, and the extents of notch monotonic and cyclic plastic zones were computed from finite element analysis. The main conclusions are the following:

1. Crack initiation life is short whatever the nominal stress range.
2. Short crack behavior in a V-notch is essentially characterized by an initial transient variation of the opening level within

FATIGUE 87

the notch cyclic plastic zone.

3. The lower the R-ratio, the more pronounced discrepancies between short and long crack growth rates; this results from important differences between the amplitudes of the opening level variation.
4. The effective SIF range correlates both short and long crack growth rates.

ACKNOWLEDGEMENTS

The authors are grateful to Natural Science and Engineering Research Council for its partial financial support.

REFERENCES

1. El Haddad, M.H. et al. ASTM STP 677, 1979, pp. 274-289.
2. Tanaka, K. and Nakai, Y., Fatigue Engng. Mater. Struct., Vol. 6, No 4, 1983, pp. 315-327.
3. Smith, R.A. and Miller K.J., Int. J. Mech. Sci., Vol. 20, 1978, pp. 201-206.
4. Leis, B.N., Int. J. Pressure Vessels Piping, Vol. 10, 1982, pp. 141-158.
5. Lankford, J., Fatigue Fracture Engng. Mater. Struct., Vol. 8, 1985, pp. 161-175.
6. Ohji, K. et al. Engng. Fract. Mech., Vol. 7, 1975, pp. 457-464.
7. Newman, J.C., Jr., "A Non-Linear Fracture Mechanics Approach to the Growth of Short Cracks", Proceedings of AGARD specialists meeting on behaviour of short cracks, Toronto, Canada, 1982.
8. Verreman, Y., et al., "Fatigue Life Prediction of Welded Joints: A Re-Assessment", to be published in Fatigue Fracture Engng. Mater. Struct.
9. Usami, S. et al. Trans. Jap. Weld. Soc., Vol. 9, 1978, pp. 118-127.
10. Holm, D.K. et al. Engng. Fract. Mech., Vol. 23, No 6, 1986, pp. 1097-1106.
11. Verreman, Y. et al., "Fatigue Short Crack Propagation and Plasticity-Induced Crack Closure at the Toe of a Fillet Welded Joint", The Behaviour of Short Fatigue Cracks (Ed by K.J. Miller) 1986, Mechanical Engng Publications, London, U.K.

FATIGUE 87

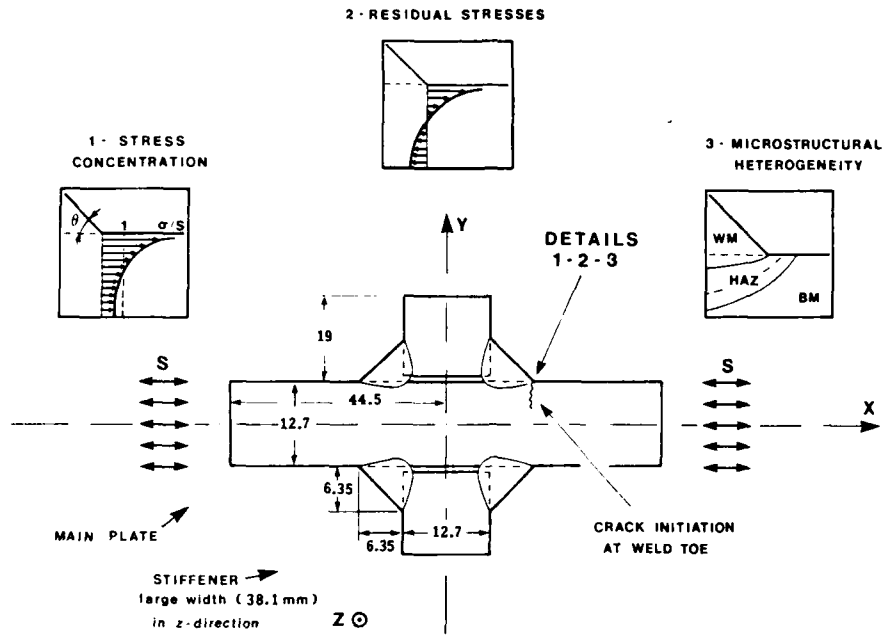


Figure 1 The cruciform welded joint (dimensions in mm).

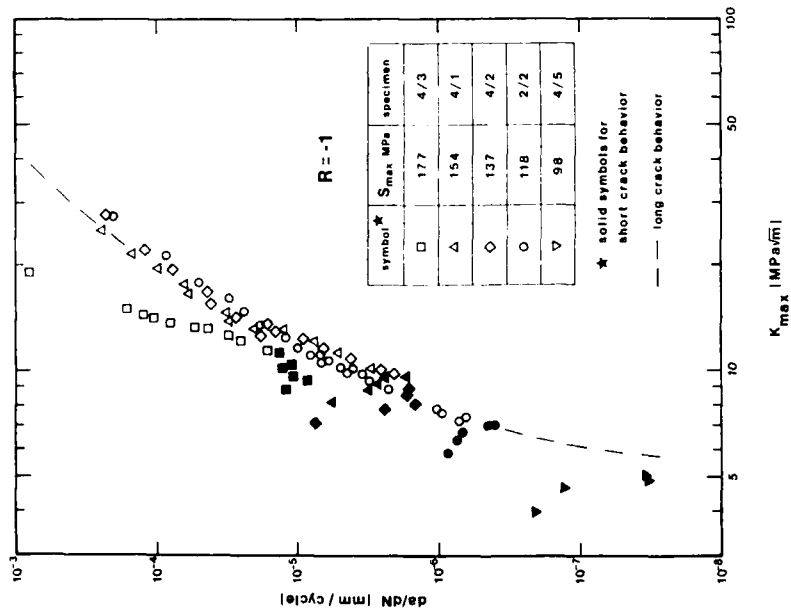


Figure 2 Crack growth rate vs K_{max} at $R = -1$.

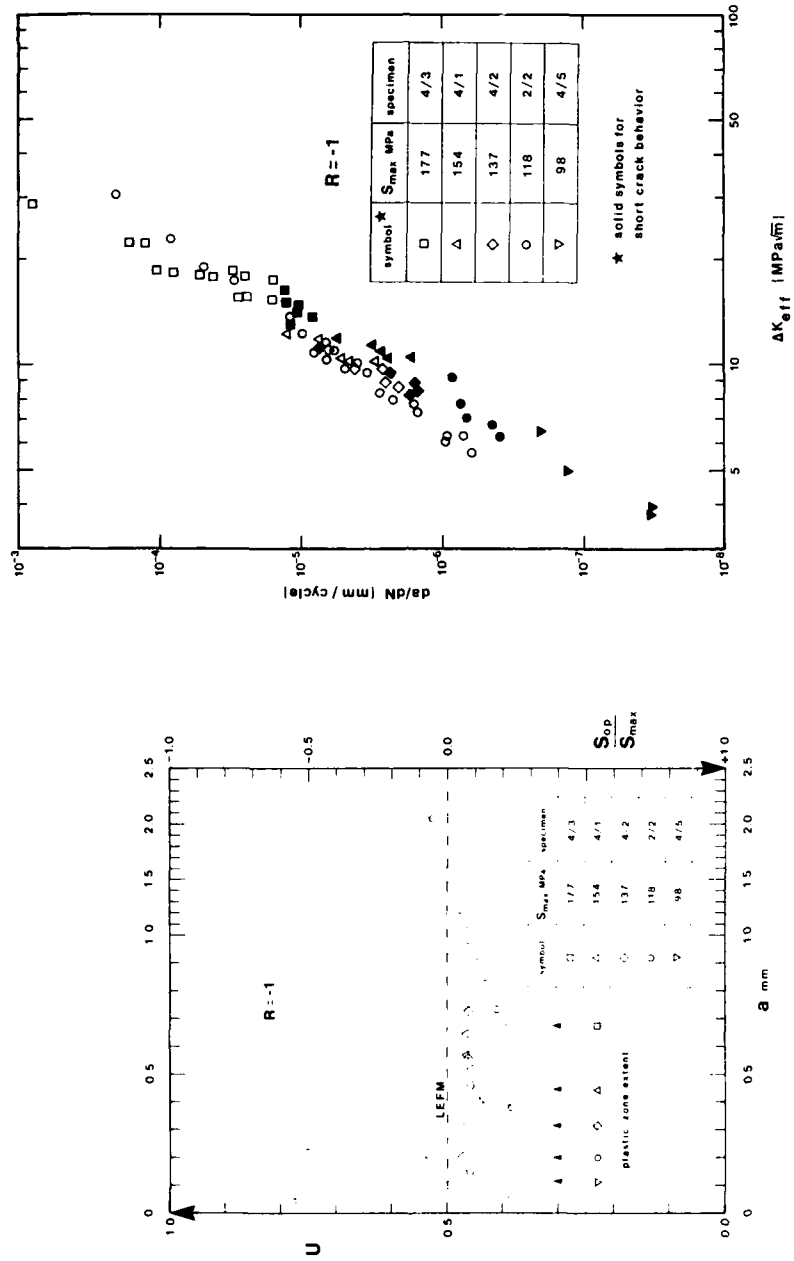


Figure 3 Crack opening level vs crack length at $R = -1$ Figure 4 Crack growth rate vs ΔK_{eff} at $R = -1$.

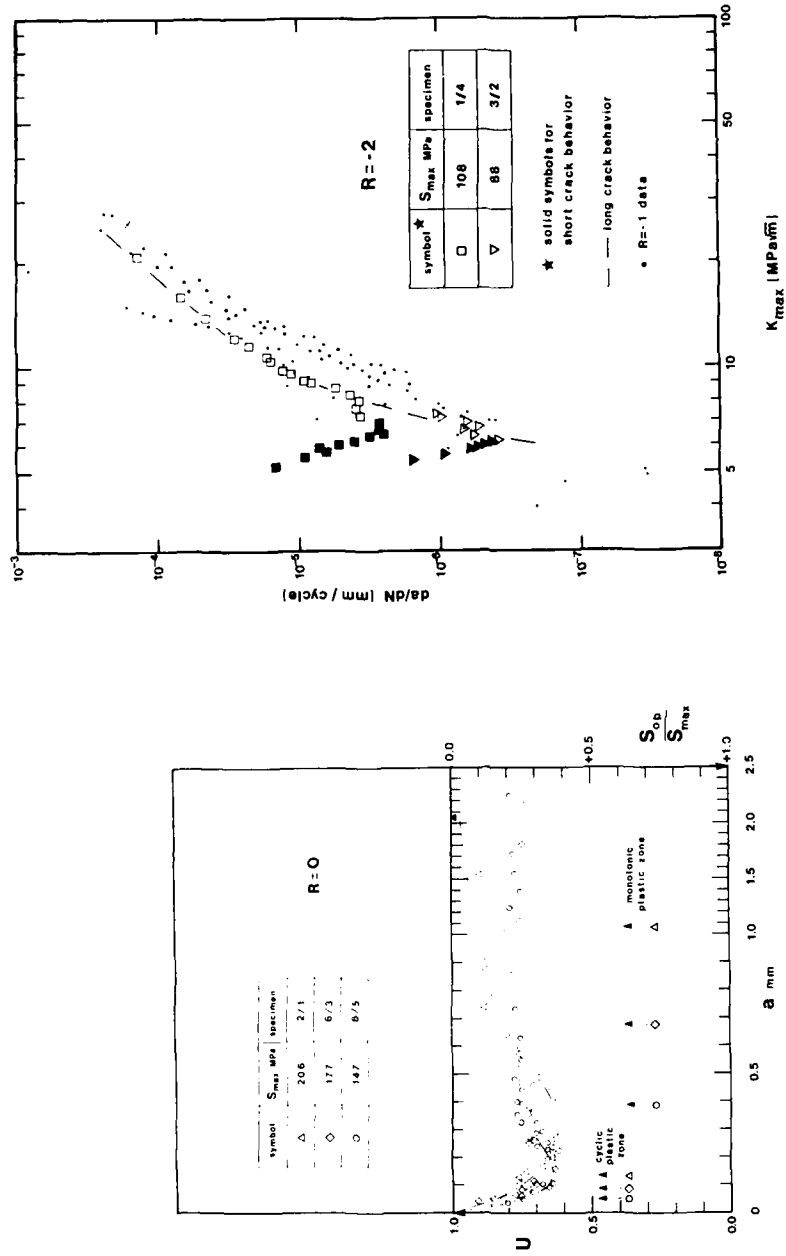


Figure 5 Crack opening level vs crack length at R=0. Figure 6 Crack growth rate vs K_{max} at R = -2.

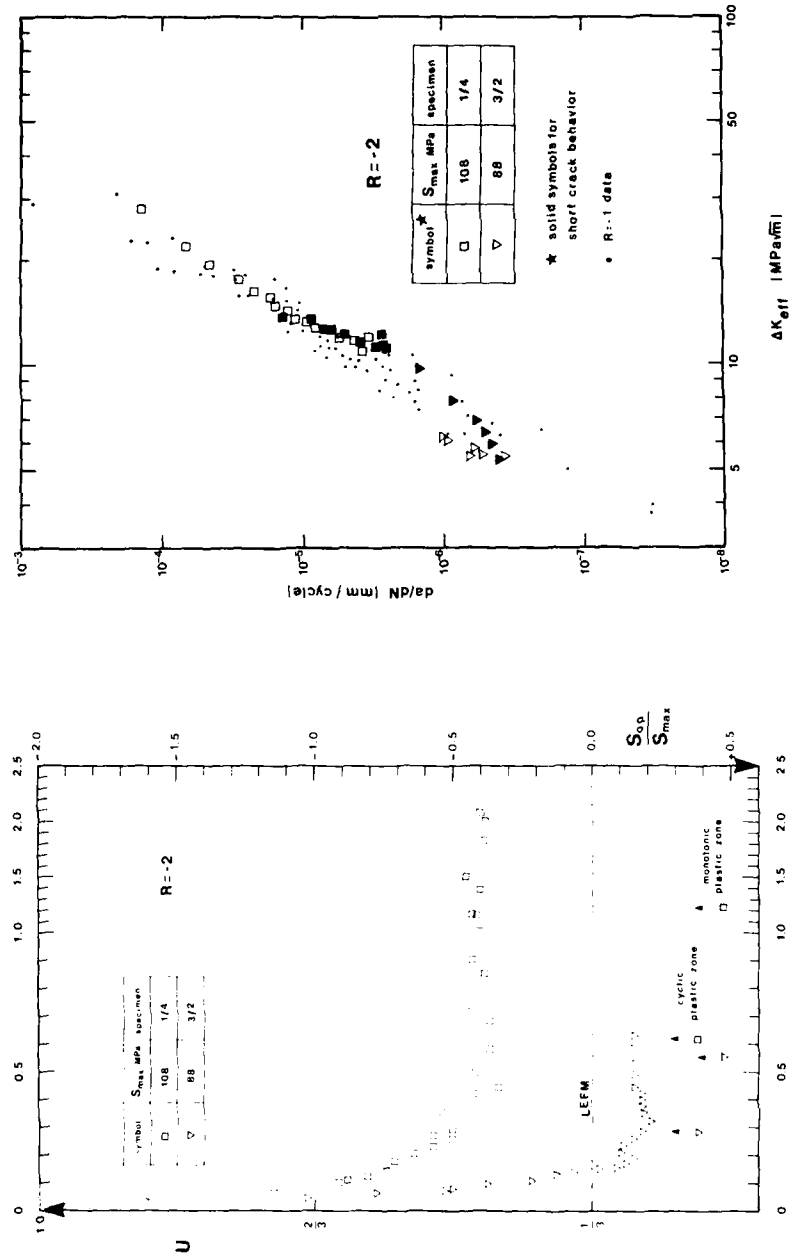


Figure 7 Crack opening level vs crack length at $R=-2$. Figure 8 Crack growth rate vs ΔK_{eff} at $R = -2$.

A UNIFIED MODEL FOR FATIGUE CRACK INITIATION, SHORT CRACK GROWTH, LONG CRACK PROPAGATION, AND CLOSURE EFFECTS.

A. O. Obabueki *, C. H. Lee*, T. Tanaka* and A. K. Miller*

A unified, physical-phenomenological model has been developed for predicting fatigue crack initiation and growth under uniaxial far-field loadings. In the model, Stage I fatigue crack advance (initiation and growth) is predicted using the range in crack tip non-elastic shearing displacement, whereas Stage II fatigue crack advance (initiation and growth) is calculated using the range in non-elastic crack tip opening displacement and the local peak tensile stress. The effects of "weak" surface grains, grain boundaries or relevant microstructural features, and redistribution of the local stresses during crack closure and re-opening have been incorporated into the model in order to represent the actual local mechanical conditions at the crack tip under various loading conditions.

INTRODUCTION

Prediction and prevention of fatigue failures have received major consideration in recent years especially in materials-limited aspects of energy technology such as fusion, solar-thermal, high-temperature gas-cooled reactors, and synthetic fuels production. In these applications there is a need for a method for the evaluation of new alloys, design optimization studies, demonstration that the systems meet safety and reliability criteria and the prediction of deformation and fracture of the major component materials. Two key needs are breadth and generality.

In conventional fatigue analysis, it is a common practice to separate the fatigue failure process into the two stages of crack "initiation" and "propagation". Crack initiation is commonly regarded as being more important in low strain (high cycle) fatigue while crack propagation is more dominant in high strain (low cycle) fatigue. Unfortunately, such a separation of fatigue failure into crack initiation and propagation has no basis in terms of the governing physical mechanisms (e.g. dislocation motion, diffusion, etc.) and is thus arbitrary. In addition, it can be quite cumbersome in predicting the response to complex loading histories. Also,

* Department of Materials Science and Engineering, Stanford University, Stanford, Ca 94305.

as NDT (non-destructive testing) methods improve and the ability to detect small flaws increases, this separation of fatigue crack initiation and growth will be more difficult to define and its arbitrariness more obvious. In addition, many studies have shown that neither "smooth specimen" methodologies (e.g. $S - N_f$ curves) nor fracture mechanics based methodologies (e.g. da/dn vs. ΔK curves) are conservative predictive tools in the short crack regime. Higher crack growth rates have been observed for "short" cracks compared to long cracks at the same stress intensity range, ΔK . Also, growth below the long crack threshold ΔK_{th} has been observed. Use of elastic-plastic fracture mechanics has not rectified these problems[1-3].

Extension of most current methodologies to include elevated temperature fracture is also problematic. Most methods directly calculate the number of cycles to failure for a given strain range, temperature, frequency, waveshape etc. This tends to limit their applicability to isothermal, constant amplitude cycling and the waveshapes and frequencies which were studied experimentally. There is thus a need for a fairly broad, general and physically based model for predicting fatigue crack initiation and propagation. Our approach in developing this model is to keep track of local damage, representing (in an approximate but physically - meaningful way) the more basic internal processes by which small "elements" of material fail locally under cyclic loading. We then numerically integrate these more fundamental local failure events into quantitative predictions of crack initiation, short crack growth, long crack propagation, crack closure and eventual total fracture. By representing the microscopically observed local failure mechanisms such as transgranular crack tip shearing (Stage I) and crack tip stretching/collapse (Stage II), a wide range of conditions can be treated by the model, which gives it breadth. At the same time, since we can numerically integrate the occurrence of these basic local failure mechanisms for any loading sequence, this kind of physically based model for fatigue can automatically predict failure under complex histories (cumulative damage). Extension of the model to include intergranular cavitation and multiaxial loadings can be accomplished, which thus gives the model the needed generality. In other words, by interpreting the existing data in terms of a quantitative representation of the internal processes which control the deformation and fracture behavior, the data are made applicable to a much wider range of conditions than only those which were tested.

The model has been used to predict the differences in the growth behavior of short and long cracks, using 304 stainless steel as an example. An overview of the model is given here. A more detailed treatment of the model is given elsewhere[4].

MODEL DEVELOPMENT

A. General Approach

The geometric idealization utilized in this model is a linear array of elements which lie parallel to the maximum principal stress axis. For a given cyclic load history, the stress and strain states of each element are followed. Based on these values, the rates of crack extension by Stage I and Stage II are computed. The operating mechanism is the one with the higher crack growth rate,

and the element at the crack tip is then said to fail under this mode. Alternatively, an element fails by rupture if its local tensile strain exceeds the critical rupture strain for that element. If the failed element is located ahead of a crack, its failure results in crack growth. On the other hand, crack initiation is predicted if the failed element is situated on the surface of the specimen.

Deformation in the model is predicted from a set of unified constitutive equations for non-elastic deformation capable of representing a wide range of phenomena such as primary and secondary creep, cyclic hardening to a stable cyclic stress-strain loop, conventional "plasticity" behavior, Baushinger effect and the interaction of these due to complex loading histories as well as other phenomena. The numerical scheme and the specific equations were developed by many investigators over the years [4,5]. The unified approach for predicting fatigue crack initiation and growth is summarized in figure 1.

B. Crack Advance Criteria

Crack initiation and propagation are treated in a unified manner in the model as there is no physical evidence to support the traditional approach of separating "initiation" and "propagation". The approach taken is that fatigue failure takes place one material "point" at a time and that all points are identical in their intrinsic resistance to fatigue failure. Differences between, for example, behavior within the first surface grain and behavior at the tip of a deep crack must arise from differences in the "local" boundary conditions at these points (e.g. triaxiality of the stress state or proximity to a grain boundary or free surface), not from differences in the intrinsic fracture properties. Failure of a material point is therefore described in terms of the local stress and local strain. The term "local" refers to the conditions at some position (r^*) ahead of the crack tip within the fracture process zone. Stage I fatigue, Stage II fatigue and ductile fracture are represented in the model. Intergranular failure has also been included but will not be discussed in this paper.

1. Stage I Fatigue Crack Advance. Experimentally, Kikukawa[6] has observed that the Stage I growth rate is directly related to the crack tip shearing displacement(ΔS). Specifically,

$$\Delta a = K_I \Delta S \quad (1)$$

where $K_I = 0.56$. This is essentially "geometric" Stage I crack growth and has been adopted for use in our model. Mathematically, we represent Stage I failure by the expression:

$$\frac{da}{dN} = \beta_1 \cdot h_2 \cdot h_1 \cdot (\Delta \epsilon^n)^1 \quad (2)$$

where the values h_1 and h_2 govern the conversion from axial non-elastic strain range ($\Delta \epsilon^n$) to shear displacement. The material constant β_1 in our expression is based on the value K_I in Kikukawa's observations.

2. Stage II Fatigue Crack Advance. A number of models have been presented to explain the mode of crack growth in the Stage II regime. These models can generally be classified into three types : crack growth based on limiting strength; crack growth by damage accumulation, e.g. Weertman's model for crack advance by accumulated plastic displacement or accumulated plastic work [7]; crack growth by a plastic sliding-off process at the crack tip, e.g. Laird and Smith[7] , Neumann[7], Tomkins and Biggs[8]. Clearly, models in the first set are inadequate. Changes in material constitutive relations with cycling occur in most metals and can result in either hardening or softening hence dependence of crack advance on a limiting strength is inappropriate. Although physical observation of crack tip processes agrees with the third type of model (the purely geometric type), their predicted two-power dependence of the growth rate on the stress intensity factor range (ΔK) has been a cause for concern as most real materials tend to have close to a four-power dependence. The models in the second set give a four-power dependence on ΔK ; however, accumulated plastic work density is not appropriate to correlate high temperature growth rate as a lower accumulated plastic work might be more damaging at a high temperature compared with a higher one at a lower temperature.

On re-interpreting the mechanisms for Stage II using the B-C-S model[8,9] for localized yielding, we arrived at

$$\frac{da}{dN} = \beta_{II} \sigma_{max}^2 (\Delta \epsilon^n)^1 a^* \quad (3)$$

Where β_{II} is a material constant, σ_{max} is the peak stress and a^* is an effective crack length($a + r^*$). At any time, crack extension is said to occur by Stage I or Stage II depending on whichever rate is greater. The implication of this approach is that a crack can initiate or propagate either by Stage I or Stage II depending on the prevailing conditions, in agreement with observations in the literature[10].

3. Ductile Fracture. The existence of a critical fracture strain at which instantaneous ductile fracture occurs is a common feature of most models for this process. Thomason[11] recently developed a three-dimensional model for ductile fracture by the growth and coalescence of microvoids. However effects such as strain hardening of the matrix and strain-rate sensitivity of the yield stress are not treated.

Earlier, McClintock[12] developed a simpler model using the same idea of growth and coalescence of microvoids which incorporates effects of strain-hardening. We have adopted McClintock's model for representation of ductile fracture with an added correction term (q_7) to get it to agree with the observed trend in the literature in the limit of high stress triaxiality. For any element, the fracture strain is given by

$$\epsilon_f = \frac{(1-n) \ln F_r}{\sinh \left[(1-n) (\sigma_x + \sigma_z) / (2\bar{\sigma}/\sqrt{3}) \right]} + q_7 \quad (4)$$

where n is the strain hardening exponent, $\bar{\sigma}$ is the equivalent stress and q_7 is a material constant.

C. Near-Surface Strain Concentration

It is now generally accepted that short fatigue cracks propagate differently from long cracks when the correlation is done using ordinary fracture mechanics parameters such as ΔK . Experimental results in the literature show that cracks whose plastic zone is smaller than the relevant microstructural feature (e.g. grain size) grow at rates which are faster than those of long cracks at the same ΔK . In addition, these high growth rates have been observed at stress intensities well below the threshold stress intensity range for long cracks. The growth rates have been observed to progressively decrease (and even arrest in some cases) as the crack approaches the first grain boundary. Many factors have been cited in the literature as being responsible for this anomalous behavior. One key factor is the fact that as a crack gets shorter and shorter, the stress at a small distance ahead of the crack tip increasingly gets larger than that predicted by fracture mechanics (figure 1, item #4). This loss of mechanical similitude is treated by our submodel for calculating the "continuum" stresses and strains ($\Delta \epsilon^{T,NOM}$) ahead of a crack of any length[4,5].

A second factor which is very important in the growth of short fatigue cracks is microstructural in origin. Concentration of the "continuum" strain into a peak local strain within persistent slip bands is represented in the model by the expression:

$$\Delta \epsilon^{T,CONC} = \Phi_1 \Delta \epsilon^{T,NOM} \quad (5)$$

where the function Φ_1 is influenced by the various factors that cause this breakdown in metallurgical similitude:

1. Free Surface Effect. A surface grain, being less constrained against slip than an "interior" grain, is weaker than the "interior" matrix. This weakness leads to the easy initiation of persistent slip bands (PSBs) in surface grains which causes concentration of plastic strain in the PSBs causing the peak local non-elastic strains (inside the persistent slip bands) to be higher than the average strain over the grain as a whole. This leads to high crack growth rates. To represent this effect we define the function Φ_1 in the form

$$\Phi_1 = \Phi_2 \left\{ 1 - \exp \left[-q_1 \left(\frac{d}{x + r^*} \right)^4 \right] \right\} + 1 \quad (6)$$

where x is the distance from the surface of the material, q_1 is a material constant

and d is the size of the relevant microstructural feature which is the grain size for most materials. This function is high initially (i.e. for small x) and gradually decreases to the value 1.0 after the crack tip is a few grains deep (if d is the grain size)(figure 1, item #5). The maximum value for Φ_1 depends on the function Φ_2 given by

$$\Phi_2 = q_2 - q_3 \Phi_3 \quad (7)$$

Where Φ_3 will be discussed below.

2. Microstructural Effect. The observed minimum or "well", in the growth rates for short cracks is generally observed at crack lengths equal to the size of the first grain. The decrease in growth rates has been attributed to the pinning of slip bands emanating from the plastic zone at the tip of the crack by the microstructural boundary, e.g. a grain boundary [1-3]. It is expected that the effect of the microstructural boundary should increase with the proximity of the crack tip to the boundary and should be a maximum at the boundary. A particular function which represents this effect is based on the normal distribution and is given by

$$\Phi_3 = \Phi_4 \exp \left\{ - \left[\frac{(x-d)}{d} \right]^2 \right\} \quad (8)$$

It therefore follows that in equation 8, the maximum influence of the grain boundary will occur when the crack tip plastic zone is at the grain boundary. Consequently, from equations 6,7, and 8, the minimum strain concentration will occur at a crack length approximately equal to the size of the relevant microstructural feature.

3. High Strain Effect. The concentration of nominal plastic strain in the available PSBs has been included in the free surface effect. However at large strains, a new structure develops and the grains are filled by PSBs. The blockage of slip by the grain boundary decreases as the entire specimen becomes filled with slip bands. This effect leads to the observation of shallower "wells" in the growth rate plots at higher applied stress values. We represent this effect through the function, Φ_4 given by:

$$\Phi_4 = 1 - \exp \left\{ - \left(\frac{q_4}{\Delta \epsilon^T} \right)^8 \right\} \quad (9)$$

The function, Φ_4 decreases from 1.0 to 0 as the nominal strain range, $\Delta \epsilon^T$ increases.

D. Crack Closure Effects.

The influence of closure on crack propagation is another factor that the literature cites in explaining the behavior of short cracks. The source of crack closure can be plasticity in the wake of the crack, roughness of the crack faces, or the presence of particles such as oxides in the crack [1]. Short cracks by definition possess a limited wake and are thus subjected to less closure. Hence at the same nominal ΔK , a short crack will experience a larger effective ΔK compared to a long, propagating crack. Also, short cracks can initiate and grow at a nominal ΔK which is less than the long crack threshold ΔK_{th} due to the absence (or near absence) of closure effects, but as the crack length increases, the build up of plasticity in the wake promotes a contribution from crack closure which leads to a reduction in crack growth rate (sometimes complete arrest). Closure effects are also thought to be responsible for load-interaction effects (retardation and acceleration) under variable amplitude loading.

To treat closure in the model, an explicit calculation is made of the amount of opening, V , of the opposing faces of fractured elements (see figure 2). The opening mV at each fractured element m depends on both an elastic term and a plastic term. Within the plastic term, the crack opening at element m is reduced as the residual plastic strain in that element (${}^m\epsilon^n$) increases. This represents plastic "wake" effects. V increases as the plastic strain in the element at the crack tip (${}^{N3}\epsilon^n$) increases representing crack face opening by plastic flow ahead of the crack. The specific equation utilized is

$${}^mV = q_5 (\sigma_y^m / E) \sqrt{a^2 - ({}^mx)^2} + q_6 ({}^{N3}\epsilon_y^n - {}^m\epsilon_y^n) \quad (10)$$

where the first term is the elastic contribution from the far-field load.

In the model, the parameter V equals zero until an element fractures. Thereafter as long as the element is open, changes in V (increases or decreases) are calculated from equation 10 above. When V decreases to zero, the element is closed, i.e. the crack is closed at that point along its face. Once an element is closed, it can support compressive stress and is governed by the same constitutive equations as when the element was intact. Compressive stress can increase or decrease in magnitude in response to the imposed loading history. When the stress in a closed element rises to zero, the element is assumed to open again (i.e. the crack opens at that location), the stress stays at zero and changes in the element's crack opening are again computed using equation 10 above. A schematic of this behavior is shown in figure 2.

RESULTS

Using material constants obtained from constant amplitude axial fatigue data ($S - N_f$ and $da/dN - \Delta K$ data) the model has been used to predict fracture behavior of type 304 stainless steel subjected to both constant and variable amplitude loading. Some of the results are shown in figures 3 - 5. Results for long crack growth

tests show a four-power dependence in the Stage II regime. For tests run under K-decreasing mode, the simulated threshold ΔK_{th} is 17.8 MPa \sqrt{m} and the crack opening load ($P_{opening}$) reaches the maximum load (P_{max}) when $\Delta K = \Delta K_{th}$. These observations are in good agreement with experimental results in the literature. Further, the model predicts a substantially lower ΔK_{th} for tests run under constant stress amplitude starting with a flaw which has no plastic "wake" (figure 3). This important point is often neglected by designers who base analyses on results in the literature that were obtained using K-decreasing tests.

Figure 4 shows that small flaws are predicted to grow below ΔK_{th} with rates which decrease as the crack approaches the first grain boundary. At lower applied stress levels, cracks arrest while at higher applied stresses they do not, and on passing the grain boundary propagate at increasing da/dN until merging with the long crack results. Shallower "wells" are also predicted for higher applied stress levels in agreement with trends in the literature. The internal workings of the model which underlie these predicted external behaviors are summarized in figure 5.

CONCLUSIONS

A unified model has been developed for predicting fatigue crack initiation and growth under uniaxial far-field loadings. The model can predict the observed anomalous behavior of short cracks. This behavior has been modeled numerically in terms of:

- 1) absence of crack closure in short cracks due to absence of a well-developed plastic wake,
- 2) "weakness" of surface grains due to lack of constraint by surrounding grains,
- 3) effect of grain boundaries in inhibiting plastic flow concentration,
- 4) the fact that as a crack gets shorter and shorter, the stress at a small distance ahead of the crack tip increasingly gets larger than that predicted by fracture mechanics.

The same crack closure ingredient in the model causes it to predict that the ΔK_{th} for "new" cracks (without a plastic "wake") is substantially less than that for long cracks for tests run under the K-decreasing mode.

ACKNOWLEDGMENTS

Financial support of this research by the office of Basic Energy Sciences of the U.S. Department of Energy under grant #DE-FG03-84ER45119 is gratefully acknowledged.

REFERENCES

- (1) Ritchie, R.O. and Suresh, S., "Mechanics and Physics of the Growth of Small Cracks," Proc. 55th of AGARD Struc. and Mat'ls panel, Toronto, Canada, Sept. 1982.
- (2) Lankford, J., "The Influence of Microstructure in the Growth of Small Fatigue Cracks," Fat. Fract. Eng. Matls. and Struc., Vol. 8, No. 2, 1985, pp. 161-175.
- (3) Leis, B.N., Kanninen, M.F., Hopper, A.T., Ahmad, J., Broek, D., "Critical Review of the Fatigue Growth fo Short Cracks," Eng. Frac. Mech., Vol. 23, No. 5, 1986, pp. 883-898.
- (4) Obabueki, A.O., "A New Unified Phenomenological Model for Fatigue Crack Initiation, Short Crack Propagation, Long Crack Propagation and Closure Effect," Ph. D dissertation, Stanford University, Department of Materials Science and Engineering, in progress.
- (5) Lee, C. H., "A Unified Method for Predicting the Stress and Strain Distributions around cracks of any length," Ph. D dissertation, Stanford University, in progress.
- (6) Kikukawa, M., Jono, M., and Adachi, M., "Direct observation and Mechanism of Fatigue Crack Propagation," Fatigue Mechanisms, ASTM STP 675, 1979, pp. 234 -253.
- (7) Weertman, J., "Fatigue Crack Propagation Theories," Fatigue and Microstructure, ASM, 1978, pp. 279 - 306.
- (8) Tomkins, B., "The Development of Fatigue Crack Propagation Models for Engineering Applications at Elevated Temperatures," J. Eng. Matls. and Tech., Oct. 1975, pp. 289 - 297.
- (9) Bilby, B. A., and Swinden, K. H., "Representation of plasticity by linear dislocation arrays," Proc. Roy. Soc. A, Vol. 285, 1965, pp. 22-23.
- (10) Wells, C.H., Sullivan, C.P., and Gell, M., "Mechanisms of Fatigue in the Creep Range," Metal Fatigue Damage-Mechanism, Detection, Avoidance, and Repair, ASTM STP 495, 1971, pp. 61-122.
- (11) Thomason, P.F., "A Three - Dimensional Model for Ductile Fracture by the Growth and Coalescence of Microvoids," Acta Metall. Vol. 33, No 6, 1985, pp. 1087 - 1095.
- (12) McClintock, F.A., "A Criterion for Ductile Fracture by the growth of Holes," J. App. Mech., June 1968, pp. 363 - 371.

SUMMARY OF INGREDIENTS IN THE MODEL

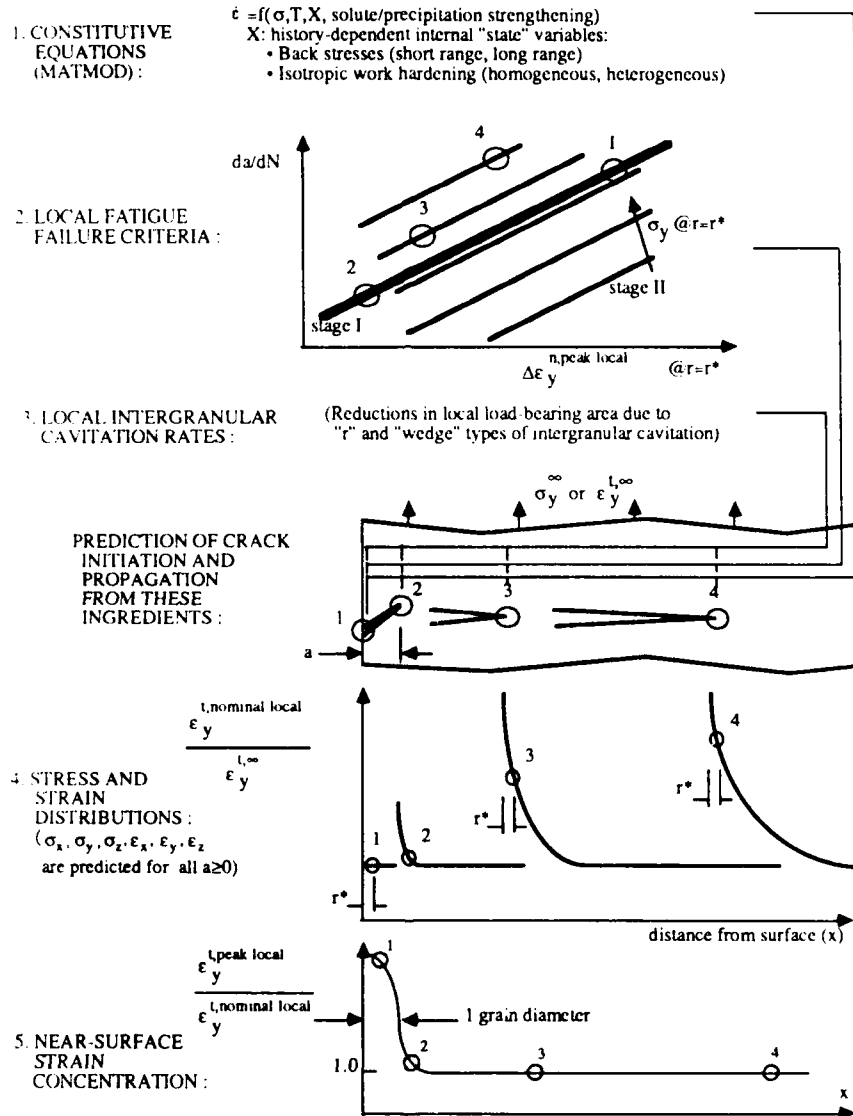


Figure 1. Summary of ingredients in the model.

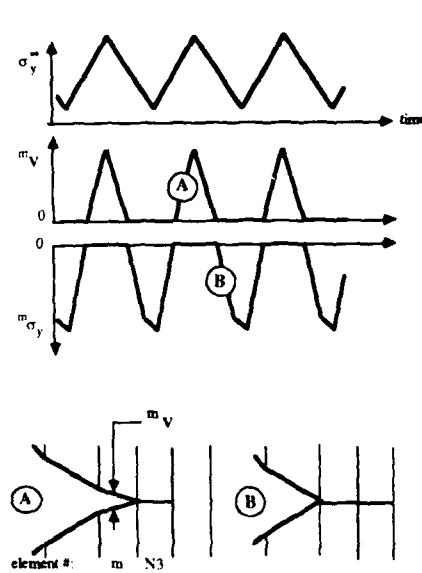


Figure 2. Schematic of the closure scheme.

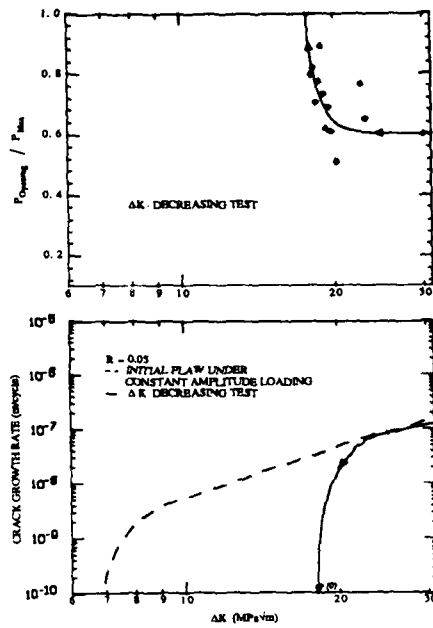


Figure 3. Long crack threshold simulations.

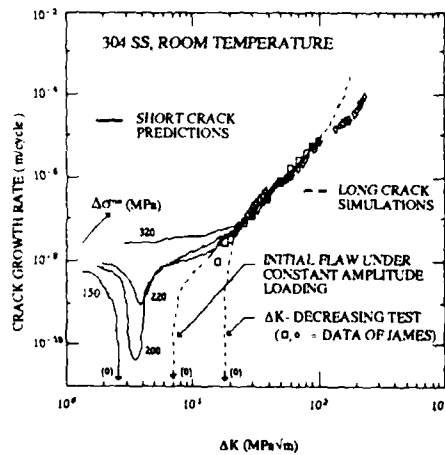


Figure 4. Short and long crack growth rates.

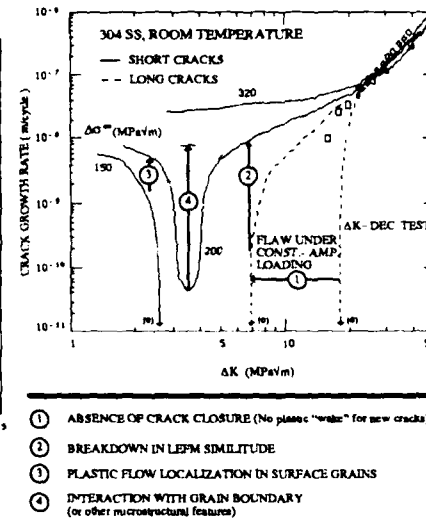


Figure 5. Reasons for the predicted growth rates.

FATIGUE 87

FATIGUE 87

**VARIABLE AMPLITUDE
LOADING**

FATIGUE 87

FATIGUE CRACK RETARDATION IN ALUMINIUM ALLOYS

D.J. Alexander* and J.F. Knott*

Fatigue crack retardation due to single tensile over-loads has been studied in aluminium alloys 7010-T7651 and 8090-T851, for $\Delta K = 7 \text{ MPa}\sqrt{\text{m}}$, $R = 0.1$ and 0.5 , and specimen thicknesses of 6.35 , 13 and 35 mm . Retardation lasts for many more cycles and extends over a greater distance in the 8090 alloy, for similar test conditions. Crack closure cannot explain retardation in the 7010 alloy. Retardation is apparently due to residual stress effects and crack deflection. In the 8090 alloy at $R = 0.1$, closure is a significant factor in the retardation, but not at $R = 0.5$. Crack deflection appears to be the primary mechanism of retardation in this case.

INTRODUCTION

It is commonly observed that the occurrence of a single overload or multiple overloads during fatigue crack propagation produces a reduction in the subsequent growth rate. Fatigue crack retardation has been observed in a variety of materials, and depends on mechanical factors, such as the range of cyclic loading prior to overload (ΔK), the load ratio ($R = K_{\min}/K_{\max}$), the magnitude of the overload (K_{OL}), the number of overloads applied and the stress state at the crack tip^(1,2,3). In addition, there are several metallurgical factors which are believed to be related to the delay, such as yield strength and the cyclic stress-strain properties⁽⁴⁾. A more complete understanding of the reasons for fatigue crack retardation would permit better models to be developed, which would in turn allow more accurate predictions of crack growth and component lifetimes under variable amplitude loading conditions such as those found in service.

Several theories have been proposed to explain fatigue crack retardation. There are three primary candidates: i) residual stresses⁽⁵⁾ ahead of the crack, created as the elastic bulk of the specimen forces the monotonic overload plastic zone into reverse

* University of Cambridge, Department of Materials Science and Metallurgy, Pembroke Street, Cambridge, England, CB2 3QZ

FATIGUE 87

compression as the sample is unloaded from the maximum load; ii) increased closure⁽⁶⁾ behind the crack tip, which arises after the crack propagates into the highly strained monotonic overload plastic zone, which will have increased residual displacements due to the overload, giving rise to increased closure and a reduced effective ΔK ; iii) crack tip deflection⁽⁷⁾, when the overload causes the crack to deviate, and the effective driving force for crack growth at the tip of the deflected crack is thus reduced, slowing the crack growth and prolonging the retardation. There is considerable controversy in the literature as to which of these mechanisms controls crack retardation. Differences in test technique and materials may account for some of the different results found.

EXPERIMENTAL PROCEDURE

The present research was designed to study fatigue crack retardation in aluminium-lithium alloys, a new generation of alloys which have a higher stiffness and lower density than conventional aluminium alloys. In addition, it was hoped to determine which mechanisms controlled retardation in these alloys.

Two aluminium alloys, provided by Alcan Ltd, and tested in the as-received condition, were selected. The first, 7010-T7651 is a typical high-strength Al-Zn-Mg-Cu alloy, while the second, 8090-T851, is an Al-Li-Cu-Mg alloy with promise for aeronautical applications. The 7010 alloy was supplied in 35 mm plate, and the 8090 in 44 mm plate. The compositions of the alloys are given in Table 1. The mechanical properties of the alloys were measured with Hounsfield No.12 specimens, at an initial strain rate of 10^{-3} s^{-1} .

TABLE 1 - Alloy Composition (wt %)

	Li	Zn	Mg	Cu	Zr	Fe	Si
7010	—	6.1	2.2	1.81	0.13	0.13	0.03
8090	2.43	—	0.74	1.17	0.12	0.09	0.09

Single tensile overloads were used to generate retardation. In order to achieve reasonable baseline crack growth rates, but minimise static fracture modes during the overloads, a ΔK value of 7 MPa $\sqrt{\text{m}}$ was selected for the baseline loading, with 100% overloads ($K_{\text{max}} - K_{\text{min}} = 7$, $K_{\text{OL}} - K_{\text{min}} = 14$). R values of 0.1 and 0.5 were chosen, to obtain high and low closure levels, respectively. Notched bend bars (W=25 mm) were tested in four point loading. Crack length was monitored by a d.c. electric potential method ().

FATIGUE 87

Probes were spot welded to either side of the notch mouth and were then reinforced with epoxy. Constant ΔK conditions, which eliminated possible effects of a varying plastic zone size, were obtained by manually shedding the load at increments of a/W of .0025, that is, a change in crack length of .0625 mm. Specimens 6.35, 13 or 35 mm thick were machined from the plates. For the 35 mm thick 7010 plate, the 13 mm specimens were taken from either side of the centre of the plate, while the 6.35 mm specimens were taken from several locations through the thickness. For the 44 mm 8090 plate, the 35 and 13 mm specimens were taken from the plate centre, and the 6.35 mm specimens were taken from several positions through the thickness.

In order to determine the role of closure, the opening load for the crack was determined using the back-face-strain technique. A single Cu-Ni foil strain gauge 6 mm long by 1 mm wide with an epoxy backing was glued to the back face of the bar opposite the notch, using cyanoacrylate adhesive. A third-order low-pass filter of cut-off frequency 1.0 Hz was used to reduce noise on both the load and strain signal, the latter of which was fed through a 1000 x strain-gauge amplifier. The load versus strain output was recorded at 0.03 Hz by interrupting the test and reducing the frequency of the test machine (10 Hz for $R = 0.5$, 30 Hz for $R = 0.1$). The initial deviation from linearity of the load-strain signal during unloading was taken as the closure load. The overloads were applied by manually raising the load to the desired level, decreasing to the minimum load, and then returning to the same mean load as that prior to the overload. Cycling was resumed at 0.03 Hz with the load-strain signal recorded initially for several cycles immediately after the overload, and then less frequently, with the previous test frequency being restored between measurements where suitable. These changes in frequency were not expected to affect the crack growth. After the tests, the fracture surfaces were examined in a Camscan scanning electron microscope operating at 30 kV.

RESULTS

The tensile properties of the two materials are given in Table 2. The ductility, as measured by elongation to fracture, was lower for the 8090 alloy, but typical for these alloys.

Both alloys showed a pancake structure typical of rolled aluminium plate, with large grains in the plane of the plate, and much thinner through-thickness dimensions.

Both materials exhibit crack retardation after the overloads. Typical examples of the response to overload of the two alloys in different thicknesses of test piece are given in Figures 1 and 2, and summarised in Table 3. The 7010 alloy shows relatively little change in the number of cycles of delay as thickness is

FATIGUE 87

TABLE 2 - Mechanical Properties

Alloy	Orientation	Yield Strength (MPa)	Tensile Strength (MPa)	Elongation (% 16mm)
7010-T7651	L	468	517	13.1
	T	463	510	13.5
8090-T851	L	408	461	5.4
	T	408	467	4.1

altered. With the increase in R from 0.1 to 0.5 the delay is reduced by a factor of 2 to 3. The delay period for the 8090 alloy is about 40 times longer, and is reduced by a factor of 3 with increase in R. As thickness increases from 6.35 to 13 to 35 mm the delay decreases substantially and then returns to a similar high level.

TABLE 3 - Average Number of Kilocycles of Delay

Alloy	R	6.35 mm	13 mm	35 mm
7010	0.1	10.9	9.5	9.5
	0.5	3.8	4.6	3.1
8090	0.1	420	285	435
	0.5	127	40	120

Figures 1 and 2 include the values of K_{op} as determined from the measured opening loads. The 7010 alloy, for $R = 0.1$, has some closure present before the overload ($U = \Delta K_{eff} / \Delta K = 0.85$). After the overload, K_{op} is reduced below its original value, to which it eventually returns as the crack growth rate stabilises (Figure 1). At $R = 0.5$, no closure is observed before or after the overload.

Much more closure is present in the 8090 alloy before the overload, for $R = 0.1$ ($U = 0.40$). Immediately after the overload, K_{op} is lower, but then quickly increases to values well above the pre-overload conditions (figure 2). The load-strain curves have two linear sections, with an upper and lower K_{op} . The upper level is at roughly 6.5 MPa/m, while the lower K_{op} is near 5.5 MPa/m, similar to the baseline conditions. As the retardation period ends, the upper K_{op} decreases towards the lower K_{op} , and returns to the baseline value. For $R = 0.5$, K_{op} decreases after the overload,

and remains below the baseline conditions. In many cases, no closure is observed after the overload.

The fractography shows a number of differences between the two alloys (Figures 3, 4 and 5). Prior to the overload, the 7010 alloy shows a series of ridges, parallel to the direction of crack growth, reflecting the aligned microstructure beneath. The overload location is readily revealed by a line across the fracture surface, marking the crack tip at overload. Immediately after this line, particularly for $R = 0.1$, the surface is often relatively featureless in some areas, appearing quite dark on the SEM fractographs (Figure 3). There is a higher incidence of flat faceted regions after the overload for both R ratios. At $R = 0.5$, the line of the crack front at the overload is very clear, with fewer featureless regions (Figure 4). Occasionally evidence of static fracture modes, such as dimples around inclusion clusters, can be found, despite the relatively low overloads used.

The 8090 alloy has a much more rugged fracture surface, which is reflected in the higher closure loads. Once again, the surface features reflect the aligned microstructure beneath them. Also, the line of the crack at the overload is again marked by a dark relatively featureless band. There are also facets on the surface, and the incidence of these increases after the overload. Secondary cracks along the grain boundaries perpendicular to the surface can be seen after the overload. Stereo pairs clearly reveal the rugged, faceted nature of the surface after the overload (Figure 5). These facets persist over quite a long distance, until the surface gradually returns to its pre-overload character.

DISCUSSION

Crack closure is frequently cited as one of the reasons for retardation after overloads, but there is considerable controversy in the literature as to whether or not this is the dominant factor. Several investigations have shown that K_{op} increases after an overload, and the reduction in ΔK_{eff} explains retardation (9-13). However, there are also many reports in which no such agreement is found (14-17). It is intriguing to note that work by Fleck et al. shows that closure can account for retardation due to single overloads at low R values ($R = .05$) (11-13) but cannot explain retardation due to periodic overloads observed at high R levels ($R = 0.5$) in the same material (18). Much of the confusion and controversy appears to arise from the wide variety of techniques employed, and the different sensitivities of these techniques. When the possible effects of different specimen geometries and different materials are added, it is perhaps not surprising that the role of closure is ambiguous.

The present results show that the effect of the overload on closure is quite different for the two alloys, and that the behaviour is

FATIGUE 87

different at the two R values. For the 7010 alloy, at $R = 0.1$, K_{op} is actually slightly lower after the overload (Figure 1), but the growth-rate, da/dN , is greatly reduced, despite the fact that ΔK_{eff} is fact larger. At $R = 0.5$, no closure is present before or after the overload, yet retardation is still present. Clearly, closure cannot explain the reduced growth rates observed for the 7010 alloy.

The 8090 alloy shows a large increase in K_{op} after the overload for $R = 0.1$ (Figure 2). The value of ΔK_{eff} is reduced from about 2.5 to 1.5 MPa/m which results in a significant decrease in da/dN values. At $R = 0.5$, K_{op} decreases, so that ΔK_{eff} increases, yet da/dN is still reduced. Closure has a significant role at $R = 0.1$, therefore, but no effect at $R = 0.5$.

The two, separate closure loads observed at $R = 0.1$ are similar to these reported by Hermann and Paris (9) and Schijve (19). It is believed that a "hump" of material is created by the overload, which gives rise to the upper K_{op} . The lower K_{op} is due to subsequent crack contact well behind the "hump" created by the overload. Eventually, when the crack has grown well past the overload location and its "hump" of material, conditions similar to those prior to the overload are restored, and the upper and lower K_{op} values approach each other, as is observed here.

A crucial issue is the question of the sensitivity of the closure measurements. Several steps were taken to ensure accuracy in the experimental values, and that sufficient sensitivity was obtained to observe slight but possibly significant changes in closure. The load and strain signals were effectively filtered to reduce noise. The recordings were made at low frequencies to allow optimum performance of the X-Y plotter, and to ensure that the filter used did not affect the results. The load-strain results were carefully examined to observe the initial deviations. Trials using a subtraction circuit to amplify the non-linear part of the load-strain trace were conducted; however, it was decided that such measures were unnecessary if sufficient care was taken in obtaining and examining the original load-strain curves.

Another possible reason for retardation is the residual stress distribution. The large monotonic plastic zone created by the overload will result in significant compressive stresses at the crack tip as the load is reduced from its maximum. Table 4 shows the length of the zone of affected crack growth; that is, the distance from the point of overload until steady state crack growth resumes. This distance is compared to the length of the overload monotonic plastic zone, given by

$$MPZ = 0.16 \left(\frac{K_{OL}}{\sigma_y} \right)^2 \quad (1)$$

FATIGUE 87

except for the 6.35 mm specimen at R = 0.5, for which a plane stress estimate of the plastic zone is used i.e.

$$MPZ = \frac{\pi}{8} \left(\frac{K_{OL}}{\sigma_y} \right)^2 \quad (2)$$

TABLE 4 - Comparison Between Length of Affected Growth Zone (L) and Overload Monotonic Plastic Zone (MPZ)

Alloy	R	K _{max} (MPa√m)	σ _y (MPa)	MPZ (μm)	Thickness (mm)	L(avg.) (μm)	L MPZ
7010	0.1	14.78	465	162	6.35	330	2.04
					13	200	1.23
					35	250	1.54
	0.5	21.0	465	326	6.35	175	0.54
					13	212	0.65
					35	106	0.33
8090	0.1	14.78	408	210	6.35	450	2.14
					13	360	1.71
					35	625	2.98
		21.0	408	424	6.35	800	0.77*
					13	325	0.77
					35	700	1.65

* Use plane stress value MPZ = 1040 μm

These estimates of the plastic zone size can be considered as upper limits for the possible extent of residual stress effects. Table 4 shows that the affected growth zone is similar in size to these estimates for both alloys at R = 0.5, but, for R = 0.1, the affected growth zone is much larger. Therefore, for these alloys, residual stress seems to be an important factor, at least for R = 0.5, but is probably of less importance for the R = 0.1 alloy.

The final mechanism which has been suggested to explain retardation is crack branching. Analysis of the stresses and strains at the tip of a branched or deflected crack reveals that the effective stress intensity is substantially reduced compared with that observed for a straight crack, (7) although it is difficult to estimate how significant this effect may be. After the overload, the crack may deflect in several ways, and the effect of these combined deflections is difficult to assess. The size of the crack tip plastic zone may be an appreciable fraction of the deflection, in which case the use of elastic analyses is clearly inappropriate. Recent calculations have shown, however, that plasticity further enhances the reduction of the local effective stress intensity,

FATIGUE 87

(20) which provides further evidence that deflection may indeed be a potent mechanism for retardation.

The fractography for the 7010 alloy indicates that there is relatively little difference between the fracture surfaces before and after the overloads. There is a slight increase in the number of flat faceted regions, although the increase is not dramatic. Thus, it seems unlikely that crack deflection is playing a major role in reducing the growth rates in the 7010 alloy. However, the 8090 alloy has a much more noticeable change in appearance after the overload. The fracture surface consists of many facets. Stereo pairs clearly indicate that this faceted region is much rougher than the fracture surface prior to overload (Figure 5). Furthermore, the faceted area persists for a large distance, comparable to the length of affected crack growth. For example, in Figure 5 the faceted region extends some 700 μm , which is much greater than the plastic zone size, and agrees quite well with the length of affected crack growth, Table 4 (8090, $R = 0.5$, 35 mm). Therefore, it appears that crack deflection and the resultant reduction of the effective stress intensity for crack growth, is a major contributor to the observed retardation.

The question remains as to what causes the crack growth mechanism to change to produce the faceted fracture observed, and why this mode of fracture persists for such large distances. Initially deflection may be due to crack propagation along one branch of the intensely strained overload plastic zone, as observed in several previous studies (see (9) for a recent review). However, the fractography does not reflect such a pattern; instead the crack advances in many different directions after the overload. Nor can such a mechanism account for the length of the faceted region, which is much greater than the plastic zone size. As yet these questions are unanswered.

There are several other interesting features of the present work, concerning the effects of specimen thickness and R ratio. The 7010 alloy is relatively insensitive to changes in specimen thickness. The 8090 alloy however, shows minimum retardation for the 13 mm specimen, which is an unusual feature. The effect of the R ratio is similar for both alloys. In all cases, increasing R for the AK prior to and following the overload from 0.1 to 0.5 substantially reduced the amount of retardation by a factor of roughly 3. This occurs despite an increase in the length of affected crack growth after overload. The one exception is again the 13 mm 8090 result. These tests are being repeated to ensure that the effect is genuine.

CONCLUSIONS

1. Fatigue crack retardation occurs in both 7010-T7651 and 8090-T851 following single tensile overloads of 100%, for $\Delta K = 7$, at $R = 0.1$ or 0.5 . Retardation in the 8090 alloy persists for many more cycles and over much longer distances than in the 7010 alloy.
2. Increasing R from 0.1 to 0.5 reduces the retardation by about a factor of three. There is little effect of changes in specimen thickness from 6.35 up to 35 mm, with the possible exception of the 8090 alloy at 13 mm.
3. In the 7010 alloy, closure cannot explain retardation. At $R = 0.1$, ΔK_{eff} is actually larger during the retardation period, and at $R = 0.5$, no closure is observed, yet retardation still occurs. Residual stresses and crack deflection may account for the retardation.
4. In the 8090 alloy, closure plays a significant role in the retardation at $R = 0.1$. There is an increase in K_{op} and a large decrease in ΔK_{eff} . However, at $R = 0.5$, ΔK_{op} is increased. In this case, crack deflection rather than closure appears to be the dominant mechanism for retardation.

ACKNOWLEDGEMENTS

We would like to thank Alcan International Ltd for their generous donation of the alloys used in this study. This work was sponsored by the Natural Sciences and Engineering Research Council of Canada through the grant of a Postdoctoral Fellowship (DJA). Thanks are also due to Prof D Hull for provision of research facilities.

REFERENCES

1. Wei, R.P. and Shih, T.T., Int. J. Frac., Vol.10, 1974, p.77.
2. von Ew, E.F.J., Hertzberg, R.W. and Roberts, R., "Stress Analysis and Growth of Cracks", ASTM STP 513, ASTM, Philadelphia, PA, 1972, p.230.
3. Bernard, P.J., Lindley, T.C. and Richards, C.E., Metal Sci., Vol.11, 1977, p.390.
4. Knott, J.F. and Pickard, A.C., Metal Sci., Vol.11, 1972, p.399.
5. Wheeler, O.E., Trans. ASME, J. Basic Eng., Vol.94, 1972, p.181.
6. Elber, W., "Damage Tolerance in Aircraft Structures", ASTM STP 486, ASTM, Philadelphia, PA, 1971, p.230.

FATIGUE 87

7. Suresh, S., Eng. Frac. Mech., Vol.18. 1983, p.577.
8. Ritchie, R.O., Garrett, G.G. and Knott, J.F., Int. J. Frac. Mech., Vol.7 1971, p.462.
9. Paris, P.C. and Hermann, L., "Fatigue Thresholds", J. Blacklund, ed., EMAS Ltd, Warley, U.K. Vol.2, p.11.
10. Tanaka, K., Matsuoka, S., Schmidt, V. and Kuna, M., "Advances in Fracture Research", ICF 5, D. Francois, ed., Pergamon Press, New York, Vol.4, 1982, p.1789.
11. Fleck, N.A., Smith, I.F.C. and Smith, R.A., Fat. Eng. Mat. Struct., Vol.6, 1983, p.225.
12. Tokaji, K., Ando, Z., Imai, T. and Kojima, T., Trans. ASME, J. Eng. Mat. Tech., Vol.105, 1983, p.88.
13. Fleck, N.A., "Fundamental Questions and Critical Experiments on Fatigue", ASTM, Philadelphia, PA, to be published.
14. Chanani, G.R. and Mays, B.J., Eng. Frac. Mech. Vol.9, 1977, p.65.
15. Gan, D. and Weertman, J., Eng. Frac. Mech., Vol.15, 1981, p.87.
16. de Castro, J.T.P. and Parks, D.M., Scripta Metall., Vol.16, 1982, p.1443.
17. Robin, C., Louah, M. and Pluvinaige, G., Fat. Eng. Mat. Struct., Vol.6, 1983, p.1.
18. Fleck, N.A., Acta Metall., Vol.33, 1985, p.1339.
19. Schijve, J., "Fracture Mechanics", ASTM STP 700, ASTM, Philadelphia, PA, 1980, p.3.
20. Suresh, S., and Shih, C.F., Int. J. Frac., Vol.30, 1986, p.237.

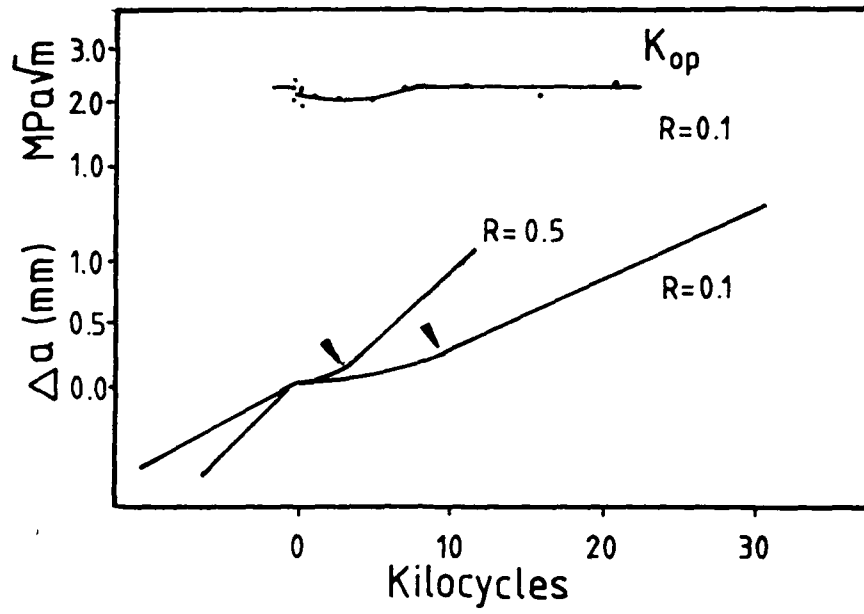


Figure 1. Crack growth after overload for 7010, 35 mm.

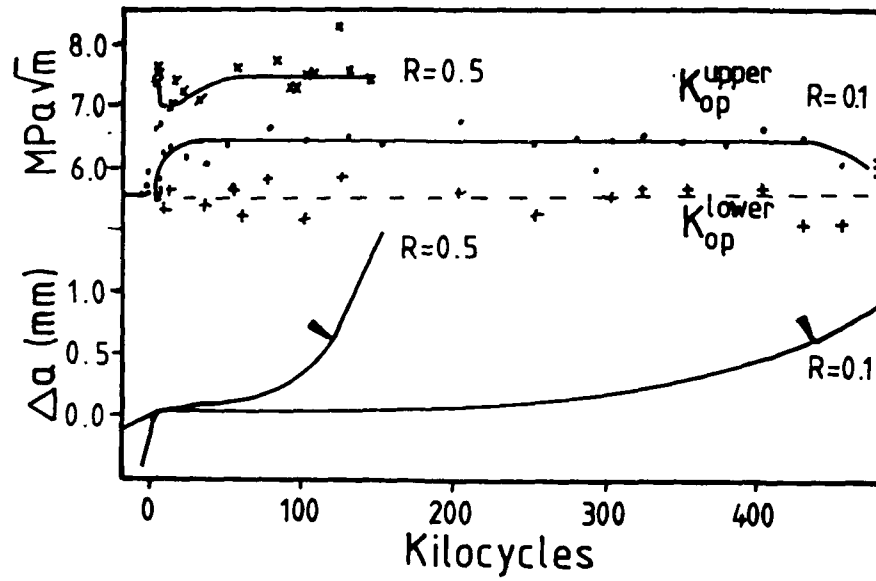


Figure 2. Crack growth after overload for 8090, 35 mm.



Figure 3. Overload location,
7010, 13 mm, $R = 0.1$.



Figure 4. Overload location,
7010, 13 mm, $R = 0.5$.



Figure 5. Stereo pair of overload location, 8090, 35 mm, $R = 0.5$.

FATIGUE 87

FATIGUE CRACK GROWTH UNDER RANDOM OVERLOADS

R. Arone*

Retardation effects associated with random overload peaks are considered. A Poisson flow of overloads superimposed on a base-line constant amplitude cyclic load is assumed. Under the above assumptions the total retardation time is presented as a stochastic process governed by the intensity of overloads. Expressions estimating reliability level for a given life-time are derived.

INTRODUCTION

Prediction of fatigue crack growth under spectrum loading is complicated by loading interaction effects. Life predictions involve time-consuming numerical procedures and their results varies widely. The reliability of the above predictions might be questionable when based on single realisations. With regard to retardation effects, when the loading history is of a relatively simple stochastic nature, fatigue crack growth may be described as a stochastic process governed by the loading history.

As is known sharp overloads in the spectrum loading mostly cause retardation of crack growth. While such overloads are generally rare their influence could be significant. This permit to describe many loading histories as a superposition of base-line cyclic loading and random peaks of overload. If overload retards crack propagation the delay time associated with this specific overload is determined as a difference between the time required

* The Israel Institute of Metals, Technion Research & Development Foundation, Haifa, Israel.

FATIGUE 87

for crack to transverse the zone affected by overload and the time required for the crack to transverse the same distance in the absence of overload. Total delay time up to observation moment is the sum of individual delay times. In what follows a Poisson flow of overloads is assumed which permits description of total delay time as stochastic process. Determining effective time as a difference between elapsed time and total delay time the stochastic description of the latter is obtained. Within the above formalization effective time is the time of undisturbed crack growth associated with base-line cyclic loading.

BASIC APPROACH

Consider a constant amplitude cyclic loading with superimposed rare random overloads characterized by random interoverload times τ_i . The term "rare" signified that probability of occurrence of an overload in the time interval Δt (base-line single cycle time) is low and can be given as

$$p = \lambda \Delta t; \quad \Delta t \ll \tau_j \quad (1)$$

The probability of two or more overloads over the interval is smaller by one order. It is also assumed that the probability of k overloads is history-independent and that the flow of overloads is stationary.

Under the above assumptions the number of overloads n is described by a Poisson process characterized by an exponential distribution of the interoverload times with parameter λ . In addition, it is also assumed that the probability of occurrence of one or more overloads within the delay time of one of them is negligibly small.

The magnitude of the overload stress σ_o is also considered as a random value. The sequence of overloads $\sigma_{o1}, \sigma_{o2}, \dots, \sigma_{oi}, \dots, \sigma_{on}$ is considered as a set of realizations of identically distributed mutually independent random variables with probability density function $f(\sigma)$. It is also assumed that:

(1) Crack growth under base-line constant amplitude cyclic loading is described by the power law

$$\frac{dk}{dt} = C(\Delta k)^m \quad (2)$$

where $\Delta k = A \Delta \sigma \sqrt{a}$ is the stress intensity factor range, $\Delta \sigma$ - the cyclic stress range, a - crack length, t - time (which can be measured in numbers of cycles) and A , C and m - are constants for a given material, a given component geometry and given parameters of the base-line cyclic loading.

(2) Crack growth after overload within the overload-affected zone is given by the following expression.

$$\left(\frac{da}{dt}\right)_R = C_R \frac{da}{dt} = C(\Delta k_{eff})^m \quad (3)$$

(3) For a given material, given component geometry and given parameters of the base-line constant amplitude cyclic load, the retardation factor C_R is function of the overload ratio R_0 and crack length ratio γ :

$$\begin{aligned} C_R &= C_R(R, \gamma); \quad 0 < C_R < 1 \\ R_0 &= \sigma_0/\sigma > 1; \quad 1 < \gamma = a/a_0 < \gamma_{max} = a_f/a_0 \\ a_0 &< a < a_f \quad a_f = a_0 + d_0 \end{aligned} \quad (4)$$

where σ_0 - is the overload peak stress, σ - the maximum stress of base-line cyclic load, a_0 - crack length at overload and d_0 - the overload-affected zone.

(4) The time interval during which crack growth is affected by overload is given in accordance with equation (3), by the following expression:

$$\begin{aligned} t_a &= \int_{a_0}^{a_f} da / C R(\Delta k)^m = \frac{1}{C_R(R_0, \gamma^*)} \int_{a_0}^{a_f} da / C(\Delta k)^m = \\ &= S_R^* \int_{a_0}^{a_f} da / C(\Delta k)^m \end{aligned} \quad (5)$$

where γ^* (assumed to be independent of crack length) corresponds to some internal point within the overload affected zone, and S_R^* is the reciprocal of $C_R(R_0, \gamma^*)$.

Under the above assumptions, the following expression can be obtained for the time of crack growth delay:

$$t_d = t_a - t_f = (S_R^* - 1) \int_{a_0}^{a_f} da / C(\Delta k)^m \quad (6)$$

where t_a - is the time affected by overload and t_f - the time required for crack extension from a_0 to a_f with no overloads occurring. In the latter event, the time necessary for the crack to reach length a_0 is:

FATIGUE 87

$$t_p = \int_{a_i}^{a_o} da / C(A\Delta\sigma/a)^m = B \left(\frac{1}{\frac{m-2}{2}} - \frac{1}{\frac{m-2}{2}} \right); \quad m > 2 \quad (7)$$

$a_1 \qquad a_o$

where a_i is the initial crack length and $B=2/[C(A\Delta\sigma)^m \cdot (m-2)]$. Accordingly, the time required to reach the critical crack length (time to failure) with no overloads occurring is:

$$t_{cr} = \int_{a_i}^{a_{cr}} d/a(C\Delta k)^m = t_\infty - \frac{B}{\frac{m-2}{2}} \quad (8)$$

$a_{cr} \qquad \frac{m-2}{2}$

where a_{cr} is the critical crack length and $t_\infty = B/a_i^{\frac{m-2}{2}}$. It follows from equation (6) that

$$t_d = (S_R^* - 1) \int_{a_o}^{a_f} da / [C(A\Delta\sigma/a)^m] = B \cdot (S_R^* - 1) \left(1 - 1/\frac{m-2}{2} \right) \cdot 1/a_o^{\frac{m-2}{2}} \quad (9)$$

Combination of (7) and (9) yields

$$t_d = \phi(t_\infty - t_p) \quad (10)$$

$\frac{m-2}{2}$

where $\phi = (S_R^* - 1) \left(1 - 1/\gamma_{\frac{m-2}{2}} \right)$ is a function of the overload stress ratio r_o and t_∞ is constant for given base-line cyclic loading conditions, a given material and a given initial crack length a_i . The total time elapsed from the beginning of crack growth to an arbitrary moment t corresponding to crack length "a", consists of two components: the total time of crack growth delay t_r and the total time of effective crack growth t_p (effective time). The latter is equivalent to the time required for crack growth to length "a" with no overloads occurring.

According to the above considerations the total effective time is

$$t_p = t - t_r \quad (11)$$

The total delay time t_r , being the sum of the individual delay times t_{di} ($i=1,2 \dots n$), is a random process, due to randomness of the individual delay times and of their number n . Accordingly, the total effective time is also a stochastic process.

Consider an arbitrary realization of the loading process characterized by n overloads with the sequence of peak values $\sigma_{o1}, \sigma_{o2}, \dots \sigma_{oi} \dots \sigma_{on}$, to which corresponds the sequence of delay times $t_{d1}, t_{d2}, \dots t_{di} \dots t_{dn}$.

According to (10)

$$t_{d_i} = \phi_i(t_\infty - t_{p_i}) \quad (12)$$

where t_{p_i} is effective time preceding the i -th overload.

On the other hand a

$$t_{p_i} = \sum_{k=1}^i \tau_k - \sum_{k=1}^{i-1} t_{dk}; \quad t_{p_i} \approx t - \sum_{k=1}^{i-1} t_{dk} \quad (13)$$

where $t_r = \sum_{k=1}^n t_{dk}$ is total delay time

$$t_{d1} = \phi_1(t_\infty - t_{p1}) = \phi_1(t_\infty - \tau_1)$$

$$t_{d2} = \phi_2(t_\infty - t_{p2}) = \phi_2(t_\infty - (\tau_1 + \tau_2 - \phi_1(t_\infty - \tau_1)))$$

$$\dots\dots\dots$$

$$t_{dn} = \phi_n(t_\infty - t_{pn}) = \phi_n(t_\infty - (\tau_f + \sum_{k=1}^n (\tau_k - t_{dk}))) \quad (14)$$

Summation of (14) yields the following expression for the total delay time:

$$t_r = \begin{cases} \sum_{i=1}^n (\prod_{j=1}^i (1 + \phi_j) - 1) t_\infty + \sum_{k=1}^{n+1} \tau_k \cdot (\prod_{l=k}^n (1 + \phi_l) - 1) & \text{if } n > 1 \\ 0 & \text{if } n = 0 \end{cases} \quad (15)$$

where taken into account that τ_f is the backward recurrence time characteristic of a limiting distribution identical with the original exponential distribution of each τ_i .

Equation (15) can be rewritten in the form

$$t_r = \begin{cases} a_n t_\infty - \sum_{k=1}^{n+1} \tau_k b_{n,k} & \text{if } n > 1 \\ 0 & \text{if } n = 0 \end{cases} \quad (16)$$

where a_n and $b_{n,k}$ are as per (15). For a given number of overloads n , these coefficients depend only on the overload stresses $\sigma_{01} \dots \sigma_{0i} \dots \sigma_{0n-1}$ realized in the sequence in question.

For a given n and a given overload stress sequence $\sigma_{01} \dots \sigma_{0n-1}$, the sum

FATIGUE 87

$$W_n = \sum_{k=1}^{n+1} \tau_k b_{n,k} \quad (17)$$

is a random variable, a linear combination of stochastically independent random variables τ_k with the same distribution. Hence, the random variables $\omega_{n,k} = \tau_k \cdot b_{n,k}$ are also exponentially distributed with parameters

$$\lambda_{n,k} = \lambda / b_{n,k} \quad (18)$$

The sum of j exponentially distributed random variables with different parameters λ_{ij} has the following probability distribution function

$$F_W(x) = P\{W_j < x\} = 1 - \sum_{i=1}^j h_{ij} e^{-\lambda_{ij}x}$$

$$h_{ij} = \begin{cases} \prod_{\substack{k=1 \\ i \neq k}}^j \frac{\lambda_{kj}}{(\lambda_{kj} - \lambda_{ij})} & \text{if } j \geq 2 \\ 1 & \text{if } j = 1 \end{cases} \quad (19)$$

Since the total delay time is a non-negative value, the following inequality follows from equations (16) and (17).

$$a_n t_\infty > W_n \quad (20)$$

This leads to the following expression for probability distribution function of W_n

$$P\{W_n < x\} = F_W(x) = \begin{cases} \frac{1 - \sum_{i=1}^{n+1} h_{in} e^{-\lambda_{in}x}}{1 - \sum_{i=1}^{n+1} h_{in} e^{-\lambda_{in} a_n t}} ; & \text{if } x < a_n t_\infty \\ 1 & ; \text{if } x > a_n t_\infty \end{cases} \quad (21)$$

From equations (13), (16) and (21) it follows that the probability distribution function for the total effective time t_p with a given number of overloads n and given sequence σ_{oi} , can be obtained as

follows

$$F_{n\sigma}(\chi) = p\{t_p < \chi/n\sigma_{oi}\} = p\{t - t_{r1} < \chi/n\sigma_{oi}\} =$$

$$F_w(a_n t_\infty - (t - \chi); \quad \text{if } n \geq 1 \text{ and } \chi < t$$

$$= \begin{cases} E(t - \chi) & ; \quad \text{if } n = 0 \text{ or } \chi > t \end{cases} \quad (22)$$

where $E(\chi)$ is unity function. Thus, the unconditional probability distribution function for an arbitrary sequences of overloads will be:

$$F(\chi) = \sum_{n=0}^{\infty} \int \dots \int F_{n\sigma}(\chi) p(n) \cdot f(\sigma_{oi} \dots \sigma_{on}) d\sigma_{oi} \dots d\sigma_{on} =$$

$$= \sum_{n=0}^{\infty} p(n) \int \dots \int F_{n\sigma}(\chi) f(\sigma_{oi}) \cdot f(\sigma_{o2}) \dots f(\sigma_{on}) \cdot d\sigma_{oi} \dots d\sigma_{on} \quad (23)$$

where $p(n) = (\lambda t)^n \cdot e^{-\lambda t} / n!$ is the Poisson distribution of the number of overloads and $f(\sigma)$ the probability density of the overload stresses.

Reliability of a component is considered as the probability of nonfailure during time t . Fracture will not occur until the crack has reached its critical value a_{cr} , or in other words so long as the effective time t_p or total time t elapsed up to the moment of observation is less than the critical time t_{cr} (see equation (8)). Thus the reliability can be expressed as follows:

$$R = \begin{cases} p\{t_p \leq t_{cr}\} = F(t_{cr}) & \text{if } t > t_{cr} \\ 1 & \text{if } t < t_{cr} \end{cases} \quad (24)$$

or bearing in mind (22) and (23) to

$$R = \sum_{n=0}^{\infty} p(n) \int \dots \int F_w\{a_n t_\infty - (t - t_{cr})\} \cdot f(\sigma_{oi}) \dots f(\sigma_{on}) \cdot$$

$$\cdot d\sigma_{oi} \dots d\sigma_{on} \quad \text{for } t > t_{cr} \text{ and } n \geq 1. \quad (25)$$

FATIGUE 87

FATIGUE 87

A DISLOCATION MODEL FOR FATIGUE CRACK PROPAGATION UNDER VARIABLE AMPLITUDE LOADING.

A. BIA*, C. ROBIN*, G. PLUVINAGE*.

A dislocation model based on the Bilby-Cottrell-Swinden model is proposed to describe the fatigue crack propagation under variable amplitude loading. Only the simple case of overload applications is investigated. The determination of the crack tip opening displacement enables us to calculate the fatigue crack propagation through the overload plastic zone.

The results are respectively compared with experimental data, analytical and numerical analysis.

INTRODUCTION.

Dislocation theory has been largely used to model the propagation of fatigue cracks. Most of the investigations are related to constant amplitude loading (Bilby et al(1), Weertman(2), Tomkins et al(3), Yokobori et al(4), Shiratori et al(5). However, variable amplitude loading and the crack closure concept have been considered by authors such as Mc. Cartney (6), Kanninen (7) and Ma Delin (8).

The present paper is concerned with the prediction of fatigue crack growth retardation following overload application. Calculation of the evolution of the fatigue crack growth rate as a function of the crack length is proposed and results are compared with experimental data.

*Laboratoire de Fiabilité Mécanique
Université de METZ, FRANCE.

DESCRIPTION OF THE MODEL.

Representation of the crack (B.C.S. model (1,9)).

The crack and the plastic zone are supposed to form a fictitious crack of length a containing a pile-up of dislocations (Figure 1). Under the action of an external applied stress σ , the equilibrium of the distribution of dislocations is obtained:

if the resulting stress due to the dislocations is equal :

- i) to the applied stress along the real crack : ($x < a_0$).
- ii) to the applied stress minus a friction stress σ_f in the plastic zone : ($a_0 < x < a$).

$$D_0 \int_0^a \frac{\rho(\xi) d\xi}{x - \xi} = \begin{cases} -\sigma & \text{if } x < a_0 \\ \sigma_f - \sigma & \text{if } a_0 < x < a \end{cases} \quad (1)$$

ρ represents the density of dislocations, D_0 is a constant.

The Muskhelishvili solution (10) is used to describe the evolution of $\rho(\xi)$ and the size of the plastic zone X_g is found to be equal to :

$$X_g = a_0 \sec\left(\frac{\pi \sigma}{2 \sigma_f}\right) \quad (2)$$

The crack tip opening displacement (CTOD) is then equal to :

$$CTOD = b \int_x^{X_g} \rho(\xi) d\xi \quad (3)$$

b is the Burgers' vector.

Application of the model to the fatigue crack propagation after overloads.

Using the principle of superposition, the model can be extended to the case of fatigue crack propagation. Let us describe it by considering the loading history represented in Figure 2.

The overload is applied at point A with a stress equal to σ_A . A plastic zone X_{gA} is generated where the friction stress σ_{fA} is supposed to be equal to the yield stress σ_{yA} . (Figure 3.a). The equilibrium is given by :

$$D_0 \int_0^{a_A} \frac{\rho_A(\xi) d\xi}{x - \xi} = \begin{cases} -\sigma_A & \text{if } x < a_0 \\ \sigma_{yA} - \sigma_A & \text{if } a_0 < x < a \end{cases} \quad (4)$$

on unloading (point B), a new state of equilibrium is created, corresponding to :

$$D_0 \int_0^{a_B} \frac{p_B(\xi) d\xi}{x-\xi} = \begin{cases} -\sigma_B & \text{if } x < a_0 \\ -\sigma_{yB} - \sigma_B & \text{if } a_0 < x < a_B \end{cases} \quad (5)$$

which can be expressed as :

$$D_0 \int_0^{a_B} \frac{p_A(\xi) d\xi}{x-\xi} + D_0 \int_0^{a_0} \frac{p_B(\xi) - p_A(\xi)}{x-\xi} d\xi = \begin{cases} -\sigma_B & \text{if } x < a_0 \\ -\sigma_{yB} - \sigma_B & \text{if } a_0 < x < a_B \end{cases} \quad (6)$$

By subtracting equation (5) from equation (6), the following is obtained :

$$D_0 \int_0^{a_B} \frac{\Delta p_{BA}(\xi) d\xi}{x-\xi} = \begin{cases} \sigma_A - \sigma_B & \text{if } x < a_0 \\ -\sigma_{yA} - \sigma_{yB} + \sigma_A - \sigma_B & \text{if } a_0 < x < a_B \end{cases} \quad (7)$$

where

$$\Delta p_{BA} = p_B(\xi) - p_A(\xi)$$

As shown in Figure 3, the final state at point B is considered to be the superposition of two solutions corresponding respectively to the applied tensile stress σ_A and the friction stress σ_{yA} for the first one (Figure 3.a) and to the applied compressive stress $-(\sigma_A + \sigma_B)$ and the friction stress $\sigma_{yA} + \sigma_{yB}$ for the second one (Figure 3.b).

Let us see now what is happening when the specimen is loaded again at point C. The following is obtained :

$$D_0 \int_0^{a_C} \frac{p_C(\xi) d\xi}{x-\xi} = \begin{cases} -\sigma_C & \text{if } x < a_0 \\ \sigma_{yC} - \sigma_C & \text{if } a_0 < x < a_C \end{cases} \quad (8)$$

which can also be expressed as :

$$D_0 \int_0^{a_C} \frac{\Delta p_{CB}(\xi) d\xi}{x-\xi} = \begin{cases} \sigma_B - \sigma_C & \text{if } x < a_0 \\ \sigma_{yB} + \sigma_{yC} + \sigma_B - \sigma_C & \text{if } a_0 < x < a_C \end{cases} \quad (9)$$

Then, the final state will be equal to the superposition of the two previous solutions and a third one corresponding to the applied tensile stress ($\sigma_c - \sigma_B$) and to the friction stress ($\sigma_{yB} + \sigma_{yC}$) (Figure 3.d).

Determination of the crack tip opening displacement.

Equation (3) is used to calculate the CTOD. After superposition, it will be equal to :

$$\text{CTOD}(\alpha_0) = \text{CTOD}_A(\alpha_0, \sigma_A, \sigma_{yA}) - \Delta \text{CTOD}_{BA}(\alpha_0, \sigma_A - \sigma_B, \sigma_{yA} + \sigma_{yB}) + \Delta \text{CTOD}_{CB}(\alpha_0, \sigma_c - \sigma_B, \sigma_{yB} + \sigma_{yC}) \quad (10)$$

By using the Muskhelishvili solution (10), the final solution is given by :

for $0 \leq X - \alpha_0 \leq X_{CB}$

here X represents the abscissa of the crack tip.

$$\begin{aligned} \text{CTOD}(x) = A b_1 \left\{ R_{\text{peak}} \sum_{i=3}^4 \left[\sqrt{1-M_i} - \left(\frac{M_i}{2}\right) \ln \left| \frac{1+\sqrt{1-M_i}}{1-\sqrt{1-M_i}} \right| \right] \right. \\ \left. - \left(\frac{R_{\text{peak}}-R}{2}\right)^2 \sum_{i=5}^6 \left[\sqrt{1-M_i} - \left(\frac{M_i}{2}\right) \ln \left| \frac{1+\sqrt{1-M_i}}{1-\sqrt{1-M_i}} \right| \right] \right. \\ \left. + \left(\frac{M_2}{2}\right)^2 \left[\sqrt{1-M_7} - \left(\frac{M_7}{2}\right) \ln \left| \frac{1+\sqrt{1-M_7}}{1-\sqrt{1-M_7}} \right| \right] + \left(\frac{M_1}{2}\right)^2 \right\} \quad (11) \end{aligned}$$

where :

$$A b_1 = \frac{8\pi\alpha_0 b \sigma_{\text{max}}^2}{E' \sigma_y'} \left(\frac{R_{\text{peak}}(1+R)}{R^2} \right) \cdot \frac{1}{X}$$

The values of M_i parameters are given in Table 1.

When the crack tip has reached the boundary of the overload cyclic plastic zone, the following equations apply :

$$X_{CB} \leq X - \alpha_0 \leq X_{CA}$$

$$\begin{aligned} \text{CTOD}(x) = A b_2 \left\{ R_{\text{peak}} \sum_{i=3}^4 \left[\sqrt{1-H_i} - \left(\frac{H_i}{2}\right) \ln \left| \frac{1+\sqrt{1-H_i}}{1-\sqrt{1-H_i}} \right| \right] \right. \\ \left. - \left(\frac{H_2}{2}\right)^2 \left[\sqrt{1-H_5} - \left(\frac{H_5}{2}\right) \ln \left| \frac{1+\sqrt{1-H_5}}{1-\sqrt{1-H_5}} \right| \right] + \left(\frac{H_1}{2}\right)^2 \right\}^{-1} \quad (12) \end{aligned}$$

where :

$$Ab_2 = \frac{\sigma'_y b E'}{8 \pi \alpha_o \sigma_{max}^2} \left(\frac{R_{peak}(1+R)}{R^3(1+R^2)} \right) \cdot X$$

The parameters H_i are given in Table 1.

TABLE 1 - Values of the M_i parameters and the H_i parameters.

$M_0 =$	$(X - X_{gA}) / X$
$M_1 =$	$M_0 / (1 - R) - (1 - R)$
$M_2 =$	$M_0 / (1 - R) + (1 - R)$
$M_3 =$	M_0 / R_{peak}
$M_4 =$	$M_2^2 / (2 R_{peak})^2$
$M_5 =$	$4 M_0 / (R_{peak} - R)^2$
$M_6 =$	$M_2^2 / (R_{peak} - R)^2$
$M_7 =$	$4 M_0 / M_2^2$
$H_1 =$	$M_0 / (1 - R_{peak}) - (1 - R_{peak})$
$H_2 =$	$M_0 / (1 - R_{peak}) + (1 - R_{peak})$
$H_3 =$	M_0 / R_{peak}
$H_4 =$	$(H_2 / (2 \cdot R_{peak}))^2$
$H_5 =$	$4 M_0 / H_2^2$

FATIGUE 87

Determination of the fatigue crack growth rate.

The fatigue crack growth rate is supposed to be related to the CTOD by the following equation :

$$da/dN = A \cdot CTOD^\beta \quad (13)$$

CTOD is the crack tip opening displacement deduced from the dislocation model. The constants A and B are related to the Paris law parameters m and c as follows :

$$A = C (E \cdot \sigma_y / 0.73)^2$$
$$\beta = 2 m \quad (14)$$

They are deduced from constant amplitude loading data.

RESULTS AND DISCUSSION.

Experimental conditions (11).

The experimental study was performed on a low strength steel whose cyclic yield stress is equal to 350 MPa. CT specimens of width 15 mm were used. The tests were conducted at a constant value of the maximum stress intensity factor ($K_{max} = 18 \text{ MPa}\sqrt{m}$) with a load ratio R equal to 0.1 and different values of the overload ratio ($R_{peak} = 1.6, 1.9$ and 2.2). Fifty overload peaks were applied.

Results.

The evolution of the crack growth rate as a function of the crack length is plotted in figure 4. Experimental data and calculation are compared.

It is observed that the curves are quite similar : delayed retardation is observed when the overload ratio is equal to 1.6 and 1.9. Crack arrest is obtained in the last case ($R_{peak} = 2.2$). The values of the minimum crack growth rate $\sqrt{m \cdot n}$ are quite similar as well as the values of the affected crack length a_d .

Discussion.

A quite good agreement is observed between the experimental data and the calculation in spite of the rough assumptions assumed in the model. The results are analogous to those obtained by two other methods : a finite element calculation (12) and an analysis based on the Glinka's model (13).

The advantage of the method presented in this paper is that its application does not need heavy calculations and is easily con-

FATIGUE 87

ducted on a microcomputer. Moreover, only a few informations, the constants of the Paris' law and the mechanical properties of the material, are necessary.

CONCLUSION.

A model describing the evolution of the fatigue crack growth rate following overload applications has been proposed. Based on the Bilby-Cottrell-Swinden model, it permits to calculate the crack tip opening displacement. Good agreement with experimental data is observed.

SYMBOLS USED.

a_d	= affected crack length (mm).
b	= Burgers' vector.
$D_0 = E'/4\pi$	= material constant.
$E' = E$	= Young's Modulus of Elasticity in plane stress conditions.
$E' = E/(1-\nu^2)$	= Young's Modulus of Elasticity in plane strain conditions.
K_{peak}	= maximum stress intensity factor during overload (MPa m).
$R_{peak} = K_{peak}/K_{max}$	= overload ratio.
V_{min}	= minimum crack growth rate after overload (mm/cycle).
X_g	= plastic zone size calculated with the B.C.S. model (mm).
ρ	= density of the dislocations.
σ'_y	= cyclic yield stress (MPa).

REFERENCES.

- (1) Bilby, B.A., Cottrell, A.H., and Swinden, K.H., Proc. Roy. Soc., A272, 1963, pp. 304-314.
- (2) Weertman J., Int. Fract. Mech., Vol.5, 1969, p. 13.

FATIGUE 87

- (3) Tomkins, B., Wareing, J., and Summer, G., I.C.F.3, Vol. 6, München, 1973, V-422.
- (4) Yokobori, T., Konosu, S., and Yokobori Jr, A.T., I.C.F.4, Vol.1, Waterloo, Canada, 1977, pp. 665-682.
- (5) Shiratori, M., Miyoshi, T., Miyamoto, H., and Mori, T., I.C.F.4, Vol.2, Waterloo, Canada, 1977, pp. 1091-1098.
- (6) Mc. Cartney, L.N., Int. J. Fract., Vol.14, N°2, 1978, pp. 213-232.
- (7) Kanninen, M.F., and Atkinson, C., Int. J. Fract., Vol.16, N°1, 1980, pp. 53-69.
- (8) Ma Delin, I.C.F.6, Vol.2, New Dehli, India, 1984, pp.955-962.
- (9) Bilby, B.A., and Heald, P.T., Proc. Roy. Soc., A305, 1968, p.429.
- (10) Muskhelishvili, N.I., Singular Integral Equations, P. Noordhoff N.V.,
- (11) ROBIN, C., CHEMIHI, C., LOUAH, M., PLUVINAGE, G., SCHNEIDER, M.L., BIGNONNET, A., TRUCHON, M., and LIEURADE, H.P., I.C.F.6, Vol.3, New Dehli, India, 1984, pp. 2007-2014.
- (12) BIA, A., ROBIN, C., PLUVINAGE, G., 4 Int. Symp. on Num. Meth. Engng., Atlanta, USA, 1985.
- (13) BIA, A., Ph. D. Thesis, University of METZ, FRANCE, 1986.

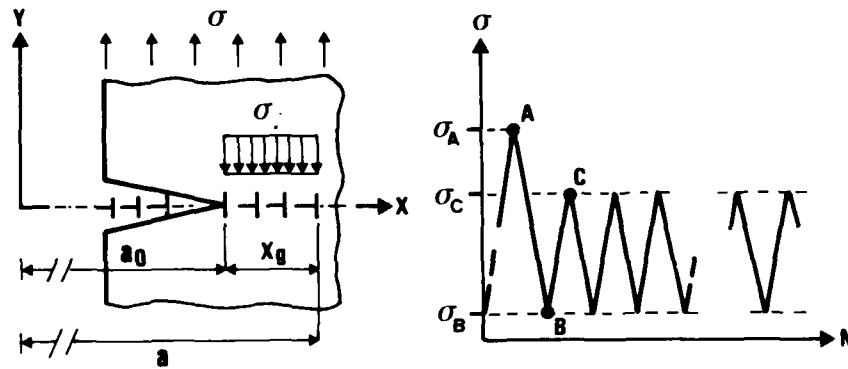


Figure 1 Representation of the crack by a pile-up of dislocations. Figure 2 Loading sequence assumed in the model.

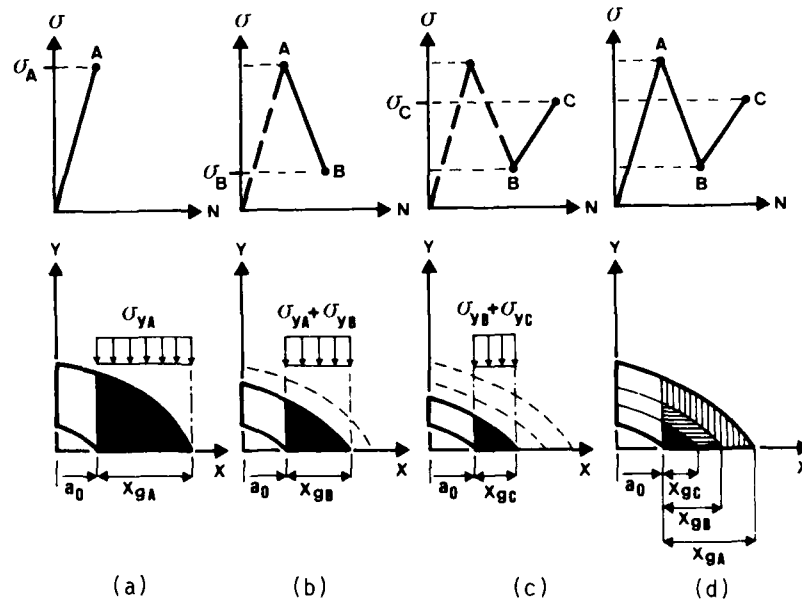


Figure 3 Application of the model to variable amplitude loading.

FATIGUE 87

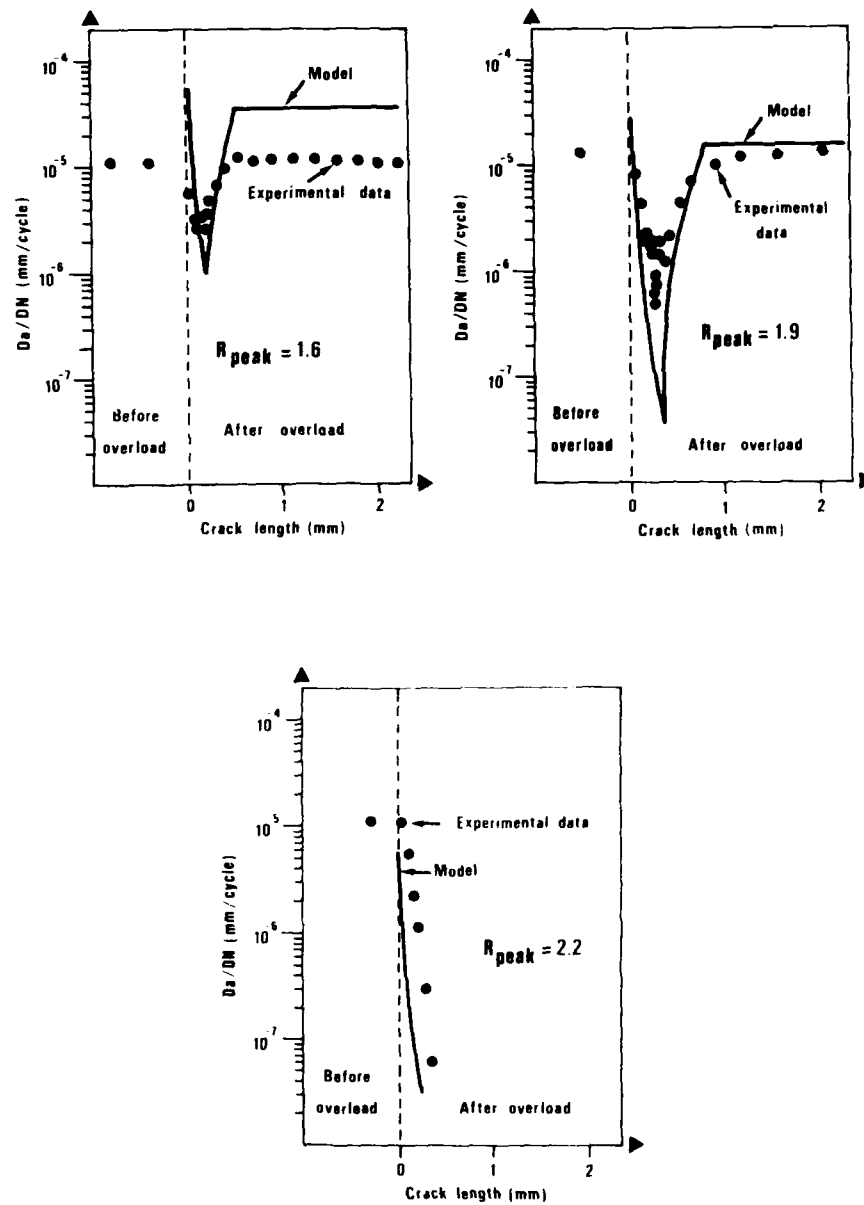


Figure 4 Evolution of the fatigue crack growth rate as a function of the crack length (E36 steel ; $K_{max} = 18 \text{ MPa m}$).

OBSERVATIONS ON THE EFFECT OF OVERLOADS ON FATIGUE CRACK GROWTH

S.K.P. Cheung-Mak* and I. Le May*

The crack growth behavior of an aluminum 2219-T831 alloy has been studied under variable amplitude loading. Experimental data were obtained for both single spike and repeated overloads. The retardation following overload application depended on the overload ratio and the number of overload cycles. Analytical studies using Chang's model have demonstrated good agreement with the experimental data for number of delay cycles and overload plastic zone size.

INTRODUCTION

Numerous researchers have discussed the significant delay in fatigue crack growth rate that occurs during low stress amplitude cycling following a high tensile overload (1-7). This effect is caused by the residual stress field developed at the crack tip and by crack closure. In order to predict fatigue crack growth in aircraft structures and components, as well as in other applications where variable amplitude loading is applied, a clear understanding of the relations governing the effects of overload level and of the number of overload cycles is required. Only from such information can a comprehensive model for crack growth under spectrum loading be developed. While various such models have been formulated, there are still many uncertainties, and the work described in this paper is intended to resolve some of these by reporting and evaluating experimental data concerning the effects of overload level or ratio on the subsequent growth rate, and of the number of overload cycles on the delay period. A model has also been developed for prediction of the retardation effects, based on the work of Chang (8-10), and the results of the analysis are compared with the experimental data.

* Metallurgical Consulting Services Ltd., P.O. Box 5006, Saskatoon, Canada S7K 4E3

FATIGUE 87

CRACK GROWTH MODELLING

The basic crack growth curve depends to some extent on the stress ratio, R . Thus, in the present analysis the equation of Walker (11), which accounts for the layering effect of the growth curves as R changes, was considered to be appropriate. This may be written as:

$$da/dN = C_1 [(1-R)^{m'-1} \Delta K_{eff}]^{n'} \quad R > R_{co}, R = R_{co} \quad (1)$$

The constants in the Walker equation can be determined from constant amplitude baseline experimental data using least squares fitting procedures.

The retardation model of Chang (8-10) is based on that of Vroman (12), modified to take account of underloads or the compressive load acceleration effect. The effective stress intensity factor range, ΔK_{eff} , for tension-tension loading, in the Vroman/Chang model, is:

$$\Delta K_{eff} = (K_{max} - K_{min}) - 0.333 \{ [(a_{ol} + r_{yol} - a)/r_{yol}]^2 \} \quad (2)$$

$$K_{hmax} - K_{max}$$

The overload plastic zone radius in this expression, r_{yol} , is given by:

$$r_{yol} = (1/\beta\pi) (K_{hmax}/\sigma_y)^2 \quad (5)$$

where $\beta = 2$ for plane stress and $\beta = 6$ for plane strain.

For the condition of variable amplitude loading, the incremental crack growth rate can be evaluated using Eqns. (1) and (2).

EXPERIMENTAL

The material used in the study was 2219-T851 aluminum with $\sigma_y = 549$ MPa, UTS = 461 MPa, and $E = 72$ GPa. Compact tension (CT) specimens were prepared from this, of width $W = 50.8$ mm and thickness $B = 12.7$ mm. They were subjected to tension-tension loading parallel to the rolling direction with values of stress ratio of 0.01, 0.5 and 0.7. The loading was sinusoidal in all cases and all fatigue testing was done at 5 Hz, while all overload cycles were applied at 0.05 Hz.

Baseline constant amplitude crack growth tests were run to establish the crack growth rate constants. Subsequently, different magnitudes of spike loading were applied as well as different

FATIGUE 87

numbers of overload cycles. During this testing, constant load cycling was run at $R = 0.3$ and the load levels during overload cycling were also maintained such that $R = 0.3$.

Experimental crack growth data were obtained using the Fractomat and Krak-gage system, this being based on an indirect potential method in which a thin, electrically insulated metal foil (the Krak-gage) is bonded to the CT test specimen. It acts as a simple DC transducer to produce a continuous DC output voltage linearly proportional to crack length, which is read out using the Fractomat. The resolution on the crack length measurement is 0.01 mm for a 20 mm gage, and separate front and rear surface crack lengths can be recorded.

RESULTS

The experiments were performed in accordance with ASTM E647. Crack growth was observed to be at roughly the same rate on both surfaces although at times it appeared to slow on one side while it accelerated on the other. Baseline data was processed using the seven point incremental polynomial method to derive the plots of da/dN versus ΔK for different values of R , as shown in Fig. 1. The constants in the Walker equation were evaluated by best fitting lines to the test data in the straight line region, the values obtained being:

$$C_1 = 3 \times 10^{-11}, n' = 3.55, m' = 0.65, R_{co} = 0.6$$

The solid lines in Fig. 1 show the best fitted straight lines, the $R = 0.6$ and $R = 0.7$ lines being identical because $R_{co} = 0.6$.

Figure 2 shows the decrease in crack growth rate following a single spike overload applied at cycle 5001 for specimen T. It is seen that the retardation on both surfaces (from gages A and B) was the same and that steady growth rate was resumed at the same time. Using the incremental polynomial technique, Fig. 2 can be replotted as Fig. 3. The latter illustrates the very large reduction in growth rate following the overload. Once the retardation has been overcome, the crack resumes the same growth rate as occurs in a specimen tested under constant cyclic load (specimen H in Fig. 3).

Figure 4 shows the variation in crack growth rate in specimen T following overload, as a function of crack length. There was an immediate crack extension following the overload, and the minimum growth rate was reached some 7000 cycles after the overload. At this point the crack had progressed about one quarter of the distance through the overload plastic zone. The baseline crack growth rate was resumed after the crack had grown by one overload plastic zone radius following overload.

FATIGUE 87

Table 1 provides a comparison between the measured delay cycles, N_D , and N_R , the number of cycles required for the crack to grow through the overload plastic zone of size r_{y01} , estimated from Eqn. (3). Also listed is the distance that the crack tip travels from application of the overload to the position corresponding to minimum growth rate. This is designated d_{min} . It may be seen that minimum growth rate occurred after the crack had grown approximately one quarter of the way through the overload plastic zone, the scatter being relatively small.

TABLE 1 - Comparison between Number of Delay Cycles and Cycles to traverse the Overload Plastic Zone

Specimen No.	Overload Plastic Zone Size, r_{y01} (mm)	Cycles to Traverse r_{y01} , N_R	Observed Delay Cycles, N_D	Crack Growth to Minimum Growth Rate, d_{min} (mm)	$\frac{d_{min}}{r_{y01}}$
T	1.054	15 531	15 015	0.285	0.27
u	0.376	2 280	2 100	0.086	0.23
u	0.808	6 027	5 905	0.193	0.24
u	0.880	5 645	5 552	0.246	0.28
u	1.368	16 786	16 770	0.342	0.25
v	1.852	83 512	87 160	0.593	0.32
v	0.568	1 430	1 189	0.114	0.20
v	1.892	4 171	4 489	0.303	0.16
w	0.672	3 142	3 356	0.188	0.28
w	1.170	7 631	8 000	0.199	0.17
x	0.346	1 907	1 821	0.080	0.23
				Average	0.24

The effect of the magnitude of spike overload on the crack growth retardation is shown in Fig. 5, curve a. It is plotted as percent overload versus delay cycles, with percent overload being defined as:

$$\% \text{ overload} = [(K_{hmax} - K_{lmax}) / K_{lmax}] \times 100 \quad (4)$$

It may be seen that the number of delay cycles increased with increase in the degree of overload, until net section yielding took place. The higher the overload, the greater is the decrease in growth rate, or the lower is the minimum crack growth rate, as shown in Fig. 5, curve b.

In addition to single overloads, multiple overload applications were performed. The results are shown in Fig. 6, showing that multiple overloads produce a greater number of delay cycles (curve a), the minimum observed crack growth rate decreasing as the

number of overloads increases (curve b).

ANALYSIS AND DISCUSSION

The predictions of crack growth under variable amplitude were developed on the basis of Chang's equations. Thus, Eqns. (1), (2) and (3) were utilized in the analysis.

Figure 7 shows a comparison between the prediction for a single spike overload and the observed behavior. The model does not predict the delay in reaching minimum growth rate observed from surface crack measurements, and the predicted minimum growth rate is 5 to 10 times greater than was the experimentally recorded value. Both the experimental and analytical curves may be seen to return to the baseline crack growth curve after the delay period.

Predicted values of delay cycles (N_{Dt}) following a single spike overload, obtained using the analysis of Chang, compare well with observed values, as is shown in Fig. 8.

The model used the Walker equation constants as its baseline crack growth constants. As seen in Fig. 7, the growth prediction has the characteristics of the Walker equation, in that it predicts well in the steady state region (regime II), but overestimates growth rate in the low ΔK region (regime I) and underestimates it in the high ΔK region (regime III).

The crack surface is under plane stress conditions whereas the mid-thickness region of the crack tip is under plane strain conditions, and retardation effects may differ between plane stress and plane strain conditions. From the gage readings on the surface, the affected crack length after overload was extensive and growth rate falls off progressively before returning to the baseline level as the crack passes through the overload plane stress plastic zone. The retardation is caused by the effect of the plane stress field at the specimen surface. For single spike overloads, where the crack propagates predominantly in plane strain, the Chang model gives satisfactory predictions of the delay cycles. The model predicts quite well for cases where the crack closure effect (13-20) is not a significant cause of retardation. The predictive curve shown in Fig. 7 has plane strain retardation characteristics, i.e., immediate retardation following overload, and the model does not predict delayed or progressive retardation.

The crack closure effect is large when the crack is under plane stress conditions. The crack closure mechanism explains the observed delayed retardation, assuming the crack has to penetrate into the overload plastic zone before crack closure can become effective. Newman (20) and Cheung and Le May (21) have analyzed the case of a plate specimen under positive stress ratio where plane strain predominated and the closure effect was found to be

FATIGUE 87

small. However, the surface measurements used in this study correspond to plane stress conditions, and the plastic overload zone has a three dimensional nature, varying from plane stress at the surface to plane strain within the plate thickness. As the penetration of the crack into the overload zone takes place, the operative stress state changes towards that of plane strain.

The longer retardations observed when multiple overloads are applied may also be explained from crack closure. Increasing the number of overloads increases the closure effect, producing higher crack opening stresses and, hence, lower minimum growth rate and increased retardation. The Chang model predicts retardation based on residual compressive stresses at the crack tip, and does not account for closure along the wake of the crack. Hence, although it does predict the effect of single overloads reasonably well, it would not be so satisfactory for multiple overloads.

CONCLUSIONS

Data have been presented for the retardation of fatigue crack growth in alloy following application of single and multiple overloads. Chang's model has been applied to predict the delaying effect on crack growth following an overload and good agreement between experimental and predicted values of delay cycles has been obtained.

Differences were noted between the progressive slowing down in crack growth rate following overload and the predicted immediate drop in growth rate, and these have been explained in terms of the change in stress state at the crack tip through the thickness of the plate. Because Chang's model is based on residual stresses in the crack tip region and does not include crack closure along the wake of the crack, the model is less effective when crack closure becomes significant as when a series of overloads are applied. However, it is concluded that the model has significant engineering importance because of its ease of application and of its ability to predict crack growth interaction effects.

SYMBOLS USED

a_{ol}	= overload crack length (mm)
d	= surface crack growth distance from overload (mm)
da/dN_{min}	= minimum crack growth rate (nm/cycle)
d_{min}	= the distance of crack traverses from the overload to the location of minimum growth rate (mm)
K_{hmax}, K_{lmin}	= maximum stress intensity factor at high and low stress levels respectively (MPa \sqrt{m})

FATIGUE 87

m'	= layering effect exponent
n'	= experimental material constant
N_D	= number of delay cycles
N_{Dt}	= theoretical delay cycles
N_R	= number of cycles the crack required to grow through overload plastic zone after the spike overload
R_{co}	= cutoff stress ratio
r_{vol}	= overload plastic zone size (mm)
β	= plane stress/plane strain coefficient
ΔK_{eff}	= effective stress intensity factor range (MPa \sqrt{m})

REFERENCES

- (1) von Euw, E.F.J., Hertzberg, R.W. and Roberts, R. "Delay Effects in Fatigue Crack Propagation", ASTM STP 513, 1972, pp. 230-259.
- (2) Corbly, D.M. and Packman, P.F., Eng. Fract. Mech., Vol. 5, 1973, pp. 479-497.
- (3) Katchner, M., Eng. Fract. Mech., Vol. 5, 1973, pp. 793-818.
- (4) Probst, E.P. and Hillberry, B.M. "Fatigue Crack Delay and Arrest due to Single Peak Tensile Overloads", AIAA Paper No. 73-525, 1973.
- (5) Trebules, V.M., Jr., Roberts, R. and Hertzberg, R.W. "Effect of Multiple Overloads on Fatigue Crack Propagation in 2024-T3 Aluminum Alloy", ASTM STP 536, 1973, pp. 115-139.
- (6) Elber, W. "Equivalent Constant-Amplitude Concept for Crack Growth Under Spectrum Loading", ASTM STP 595, 1976, pp. 236-250.
- (7) Schijve, J. "Observations on the Prediction of Fatigue Crack Growth Propagation under Variable-Amplitude Loading", ASTM STP 595, 1976, pp. 3-23.
- (8) Chang, J.B., Stolpestad, J.H., Sinozuka, M. and Vacaitis, R. "Improved Method for Predicting Spectrum Loading Effects — Phase I Report, Volume I — Results and Discussion", AFEDL-TR-79-3036-VOL-I, 1979.

FATIGUE 87

- (9) Chang, J.B. and Stolpestad, J.H. "Improved Methods for Predicting Spectrum Loading Effects -- Phase I Report, Volume II", AFFDL-TR-79-3036-VOL-II, 1979.
- (10) Chang, J.B., Engle, R.M. and Stolpestad, J.H. "Fatigue Crack Growth Behavior and Life Predictions for 2219-T851 Aluminum Subjected to Variable-Amplitude Loadings", ASTM STP 743, 1981, pp. 3-27.
- (11) Walker, K. "The Effect of Stress Ratio During Crack Propagation and Fatigue for 2024-T3 and 7075-T6 Aluminum", ASTM STP 462, 1970, pp. 1-14.
- (12) Vroman, G.A. "Analytical Prediction of Crack Growth Retardation using a Residual Stress Concept", TFR71-701, Rockwell International, B-1 Division, 1971.
- (13) Elber, W., Eng. Fract. Mech., Vol. 2, 1970, pp. 37-45.
- (14) Elber, W. "The Significance of Fatigue Crack Closure", ASTM STP 486, 1971, pp. 230-242.
- (15) Lindley, T.C. and Richards, C.E., Mat. Sci. Engng., Vol. 14, 1974, pp. 281-295.
- (16) Shaw, W.J.D. and Le May, I. "Crack Closure During Crack Propagation", ASTM STP 677, 1979, pp. 233-246.
- (17) Lal, K.M. and Le May, I., Fat. Eng. Materials and Structures, Vol. 3, 1980, pp. 99-111.
- (18) Newman, J.C., Jr. "A Crack-Closure Model for Predicting Fatigue Crack Growth Under Aircraft Spectrum Loading", ASTM STP 748, 1981, pp. 53-84.
- (19) Newman, J.C., Jr. "A Nonlinear Fracture Mechanics Approach to the Growth of Small Cracks", AGARD-CP-328, 1983, pp. 6.1-6.26.
- (20) Newman, J.C., Jr. "Prediction of Fatigue Crack Growth Under Variable-Amplitude and Spectrum Loading Using a Closure Model", ASTM STP 761, 1982, pp. 255-277.
- (21) Cheung, S.K.P. and Le May, I. "Modelling Problems in Crack Tip Mechanics", J.T. Pindera, Ed., Martinus Nijhoff Publishers, Dordrecht, 1984, pp. 197-206.

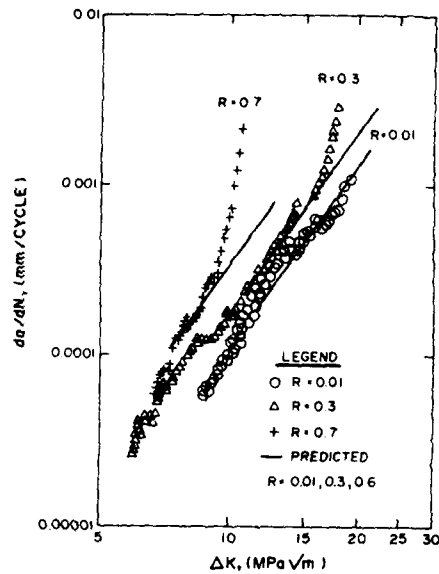


Figure 1 The experimental data and prediction crack growth rate curves for different R values

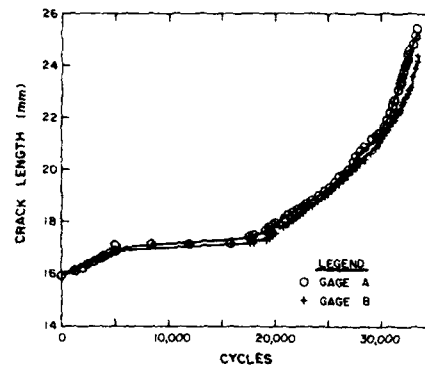


Figure 2 Crack growth curve showing the effect of a single spike overload. Overload applied at 5001 cycles. Maximum load 13.38 kN; minimum load 3.93 kN; delay cycles ~15000

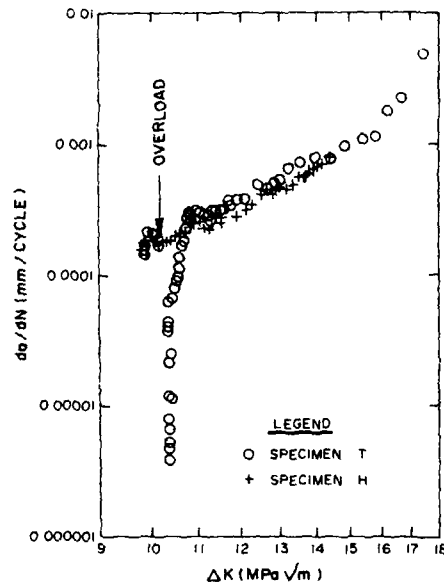


Figure 3 Crack growth rate plots for constant load cycles and for spike overload shown in Fig. 2

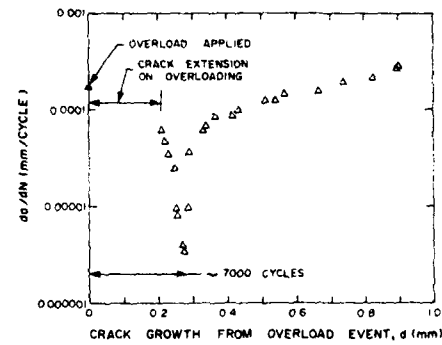


Figure 4 Surface crack growth retardation following spike overload shown in Figs. 2 and 3

FATIGUE 87

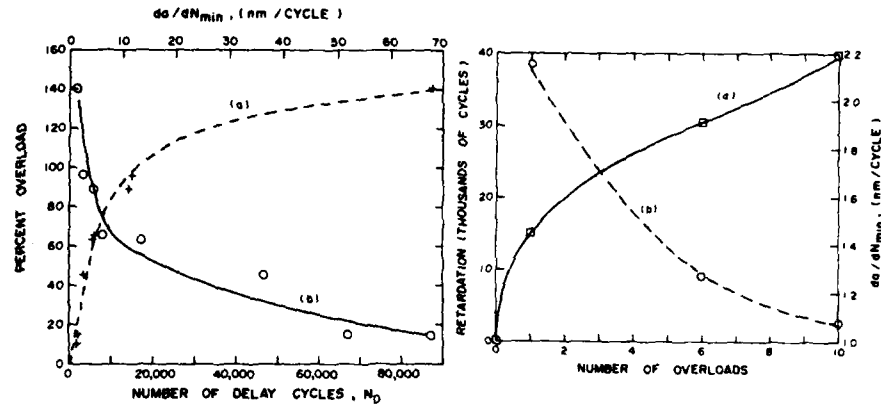


Figure 5 The effect of overload level on crack growth. (a) Number of delay cycles. (b) Minimum crack growth rate following overload

Figure 6 The effect of number of overloads on crack growth. (a) Number of delay cycles. (b) Minimum growth rate following overload

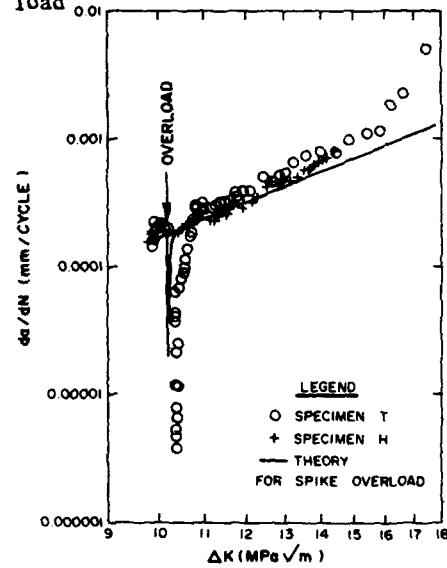


Figure 7 Comparison between experimental and predicted crack growth rate following a spike overload. Also shown are baseline data

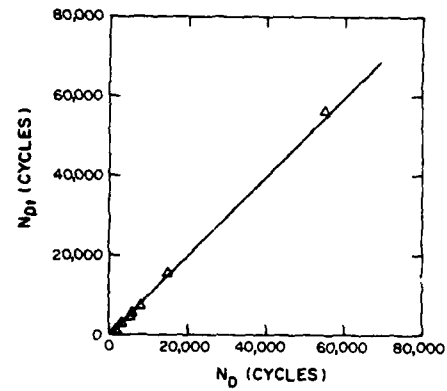


Figure 8 Theoretical delay cycles versus observed delay cycles

FATIGUE 8/

A STUDY OF FATIGUE CRACK GROWTH LIFE UNDER RANDOM STRESSES

J.M. Hu, W.P. Yao and K.X. Li*

In the view of statistics, the expressions of characteristic stress intensity range ΔK_{char} which is related to da/dt are discussed herein by using MTS-880 material test system. The central crack tests (CCT) of low carbon steel were controlled by pseudo random signal in order to investigate the influences of different ΔK_{char} on da/dt . A formula by which the fatigue crack growth life under narrow-band random stress can be estimated is derived. The result of calculation using the formula is accord with the experimental result quite well.

INTRODUCTION

Most cases of failure in many engineering structures result from fatigue. In some situations, such as offshore structures, ships are subjected to sea wave forces and airplanes, spacecrafts are loaded by wind; car and automobile are acted by rough road, all the stresses of those structures above are often belong to random category. Thus, the dynamic strength of structures has a close relation with random fatigue. The fatigue failure under random loading is more complicated than that under regular loading.

For lack of test technology and large computer, the research on the rate of fatigue crack propagation and estimation of the fatigue life under random loading were limited in the past. Recently, electric-hydraulic-servo test system and development of the calculate technology make it possible to reapper random signal or simulate service loading, on the other hand, safety of design and the accuracy of life estimation for fatigue strength are required more urgently. So the research on random fatigue are paid more attention by lots of countries gradually.

* Dept. of Engineering Mechanics, Shanghai Jiao Tong University
Shanghai, P.R. China.

So far, the research methods for random fatigue are divided into two distinct categories, the cycle-by-cycle approach and characteristic approach. The first approach estimates life according to the crack propagation growth which is counted cycle-by-cycle under spectral loading(1). The characteristic approach is a method based on statistics, that is, it substitutes a statistical characteristic for stress term in expression of stress intensity range and estimates the fatigue life using statistical characteristic stress intensity range (ΔK_{char})(2)(3).

The most common expression of ΔK_{char} is root-mean square. Although references (4)(5) provided some examples of its successful application, there are some different forms of ΔK_{char} .

The comparison between different expressions of crack propagation rate and the differences of their lives has not been taken previously, so the influences of different ΔK_{char} on da/dt are compared by experiments under random loading and a formula by which the life of fatigue crack propagation under narrow-band random stress can be estimated is derived in this paper. A statistical characteristic in the formula is root-mean square (RMS) of random stress process and RMS only depends on auto-power spectral density (P.S.D.) of stress process. Thus, this method is one kind estimation of fatigue crack propagation life using P.S.D.(6)

DIFFERENT FORMS OF CHARACTERISTIC STRESS INTENSITY FACTOR RANGE

Because the cycles of random stress history are difficult to be determined and the results of all counting methods are not same perfectly(5)(4), the characteristic of crack propagation can be described by using crack growth rate with time t . We defined:

$$da/dt = f_0 \cdot da/dN \quad (1)$$

where

$$f_0 = \sqrt{\frac{\int_0^\infty f^2 G(f) df}{\int_0^\infty G(f) df}} \quad (2)$$

f_0 is an expected zero-crossing rate with positive slope of stochastic stress process and $G(f)$ is one-sided power spectral density of random stress process.

The Paris formula can be written as: (7)

$$da/dN = C(\Delta K)^m \quad (3)$$

also, we have:

$$da/dt = C f_0 (\Delta K_{char})^m \quad (4)$$

in which, ΔK_{char} is a characteristic stress intensity range.

There are a lot of forms of ΔK_{char} , generally used as follow:

$$\Delta K_{char1} = (S_{maxrms} - S_{minrms}) \sqrt{\pi a} F \quad (5)$$

$$\Delta K_{\text{char2}} = 2 S_{\text{rms}} \sqrt{\pi a} F \quad (6)$$

$$\Delta K_{\text{char3}} = (S_{\text{pm}} - S_{\text{vm}}) \sqrt{\pi a} F \quad (7)$$

where

$$S_{\text{maxrms}, (\text{or minrms})} = \left[\lim_{K \rightarrow \infty} \frac{1}{K} \sum_{i=1}^K S_{\text{maxi}, (\text{or mini})}^2 \right]^{\frac{1}{2}} \quad (8)$$

$$S_{\text{rms}} = \left[\lim_{T \rightarrow \infty} \frac{1}{T} \int_0^T (S_i - S_m)^2 dt \right]^{\frac{1}{2}} = \left[\int_0^{\infty} G(f) df \right]^{\frac{1}{2}} \quad (9)$$

$$S_{\text{pm}, \text{vm}} = \lim_{K \rightarrow \infty} \frac{1}{K} \sum_{i=1}^K S_{\text{maxi}, \text{mini}} \quad (10)$$

Because, in Eq(8) and (10), the values of peak $S_{\text{max}, i}$ and valley $S_{\text{min}, i}$ have to be obtained by rain-flow counting method, so the Eq(9) is most convenient to calculate.

EXPERIMENTS

There are two purposes in the random loading test, they are to get the rate and the life of crack propagation separately under random stress. The former can be compared with the rate of crack propagation under constant amplitude loading and also be in order to evaluate three different expressions of characteristic stress intensity range; the latter can be compared with the calculating result which is obtained by theoretical formula.

The experiment was conducted by MTS-880 material test system, reference(8), and the loading was controlled by white noise filtered with narrow-band filter. The random stress history is a narrow band Gaussian process with central frequency $f_0=19.34$ Hz and the specimens are central crack plate of low carbon steel. The yield strength of the material is:

$$S_y = 9.5 \text{ Mpa} ;$$

the constants which were used in Eq(3) are:

$$C = 1.1 \times 10^{-9} ; \quad m = 2.9 .$$

Also, the size of specimen is:

$$\text{width } W = 75.5 \text{ mm} ;$$

$$\text{thick ness } B = 7.8 \text{ mm} ;$$

and the shape factor

$$F = \sqrt{\text{Sec } \frac{\pi a}{W}} .$$

The wave of testing loading and its auto-power spectral density are shown in Fig (1), the a-t curve obtained by experiment shown

FATIGUE 87

in Fig (2).

Analysing the data of response stress, we have:

$$S_{\max \text{ rms}} = 63.501 \text{ Mpa}, \quad S_{\text{pm}} = 62.913 \text{ Mpa},$$

$$S_{\min \text{ rms}} = 37.629 \text{ Mpa}, \quad S_{\text{vm}} = 36.795 \text{ mpa},$$

$$f_o = 19.34 \text{ Hz}.$$

The relationship between da/dt and $\Delta K_{\text{char},i}$ ($i=1,2,3$) which are obtained by test results are shown in Fig (3). After plotting the data points, we find that the $\Delta K_{\text{char}3}$ is the largest one and

$\Delta K_{\text{char}2}$ is the smallest one at the same level of da/dt , but the error among them are less than 2%. So the $\Delta K_{\text{char}2}$ which is most convenient to calculate can be considered as the best expression, at least in this case.

There is a difference from some results provided by several references, that is, although the slope of the straight line of $da/dt - \Delta K_{\text{char}}$ under random loading is the same as that under constant loading, the constant C is different, that is, the data from random loading is not within a scatter band which is obtained from constant loading. It makes us know that the ΔK in Paris formula can not be simply replaced by ΔK_{char} to estimate the life of crack propagation under random loading.

A FORMULA FOR ESTIMATING FATIGUE LIFE UNDER RANDOM STRESS

A formula has been derived to estimate the life of crack propagation under random stress. In narrow band case, the random stress is described only use one statistical characteristic ΔK_{char} so it is rather simple. Integrating Eq (3) we have, (6)

$$N = \frac{1}{C} \frac{2}{m-2} \frac{a_f}{(\sqrt{\pi} a_f \cdot F)^m} \cdot \left\{ \left(\frac{a_f}{a_o} \right)^{\frac{m}{2}} - 1 \right\} \cdot (\Delta S)^{-m} \quad (11)$$

according to Miner's law, (9) when

$$\sum \frac{n}{N} = 1 \quad (12)$$

the failure occurs. Here we have:

$$n = T f_o p(S_p) dS \quad (13)$$

$p(S_p)$ is the probability density of stress peaks.

If we write:

$$H = \frac{1}{C} \frac{2}{m-2} \frac{a_f}{(2\sqrt{\pi} a_f F)^m} \left\{ \left(\frac{a_f}{a_0} \right)^{\frac{m}{2}-1} - 1 \right\} \quad (14)$$

From Eq (12) we get,

$$T = \frac{H}{f_0 \int_0^\infty (S_p)^{-m} p(S_p) dS_p} \quad (15)$$

When the stress process is of narrow-band Gaussian, the peaks of stress obey the Rayleigh distribution:

$$p(S) = \frac{S}{S_{rms}^2} \exp \left(-\frac{S^2}{2S_{rms}^2} \right) \quad (16)$$

Substituting it into Eq (15), we get:

$$T = \frac{H}{f_0 (\sqrt{2})^m \Gamma(\frac{m+2}{2})} S_{rms}^{-m} \quad (17)$$

where $\Gamma(\frac{m+2}{2})$ is a Gamma function (6).

Substituting the data of specimen and stress value into Eq(17)

$$T = \frac{3.9 \cdot 10^6 \cdot (1.28)^{-2.9}}{19.34 \cdot (\sqrt{2})^{2.9} \cdot 1.2842} = 28148 \text{ (Sec)}$$

The calculated results are quite satisfied compared with experimental results (20125 Sec), the error is about 40%.

CONCLUSION

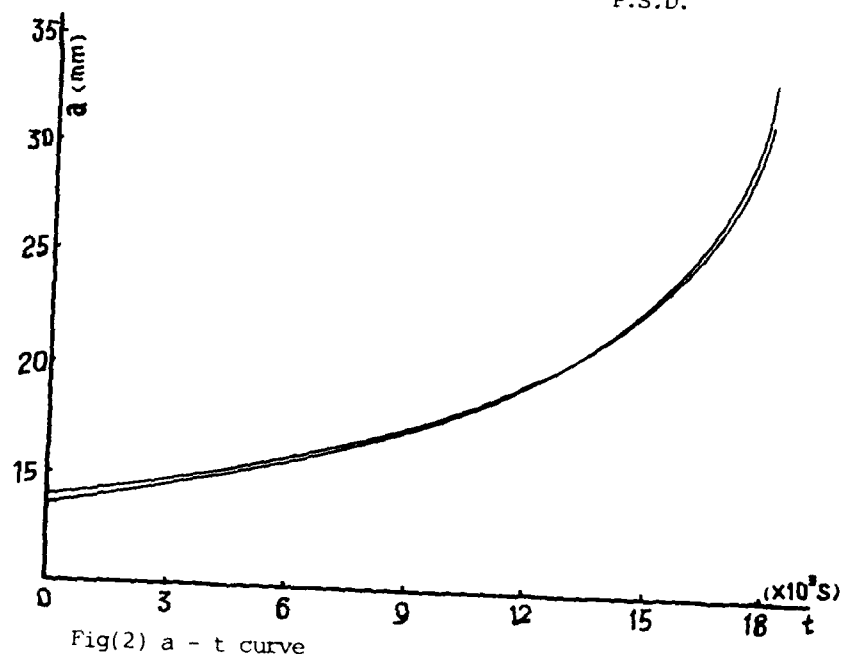
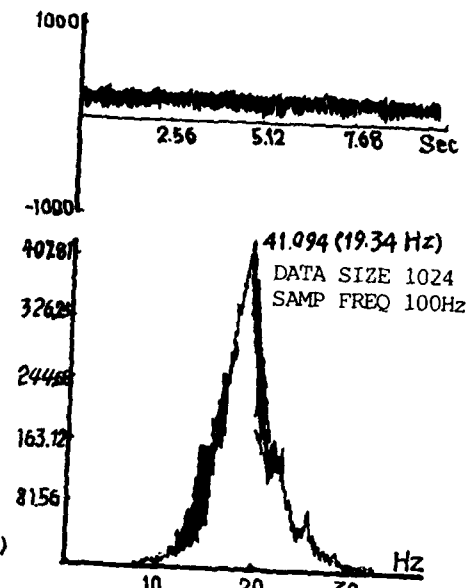
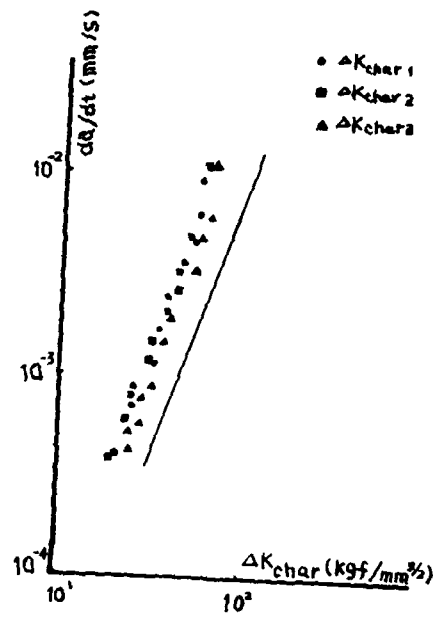
- 1) The differences between three expressions of characteristic stress intensity range are very small and $\Delta K_{char2} = 2S_{rms} \sqrt{\pi} a$ is one of the best expressions because it is convenient to calculate.
- 2) The random loadings which obey any kind of distributions can be recreated in MTS-880 material test system according to functions of the machine. (Hardware and Software).
- 3) The Eq (17) is a practical formula. If the length of the original crack, the power spectral density of random stress process and the expression of stress intensity range have been obtained, the formula can be used to estimate the life of fatigue crack growth with satisfaction in engineering.

FATIGUE 87

REFERENCES

- (1) Fleck, N.A. And Smith, R.A., "Fatigue Life Prediction of a Structural Steel Under Service loading", Int. J. Fatigue, Vol.6., No.4, 1984, pp.203.
- (2) Barson, J.M., "Fatigue Crack Growth Under Variable-Amplitude Loading in Various Bridge Steels", ASTM. STP, 595, 1976, pp. 217-229.
- (3) Priddle, E.K., "High Cycle Fatigue Crack Propagation Under Random and Constant Amplitude Loadings", Int. J. Press, Ves and Piping, 89, No. 4, 1976.
- (4) Schijve, J., "Four Lectures on Fatigue Crack Growth", Engrg. Fract. Mech., June., 1978.
- (5) Hudson, C.M., "R-M-S Approach for Predicting Fatigue Crack Growth Under Random Loading", ASTM. STP, 748, 1981, pp. 45-48.
- (6) Hu, J.M., Yao, W.P. and Hu, S.R., "Estimation of the Fatigue Life Under Random Loading Using Power Spectral Density Method", National Second Fatigue Congress Proceedings, P.R. China, Vol.2., 1984.
- (7) Chen, C., "Engrg. Fract. Mech.", National Defence Industry Press, Piking, P.R.C., 1978.
- (8) Lee, J.M. and Meconnell, K.C., "Random Load Simulation in Laboratory Fatigue Testing", SAE, 1979, pp. 780101.
- (9) Kujawsky, D. and Ellyin, F., "Accumulative Damage Theory for Fatigue Crack Initiation and Propagation", Int, J. Fatigue, Vol. 6., No. 2, 1984.

FATIGUE 87



FATIGUE 87

CRACK GROWTH IN CONTRASTING TITANIUM ALLOYS UNDER THE CONJOINT
ACTION OF HIGH AND LOW CYCLE FATIGUE

B.E. Powell*

Fatigue crack propagation rates have been measured for Ti-6Al-4V and Ti-5331S aeroengine disc materials using compact tension and corner notched tensile test-pieces. The loadings used simulate both the start-stop operations of aeroengines which lead to low cycle fatigue and the in-flight vibrations which may cause high cycle fatigue. It is suggested that the different fatigue crack growth behaviour of Ti-5331S, relative to that of Ti-6Al-4V, arises largely from the greater proportion of crack closure and short crack growth occurring in this alloy.

INTRODUCTION

The current design limitation for aeroengine discs is that of low cycle fatigue (LCF). In such rotating components the LCF loading arises from the cyclic variation of both the centrifugal and the thermal stresses. In the simplest case this major stress variation occurs once per flight. However, rotating engine components have also experienced high cycle fatigue (HCF) failures as a direct result of excessive vibrational stresses. These minor stress cycles are characterised by a high frequency and are superimposed on part of the major cycle. Consequently, in order that the fatigue integrity of these critical components might be fully assessed, it is necessary to establish the resistance of various disc and blade materials to the conjoint action of LCF and HCF loadings.

EXPERIMENTAL DETAILS

The two alloys selected for this study are the general purpose $\alpha + \beta$ alloy Ti-6Al-4V and the near- α creep resistant alloy Ti-5331S, which is also known as IMI829. These alloys show a marked contrast

*Department of Mechanical Engineering, Portsmouth Polytechnic.

in terms of their microstructure, crack growth behaviour and temperature of application. Samples of both materials were cut from unused aeroengine discs. In the final stages of manufacture these discs were heat treated: the Ti-6Al-4V being solution treated at 960 °C, water quenched and aged at 700 °C; whilst the Ti-5331S was solution treated at 1050 °C, oil quenched and aged at 650 °C. As a consequence the Ti-6Al-4V consisted of regions of primary α and transformed β whose widths were approximately 25 μm , whilst the Ti-5331S possessed a prior β grain size of 0.6 mm. At room temperature the values of the 0.1% proof stress were 873 MPa and 760 MPa respectively.

Fatigue crack growth (FCG) rates have been determined using two specimen designs. A conventional compact tension (CT) test-piece generates data for long, through-the-thickness cracks; whilst a corner notched (CN) test-piece (Fig. 1), consisting of a square sectioned bar containing a shallow notch at one corner, and loaded in remote tension, produces data for quarter circular cracks (Hicks and Pickard(1)). The corner notches employed were 0.25 mm deep and 0.10 mm wide, and located in test-pieces with cross-sectional areas of 50 or 100 mm² at their gauge lengths. The CT specimens were 26 mm wide and 13 mm thick and conformed to the ASTM(2) specified design.

A major cycle is represented in the fatigue testing by a trapezoidal stress wave which is applied by a servohydraulic machine at a frequency of 0.1 Hz (Fig. 2a). The minor cycles are simulated by a 150 Hz sinusoidal stress wave of constant amplitude generated by an electromagnetic vibrator which is positioned between the servohydraulic actuator and the specimen. With this system the minor cycles may be superimposed upon that part of the major cycle corresponding to the cruise condition; that is the dwell on maximum load, which is extended to accommodate the required number of minor cycles (Fig. 2b).

The fatigue crack propagation characteristics of the two alloys were determined having first pre-cracked the specimens to give an approximate crack length of 8 mm in the CT test-piece and 0.5 mm in the CN test-piece. During the subsequent collection of FCG data the levels of major and/or minor stress amplitude were maintained constant, so that as the test proceeded the levels of stress intensity range (ΔK) progressively rose as the crack advance accelerated. Where possible, under the conjoint action of major and minor stress cycles, the approach adopted was to grow the crack from a low level of stress intensity range at which the minor cycles caused no damage, and by allowing the stress intensity range to rise unhindered, to determine both the FCG rates and the level of stress intensity range at which the minor cycles became active.

During every test crack length was monitored using the direct current potential drop (DCPD) technique. The three point secant

FATIGUE 87

method was used to obtain crack growth rates, with input data corresponding to equal increments in the observed DCPD voltage ratio. In addition bulk measurements of the crack opening load in the CT specimens have been made from plots of load versus back face strain recorded on an X-Y plotter both on loading and unloading. In order to accommodate the slow response of the plotter it is necessary to make a temporary reduction in the major cycle rise and fall times. Clearly the plotter cannot follow the high frequency minor cycles, and the load range recorded is that of the major cycle.

RESULTS

The FCG rates in CT and CN specimens of Ti-6Al-4V subjected solely to major cycle loadings are in agreement for $\Delta K < 20 \text{ MPa}\sqrt{\text{m}}$. Above this level, slower rates of growth are associated with the CN specimen. This behaviour (Fig. 3) is the same as that reported elsewhere both for Ti-6Al-4V (Pickard et al(3)) and nickel-based superalloys (Brown and Hicks(4)). However, the results obtained for the alloy Ti-5331S are in contrast to these findings, since the growth rates observed in the two types of specimen are essentially the same at all levels of ΔK examined (Fig. 4).

Fatigue crack propagation experiments have been undertaken using 10 000 minor cycles per major cycle (n), with a ratio of minor to major stress amplitudes (Q) of 0.12. These results are presented as a function of ΔK_{total} since this parameter accounts for the increase in stress intensity resulting from the superimposition of the minors on the major cycle. In Ti-6Al-4V both the CT and CN data show that the effect of the superimposed minor cycles is to give enhanced FCG rates, relative to the growth rates for major cycles alone, above a transition level of ΔK_{total} . This transition has been labelled ΔK_{onset} since it corresponds to the onset of minor cycle crack growth. The linear summation of the crack growth associated with the individual LCF and HCF loadings, indicated by a full line in Fig. 5, gives an accurate prediction of the overall growth rates and the value of ΔK_{onset} . Thus, for this material, the linear summation predictions and the results from both the CT and the CN specimens are in accord.

In Ti-5331S, subjected to the previously stated combination of major and minor stress cycles, the measured growth rates show some departures from the linear summation predictions (Fig. 6). Relative to these predictions, the long crack growth rates generated in CT test-pieces show some retardation. In CN specimens the growth rates associated with the shorter crack lengths are greater than the linear summation predictions. Subsequently, as the length of the quarter circular cracks increases, the growth rates again display some slight retardation. The initial enhancement in growth rates, which are associated with measurements at the shortest crack lengths makes the determination of a ΔK_{onset} value difficult.

FATIGUE 87

Bulk measurements of crack closure have been determined for CT specimens using the back faced strain method. In Ti-5331S the opening of the crack occurs at a level of stress intensity (K_{op}) which is virtually constant. In Ti-6Al-4V the levels of K_{op} are not only lower but also exhibit a rise which is linearly related to ΔK . This pattern of behaviour was observed both with major cycles applied separately and with combinations of major and minor stress cycles, the typical data presented (Figs. 7 and 8) being for the combination of 10 000 minor cycles per major cycle at an amplitude ratio of 0.22.

DISCUSSION

The different crack closure mechanisms which occur in Ti-5331S and Ti-6Al-4V must give rise to the different K_{op} versus ΔK responses observed for these two materials. Thus the higher level of K_{op} observed in Ti-5331S results from the surface roughness-induced crack closure which derives from this material's larger grain size. The extent of this closure mechanism is largely controlled by the material's microstructure, thus the level of K_{op} remains virtually constant, at least in tests which largely span the intermediate region of FCG. This effect is much reduced in Ti-6Al-4V which exhibits a lower level of K_{op} by virtue of plasticity-induced closure. The size of the plastic zone at the crack tip will increase as ΔK increases, and as a consequence a progressive rise in K_{op} is to be expected.

The different FCG behaviour of the two titanium alloys, apparent when tested solely under a major cycle loading, can be rationalised on the basis of their crack closure characteristics in conjunction with the explanation for the growth rate discrepancy between specimen types advanced by Brown and Hicks(4). They argue that the effect arises from a greater proportion of plane stress to plane strain in the CN specimen. In materials exhibiting a low level of crack closure due solely to crack tip plasticity it may be expected that the extent to which a crack front is affected by crack closure will be influenced by the proportion of plane stress to plane strain, and that a greater retardation in the rate of growth is to be expected if this proportion is increased. However this effect will be insignificant for materials characterised by a high level of surface roughness-induced crack closure which is microstructurally determined, as was observed for Ti-5331S.

In the absence of minor cycles the fatigue crack propagation lives associated with flaws in aeroengine discs are more accurately predicted using crack growth data from CN specimens, as Brown and Hicks(3) have shown. Where damaging minor cycles are present in substantial numbers their contribution to the overall growth rate is dominant. In these circumstances, differences between the FCG rates for major cycle loadings at $\Delta K > 20 \text{ MPa}\sqrt{\text{m}}$ become unimportant. This is the reason why the results from CN and CT specimens of Ti-

FATIGUE 87

6Al-4V subjected to combined low and high cycle fatigue, together with the linear summation predictions, can be in total agreement, although there is apparently a variation in one of the contributions to the overall crack growth.

The FCG rates predicted for Ti-5331S by the method of linear summation do not coincide entirely with those observed in either specimen design; thereby indicating the presence of additional forms of crack growth behaviour in this alloy. The growth rates which exceeded the linear summation predictions, observed in the CN specimens at the lowest levels of applied ΔK_{total} , corresponded to measurements taken when crack lengths were 1 to 3 times that of the grain size of the material; that is to say, at crack lengths for which the occurrence of microstructurally short crack effects might be expected. Brown and Hicks(5) have studied the extent of the microstructural short crack effect for a variety of materials, including the influences of grain size and crystal structure, and have shown that the effect is substantial in a similar material, namely Ti-65S. Some additional tests have therefore been conducted using grain coarsened Ti-5331S, and a similar enhancement in the FCG rates due to the behaviour of microstructurally short cracks has been observed.

Towards the end of tests on Ti-5331S having grains of conventional size, when the crack length would be at its longest and the values of ΔK_{total} at their greatest, the results from both specimen designs indicated a slight retardation relative to the linear summation predictions. This slight retardation in the long crack growth rate data arises, at least in part, from the interference to the mechanism of minor cycle crack growth which is caused by the periodic marking of the fracture surfaces with fatigue striations generated in response to the major cycle loading. The fractographic observation (Powell and Duggan(6)) of the regeneration of tear ridges at the major cycle striation marking indicated the effective lengthening of the crack front which would give a reduction in the crack growth rate (Forsyth(7)).

CONCLUSIONS

1. When the advance of a fatigue crack is used to generate a progressive increase in the stress intensity range applied to a compact tension test-piece, the bulk measurement of crack opening stress intensity in Ti-5331S remains almost constant, but rises linearly in Ti-6Al-4V.
2. Under a major cycle only loading the discrepancy in fatigue crack growth rates generated in compact tension and corner notched test-pieces above a stress intensity range of $20 \text{ MPa}\sqrt{\text{m}}$, observed in Ti-6Al-4V, is absent in Ti-5331S.
3. In Ti-6Al-4V subjected to a combination of major and minor stress

FATIGUE 87

cycles there is a good agreement between the fatigue crack growth rates obtained from tests carried out on compact tension and corner notched test-pieces and those predicted by the linear summation of crack growth associated with the low and high cycle fatigue loadings. In Ti-5331S both accelerations and retardations in growth rates relative to the linear summation predictions have been observed.

ACKNOWLEDGEMENTS

This work has been sponsored by Rolls-Royce, Derby Aeroengine Division, under Research Contract URC 116; the European Office of Aerospace Research and Development, under Grant AFOSR-82-0077; and the Air Force Wright Aeronautical Laboratories (AFSC), under Contract F 49620-85-C-0116. The United States Government is authorised to reproduce and distribute reprints for governmental purposes notwithstanding any copyright notation hereon. The provision of funding, materials and technical support is gratefully acknowledged.

SYMBOLS USED

$K_{\text{major max}}$	maximum stress intensity associated with the applied trapezoidal major cycle ($\text{MPa}\sqrt{\text{m}}$).
K_{min}	minimum stress intensity ($\text{MPa}\sqrt{\text{m}}$).
K_{op}	stress intensity associated with crack opening ($\text{MPa}\sqrt{\text{m}}$).
Q	ratio of minor amplitude to major amplitude.
n	number of minor cycles per major cycle.
ΔK_{onset}	value of ΔK_{total} corresponding to the onset of minor cycle damage ($\text{MPa}\sqrt{\text{m}}$).
ΔK_{total}	stress intensity range associated with the total, or overall, stress cycle ($\text{MPa}\sqrt{\text{m}}$).

REFERENCES

- (1) Hicks, M.A. and Pickard, A.C., Int. J. of Fracture, Vol. 20, 1982, pp. 91-101.
- (2) ASTM, "Tentative Test Methods for Constant Amplitude Fatigue Crack Growth above 10^{-8} m/cycle - ASTM Standard E647-78T", ASTM Book of Standards, Part 3, 1983, pp. 710-730.
- (3) Pickard, A.C., Brown, C.W. and Hicks, M.A., "The Development of Advanced Specimen Testing and Analysis Techniques Applied to Fracture Mechanics Lifing of Gas Turbine Components", Conference on "Advances in Life Prediction Methods", New York,

FATIGUE 87

1983, pp. 173-178.

- (4) Brown, C.W. and Hicks, M.A., Int. J. of Fatigue, Vol. 4, 1982, pp. 73-81.
- (5) Brown, C.W. and Hicks, M.A., Fatigue of Engrg. Mater. and Struts., Vol. 6, 1983, pp. 67-76.
- (6) Powell, B.E. and Duggan, T.V., "The Influence of Minor Cycles on Low Cycle Fatigue Crack Growth in Ti-5331S", in 2nd Int. Conf. on "Low Cycle Fatigue and Elasto-Plastic Behaviour of Materials", Munich, 1987, to be published.
- (7) Forsyth, P.J.E., "A Unified Description of Micro and Macroscopic Fatigue Crack Behaviour", Technical Report 82065, Royal Aircraft Establishment, Farnborough, U.K., 1982.

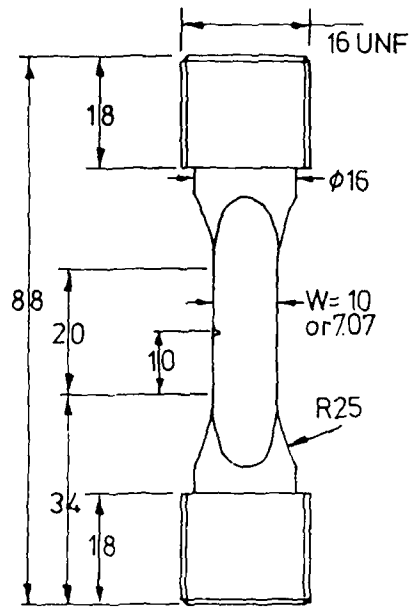


Fig. 1 Corner notched specimen.

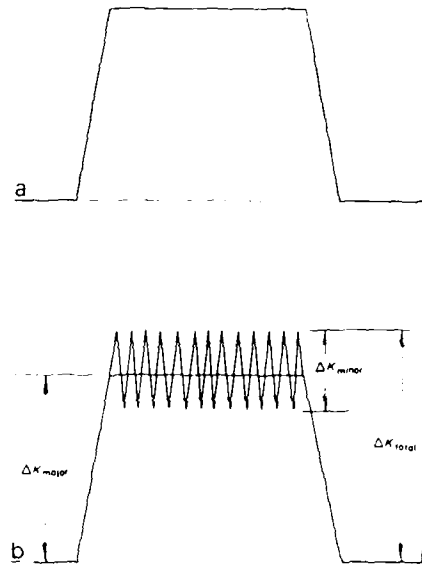


Fig. 2(a) Major cycle: (b) major and minor cycles.

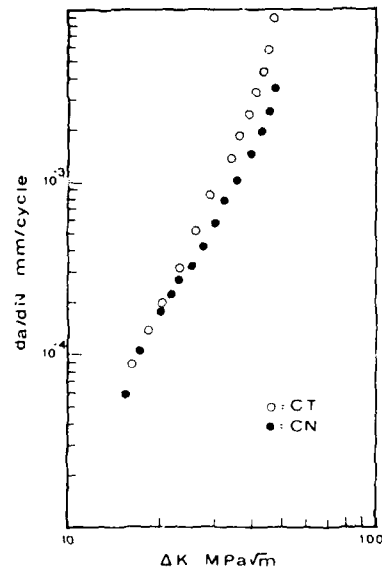


Fig. 3 Major cycle FCG rates in Ti-6Al-4V.

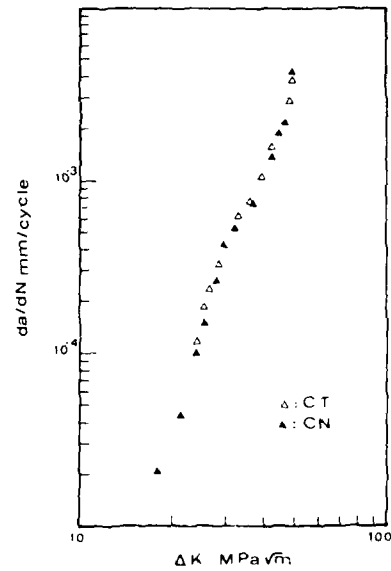


Fig. 4 Major cycle induced FCG rates in Ti-5331S.

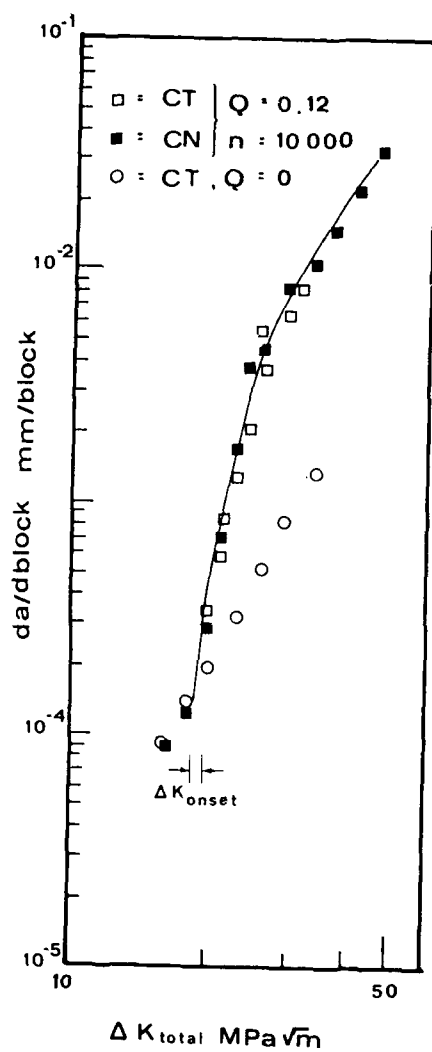


Fig. 5 FCG rates in Ti-6Al-4V under combined cycles.

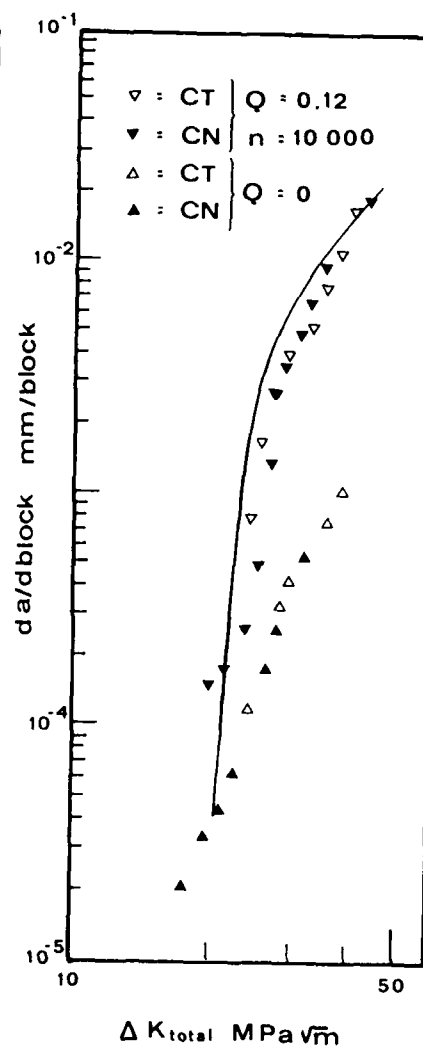


Fig. 6 FCG rates in Ti-5331S under combined cycles.

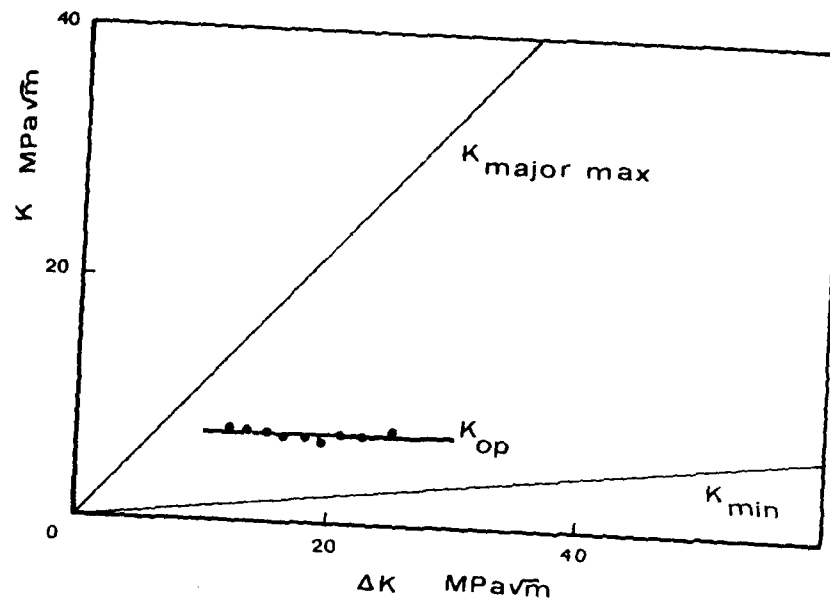


Fig. 7. Typical crack closure behaviour in Ti-5331S.

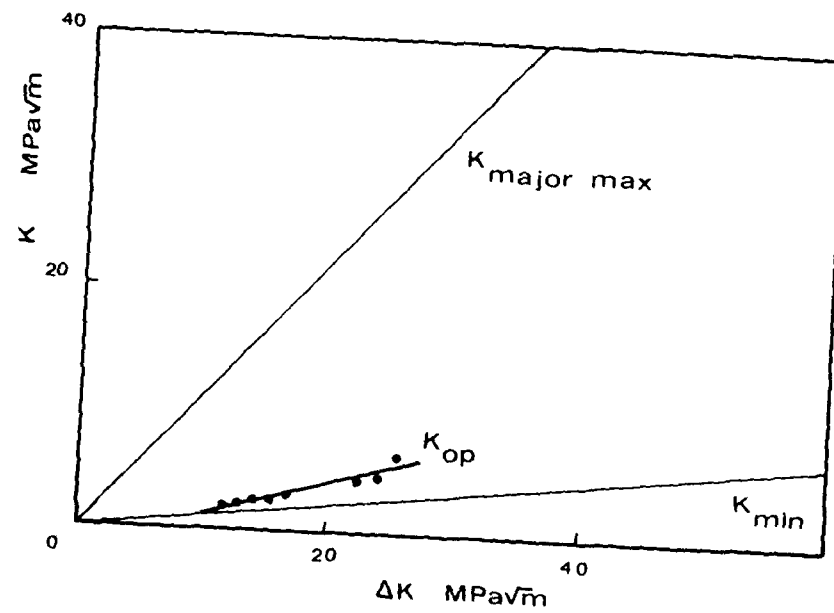


Fig. 8. Typical crack closure behaviour in Ti-6Al-4V.

FATIGUE 87

VARIABLE AMPLITUDE FATIGUE CRACK GROWTH IN ALUMINUM ALLOYS 2090-T8E41 AND 7075-T651

J.S. Thomas, Jr.*, J.C. Van Sice*, A.F. Grandt, Jr.**

Fatigue crack growth experiments were conducted to compare the variable amplitude fatigue crack growth behavior of aluminum-lithium alloy 2090-T8E41 and aluminum alloy 7075-T651. Fixed-end-single-edge-notch-tension specimens were subjected to the MINITWIST loading spectrum. The results indicate that the 2090-T8E41 alloy has significantly superior fatigue crack growth resistance to the MINITWIST load history.

INTRODUCTION

The work reported here compares the fatigue crack growth behavior of aluminum alloys 2090-T8E41 and 7075-T651 when subjected to the MINITWIST load spectrum. The 2090 aluminum-lithium alloy is being developed as a lighter and stiffer replacement for 7075-T6 in aircraft structural applications. The goal of this particular effort was to provide a direct comparison between the variable amplitude fatigue crack growth resistance of 2090-T8E41 and 7075-T651. Other investigators have studied other property comparisons (1).

Both materials were provided in plate form with a nominal thickness of 1.3 cm (0.5 in.) by the Aluminum Company of America. The particular 2090-T8E41 plate examined was from the first production run of this new alloy. Mechanical properties measured from specimens obtained from the two plates were provided by the

* U.S. Coast Guard aeronautical engineers and former graduate students.

** Professor and Head, School of Aeronautics and Astronautics, Purdue University, W. Lafayette, IN 47907

FATIGUE 87

Aluminum Company of America (1), and include an ultimate tensile stress of 580 MPa (84 ksi) for the 2090-T8E41 alloy, and 600 MPa (87 ksi) for the 7075-T651 material. Both materials exhibited an average tensile yield stress of 545 MPa (79 ksi). It was noted that the 7075-T651 plate properties are slightly higher than typical values. The density of the aluminum-lithium alloy is approximately five percent less than that of 7075.

The load history investigated consisted of the MINITWIST spectrum. MINITWIST is a shortened version of the standardized TWIST fatigue load spectrum (2). It is a variable amplitude loading that simulates the operational loads imposed on transport aircraft wings. MINITWIST is composed of ten different flight types in blocks of 4000 flights. Each block of 4000 flights consists of 62,442 cycles. The first 100 cycles and exceedence curves for 40,000 flights of TWIST and MINITWIST are shown in Figures 1 and 2, respectively. The mean 1.0 g stress level was set at 46 MPa (6.7 ksi) for the present investigation.

EXPERIMENTAL PROCEDURE

The fatigue crack growth tests were conducted on an electro-hydraulic fatigue machine which employed computer control to administer the MINITWIST loading spectrum and record all data. Details of the hardware and software employed are described in Reference 3. Since the MINITWIST loading spectrum subjects the test specimen to compressive stresses, the fixed-end-single-edge-notch (FESSENT) specimen (Figure 3) was used along with locally manufactured grips for all tests. The grips provided clamped end conditions to prevent buckling during the compressive loads. The stress intensity factor solution for the FESSENT specimen is given in Reference 4.

The specimens were machined locally to the dimensions shown in Figure 3, and the area of anticipated crack growth was polished. Specimens were oriented in both the L-T and T-L direction to study potential anisotropy in crack growth properties. The machined starter notch was sharpened by pressing a single edge razor blade across the notch tip. A 350 ohm strain gage was attached to each side of the specimens to assist in aligning the specimens in the grips so that bending was minimized. A clip gage was inserted in the notch to permit compliance measurements of crack length by the computer controlled data acquisition system.

Five aluminum alloy 2090-T8E41 specimens were tested. The tests were designated LIFE1 T-L, LIFE2 L-T, LIFE3 T-L, LIFE4 T-L and LIFE5 L-T, where LIFE stands for lithium fixed end and the two letter designation (i.e. L-T) defines the rolling direction relative to the crack propagation. The three aluminum alloy 7075-T651 specimens tested were designated ALFE1 L-T, ALFE2 L-T and ALFE3 T-L.

FATIGUE 87

Since there is not an established criterion for the minimum crack length relative to the notch length for fixed-end-single-edge-notch specimens, the criteria for compact tension specimens was adopted as a guideline for precracking (5). All specimens were initially precracked at a constant remote stress amplitude of 69 MPa (10 ksi). The stress ratio was fixed at 0.1 and the test frequency maintained at 10 Hz. Once visible cracks initiated, load was shed under computer control down to a final nominal stress of 62 MPa (9.17 ksi), following the procedure recommended in Ref. 5. In three of the specimens, LIFE1 T-L, LIFE2 L-T, and LIFE3 T-L, the precrack load was fixed at 69 MPa (10 ksi).

Following precracking to an initial crack length (including notch) of 0.56 cm (0.22 inch), the specimens were subjected to the MINITWIST load history. The variable amplitude stresses were applied through an IBM 9000 laboratory computer interfaced with the MTS materials testing machine. The spectrum loads were applied at a cyclic frequency of 2 Hz. Details of the computer controlled test apparatus are given in Reference 3.

The mean 1.0 g load in the MINITWIST spectrum was set at a nominal stress of 46 MPa (6.67 ksi). Note from Figure 1, that the 69 MPa (10 ksi) precrack load, which corresponds to 1.5 g, is exceeded four times in the first 100 cycles of MINITWIST, so that any crack retardation effects resulting from the precrack procedure are quickly eliminated during the variable amplitude testing. Crack lengths were measured both optically by a traveling microscope, and through compliance measurements obtained with the clip gage. Only the optical measurements are reported here. The compliance measurements of crack length generally agreed quite well with the optical measurements for large crack sizes, but exhibited considerable scatter at shorter flaw sizes. This latter variation at small crack sizes, is attributed to the relative stiffness of the FESENT specimen, and the resultant difficulty of accurately measuring compliance changes when the crack length is small.

EXPERIMENTAL RESULTS

Composite fatigue crack growth curves for the eight tests are given in Figure 4. All aluminum alloy 7075-T651 specimens were cycled to fracture, and gave quite consistent results, with the T-L orientation giving a slightly shorter life. Specimen ALFE1 L-T fractured after 105,069 cycles at a peak spectrum load of 115 MPa (16.7 ksi) and a crack length of 2.36 cm (0.93 in.). Specimen ALFE2 L-T fractured after 116,840 cycles at a peak stress of 98.6 MPa (14.3 ksi). The final crack length was not recorded for this specimen. The third 7075-T651 specimen, ALFE3 T-L, fractured after 66,488 cycles, at a peak stress of 63.2 MPa (9.17 ksi) and a final crack length of 2.59 cm (1.018 in.)

The aluminum alloy 2090-T8E41 specimens all exhibited

FATIGUE 87

significantly longer fatigue crack growth lives when compared to the aluminum alloy 7075-T651 specimens as shown in Figure 4. It was observed that in the L-T configured aluminum 2090-T8E41 specimens cracks would bifurcate or split as the crack grew, with one of the bifurcated crack tips finally becoming dominant. The T-L specimens propagated mode I cracks with fewer bifurcations and in a flatter plane than the L-T specimens.

The two aluminum alloy 2090-T8E41 L-T specimens both reached 1.8 million cycles without failure, at which time the test was terminated. LIFE2 L-T grew to a crack length of 12.4 mm (0.488 in) with the crack propagating across and up on one face and across and down on the other face, while LIFE5 L-T only reached a crack length of 5.97 mm (0.235 in.). The difference in crack growth rates could be attributed to a variation in the microstructure. Although strain gage readings were used to aid alignment of the specimen in the grips, bending might have developed in LIFE2 L-T, since the front and back face crack lengths were 12.40 mm (0.488 in.) and 10.97 mm (0.432 in.), respectively. Note that the difference between front and back crack lengths of 1.42 mm (0.056 in.) for this specimen exceeds the 0.025W criterion (0.95 mm or 0.0375 inches) specified in ASTM Test Specification E647-83 for constant amplitude fatigue crack growth, but does satisfy the 0.25B (1.3 mm = .05 in.) criterion for minimum crack length deviation.

Three 2090-T8E41 specimens were tested in the T-L direction. Specimen LIFE1 T-L was cycled for 320,000 cycles with 0.36 mm (0.014 in.) of measured crack growth. The mean load was then increased from 46 MPa (6.67 ksi) to 63.9 MPa (10 ksi), and the specimen fractured after 42,300 additional cycles. Figure 4 only shows the initial crack growth at the original 46 MPa (6.67 ksi) mean load. Specimen LIFE3 T-L fractured after 417,280 cycles. The third T-L specimen, LIFE4 T-L, saw 3 million cycles with only 2.06 mm (0.081 in.) of crack growth. (Figure 4 only shows the first 1.8 million cycles of crack growth for this specimen).

Although there is considerable variation in the crack growth observed for the aluminum-lithium specimens, all demonstrated significantly slower growth rates than the 7075-T651 members. The variation in crack growth observed in the aluminum-lithium material might be due to the tendency for the crack tip to bifurcate. It is suggested that further variable amplitude tests be conducted with this alloy to more completely characterize the crack growth variability. If the MINITWIST load history was employed, it would perhaps be useful to increase the mean stress level in order to provide shorter test times.

ACKNOWLEDGEMENTS

All of the test material was provided by the Aluminum Company of America, along with support for specimen preparation. The support and suggestions of Mr. R.L. Brazill are gratefully acknowledged.

FATIGUE 87

J.S. Thomas, Jr. and J.C. Van Sice (Aeronautical Engineering Officers in the United States Coast Guard) conducted the research described here while on an educational assignment to Purdue University.

REFERENCES

- [1] Private correspondence with R.L. Brazill, Aluminum Company of America.
- [2] Lowak, J.B., deJong, J.B., Franz, J., and Shultz, D., "MINITWIST: A Shortened Version of TWIST," NLR-MP-79018-U, National Aerospace Laboratory NLR, The Netherlands, 1979.
- [3] Morrison, A.S., "Development of Software for the Control of Spectrum Loading Fatigue Tests," MS Thesis, Purdue University, 1985.
- [4] Rooke, D.P., and Cartwright, D.J., "Compendium of Stress Intensity Factors," Her Majesty's Stationary Office, London, 1976.
- [5] "Standard Test Method for Constant-Load-Amplitude Fatigue Crack Growth Rates Above 10^{-8} m/cycle," ASTM E647-83, American Society for Testing and Materials, June 1983.

MINITWIST

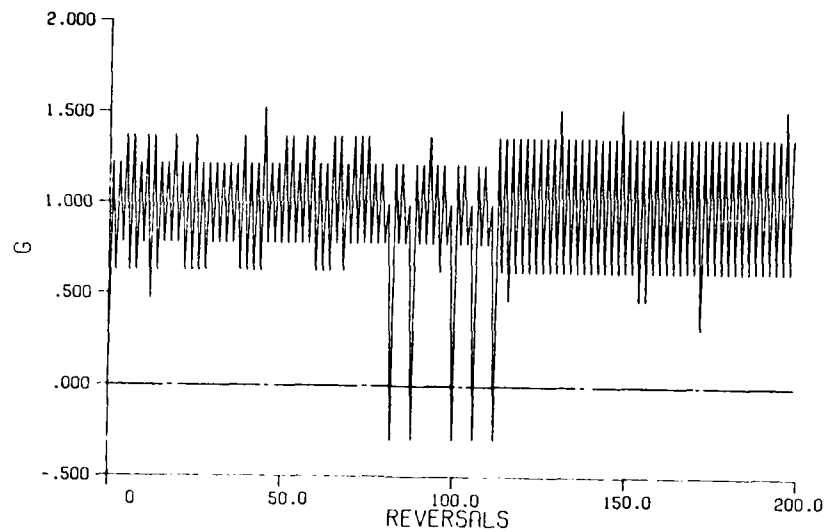


Figure 1 First 200 reversals of MINITWIST load spectrum expressed in g levels.

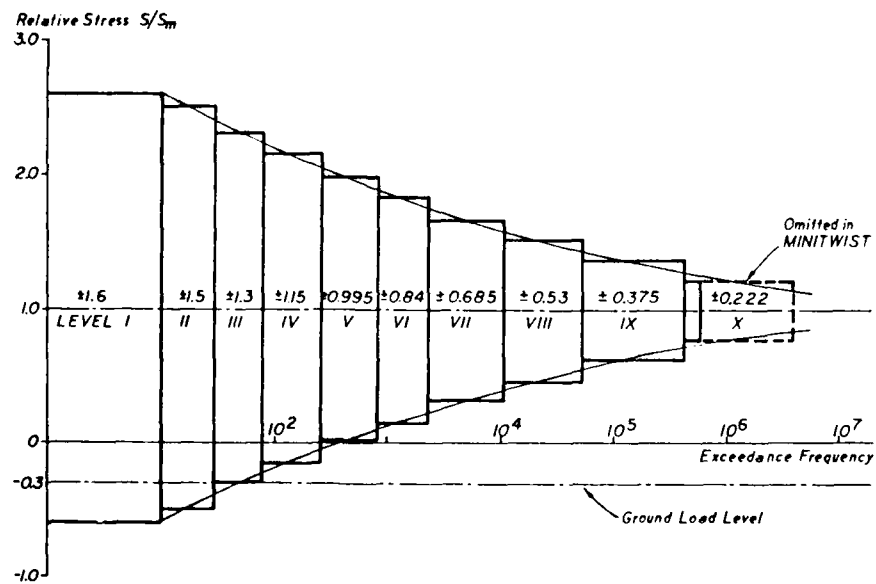


Figure 2 Load exceedance curve for 40,000 flights of TWIST and MINITWIST load spectra.

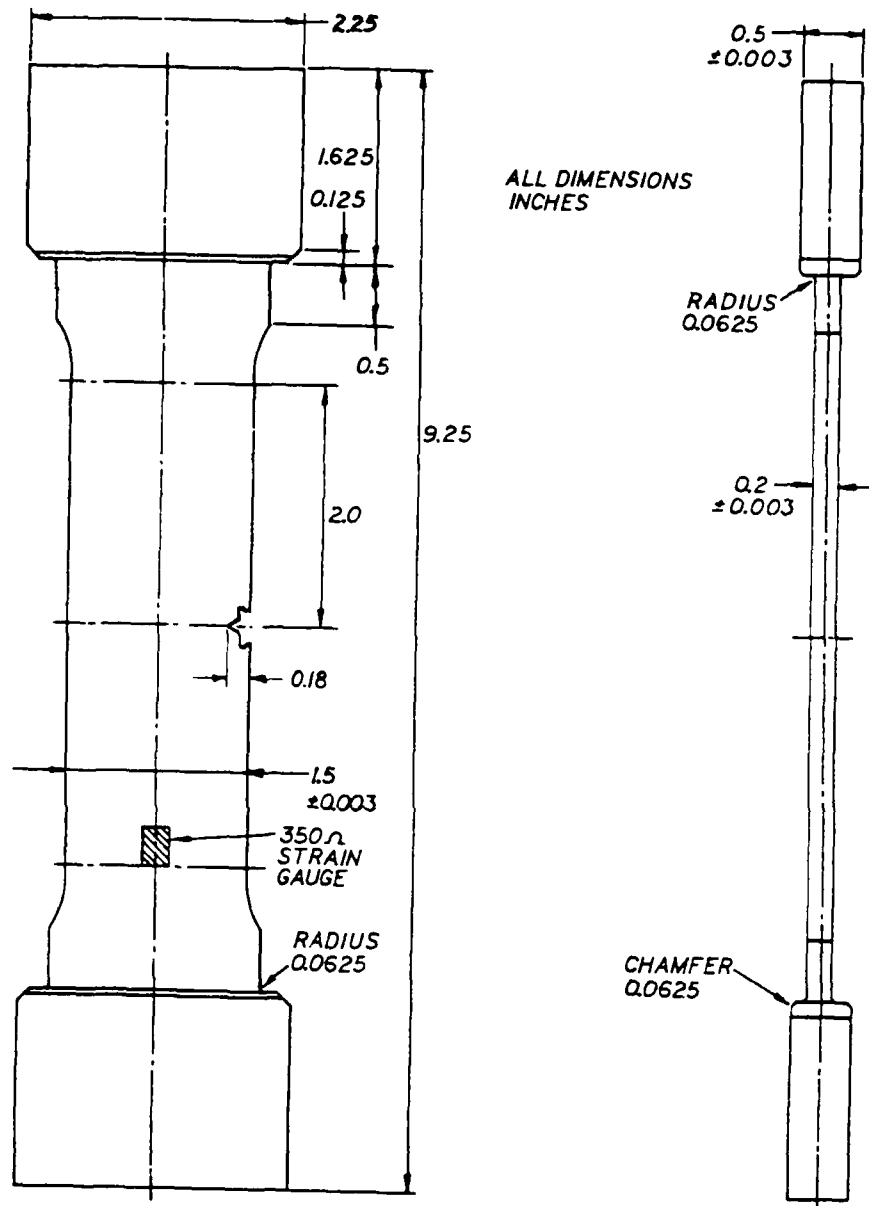


Figure 3 Fixed-end-single-edge-notch test specimen.

FATIGUE 87

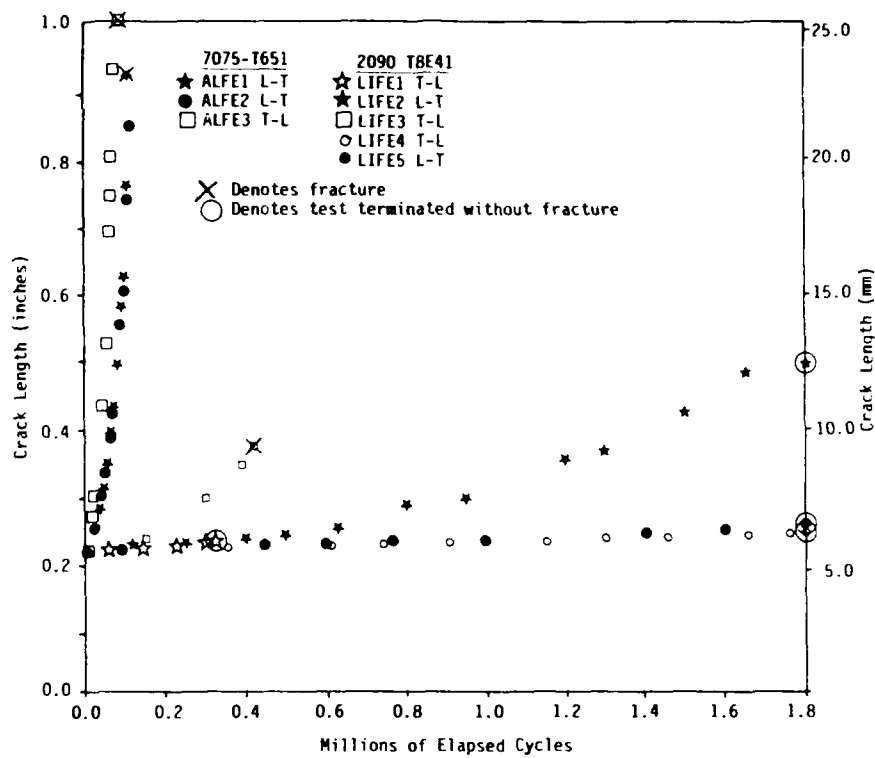


Figure 4 Composite plot of fatigue crack growth curves obtained for MINITWIST load history in 7075-T651 and 2090-T8E41 test specimens.

FATIGUE 87

CRACK GROWTH PREDICTION IN 3D STRUCTURES UNDER AERONAUTICAL-TYPE SPECTRUM LOADINGS

R. Labourdette, G. Baudin, M. Robert*

SYNOPSIS

A model describing crack growth in 3D structures submitted to aeronautical spectrum loadings is presented. Examples of predictions for 7075-T7351 alloy bending specimens undergoing FALSTAFF and mini TWIST sequences are compared with experiment. The general accuracy of predictions appears reasonably good since almost all points fall in the "classical" (± 2 ; $\times 2$) area. Suggested improvements can result from a better description of plastic behavior.

INTRODUCTION

Since the original works of Paris (1), a lot of attention has been paid to the mechanical description of the stable crack growth process.

For two-dimensional structures (plates) under spectrum loadings, several models have been proposed in order to express the crack growth rate in presence of "load-history" effects ; in a more or less chronological order, we can mention, for instance, the works of Wheeler (2), Willenborg et al. (3), Baudin (4), Newman (5), De Koning (6), Chang et al. (7).

The work presented here is an extension of (4), coupled to a description of crack growth in 3D structures submitted to constant amplitude loadings, (Labourdette and Baudin (8)) in order to predict the behavior of crack fronts in 3D structures under spectrum loadings.

* Office National d'Etudes et de Recherches Aérospatiales
Châtillon-Sous-Bagneux, France

POSITION OF THE PROBLEM

In a 3D structure submitted to spectrum loadings, the prediction of crack growth must answer two questions :

- i) - at each point of the crack front, what will be the orientation of the surface of separation during the next cycle of loading ?
- ii) - what increment of crack length will occur in the surface ?

In our work, we restricted our attention to the second point, since some interesting results have already been provided for the first (Hussain et al. (9), Boissenot and Dubois (10)).

DERIVATION OF A CRACK GROWTH MODELBasic Hypothesis

- i) - The description of the cracked growth process is made in the frame of the thermodynamics of irreversible processes.
- ii) - Following N.Q. Son (11), we assume the normality rule between the crack growth rate and the associated thermodynamical force.
- iii) - Following Elber (12), we assume the existence of an effective energy release rate, which is the driving force of the crack.

Crack Growth rate equation

Let us consider the crack body of figure 1. The definition of the virtual power of external forces, according to Germain (13) writes :

$$\mathcal{P} = - \int_{S_{\Sigma}} F(R) \cdot \dot{U}(R) \cdot dS_{\Sigma} \quad (1)$$

We can write $\dot{U}(R)$ as :

$$\dot{U}(R) = \int_{\mathcal{C}} h(M, R) \cdot \dot{v}(M) \cdot dM \quad (2)$$

which gives, finally :

$$\mathcal{P} = - \int_{\mathcal{C}} Q(M) \cdot \dot{v}(M) \cdot dM \quad (3)$$

The results of Atkinson and Eshelby (14) permit to identify :

$$Q(M) = G_{\text{eff}}(M) \quad (4)$$

The use of hypothesis ii) allows to express :

$$\dot{v}(M) = \frac{\partial \Omega}{\partial G_{\text{eff}}} \quad (5)$$

It has been shown (8) that a quadratic potential $\Omega(G_{\text{eff}})$ leads to reasonably accurate results for C.A loadings. Then :

$$\dot{v}(M) = C \cdot G_{\text{eff}}(M) \quad (6)$$

$$\text{with : } \sqrt{G_{\text{eff}}}(M) = \sqrt{G(M)} - \sqrt{G_{\text{th}}}(M) \quad (7)$$

In eq. (7), $G_{\text{th}}(M)$ is a crack growth threshold, depending on the load history, such that :

$$\begin{aligned} \dot{v}(M) &= 0 & \text{if } G_{\text{th}}(M) > G(M) \\ \dot{v}(M) &= C \cdot G_{\text{eff}}(M) & \text{if } G_{\text{th}}(M) < G(M) \end{aligned}$$

At a given instant of a crack growth process, G_{th} is the value of G (see fig. (2)), corresponding to a zero crack growth rate in a subsequent loading.

It has recently been shown by Anquez (15) that this threshold is closely correlated with the crack opening phenomenon.

We adopt here the evolution equation for G_{th} which was proposed in (4), with a redefinition of the plastic zone size.

Then :

$$\sqrt{G_{\text{th}}}(M) = \sqrt{G_{\text{ME}}}(M) \{ \alpha \cdot f_1(U(M)) + (1 - \alpha f_2)(U(M)) \} \quad (8)$$

$$U(M) = \frac{K_{\text{mE}}(M)}{K_{\text{ME}}(M)} \quad (9)$$

$$K_{\text{ME}}(M) = \sigma_y [\pi \rho(M)]^{\frac{1}{2}} \quad (10)$$

$K_{\text{mE}}(M)$ is defined by a recurrence process (4)

$$G_{\text{ME}}(M) = \frac{K_{\text{ME}}^2(M)}{E}$$

f_1 and f_2 are intrinsic functions of the material ; for 7075-T7531 they are given fig. (3).

$$\alpha = 1 - \frac{\bar{F}_{\text{MAX}}}{\text{Sup}(F_{\text{MAX}})} \quad (11)$$

Plastic Zone Size

In principle, this parameter should be computed, at each cycle at

4D-A184 045

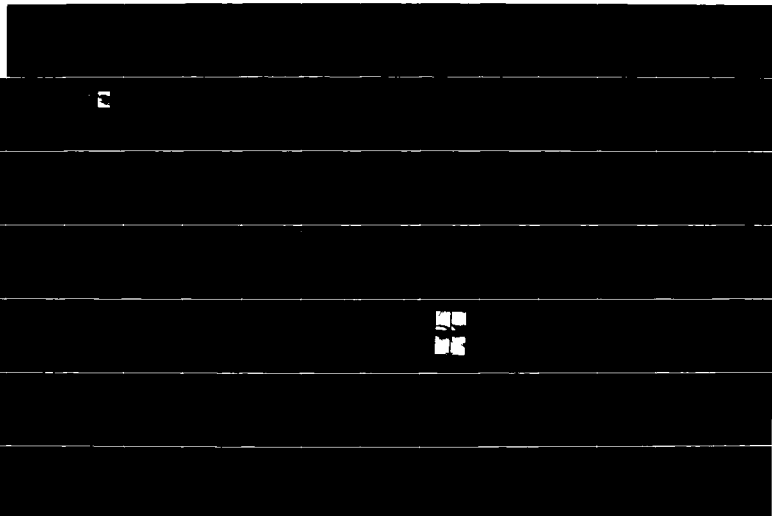
FATIGUE 87 VOLUME 1(U) VIRGINIA UNIV CHARLOTTESVILLE
SCHOOL OF ENGINEERING AND APPLIED SCIENCE
R O RITCHIE ET AL. JUN 87 ARO-24134.1-MS-CF
N00014-87-G-0008

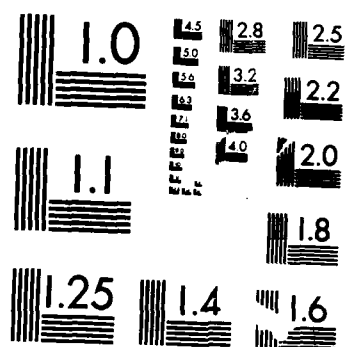
6/7

UNCLASSIFIED

PAG 20/11

NL





MICROCOPY RESOLUTION TEST CHART
NATIONAL BUREAU OF STANDARDS-1963-A

FATIGUE 87

any point M on the crack front ; the complete 3D elastoplastic-cyclic analysis of a cracked body is, at the present time, beyond our reach, at least on an economical point of view.

Consequently we propose the practical rule as follows :

- at a free surface (plane stress conditions)

$$\rho(M) = \rho_c = \frac{1}{\pi} \frac{G(M)}{\sigma_y^2} E \quad (12)$$

- at inner points, sufficiently far from a free surface we assume plane strain and :

$$\rho(M) = \rho_D = \frac{1}{6\pi} \frac{G(M)}{\sigma_y^2} \frac{E}{1-\nu^2} \quad (13)$$

The ratio of 6 between ρ_c and ρ_D is consistent with the results of (15).

- The transition between surface and inner points can assume, for instance, the same shape as the evolution of the Mises' criterion.

We found that the practical rule :

$$\begin{aligned} \rho(M) &= \rho_c - d(M) \text{ if } 0 \leq d(M) \leq \frac{5}{6} \rho_c \\ \rho(M) &= \rho_D \quad \text{if } d > \frac{5}{6} \rho_c \end{aligned}$$

gives results very similar to those obtained with the previous assumption (see figure (5) for definition of d).

PREDICTIONS AND COMPARISONS WITH TESTS

Identification of the Model

The constant C of eq. (6) has been determined for the material 7075-T7351 from constant amplitude tensile test on a prismatic bar (figure (6.a)).

The functions f_1 and f_2 were derived from bending tests on our classical 2D specimen ; the complete procedure for derivation of f_1 and f_2 is given in (4).

Figure (5) shows a typical front obtained in tests.

The classical perturbation technique of Parks (16), and Hellen (17) is used ; one quarter of the specimen (from symmetry

FATIGUE 87

reasons) is meshed with 782 nodes (2346 d.o.f) corresponding to 588 eight-nodes hexaedrons.

In order to avoid numerous computations (theoretically one by cycle) we use also the extrapolation technique of De Koning and Lof (18).

Tests

"Four points" bending tests were carried out using FALSTAFF or mini TWIST standard spectrum loadings. The cross section of the specimen is presented on fig. 4.b.

Due to the fact that no upward force could be applied, the previous spectra were truncated so that only tensile stresses were applied in the cracked region. FALSTAFF was truncated at level 8 ; mini TWIST was truncated at level 0.1 of σ_{mean} (in addition we also truncated at $2.3 \sigma_{\text{mean}}$ for high values).

Measurements

At predetermined numbers of flights, the loading was interrupted and coloured ink was injected in the crack. At the end of the test, the specimen was broken and we were able to measure the crack extension along each reference radius as a function of the number of flights.

RESULTS

Comparison was made between the "experimental" numbers of flights necessary to reach a certain crack extension and the predicted ones.

Three different mean levels were used for the mini TWIST case, namely 70, 80 and 100 MPa.

This comparison induces the following remarks (see figs. (6) and (7)) :

- almost all points fall in the $(x 2 ; \div 2)$ band, which means that the prediction is reasonably accurate,
- the "scatter" due to the lack of symmetry does not significantly appear in the discrepancy between test and prediction,
- for the mini TWIST case, predictions are on the unconservative side for points 1 and 9 (free surfaces) and conservative for the inner point 5.

FATIGUE 87

CONCLUSIONS

The predictions presented here are, roughly speaking, of the same degree of accuracy than those obtained in 2D structures under the same loadings.

The necessary improvements can be reached, in our opinion, only by a better description of the elastoplastic (viscoplastic) cyclic behavior of the material. As already pointed out, the main difficulty, in doing this lies more with the capabilities of today computers than with the state-of-the-art in modelling such behaviors, since models like those proposed by Chaboche (19) are sufficiently accurate to take into account very complex phenomena like cyclic hardening or softening, non linear kinematic hardening, recovery etc...

REFERENCES

- (1) Paris, P.C. and Erdogan, F., Trans. ASME, ser. D, J. Bas. Eng., Vol. 85, N° 4, 1963.
- (2) Wheeler, O.E., "Crack Growth under Spectrum Loading", General Dynamics Report F2M 5602, 1970.
- (3) Willenborg, J.D., Engle, R.M. and Wood, H.A., "A Crack Growth Retardation Model using an Effective Stress Concept", AFFDL-TM-FBR-71-1, 1971.
- (4) Baudin, G. and Robert, M., Proc. 5th Europ. Conf. on Fracture - ECF 5, 1984, pp. 754-779.
- (5) Newman, J.C., Jr., ASTM-STP 748, 1981, pp. 193-114.
- (6) De Koning, A.V., 11th ICAF Symposium Proc., 1981, pp. 2.6/1-43.
- (7) Chang, J.B., Szamosi, M. and Liu, K.W., ASTM-STP 748, 1981, pp. 115-126.
- (8) Labourdette, R. and Baudin, G., Proc. of 5th Int. Conf. on Fracture ICF 5, 1981, pp. 687-702.
- (9) Hussain, M.A., Pu, S.L. and Underwood, G., ASTM-STP 560, 1974.
- (10) Boissenot, J.M. and Dubois, M., Jl. Mec. Appl., Vol. 1, 2, 1977, pp. 45-52.
- (11) Son, N.Q., Jl. Mec., Vol. 19, 2, 1980, pp. 363-386.
- (12) Elber, W., ASTM-STP 486, 1971, pp. 230-242.

FATIGUE 87

- (13) Germain, P., Cours de Mécanique des Milieux Continus, Masson, Paris, 1973.
- (14) Atkinson, C. and Eshelby, J.D., Int. Jl. Fract., Vol. 4, 1968.
- (15) Anquez, L., Proc. Int. Symp. On Fatigue Crack Closure, Charleston S.C, 1986 - to be published.
- (16) Parks, D.M., Int. Jl. Fract. Vol. 10, 4, 1971, pp. 58-65.
- (17) Hellen, T.K., Int. Jl. Num. Meth. Eng., Vol. 9, 1975, pp. 122-130.
- (18) De Koning, A.U. and Lof, C.J., NLR Memorandum SC-82-016U, 1982.
- (19) Chaboche, J.L. et al., ONERA TP 1986-13, 1986.

LIST OF SYMBOLS

S_{Σ}	: external surface of the cracked body (m^2)
\mathcal{C}	: crack front
R	: point on S_{Σ}
M	: point on \mathcal{C}
$F(R)$: external force density ($N.m^{-2}$)
$\dot{U}(R)$: displacement rate ($m.s^{-1}$)
$\dot{V}(M)$: crack growth rate (m per cycle)
$h(M,R)$: operator of influence (Hz)
$Q(M)$	} : energy release rate ($N.m^{-1}$)
$G(M)$	
$G_{eff}(M)$: effective energy release ($N.m^{-1}$)
$G_{th}(M)$: threshold energy release rate ($N.m^{-1}$)
α	: scalar parameter attached to the loading sequence
K_{ME}, K_{mE}	: stress intensity factors ($N.m^{-3/2}$)
ρ	: plastic zone size (m)

FATIGUE 87

E	: Young's modulus ($N.m^{-2}$)
ν	: Poisson ratio
σ_y	: Yield stress ($N.m^{-2}$)
d	: distance of inner point to free surface (m)
F_{MAX}	: maximum of force during one cycle (N)
\bar{F}_{MAX}	: mean value of F_{MAX} during a loading sequence (N)

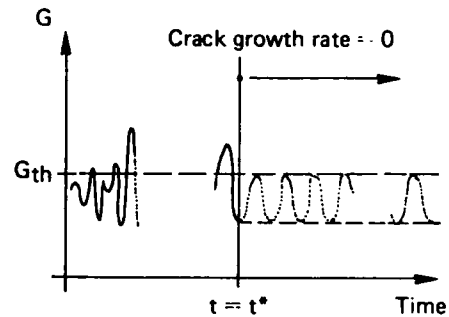
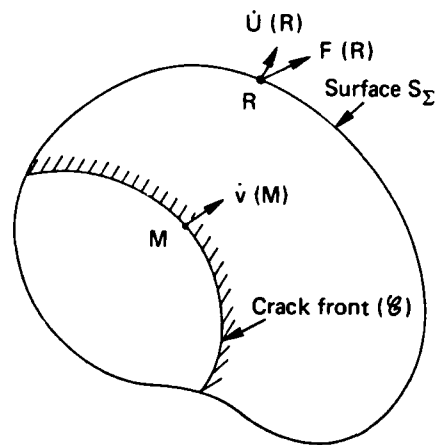


Figure 1 3D cracked body and notations

Figure 2 Definition of crack growth threshold

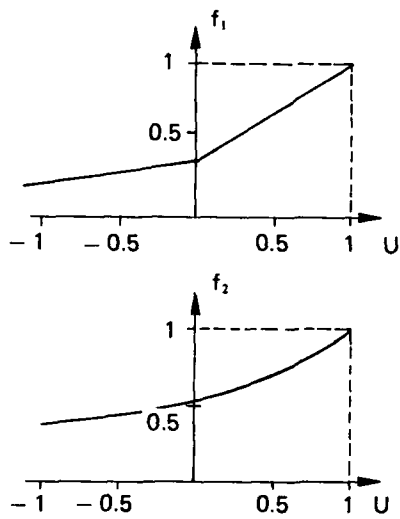


Figure 3 Functions $f_1(U)$ and $f_2(U)$ for 7075-T7351 alloy

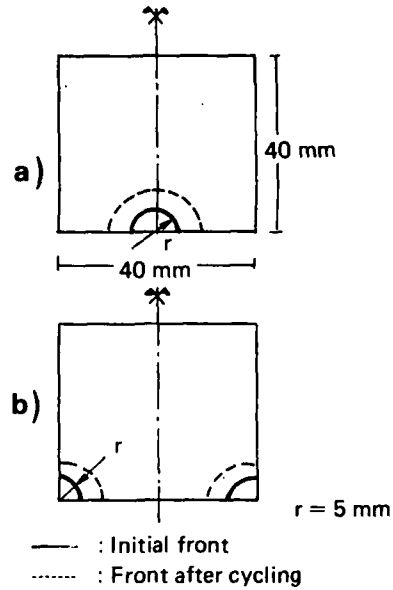


Figure 4 Tensile specimen (a) ; bending specimen (b)

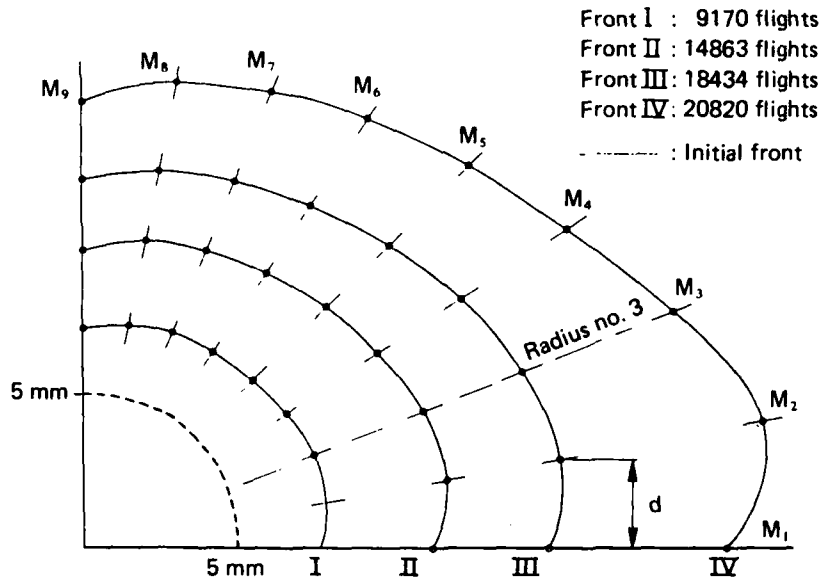


Figure 5 Examples of measured crack fronts

FATIGUE 87

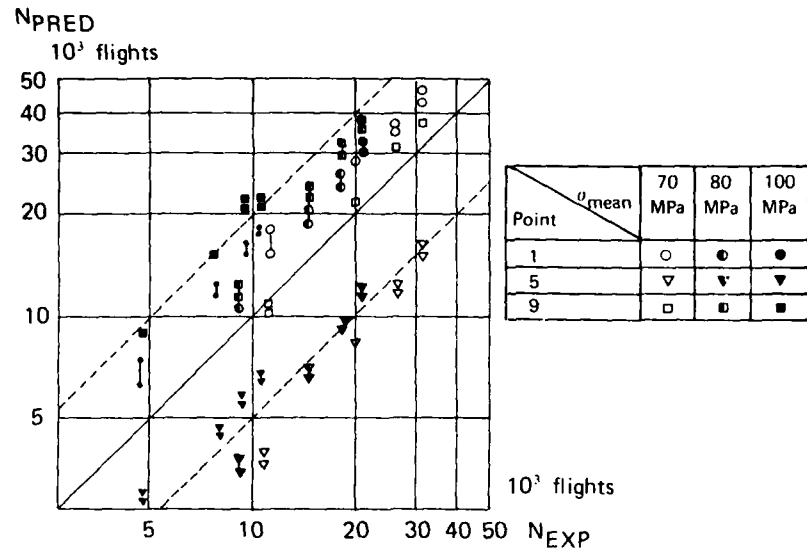


Figure 6 Comparisons tests-pre-dictions : mini TWIST loading

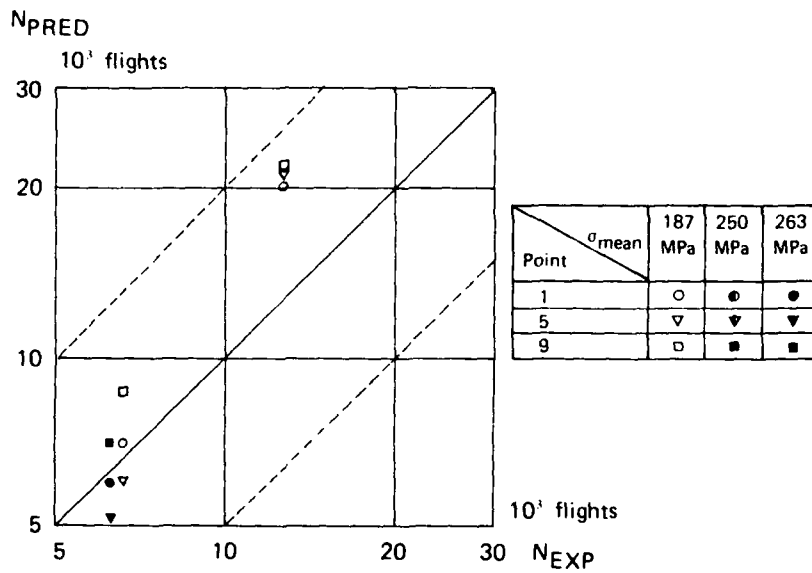


Figure 7 Comparisons tests-pre-dictions : FALSTAFF loading

FATIGUE 87

FATIGUE OF 30CrMnSiNi2A NOTCHED SPECIMENS UNDER SPECTRUM LOADING

Y.S.Wu*, J.H.Huan* and A.H.Zhou*

The fatigue tests of 30CrMnSiNi2A notched specimens were performed under a maneuver loading spectrum. The stress-strain behavior at the notch under the load spectrum was studied. The fatigue crack initiation and growth was observed microscopically and macroscopically. The fatigue crack initiation life was estimated by a simplified local stress-strain method. The fatigue crack growth life was estimated by the fracture mechanics method. The estimated results and the test results were compared. The size of initiation crack was determined based on the size of fatigue crack initiation zone in the fracture surface of the specimen.

INTRODUCTION

30CrMnSiNi2A is a high strength alloy steel. Many structure elements in aircraft, such as wing's main beam, are made of this material. These elements are subjected to service loading, such as maneuver loading. Some cracks led to fatigue failure were found in these elements. It is a important problem how to estimate the fatigue life of these structure elements under service loading. From an engineering point of view, the most accepted approach is the local stress-strain method for estimating the fatigue crack initiation life and the fracture mechanics method for estimating the fatigue crack growth life. In order to check these methods, the fatigue tests of 30CrMnSiNi2A notched specimens were performed under a maneuver load spectrum simulating the service loading. The fatigue life was estimated by these methods. The determination of the initiation crack which is a important problem for estimating the fatigue crack initiation life and the fatigue crack growth life was also studied.

* Institute of Mechanics, Chinese Academy of Sciences, Beijing, China.

FATIGUE 87

MATERIAL'S STATIC AND FATIGUE PROPERTIES

The material's static properties are given in Table. 1.

TABLE 1 - 30CrMnSiNi2A Static Properties (1)

E(Mpa)	σ_u (Mpa)	σ_y (Mpa)	δ_5 (%)	K(Mpa)	n
199920	1654	1307	13.2	2354	.091

The material's strain fatigue properties are given in Table.2.

TABLE 2 - 30CrMnSiNi2A Strain Fatigue Properties (1)

σ'_f (Mpa)	b	ϵ'_f	c	K' (Mpa)	n'
2771	-0.10	1.21	-0.78	2646	0.13

The material's fatigue crack growth properties and the fracture toughness are given in Table.3.

TABLE 3 - 30CrMnSiNi2A Fatigue Crack Growth Properties and Fracture Toughness (2)

$C(\times 10^{-10})$	p	q	t	KIc (Mpa \sqrt{m})
0.329	3.46	0.56	0.13	97.68

THE FATIGUE TESTS OF 30CrMnSiNi2A NOTCHED SPECIMENS UNDER THE SPECTRUM LOADING

Specimen and Fatigue Test Machine

The plate specimens with a central hole were adopted. The specimen's width was 22 mm and the thickness was 8 mm. The diameter of the hole was 6 mm. The theoretical stress concentration Kt was equal to 2.57. Testing was conducted on a 25T MTS hydraulic-servo test system with the computer control. The test frequency was 10HZ.

Load Spectrum

The load spectrum was a program block load spectrum simulating maneuver flight loading. It was composed of 47 levels, as shown in Figure. 1. There were 8653 cycles in a block. The tension loads prevail for this spectrum. The stress ratio R was bigger than -0.14. The detail of the load spectrum refer to (3). Testing was beginning at maximum loading and ending at maximum loading for every cyclic block in order to be easy to observe the crack.

Strain Measurement

The strain in the neighbourhood of the hole was measured by the "Moire" gauge with 100 line/mm and 0.5 x 0.5 mm strain gauge.

FATIGUE 87

A piece of "Moire" gauge was stuck on the one surface of the specimen. Two pieces of strain gauge were stuck on the another surface near the hole. The strain measurement was performed at the beginning of the fatigue tests and the ending of every cyclic blocks. No obvious cyclic hardening or softing of the material near the hole was found during the tests.

Measurement of Crack Length

The crack length was measured by a microscope (x30). The fatigue crack about length 0.2 mm could be observed by the microscope. After fatigue crack about length 0.2 mm was initiated at the edge of the hole, fatigue crack growth became very fast, as shown in Figure. 2.

Observation of Fracture Surface

There were four zones in the fracture surface of the specimen: the fatigue crack initiation zone, the shell-like stripes zone, the thumb-like pop-in zone and the shear-lip fracture zone, as shown in Figure.3. The width of the four zones were 0.2-0.5mm, 2.2-2.6mm, 2.4-2.7mm and 2.4-2.6mm, respectively. About 90% of the fatigue life spent in the fatigue crack initiation zone. The corresponding cyclic blocks were about 33-45 blocks. About 10% of the fatigue life spent in the shell-like stripes zone. The corresponding cyclic blocks were about 3-5 blocks. The shell-like stripes observed in the electro-microscope are shown in Figure.4. The stripes may be caused by the overloads in the program block loading spectrum. The unstable crack growth was occurred in the thumb-like pop-in zone and the final fracture was occurred in the shear-lip fracture zone. The crack length at the beginning of unstable crack growth was about 3mm.

FATIGUE CRACK INITIATION LIFE ESTIMATION

T.H.Topper (4) have been shown that Neuber's formulation (5) can be applied to the notch fatigue problem. In this investigation, the nominal stress and strain was elastic, the relation between the local stress-strain range and the nominal stress range is as following:

$$E\Delta\sigma\Delta\epsilon = K_f\Delta S^2 \quad (1)$$

Based on Peterson's proposal (6)

$$K_f = K_t / (1 - a' / r) \quad (2)$$

a' was taken as 0.0635 mm and K_f was equal to 2.54.

Based on the results of the strain measurement, the variation of the local stress-strain is illustrated in Figure. 5. During the load variated from 0 to P_{max} , the stress-strain variated along the

FATIGUE 87

monotonic loading stress-strain curve OA

$$\Delta \epsilon = \Delta \sigma / E + (\Delta \sigma / K)^{1/n} \quad (3)$$

Afterwards, the stress-strain varied along the elastic unloading line AB.

$$\Delta \epsilon = \Delta \sigma / E \quad (4)$$

Substituting (4) into (1), the formulation (1) become

$$\Delta \sigma^2 = K f \Delta S^2 \quad (5)$$

In this case, the local stress-strain analysis become very simple. During the load varied from 0 to Pmax, the variation of the stress-strain was calculated using formulation (1) and (3). Thereafter the variation of the stress-strain was calculated using formulation (4) and (5). The damage of every stress-strain cycles was calculated based on the material strain-life curve and the effect of average stress on fatigue was considered.

$$\epsilon_a = \frac{\sigma'_f - \sigma_a}{E} (2Nf)^b + \epsilon'_f (2Nf)^c \quad (6)$$

Nf was calculated based on ϵ_a using formulation (6). The damage per cycle Di and the cumulative damage D of a block are as following:

$$D_i = 1/Nf \quad (7)$$

$$D = \sum_{i=1}^k D_i \quad (8)$$

Where k is number of cycles in a block. The blocks to failure (BTF) are given as follow:

$$BTF = 1/D \quad (9)$$

The estimated fatigue crack initiation life and the test results are given in Table. 4.

FATIGUE CRACK GROWTH LIFE ESTIMATION

The fatigue crack growth life was calculated using Walker formulation (7):

$$da/dn = C [K_{max}(1-R)^q]^P, R \geq 0 \quad (10)$$

$$da/dn = C [K_{max}(1-R)^t]^P, R < 0 \quad (11)$$

The fatigue crack growth was calculated on a cycle by cycle basis.

FATIGUE 87

$$a = a_0 + \sum \Delta a \quad (12)$$

Δa was calculated based on the K_{max} and R of every cycles. The critical crack size obtained from the material's fracture toughness K_{Ic} was 3 mm. The estimated fatigue crack growth life from 0.2 mm to 3 mm was about 2.5 cyclic block, close to the test results, as shown in Table. 4 and Figure. 6.

TABLE 4 - The Estimated Fatigue Life Results and The Test Results

	Initiation Life (0.2mm)	Growth Life (0.2mm-3mm)
Estimated results (Blocks)	41	2.5
Test Results (Blocks)	33,36,44,45	3,3,6,4

CONCLUSION

1. For the 30CrMnSiNi2A notched specimens subjected to spectrum loading, the fatigue crack initiation life is important part of the total fatigue life. As soon as fatigue crack of length 0.2 mm was initiated at the hole edge, fatigue crack would grow very quickly.
2. The width of the fatigue crack initiation zone is about 0.2-0.5 mm. The fatigue crack initiation life estimated by the local stress-strain method was agreement with the fatigue life spent in the fatigue crack initiation zone.
3. The fatigue crack growth life estimated by Warker formulation and on a cycle by cycle basis was close to the test results, but a little less than the test results.

SYMBOLS USED

E = elastic modulus
 $\Delta\sigma$ = local stress range
 $\Delta\epsilon$ = local strain range
 ΔS = nominal stress range
 σ_0 = average stress
 R = stress ratio
 K_t = theoretical stress concentration factor
 K_f = fatigue strength reduction factor
 a' = the material constant in Peterson formulation
 r = the radius of the hole
 a_0 = initiation crack length
 t, q, p = the material constants in Walker formulation

FATIGUE 87

REFERENCES

- (1) H.Ouyang and B.C.Gou, "LC4-CS and 30CrMnSiNi2A Strain Fatigue Properties", The Second National Conference of Fatigue, E-Mai, China, Sep.8 - 12, 1984.
- (2) W.Zhao, C.F.Ding, M.D.Gu and M.G.Yan, *Acta Aeronautica Et Astronautica Sinica*, No.6, 1985, pp. 602-609.
- (3) Y.S.Wu, X.C.Jiang, S.Y.Xi and H.Li, *Acta Mechanica Solida Sinica*, No.2, 1985, pp. 181-194.
- (4) T.H.Topper, R.M.Wetzel and JoDean Morrow, *J. of Materials*, 1969, pp.200 - 209.
- (5) H.Neuber, *J. of Applied Mechanics*, Vol.8, 1961, pp. 544 - 550.
- (6) R.E.Peterson, "Notch - Sensitivity," *Metal Fatigue, Sines and Waisman*, eds., McGraw-Hill, New York, 1959, pp. 293 - 306.
- (7) K.Walker, ASTM STP 462, 1970.

FATIGUE 87

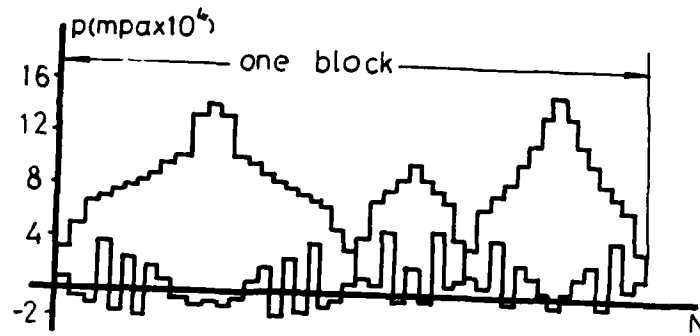


Figure 1 The Program Block Fatigue Loading Spectrum

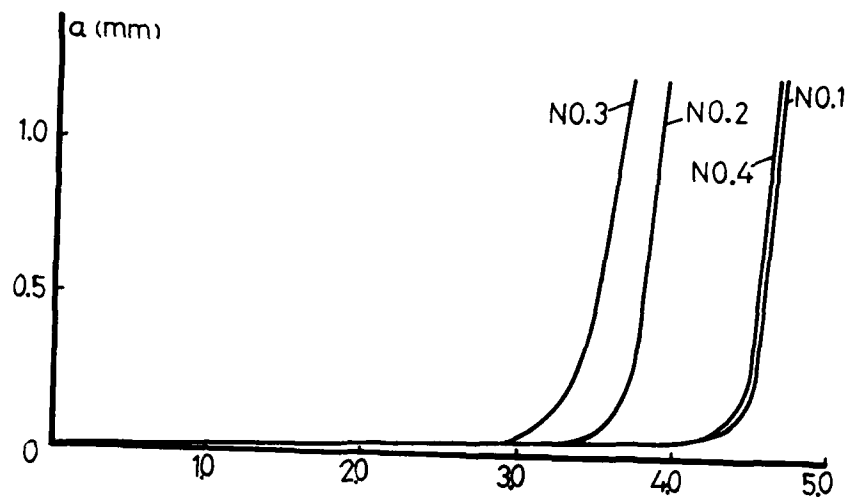
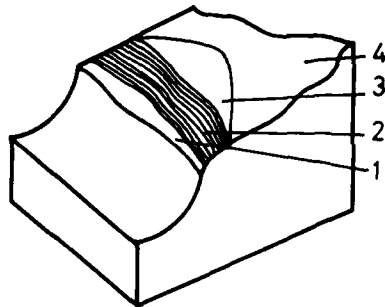


Figure 2 Fatigue Crack Growth Curve

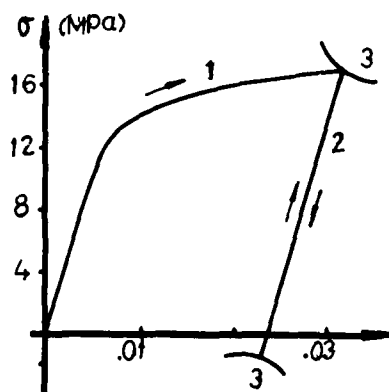


- 1.Fatigue Crack Initiation Zone
- 2.Shell-Like Stripes Zone
- 3.Thumb-Like Pop-in Zone
- 4.Shear-Lip Fracture Zone

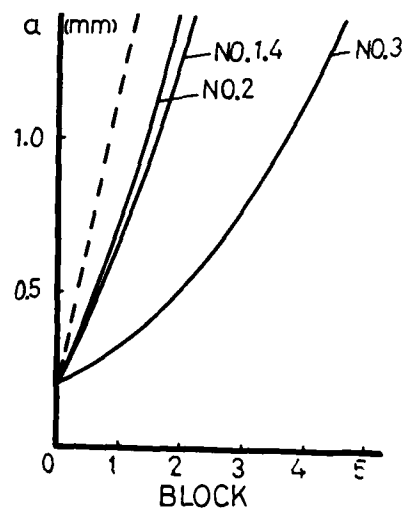


Figure 3 The Specimen's Fracture Surface

Figure 4 Shell-Like Stripes under Electro-Microscope



- 1.Monotonic Stress-Strain Curve
- 2.Elastic Unloading Curve
- 3.Neuber Curve



- Estimated Results
 ——— Test Results

Figure 5 Local Stress-Strain Analysis

Figure 6 Fatigue Crack Growth

THE HOW AND WHY OF VARIABLE AMPLITUDE TESTING

W. SCHÜTZ* AND P. HEULER*

Fatigue life prediction by experiment, that is variable amplitude testing, is becoming more and more widespread in industry. The many engineering decisions necessary before a useful variable amplitude test can be carried out are explained in detail, such as

- measurement of the stress time history in service
- which counting procedure to use and why
- scatter of measured stress spectra
- manipulation of measured stress spectra
- reconstitution (synthesis) of the test spectrum as a basis for a realistic variable amplitude test sequence
- predicted fatigue life under this sequence etc.

INTRODUCTION

In recent years the experimental determination of fatigue strength or life under variable amplitudes has become an important topic for industry, as can be judged from the large number of relevant papers. One of the reasons for this is that it is not possible - despite many claims in the literature - to predict this fatigue life reliably enough by calculation, i.e. by using a damage accumulation model (5).

However, outside of the aircraft industry very little has been published on how to carry out the actual test itself. As soon as one leaves the constant amplitude test - which is completely defined by two numbers, i.e. stress amplitude and mean stress - in principle an infinite number of different stress time histories are possible, even for the same spectrum shape. Many of them have been employed, often quite haphazardly and therefore with more or less useless results.

* Department of Fatigue and Fracture Mechanics, Industrieanlagen-Betriebsgesellschaft mbH, Ottobrunn

OBJECTIVES OF VARIABLE AMPLITUDE TESTS

The primary objective from Gassner's block programme test (1) onward was to obtain allowable stresses or safe fatigue lives. The variable amplitude (v.a.) test therefore is used for experimental fatigue life prediction mainly in industrial applications.

In addition it is used to investigate processes for improving fatigue life, like shot peening or surface rolling, and to compare new materials. A number of examples from the literature have shown that the effect of such processes on fatigue life under variable amplitude loading can only be judged correctly from variable amplitude tests. SN-tests can even give qualitatively wrong answers (2, 3) or, in complex components, different failure locations (4).

Last, but not least, variable amplitude tests must be used if fatigue life prediction models are to be checked (5, 6, 7). Without such checks, employing realistic stress sequences, fatigue life prediction models are useless.

HOW TO PERFORM A VARIABLE AMPLITUDE TEST

Such a test looks deceptively simple - simulate what happens in service - but only at first glance. Besides the question of what actually happens in service, in addition a large number of engineering decisions have to be taken before a meaningful v.a. test can be carried out. Most of them are shown in Fig. 1.

If at all possible, the stress time history should be measured in service. It must then be evaluated (or counted) statistically for at least two reasons:

- The measurement period will usually not have been long enough to be used directly in test and the measured stress time history therefore has to be expanded (extrapolated), see below. This cannot be done directly, it is only possible via the result of the counting procedure, the stress spectrum.
- The stress spectrum is also needed for comparison with other, previously determined spectra. Only in this way is it possible to accumulate generalised data for load assumptions, standards, building codes and so on, and to recognise if the service loads are, for example, more severe than assumed in the design phase.

There are many counting procedures available, which in the general case result in as many different spectra from the same stress time history. The "Rainflow" procedure, which was developed at about the same time in Japan (8) and in the Netherlands by the NLR (who called it "range-pair-range") (9) is considered the optimum counting procedure, because it counts the stress ranges and the associated mean stresses correctly. Some authors (10) claim that a Rainflow count cannot be extrapolated, and therefore is useless for industrial applications. However, this is not correct; for details on one extrapolation procedure see (11), but others, simpler ones than in (11) can be employed.

The "range-pair" counting method counts nearly identical ranges, without regard to the associated mean stress. Some experts consider both counting procedures to be equal. However, Goodman diagrams for different materials show that the mean stress sensitivity of some is high, while that of others is low (12); so in the general case, both counting procedures are not equal.

One aspect of the rainflow method needs some further consideration (13): It will always yield as largest range counted the load variation between the lowest trough and the highest peak. Suppose that this lowest trough occurs very early in the load sequence and the highest peak at the end. If the load sequence in question is a very long one, one may ask whether it physically makes sense to combine these "remote" occurrences into one cycle. Specifically, in the case of a growing crack, one can imagine that the peak at the end will be seen by a crack which is very different in size and crack tip condition from the one prevailing at the occurrence of the lowest trough.

In other words, it is advisable to restrict the size of the load history on which the rainflow method is applied at one time. Very long load histories should be split up, and each part counted separately and later on added up again. De Jonge suggests in (13) "one flight" as a reasonable choice of maximum length for the analysis of helicopter rotor loads. By the way, this is a typical example of one of the many engineering decisions mentioned before.

After the counting procedure, the measured stress spectrum is now available, see Fig. 1. However, before it's utilisation in the following steps, it should be considered what has actually been measured:

- Is the measured spectrum representative of actual usage?

FATIGUE 87

- What is the variability of the service stress spectra of nominally identical components?

Both questions actually refer to the most severe problem most industries have to face in v.a. fatigue testing, and in fatigue life prediction by calculation as well. An automobile maker, for example, does not know with any exactness how his products will be driven by customers; some automobile makers therefore try to define the so-called one-percent driver, that is the most severe driver out of one hundred for whom the car must be designed fatigue-wise (14).

In the next step the measured stress spectrum must be "manipulated", see Fig. 1, because in practically all cases the measurement period is too short: Assuming that it contains 10^6 cycles (a very large measuring and evaluation effort, corresponding to about 2000 to 4000 km for automobiles or about 10 weeks continuous measurement time in an oil rig) this is still only about one percent of the required service life of 200 000 to 400 000 km for an automobile or 20 years for the oil rig, corresponding to about 10^8 cycles in both cases.

The obvious solution is to increase the number of the measured stress amplitudes of all sizes by a factor of 100, see Fig. 2. The next question to be solved is what to do with those events with a probability of occurrence of $P < 10^{-6}$, which are not contained in the measured sequence.

There may be an upper physical limit which cannot be exceeded, for example when an automobile suspension coil spring "goes to block". Assuming this happened once during the measurement period of 10^6 cycles, this maximum amplitude occurs one hundred times in 10^8 cycles, but no higher amplitudes occur. If there is no such limit the higher stress amplitudes will have to be added to the service stress spectrum by a meaningful extrapolation procedure like the extreme value method (15). (The truncation dilemma as mentioned in Fig. 2 will be treated below.)

We now have arrived at the service spectrum, see Fig. 1.

In place of stress measurements in service quite often load assumptions have to be used, see Fig. 1, for example when the complete structure is not yet available for measurements, that is in the development phase.

Such load assumptions are usually based, for example in the automobile industry, on previous experience with similar components, especially if many stress measure-

ments have been carried out before and can be generalised. Several building codes also contain stress spectra or at least advice on how to derive them, for example BS 5400 (16) for road bridges.

The service stress spectrum arrived at by the procedures described above is, however, not yet a reasonable test spectrum because it has to be manipulated once more in two respects (Manipulation II in Fig. 1):

First, large but infrequent stress amplitudes may actually prolong fatigue life due to the beneficial residual stresses they cause. Thus, if the test is carried out with too high infrequent stress amplitudes the fatigue life in test will most probably be unconservative, at least for that percentage of the structures which do not see these stress amplitudes in service. So the correct choice of the maximum stress amplitude to be applied in test, the so-called "truncation dilemma" (17) is an important decision. Some experts have suggested that the maximum stress amplitudes in the test spectrum should occur not less than 10 times (18) before failure.

Second, longlife structures, like oil-rigs, ships, trucks, automobiles etc. see about 10^6 cycles during their required life; that is, the service stress spectrum contains 10^6 cycles, too many for an economically feasible fatigue test because at 10 Hz this means 100 days testing time. So the next question is how best to simulate this large number of cycles. The aircraft industry does not have this problem. The 10^7 cycles a commercial aircraft sees during its service life (and more so the 10^6 cycles a tactical aircraft sees) are usually applied in the full scale fatigue test.

10^7 test cycles result in a reasonable test time (10 days at 10 Hz). Figs. 3 and 4 show four solutions utilised in various industries: Using a spectrum with a more severe shape is one option (see Fig. 3, left side) a typical user is the automobile industry. The problem here is how to read across from the test spectrum to the service spectrum, which requires a relative damage accumulation hypothesis, like relative Miner's Rule (19).

10^7 test cycles can also be obtained by omitting small cycles, because this shortens testing time without an increase of the maximum stresses and without a change of spectrum shape, see Fig. 3, right side. Unrealistically high residual stresses and their possible effect on fatigue life in test are thereby avoided. In a typical straight-line spectrum, this reduction of the number of cycles by one order of magnitude means that

FATIGUE 87

all stress amplitudes lower than about 15 % of the maximum amplitude are omitted; usually they are below 50% of the fatigue limit, which has been shown to a reasonable omission criterion (32, 33). Recent German results show that in some cases even two orders of magnitude may be omitted without affecting the result.

If the number of test cycles has to be reduced still further, for example if a low test frequency is thought to be necessary, as in some corrosion fatigue tests, further omission may run into the problem of the "omission dilemma": The stress amplitudes left out may be near or even above the fatigue limit and the resulting fatigue life in test will be different.

"Scaling up" of all stress amplitudes, a further option, applies higher stress amplitudes than occur in service, with the attendant problems mentioned before, see Fig. 4, left side.

Using a more severe test spectrum shape plus higher maximum stresses than occur in service is typically the option the automobile makers utilise when they test their cars on race tracks in order to shorten testing time, see Fig. 4, right side; 5000 to 10000 km on such a race track at high speed by test drivers is supposed to be equivalent to more than 500.000 km as driven by the normal customer. In this case, neither the shape of the test spectrum nor its maximum stress amplitude agree with those of the service stress spectrum and the problems of too high test stresses and of reading across from one spectrum to another are compounded.

Considering the pros and cons of these four options, the author concludes that the omission of small amplitudes is to be preferred.

Most v.a. fatigue tests have a fixed sequence which is repeated after a certain number of cycles. The length of this so-called return period is critical: On one hand it has to be repeated at least several times; otherwise the various stress amplitudes do not occur in their correct percentages. On the other hand a too short return period means that infrequent but high stress amplitudes are not contained in the test sequence, while they do occur in service and will affect fatigue life. That is a kind of "truncation dilemma in reverse". The load spectrum applied in test is thus quite different from that in service.

The effect is shown in Fig. 5. Again assuming a service stress spectrum of 10^6 cycles, a return period of, say 10^4 cycles has to be repeated 10^2 times and a test spectrum will be applied in which all stress am-

plitudes above 50 percent of the maximum stress occurring in service have been truncated; such a test will most certainly not give the correct result.

With respect to the return period length the international literature is full of horrible blunders, the worst example probably being the well known SAE-program (20). The return periods of 1.500 to 4.000 cycles which were used because of computer limitations (21), are just not long enough, as can be seen in Fig. 6: For a fatigue life of 10^6 cycles and a return period of 1.000 cycles the maximum stress amplitude occurs one hundred thousand times and thus is practically a constant amplitude test with this maximum stress amplitude. Moreover, all stresses above 37,5% of the maximum stress are truncated with the attendant consequences discussed above. The SAE program is now being repeated with more reasonable return period lengths. By the way, the fatigue life prediction models developed in this program gave especially unconservative results (21), when employed for predicting the life under a spectrum with a reasonable return period length in which the author was involved (22).

In some cases, the length of the return period can be decided quite simply: Tactical aircraft in peacetime are flown very similarly every year for training purposes. So a logical return period is one year and this was chosen for the "Falstaff" sequence (23).

Anyway, the return period is a very important decision the test engineer has to take, before a meaningful random fatigue test can be performed.

The test spectrum now is available, see Fig. 1. It has to be reconverted into the test stress-time-history for carrying out the v.a. fatigue test, the so-called synthesis or reconstitution. If the original counting procedure was "Rainflow", a Rainflow synthesis has to be used. A number of programs have been carried out on such techniques over the last few years. There was a cooperative program between the U.K., Canada, the US and Australia (24), and in Germany a number of papers were published (11, 25, 26).

Broadly speaking, the results of all these programs show that all these different Rainflow synthesis procedures developed up to now give very similar fatigue and crack propagation test results and also give very similar results to the original stress-time history. So, the reconstitution method seems not to be very critical.

FATIGUE 87

Some decisions still have to be taken, for example: When should the maximum stress amplitude occur in the sequence? For this purpose an examination of the test stress time history is necessary, in order to prevent the accidental occurrence of the maximum stress amplitude right at the beginning of the sequence, which is highly unlikely for example in a commercial aircraft. In the standardised Gaussian load sequence developed by LBF and IABG (22) they are applied at the middle of the return period of 10 cycles, that is after about 5×10 cycles. Deterministic or "abuse" events (like hitting a curbstone), which have not been measured in service, may also need to be incorporated into the sequence at this stage.

After all the steps described above have been taken, the fatigue test can finally be carried out.

If no stress measurements are available, the relevant standardised load sequence, for tactical aircraft for example the "Falstaff"-sequence (23) can be used. All the other standards available or in progress are mentioned in (31), details are given in (22, 23, 27, 28, 29, 30).

The result of the variable amplitude test is the experimentally predicted fatigue life for a probability of survival of 50%, see Fig. 1.

However, if the service stress spectrum of the component, whose life is to be predicted is different from the test spectrum, for example if assumptions had been used for the test spectrum and had later been shown to be incorrect by measurement in service, an additional fatigue life prediction by calculation must be carried out, see Fig. 1, in order to read across from the test spectrum to the service spectrum. This is usually done employing one of the relative damage accumulation hypotheses (19).

The safe fatigue life for the high probabilities of survival required for real components is determined using a statistically derived safety factor, which can be taken directly from v.a. tests.

Usually only a small number of v.a. tests on nominally identical components under identical test conditions is performed. The confidence for the safety factor derived from these few tests is therefore low.

It is a much better idea to use previous experience from many v.a. tests on similar components and to derive different safety factors, for example, for machined surfaces, cast or forged surfaces or welded joints.

FATIGUE 87

CONCLUDING REMARKS

The quite complex procedure described in this paper is necessary to determine the allowable stresses or the safe fatigue life, that is for the main objective of v.a. tests. For the other, less important objectives like assessment of damage accumulation hypotheses simplified procedures can be employed. However, even then a correct return period length and a suitable specimen must be used.

REFERENCES

- (1) Gassner, E., Festigkeitsversuche mit wiederholter Beanspruchung im Flugzeugbau, Deutsche Luftwacht, Ausgabe Luftwissen, Febr. 1939
- (2) Ekvall, J.C., Young, L. and Kakow, L. in: Problems in the Fatigue of Aircraft, ICAF-Symposium 1975, Lausanne
- (3) Davis, C.S. and Young, L., 23rd Annual Forum of the American Helicopter Society, 1967
- (4) Branger, J., Conf. on Structural Safety and Reliability, A. Freudenthal Ed., 1969
- (5) Heuler, P. and Schütz, W., in: Durability and Damage Tolerance in Aircraft Design, Proceedings of the 13th ICAF-Symposium, Pisa, EMAS 1985
- (6) Schütz, W., Eng. Fract. Mech. 11, 1979, pp. 405-421
- (7) Schütz, W., in: Werkstoffermüdung und Bauteilfestigkeit, Vorträge des DVM-Kolloquiums, DVM, 1980
- (8) Matsuishi, M. and Endo, T., Japan Soc. of Mech. Eng., March 1968
- (9) De Jonge, J.B., Fatigue Load Monitoring of Tactical Aircraft, NLR-Report TR 69063U, August 1969
- (10) Buxbaum, O., Betriebsfestigkeit, sichere und wirtschaftliche Bemessung schwingbruchgefährdeter Bauteile, Verlag Stahleisen Düsseldorf, 1986
- (11) Petersen, J. and Krüger, W., Experimenteller Lebensdauernachweis für Kfz-Komponenten auf der Basis von rekonstruierten stochastischen Beanspruchungen in: VDI-Berichte Nr. 613, 1986
- (12) Schütz, W., in: VDI-Berichte, 214, VDI, 1979
- (13) De Jonge, J.B., in: Helicopter Fatigue Design Guide, AGARDograph No. 292, 1983
- (14) Wimmer, A. and Petersen, J., SAE Paper 790713, 1979
- (15) Buxbaum, O., Konstruktion 20, Nr. 12, pp. 483-489, 1968
- (16) N.N., Steel, Concrete and Composite Bridges, BS 5400, Code of Practice for Fatigue, B.S.

FATIGUE 87

Institution, London, Part 10, 1980

- (17) Crichlow, W., in: AGARD LS 62, 1973
- (18) Schijve, J., The Significance of Flight-Simulation Fatigue Tests, T.U. Delft, Report LR-466, June 1985
- (19) Schütz, W., in: AGARD-CP 118, 1972
- (20) Fatigue under Complex Loading: Analysis and Experiments, R.M. Wetzels, Ed., 1977
- (21) Fash, J., in: SEECON '83, Digital Techniques in Fatigue
- (22) Fischer, R., Hück, M., Köbler, H.G. and Schütz, W., Eine dem stationären Gaußprozess verwandte Beanspruchungs-Zeit-Funktion für Betriebsfestigkeitsversuche, Düsseldorf, VDI-Forschungsberichte, Reihe 5, Nr. 30, 1977
- (23) Aicher, W., Branger, J., van Dijk, G.M., Ertelt, J., Hück, M., de Jonge, J., Lowak, H., Rhomberg, H., Schütz, D. and Schütz, W., Description of a Fighter Aircraft Loading Standard for Fatigue Evaluation "FALSTAFF", Common Report of F+W Emmen, LBF, NLR, IABG, March 1976
- (24) Perrett, B.H.E., in: Review of the Work in the United Kingdom on the Fatigue of Aircraft Structures 1983-1985, U.K., ICAF Review, May 1985
- (25) Krüger, W., Schentsow, M., Beste, A. and Petersen, J., Markov- und Rainflow-Rekonstruktionen stochastischer Beanspruchungs-Zeit-Funktionen, Fortschrittsberichte, VDI-Reihe 18, Nr. 22
- (26) Bergmann, J.W., in: Review of Investigations on Aeronautical Fatigue in the Federal Republic of Germany, LBF-Report S-173, 1985
- (27) Schütz, D., Lowak, H., de Jonge, J. and Schijve, J., Standardisierter Einzelflugbelastungsablauf für Schwingfestigkeitsversuche an Tragflächen-Bauteilen von Transportflugzeugen. NLR-Report TR 73 and LBF-Report FB 106, 1973
- (28) Edwards, P.R. and Darts, J., Standardised Fatigue Loading Sequences for Helicopter Rotors (Helix and Felix). RAE-Technical Report TR-84085, August 1984
- (29) Mom, A.J.A., Evans, W.J. and ten Have, A.A., in: AGARD Conf. Proceedings No 393, 1985

FATIGUE 87

- (30) Schütz, W., Dover, W.D. and Pook, L.P., in: ASTM Symposium on Development of Fatigue Loading Spectra Cincinnati, April 1987
- (31) Schütz, W., in: ASTM Symposium on Development of Fatigue Loading Spectra, Cincinnati, April 1987
- (32) Heuler, P. and Seeger, T., Int. J. Fatigue No 4, 1986, pp. 225-230
- (33) Gassner, E., Mat. Prüf. No. 11, 1984, pp. 394-398
- (34) Fash, J.W., Conle, F.A. and Minter, G.L., SAE paper to be published

FATIGUE 87

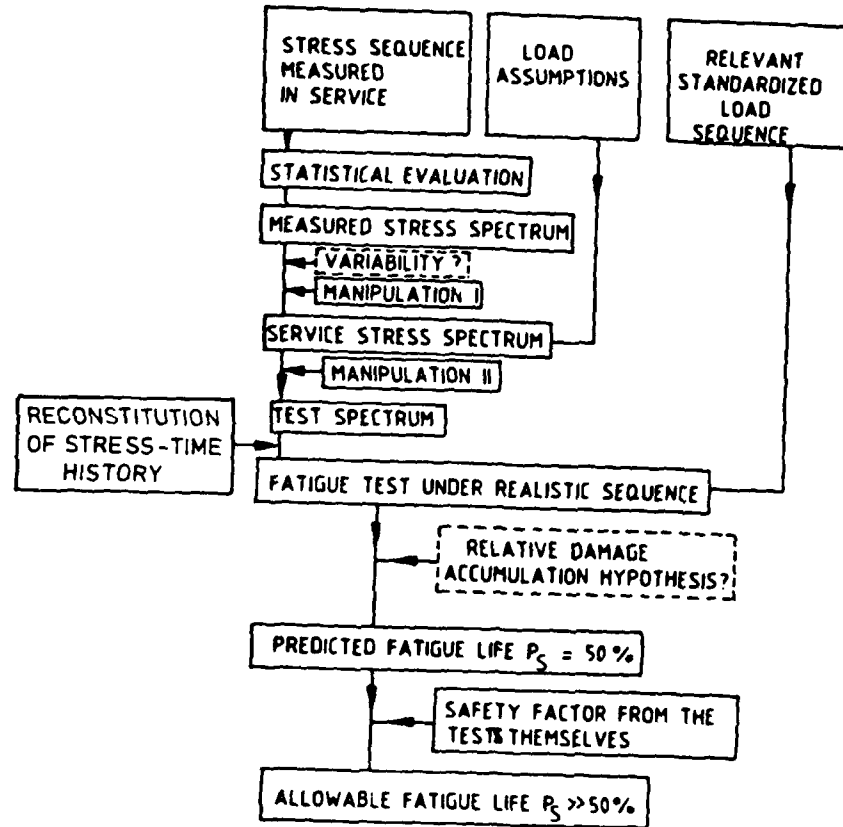


Figure 1. Flow chart for a variable amplitude test

FATIGUE 87

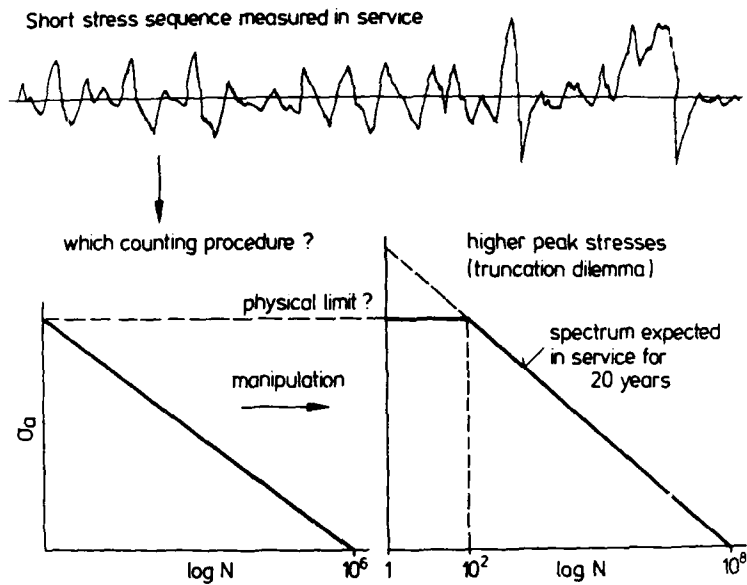


Figure 2. Extrapolation of the measured stress spectrum (Manipulation I)

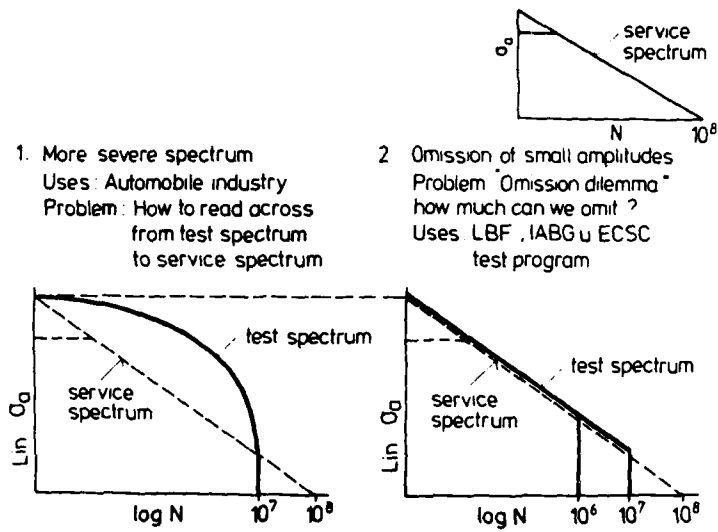


Figure 3. How to shorten the test spectrum (Manipulation II)

FATIGUE 87

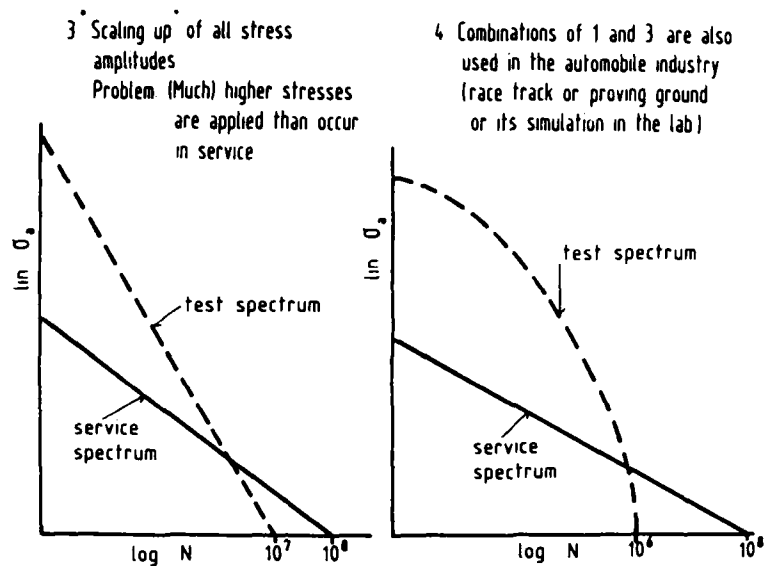


Figure 4. How to shorten the test spectrum
(Manipulation II)

1 Size of return period
if a return period is used

2 Use of random generators
with too low crest factor

for example:
return period of
 10^4 cycles much too short
no high stresses are applied

Similar effect to 1.

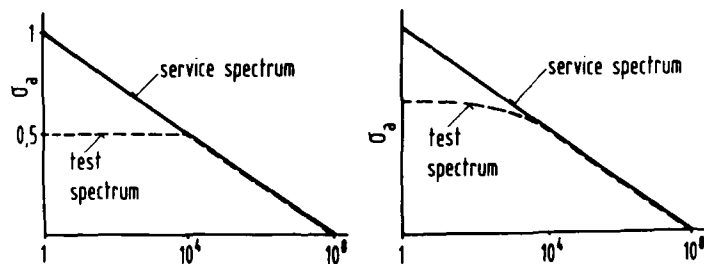


Figure 5. Further questions

FATIGUE 87

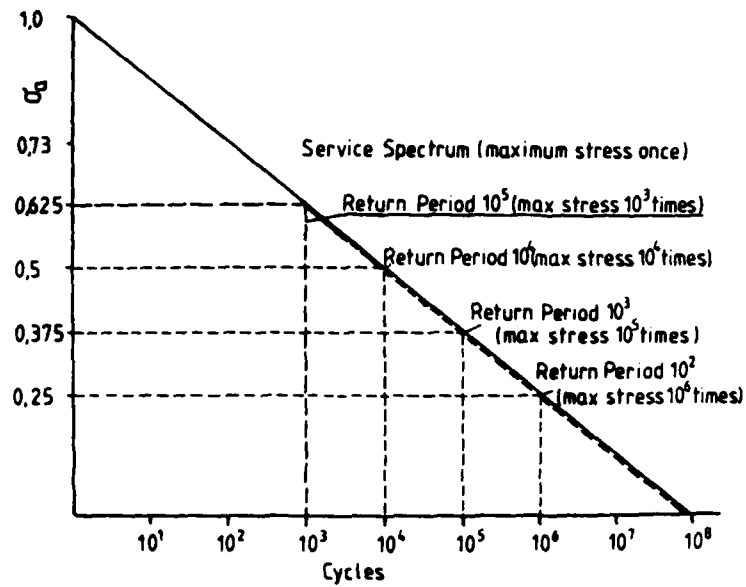


Figure 6. The spectrum shape at long lives under short return periods

FATIGUE 87

**FATIGUE
AND
MICROSTRUCTURE**

FATIGUE 87

NEAR-THRESHOLD GROWTH OF DEFECTS IN ENGINEERING MATERIALS

J.F. Knott*

ABSTRACT

The paper describes recent work on fatigue-crack growth in the near threshold region, with particular reference to the behaviour of short cracks. Attention is drawn to the importance of closure and it is suggested that a lower-bound to behaviour in steels is associated with a closure-free threshold stress-intensity-factor of approx. $3 \text{ MPam}^{1/2}$. This modifies the Kitagawa plot. Engineering design is considered with respect to two areas: structures and machine components. Closure-free threshold values are appropriate for structures. For machine components, engineering design must rest on the endurance limit. This is a function of material's defect content and a simple statistical model is described to demonstrate the sensitivity of behaviour to input variables.

INTRODUCTION

The use of linear elastic fracture mechanics (LEFM) to characterise the growth of fatigue-cracks is now well-established and it has proved to be a valuable component of engineering design in situations where structures are subjected to cyclic stresses. Research has defined limits to the original Paris-Erdogan relationship [1], which gives the crack-growth increment per cycle, da/dN , as a simple power-function of the range of stress-intensity factor, $\Delta K = (K_{\max} - K_{\min})$, where K_{\max} and K_{\min} are the maximum and minimum values in the cycle:

$$da/dN = A \Delta K^m \quad 1)$$

with A and m as constants. At high ΔK , such that K_{\max} becomes a sizable fraction of the material's fracture toughness K_{IC} , the crack growth-rate can be increased by the occurrence of "static" or "monotonic" fracture modes [2]. The growth rate is then dependent on the mean stress, as defined by the stress-ratio, $R = K_{\min}/K_{\max}$. At low ΔK , it is found that values of da/dN fall below the extrapolation of data in the "Paris Law" regime,

* Department of Materials Science and Metallurgy, University of Cambridge, Pembroke Street, Cambridge, CB2 3QZ

FATIGUE 87

eventually becoming so small that no crack growth can be detected. The associated value of ΔK , ΔK_{th} , is referred to as the "fatigue-crack threshold". It is found experimentally that ΔK_{th} varies with the stress-ratio, R , and with the environment. A number of explanations for this behaviour, invoking concepts of closure, re-welding of the crack-tip and gas adsorption on clean slip-steps at the crack-tip, have been proposed [3-6].

The engineering use of equation 1) is apparent if a defect of initial size a_0 grows by fatigue to a critical size, a_f , determined by the onset of fast fracture when $K_{max} = K_{IC}$, or by the onset of plastic collapse when crack growth has reduced the size of the load-bearing, uncracked ligament sufficiently to allow instability to occur. A sample calculation for a through-thickness crack in an infinite body, for which $\Delta K = \Delta\sigma(\pi a)^{1/2}$ where $\Delta\sigma$ is the applied stress-range, gives:

$$da/dN = A \Delta\sigma^m (\pi a)^{m/2} \quad 2)$$

It is then possible to separate variables (N and a for constant $\Delta\sigma$) and to integrate between limits a_0 and a_f , and 0 and N_f (the number of cycles to failure). This gives:

$$A \Delta\sigma^m \pi^{m/2} N_f = \{2/(2-m)\} [a_f^{(1-m/2)} - a_0^{(1-m/2)}] \quad 3)$$

for all values of m not equal to 2. For $m = 2$, the form is

$$A \Delta\sigma^2 \pi N_f = \ln(a_f/a_0) \quad 4)$$

The value, $m = 2$, holds for a number of tough engineering materials [2], but values of m in the range 3-4 are also often found in design data. If it is assumed that both a_0 and a_f are constant: a_0 fixed by the inherent defect size in the engineering component and a_f fixed by fracture toughness or plastic collapse, then it is possible, by taking logarithms, to re-cast either equation 3) or equation 4) in the form:

$$\log N_f = -m \log \Delta\sigma + \text{const.} \quad 5)$$

which is essentially a linear "S-N" curve. It is of interest to note, in passing, that the derivation of 5) does not depend on the LEFM formulation as such: it would be equally possible to perform the integrations starting from a relationship of the type:

$$da/dN = A' \Delta\sigma^v a^w \quad 6)$$

where $v \neq 2w$ [7]

If it is the case that the value of a_f is not strongly dependent on the value of σ_{max} , it is possible further to follow the integration procedures for variable amplitude loadings [7]. Envisage a series of loading blocks, $\Delta\sigma_i$ (where $i = 1, 2, 3$ etc),

FATIGUE 87

each applied for a number of cycles, N_1 . For the first block, the crack grows from a_0 to a_1 in N_1 cycles¹. The limits of integration in equation 3) are then a_1 and a_0 , rather than a_f and a_0 . Let this integral be denoted by I_{01} and let the integral between a_0 and a_f be denoted by I_{of} . If the lifetime at stress amplitude $\Delta\sigma$, is denoted by $N_{f(1)}$, it is then possible to write:

$$N_1/N_{f(1)} = I_{01}/I_{of} \quad 7)$$

Now apply a stress amplitude $\Delta\sigma_2$ for N_2 cycles, during which period the crack grows from a_1 to a_2 .² The integral over these cycles is denoted by I_{12} . If the number of cycles to failure at $\Delta\sigma_2$ is $N_{f(2)}$, we have:

$$N_2/N_{f(2)} = I_{12}/I_{of} \quad 8)$$

In general, for a sequence of stresses $\Delta\sigma_i$,

$$\sum N_i/N_{f(i)} = (1/I_{of}) (I_{01} + I_{12} + I_{23} \dots + I_{f-1,f}) \quad 9)$$

The final term in parentheses in equation 9) comprises the sequential integrals of $a^{-m/2} da$ from a_0 to a_1 to a_2 etc to a_f . By the definition of integrals, this sum is equal to I_{of} so that the resultant RHS is equal to unity. Hence:

$$\sum N_i/N_{f(i)} = 1 \quad 10)$$

which is the Palmgren-Miner law. Again, this could be derived using equation 6). i.e. not invoking LEFM formulation as such. It is unrealistic to assume that a_f is independent of stress-level, unless K_{max} is held constant and ΔK is varied by varying K_{min} , but it is often found that the fatigue lifetime does not depend on the value of a_f in a very sensitive manner. The Palmgren-Miner law may therefore serve as a reasonable approximation to behaviour, if overload effects do not produce significant retardations when $\Delta\sigma$ is reduced from a high value to a low value [as in 8].

It should be noted that fatigue lifetimes can be calculated by integration, as in the derivation of equation 3) or 4), even if the relationship between (da/dN) and ΔK is not linear on a log: log plot. The method is to approximate a curved line, dropping towards threshold, by a series of straight lines and to integrate these in a simple piecewise manner. This approach has been used by Taylor and Knott [9] to predict the S/N curves for nominally smooth specimens of aluminium-bronze castings from $(da/dN): \Delta K$ data. Calculations were made for different initial (semi-elliptical) defect sizes and the predictions were compared with actual S/N data. Agreement was good for assumed defects of sizes equal those to casting pores observed in the material, and the S/N curves showed a form of fatigue limit, deriving from the

shape of the fatigue-crack growth-rate curve in the near-threshold region.

GROWTH-RATES OF "PHYSICALLY SHORT" CRACKS (LENGTHS 0.1-2 MM)

The calculations described above are based on long-crack behaviour, such that a given value of stress intensity factor is associated with a low overall stress and LEFM conditions apply. When the initial defects are small, however, it is often found that growth rates are higher than those for long cracks and that the threshold is reduced. Measurements on short crack growth carried out by Taylor [10] for the same aluminium bronze (yield stress 235 MPa) as that for which the S/N predictions were made indicated that cracks much smaller than approx. 0.4 mm grew anomalously rapidly. In nickel-base superalloy (yield strength ~950 MPa) cracks of length 0.25 mm grew at the same rates as those for long cracks, but high rates were observed for shorter cracks [11],[12]. It is clear that use of long-crack data and LEFM calculations could lead to over-optimistic predictions of fatigue lifetimes if the standard integration procedures were applied to defects of initial size smaller than a given critical value.

Investigation of the reasons for "short-crack behaviour", particularly in the near-threshold region, is the subject of much current research. It is clear that microstructurally short cracks are unlikely to follow continuum growth laws, but even "physically short" (0.1-0.5 mm) cracks may show anomalous behaviour. One possibility is that, as cracks become short, the overall applied stress needed to produce a given stress intensity factor is increased, and yielding becomes extensive, so that LEFM conditions no longer hold. An estimate of this suggests that short-crack behaviour is associated with all stress levels greater than one-third of the yield stress [13]. Experimental results obtained on short (0.1-1 mm) cracks in bend specimens of mild steel (yield strength 280 MPa, UTS 420 MPa), however, showed that agreement with long crack growth rates could be obtained, even though the specimens had undergone general yielding when load was first applied [14]. The rates of crack-growth for defects smaller than 0.5 mm were initially high, but then merged with the long-crack curve. Possibly, cyclic hardening progressively raised the flow stress of the material, so that the response, after an initial "shakedown", became equivalent to that under LEFM loading. Comparison of cyclically hardening and cyclically softening material would clearly be instructive.

Another major point is that the amounts of closure associated with long and short cracks are likely to differ, particularly because "wind-down" procedures are used to determine long-crack threshold values. The effect of this has been demonstrated by

Minakawa et al [15] and by James and Knott [5] in their studies on HY80 steel. For a long crack, the value of ΔK_{th} , determined using a careful wind-down sequence, at $R = 0.35$, was $3.6 \text{ MPam}^{1/2}$. In one particular test, the length of crack at threshold was 2.43 mm, and this corresponded to a closure level, K_{op}/K_{max} , of 0.45, with an apparent closed length of crack, in the plastic wake, of 1.2 mm. At this point, part of the crack wake was removed by electro-discharge machining (EDM), leaving only 0.5 mm of wake behind the tip. The crack growth rate immediately increased from less than 0.05 nm/cycle to 0.35 nm/cycle, and the value of K_{op}/K_{max} decreased to 0.20. Note that the effect of the geometry change induced by EDM could only reduce the stress intensity factor at the crack tip and so, by itself, would be likely to cause a decrease, not an increase, in growth rate. The reduced value of K_{op}/K_{max} , and a calculation which shows that the value of 0.29 could be predicted from the value of K_{max} attained in the plastic wake at a position 0.5 mm behind the crack tip during the wind-down sequence, supports the fact that the increase in growth-rate is due to a decrease in plastic-wake closure. Similarly, if a short crack had been prepared by machining away material from behind the crack tip so as to leave a crack of length 0.5 mm, the closure level would again be reduced and the short crack would exhibit a higher growth rate.

This behaviour has been observed directly by Kendall [14,16] in a steel of BS4360-43A type, in which physically short cracks of lengths in the range 0.1-2 mm were prepared by grinding away material from behind the tips of cracks 5-6 mm in length, which had been grown to a near-threshold condition ($da/dN < 1 \text{ nm/cycle}$) using a load-shedding sequence. The machining was followed by a stress-relief anneal of 2h at 650°C . The growth rates of these short cracks were compared with those of long cracks at an R-ratio of 0.5, and it was found that anomalous behaviour (higher growth-rates, lower thresholds) was observed only for ΔK values (below $10 \text{ MPam}^{1/2}$) at which long crack growth rates were affected by closure at $R = 0.5$. Plasticity-induced closure is expected to act up to 1.5 mm behind the tip of a long crack, and it was determined that, for the shorter cracks, the value of K_{op}/K_{max} was reduced from 0.64 to 0.30. The anomalous behaviour of short cracks is attributed to effects of closure rather than to effects of plasticity, because the growth-rates of short cracks loaded to values of ΔK greater than $10 \text{ MPam}^{1/2}$ (i.e. more plasticity) follow the long crack curve.

Given these observations on the growth of physically short cracks, it is now pertinent to propose on a general philosophy which might be followed when considering fatigue-crack growth in the context of engineering design, rather than as a scientific exercise. The approach follows that in ref. [14].

FATIGUE CRACK GROWTH IN STRUCTURES AND MACHINE COMPONENTS

It is convenient to divide the range of objects subjected to fatigue loading into two broad categories: structures and machine components. Structures are large pieces, which have had to be fabricated by processes such as welding, rivetting or bolting. Defects will be present ab initio and control of the size of these defects will be exerted by attention to processing and fabrication schedules. Non-destructive examination (NDE) will usually be employed prior to the piece entering service and any guarantee of fatigue life can be ensured only in terms of the resolution of the NDE technique employed. This will be termed NDE Control. Magnetic particle inspection (MPI) on smooth surfaces may be capable of a resolution of 0.2 mm, but, for sub-surface defects, e.g. in welded joints, even 2 mm would be regarded as a rather good performance. The guaranteed detection limit for thick, PWR pressure vessels is more of order 20 mm. In structures, therefore, initial cracks of length at least 2 mm must be assumed.

Machine components, on the other hand, are, generally, relatively small units (although there are some exceptions, such as large alternator forging), made from worked (and hence consolidated) material, with attention to surface finish. Control of defects is exerted by the metallurgist through attention to melting practice and consistency of processing. Surface inspection by MPI or eddy-current techniques sets an upper limit of order 0.2 mm to surface defect size, but control of inclusions or porosity to much tighter limits than that which can be detected by NDE is usually necessary to give satisfactory fatigue performance. Control is exerted by consistency of processing combined with the (S/N) testing of a large number of representative test samples. This form of control is termed Process Control.

The two regimes of behaviour are conveniently represented as the extremes of the so-called Kitagawa plot [17], in which the applied stress range, $\Delta\sigma$, required to cause failure is plotted vs. initial defect size, a , on log scales. Their data, for a quenched and tempered steel, show LEFM behaviour for crack lengths greater than about 0.5 mm, i.e. fall on a straight line of slope -0.5 with $\log \Delta\sigma$ as ordinate. The straight line and the slope of -0.5 are compatible with a constant threshold, ΔK_{th} , since $\Delta K_{th} \propto \Delta\sigma(a)^{1/2}$. For crack lengths less than approx. 0.05 mm, the failure stress is given by the endurance limit, 549 MPa. "Anomalous" behaviour is then generally held to be observed for crack lengths between 0.05 mm and 0.5 mm.

It is, however, critically important to realise that the threshold data which comprise the Kitagawa plot were obtained at an R-ratio of 0.04. The associated value of ΔK_{th} is 4.8 MPa \sqrt{m} .

FATIGUE 87

($15.5 \text{ Kg mm}^{-3/2}$ from the original data, allowing for the fact that their cracks were small and semi-circular: hence $\Delta K = 0.66 \Delta \sigma (\pi a)^{1/2}$). This is comparable in magnitude with a value of $\Delta K_{th} = 4.8 \text{ MPam}^{1/2}$ obtained by James and Knott [5] for HY80 steel quenched and tempered to similar yield strength, and $R = 0.2$. In the latter case, closure measurements were made and it was clear that closure (from the "plastic wake") was significant. The "closure-free" value of ΔK_{th} , termed ΔK_c , was found to be approximately $3 \text{ MPam}^{1/2}$.

If the Kitagawa plot has added to it a line of slope -0.5 in the LEFM region corresponding to a (closure-free) value of $\Delta K_{th} = 3 \text{ MPam}^{1/2}$, this serves as a lower bound to all results for cracks of initial length greater than 0.05 mm and hence removes the regime of anomalous behaviour [14]. As in the previous section it is concluded that anomalous behaviour of physically short cracks is a result of differences in closure behaviour, rather than excess plasticity, and that the endurance limit and closure-free LEFM lines can provide adequate lower bounds for engineering design.

It is pertinent now to consider the growth of microstructurally short cracks ($< 0.5 \text{ mm}$) in machine components, i.e. those for which the failure line on the Kitagawa plot is the endurance limit. Several points need to be made. First, the number of cycles to failure in service or in a testpiece is large and the associated stress is relatively low. An automobile engine which has travelled $100,000$ miles, for example, at an average speed of 40 miles per hour and at 3000 revolutions per minute will have experienced 4.5×10^8 cycles. Under stresses corresponding to these lifetimes, crack growth occurs in what is absolutely, a large number, but, relatively, a small area fraction of surface grains. The orientations of individual grains will be important, as will local residual stress fields due to particles or transformed regions (e.g. in case-hardened surface layers). The crack path is known to follow metallographic features and is hence often tortuous.

In such circumstances, it is not fruitful, in the author's view, to attempt to pursue deterministic micro-mechanical modelling of a single microcrack for the purposes of engineering design, although study of such cracks may advance scientific understanding of important metallurgical factors. This comment is made, not least, because the practical situation involves a plethora of small cracks of different sizes, which may grow individually in response to the applied stress and then interact with near-neighbours, shedding or re-distributing stress in a complicated manner. Rather, it should be recognised that the engineering design tool is the endurance limit, noting, of course, that this is dependent on defect content (and crack growth laws, as modified by local residual stresses). In other words, the link to defects and growth-laws is conceptual, although use should

FATIGUE 87

obviously be made of scientific findings if they help to give improvements in performance.

An analogy may be made with the 0.2% proof stress of a simple metal containing an ingrown network of dislocations. Scientific studies make it clear that the longest network link will move at the lowest stress and that this may produce a plastic displacement of, say, half a network spacing. At a slightly higher stress, the second-longest link is operated and makes another contribution to plastic displacement. The stress is edged up until eventually 0.2% overall strain is obtained, and this is then the 0.2% proof stress, calculated from first principles. Conceptually, the method is sound. In practice, it is unusable because it would be necessary to make TEM foils of the whole testpiece to measure link lengths, even if the horrendous summations could be executed. In contrast, it is relatively easy to measure the 0.2% proof stress on a bar of metal and to use this as an engineering design parameter. It is, however, of value to know, from the scientific studies, that link length is important and to know that processes such as cold-working serve to reduce link lengths, so that the flow stress is increased.

Once the concept of the dependence of the endurance limit on the initial sizes of defect has been established, the question of quantification is raised. The following section is devoted to a simple model, for illustrative purposes.

CRACK GROWTH AND THE ENDURANCE LIMIT

A method of treating slow crack growth in material which contains an initial distribution of defects is to be found in ceramics literature, dealing with stress-corrosion crack growth [18]. Here, the defect distribution gives rise to a distribution in fracture stress, which is often taken as a three-parameter Weibull function, such that the probability of survival $P_s(V)$ of a volume V is given by:

$$P_s(V) = \exp[-V\{\sigma-\gamma\}/\eta]^\beta \quad 11)$$

where η is a scale factor, γ is a lower-bound cut-off and β is the Weibull modulus. (see also [19] and [20].) The cumulative probability plots as a straight line on Weibull probability paper, e.g. by taking logs twice:

$$\ln \ln(1/P_s) = \ln V + \beta \ln(\sigma-\gamma) - \ln \eta \quad 12)$$

and $\ln \ln(1/P_s)$ is plotted vs $\ln(\sigma-\gamma)$. The best value of γ may be found by trial and error. The stress-corrosion crack growth-rate, da/dt , is expressed as a simple power of the stress intensity, K ,

through the expression:

$$da/dt = CK^n \quad (13)$$

where C and n are constants: n is usually large (>10). Failure stresses are normalised to failure in a given time, e.g. 1s, and it may be shown that each decade increase of time produces a failure line parallel to the 1s failure line on Weibull probability paper: for n = 10, a reduction in stress of 21% is found for each decade increase in failure time [18]. These diagrams are known as SPT (strength, probability, time) diagrams.

The Weibull approach is not followed directly in the present paper; first, because the endurance limit is not an identifiable fracture stress; second, because the growth-rate curve exponents (m in equation 1)) are not large (as is n in equation 13)); third, because it is desirable to maintain a link as direct as possible between defect distribution and endurance limit, rather than between any sort of "fatigue strength" and endurance limit. This is the only fault with the otherwise excellent treatise by Bompas-Smith [19].

The model is highly simplified. Defects are treated as spherical particles of radius, r, which crack in the first cycle to give a distribution of penny-shaped cracks, free from internal stress. The number of particles of radius r, M(r), is taken as a negative exponential, such that:

$$M(r) = B \exp(-r/\rho) \quad (14)$$

where B and ρ are constants. This could be regarded as a simple Weibull distribution, with $\beta = 1$, $\gamma = 0$ but the distribution now refers to defects, not strengths. It is desirable to choose a population of particles slightly larger than features of the heat-treated microstructure, so that it controls fatigue-crack growth, and the population should decrease fairly rapidly as r increases, consistent with observed behaviour of inclusions, such as deoxidation products in weld metals [21,22]. A typical value for ρ might then be chosen as 5 μm , with the values of r of interest ranging from ρ to 10ρ . When $r = \rho = 5 \mu\text{m}$, the stress corresponding to $\Delta K_{th} = 3 \text{ MPa}\sqrt{\text{m}}$ for a penny-shaped crack is 1200 MPa, which is somewhat above the yield stress of a medium-strength quenched-and-tempered forging steel, (although approximately equal to that of a gun-barrel steel). The upper limit, $r = 10\rho = 50 \mu\text{m}$, corresponds to that of the end of the "endurance limit"-controlled region on the Kitagawa plot [17]. The value of B may be obtained from equating the total volume of inclusions to the overall volume fraction i.e.

$$\int_0^{10\rho} M(r) (4\pi/3)r^3 dr = V_f \quad (15)$$

FATIGUE 87

$$(4\pi/3)(B/\rho) \int_0^{10\rho} \exp(-r/\rho) r^3 dr = V_f \quad (16)$$

$$B = V_f / (8\pi\rho^3) \quad (17)$$

For a volume fraction, $V_f = 0.1\% = 0.001$, and $\rho = 5 \mu\text{m}$, this gives $B = 3 \times 10^{-11} \text{ m}^3$.

Now write equation 2) as for a penny-shaped crack, for which $\Delta K = (2/\sqrt{\pi}) \Delta\sigma\sqrt{r}$, and take $m = 2$, to give:

$$dr/dN = A(4/\pi) \Delta\sigma^2 r \quad (18)$$

Separating variables and integrating (c.f. equation 4)):

$$A(4/\pi) \Delta\sigma^2 N_f = \ln(r_f/r_o) \quad (19)$$

where r_f and r_o are the final and initial radii. Taking (natural) logarithms:

$$\ln N_f = \ln(\ln r_f - \ln r_o) - 2 \ln \Delta\sigma - \ln(4A/\pi) \quad (20)$$

For ideally consistent material, r_o is constant. If it is assumed that r_f is constant (independent of σ_{\max}), we have a linear $(\ln)S-(\ln)N$ curve, as in equation 5). i.e. for a specified number of cycles, e.g. $N_f = 10^8$, there is a unique endurance limit, $\Delta\sigma$.

Now consider equation 20), not with a fixed initial crack size, r_o , but with a variable initial size, r , ($<10\rho = 50 \mu\text{m}$) distributed as given by equation 14). It is therefore expected that there will be a corresponding distribution in lifetime at a constant stress level, $\Delta\sigma$, given by $P(\ln N_f)$. A rough estimate of this is obtained as follows: a) Estimate r_f from the value of σ_{\max} in the fatigue cycle and the material's fracture toughness, K_{IC} (or from consideration of plastic collapse on the final ligament). For illustrative purposes, we assume $\sigma_{\max} = 1200 \text{ MPa}$, $K_{IC} = 100 \text{ MPa}\sqrt{\text{m}}$, hence $r_f = 5.45 \text{ mm}$. b) for convenience and clarity, it is possible to represent the smooth function in equation 14) as a discrete histogram with blocks centred on ρ , 2ρ , $3\rho \dots 10\rho$, running from 0.5ρ - 1.5ρ , (2.5 - $7.5 \mu\text{m}$), 1.5 - 2.5ρ (7.5 - $12.5 \mu\text{m}$) ... etc. The fractions of defects in each block are then virtually equivalent to the values of the mean centres as given by equation 14), as the following calculation shows. Total area under the curve represented by equation 14)

$$= \int_0^{10\rho} \exp(-r/\rho) dr = -4.54 \times 10^{-5} \rho + \rho \approx \rho. \text{ Area between } 1.5\rho$$

and 2.5ρ , as an example, $= 0.141\rho$, so fraction $= 0.141$. Value of equation 14) at $2\rho = 0.135$. These fractions are given in Table I and it can be seen that, within rounding-off errors, the whole

FATIGUE 87

distribution is effectively catered-for by values of r up to 7ρ only. This is, of course, a feature of the chosen distribution and ignores outliers.

TABLE I - Frequency of Defect Occurrences

Value of $\frac{r}{\rho}$ Centre	Block Size r/ρ	Centre Fraction	Block Fraction	Cumulative Probability (Blocks)
0	<0.5	-	0.394	0.394
1	0.5-1.5	0.37	0.383	0.777
2	1.5-2.5	0.135	0.141	0.918
3	2.5-3.5	0.05	0.052	0.970
4	3.5-4.5	0.018	0.019	0.989
5	4.5-5.5	0.007	0.007	0.996
6	5.5-6.5	0.003	0.003	0.999
7	6.5-7.5	0.0009		~1
8	7.5-8.5	0.00035		
9	8.5-9.5	0.0001		
10	9.5-10	0.000045		

For each block, it is then possible to evaluate equation 19) or 20) to calculate the probability with which N_f or $(\ln N_f)$ will be distributed as a result of the distribution of defect sizes. It is, of course, necessary to choose a datum which represents the "best" endurance limit for the material and then to examine the shift in N_f or $(\ln N_f)$ relative to this datum.

Choice of the datum is not easy and must involve the volume of sample exposed to high stress. For a conventional "hour-glass" S/N fatigue specimen, subjected to axial fatigue, and assuming surface initiation this might be an annular volume, given by πd (where d is the specimen diameter) multiplied by a height, h , which is a function of the "hour glass" profile, multiplied by a depth, δ , representing that over which the early stages of

FATIGUE 87

fatigue-crack growth may be assumed to occur with equal probability. It is difficult to estimate δ , for two reasons. If too large a depth is chosen, it may be argued that penetration of the surrounding environment into a crack is insufficient for the depth to be representative of "surface" condition (and "surface initiation" has been assumed). If the depth is too small, it becomes less than an inclusion radius, so that the frequency of occurrence of inclusions in the surface annulus is difficult to establish. For the purposes of illustration, a depth of 10 μm is chosen, although it is appreciated that this calls into question the frequency distribution of the larger inclusions. Values of $d = 10\text{ mm}$ and $h = 1\text{ mm}$ are reasonable for testpieces and with these values, the volume of the surface annulus becomes $\pi \times 10^{-2} \times 10^{-3} \times 10^{-3} = \pi \times 10^{-10}\text{ m}^3$. (Note that r_f , calculated as 5.45 mm, is less than d .) From equation 16) the pre-exponential constant, B , was calculated as $3 \times 10^{11}\text{ m}^{-3}$, so that the numbers of defects of given size "in" the surface layer comprise the frequencies given in Table I, multiplied by approx. 100. The resultant effects on N_f and $(\ln N_f)$ may be calculated using equations 18) and 19) respectively. If $\Delta\sigma$ and r_f are constant, N_f is directly proportional to $\ln(r_f/r)$, and the value of $\ln(N_f)$ is shifted by $\ln\{\ln(r_f/r)\}$ with respect to the datum. The figures are given in Table II.

TABLE II - Effects of Defect Size on Endurance Limit

Block Centre r/ρ	Frequency of Occurrence	Number in Test Volume	$\ln \frac{r_f}{r}$	$\ln \ln \frac{r_f}{r}$	Cumulative Frequency
<0.5	0.394	many	immaterial		0.394
1	0.383	38	7.0	1.95	0.777
2	0.141	14	6.3	1.84	0.918
3	0.052	5	5.9	1.77	0.970
4	0.019	2	5.61	1.72	0.989
5	0.007	0.7	0.7	1.68	0.996
6	0.003	0.3	5.20	1.65	0.9985
7	0.0009	0.1	5.05	1.62	0.9995
8	0.0003	0.03	4.91	1.59	0.9998
9	0.0001	0.01	4.78	1.57	0.9999
10	0.00005	0.005	4.69	1.55	~1

The model contains a number of simplifications, particularly with respect to the treatment of defect content in the "surface layer" ($\delta = 10 \mu\text{m}$) but, with these qualifications, it is possible to use Table II to make a number of observations. First, the obvious choice of datum is the value of N_f for the $20 \mu\text{m}$ defect ($r/\rho = 4$) because >1 defect is always present in the test volume, so that, with respect to the assumptions, a cumulative frequency of 98.9% of the population will all possess the value of N_f corresponding to that for the $20 \mu\text{m}$ defect, since at least one will always be present in the test volume. (If inclusions, in general, do not crack equally easily or are oriented at angles to the stress axis, it may be necessary to sample, on average, more than one per test volume, so that the datum may shift to a smaller defect size.) Clearly, an increase in test volume should lead to more reproducible values, although a cumulative frequency of 98.9% is already higher than commonly observed. The variation in Table II is given as a variation in N_f or $\ln(N_f)$ at constant $\Delta\sigma$ and this is often what is observed experimentally. It would, however, be quite possible to fix N_f as, say, 10^8 cycles for the $20 \mu\text{m}$ defect and then explore the variation in $\Delta\sigma$ at 10^8 cycles. Proceeding from Table II, however, it is possible first to estimate the endurance limit, assuming that 98.9% is so close to unity that experimental results would show an LEFM line, for the closure-free ΔK_{th} value of $3\text{MPa}\sqrt{\text{m}}$, intercepting the "endurance limit" at a $20 \mu\text{m}$ defect (rather than at $50 \mu\text{m}$, as in Kitagawa's results). The associated value of $\Delta\sigma$ for a penny-shaped crack is then 600 MPa , which is, at least, the right order of magnitude, and, in fact, close to Kitagawa's value of 549 MPa .

The prediction of the model is that, for a $20 \mu\text{m}$ datum, 98.9% of the population exhibit an endurance limit equal to that for the $20 \mu\text{m}$ datum. It is found that, if $\ln(r_f/r)$ or $\ln\ln(r_f/r)$ are plotted vs. cumulative frequency on Gaussian probability paper, straight-line fits are obtained for cumulative frequencies of 0.97 or greater, so that normal distributions of N_f or $\ln(N_f)$ could plausibly be assumed for defects larger than the datum. Few data points are, of course, involved, and a simple linear plot does not give unequivocal proof of normality. Greater scatter in endurance limits than that predicted is often observed experimentally and the explanation of such scatter rests on careful experimentation, both in fatigue testing and in characterisation of defects. Sintered pure metals might provide good model material.

The endurance limit is usually defined at constant N_f , e.g. 10^8 cycles, but, if N_f is allowed to vary as in the determination of the full S-N curve, it is of interest to note that the model predicts the same distribution of N_f with defect size at all stress levels, since r_f has been assumed to be independent of σ_{max} . If this could be achieved in tests, e.g. by holding σ_{max} constant and varying $\Delta\sigma$ by altering σ_{min} , and the defect distribution were fixed, it is possible, in theory, to employ any

observed deviations from single-crack LEFM calculations to derive stress: crack growth-rate relationships for small cracks as follows. First, derive a defect distribution. Second, use LEFM to calculate from this the predicted distribution in N_f or $\ln(N_f)$. Third, determine experimental values of N_f or $\ln(N_f)$ distributions at different stress levels. Fourth, (particularly if the distributions agree at low stress levels, but not at high stress levels) back-calculate (using trial-and-error if necessary) to derive an appropriate growth law. In practice, this requires a vast number of experiments with non-standard cycles (tension-tension, varying σ_{min}) and attention must be paid to effects such as those of closure, but there are applications, e.g. gas turbine discs, where service failure lives are designed to be as low as 10^5 cycles. and high-stress growth laws are needed.

The description of the defect distribution as negative exponential, over a range 5-50 μm , is clearly a simplifying assumption. Data are available for weld-metals, where it has been suggested that deoxidation products are distributed in log-normal manner [21,22], with sizes generally up to a few μm . These particles, however, are associated with local residual, "tessellated", stress fields which will affect crack growth (see next section) and, in this size range, other particles, such as carbides, could be equally effective in serving as initiation sites. In the absence of these complications, the effect of simply altering the particle radius is two-fold. If, for example, ρ were 1 μm , rather than 5 μm (as might be appropriate for a weld-metal), then B, in equation 16) would be increased to $4.75 \times 10^{13} \text{ m}^{-3}$. The values of N_f or $\ln(N_f)$, equations 18) or 19) would be shifted by a constant amount, $\ln(5)$, but pairing with appropriate frequencies and the resulting choice of datum (Table II) requires step-by-step recalculation. Alternative distributions might be devised to take account of the fact that a 50 μm defect must have occurred with high probability in Kitagawa's results, since his endurance limit coincided with the stress level for a defect of this size.

To summarise, the intention of this section is to indicate a general method by which the conceptual relationship between endurance limit and defect content might be quantified. In theory, back-calculation could enable appropriate growth-rate laws to be derived. There have, in the past, been a number of statistical treatments of endurance limit as a function of "fatigue strength", e.g. [19], but it is important to incorporate a description of defect content, since this is the parameter directly amenable to metallurgical control. The model is, however, greatly simplified and, once cracks are of microstructural dimensions, attention must be paid to microstructure, crystallography and local residual stress fields. Comments on residual stress fields are made in the following section.

DEFECTS AND LOCAL RESIDUAL STRESS FIELDS

It must be recognised that it is not sufficient to classify a set of defects as "short cracks", simply on the basis of geometry, because the generation of these defects in engineering components may have induced very different local, residual stress fields. Solidification cracking or porosity in a casting or weld deposit, for example, may be relatively free of local stress, because the defects form at high temperature and any plasticity can be removed by solid-state diffusion. Hydrogen cracking in the heat-affected-zone (HAZ) of a weldment which has not been stress-relieved, however, may be associated with a monotonic plastic zone at the end of the arrested crack. Stress-relief of the weldment may partially remove this plasticity. The early stages of fatigue-crack growth from the HAZ hydrogen crack may then be affected by residual stress from the monotonic plasticity, analogous perhaps to effects of single overloads on fatigue crack growth e.g. [8].

Macroscopic elastic fields can, of course, produce changes in the stress experienced by a crack and therefore affect growth-rates. Typical practical examples of such fields are to be found in weldments (where thermal contraction of the weld metal and phase changes in the HAZ give rise to volume changes) in autofrettaged gun-barrels (where initial over-pressurisation leaves residual compression close to the bore), in case-hardened components (where martensite formation in the surface layers produces compression) and in "ballised" lugs (where the forcing of an oversized ball through the hole leaves residual compression). It is possible to assess the effects of these elastic fields using weight functions. If the residual stress distribution over the crack is $\sigma(t)dt$, the contribution to the stress intensity from residual stresses, K_{res} , is given by:

$$K_{res} = 2(a/\pi)^{\frac{1}{2}} \int_0^a \sigma(t)dt/(a^2-t^2)^{\frac{1}{2}} \quad (21)$$

This can then be added to the stress intensity generated by the applied stress. Excellent agreement between predictions and experiment has been obtained by Clark [23] for auto-frettaged cylinders, and by Braid [24] who studied crack growth in centre-cracked plate, with residual stresses generated by indentation of rollers into the plate a substantial distance above and below the crack line. The strong effects observed in this case call into question the practice of using hardness indents to serve as markers when measuring the growth-rates of small surface cracks. The residual stress fields generated could affect crack growth.

In principle, macroscopic elastic fields can therefore be allowed for, but the crucial point is that it is unreasonable to expect all small cracks to show similar growth-rate behaviour, regardless of their method of generation, and any model which attempts to predict a general pattern of behaviour, without recognising this, must be open to question. Experimental results obtained by James and Knott [5] have demonstrated that small cracks prepared by machining away long cracks have closure properties and thresholds different from those exhibited by short cracks grown from inclusions at stress levels greater than surface yield. These observations are plausibly related to differences in local residual stress fields.

The effects of local stress fields are likely to be even more important when the initiating defect is an inclusion. The inclusion is essentially in equilibrium with a metal matrix at high temperature, but, on cooling to a lower temperature, through a range ΔT , differences in thermal expansion coefficient lead to a set of internal, or "tessellated", stresses, whose magnitude depends on the difference in thermal expansion coefficient ($\alpha_m - \alpha_i$) and on ΔT , see [25-25]. Oxides and silicates in steel or nickel-base alloys have $\alpha_i < \alpha_m$, so compression is developed in the particle, and tension in the matrix: manganese sulphide in steel has $\alpha_i < \alpha_m$, so the particle is in tension. Effects on crack growth can be treated using the appropriate form for $\sigma(t)$ in equation 21). It is, however, clear that different types of inclusion can affect the value of K_{res} and hence early values of growth-rates. Equally, different test temperature affect the value of ΔT , so any effect of K_{res} varies with temperature.

To summarise, even in the absence of strong effects of crystallography, grain size, or microstructural alignment, it is necessary to account for effects of local stress fields on the growth-rates of short cracks. Many of these stress distributions are inherent to the way in which the short crack has been generated. If the complexity of such stress distributions is compounded with the multiplicity of possible initiating defects in a nominally smooth machine component, the expectation of deriving a single, deterministic model to characterise all short crack growth is low. For engineering design of machine components, the sound approach is to use fracture mechanics in a conceptual sense to link endurance limit to process control via defect content. This could perhaps be supported by statistical models based on defect distributions and crack growth-rate relationships.

FATIGUE 87

CONCLUSIONS

The paper has summarised some recent research on the characteristics of the growth-rates in fatigue of short cracks and has emphasised the important role of closure. Even for physically short cracks, it is necessary to be aware of local, residual stress fields which are inherent to the way that the crack has been generated, because these will affect local values of stress intensity and closure. An attempt has been made to assess short crack behaviour, from the point of view of engineering design and two main areas of application have been highlighted. For structures, NDE control applies and a closure-free value of ΔK_{th} should provide a lower-bound to behaviour. For machine components of high quality, the view is taken that engineering design should rely on process control and the endurance limit (or stress-range at a specified, lower number of cycles). In this respect, the main use of fracture mechanics is viewed as conceptual, rather than deterministic. Given the complications of defect distributions, it is suggested that the link between endurance limit and defects should be placed on a probabilistic basis and a simple model has been suggested, to illustrate the main features of such an approach.

ACKNOWLEDGEMENTS

Thanks are due to Professor D. Hull, F.Eng. for provision of research facilities and to Dr M.N. James, Dr J.M. Kendall and Mr P. Woollin for useful discussions and for permission to quote previously unpublished results.

REFERENCES

- (1) Paris, P.C. and Erdogan, F., Trans ASME Jnl Basic Eng., 85, 1963, p.538.
- (2) Ritchie, R.O. and Knott, J.F., Acta Met., 1973, p.639.
- (3) Suresh, S., Zavinski, G.F. and Ritchie, R.O., Met. Trans, 12A, 1981, p.435.
- (4) Beevers, C.J. and Carlson, R.L. Fatigue Crack Growth - 30 Years of Progress, ed. R.A. Smith Pergamon, 1985, p.89.
- (5) James, M.N. and Knott, J.F., Fat. and Fract. of Eng. Matls. & Structures, 8, 1985, p.177.

FATIGUE 87

- (6) Kendall, J.M. and Knott, J.F., Fatigue 84, ed. C.J. Beevers et al, EMAS, 1984, p.307.
- (7) Knott, J.F., Fatigue Crack Growth - 30 Years of Progress, ed. R.A. Smith Pergamon, 1985, p.31.
- (8) Alexander, D. and Knott, J.F., this Conf, 1987.
- (9) Taylor, D. and Knott, J.F., Metal Technology, 9, 1982, p.221.
- (10) Taylor, D. and Knott, J.F., Fat. Eng. Matls. & Structures, 4, 1981, p.147.
- (11) Brown, C.W. and Hicks, M.A., Intl. Jnl. Fatigue, 4, 1982, p.73.
- (12) Brown, C.W., King, J.E. and Hicks, M.A., Metal Sci., 18, 1984, p.374.
- (13) Miller, K.J., Eshelby Memorial Symposium, Sheffield, Roy. Soc., 1984, p.477.
- (14) Kendall, J.M., James, M.N. and Knott, J.F., The Behaviour of Short Fatigue Cracks, ed. K.J. Miller and E.R. de los Rios, ECFI Mech. Eng. Publ. Ltd. (London), 1986, p.241.
- (15) Minakawa, K., Newman, J.C. and McEvily, A.J., Fat. Eng. Matls. & Structures, 6, 1983, p.359.
- (16) Kendall, J.M., "Aspects of Fatigue Crack Growth in a Low-Carbon Steel" Ph.D. thesis, University of Cambridge, 1986.
- (17) Kitagawa, H. and Takahashi, S., Proc 2nd Intl. Conf. on Behaviour of Materials, Boston, 1976, p.627.
- (18) Davidge, R.W., Mechanical Behaviour of Ceramics, Cambridge Univ. Press, 1979, p.143 et seq.
- (19) Bompas-Smith, J.H., Mechanical Survival, ed. R.H.W. Brook McGraw Hill (UK), 1973 p.59 et seq.
- (20) Neville, D.J. and Knott, J.F., Jnl. Mech. Phys. Solids, 34, 1986, p.243.
- (21) Widgery, D.J. and Knott, J.F., Metal Sci., 12, 1978, p.8.
- (22) Bowen, P., Ellis, M.B.D., Strangwood, M. and Knott, J.F., Proc. 6th Europ. Conf. on Fracture, ed. H.C. Van Elst and A. Bakker EMAS, Vol.III, 1986, p.1751.

FATIGUE 87

- (23) Clark, G., Fracture Mechanics Technology Applied to Materials Evaluation and Design, ed. G.C. Sih, N. Ryan and R. Jones, 1983, p.417.
- (24) Braid, J.E.M., "Fatigue Crack Propagation in Residual Stress Fields" Ph.D. thesis, University of Cambridge, 1983.
- (25) Brooksbank, D. and Andrews, K.M., J. Iron and Steel Inst., 210, 1972, p.246.
- (26) Tsubota, M., King, J.E. and Knott, J.F., Proc. 1st Parsons Turbine Conference, Trinity College, Dublin, Parsons Press/Inst. Mech. Engrs., 1984, p.189.
- (27) Woollin, P. and Knott, J.F., this conf, 1987.

FATIGUE 87

EFFECTS OF MN DISPERSOIDS ON NEAR THRESHOLD FATIGUE CRACK GROWTH
IN 2134 TYPE ALLOYS +

K. V. Jata, J. A. Walsh, and E. A. Starke, Jr. *

The near threshold fatigue crack growth resistance of high purity 2134 type alloys with Zr as the major dispersoid forming element, has been examined in the under and overaged conditions as a function of Mn additions ranging from 0 to 1.02 weight percent. The additions of manganese resulted in a continuous decrease of the nominal threshold in both the aging conditions with the effect more pronounced in the overaged condition. Crack deflections, closure and fractography suggest that roughness induced crack closure is dominant in all alloys. Besides, fractographic evidence suggests that large Mn particles could contribute to local microcrack acceleration resulting in an intrinsic lowering of the fatigue thresholds and faster crack propagation rates.

INTRODUCTION

Dispersoid forming elements such as Zr, Mn and Cr control the grain structure in aluminum alloys. Additionally Mn and Cr rich particles can homogenize slip and impede slip band impingement at the grain boundaries resulting in a reduced low energy brittle intergranular fracture. Although these effects could play a role in improving fracture toughness, homogeneous slip might not necessarily improve fatigue threshold behavior. In precipitation hardened alloys slip reversibility arguments suggest that homogeneous slip (e.g. in the overaged conditions with non shearable particles) reduces the fatigue crack growth resistance in comparison to inhomogeneous (e.g. underaged condition with shearable particles) slip (1,2). There is however evidence in the literature that Mn dispersoids can substantially improve near threshold fatigue crack growth resistance by suppressing intergranular fracture (3). Results on the effect of Mn additions to Al-Si-Mg alloys show that the fatigue crack resistance in the peak condition is improved due to a decrease in the grain boundary fracture by homogenization of slip by the Mn rich particles in spite of reduced slip reversibility. Literature on other alloys

*Department of Materials Science, University of Virginia,
Charlottesville, VA 22901

+This research was sponsored under Grant AFOSR-83-0061, Dr. Alan
Rosenstein, Program Manager.

FATIGUE 87

such as steels suggest that inclusions such as MnS either do not have any influence on near threshold crack growth rate (4) or could result in an improved fatigue threshold due to crack closure effects. After correcting for crack closure the intrinsic fatigue threshold of alloys containing lower MnS content exhibit higher values (5,6).

A thorough literature search has shown that a systematic evaluation on the effect of second phase particles on the fatigue threshold behavior, crack closure, crack deflection, load ratio effects and fractography has not been conducted. The present work was carried out to document the effects of Mn particles on the near threshold fatigue crack growth, crack closure, crack deflections in 2134 type alloys whose grain structure has already been stabilized by Zr. Thus Mn should not have any effect on the grain size and recrystallization. The yield strength of all the alloys was kept approximately the same by choosing appropriate aging times. Both under and overaged conditions were developed to study the effect of the deformation mode on the fatigue threshold behavior.

EXPERIMENTAL PROCEDURES

The 2134 type alloys were obtained from Reynolds Metals Company in the form of 20 mm thick plates. All plates were hot rolled, (744K-644K), solutionized 1.5 hours, at 766K, then water quenched and stretched approximately 2.5% to T351 temper. The actual chemical compositions of these alloys are shown in Table I. The alloys were aged in an oil bath at 463K to obtain under and overaged conditions. Tensile samples were tested at a strain rate of $3 \times 10^{-3} \text{ sec}^{-1}$ and the results are shown in Table II. Crack propagation tests were conducted on compact tension specimens at 30 Hz in laboratory air at 295K and at a R.H. of 45% at R ratios of 0.1 and 0.5 in the L-T orientation. Crack closure curves were obtained by the back face strain gage and the crack growth rates were generated by the standard load shedding scheme.

RESULTS

A. Crack growth rates. The results obtained from the fatigue crack growth tests conducted in air at a R ratio of 0.1 are shown in Figure 1 and 2 for the under and overaged conditions. In both aging conditions the effect of Mn is to increase the crack propagation rates at lower ΔK 's with the effect more pronounced in the overaged. A comparison of the crack propagation rates for any one Mn level show that underaged structures are superior to overaged at near threshold consistent with previous results on under and overaged aluminum alloys (eg.7), Figure 3 and 4. This is also reflected in the nominal threshold stress intensity factor range for the underaged alloys being higher than the overaged at all Mn levels, Table III. Fatigue crack growth rates as a function of Δ

K at a higher R ratio of 0.5 did not show any significant differences with Mn content. The differences were only observed between the two aging conditions with the underaged again exhibiting superior fatigue crack growth resistance, Table III. The differences in the crack growth rates between the two R ratios were seen only below ΔK of $7 \text{ Mpa m}^{1/2}$ suggesting that crack closure was a role in reducing growth rates at the lower R ratio and at low ΔK levels. Crack closure was observed at 0.1 R ratio and the values are shown in Figure 5. At the high R ratio only #3 alloy in the overaged condition exhibited crack closure at growth rates of 10^{-10} m/cycle .

B. Crack deflections. Crack path profiles of both the under and overaged alloys at lower R ratio were found to be non linear. Since the fracture morphology changed considerably from shear faceted mode at the near threshold to ductile tearing at ΔK of $5 \text{ Mpa-m}^{1/2}$ the crack deflection angles only below this K level were measured. The lineal roughness values were also measured only below K of 5 Mpa m , Table III. The #1 UA alloy exhibited the highest values of lineal roughness and crack deflection in agreement with the most inhomogeneous slip mode. The trend of these values for other alloys along with the crack closure results Figure 5, strongly suggest that roughness induced crack closure is dominant in all the alloys tested at $R=0.1$. This is also supported by the disappearance of closure as well non linearity in the crack path at the higher R ratio (0.5) test.

C. Fractography

The fracture surface features of the underaged alloys were more crystallographic than the overaged alloys. The crystallographic mode was not significantly affected by the presence of Mn rich particles. However it diminished in the overaged alloys and more grain boundary facets were observed. Out of plane cracking was also found to be still prevalent in the overaged conditions. Two near threshold micrographs illustrating the fracture surface asperities, out of plane cracking, grain boundary facet and slipband intersections for alloys #1 and #3 for overaged condition are shown in Figure 6. These features were typical of all the alloys in the overaged condition. In addition to these characteristics the #3 alloy clearly showed larger than average size particles on grain boundary facets interacted with the crack front, Figure 7. In this micrograph trails pointing towards the crack growth direction can be seen. At higher magnifications these trails were associated with either microfacets or striations. When the sample was properly oriented the striations could be clearly observed and the crack growth rate obtained from high magnification shots revealed 1 to 2 orders of magnitude higher crack growth rates than the measured growth rates.

DISCUSSION

The decrease in ΔK_{th} in the overaged condition for all the alloys can be explained on the basis of reduced non linearity of the crack path and reduced slip reversibility proposed in the literature (8). Surface roughness induced crack closure is dominant in all the alloys in both aging conditions. The decrease of the closure level with increasing ΔK level and the disappearance with increasing R ratio (9) support this observation. However crack closure results and fretting corrosion deposits were found on fracture surfaces of some alloys suggest that other closure mechanisms may be operating. For instance in the alloy #3 in the overaged condition at R=0.1 crack closure levels were found to be as high as that of #1 alloy. Again the closure persisted at R=0.5, whereas other alloys did not exhibit this behavior. This may be due to some contribution to closure arising from the pulled out Mn particles acting as asperities and acting as contact points at levels above K_{min} . Further investigation is necessary before contribution from these mechanisms are ruled out. The fracture surfaces also demonstrated that second phase particles can cause void nucleation at near thresholds. However in low Mn alloys there do not seem to be a clear indication of crack front interaction with the particles or voids. In many cases there was only evidence of slight plasticity around the void. In alloy #3 wherever the fracture was composed of intergranular facets the Mn particles and the associated voids interacted with the crack front.

The present results demonstrate that when sufficiently large size and volume fraction of void nucleating particles are present near threshold fatigue crack growth rates could be influenced. In the present study the Mn rich particles which were equiaxed in the #2 alloy did not seem to have influenced the fatigue threshold behavior although they were associated with voids. However when the Mn rich particles assumed a more non-equiaxed shape the effect was to increase the crack growth rates by local acceleration of the crack front. Striation formation was observed in the vicinity of the cracked particle or void. The creation of the voids in the near threshold region implies that a critical tensile strain is being reached even at these low ΔK levels. Although the overall tensile fracture strain Table II, for #3 is .268 the void nucleation tensile strain has been determined to be less than .02 to create .1 volume percent of voids (10).

CONCLUSIONS

1. The fatigue crack growth rates in 2134 alloys increase with increasing Mn content. The roughness induced crack closure in all the alloys tested arises from fracture surface roughness. Substantial mode II displacements and fracture surface asperities comparable to the crack tip opening displacement were observed in

FATIGUE 87

all cases.

2. Although the highest Mn level alloy exhibited closure levels comparable to the lower Mn alloys the nominal and also the effective fatigue thresholds were lower in the overaged condition.
3. Fractography suggests that in the highest Mn level alloy there is a crack front particle interaction which causes local faster crack propagation. The regions near the Mn particles exhibited striations which showed 1 to 2 orders of magnitude higher crack growth rates than the macroscopic or measured growth rates.

REFERENCES

1. Hornbogen, E. and Gahr, K.H. Zum: Acta Metall., 1976, vol. 24, p. 581
2. Carter, R.D., Lee, E.W., Beevers, C. J., and Starke, E.A.: Metall. Trans. A, 1984, vol. 15A, p. 555
3. Edwards, L. and Martin, J.W.: Metal Science, 1983, vol. 17, p. 511
4. Fowler, G.J.: Mater. Sci. and Engg., 1979, vol. 39, p. 121
5. Cadman, A.J., Nicholson, C.E., and Brooks, R.: paper #34, International Symposium on Fatigue Thresholds, Stockholm, Sweden, June 1981
6. Wilson, A.D.: Fracture: Interactions of Microstructure, Mechanisms, Mechanics, eds. J.M. Wells and J. D. Landes, AIME, 1984, p. 235
7. Jata, K.V. and Starke, E.A.: Metal. Trans. A, 1986, vol. 17, p. 1011
8. Suresh, S.: Metall. Trans.A, 1985, vol. 16A, p. 249
9. Suresh, S. and Ritchie, R.O.: Metall. Trans.A, 1982, vol. 13A, p. 1627
10. Walsh, J.A., Jata, K.V., and Starke, E.A.: 1986, TMS Fall Meeting, Orlando, Florida, USA.

TABLE 1- Chemical Composition in weight percent

Alloy	Cu	Mg	Mn	Fe	Si	Zr
#1	3.96	1.48	0.00	.06	.04	.14
#2	3.96	1.46	0.31	.06	.04	.12
#3	4.51	1.47	1.02	.06	.04	.12

FATIGUE 87

TABLE II- Room Temperature mechanical properties

Alloy	σ_{ys}	σ_{uts}	n	%el.	ϵ_f	K_{Ic}
#1 UA	376	431	.052	11.2	.409	52
OA	447	481	.052	13.5	.573	39
#2 UA	403	443	.065	15.7	.444	53
OA	448	478	.037	10.3	.644	45
#3 UA	425	491	.057	13.4	.217	32
OA	451	493	.041	9.5	.268	27

TABLE III- Fatigue Thresholds

Alloy	Threshold			Mean Crack Deflection	Lineal Roughness Parameter
	nominal	effective			
		R=0.1	R=0.5		
#1 UA	3.3	2.0	2.2	29	1.14
OA	3.0	1.34	1.67	14	1.01
#2 UA	3.1	1.85	2.16	25	1.1
OA	2.4	1.89	1.55		
#3 UA	2.8	1.26	1.85	12	1.02
OA	1.9	0.93	1.55	16	1.02

FATIGUE 87

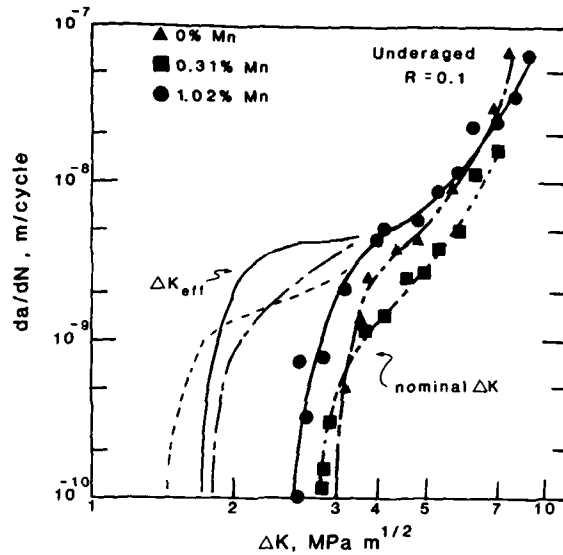


Figure 1: Comparison of fatigue crack growth rates (da/dn) as a function of nominal and effective stress intensity range for different Mn levels in the underaged condition ($R=0.1$).

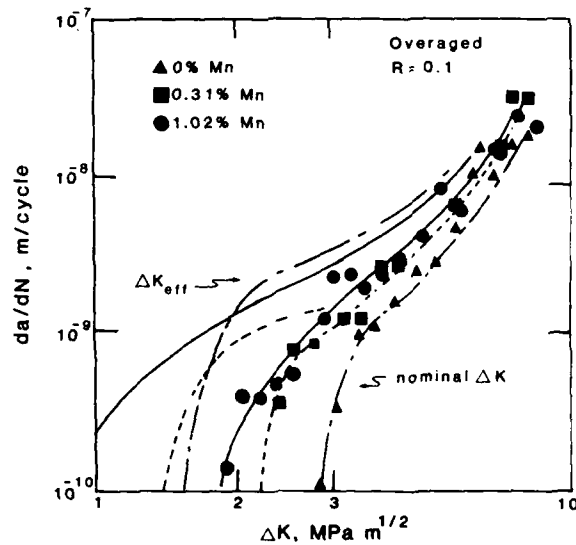


Figure 2: Comparison of fatigue crack growth rates as a function of nominal and effective stress intensity range for different Mn levels in the overaged condition ($R=0.1$).

FATIGUE 87

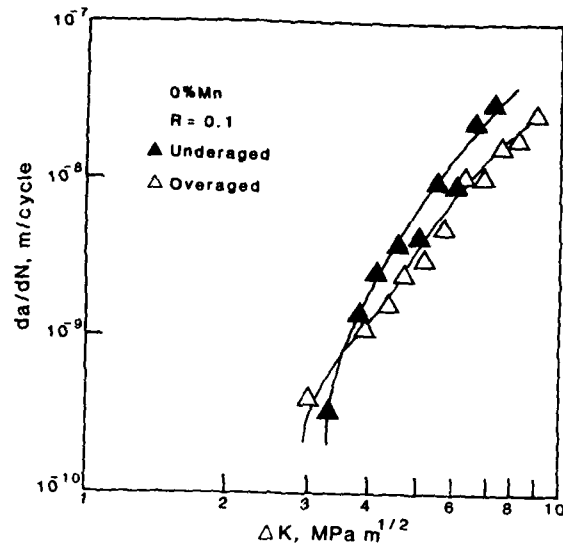


Figure 3: Comparison of fatigue crack growth rates as a function of nominal stress intensity range for a 0% Mn alloy in the under and overaged conditions ($R=0.1$).

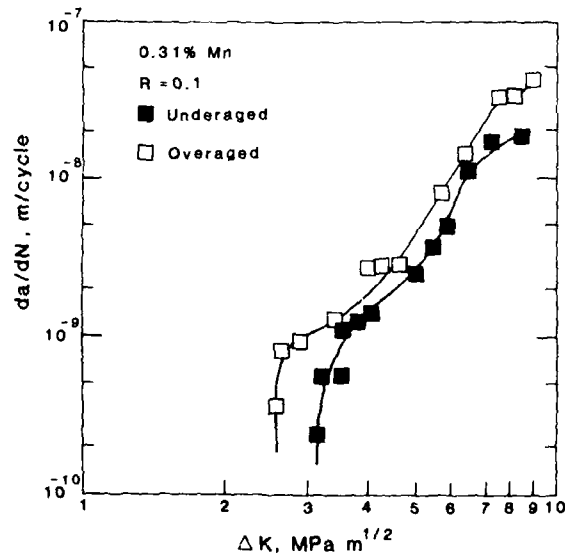


Figure 4: Comparison of fatigue crack growth rates as a function of nominal stress intensity range for 0.3% Mn alloy in the under and overaged conditions ($R=0.1$).

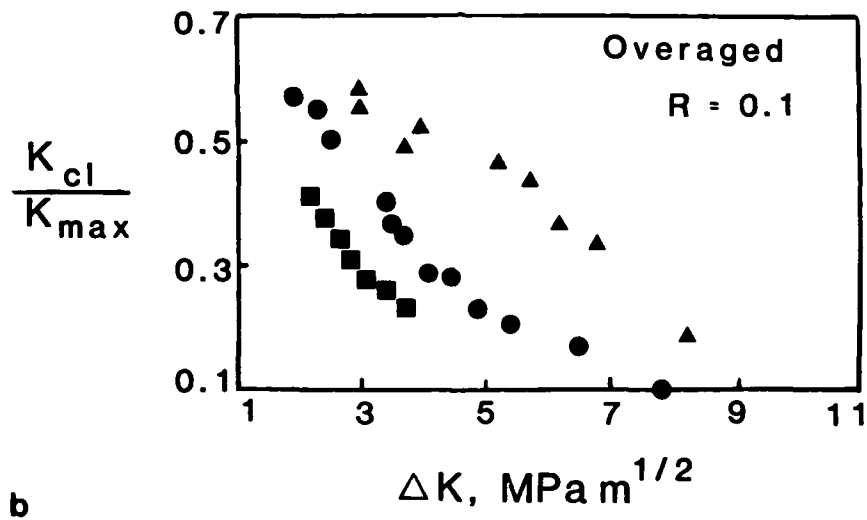
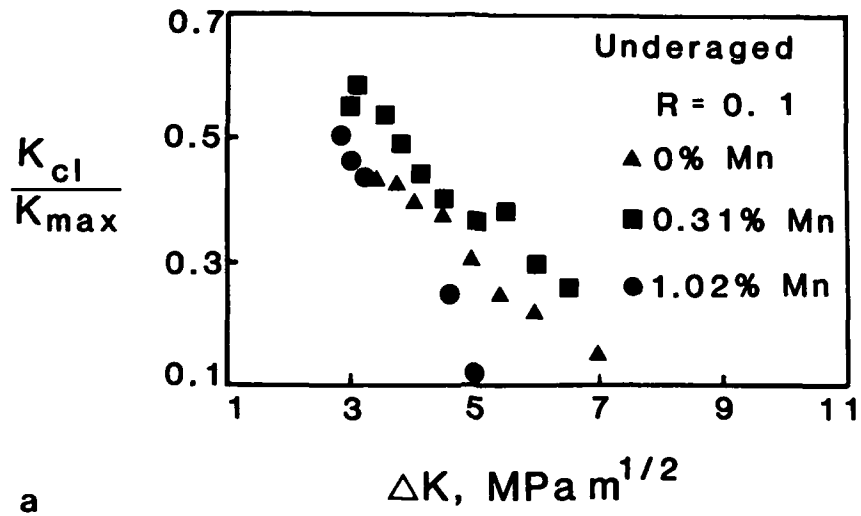


Figure 5: Variation of crack closure with nominal stress intensity range in the underaged condition (a) and overaged condition (b).



Figure 6: Near-threshold fractographs of overaged alloys 0% Mn (a) and 1.02 % Mn, overaged alloy (b).

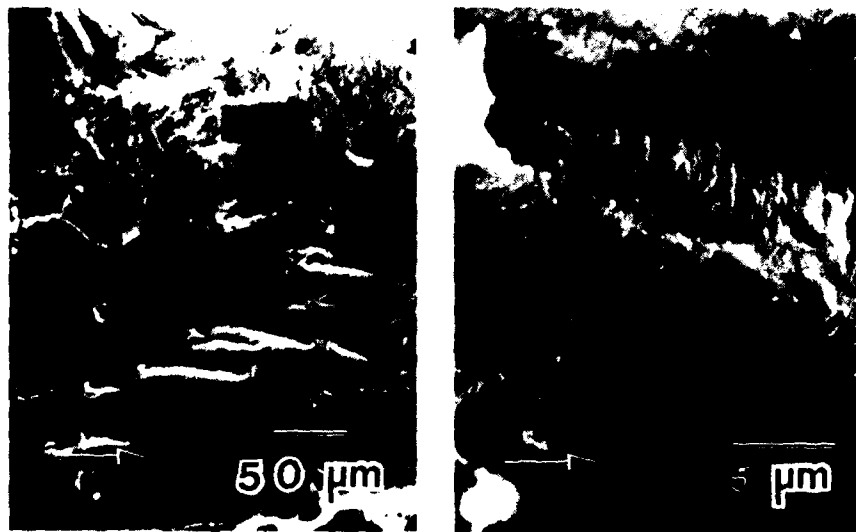


Figure 7: Voids around Mn dispersoids and subsequent striated crack growth in 1.02% Mn, overaged alloy.

FATIGUE 87

INTERACTION OF MICROSTRUCTURE AND FATIGUE IN TOOL STEELS

H. BERNS*

Different grades of cold working, hot working and high speed steels were investigated as to their behaviour in rotating bending and stable crack growth tests with longitudinal and transverse specimens. Hard phases like carbides and nonmetallic inclusions vary in size and content because of carbon contents from 0.27 to 2.25 % and conventional, hiped and vacuum sintered manufacturing. The tempered matrix consists of martensite and/or bainite with some retained austenite. The macrohardness ranges from 400 to 900 HV.

INTRODUCTION

The aim of this paper is to summarize our recent work on the fatigue behaviour of hard steels (Berns et al. (1) to (4), Weber (5)). Their microstructure consists of hard phases like carbides and nonmetallic inclusions (NMI) which are embedded in a quenched and tempered matrix of martensite (M) and/or bainite (B) with or without some retained austenite (RA). Stress controlled push/pull-tests were carried out on tool steels, by Rogan (6) in the wholly compressive and a 6 to 1 compressive to tensile stress region. Kocanda (7) used strain controlled push/pull-test. Rotating bending and rolling contact fatigue tests showed crack initiation at NMI (Tricot et al. (8) and carbides (Vincent (9)) in ball bearing steels.

Most tools have to withstand cyclic compressive and tensile stresses. Examples are dies under radial

* Institut für Werkstoffe, Lehrstuhl Werkstofftechnik, Ruhr-Universität Bochum, Postf. 102148, D-4630 Bochum

FATIGUE 87

pressure and punches under unintentional bending stresses. Therefore, smooth rotating bending specimens are used in the present work to study the crack initiation and failure while the stable crack growth is followed up in CT specimens. Thermal fatigue tests are carried out on hot working tool steels.

MICROSTRUCTURE

Cold working (CW), hot working (HW), and high speed (HSS) tool steel specimens are investigated in the quenched and tempered or isothermally transformed condition (tables 1 and 2). A rough characterization of the microstructure is given in table 3.

CW 1: This hypoeutectoid steel is tempered to three different hardness levels.

CW 2: After quenching from 820 or 880°C this hypereutectoid tool and ball bearing steel contains 7 % or 16 % RA in the tempered martensite. Starting from the same austenitizing temperatures an isothermal transformation at 250°C 1h or 215°C 6h is performed to gain an untempered bainitic microstructure with 0 or 2,5 % RA respectively. The RA content is measured by X-ray diffraction.

CW 3: In this variety of hypoeutectic chromium steels, the carbide content grows with the carbon content. The maximum carbide size depends on the ingot diameter and hot working ratio λ . In hot isostatically pressed (HIP) material it is smaller by one order of magnitude. The range of hardening temperatures renders RA contents up to 40 %, which vanish during secondary hardening at tempering temperatures above 500°C or by deep cooling to -196°C.

HW 1 and 2: The amount and size of segregated eutectic carbides decreases as the carbon content is lowered. In addition to a structure of tempered martensite, a mixed one of martensite with 30 % bainite is produced by controlled cooling (in 910 s from 800 to 500°C). Tempering at 620°C brings about a hardness equal to that of pure tempered martensite.

HSS: Hot isostatically pressed (HIP), vacuum sintered (VS), and conventionally cast (C) materials are compared after hot working at two different hardness levels. The maximum carbide size of powder metallurgical (PM) steel is smaller (HIP = 5 μm , VS = 10 μm) than in conventional steel as given in table 2.

CRACK INITIATION

Four point rotating bending. After heat treatment and circumferential grinding to a smallest diameter of 5 mm, the rotating bending specimens are ground and polished in an axial direction to avoid any notches, and to produce a surface finish that allows an observation under a light microscope (LIMI) at 1000 x magnification.

CW 1: At a hardness level of 400 and 480 HV crack initiation is preceded by the formation of dislocation cell structures (as revealed by transmission electron microscopy TEM) and glide traces around NMI at the surface. Cracks start in these traces. At 550 HV no subgrains or signs of local plasticity are noticeable. As before, cracks solely arise at NMI in the surface. Inclusions of less than 10 μm size may act as crack starters. Crack formation is retarded by an increase in steel hardness.

CW 2: Cracks are initiated at Ti(C,N) inclusions in or below the surface, as can be seen in the fracture face under the scanning electron microscope (SEM). Their size may be less than 10 μm . Sulfides of equal diameter give far less rise to cracking as their Young's modulus is only half that of steel, and their cross section is round. Ti(C,N) particles are square, and their Young's modulus exceeds that of steel by about 50 %. Since their volume content is small, subsurface crack start is common. The number of cycles to crack initiation N_i is reduced in bainitic specimens and increased by a higher hardness. As the RA-content is raised the amount of stress induced transformation to martensite near the surface grows. This induces compressive residual stresses which cause a delay in the crack start.

CW 3: At 850 HV the cracks form in the matrix/carbide interface; at ≤ 770 HV the carbides crack. Due to the large volume of coarse eutectic and primary carbides, cracks always start at the surface. $N_i \leq 0,1 N_f$ (N_f = number of cycles to fracture). At high stress amplitudes, cracks of carbide length appear after a single or a few cycles. However, it may take a considerable number of cycles until they penetrate into the matrix.

HW 1 and 2: In longitudinal (l) specimens cracks develop from fractured sulfides and eutectic carbides at the surface and in rare cases below. Transverse (t) specimens begin with a decohesion between the matrix and the coarse hard phases. A lower carbon and eutectic carbide content improves N_i , especially for t-specimens. 30 % bainite have no significant influence on N_i .

FATIGUE 87

HSS: While in conventional steel cracks start from coarse carbides at the surface, hard round Ca, Si, Al oxides cause mostly subsurface cracks in hipped l and t specimens. Inclusion filled hose-like sinter pores in VS steel lead to stretched NMI of up to 150 μm length after hot working. As a result we find subsurface cracks in l-specimens and surface cracks in t-specimens where the NMI penetrate the surface. As in CW 3 cracks may appear in conventional steel after the first cycle.

Thermal fatigue. Thermal fatigue tests are carried out with polished plates 50 x 55 x 10 mm of steel HW 1 and HW 2. After thermal cycling by repeated induction heating (50°C/s to 650°C) and subsequent water quenching (500°C/s), a metallographic sample of 10 x 10 x 50 mm is taken and investigated for surface cracks. Crack start at NMI is observed frequently.

STABLE CRACK GROWTH

CT-specimens. The tests are performed in accordance with ASTM-E 399/83 and 647/83. The threshold ΔK_0 , at a crack velocity da/dN of about 10^{-6} mm/cycle, is measured rather independently of the hardness between 5 and 10 $\text{MPa}\cdot\text{m}^{1/2}$ for CW 1, CW 3 and HW 1 and between 3 and 4 for HSS. In CW 2 an increase from 5 to 15 $\text{MPa}\cdot\text{m}^{1/2}$ is found as the hardness is lowered from 790 to 700 HV. At 40 % RA, ΔK_0 of CW 3 is raised to 20 $\text{MPa}\cdot\text{m}^{1/2}$. This is probably due to an austenite/martensite transformation in the plastic zone at the crack tip. Higher stress intensities cause instability. On the fracture face only half of the bulk RA is measured. At $da/dN = 10^{-11}$ mm/cycle CW 1 comes down to $\Delta K_0 = 2.5 \text{ MPa}\cdot\text{m}^{1/2}$.

The crack velocity is apparently governed by the matrix and therefore rather independent of hard phases and longitudinal or transverse taking. An increase in hardness raises the crack velocity and lowers the critical ΔK_0 . There is no significant influence of bainite. Hipped CW 3 and HSS show considerably lower ΔK_0 values as compared to conventional steel. A possible reason may be that the carbide spacing of PM steel is smaller than the plastic zone size thus initiating cracks at carbides ahead of the main crack tip.

Thermal fatigue. Due to the decrease in temperature below the surface the crack velocity of HW 1 and 2 at first increases. With a growing distance of the crack tip from the surface the local thermal stress amplitude drops and the crack growth slows down again. A lower carbon content retards the crack extension.

FATIGUE 87

FATIGUE LIFE

The fatigue fracture area in fractured rotating bending specimens decreases from more than 10 % at 500 HV to less than 0.1 % of the cross section at 850 HV. This and the weak interaction of stable crack growth and hard phases reveals that the life to fracture of hard steels is strongly depending on N_i . A higher hardness of CW 1, for instance, raises N_f due to an increase of N_i in spite of a reduction in the stable crack growth period ($N_f - N_i$). A statistical evaluation of the experimental results is given in table 4 and figure 1.

Cracks are initiated at the most effective and largest stress raising hard phases. In CW 1, CW 2, HW 1, HW 2, CW 3 (HIP) and HSS (HIP, VS) these are NMI, in conventional CW 3 and HSS primary and eutectic carbides. If such a hard particle is resembled by an equivalent crack size, a local stress intensity ΔK_1 may be calculated using the local bending stress for subsurface crack origins. N_f then is found inversely proportional to ΔK_1 .

Stress or strain induced transformation of retained austenite retards crack initiation and growth due to counteracting local compressive stresses. The fatigue life of CW 2 and CW 3 is improved by RA. Bainite accelerates crack formation and therefore, reduces N_f .

FATIGUE LIMIT

Results of martensitic and bainitic CW 2 show that there is a poor correlation between hardness and fatigue limit, but a rather good one between RA and fatigue limit in rotating bending as shown in figure 2.

CONCLUSIONS

Under rotating bending fatigue cracks start at the largest hard phase particle in the surface (high content of coarse carbides) or subsurface (small content of nonmetallic inclusions). Crack start is delayed by an increase in matrix hardness.

Stable crack growth is governed by the matrix hardness and rather independent of coarse hard phases. The threshold stress intensity, ΔK_0 , was found as low as $2.5 \text{ MPa}\cdot\text{m}^{1/2}$. Retained austenite retards the crack velocity.

FATIGUE 87

Fatigue life, N_f , is strongly depending on N_i . N_f is inversely proportional to the local stress intensity at the crack origin. Bainite reduces N_f while retained austenite improves fatigue life and limit.

Thermal fatigue starts at coarse hard phases. The crack velocity reaches a subsurface maximum.

TABLE 1 - Average chemical composition of the tool steels investigated

Steel Type	C	Cr Weight Percent	Mo	V	other
CW 1	0.55	0.8			0.8 Mn
CW 2	1.0	1.5			
CW 3	$\sim 2^a)$	12	1	4	2 Ti
HW 1	~ 0.4	5	1.3	1	1 Si
HW 2	0.27	5	1.3	1	1 Si
HSS	1.3	4	16 ^{b)}	3	9 Co
a) 1.5 to 2.3		b) 2 Mo + W			

TABLE 2 - Heat treatment and hardness

Steel Type	HT °C	TT °C	Hardness HV
CW 1	860	340, 420, 490	550, 480, 400
CW 2	820, 880	180 250 c) 215	730, 790 700, 780
CW 3	950 to 1100	180 to 550	850 to 630
HW 1	1060 1060d)	610 620	460 460
HW 2	1060	600	460
HSS	1075, 1180	560	800, 900
HT = hardening temperature, TT = highest tempering temp.			
c) isothermal bainite transformation temperature			
d) controlled cooling to give martensite + 30% bainite			

FATIGUE 87

TABLE 3 - Characterisation of microstructure in the quenched and tempered condition
(conventionally cast and hot worked steel)

Steel Matrix			Carbides		Nonmetallic Inclusions	
		Type	Size+)	Amount	Type	Size+)
			μm	vol. %		μm
CW 1	M	tp M_3C	~0.1			
CW 2	M, RA	s M_3C	1	6 or 9	MnS Ti(C,N)	50 30
CW 3	M, RA	p MC	10	<3		
		e M_7C_3	50	10		
		s M_7C_3	1	15		
HW 1	M, B	e MC	30	<1	MnS	50
		s M_7C_3	1			
HW 2	M	e MC	20			
		e M_7C_3	1			
HSS	M	p, e MC	50	15	oxides	50
		M_2C				
		M_6C				

M = martensite, B = bainite, RA = retained austenite
p = primary, e = eutectic, s = secondary, tp = temper
+) maximum size encountered

Table 4 - Statistical evaluation of fatigue life by the arc sin \sqrt{P} - transformation for a probability of P = 50 %

- Life to fracture N_f (or to crack initiation N_i as designated) at a stress amplitude $\sigma_a = 1000 \text{ MPa}$
- stress dependence of N_f (N_i) as given by $\log N = A - B\sigma_a$; σ_a in MPa
longitudinal or transverse (t) taking; B = bainite; M/B = martensite with 30 % bainite,
1) small ingot, low hot working ratio,
2) 1.58 % C (X 155 CrVMo 12 1) 13 % RA
3) 2.25 % C (X 225 CrVMo 13 4) 15 % RA

FATIGUE 87

Steel		Hardness HV	$N_f(N_i)$ 10^3	A	B 10^{-3}
CW 1		400	11.4	7.3734	3.3171
		480	26.8	7.6334	3.2048
		550	33.0	6.8114	2.2924
CW 2		730	1127.0	10.4740	4.4220
		790	512.7	9.4620	3.7521
	B	700	81.3	7.4633	2.5531
	B	780	230.3	8.6029	3.2406
CW 3	2)	770	39.4	11.1285	6.5325
	t2)	770	3.0	12.0729	8.5941
	HIP3)	760	10.2	13.1455	9.1385
HW 1	N _i	460	14.5	6.8145	2.654
		460	31.3	6.7391	2.243
	M/B	460	27.3	6.8937	2.458
HW 1 1)	N _i	460	9.0	7.2128	3.260
		460	30.3	6.8274	2.345
	N _i , t	460	1.4	4.0884	0.949
		460	14.0	6.4966	2.349
HW 2 1)	N _i	460	6.2	5.8653	2.027
		460	29.0	6.9786	2.515
	N _i , t	460	1.7	5.2405	2.000
		460	14.2	6.6872	2.535
HSS	C	900	62.2	8.2389	3.4454
	C,t	900	3.5	5.6426	2.0939
	C,t	800	5.8	6.2432	2.4794
	HIP	900	1354.1	9.7518	3.6202
	HIP,t	900	297.6	9.3868	3.9132
	VS	900	640.1	8.8883	3.0820
	VS,t	900	5.7	7.8151	4.0625
	VS,t	800	2.4	5.4412	2.0701

REFERENCES

- (1) Berns, H. and Siekmann, G., Wire, Vol.35, 1985, pp.8-15
- (2) Berns, H. and Trojahn, W., VDI-Z, Vol.125, 1985 pp.889-892
- (3) Berns, H. and Wendl, F., Härtereitechn.Mitt., Vol.41, 1986, No.6

FATIGUE 87

- (4) Berns, H., Lueg, J., Trojahn, W., Wähling, R. and Wisell, H., "Fatigue Behaviour of High Speed Steels"; Proc.Int.Conf. Powder Metallurgy, pp.515-519, Edited by W.A. Kaysser and W.J. Huppmann, Verlag Schmidt, Freiburg, 1986
- (5) Weber, L., Wechselwirkung zwischen Randschichtzustand und Schwingungsrißausbreitung, Doctoral Thesis, Ruhr-Universität Bochum, FRG, 1986
- (6) Rogan, J. and Parry, J.S.C., High-Pressure Science and Technology, 6. AIRAPT Conf., Vol.2, Edition K.D. Timmerhaus and M.S. Barber, Plenum Press, New York, 1979
- (7) Kocanda, A., 7th Congress on Material Testing, Budapest, 1978, pp.147-150
- (8) Tricot, R., Monnot, J. and Lluansi, M., Metals Engineering Quaterly , Vol.12, 1972, No.5, pp.39-47
- (9) Vincent, L., Coquillet, B. and Guiraldenq, P., Metallurg. Transact. , Vol.11A, 1980, pp.1001-1006

FATIGUE 87

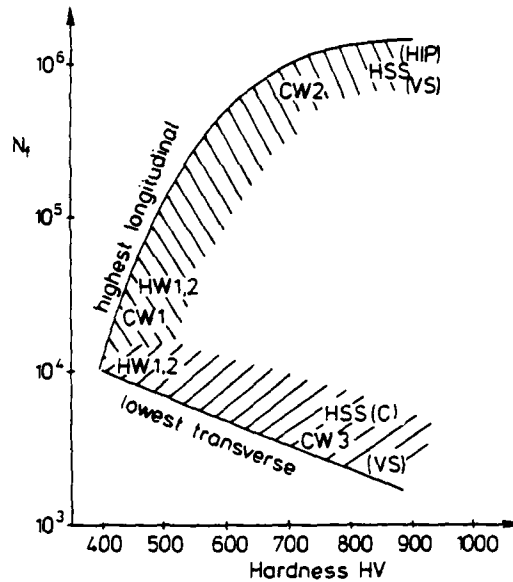


Figure 1 Fatigue life N_f in rotating bending ($\sigma_a = 1000$ MPa, $P = 50\%$)

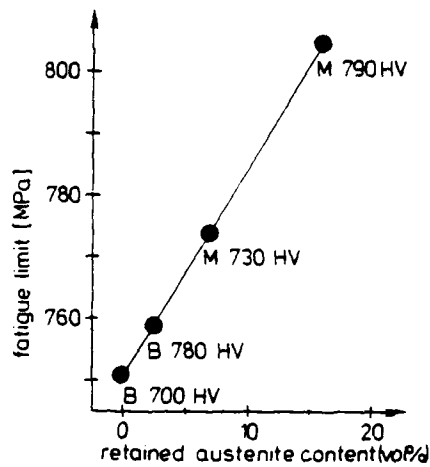


Figure 2 Fatigue limit and retained austenite content of steel CW2. M = martensitic, B = bainitic, probability of survival $P_S = 95\%$

TENSILE MEAN STRESS EFFECTS ON UNIAXIAL
FATIGUE BEHAVIOR OF 1045 HR STEELA. Fatemi¹ and R.I. Stephens²

The effect of tensile mean stress/strain on axial fatigue and cyclic deformation behavior of SAE 1045 steel in the hot-rolled condition was investigated using strain-controlled smooth specimens at room temperature. It was found that mean strain is not detrimental to fatigue life unless it produces a mean stress. In tests where the mean stress was significant, a reduction in fatigue lives up to a factor of 3 was observed. Mean stress relaxation and mean strain effect on the cyclic stress-strain curve is discussed and the use of several damage parameters to predict the mean stress effect on fatigue life is examined.

INTRODUCTION

Components and structures are usually subjected to fluctuating strains (stresses) with different values in tension and compression. This means the presence of some mean static strain and/or stress superimposed on an alternating strain (stress). Even though strain-life, ϵ -N, data are widely used to describe low cycle fatigue behavior, the traditional S-N approach is still commonly used to predict fatigue life in the presence of mean stresses. A popular approach has been the use of the modified Goodman diagram (1). Nihei et al (2) have reviewed the capability and accuracy of several damage parameters to predict the mean stress effect on fatigue life as applied to strain-controlled fatigue data. The most commonly used methods to include mean stress or mean strain

¹Assistant professor of Mechanical Engineering, Purdue University at Fort Wayne, Fort Wayne, IN 46805, USA

²Professor of Mechanical Engineering, The University of Iowa, Iowa City, IA 52242, USA

effects in fatigue life prediction involving strain-life data are those proposed by Morrow (3) and Smith et al (4). In this work, the accuracy of these two methods in addition to a recent approach proposed by Lorenzo and Laird (5) is examined based on the results of strain-controlled fatigue tests with mean strain and/or stress. Mean stress relaxation and the influence of mean strain/stress on the cyclic stress-strain relationship for the material are also discussed.

EXPERIMENTAL PROGRAM

The material used in this work was hot-rolled 1045 steel in the normalized condition. The microstructure consisted of fine grained pearlite and ferrite which contained up to 0.1 mm long sulfide inclusions in the rolling direction. Mechanical properties of this material are shown in Table 1 (6).

Standard uniaxial fatigue specimens with a nominal diameter of 6 mm and gage length of 12.7 mm were used. The specimens had a polished surface with polishing marks in the longitudinal direction. Tests were performed with a 89 kN closed-loop electro-hydraulic test system using Wood's metal grips. Strains were measured and controlled with a 12.7 mm extensometer attached to the specimens through scotch tape and clamped by small springs. For tests with strain amplitudes greater than 0.25 percent, the frequency used was between 0.7 and 2.5 Hz, while for tests with smaller strain amplitudes, the frequency was between 5 and 15 Hz. A sinusoidal waveform was applied in all tests. An X-Y recorder was used to periodically plot hysteresis loops. Loads and strains were also monitored with a strip chart recorder and a digital indicator panel. The total strain was controlled in all tests. The imposed strain ratio R_ϵ , ranged between 0 and 0.9 resulting in mean strains between 0.15 and 9.5 percent. Failure was defined as 20 percent load drop in all tests. The completely reversed data for the material was already available from a previous study (6). Several tests with zero or very small mean strains were conducted and the results were compared to the completely reversed data taken from reference 6. Very good agreement was found verifying the appropriateness of using the two separate sets of data together.

All test results are summarized in Table 2.

FATIGUE 87

TABLE 1 - Axial Monotonic and Cyclic
Properties of 1045 Steel (6)

Yield Strength (0.2%), σ_y	382 MPa
True Fracture Stress, σ_f	985 MPa
True Fracture Strain, ϵ_f	0.71
Percent Reduction in Area, %RA	51
Strain Hardening Exponent, n	0.23
Strain Hardening Coefficient, K	1185 MPa
Modulus of Elasticity, E	202 GPa
Brinell Hardness, BHN	153
Fatigue Ductility Coefficient, ϵ'_f	0.26
Fatigue Ductility Exponent, c	-0.445
Fatigue Strength Coefficient, σ'_f	948 MPa
Fatigue Strength Exponent, b	-0.092
Cyclic Strain Hardening Coefficient, K'	1258 MPa
Cyclic Strain Hardening Exponent, n'	0.208

Plastic strains and alternating and mean stress values reported were measured at approximately half-life when the stress-strain response was stable. Plastic strains were directly measured from stable hysteresis loops at approximately half-life.

CYCLIC RESPONSE

Mean stress relaxation for the material is shown in Figure 1 where the mean stress versus the applied number of cycles has been plotted for some typical tests with the same strain amplitude but different amounts of mean strain. Substantial mean stress relaxation has occurred as can be seen from this figure. Also note that the rate of mean stress relaxation increases with increasing the amount of mean strain. A similar behavior was observed at other strain amplitudes. It should be noted here that the mean stress relaxation continued throughout the life. This is in contrast to the results obtained by Ellyin (7) for ASTM A-516 Grade 70 carbon low alloy steel where it was shown that after a small fraction of life the mean stress dropped to about 10 percent of its initial value. Ellyin concluded that metals tend to a steady state cyclic condition independent of the prestrain (mean strain) level when cycled in a strain-controlled mode for about one thousand cycles. This conclusion cannot be supported with the 1045 data.

FATIGUE 87

TABLE 2 - Summary of Fatigue Test Results

ϵ_a (%)	R_ϵ	ϵ_m (%)	$\Delta\epsilon$ $p/2$ (%)	σ_a (MPa)	σ_m (MPa)	$2N_f$
0.15	-1	0	0.031	241	0	4,901,750
0.15	0	0.15	0.025	243	12	>3,911,400
0.15	0.80	1.35	0.026	231	75	1,960,360
0.20	-1	0	0.070	270	0	523,222
0.20	-1	0	0.070	269	0	762,902
0.20	0	0.20	0.054	275	6	568,760
0.20	0.5	0.60	0.059	265	20	329,060
0.20	0.75	1.40	0.058	263	32	244,000
0.20	0.75	1.40	0.056	263	39	219,720
0.25	-1	0	0.103	298	0	234,268
0.25	-1	0	0.091	302	0	244,384
0.25	0.5	0.75	0.091	295	13	147,036
0.25	0.75	1.75	0.086	286	26	95,360
0.25	0.90	4.75	0.083	281	48	126,090
0.25	0.90	4.75	0.079	281	55	99,380
0.30	-1	0	0.144	315	0	73,860
0.30	0	0.30	0.129	320	0	72,580
0.30	0.5	0.90	0.128	318	7	71,600
0.30	0.75	2.10	0.128	310	19	60,938
0.30	0.90	5.70	0.107	311	41	43,468
0.40	-1	0	0.227	351	0	35,970
0.40	-1	0	0.226	353	0	40,398
0.40	0	0.40	0.204	360	0	33,800
0.40	0.90	7.60	0.191	338	30	17,904
0.50	-1	0	0.316	372	0	25,826
0.50	0.90	9.5	0.263	366	20	17,472
0.60	-1	0	0.402	400	0	13,344
0.60	-1	0	0.393	420	0	13,650
0.80	-1	0	0.581	445	0	6,088
0.80	-1	0	0.583	440	0	4,092
1.00	-1	0	0.777	452	0	3,054
1.00	-1	0	0.770	465	0	2,922
1.50	-1	0	1.253	499	0	770
2.00	-1	0	1.741	524	0	514

Cyclic true stress-true strain curves for completely reversed and mean strain tests are shown in Figure 2. The monotonic curve taken from reference 6 is also included in order to observe relative cyclic hardening and/or softening for the material. The mean strain does not affect the cyclic stress-strain response at lower strains (less than 0.25 percent)

while slight additional hardening compared to that for $\epsilon_m = 0$ is observed at larger strains.

LOW CYCLE FATIGUE BEHAVIOR

The strain amplitude versus number of reversals to failure is plotted in Figure 3 for all tests with or without mean strain. From this figure and Table 2 it can be concluded that mean strains (prestrains) are not detrimental to fatigue life unless they produce a mean stress that does not relax to zero. For example in a test with an alternating strain of 0.5 percent and a mean strain as high as 9.5 percent, only a 30 percent reduction in fatigue life was observed since the mean stress had relaxed to only about 5 percent of the alternating stress at midlife. Topper and Sandor (8) from their tests on 2024-T4 aluminum alloy and SAE 4340 steel found that small plastic prestrains cause considerable life reductions at nominally elastic strain levels and that larger prestrains have little additional adverse effects. They showed that the life reduction for specimens prestrained 10 cycles at 2 percent was no greater than the life reduction for specimens prestrained 1 cycle at 1 percent. Here, for tests in which the mean strain produced a mean stress greater than 10 percent of the alternating stress at midlife, fatigue lives were reduced by a factor of 2 to 3 depending on the mean stress level.

In order to account for the effect of mean stress on fatigue life, Smith et al (4) proposed the following parameter:

$$(\sigma_{\max} \epsilon_a E)^{1/2} = \text{constant} \quad (1)$$

Where $\sigma_{\max} = \sigma_a + \sigma_m$. Mean stress fatigue life correlation using this parameter is shown in Figure 4. The solid line is passed through the data with no mean strain. As can be seen a very good fit for the experimental data is obtained using this parameter. Combining this parameter with the low cycle strain-life relationship:

$$\epsilon_a = \frac{\Delta \epsilon}{2} = \frac{\Delta \epsilon_e}{2} + \frac{\Delta \epsilon_p}{2} = \frac{\sigma'_f}{E} (2N)^b + \epsilon'_f (2N)^c \quad (2)$$

the following relation is obtained:

$$\sigma_{\max} \epsilon_a E = (\sigma'_f)^2 (2N)^{2b} + \sigma'_f \epsilon'_f E (2N)^{b+c} \quad (3)$$

FATIGUE 87

In order to adjust for mean stress sensitivity of different materials, the maximum stress σ_{max} , in the Smith et al parameter can be replaced by an effective stress proposed by Bergmann et al (9) to be: $\sigma_{eff} = \sigma_a + k \sigma_m$ and by Nihei et al (2) to be: $\sigma_a = \sigma'_a \cdot \sigma'^{-1}_{max}$. The constants k and γ are obtained by individual fits to experimental data.

Morrow (3) assumed that the mean stress influences only the elastic portion of the strain-life relationship in equation 2 and proposed the following parameter:

$$\sigma_a = (\sigma'_f - \sigma_m)(2N)^b \quad (4)$$

Landgraf (10) showed that this parameter satisfactorily predicts the mean stress effect for SAE 1045 steel at several hardness levels. The adequacy of this parameter for the present data is shown in Figure 5. As can be seen the degree of correlations is less than that obtained using the Smith et al parameter.

Based on their study of the cyclic creep of copper, Lorenzo and Laird (5) found that for constant values of maximum stress, a family of straight lines is obtained by a semi-log plot of the plastic strain range versus the mean stress. Plotting plastic strain amplitude versus mean stress in this manner for the present data resulted in a family of parallel straight lines as can be seen in Figure 6. Lorenzo and Laird then suggest that this relationship between cyclic plastic strain and mean stress may be used to relate the mean stress to fatigue life. This is done using a parameter similar to Smith et al's parameters:

$$\sigma_a \Delta \epsilon_p / 2 = \sigma_{max} \Delta \epsilon_{pm} / 2 = \text{constant} \quad (5)$$

where $\Delta \epsilon_{pm}/2$ is the plastic strain amplitude associated with the mean stress. Using this parameter it is possible to draw "isolongevity lines" on a plot of plastic strain amplitude versus mean stress in order to predict fatigue lives under mean stress cycling conditions.

SUMMARY AND CONCLUSIONS

1. Substantial mean stress relaxation occurred with this 1045 HR steel throughout the life of mean strain-controlled fatigue tests.

FATIGUE 87

2. The mean strain did not affect the cyclic stress - strain curve at low strain amplitudes, however slight additional cyclic hardening of the material was observed at higher strain amplitudes.
3. Mean strains (prestrains) were not detrimental to fatigue life unless they produced a mean stress that did not relax to zero.
4. Reduction of fatigue lives between a factor of 2 to 3 was observed for tests with the mean stress greater than 15 percent of the stress amplitude at half-life.
5. Satisfactory correlation of the mean strain data was obtained using the Smith et al parameter. The degree of correlation was better than that obtained using Morrow's parameter.
6. A semi-log plot of the plastic strain amplitude versus the mean stress for constant values of mean stress revealed a family of parallel straight lines. The concept of an isolongevity map proposed by Lorenzo and Laird to predict mean stress fatigue lives seems promising.

REFERENCES

- (1) Fuchs, H.O. and Stephens, R.I., "Metal Fatigue in Engineering," Wiley Interscience, New York, N.Y., 1980.
- (2) Nihei, M., Heuler, P., Boller, C. and Seeger, T., Int. J. of Fatigue, Vol. 8, No. 3, 1986, pp. 119-126.
- (3) Morrow, J.D., ASTM spec. publ. 378, 1965, p.45.
- (4) Smith, K.N., Watson, P. and Topper, T.M., J. of Materials, Vol. 5, No. 4, 1970, pp. 767-778.
- (5) Lorenzo, F. and Laird, C., J. of Materials Science and Engineering, 62, 1984, pp. 205-210.
- (6) Leese, G.E., FCP Report No. 43, College of Engineering, U. of Illinois, 1982.
- (7) Ellyin, F., J. of Engineering Materials and Technology, Vol. 107, 1985, pp. 119-125.

FATIGUE 87

- (8) Topper, T.H. and Sandor, B.I., TAM Report No. 318, U. of Illinois, 1968.
- (9) Bergmann, J.W. and Steeger, T., Proc. 2nd European Coll on Fracture, Darmstadt, FRG, VDI-Report of Progress 18, No. 6, 1979.
- (10) Landgraf, R.W., TAM Report No. 662, U. of Illinois, 1966.

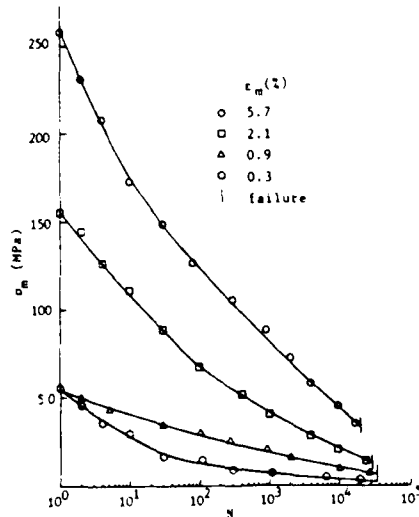


Figure 1. Mean stress relaxation with $\epsilon_a = 0.3\%$

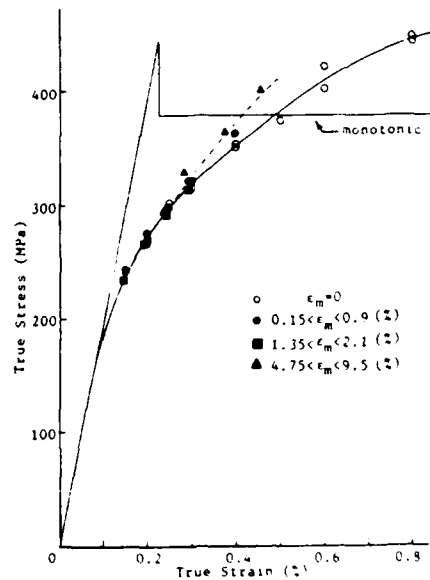


Figure 2. Cyclic and monotonic true stress-true strain

FATIGUE 87

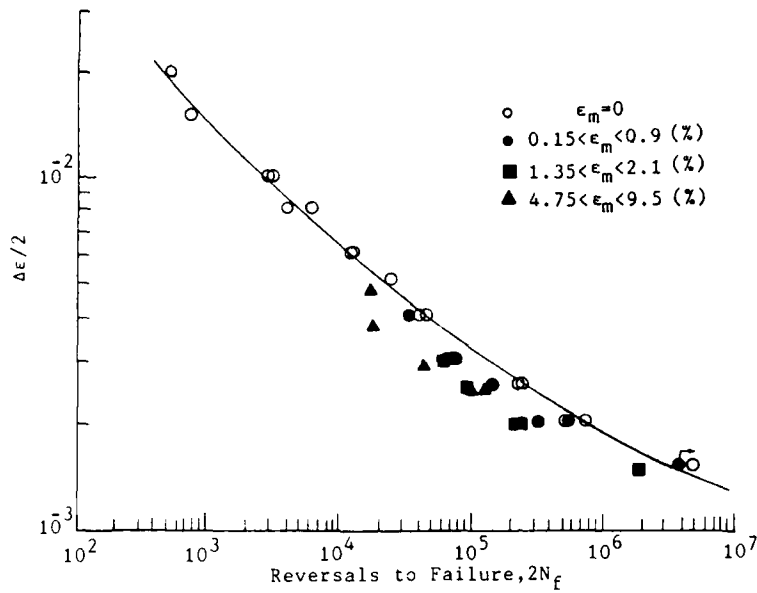


Figure 3. Total strain amplitude versus reversals to failure

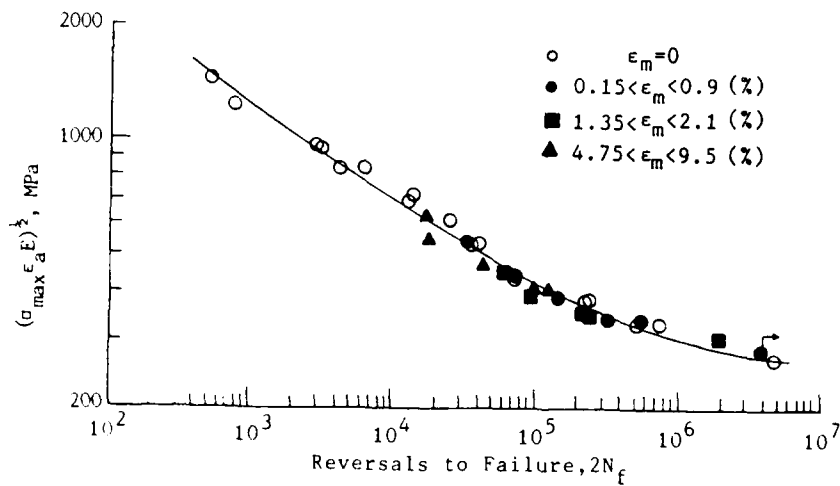


Figure 4. Correlation of data using Smith et al parameter

FATIGUE 87

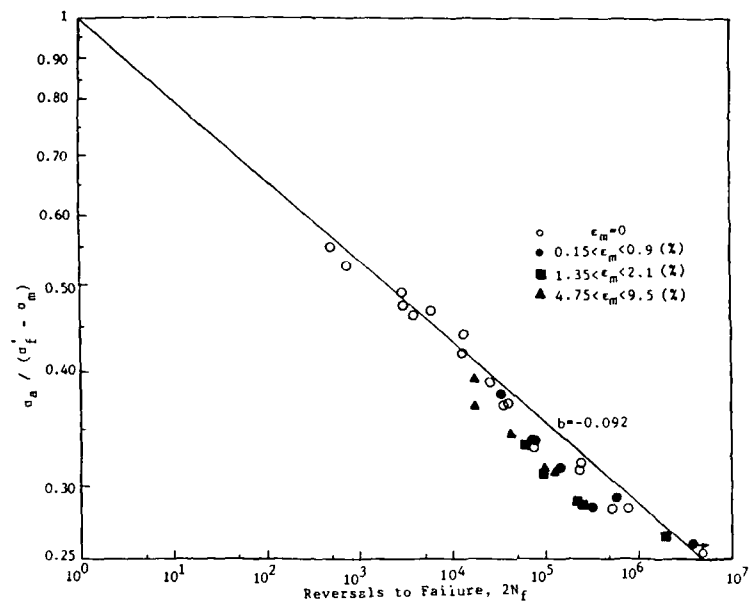


Figure 5. Correlation of data using Morrow's parameter

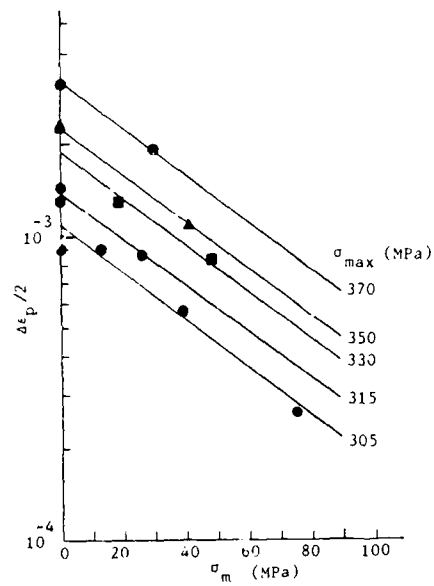


Figure 6. Plastic strain amplitude vs. the mean stress

FATIGUE STRENGTH OF ALLOY A286 AT CRYOGENIC TEMPERATURE

A. Inoue*, S. Yoshioka*, S. Takayanagi**, K. Hiraga***, T. Ogata***, K. Nagai***, T. Yuri*** and K. Ishikawa***

The fatigue strength at 4 and 300K of alloy A286 and its weld was investigated. Load controlled low cycle fatigue tests were carried out on the base material, weldment and heat-treated weldment of the alloy by using smooth and notched specimens. The experimental results revealed a close correlation between the fatigue strength of these specimens and their tensile strength. The notch sensitivity for fatigue strength of the base and welded materials was low even at 4K.

INTRODUCTION

A286 is an iron-base superalloy which is recently regarded as a potential candidate material for cryogenic machinery. Since the alloy has higher strength at room temperature than that of nitrogen strengthened alloys (ex., SUS304LN, 316LN), it is suitable for components having a wide temperature gradient from room to cryogenic temperatures such as the rotor of superconducting generator and the support of superconducting magnet (Horiuchi et al. (1), Morris et al. (2), Kohno et al. (3)). For this alloy, however, only a few data have been reported about its cryogenic (or low temperature) fatigue strength which is necessary for structural designing. Moreover, though the components tend to be constructed by welding owing to an increase in the

- * Central Research Laboratory, Mitsubishi Electric Corp., Amagasaki, Japan.
- ** Kobe Works, Mitsubishi Electric Corp., Kobe, Japan.
- *** National Research Institute for Metals, Niihari, Japan.

FATIGUE 87

capacity of the cryogenic machinery, no data have been made on the fatigue strength of thick plate welds.

Therefore, we have studied the low cycle fatigue strength and notch sensitivity of the base and welded materials of alloy A286 at 4 and 300K.

SPECIMEN AND EXPERIMENTAL PROCEDURE

Specimen

The material used is 35 mm thick forged plate of electroslog remelted alloy A286 aged at 998K for 16 hours after solution treatment at 1253K for 2 hours. The chemical compositions of the alloy are shown in Table 1. The materials were GTA welded under an argon gas shielding by using the filler metal (alloy A286) shown in Table 1. The welding conditions are 20 V, 100 A and 100 mm/minute. To a half of the butt welded joints, the same solution and aging treatments mentioned above were applied after welding to restore the strength of the weld. Thus the base material (material B), weldment (material W) and heat-treated weldment (material HW) were used for the experiment. The tensile specimens and fatigue specimens shown in Figure 1 were prepared from these materials. The stress concentration factor (K_t) of the notched specimens is 2.99. The fatigue specimens for 300K have the same configurations as Figure 1 (b) and (c) except for a slight modification of the grip. For material W and HW, the gage center of the smooth specimen or the notch root of the notched specimen was centered in the weld bead, and the longitudinal direction of the specimens was perpendicular to the welding direction.

TABLE 1 - Chemical Compositions of Base Material and Filler Metal.

	(wt.%)											
	C	Si	Mn	P	S	Ni	Cr	Mo	V	Al	Ti	B
Base material	0.016	0.11	1.19	0.005	0.003	25.59	14.37	1.44	0.24	0.26	2.04	0.0003
Filler metal	0.014	0.09	1.19	0.015	0.004	25.67	14.31	1.23	0.25	0.27	2.14	-

Experimental Procedure

The tensile tests were carried out at 4 and 300K. The low cycle fatigue tests were also performed at the same temperature under pulsating tensile load control

FATIGUE 87

(stress ratio $R = 0$) and 0.5 Hz frequency by using a servohydraulic fatigue testing machine. For the tests at 4K, a cryostat was used which could immerse the specimens in liquid helium.

EXPERIMENTAL RESULTS AND DISCUSSION

Tensile Properties

Table 2 shows the tensile properties of material B, W and HW. For material B, 0.2% yield strength ($\sigma_{0.2}$) and tensile strength (σ_u) at 4K are higher by about 1.3 and 1.5 times than those at 300K, respectively, and elongation (δ) at 4K is also larger than that at 300K. For material W, $\sigma_{0.2}$ and σ_u at 4 and 300K are lowered respectively to about 85% and about 70 ~ 80% of those of material B, and δ is also lowered due to local deformation at the welded zone (Strum et al. (4)). For material HW, $\sigma_{0.2}$, σ_u , δ , reduction of area (ψ) at 4 and 300K are larger than those of material W. By the post-weld heat-treatment, strength and ductility of material W are recovered close to the level of material B.

TABLE 2 - Tensile Properties at 4 and 300K of Base Material (B), Weldment (W) and Heat-treated Weldment (HW).

Material	T (K)	$\sigma_{0.2}$ (MPa)	σ_u (MPa)	δ (%)	ψ (%)
B	300	708	1069	29.7	42.9
	4	932	1548	45.7	37.7
W	300	611	724	15.1	34.5
	4	790	1184	22.9	34.1
HW	300	665	1033	31.1	47.8
	4	830	1424	40.1	46.2

The weld metal of material W and HW are featured by the dendritic solidification structure (material W) and by the scattered micro-defects (material W and HW). Though the micro-defects reduced the ductility (δ , ψ) of material W and HW to some extent, they did not degrade the strength ($\sigma_{0.2}$, σ_u).

Fatigue Strength

Temperature dependence and notch sensitivity of fatigue strength. S-N curves of smooth and notched specimens are shown in Figure 2 and Figure 3, respectively. For material B, the fatigue strength at 4K of smooth and notched specimens is much higher than that at 300K, which is showing the excellent fatigue properties of alloy A286 at 4K. While the fatigue strength of material W is also increased with the decrease in temperature, it is lower than that of material B at both 4 and 300K. For the notched specimen of material HW, the fatigue strength is restored by the post-weld heat-treatment and shows the same temperature dependence of materials B and W. For the smooth specimens, however, the S-N data at 4K are scattered between those at 4 and 300K of material B. In the notched specimens of material W and HW, fractographs revealed that fatigue crack initiated at the notch root and not at the micro-defects. In some of the smooth specimen of material W, fatigue crack initiated at the micro-defects. Compared with the data of the specimens in which fatigue crack did not initiate at the micro-defects, however, the fatigue strength is not lowered. In the smooth specimen of material HW at 4K, on the other hand, the fatigue strength for which the fatigue crack initiated at the micro-defects tends to be lower. Thus, the large scattering of the fatigue data shown in Figure 2 can be attributed to this type of crack initiation.

For quantitative comparison of fatigue strength, the fatigue strength at 2×10^4 cycles ($\Delta\sigma_0$) was determined under each test condition. Figure 4 shows the relationship between the $\Delta\sigma_0$ and temperature. It is evident that the $\Delta\sigma_0$ value increases as temperature goes down from 300K to 4K in both of smooth and notched specimens. The values of $\Delta\sigma_0$ at 4 and 300K are high in the order of material B, HW and W.

To evaluate the notch sensitivity for fatigue strength, the notch factors (K_f) at 2×10^4 cycles were also determined. Figure 5 shows the relationship between K_f and temperature. At 4 and 300K, the K_f values are within the range from 1.3 to 1.6, which are considerably lower than the K_t value (2.99). The notch sensitivity of these specimens except for the material HW at 4K is estimated to be low and almost independent of the temperatures.

Correlation between fatigue strength and tensile strength. The relationship between $\Delta\sigma_0$ and σ_u is shown

FATIGUE 87

in Figure 6. The $\Delta\sigma_0$ for both smooth and notched specimens is closely related with the σ_u of the respective materials. In other words, the $\Delta\sigma_0$ is approximately proportional to the σ_u . Higher fatigue strength of each material at 4K than at 300K is attributed to the higher σ_u at 4K.

Figure 7 shows the replotted S-N curves by the ratio of stress range to tensile strength ($\Delta\sigma/\sigma_u$). All of the data can be divided into two scatter bands for smooth specimen and notched specimen. Based upon this diagram, the low cycle fatigue strength of each material can be approximately estimated from the σ_u . In Figure 7, the 4K data of smooth specimens of material HW including micro-defects, which are parenthesized, are in the scatter band of notched specimens.

CONCLUSION

- (1) Except for smooth specimens of heat-treated weldment at 4K, low cycle fatigue strength is higher in the order of base material, heat-treated weldment and weldment, and increases as temperature goes down.
- (2) The notch factor of fatigue strength at 2×10^4 cycles of the respective materials is about $1.3 \sim 1.6$, which is considerably smaller than stress concentration factor ($K_t = 2.99$) and is almost independent of temperature.
- (3) Low cycle fatigue strength is strongly correlated with tensile strength. Except for the data of smooth specimen of heat-treated weldment at 4K, two scatter bands for smooth specimens and notched specimens were obtained by replotting the S-N curves by the ratio of stress range to tensile strength.

FATIGUE 87

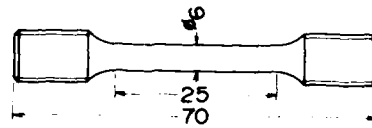
SYMBOLS USED

K_f	= notch factor of fatigue strength at 2×10^4 cycles
K_t	= stress concentration factor
N_f	= number of cycles to failure
R	= stress ratio (minimum stress/maximum stress)
T	= temperature (K)
$\sigma_{0.2}$	= 0.2% yield strength (MPa)
σ_u	= tensile strength (MPa)
$\Delta\sigma$	= stress range (MPa)
$\Delta\sigma_0$	= fatigue strength at 2×10^4 cycles (MPa)
δ	= elongation (%)
ψ	= reduction of area (%)

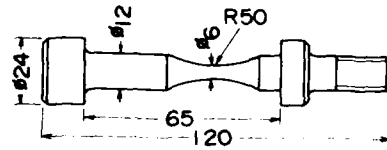
REFERENCES

- (1) Horiuchi, T., Ogawa, R., Shimada, M. and Tone, S., Kobe Steel Engineering Reports, Vol. 34, 1984, pp.47-52.
- (2) Morris, J.W. Jr. and Dalder, E.N.C., J. Metals, Vol. 37, 1985, pp.24-32.
- (3) Kohno, M., Moriyama, T., Shimada, M. and Suzuki, A., J. of Iron and Steel Institute of Japan, Vol. 71, 1985, pp.1956-1964.
- (4) Strum, M.J., Summers, L.T. and Morris, J.W. Jr., Welding J., Vol. 62, 1983, pp.235S-242S.

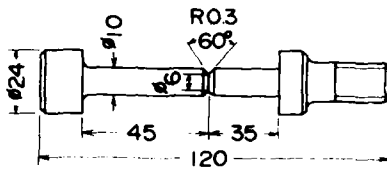
FATIGUE 87



(a) Tensile specimen for 4K and 300K



(b) Smooth fatigue specimen for 4K



(c) Notched fatigue specimen for 4K

Figure 1 Configuration of specimen (mm)

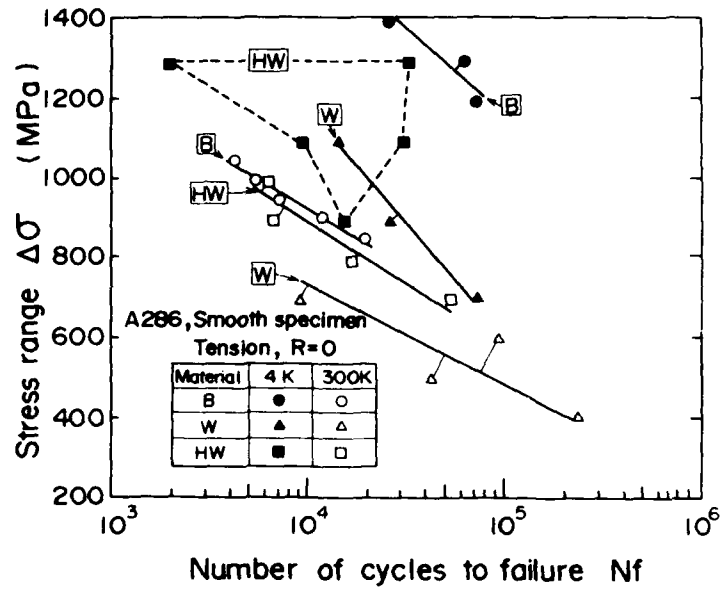


Figure 2 S-N curves for smooth specimen

FATIGUE 87

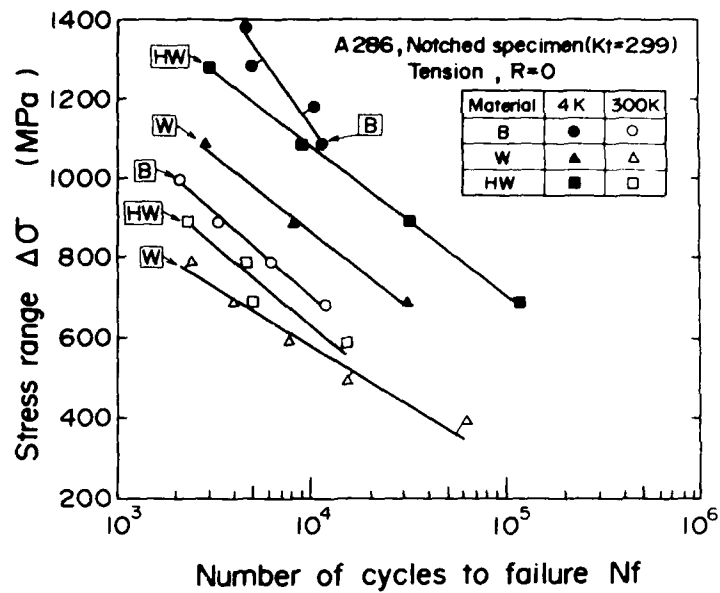


Figure 3 S-N curves for notched specimen

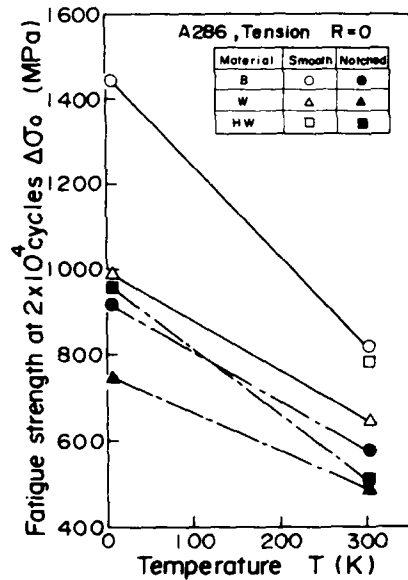


Figure 4 Relationship between fatigue strength and temperature

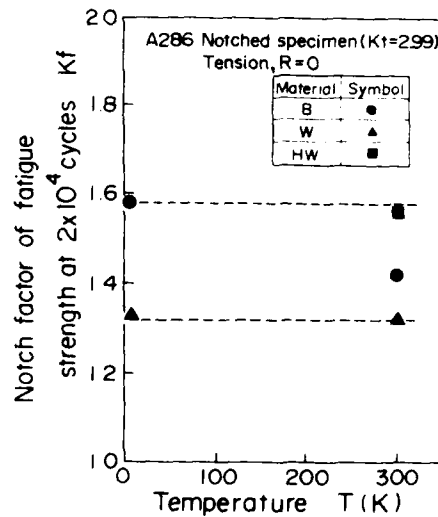


Figure 5 Relationship between notch factor and temperature

FATIGUE 87

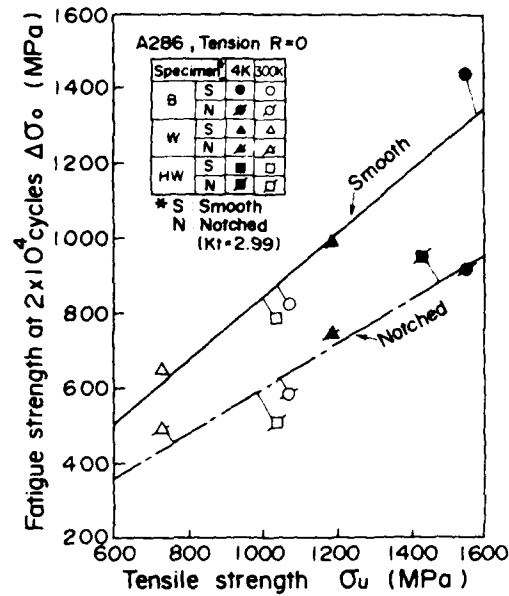


Figure 6 Fatigue strength at 2×10^4 cycles as a function of tensile strength

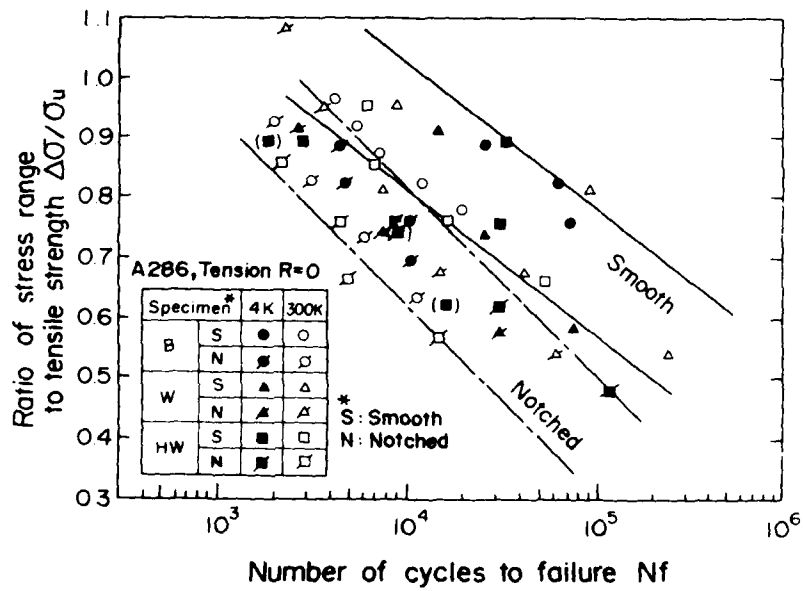


Figure 7 Replots of S-N curves by using ratio of stress range to tensile strength

FATIGUE 87

THE INITIATION AND GROWTH OF FATIGUE CRACKS IN
CARBURISED 9Cr1Mo STEEL

P. J. Jeffcoat*

The high temperature fatigue endurance of carburised 9Cr1Mo ferritic steel is determined by the conditions under which fatigue cracks are initiated. At high loads, cracks are initiated at the carburised surface and endurance is little changed. By contrast, at lower loads, cracks are initiated internally at oxide inclusions randomly distributed in the steel, and marked improvements in endurance are measured. A simple semi-empirical model is presented which relates fatigue endurance to the inclusion population of the steel.

INTRODUCTION

Surface carburisation of 9Cr1Mo ferritic steel components may occur during service in Fast Reactor and UK Advanced Gas cooled Reactor systems. In order to more fully understand the possible consequences of this effect the fatigue and fracture characteristics of the alloy have been determined following simulated high intensity surface carburisation treatments.

EXPERIMENTAL PROCEDURES

Preparation of Test Specimens

Specimen manufacture. HCF and LCF fatigue specimens were fabricated from a single cast of 9Cr1Mo ferritic steel the composition and heat treatment (normalised and tempered), of which are given in Table 1.

Environmental testing. The specimens were carburised by exposure to static, carbon contaminated liquid sodium at temperatures of 475° and 525°C for periods of

*UKAEA, Risley Nuclear Laboratories, England

FATIGUE 87

up to 180 days as detailed in Table 2. Full details of the techniques used have been given previously by Jeffcoat and Thorley(1).

Mechanical Testing

N+T and carburised HCF and LCF specimens were tested in air at 475° and 525°C. The HCF specimens were tested to failure, about a mean stress of 69 N/mm² and with a peak alternating stress varied between +226 to +293N/mm². Testing of the LCF specimens to failure was carried out with a TSR varied between 0.4 and 1.0% about zero mean strain.

Microstructural, Analytical and Fractographic Studies

The microstructures of the N+T and of the carburised 9Cr1Mo specimens were examined by standard optical microscopy and hardness measurement techniques. In addition, a quantitative metallographic assessment of the inclusion population in the N+T 9Cr1Mo steel was carried out using an IBAS 2 image analysis system. The carbon contents of the carburised specimens were determined by electron probe micro-analysis techniques. Finally, the fatigue fracture characteristics of the specimens tested under all conditions were studied in a scanning electron microscope, where use was also made of energy dispersive X-ray analytical facilities.

RESULTS

Microstructural Examinations

N+T 9Cr1Mo steel. Figure 1(a) shows the original tempered martensite structure of the N+T 9Cr1Mo steel, which had a prior austenite grain size of ca. 30 µm and a hardness, Hv25, of ca. 220. The quantitative metallographic measurements detected and measured 933 oxide inclusions randomly distributed within the steel, in a total area of 8.25 mm², of which 97% lay in the size range 0.5-10 µm (mean ca. 2.7 µm) and the maximum particle size detected was 50 µm.

TABLE 1 - Details of 9Cr1Mo ferritic steel

Cr	Mo	C	Mn	Si	Ni	S	P	Fe(wt%)
8.85	0.95	0.1	0.5	0.66	0.21	0.008	0.013	Bal

Normalised; 950°C, 0.5 h : Tempered; 750°C, 0.5 h

FATIGUE 87

TABLE 2 - Sodium carburisation treatments; summary of carbon EPMA analyses and hardness levels

	Temp °C	Period days	Carbon profile Cs%, Depth μm		Surface hardness Hv25
HCF	525	30	2.4	217	473
	"	90	2.0	371	682
	475	30	1.72	220	906
	"	90	1.88	260	700
LCF	525	84	2.4	420	405
	"	187	2.82	>550	460
	475	90	1.5	>250	650
	"	185	1.5	>300	650

Carburised material. Examples of the carburised surface microstructures in 9Cr1Mo steel arising from sodium exposure at 475° and 525°C are shown in Figure 1(b) and 1(c) respectively. Details of the surface carbon levels, depths of carbon penetration and the maximum surface microhardness values are also summarised in Table 2.

Fatigue Tests

Fatigue endurance data. The LCF and HCF endurance data at 475° and 525°C are shown in Figures 2-5. The data at 525°C are supplemented by the results of Wood et al (2)(3) for this same cast of N+T 9Cr1Mo steel.

Fractographic Examinations

Normalised and tempered material. In all instances, irrespective of test mode, stress level or temperature the N+T 9Cr1Mo steel failed by the expected mechanisms of crack initiation at the specimen surface, and transgranular growth across the section.

Carburised material. The fracture surface of the carburised materials were primarily determined by the imposed fatigue loadings. Two types of behaviour were observed, these being:

1. High stress/strain fracture. For such specimens (identified by superscript S in Figures 1-5) crack initiation was initiated at the steel surface. In addition, it should be noted that when failure occurred by such a mode, little or no fatigue crack growth resulted, (Figures

AD-A184 045

FATIGUE '87 VOLUME 1(U) VIRGINIA UNIV CHARLOTTESVILLE

7/7

SCHOOL OF ENGINEERING AND APPLIED SCIENCE

R O RITCHIE ET AL JUN 87 ARO-24134.1-MS-CF

UNCLASSIFIED

NO0014-87-G-0008

F G 30/11

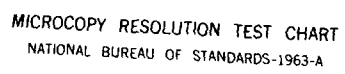
NL

END

DATE

FILED

10-87



MICROCOPY RESOLUTION TEST CHART
NATIONAL BUREAU OF STANDARDS-1963-A

2. Moderate stress/strain fracture. At lower fatigue loadings complex fractures were observed, (eg Figure 7(a)), which were characterised by a disc region (Zone A), located at a random position within the uncarburised core region of the specimen, at the centre of which a large oxide inclusion was observed, (Figure 7(b)). Energy dispersive X-ray analysis showed the inclusions to be a mixed oxide rich in aluminium and iron with an outer crust containing primarily calcium and silicon. Such inclusions had a maximum dimension typically 20-35 μm though in one instance a 52 μm particle was observed. The local fracture morphology indicated that fatigue cracks were initiated at the matrix/inclusion interface and propagated circumferentially across the section. Similar inclusion particles, but significantly smaller (2-10 μm), were also occasionally found on the fracture surface; however they did not influence the local fatigue crack morphology, and there was no evidence of secondary crack initiation at such sites. It is significant that carburised samples which failed in this manner showed marked increases in endurance.

DISCUSSION

Microstructural Observations

N+T. The oxide inclusions in the tempered martensite matrix of the N+T 9Cr1Mo steel are considered to have originated from the slagging operations during the manufacture of the steel by the basic electric arc process. A linear regression analysis of the quantitative metallographic data showed that the cumulative inclusion frequency and inclusion size are related by:

$$8.25 \log N_i = -0.1688 \text{ FERET } (X, Y) + 3.0746 \dots (1)$$

Fatigue behaviour of carburised 9Cr1Mo steel.

In considering the effects of pre-carburisation on the properties of 9Cr1Mo steel, the results have shown how depending on the imposed fatigue loadings, surface carburisation may modify the fracture characteristics of the alloy, particularly with regard to the factors controlling fatigue crack initiation. These changes are considered to be instrumental in determining the overall fatigue endurance of the alloy.

At high stresses and strains, fatigue crack initiation in the carburised steel remained related to the surface showing that despite the increased tensile

strength of the carburised layer (1), it could not totally impede the normal surface dominated processes of crack initiation observed in the N+T steel. An estimate of the surface fatigue loadings and strains relevant to this regime may be made by considering the strength and cyclic stress strain properties of the alloy in the N+T and carburised conditions ((3), Skelton (4)), from which it is considered that surface fatigue crack initiation remains dominant at specimen total strains in excess of ca 0.8%, corresponding to plastic strains in the surface carburised layer of ca. 0.2%.

The situation under more moderate loadings where cracks are initiated internally at large oxide inclusions, is considerably more complex. Frost et al (5) have identified the importance to fatigue crack initiation of inclusions and discontinuities in the internal boundary regions of surface hardened materials. By contrast, in this work where although surface strength properties are important in suppressing the normal mechanisms of fatigue crack initiation, the subsequent initiation and early growth of fatigue cracks is not influenced by either the extent or microstructure of the carburised surface layer, but rather is simply related to the occurrence of a suitable inclusion at some random point within the alternating stress field of the specimen.

The general conditions favouring particle-initiated cracking in steels and other alloys are complicated, and although the experimentally observed threshold inclusion size for crack initiation of 20 μm cannot be fully quantitatively rationalised, it is noteworthy that the preferential cracking of large particles is a common feature in materials with an agglomerate of mixed particle sizes (e.g. Goods and Brown (6), Fisher and Gurland, (7)).

If under fatigue loading the inclusion rapidly decoheres from the local matrix, then the endurance will be determined by the growth of the resulting crack-like defect. Although a precise quantification of short crack growth is difficult, the endurance has been assessed by a combination of elastic-plastic and linear-elastic fracture mechanics treatments (eg Miller (8)). However, such an analysis seriously underestimates the fatigue endurance of carburised 9Cr1Mo by up to three orders of magnitude. This indicates that endurance is determined by the successful formation of a crack at an inclusion which is a slow process involving such factors as the impingement

of slip bands on to the inclusion surface.

It is to be recalled that in plain homogeneous materials (ie in this context uncarburised), the fatigue strength may under certain circumstances be influenced by specimens size or area effects concerned with the probability of a local soft region being subjected to the maximum stress. It is therefore suggested that in the first instance the endurance of carburised 9Cr1Mo is governed by the probability of the specimen containing an inclusion greater than the experimentally observed threshold size of 20 μm and that such an inclusion be contained and suitably oriented within a grain which itself is favourably oriented for Stage 2 crystallographic slip and cracking under the applied stress-strain system. These latter two factors are however considered to be relatively unimportant since the multiplicity of high temperature slip systems in ferritic materials suggests that all grains within the specimen are equally potent as sources of cracking. By utilising the relationship between cumulative inclusion frequency and size (eq 1) and assuming all the inclusions of interest are octahedral in shape, the number of inclusions available for crack initiation and their total surface area may be calculated. The fatigue endurance of the carburised material may then be compared to that of the N+T material in a semi-empirical manner by comparing the ratio of free surface area to that of the inclusions; ie:

$$N_f (\text{carburised}) = N_f (N+T) \times \text{area ratio} \dots\dots(2)$$

Such an analysis for threshold inclusion sizes of 20 and 25 μm predicts area ratios of ca. 70 and 400 respectively. These data are compared with the experimentally determined HCF endurance values in figure 8. Included in parentheses by each experimental point is the measured size of the inclusion at the crack initiation site.

It may be seen that this simple model based on the size and frequency of remnant oxide inclusions from the steel making process, can in general satisfactorily estimate the fatigue endurance of 9Cr1Mo steel when the surface has been hardened to resist plastic deformation. Within this stress regime, other factors such as the depth, carbon content and hardness of the carburised layer are of secondary importance.

CONCLUSIONS

The fatigue endurance of carburised 9Cr1Mo ferritic

steel is determined by the conditions under which fatigue cracks are initiated. At high fatigue loadings were specimen strains are $>ca\ 0.8\%$ and plastic strains in the carburised layers are $>ca\ 0.2\%$, fatigue cracks are initiated at the carburised surface and the endurance remains essentially unchanged. By contrast, at lower loads, fatigue crack initiation occurs at large oxide inclusions and the endurance is markedly improved.

By considering the conditions for effective crack initiation and growth from inclusions, a simple semi-empirical model is proposed which satisfactorily describes the fatigue endurance of carburised 9Cr1Mo steel.

SYMBOLS USED

HCF = high cycle fatigue

LCF = low cycle fatigue

TSR = total strain range

N_1 = cumulative inclusion frequency per mm^2

FERET(X,Y) = Inclusion size (μm)

REFERENCES

- (1) Jeffcoat, P. J. and Thorley, A. W., The influence of carburisation on the structure and properties of a 9Cr1Mo ferritic steel. Proceedings of the International Conference "Liquid Metal Engineering and Technology". BNES, Oxford, 1984.
- (2) Wood, D. S. et al., The Creep-fatigue Behaviour of 9%Cr Steel at 525°C. Proceedings of the Conference on "Time and Load Dependent Degradation of Pressure Boundary Materials". IAEA, Innsbruck, Austria, 1978.
- (3) Wood, D. S. et al., Mechanical Properties Data on 9%Cr Steel. Proceedings of the International Conference on "Ferritic Steels for Fast Reactors". BNES, London, 1977.
- (4) Skelton, P., Crack Growth and Cyclic Stress-Strain Properties of 9Cr1Mo Steel at Elevated Temperature. "Fatigue at high temperatures". International spring meeting of the French Metallurgical Society. Paris, 1986. pp185-203.

FATIGUE 87

- (5) Frost, N. E. et al., Metal Fatigue. Clarendon Press, 1974.
- (6) Goods, S. H. and Brown, L. M., Acta Metallurgica, Vol 27, 1981, pp 1-15.
- (7) Fisher, J. R. and Gurland, J., Metal Science. Vol 15, 1981, pp 185-192.
- (8) Miller, K. J., "The Short Crack Problem". Mechanical and thermal behaviour of metallic materials. Soc. Italiana di Fisica, Bologna, Italy, 1982.



Figure 1. Microstructures of test specimens.

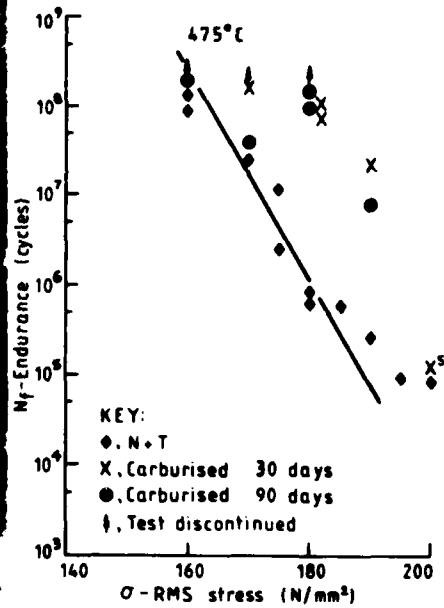


Figure 2. High cycle fatigue endurance at 475°C.

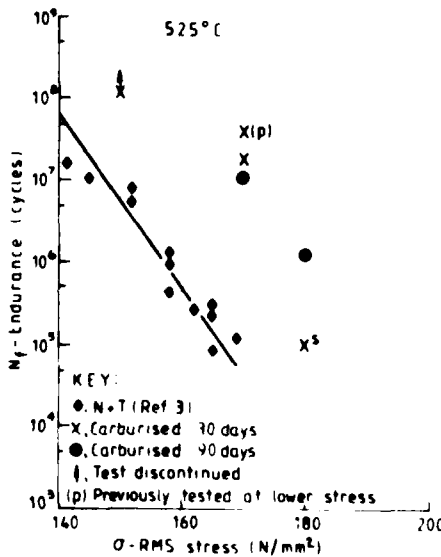


Figure 3. High cycle fatigue endurance at 525°C.

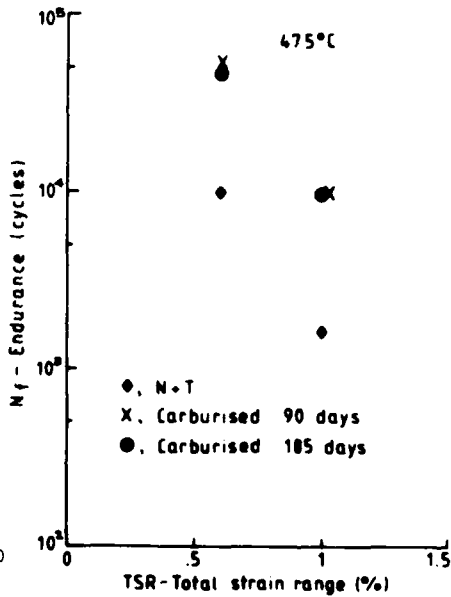


Figure 4. Low cycle fatigue endurance at 475°C.

FATIGUE 87

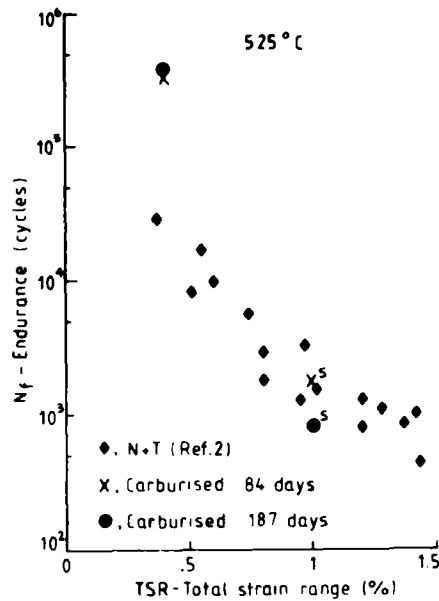


Figure 5. Low cycle fatigue endurance at 525°C.

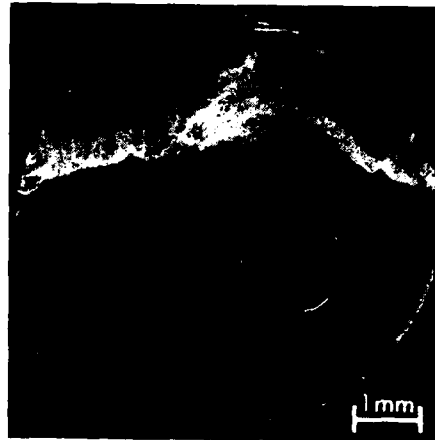


Figure 6. High load fatigue fracture.



Figure 7. Moderate load fatigue fracture.

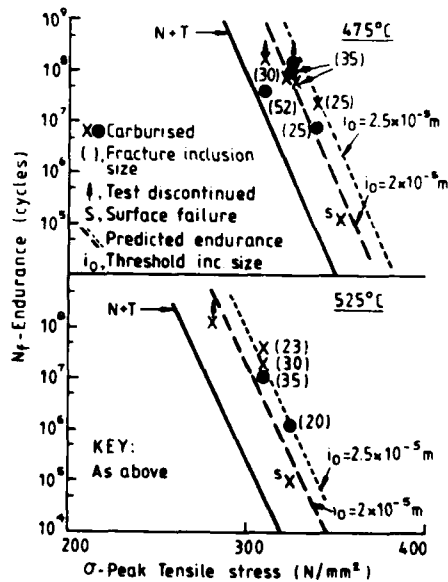


Figure 8. Effect of inclusion population on endurance.

FATIGUE 87

FRETTING WEAR AND FRETTING FATIGUE DAMAGE

C. Colombie*, Y. Berthier**, L. Vincent*, M. GODET**

Fretting wear and fretting fatigue are studied from a combined mechanical and material point of view.

Each phase of the degradation process is described by considering boundary conditions in the contact and material properties. The role of debris is shown to be very important to predict failures.

INTRODUCTION

Fretting significantly reduces fatigue life. Fretted regions are described as very sensitive to the occurrence of plastic deformation and cracks. However few results take into account the possible effect of debris due to wear. Many papers describe fretting-fatigue (FF) from a material viewpoint and thus ignore the behaviour of metal to metal contacts. Other papers describe fretting-fatigue from a theoretical point of view and do not take into account the superficial damage produced in the contact and the debris. In fact FF may be defined as fatigue combined with fretting effects. Thus several FF damages are observed following the strain or stress levels of both fatigue and fretting. In fatigue for instance if the applied stresses are very near the fatigue limit, the tensile stresses at the contact boundary are high enough to nucleate cracks. In other

* Equipe "Matériaux" - Département de Mécanique des Solides
Ecole Centrale de Lyon - B. P. 163 - 69131 ECULLY CEDEX FRANCE

** Laboratoire de Mécanique des Contacts, Institut National des
Sciences Appliquées - 69621 VILLEURBANNE CEDEX FRANCE

FATIGUE 87

cases, notches are generated as a local plastic deformation. But in the both approaches the role of debris on contact behaviour is ignored. Clearly a complete analysis requires a combine mechanical and material approach.

First, we have to emphasize that FF is not concerned with corrosion but with contact mechanics. Thus we want to describe the mechanisms that enhance damage in fretting wear and to discuss how they can cause failure in FF. Several materials are studied to point out the effects of experimental conditions on this kind of damage.

FRETTING WEAR MECHANISMS

Experimentals. The fretting rig is a tension compression hydraulic machine. Reciprocating movement of a given shape and amplitude is applied to the first specimen (1) which is connected to the piston (3). The second specimen (2) is fixed to the framework via a moveable trolley (4) enabling the application of the normal load (Figure 1). The whole fixed part of the machine is connected to the base via a ball bearing (6).

Visualisation of the contact is possible by means of a fixed transparent specimen using a binocular microscope. The specimen holder can be adjusted in two directions to permit correct location of the specimen contact region. Displacement, normal load and tangential load are measured. The three recorded signals are studied through a "tangential load-displacement-time" plot. In this paper, experimental conditions are :

Normal load : 500 Newtons
Relative displacement : $\pm 50 \mu\text{m}$
Frequency : 1 Hertz
Triangular signal.

Several allows were tested : a low alloyed steel (35 % C - 4 % Ni - 1.75 % Cr - 5 % Mo) tempered at 600° C or 200° C ; aluminium alloys (2024 or 7075) ; austenitic stainless steel (316) ; titanium alloy (Ti-6Al-4V) ; ... Tests are performed on similar metal combinations (called first bodies) in ambient laboratory air. Flat on flat or sphere (R = 1m) on flat (R = 30 m) contacts are used.

Analysis of phenomena. The variation of tangential load as a function of measured relative displacement and time shows the existence of five stages in the degradation process (Figure 2) :

- 1 - Increasing the metal to metal contact area.
- 2 - Maximal tangential load due to the existence of generalised contact after the destruction of the superficial film layers. An examination of a cross-section of the test specimens at this stage of the degradation shows very deep plastic deformation and structural changes (white etching areas) in the zone close to the surface.

If this stage lasts for a long time (several tens of cycles) it will be accompanied by cracking in the bulk of the material. Depending upon its mechanical properties, the material will accommodate the stress field imposed in the contact by plastic deformation. This phenomenon causes a change in surface geometry which in fretting is characterised by the appearance of raisers (Figure 3).

3 - Transition from two body to three-body contact. As soon as there is debris in the contact area, a drop in the tangential load is observed. These debris appear gradually. Debris is first created in the initial contact region then covers the whole contact area. Once this is formed, the debris is trapped because of the superficial plastic deformation. At the same time the specific volume of the material related to the appearance of debris increases and tends to increase the pressure field in the contact area.

These two contradictory phenomena imply that the debris is pushed with some force towards the side of the contact and continues to cause plastic deformation on the edges of the scar. This blockage related to both the existence of raisers and the existence of the debris is illustrated by an increase in the tangential load at the end of the cycle (Figure 4).

4 - Creation of the powder bed. Once the debris has been created in large quantities within the contact area, the surfaces are necessarily separated one from the other.

5 - Variations in the powder bed. At this stage of the process we are in true three-body contact (1).

Stages 4 and 5 have been described in (2) and (3). They are concerned with the load carrying capacity of wear debris and with the flow of debris.

Two-Body contact. Observations of surfaces after several fretting cycles show that surface geometry has a significant effect on the location of initial contact. The discrete contact areas determine the local stress field and therefore the depth of damage. For instance a single contact zone often induces significant damage in the sublayer. For rough surfaces wear zones are distributed very evenly over the whole contact surfaces. The depth of damage is almost significant.

The common factor in material behaviour is the way in which relative displacement is accommodated by the boundary conditions. It is remarkable to note that loads normal to the local contact surfaces are wholly transferred into first bodies but that tangential loads, transmitted via intermediate interfaces, are only transferred to the first bodies as a function of adhesion between surfaces. Relative motion between the surfaces can only occur in the case of solid materials by cracking : cracking of the interface or of the substrate. For instance because of the adhesion properties, part of the displacement is accommodated by plastic deformation of the substrate, giving rise to strain hardening of the material and structural changes. Subsequently this form of damage will not longer accommodate the imposed deformations and cracks

will occur .

Material properties in friction are to be related to the following three phenomena :

- (i) surface adhesion
- (ii) cracking related with ductility and with K_c
- (iii) progressive cracking in conjunction with low cycle (plastic) fatigue and in particular with strain hardenability.

It is possible with the three phenomena to understand the material behaviour in two body contact. Two types of good anti-wear materials are noted :

- (i) materials which sacrifice their surfaces to protect their bulk. The debris appears immediately in the contact area. The whole of the rest of the process is then governed by the behaviour of debris.
- (ii) materials capable of accommodating a high degree of plastic deformation. The appearance of debris is very long but degradation is deep.

In all intermediate cases depending on the problem posed, there must be a balance between the accommodation of plastic deformation and the cycle strain hardening.

The Two-Body / Three-Body Transition Mechanism. We have shown in (2, 3) the importance of the third body in the fretting process. The role of debris is not solely that of the powder bed : depending on the process of their rejection from the contact area, they may from the time of their creation, have a great influence on the degradation. Their role is related to the modification, which depends on wear, of the stress fields in the first body. Depending upon the surface stress fields, there are two main types of degradation :

- (i) a region of intense plastic deformation
- (ii) cracking in the bulk initiated at the surface and related to the existence of a high tensile stress due to boundary conditions.

The first debris appears at the microscopic contacts, trapping of this debris determines the mode of transition to macroscopic contact and therefore the bulk degradation of the substrates. As a function of trapping we have observed three typical cases for the development of the degradation. We would point out that once the powder bed has been formed observation of the surfaces does not show anything different.

1 - Very high rate of ejection (Figure 5) : the first debris formed is ejected very far from the scars and has not effect on contact. The type of degradation will be that described for two body contact : a region of high surface plastic deformation in which there is strain hardening and microstructural changes causing the formation of debris. A crack initiated at the surface propagates in the regions of maximum shear until a flake is removed. The process restarts on the newly created surface.

FATIGUE 87

2 - Very little debris elimination (Figure 6). Since most of the wear particles remain within the area in which they are formed they immediately insure a separation and a bearing area between the first bodies. Degradation remains very superficial, there is no deep cracking of the material related to macroscopic two-body contact.

3 - Medium elimination (Figure 7). This intermediate state corresponds to a long mixed state of two and three-body contacts. The debris is quickly thrown out from the source regions and does not have a significant effect on wear. It will however remain mostly in the contact area thus changing boundary conditions. Under the effect of the applied loading a crack may initiate at the surface without necessarily going as far as to remove a flake. However, there may be considerable plastic deformation of the surfaces thus creating raisers that result in strain hardening of surface regions.

DISCUSSION

Fretting degradations in a real contact. We have shown two types of fretting damage as a function of the transition from two to three body contacts :

- (i) wear corresponding to the formation of debris
- (ii) deep cracking which does not result in any overall material loss.

The behaviour of the third-body has a very significant influence on both the wear and the bulk degradation of the first-body. This poses the problem of simulation. How can we compare tests performed on different machines and often with different geometries ? In the same way how can we classify materials on machines with totally different designs.

In the case of flat on flat geometries there may be several surface configurations according to local conditions (Figure 8) :

1 - Debris in the contact area. The normal load is then entirely transferred to the first body but a large proportion of the shear strain is taken up by the third body. Degradation is generally very superficial and related to first and third-body interactions.

2 - Contact occurs between first bodies but with a small degree of local pressure. An area of high superficial plastic deformation occurs without any cracking in the depth related to a high normal load.

3/4 - Contact occurs between first bodies and there is a high degree of local pressure. Tangential loads transmitted to the first bodies are high : in addition to the contact area of high surface deformation a crack is initiated at the edge of the contact region and propagates into the depth of the first bodies. The depth of degradation will depend on a large extent on the contact geometry.

The mechanism described is characteristic of the existence of debris in the contact area and allows a common factor and a genera-

realisation to be drawn from fretting experiments. The behaviour of materials can only be explained and predicted by using a mechanical/material approach allowing for the third body parameter. We have shown that stainless steel (a poor friction material) exhibit better "tribological properties" than Ni-Cr-Mo steel simply by working at different frequencies. Although, as this study has shown, it is unfortunately very difficult in a real contact case to predict the behaviour of parts damaged by fretting we know that locally the degradation process described is always verified whatever materials are used. Changes in tangential loads, a characteristic of the overall contact, can be interpreted as the superposition of the various local mechanisms described above.

Fretting-Fatigue. Our entire study has shown that control of this cracking requires an understanding of the behaviour of debris and of the transition between two to three-body contacts. As in any conventional fatigue problem, any approach must be based on crack initiation and propagation concepts. We will now discuss two extreme cases based on Wohler's curve.

Let us consider a specimen loaded macroscopically near the endurance limit. The problem can then be approached in terms of local overstressing related to the contact. This phenomenon has been studied particularly by Chivers and Gordelier (4). The problem is approached from a hertzian contact view (in partial and total slip) considering crack initiation to be related to the maximum tensile stress appearing at the surface at the contact boundary. Locally the stress is the sum of the macroscopic stress and the contact stress. The fatigue strength of the part is then to be related to the value of this stress in relation to endurance limit. The authors propose two types of solution to combat this problem :

- (i) the use of surface treatments (such as shot peening introducing residual compressive stresses in the sub-layer).
- (ii) the use of thin coatings (to reduce friction forces) so as to reduce the added stresses related to the contact.

We would point out that, in this case, if a crack is initiated it will accommodate the applied relative displacement and fretting will be stopped.

We will now consider the case where the macroscopic loading is further from the endurance limit. We know that from the mechanism for two or three-body transition the crack may appear in the bulk of the substrate. Crack initiation must then be approached using plasticity theory in terms of tensile stresses at the surface and boundary conditions. According to the length of crack created (see Figure 8), the fatigue strength of the parts can be related to the notion of critical crack length which can propagate, and possibility to the crack closure.

If we accept that according to the dynamic contact conditions a crack is always capable of being initiated at the surface, the

FATIGUE 87

lifetime of parts subjected to FF loads corresponds to the time of crack propagation (elimination of the initiation stage). The search for solutions can be considered as the development of a base structure having a good resistance to propagation independent of the endurance properties of coatings.

We are therefore confronted with two opposite tendencies : the resistance of parts subjected to loading involve the selection of material having a low tendency to crack propagation and to short cracks (notion of ΔK_{th} , the Paris law) ; however, the resistance to the appearance of cracks in the bulk, since it is related in fretting to the mechanism of debris creation and rejection, involves materials having a great tendency to cracking (cyclic strain hardening, notion of K_c). Any research for a solution should therefore tend towards a brittle surface treatment accepting that the fatigue strength of the part will be reduced.

CONCLUSION

The problems of fretting wear and fretting fatigue are therefore difficult to approach in a complex industrial situation. Each must be dealt with as a special case. We have defined wear as being the interaction at a given moment of the following three phenomena :

- (i) a purely mechanical phenomenon of stress distribution in the first body
- (ii) a material phenomenon related to its properties and its development in relation to the environment both mechanical and chemical and physical chemical.
- (iii) a phenomenon of interaction between surfaces (adhesion, surface geometry, ...) which also involves the first two. This then defines the boundary conditions of the problem.

As a material point of view fatigue strength, ductility, hardness and so on are not useful to describe FF. We must consider strength to short crack propagation, threshold value of stress intensity factor or fracture toughness to predict appearance of debris. A main difficulty remains in the definition of the opening mode in contact or beneath the surface.

REFERENCES

- (1) Godet, M., Wear, 100, 1984, pp. 437-452.
- (2) Colombie, C., Berthier, Y., Vincent, L. and Godet, M. Trans. of ASME, vol. 106, 1984, pp. 194-201.
- (3) Colombie, C., Berthier, Y., Vincent, L. and Godet, M. Proc. of Leeds-Lyon Symposium, 1985
- (4) Gordelier, S. C., Chivers, T. C., G.E.G.B. Report, TPRD/B/C312/N83, 1983.

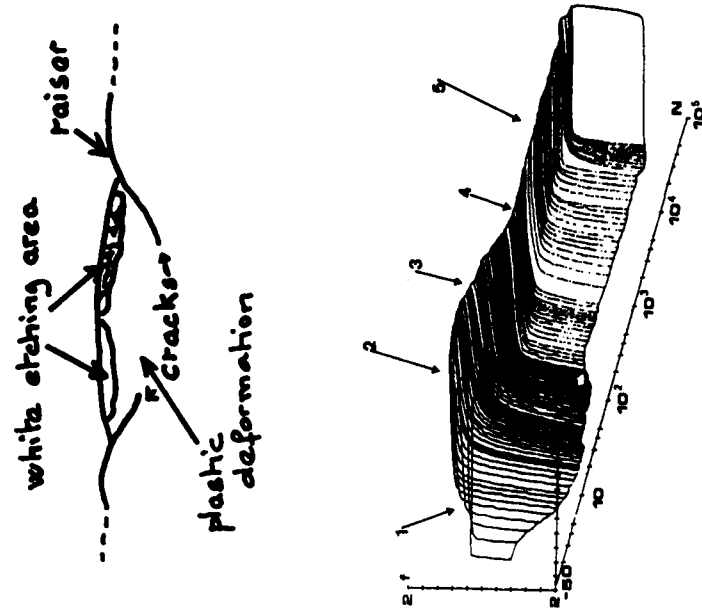


Figure 1 Apparatus (numbers refer Figure 2 General variation during test to text)

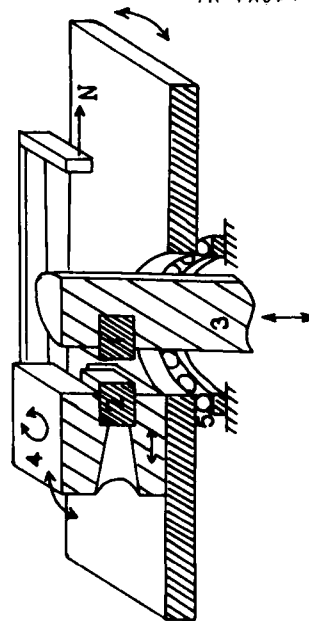


Figure 3 Scheme of a contact section

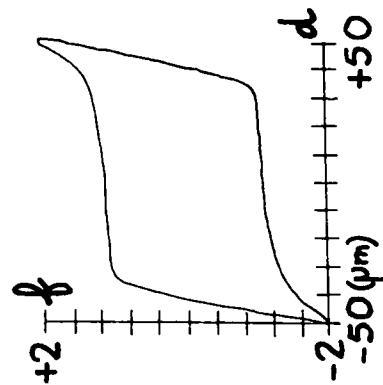


Figure 4 Increase at the end of cycle for an aluminium alloys

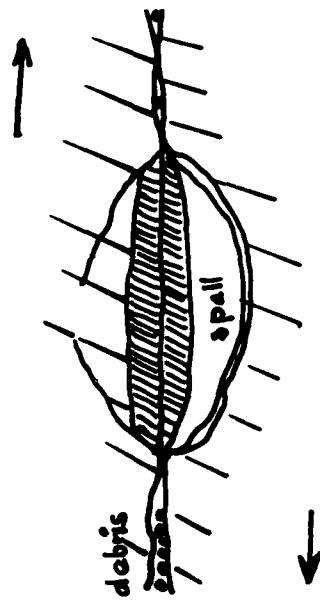


Figure 5 Very high elimination rate

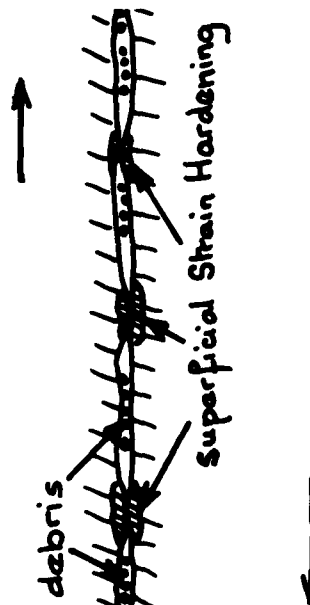


Figure 6 Very little elimination

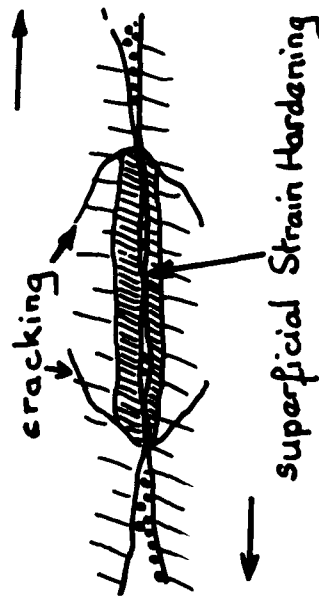


Figure 7 Medium elimination

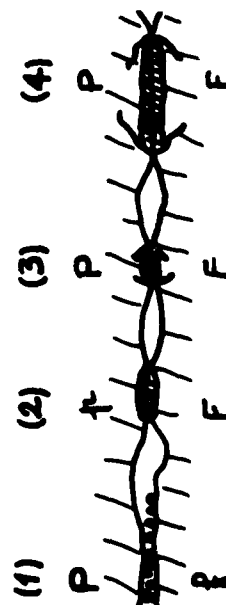


Figure 8 Global scheme of a real contact

FATIGUE 87

CRACK PROPAGATION PROPERTIES OF SINTERED STEEL

I. Bertilsson* and B. Karlsson*

The crack propagation properties of sintered steels with porosities ranging from 0 to 16 % have been investigated. The most important variable affecting the crack propagating resistance was found to be the porosity. A higher porosity normally leads to lower resistance. The microstructure has a smaller influence.

The crack mainly follows the pore system. Most of the straining is concentrated to the sintering necks between the original powder particles. The localised deformations give rise to a large amount of microcracks. These microcracks increase the crack closure which leads to lower propagation rates.

INTRODUCTION

Sintered steel is produced by cold compacting of steel powder. The compacting is made in a die with the shape of the finished product. This procedure reduces or eliminates machining. Sintered steels are normally manufactured with 80 - 95 % of full density. To obtain sufficient strength sintering at typically 1120 °C is performed. Components manufactured according to this route have economical advantages when many identical parts are produced. Large quantities are for example used in cars and office-machines. Many of these parts are subjected to dynamic loadings. In this work the effect of porosity and microstructure on the crack propagation properties of sintered steel is investigated.

The mechanical properties of sintered steels are mainly determined by the density, e.g. Karlsson and Bertilsson (1). A higher density results in better properties. Different alloying additions and heat treatments normally affect the properties to a smaller extent. Properties as elongation to fracture and impact energy are much dependent on changes in the density, whereas for

* Department of Engineering Metals, Chalmers University of Technology, S-412 96 Göteborg, Sweden. I.B. now at Volvo Flygmotor AB, S-461 81 Trollhättan, Sweden.

FATIGUE 87

example the fracture toughness is less sensitive (Bertilsson and Karlsson (2-4), Fleck and Smith (5)). The fatigue crack propagation resistance normally increases with the density ((2-5), Esper et al. (6), Sonsino (7)).

EXPERIMENTAL

Materials and microstructures

Three different microstructures obtained from three different powders were investigated. Two of the powders had the same nominal composition (1.75Ni, 0.5Mo, bal. Fe), but the alloying techniques were different. The third powder consisted of 0.8P with balance of Fe. The powder particle sizes ranged approximately from 20 to 175 μm . Graphite was mixed into the powders before pressing. The final carbon content was 0.5% in the Ni-Mo steels and 0.3% in the P-steel.

The effect of chemical heterogeneity was studied in the Ni-Mo steel by comparing the properties of samples produced from homogeneous and inhomogeneous powders respectively. The homogeneous powder was water-atomized from a prealloyed melt. In the inhomogeneous powder the alloying additions were diffusion bonded to iron powder. To obtain similar pore structures water-atomized powders were used in both alloys.

The powder for the P-steel was produced by mixing Fe_3P -powder with water-atomized iron powder (Höganäs ASC 100.29) to obtain 0.8% phosphorous in the final specimens.

Four densities were produced: 6.6 (16% pores) and 7.1 kg/dm^3 (10% pores) by single-pressing, 7.5 kg/dm^3 (5% pores) by double-pressing with an intermediate sintering at 900°C, and 7.85 kg/dm^3 (0% pores) by hot forging at 1100°C. All porous samples were pressed to final shape, while the fully dense specimens were machined from larger bars. The sintering was done in a belt furnace at 1120°C for 30 min with endogas as a protective atmosphere. The cooling rate after sintering was about 1°C/s. In the fully dense specimens the oxygen content was 120 ppm in the homogeneous Ni-Mo steel and 100 ppm in the inhomogeneous one. The oxygen level in the porous samples ranged between 210 and 410 ppm for the Ni-Mo steels. The oxygen content in the P-steel was 330 ppm in the fully dense samples and between 690 and 1050 ppm in the porous samples. In the porous samples inclusions have similar effects as pores on the mechanical properties. Since the volume fraction of pores is much larger than that of inclusions the latter can be neglected.

The three different powders resulted in three different microstructures. The homogeneous Ni-Mo steel had a microstructure consisting of coarse divorced pearlite (microhardness, $\text{HV}_{0.02} = 270$). The inhomogeneous Ni-Mo steel consisted of ferrite, pearlite (lamellar and divorced) and about 7% martensite. The microhardnesses of these constituents were 140 for the ferrite, 200-270 for

FATIGUE 87

the pearlite (variation due to differences in the cementite morphology) and 450 for the martensite.

The phosphorous-alloyed steel had a regular ferritic-pearlitic microstructure. The strong solid solution hardening effect of phosphorous gave the ferrite a microhardness of 200 and 380 dependent on the local phosphorous content set up during sintering (2-3). The microhardness in the pearlite was 450.

After single-pressing (density 6.6 and 7.1 kg/dm³) the pores are slightly rounder in the P-steel than in the Ni-Mo steel. The pore rounding is due to the phosphorous addition. More details about the phosphorous distribution can be found in refs. (2-3). Photos of the different investigated microstructures are shown in fig. 1.

Mechanical testing

The fatigue crack propagation rates were measured both in 3-point bending and in tension, with $R = F_{\min}/F_{\max} = 0.05$. The size of the samples was 100x15x5mm, with the crack propagating in the 15 mm direction from notches sawed with a 0.2 mm thick blade. The crack length was measured with two microscopes, placed on each side of the specimens. The mean value of these two readings was taken as the actual crack length. The load amplitude was held constant during the testing, leading to an increased stress intensity range as the crack grew. In bending the stress intensity range was calculated according to the formula in ASTM E-399 (8). In tension a formula derived by the finite element method was used (4). Normally 4 to 6 samples of each variant were tested.

The crack opening load was determined from curves of the load versus COD (crack opening displacement). An Instron clip-gauge was used to obtain the COD-values.

RESULTS

Static properties

The yield strength as well as the ultimate tensile strength increase with the density, fig. 2a. The mixture of hard and soft phases in the inhomogeneous Ni-Mo steel causes a pronounced microplasticity which results in a lower yield strength. The lower yield strength is compensated for by a larger workhardening, and thus the ultimate tensile strengths are virtually the same for all three microstructures tested.

For sintered steels the elongation to fracture normally increases with the density. Such is the case for the Ni-Mo steel, whereas the fracture strain in the P-steel is almost unaffected by changes in the density, fig 2b. This is related to a transition from ductile to brittle fracture as the density is increased. The

FATIGUE 87

Ni-Mo steel has a ductile fracture at all densities, except at full density where some brittle fracture is found.

The differences in fracture strain between the Ni-Mo steel and the P-steel at low densities, when all fractures are ductile, can be explained by differences in the pore shape. The rounder pores in the P-steel result in a larger elongation to fracture.

Crack propagation properties

The crack propagation resistance normally increases with the density. This is evident for the Ni-Mo steel, fig 3. The differences between the homogeneous and the inhomogeneous steels are small, although the homogeneous one is slightly better. For the P-steel, fig. 4, the crack propagation resistance is affected by the density, but at higher densities also by a transition in the fracture behaviour.

For the P-steel it can be seen in fig. 4 that at low stress intensity ranges, the fully dense steel is better than the density level 7.5 kg/dm^3 . At high stress intensity ranges the order is reversed. As mentioned above this is related to a transition in the fracture type. At 7.5 kg/dm^3 mainly ductile fractures are formed. At full density the fracture type is affected by the stress intensity range. Ductile fracture dominates at low stress intensity ranges, while at high stress intensity ranges brittle fracture dominates. The transition from ductile to brittle fracture causes a relative lowering of the crack propagation resistance. Fracture toughness measurements have revealed corresponding results, i.e. the density 7.5 kg/dm^3 has a higher fracture toughness than 7.85 kg/dm^3 (2-3).

The crack propagation properties of the Ni-Mo steel and the P-steel are compared in fig. 5. It can be seen that the P-steel is better at lower densities but worse at higher densities. This might be explained by rounder pores in the P-steel at low densities, and the transition to a more brittle behaviour in the P-steel at high densities.

No differences were found between results obtained from tests made in bending or tension. This indicates validity of the derived formula.

Crack closure

The different deformation behaviour in a porous sintered steel compared to a dense steel results in differences in the crack closure. In fig. 6, the relation between K_{op} (stress intensity for crack opening) and K_{max} (largest applied stress intensity) can be seen. For the porous samples K_{op} increases with K_{max} , while for the dense samples K_{op} is independent of K_{max} , similar to what have been found for cast and wrought steels (9,10).

DISCUSSIONCrack propagation properties

Several different mechanisms affect the crack propagation properties of sintered steels. Most of them have their origin in the very inhomogeneous deformations caused by the pore system. Important mechanisms are microcracking and repeated crack initiation in the sintering necks, crack blunting by the pores, crack branching caused by the pore system, and local shear (mode II and III displacements). Upon macroscopic deformation most of the straining is concentrated to the sintering necks between the original powder particles. The plastic deformations might eventually cause local fractures, which can be seen as microcracks.

A crack in a fully dense steel is surrounded by a plastic zone. Due to the inhomogeneous deformations a crack in a sintered steel is surrounded by a zone containing plastically deformed sintering necks and microcracks. The microcracks affect the crack propagation rate by consuming energy on several parallel cracks, by increasing the crack closure, and also by reducing the local stress intensity at each crack tip. All these mechanisms cause a decrease in the propagation rate.

Measurements on internal crack profiles have revealed strong dominance of pores in a crack profile. For example, at the porosities 10 and 16 % the portions of the crack following the pores were found to be about 60 and 75 % respectively (11). That is, only 40 and 25 % of the crack length respectively are found in the solid material.

The dominance of the pores is even more evident if the fracture surfaces are studied. It can be seen that the pore system is continuous, while the bulk material is found as isolated islands. As the material does not form a continuous phase on a fracture surface, a new crack has to be initiated in each sintering neck. As initiation normally is considered to be a slower process than propagation, the macroscopic propagation rate might be decreased, although a large distance is passed as the crack follows a pore.

Another effect of the pores is crack blunting since the radii of the pores are larger than that of the crack tip. The crack blunting influences both the propagation and the initiation of microcracks, and might therefore decrease the macroscopic propagation rate.

Studies on the crack profiles revealed a strong tendency of the propagating crack to advance from one pore to the closest neighbouring pore rather independently of the main propagation direction. This was supported by results from measurements of the directions of the local crack elements in relation to the main propagation direction. The recorded angular distribution is very

wide, with a standard deviation of about 45° . This angular deviation is much larger than what is usually found in fully dense steels (Karlsson et al., 12) indicating a dominance of shear modes at the crack tip. The macroscopic stress field might therefore be less effective in advancing the crack.

Crack closure

The relatively large crack closure in sintered steels is related to the inhomogeneous deformations and the microcracks. Each microcrack adds to the total crack closure. A raise in K_{max} increases the size of the affected zone around the crack tip in which microcracks are formed. Thus the number of microcracks increases, and as a result of that also the crack closure.

The crack propagation resistance of sintered steels is better than what would be expected if the dominance of the pores in a fracture surface is considered. At low crack propagation rates the resistance is almost comparable with cast and wrought steels. The relatively large values of K_{op} is an important characteristic of the rather good crack propagation resistance of sintered steels. The high values of K_{op} is mainly caused by the large amount of microcracks that exist around a crack in a sintered steel.

Fractographic appearance

Even if the fracture strain is low, indicating a macroscopically brittle fracture, studies of fracture surfaces in the scanning electron microscope reveal a ductile, dimple type of fracture. The fracture is concentrated to the sintering necks between the original powder particles. The necks are typically 10 μm in diameter. This very localised fracture results in a macroscopically low elongation to fracture, even if the local fracture mechanism is ductile.

The pores promote ductile fracture (Karlsson and Bertilsson, 13). A normally brittle matrix will exhibit a ductile fracture provided that the porosity is high enough. This behaviour is most evident in the P-steel, since the strong solid solution hardening effect of phosphorous causes a brittle matrix. In conventional steels phosphorous is known to give brittleness, but at high porosities sintered phosphorous alloyed steels have a ductile fracture. Thus at low densities the P-steel has a ductile fracture, while at high densities brittle fracture dominates. Also in the Ni-Mo steel the amount of brittle fracture increases at higher densities, but the transition from mainly ductile to mainly brittle fracture is found close to full density.

FATIGUE 87

CONCLUSIONS

The crack propagation properties of three sintered steels were investigated. Two of the steels had the same nominal composition (1.75 Ni, 0.5 Mo, 0.5 C, bal. Fe), but different microstructures due to different degree of chemical heterogeneity. The microstructures were coarse pearlite in the homogeneous steel and pearlite, ferrite with some martensite in the inhomogeneous steel. The third steel consisted of 0.8 P, 0.3 C, bal. Fe, with a ferritic-pearlitic microstructure. Four different densities ranging from 6.6 to 7.85 kg/dm³ (0-16 % pores) were investigated. The results of the investigation allow the following conclusions to be drawn:

1. The crack propagation resistance increases with the density as long as the fracture type is ductile. The Ni-Mo steel has such a behaviour.
2. The solid solution hardened P-steel has a more brittle matrix. At full density and high stress intensity ranges, the brittle matrix causes a brittle fracture and a relative lowering of the crack propagation resistance.
3. The crack propagation properties are normally more affected by the density than by the microstructure.
4. The crack mainly follows the pore system, propagating from one pore to the closest one almost independently of the main propagation direction. The cracks are found in the sintering necks between the original powder particles.
5. The pores are continuous on a fracture surface, while the solid material is found as isolated islands.
6. The crack tip is surrounded by a zone of microcracks, which increase the crack closure and decrease the propagation rate.
7. The crack closure increases with the stress intensity in porous steels. In the fully dense steel no such K_{max} -dependence is found.

ACKNOWLEDGEMENT

The manufacturing of the powders and the test samples by Höganäs AB is gratefully acknowledged. Financial support of this project has been provided by the Swedish Board for Technical Development.

FATIGUE 87

REFERENCES

- (1) Karlsson, B., and Bertilsson, I., Scand. J. Metall., Vol. 11, No. 6, 1982, pp. 267-275.
- (2) Bertilsson, I., and Karlsson, B., "Horizons of Powder Metallurgy". Edited by Kaysser, W.A., and Huppmann, W.J., 1986, Vol. 1, pp. 483-486.
- (3) Bertilsson, I., and Karlsson, B. To be published in Metal Powder Report, April 1987.
- (4) Bertilsson, I., and Karlsson, B., "Preprint supplement, 1986 Powder Metallurgy Group Meeting, Buxton, England, pp 15.1-15.7.
- (5) Fleck, N.A., and Smith, R.A., Powder Metall., 1981, Vol. 24, No. 3., pp 121-125.
- (6) Esper, F.J., Leuze, G. and Sonsino, C.M., Powder Metall. Int., 1981, Vol. 13, No. 3, pp 203-208.
- (7) Sonsino, C.M., Z. Werkstofftechn., 1984, Vol. 15, No. 4, pp. 109-117.
- (8) ASTM standard E-399, 1984.
- (9) Klensil, M., Proc. "Fatigue thresholds, Fundamentals and engineering applications", 1981, EMAS, Warley, U.K. (1982), p. 155.
- (10) Horng, J.L., Ph. D. Thesis, Northwestern Univ., Evanstone, IL, USA, 1983.
- (11) Bertilsson, I., and Karlsson, B., "Modern Developments in Powder Metallurgy". Edited by Aqua, E.N., and Whitman, C.I., 1985, Vol. 16, pp. 19-32.
- (12) Karlsson, B., Wasén, J. and Hamberg, K., To be presented at Fatigue '87.
- (13) Karlsson, B., and Bertilsson, I., "Horizons of Powder Metallurgy". Edited by Kaysser, W.A., and Huppmann, W.J., 1986, Vol. 2., pp. 1011-1014.

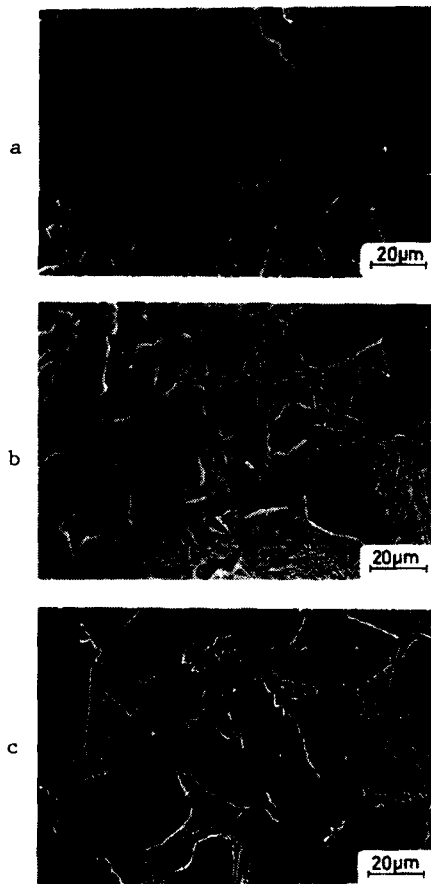


Fig. 1. Typical microstructures at 7.1 kg/dm^3 . The black areas are pores.

a. Homogeneous Ni-Mo steel. Mainly irregular cementite. SEM image.

b. Inhomogeneous Ni-Mo steel. Ferrite, pearlite (lamellar and irregular cementite) and martensite. Martensite denominated M. SEM image.

c. P-steel, Ferrite and pearlite. SEM image.

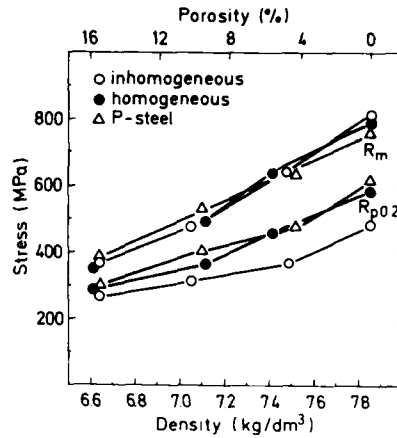


Fig. 2a. Yield ($R_{p0.2}$) and ultimate tensile strength (R_m) vs. density.

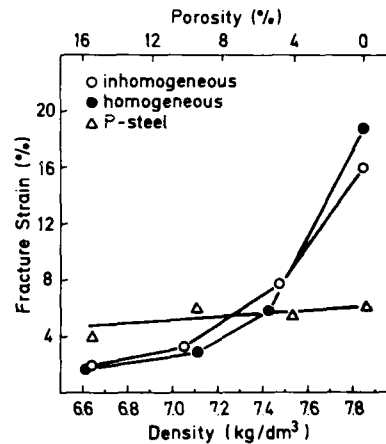


Fig. 2b. Fracture strain vs. density. Fracture strain approximates the elongation to fracture.

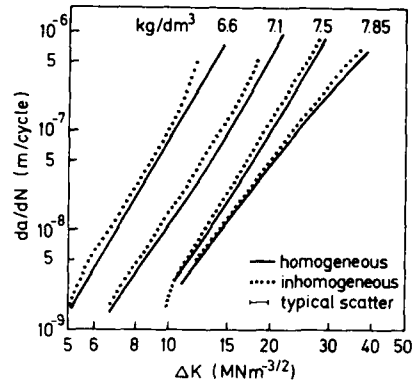


Fig. 3. Fatigue crack propagation rate (da/dN) vs. stress intensity range (ΔK) for the Ni-Mo steel.

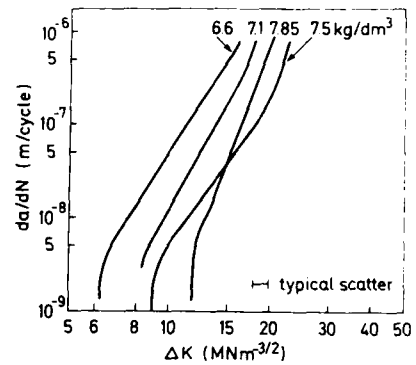


Fig. 4. Fatigue crack propagation rate (da/dN) vs. stress intensity range (ΔK) for the P-steel.

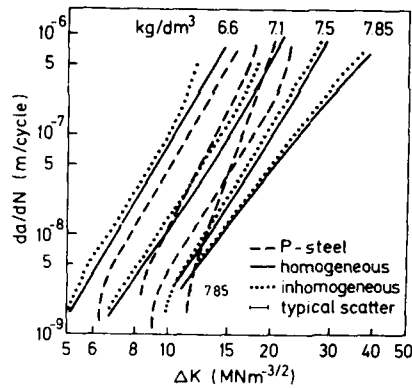


Fig. 5. Fatigue crack propagation rate (da/dN) vs. stress intensity range (ΔK) for all tested steels.

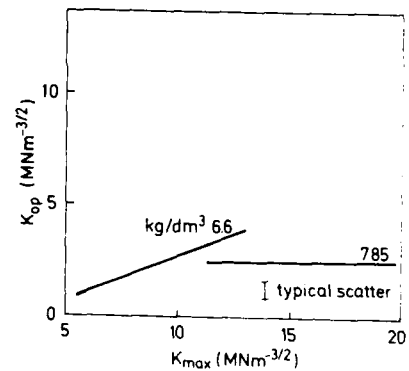


Fig 6. Stress intensity for crack opening (K_{op}) vs. max. stress intensity (K_{max}). 6.6 kg/dm³ represents typical behaviour of porous samples.

THE ROLE OF INCLUSIONS IN CORROSION FATIGUE CRACK INITIATION IN Q1N

R.A. Cottis and A. Markfield*

The role of inclusions in the initiation and early stages of growth of fatigue cracks has been studied for Q1N in sodium chloride solution. The test conditions are such that the effect of corrosion is exclusively the dissolution associated with the crack, with no hydrogen embrittlement. Oxide inclusions are found to initiate fatigue cracks in air, while sulphides are more effective in corrosion. This is attributed to the effect of sulphur species produced by dissolution of the inclusions in enhancing the rate of corrosion of the steel around the inclusion. The addition of thiosulphate spreads the enhanced corrosion over a larger surface area, and thereby reduces the local rates of attack, and transfers the initiation site back to the oxide inclusions. Corrosion is thought to accelerate the growth of the short cracks by the dissolution of microstructural barriers, and by the elimination of closure effects.

INTRODUCTION

The effect of moderately corrosive environments, such as seawater and sodium chloride solution, on the growth of long fatigue cracks in steels has been widely studied, and the observed accelerations have been clearly attributed to the damaging effect of hydrogen produced by the cathodic reaction within the crack. Conversely, the corrosion fatigue crack initiation behaviour, as determined by the measurement of S-N curves on plain specimens, has long been associated with the metal dissolution effects of corrosion, and particularly the effects of pitting corrosion. Recently the actual formation of a crack nucleus in air fatigue has been shown to occur very early in the fatigue life. Thus the results of S-N tests, and even the fatigue limit itself, have been shown to be controlled by the growth of very short cracks. Being of size comparable to the grain size and/or the size of the reversed plastic zone, these cracks do not follow normal long-crack growth laws. Cracks grow rapidly in favourably oriented grains, but are held up at high angle grain boundaries and other microstructural barriers. The absence of closure effects allows short cracks to grow relatively fast, although plasticity- and roughness-induced closure develops quite quickly. As a result of the work of Ritchie, Suresh, Miller, Lankford and others, we now have a reasonably clear view of the factors governing fatigue crack growth from the beginning of an S-N test.

* Corrosion and Protection Centre, UMIST,
P.O. Box 88, Manchester, M60 1QD.

FATIGUE 87

Rather little work in this area has considered the effect of corrosion on these early stages of the growth of the crack, notable exceptions being the work of Congleton et al.(1) and Ray et al.(2).

In the work presented here the early stages of growth of corrosion fatigue cracks in Q1N have been investigated, and the results observed related to the pitting behaviour of the steel.

MATERIAL

The material used for this study was a sample of Q1N, a steel to a British Naval specification, which is for most practical purposes identical to HY80. The material was supplied in the form of 30 mm plate. It was tested in the as-received, quenched and tempered condition. The material analysis and mechanical properties are given in Tables 1 and 2.

TABLE 1 - Chemical Composition of Q1N Test Plate

C	Mn	Si	S	P	Ni	Cr	Mo	Va	Cu	Al
0.15	0.35	0.32	0.007	0.010	2.61	1.62	0.39	<0.05	0.12	0.021

TABLE 2 - Mechanical Properties of Q1N Test Plate

0.2% PS	UTS	Elongation	R of A
610 MPa	730 MPa	23%	69.5%

EXPERIMENTAL PROCEDURE

Test Machine and Specimen Configuration

The fatigue tests were performed in an Avery-Denison Type 7303 reversed bend fatigue testing machine. This applies reversed bending loading to the specimen, the configuration of which is shown in Figure 1. This machine uses displacement-controlled loading through an eccentric, but a relatively soft spring attached to the other end of the specimen converts the loading into approximately constant stress. The spring also serves as a dynamometer for the measurement of the load applied to the specimen, the displacement of the spring being measured by two dial gauges. The loading frequency for all of the tests reported here was 25 Hz, and the stress ratio was -1.

Corrosive Environments

Two corrosive environments were studied :

- (a) 0.6 M NaCl solution
- (b) 0.6 M NaCl + 0.03 M $\text{Na}_2\text{S}_2\text{O}_3$.

FATIGUE 87

In both cases the solutions were prepared with analytical grade reagents and deionized water. No pH adjustment was made, the initial pH typically being 6.7.

For corrosion experiments the solution was aerated, while for the fatigue tests the agitation induced by the fatigue cycling is assumed to have maintained the solution in a fully aerated condition. All experiments were conducted at room temperature (approximately 20°C).

The solution was maintained around the specimen in a silicone rubber cell. For tests in which the specimen potential was controlled the cell also contained a reference electrode and a platinum counter electrode.

Crack Growth Measurements

The initiation and growth of small cracks during testing was monitored by examination of the polished surface of the specimen under the optical microscope. Once cracks had been detected their development was monitored at regular intervals throughout the test. The rather more convenient replication technique was not used because previous work with stress corrosion cracking tests (3) had shown that the replication process seriously disrupted the corrosion behaviour.

Micro-Corrosion Tests

In addition to the fatigue tests, polished but unstressed samples of Q1N were exposed to the same test environments for periods of 5 seconds to 5 minutes in order to study the initial stages of the development of localized corrosion around the inclusions. These tests were based on the micro-corrosion tests developed by Noren-Brandel and reported by Wranglen(4). In order to obtain valid results care was taken to ensure that all surfaces of the specimen exposed to the solution were thoroughly polished. Even fine scratches showed a strong tendency for preferential attack.

RESULTS

S-N Curves

The S-N curves obtained in air and in the two corrosive environments are shown in Figure 2. The S-N curve in air shows the expected behaviour with a fatigue limit of ≈ 440 MPa. In the 3.5% NaCl solution the fatigue life is markedly reduced, particularly at the longer lifetimes. There is no evidence of a fatigue limit, the 10^7 cycle endurance limit being ≈ 155 MPa. The addition of sodium thiosulphate in the sodium chloride solution resulted, somewhat unexpectedly, in an improvement in the corrosion fatigue behaviour, the 10^7 cycle endurance limit being raised to ≈ 190 MPa.

The Effect of Applied Potential

The endurance at an applied stress amplitude of 490 MPa is shown in Figure 3 as a function of applied potential. It can be seen that for potentials

below about -900 mV (SCE) the endurance is essentially the same as that in air. The scatter observed for the tests under cathodic polarization is rather large; the reason for this is uncertain, but it may in part have been attributable to difficulties in ensuring that the cathodic polarization was applied without interruption. The observed effect of applied potential implies that the damaging effect of corrosion does not involve hydrogen embrittlement. This is in agreement with the observations of many earlier workers.

Crack Growth Rates

Crack growth rates measured in air and in corrosion with an applied stress amplitude of 530 MPa are presented in Figure 4. Strictly this graph should be regarded as a plot of the crack growth rate at the surface as a function of the surface crack length. In order to provide a comparison with long crack data the maximum K during the cycle (K_{\max}) has been calculated on the basis of the simple relationship $K_{\max} = \sigma_a \sqrt{\pi a}$, where σ_a = stress amplitude (or maximum stress for this fully-reversed loading). Detailed consideration (5) of the correction factors applicable to the case of a semi-elliptical surface crack suggests that a more accurate value of K_{\max} will be 0.77 times that presented. The use of K_{\max} in place of ΔK also assumes that the compressive component of the cycle has no effect, i.e. closure occurs when the applied stress is zero.

Crack Initiation Sites

In fatigue in air the cracks initiated at persistent slip bands and at oxide inclusions. At high stress amplitudes initiation at persistent slip bands dominated; Figure 5 shows two stages in the development of a crack at a stress amplitude of 590 MPa (97% of the yield stress). An array of persistent slip bands leads to the development of a network of small cracks which propagate by growth of individual cracks, together with crack coalescence. Even in this example, however, inclusions provide a focus for the nucleation of some of the major cracks.

At low stress amplitudes oxide inclusions, primarily alumina, tend to dominate the crack initiation process. Figure 6 shows a crack forming from an alumina inclusion at a stress amplitude of 530 MPa. Cracks also initiated at duplex oxide-sulphide inclusions, but there was little evidence of initiation from sulphides alone.

In sodium chloride solution crack initiation transferred to the sulphide or duplex sulphide-oxide inclusions, with sulphide components of the inclusion generally showing signs of dissolution. Figure 7 shows a crack formed during a test at 490 MPa. The inclusion responsible for the right-hand crack has been lost by corrosion/dislodgement. The inclusion which has nucleated the left-hand crack is a duplex oxide-sulphide. The oxide phase is a rather angular Mg-aluminate, probably an $\text{MgO} \cdot \text{Al}_2\text{O}_3$ spinel. The sulphide phase, much of which has been dissolved, is $(\text{Mn,Ca})\text{S}$ with a high manganese content. It can be seen that a shallow region of localized corrosion has formed around these inclusions, and relatively sharp, but open fatigue cracks have grown in this region.

On the addition of thiosulphate to the sodium chloride solution the crack initiation site becomes less dependent on inclusion composition, with crack initiation at alumina and Ca-aluminate inclusions as well as sulphides and duplex oxide-sulphides. Figure 8 shows an example of crack initiation at an alumina inclusion. The corroded region is covered with a heavy scale of FeS, which makes detailed examination difficult.

Micro-Corrosion Experiments

The micro-corrosion experiments gave results which were consistent with the observations made during the fatigue tests. In 3.5% NaCl pits initiated around sulphide or duplex oxide-sulphide inclusions, particularly the more soluble calcium containing sulphides. On the addition of thiosulphate the pitting was more widespread, and nucleated on minor scratches as well as all inclusion compositions. The depth of attack tended to be less than that observed in the plain chloride solution.

DISCUSSION

Crack Initiation

The tendency for cracks to initiate at oxide inclusions in air may be explained in terms of the higher tessellated stresses (as compared to sulphide inclusions), on the angular inclusion shape. In the corrosive environments it seems clear that the corrosion process enhances crack initiation. In the plain sodium chloride the sulphide inclusions are most active in accelerating the corrosion of the adjacent steel, and consequently in initiating corrosion fatigue cracks. On the addition of thiosulphate the availability of sulphur from the solution leads to more widespread pitting attack, and the factors which control crack initiation sites in air re-assert their importance. However, because the area of active dissolution is increased and the total loss of metal is limited by the rate at which oxygen can be supplied to the metal from the solution, the local rates of corrosion are reduced, and the rate of crack initiation and the early stages of growth are less than for plain chloride solution.

Short Crack Growth

Considering the growth of cracks initiated from inclusions in air, there are known to be two factors tending to restrict growth rates. For microstructurally short cracks the microstructural barriers, principally grain boundaries, hold up or stop the crack growth process. For longer cracks the development of plasticity- and roughness-induced closure leads to a lower growth rate than would be predicted. For the experiments reported here there were indications of delays in the crack growth at intervals of the order of the grain size, particularly over the first few grain diameters. However the frequency of crack length measurement was too low to determine the instantaneous crack velocities in these early stages, and the crack velocities plotted in Figure 4 are averages.

It can be seen from Figure 4 that the corrosive environment affects the growth of fatigue cracks throughout the ΔK range. For very short cracks it is

suggested that the effect of corrosion is to facilitate the passage of the crack through the microstructural barriers. When a fatigue crack growing in air meets a grain boundary, the barrier to continued growth is provided by the misalignment of the crystal structures and the constraint at the crack tip. If the crack is broadened by corrosion the constraint on the crack tip will be reduced, the situation becoming more like that existing at the tip of a relatively sharp notch. This will facilitate the reinitiation of the crack in the new grain. An alternative view of this process is that pitting corrosion produces a defect which is sufficiently large to overcome the microstructural barriers. While this provides a useful quantitative description, as will be discussed below, it should be clear from Figure 7 that the pitting process is heavily modified by the applied cyclic stresses.

At higher crack growth rates, where the crack is no longer significantly influenced by grain boundaries and other microstructural features, it is thought that the effect of corrosion is to eliminate closure effects by dissolution of the crack walls. It can be seen from Figures 5 and 7 that the crack produced in corrosion is much wider than that produced in air. While the crack may be narrower below the surface, it is clear that at least at the surface closure is unlikely to occur, even at the maximum compressive stress. Assuming that the corrosion crack remains open throughout the cycle and the crack closure occurs at zero load in air, it is clear that the effective ΔK in corrosion will be twice that in air for the stress cycle studied in this work. It can be seen in Figure 9 that the corrosion curve is approximately coincident with the air data if it is displaced to double the ΔK .

Threshold Behaviour

The link between the fatigue limit (or threshold stress amplitude) and the threshold stress intensity range can conveniently be presented in the stress-crack length diagram proposed by Kitagawa (6). Such a plot is shown in Figure 9. The value of the endurance limit, σ_e in air from this work is used to define a stress amplitude threshold, while the threshold stress intensity range determined by James and Knott (7,8) is used to define the behaviour at lower stresses. A second line shows ΔK_{th} modified to allow for closure effects. The solid points plotted on this diagram correspond to the "pit" diameter measured on corrosion fatigue specimens at failure at a range of stresses below the air fatigue limit. It can be seen that these pit depths fit remarkably well on to the Kitagawa diagram. Micrographs of typical pits are shown in Figure 10.

CONCLUSIONS

1. In air fatigue cracks in Q1N initiate primarily at angular oxide inclusions. The crack growth rate is higher than that expected for long cracks in this material. Some p.s.b. initiation is observed at high stress amplitudes.
2. In 3.5% NaCl the fatigue cracks initiate at chemically-active sulphide inclusions and the accelerated initiation is attributed to strain-enhanced corrosion processes.
3. The growth of "chemically-short" cracks in 3.5% NaCl is initially

accelerated by the action of corrosion in overcoming microstructural barriers. As the crack grows, corrosion of the crack walls prevents the development of closure effects, giving a continued acceleration of crack growth rate.

- 4 Below the air fatigue limit the crack length at which there is a transition from the effect of dissolution on the initiation process (or the growth of the microstructurally-short crack), to the effect of dissolution on closure processes for longer cracks may be expressed in terms of the pit diameter necessary to reach the closure-free threshold stress intensity factor.
- 5 The addition of thiosulphate to the solution results in more widespread anodic regions, thereby limiting the severity of the attack at specific sites. This reduces the rate of corrosion fatigue crack growth.

SYMBOLS USED

σ_e = endurance limit (expressed as stress amplitude).

σ_a = stress amplitude

REFERENCES

- 1 Congleton, J., Olieh, R.A. and Parkins, R.N., *Metals Technology*, Vol. 9, 1982, pp 94-103.
- 2 Ray, G.P., Jarman, R.A. and Thomas, J.G.N., *Corrosion Science*, Vol. 25, 1985, pp 171-184.
- 3 Cottis, R.A. and Loto, C.A., *Materials Science Forum*, Vol. 8, 1986, pp 201-214.
- 4 Wranglen, G., in "Localized Corrosion", NACE-3, eds Staehle, R.W. et al., NACE, Houston, 1974.
- 5 "The Role of Inclusions in the Corrosion Fatigue of a Marine Structural Steel", A. Markfield, PhD Thesis, UMIST (1986).
- 6 Kitagawa, H. and Takahashi, S., in "Proc. of the Second Int. Cong. on Mechanical Behaviour of Materials", ASM, Metals Park, Ohio, 1976.
- 7 James, M.N. and Knott, J.F., *Fatigue Fracture of Engineering Materials and Structures*, Vol. 8, 1985, pp 177-191.
- 8 Kendall, J.M., James, M.N. and Knott, J.F., *EGF Publication No. 1*, European Group on Fracture, *in press*.

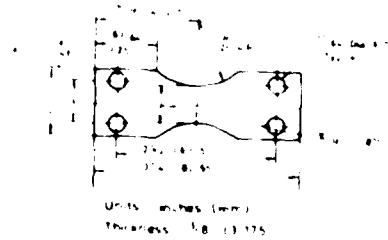
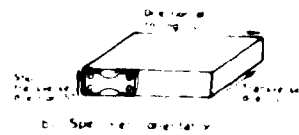


Figure 1 Specimen Configuration

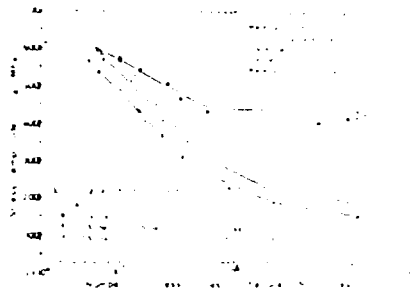


Figure 2 S-N Curves

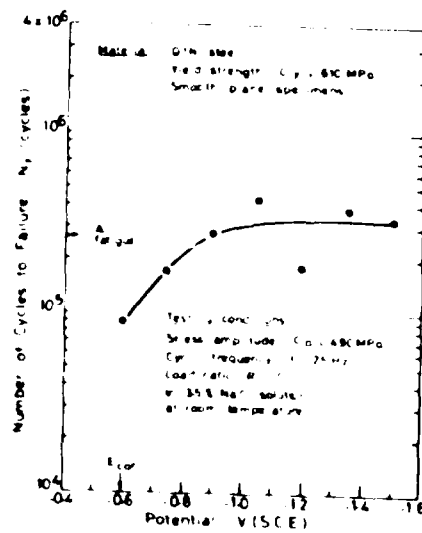


Figure 3 The Effect of Applied Potential on Endurance

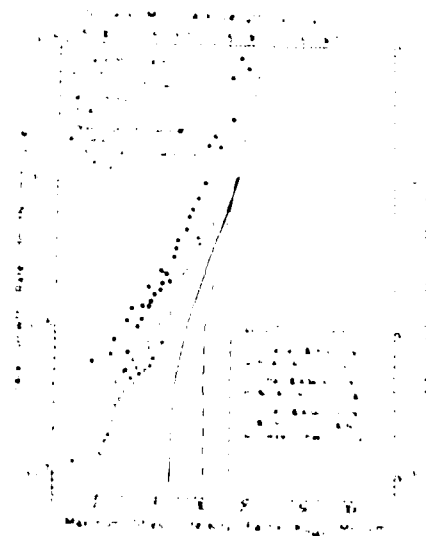


Figure 4 Crack Growth Rates



Figure 5. Crack Development at $\sigma_a = 540$ MPa, air.

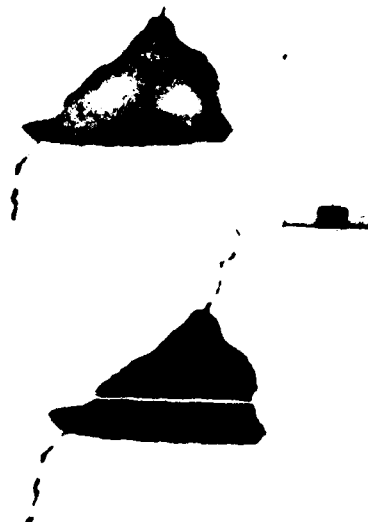


Figure 6. Crack Forming from an Alumina Inclusion, 530 MPa, air.



Figure 7. Crack at Oxide-Sulphide Inclusions, 490 MPa, NaCl.

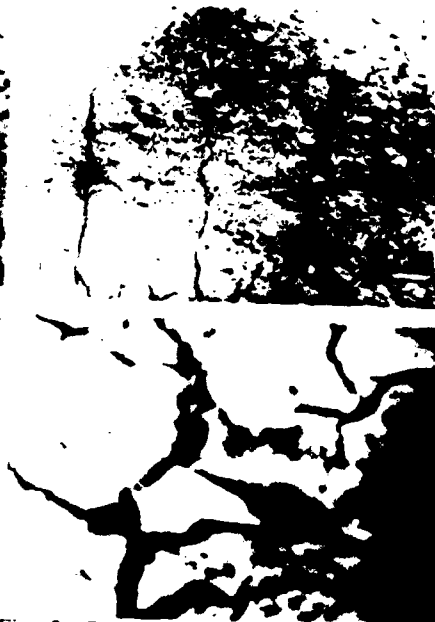


Fig. 8. Cracking at Alumina Inclusions, $\sigma_a = 450$ MPa, NaCl/Na₂S₂O₃.

FATIGUE 87

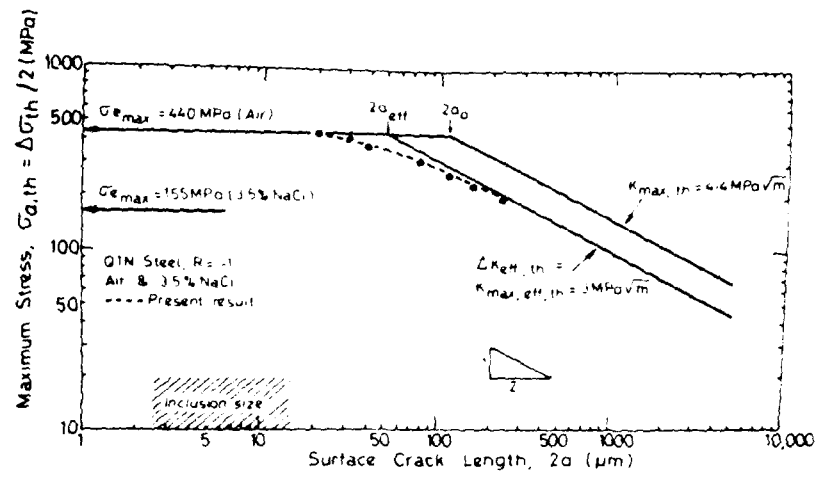


Figure 9. "Kitagawa" Plot for Q1N.

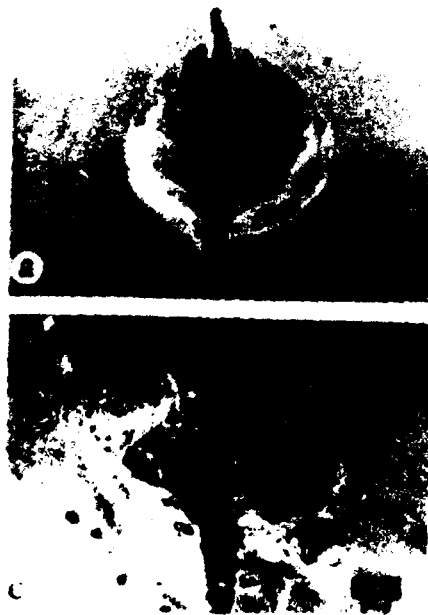


Figure 10. Pits Associated with Crack Initiation.

LMED
-8